

Ultrananocrystalline Diamond

Ultrananocrystalline Diamond

Synthesis, Properties,
and Applications

Second edition

Edited by

Olga A. Shenderova

International Technology Center
Research Triangle Park, NC, USA

Dieter M. Gruen

Argonne National Laboratory
Argonne, IL, USA



AMSTERDAM • BOSTON • HEIDELBERG • LONDON
NEW YORK • OXFORD • PARIS • SAN DIEGO
SAN FRANCISCO • SINGAPORE • SYDNEY • TOKYO
William Andrew is an imprint of Elsevier



William Andrew is an imprint of Elsevier
The Boulevard, Langford Lane, Kidlington, Oxford OX5 1GB, UK
225 Wyman Street, Waltham, MA 02451, USA

First edition 2006
Second edition 2012

Copyright © 2012 Elsevier Inc. All rights reserved

No part of this publication may be reproduced, stored in a retrieval system or transmitted in any form or by any means electronic, mechanical, photocopying, recording or otherwise without the prior written permission of the publisher.

Permissions may be sought directly from Elsevier's Science & Technology Rights Department in Oxford, UK: phone (+44) (0) 1865 843830; fax (+44) (0) 1865 853333; email: permissions@elsevier.com. Alternatively you can submit your request online by visiting the Elsevier web site at <http://elsevier.com/locate/permissions>, and selecting *Obtaining permission to use Elsevier material*.

Notice

No responsibility is assumed by the publisher for any injury and/or damage to persons or property as a matter of products liability, negligence or otherwise, or from any use or operation of any methods, products, instructions or ideas contained in the material herein. Because of rapid advances in the medical sciences, in particular, independent verification of diagnoses and drug dosages should be made.

British Library Cataloguing in Publication Data

A catalogue record for this book is available from the British Library

Library of Congress Cataloging-in-Publication Data

A catalog record for this book is available from the Library of Congress

ISBN: 978-1-4377-3465-2

For information on all William Andrew publications
visit our web site at books.elsevier.com

Typeset by MPS Limited, Chennai, India
www.adi-mps.com

Printed and bound in Great Britain
12 13 14 15 16 9 8 7 6 5 4 3 2 1

Working together to grow
libraries in developing countries

www.elsevier.com | www.bookaid.org | www.sabre.org

ELSEVIER

BOOK AID
International

Sabre Foundation

Table of Contents

 [Show preview](#) |  [PDF \(176 K\)](#) | [Related articles](#) | [Related reference work articles](#)


Copyright, Page iv

 [Show preview](#) |  [PDF \(57 K\)](#) | [Related articles](#) | [Related reference work articles](#)

Preface, Pages xv-xviii, Olga A. Shenderova, Dieter M. Gruen

 [Show preview](#) |  [PDF \(60 K\)](#) | [Related articles](#) | [Related reference work articles](#)

List of Contributors, Pages xix-xxi, Shashishekar P. Adiga, Raul Arenal, Jes Asmussen, Orlando Auciello, Amanda S. Barnard, Yuriy V. Butenko, Edward K. Chow, Larry A. Curtiss, Vycheslav Danilenko, Yury Gogotsi, Timothy A. Grotjohn, Dieter M. Gruen, Dean Ho, Alon Hoffman, M.G. Ivanov, D.M. Ivanov, Vladimir L. Kuznetsov, Jonathan B. Lin, Han B. Man, Neil B. Manson, *et al.*

 [Show preview](#) |  [PDF \(48 K\)](#) | [Related articles](#) | [Related reference work articles](#)

Part 1: Advances in Synthesis and Processing

Chapter 1 - Stability of Diamond at the Nanoscale, Pages 3-52, Amanda S. Barnard

 [Show preview](#) |  [PDF \(3456 K\)](#) | [Related articles](#) | [Related reference work articles](#)

Chapter 2 - Advances in Plasma Synthesis of UNCD Films, Pages 53-83, Jes Asmussen, Timothy A. Grotjohn, Thomas Schuelke

 [Show preview](#) |  [PDF \(2606 K\)](#) | [Related articles](#) | [Related reference work articles](#)

Chapter 3 - Theoretical Studies of UNCD Properties, Pages 85-102, Shashishekar P. Adiga, Peter Zapol, Larry A. Curtiss

 [Show preview](#) |  [PDF \(2240 K\)](#) | [Related articles](#) | [Related reference work articles](#)

Chapter 4 - *n*-Type Nanocrystalline Diamond Films: Synthesis, Structure, Composition, Properties, and Applications, Pages 103-132, Raul Arenal

 [Show preview](#) |  [PDF \(2561 K\)](#) | [Related articles](#) | [Related reference work articles](#)

Chapter 5 - Advances in Synthesis of Nanodiamond Particles, Pages 133-164, Vycheslav Danilenko, Olga A. Shenderova

 [Show preview](#) |  [PDF \(2471 K\)](#) | [Related articles](#) | [Related reference work articles](#)

Chapter 6 - Deagglomeration of Detonation Nanodiamond, Pages 165-179, Eiji Osawa, Shuichi Sasaki, Ryoko Yamanoi

 [Show preview](#) |  [PDF \(709 K\)](#) | [Related articles](#) | [Related reference work articles](#)

Chapter 7 - Diamond Phase Transitions at Nanoscale, Pages 181-244, Vladimir L. Kuznetsov, Yuriy V. Butenko

 [Show preview](#) |  [PDF \(7394 K\)](#) | [Related articles](#) | [Related reference work articles](#)

Part 2: Advances in Nanodiamond Characterization and Property Measurements

Chapter 8 - Bonding and Concentration of Hydrogen and Thermal Stability of Nanocrystalline Diamond Films, Pages 247-289, Shaul Michaelson, Alon Hoffman

 [Show preview](#) |  [PDF \(3562 K\)](#) | [Related articles](#) | [Related reference work articles](#)

Chapter 9 - Recent Results on Characterization of Detonation Nanodiamonds, Pages 291-326, Igor I. Vlasov, Stuart Turner, Gustaaf Van Tendeloo, Andrei A. Shiryayev

 [Show preview](#) |  [PDF \(3715 K\)](#) | [Related articles](#) | [Related reference work articles](#)

Chapter 10 - Optical and Spin Properties of Nitrogen-Vacancy Color Centers in Diamond Crystals, Nanodiamonds, and Proximity to Surfaces, Pages 327-354, Andrei V. Zvyagin, Neil B. Manson



 [Show preview](#) |  [PDF \(2179 K\)](#) | [Related articles](#) | [Related reference work articles](#)

Part 3: Emerging Applications

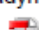
Chapter 11 - Nanocarbons in Energy Conversion, Pages 357-381, Dieter M. Gruen

 [Show preview](#) |  [PDF \(2140 K\)](#) | [Related articles](#) | [Related reference work articles](#)

Chapter 12 - Science and Technology of Ultrananocrystalline Diamond (UNCD™) Film-Based MEMS and NEMS Devices and Systems, Pages 383-420, Orlando Auciello

 [Show preview](#) |  [PDF \(2943 K\)](#) | [Related articles](#) | [Related reference work articles](#)



Chapter 13 - Advances in Surface Chemistry of Nanodiamond and Nanodiamond-Polymer Composites, Pages 421-456, Ioannis Neitzel, Vadym Mochalin, Yury Gogotsi

 [Show preview](#) |  [PDF \(4693 K\)](#) | [Related articles](#) | [Related reference work articles](#)

Chapter 14 - Nanodiamond Nanoparticles as Additives to Lubricants, Pages 457-492, M.G. Ivanov, D.M. Ivanov

 [Show preview](#) |  [PDF \(2863 K\)](#) | [Related articles](#) | [Related reference work articles](#)


Chapter 15 - Engineering Nanoparticulate Diamond for Applications in Nanomedicine and Biology, Pages 493-518, Han B. Man, Kangyi Zhang, Erik Robinson, Edward K. Chow, Dean Ho

 [Show preview](#) |  [PDF \(1826 K\)](#) | [Related articles](#) | [Related reference work articles](#)

Chapter 16 - Characterization of Detonation Nanodiamonds for Biocompatibility, Pages 519-548, Amanda M. Schrand, Jonathan B. Lin

 [Show preview](#) |  [PDF \(2473 K\)](#) | [Related articles](#) | [Related reference work articles](#)

Index, Pages 549-558

 [Show preview](#) |  [PDF \(183 K\)](#) | [Related articles](#) | [Related reference work articles](#)

Preface

The first edition of *Ultrananocrystalline Diamond* was published in 2006, revealing vast synergistic relationships between two communities of scientists working largely independently with ultrananocrystalline diamond (UNCD) in one of two forms: as a dispersed powder made by detonation techniques and as a chemical vapor deposited film. Since then, important events have taken place in the fields of nanostructured carbon materials in general and UNCD in particular. The discovery of graphene was awarded the Nobel Prize in Physics in 2010, spawning further interest in carbon nanostructures worldwide. Nanostructured diamond experienced important advances in synthesis, processing, characterization, and applications, accelerated by a widely expanding research community working with UNCD. The key purpose of this second edition of the book is to give a broad overview of the forefront of research in the UNCD field, providing a focus for and giving direction to the next generation of experimental and theoretical developments.

Nanoscale diamond particles were first produced by detonation in the USSR in the 1960s, but they remained essentially unknown to the rest of the world until the end of the 1980s. Since then, a number of important breakthroughs in purification, surface functionalization, and deagglomeration led to wider interest in these particles with diameters as small as 4–5 nm, which are now known as detonation nanodiamond (DND). DND is utilized in such applications as polishing, nanocomposites, and different areas of medicine. Another class of nanoscale diamond particles is nanodiamond produced by milling of high-pressure high-temperature diamond microcrystals providing nanoscale diamond particles containing intrinsic color centers aimed at revolutionizing biomedical imaging and quantum optics applications. Research on the synthesis of UNCD films began in the early 1990s when Gruen conceived the idea of using fullerene and later hydrocarbon molecules as carbon sources in hydrogen-poor noble gas microwave plasmas so as to achieve very high renucleation rates. The films, composed of 5–10 nm randomly oriented diamond crystallites with sharp grain boundaries, have many fascinating properties not possessed by conventional microcrystalline diamond films. The discovery and subsequent development of UNCD films has already resulted in a variety of novel applications. Some of these have reached the stage of commercialization while others are likely to follow this path as the technology continues to mature.

The content of the book is divided into three parts. The first part provides an overview of basic information and recent advances in synthesis and processing of UNCD. The second part addresses advances in nanodiamond characterization and properties measurements. The third part provides in-depth discussions of several emerging applications of UNCD films and nanoparticulate diamond.

The book starts with a chapter by Barnard on modeling of nanodiamond particle stability including studies on the distribution of incidental impurities and functional defects such as photoluminescent color centers. A summary of numerous synthetic

means to produce nanoscale diamond particles that have been reported up to date is given in the chapter by Danilenko, the inventor of DND, and Shenderova. The chapter emphasizes that development of novel DND synthesis approaches is required that will significantly increase production volume and purity while decreasing aggregate sizes of as-synthesized DND. Colloidal suspensions of individual DND particles of only 4–5 nm in size (so-called single-digit nanodiamond) recently became available, as described in the chapter by Osawa and coworkers. The availability of single-digit DND particles has broadened perspectives on the application of nanodiamond particles in composites and nanomedicine. The chapter by Kuznetsov and Butenko discusses conditions of nanodiamond phase transformation through graphitization that has important practical implications. A number of modern techniques based on electron, X-ray, RF wave, and visible light interaction with materials recently helped to reveal several key questions about the structure, morphology, and presence of nitrogen impurities in DNDs. These findings are discussed in the chapter by Vlasov, Turner, Tendeloo, and Shirayev. The chapter by Zvyagin and Manson reviews the basic luminescent properties of nitrogen-vacancy (NV) color centers in diamond nanoparticles, with a focus on the hotly debated mechanisms of ground spin-state polarization and the mechanisms of photoconversion that affects photostability. Progress toward unveiling the influence of the nanometer-proximal diamond surface on the emission properties of NV centers is also addressed. Neitzel, Mochalin, and Gogotsi discuss recent advances in surface chemistry of nanodiamond and nanodiamond–polymer composites, while M. Ivanov and D. Ivanov critically examine applications of nanodiamond and other ultradispersed carbon particles in lubricating oils for reduction of wear and friction. There is increasing evidence that nanodiamonds can be effectively utilized as a platform for a variety of diagnostic and therapeutic applications. Dean Ho and colleagues demonstrate the powerful therapeutic sequestering and targeting effect of nanodiamonds and its potential for improving the ability to treat a broad spectrum of diseases such as cancer. During the pursuit for novel uses of nanoparticles, it is imperative to independently assess the biocompatibility of nanosized particles. The chapter by Schrand, concluding the book, reviews the current literature on nanodiamond biocompatibility, addresses the current methods for studying biocompatibility, and discusses specific factors responsible for nanodiamond biocompatibility through the exploration of *in vitro* and *in vivo* data.

Advances in research and development of particulate nanodiamonds are discussed in parallel with progress in the area of UNCD films. The synthesis of UNCD films both by microwave and by hot-filament techniques is discussed in the chapter by Asmussen, Grotjohn, and Schuelke. Attention is paid to theory, modeling, and diagnostics as well as to the scaling up of microwave plasma machines for the growth of homogeneous UNCD films on 8" diameter and larger wafer sizes. Cost-effective development of such processes will be key to the rapidity with which UNCD films will penetrate the marketplace.

The reasons for the unique properties of UNCD films are to be found in the fundamental ways in which UNCD particles differ from larger diamond crystallites. In particular, the highly unusual rehybridized bonding at the ubiquitous UNCD grain

boundaries is reexamined using a combination of molecular dynamics and density functional tight-binding calculations. This sophisticated approach allows Adiga, Zapol, and Curtiss to draw conclusions concerning the thermal stability and the effect of annealing on sp^2/sp^3 hybridization ratios in UNCD films. These authors also examine the complex bonding relationships that can exist for carbon nanotubes reacting with the reconstructed diamond (100)-(2 × 1) surface revealing unexpected energetically stable nanotunnel structures.

Using secondary ion mass spectrometric measurements, Michaelson and Hoffman have shown that UNCD films incorporate about 5 atomic percent hydrogen during synthesis, a fact not explicitly taken into account in the work of Adiga et al. The work of Michaelson and Hoffman explores in detail the effect by means of which hydrogen increases by several hundred degrees the thermal stability of the films relative to that found for diamond particles. Detailed studies involving isotopic exchange, Raman and high-resolution electron energy-loss spectroscopy, and theoretical calculations allow them to conclude that this effect is primarily due to “grain boundary stabilization” arising from incorporated hydrogen atoms bonded to sp^2 -bonded carbon atoms located at internal grain surfaces.

About 10 years ago, Gruen and his collaborators found that the progressive substitution of nitrogen for argon in the synthesis gas causes UNCD films to attain electrical conductivities that reach several hundred S/cm for 20% additions of nitrogen. A chapter by Arenal explores this phenomenon in detail and concludes that it depends on the formation of 3–5 nm diamond crystallites bonded end to end so as to form 80–100 nm long diamond filaments surrounded by a graphene-like sheath that is 2–3 layers thick. It is thought that complex interactions of UNCD crystallites with thermally unstable polymeric HCN, polynitrile, and polyacetylene precursors may be involved in the formation of these highly unusual densely interwoven electrically conducting “diamond wires.”

A chapter by Auciello reviews the production of UNCD MEMS and NEMS structures using both selective film deposition and photolithographic coupled with reactive ion etching techniques. Device applications frequently require the integration of UNCD films with dissimilar materials in film form including piezoelectric oxides, metal films, and biological materials for a new generation of biological applications. The range of devices developed up to now include RF MEMS/NEMS resonators, piezoactuated NEMS switches, UNCD AFM tips, and MEMS/NEMS biomedical devices and biosensors.

Synthesis and properties of core/shell nanocarbon ensembles including UNCD/graphene ensembles are described in a chapter by Gruen. The goal is to create new classes of materials with energy conversion efficiencies that can compete with electromagnetic induction. The new approach to thermoelectricity focuses on increasing the “present” and “transported” electronic entropy by the use of biphasic ensembles. Decoupling the thermopower from the carrier density in this way would enable hitherto unrealized values of power factors. This ambitious approach to thermoelectricity requires a detailed understanding of the processes associated with transport of entropy across interfaces and in a temperature gradient. Early

experimental results are reported on two of the nanocarbon model systems that have been explored in this challenging effort up to now.

We hope that this present book will attract the attention of scientists working in other areas of nanostructured materials on the opportunities for applications offered by UNCD in its various forms. We believe that a wide variety of new, unexplored areas of research within carbon nanostructures and particularly still exist.

Olga A. Shenderova and Dieter M. Gruen

List of Contributors

Shashishekar P. Adiga

Kodak Research Laboratories, Eastman Kodak Company, Rochester, NY

Raul Arenal

Laboratorio de Microscopías Avanzadas (LMA), Instituto de Nanociencia de Aragón (INA), Universidad de Zaragoza, Zaragoza, Spain; Fundacion ARAID, Zaragoza, Spain

Jes Asmussen

Michigan State University, Department of Electrical and Computer Engineering, East Lansing, MI; Fraunhofer USA, Center for Coatings and Laser Applications, East Lansing, MI

Orlando Auciello

Materials Science Division, Argonne National Laboratory, Argonne, IL

Amanda S. Barnard

CSIRO Materials Science and Engineering, Clayton, VIC, Australia

Yuriy V. Butenko

European Space Agency, ESTEC, Noordwijk, the Netherlands

Edward K. Chow

G.W. Hooper Foundation, University of California, San Francisco, CA

Larry A. Curtiss

Materials Science Division, Argonne National Laboratory, Argonne, IL

Vyacheslav Danilenko

Novogorsk, Chimki, Moscow region, Russia

Yury Gogotsi

Department of Materials Science and Engineering, Drexel University, Philadelphia, PA

Timothy A. Grotjohn

Michigan State University, Department of Electrical and Computer Engineering, East Lansing, MI

Dieter M. Gruen

Materials Science Division, Argonne National Laboratory, Argonne, IL

Dean Ho

Department of Mechanical Engineering, Northwestern University, Evanston, IL; Department of Biomedical Engineering, Northwestern University, Evanston, IL; Robert H. Lurie Comprehensive Cancer Center, Northwestern University, Chicago, IL; Institute for Nanobiotechnology in Medicine (IBNAM), Northwestern University, Chicago, IL

Alon Hoffman

Schulich Faculty of Chemistry, Technion—Israel Institute of Technology, Haifa, Israel

M.G. Ivanov

Ural Federal University named after the First President of Russia B.N. Yeltsin, Yekaterinburg, Russia

D.M. Ivanov

Adámas Nanotechnologies, Raleigh, NC

Vladimir L. Kuznetsov

Boreskov Institute of Catalysis, Novosibirsk, Russia

Jonathan B. Lin

Department of Neuroscience and Behavioral Biology, Emory University, Atlanta, GA

Han B. Man

Department of Mechanical Engineering, Northwestern University, Evanston, IL

Neil B. Manson

Laser Physics Centre, RSPE, Australian National University, Canberra, ACT, Australia

Shaul Michaelson

Schulich Faculty of Chemistry, Technion—Israel Institute of Technology, Haifa, Israel

Vadym Mochalin

Department of Materials Science and Engineering, Drexel University, Philadelphia, PA

Ioannis Neitzel

Department of Materials Science and Engineering, Drexel University, Philadelphia, PA

Eiji Osawa

NanoCarbon Research Institute, AREC, Shinshu University, Ueda, Nagano, Japan

Erik Robinson

Department of Mechanical Engineering, Northwestern University, Evanston, IL

Shuichi Sasaki

Bravus Co. Ltd, Arakawa-ku, Tokyo, Japan

Amanda M. Schrand

Air Force Research Laboratory, Munitions Directorate Eglin AFB, Eglin, FL

Thomas Schuelke

Fraunhofer USA, Center for Coatings and Laser Applications, East Lansing, MI

Olga A. Shenderova

Nanodiamond Laboratory, International Technology Center, Raleigh, NC

Andrey A. Shiryaev

Institute of Physical Chemistry and Electrochemistry, Russian Academy of Sciences, Moscow, Russia

Stuart Turner

EMAT, University of Antwerp Groenenborgerlaan, Antwerp, Belgium

Gustaaf Van Tendeloo

EMAT, University of Antwerp Groenenborgerlaan, Antwerp, Belgium

Igor I. Vlasov

General Physics Institute, Russian Academy of Sciences, Moscow, Russia

Ryoko Yamanoi

NanoCarbon Research Institute, AREC, Shinshu University, Ueda, Nagano, Japan

Peter Zapol

Materials Science Division, Argonne National Laboratory, Argonne, IL

Kangyi Zhang

Department of Biomedical Engineering, Northwestern University, Evanston, IL

Andrei V. Zvyagin

MQ Photonics Research Centre, Macquarie University, Sydney, NSW, Australia

Stability of Diamond at the Nanoscale

1

Amanda S. Barnard

CSIRO Materials Science and Engineering, Clayton, VIC, Australia

CHAPTER OUTLINE

1.1 Introduction: phase stability of carbon	4
1.2 Nanocarbon phase diagrams.....	5
1.3 Structure, stability, and morphology	8
1.3.1 Computational modeling of diamond nanoparticles.....	9
1.3.2 Theoretical modeling of nanocarbon particles	13
1.3.3 Coexistence of nanocarbon particles	16
1.4 Stability in response to external stimuli.....	17
1.4.1 Annealing and thermal activation	17
1.4.2 Pressure- and irradiation-induced transformations.....	19
1.4.3 Stability under induced anionic and cationic charge.....	20
1.5 Surface passivation and functionalization	22
1.5.1 Passivation and functionalization in oxygen-rich environments	23
1.5.2 Passivation and functionalization in nitrogen-rich environments	24
1.6 Impurities, dopants, and functional defects	25
1.6.1 Intrinsic defects	25
1.6.2 Incidental impurities	28
1.6.3 Deliberate dopants.....	30
1.6.4 Optical centers and functional defects	32
1.7 Stability of quasi-1D nanocarbon	37
1.7.1 Morphology of diamond nanorods and nanowires.....	38
1.7.2 Hybrid 1D structures.....	41
1.8 Conclusions.....	42
Acknowledgments.....	43
References	44

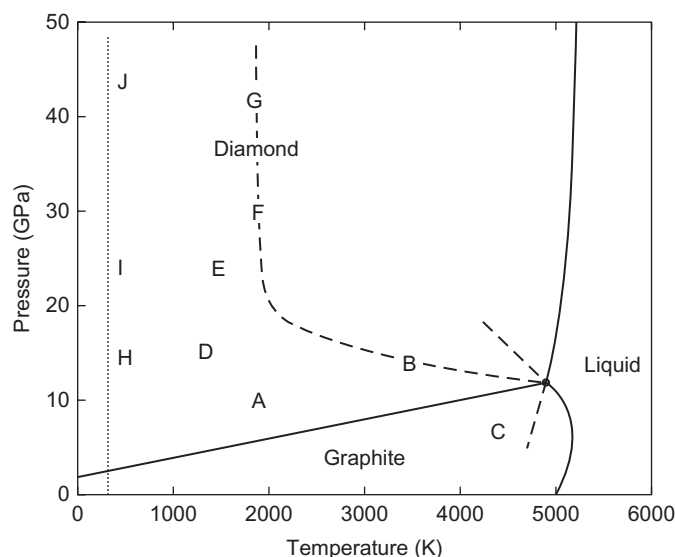
1.1 Introduction: phase stability of carbon

In order to discuss the phase diagram of nanocarbon, it is instructive to review the features of the phase diagram of bulk carbon in the macroscopic regime. A reasonable amount is known regarding the thermodynamics of the elemental carbon phases (graphite, diamond, liquid, and vapor) over a wide range of conditions. Numerous studies have been published over past decades (beginning in the 1960s) [1], iteratively improving upon previous versions of the phase diagram as new information, methods, and results become available. Much work [2] has focused on the graphite–diamond–liquid triple points at ~ 12 GPa/5000 K [3], the boundary between the graphite and diamond stable regions [4] (known as the Berman–Simon line [5]), the melting line of graphite, and the diamond melting line that runs to higher pressure and temperature above the triple point [6].

Early studies have been recently extended, via explicit calculation of the Gibbs free energy equation of state, to describe the phase diagram of carbon up to 600 GPa and 15,000 K [7] using Hugoniot analysis [8]. As early as 1979, Grover used the equation of state of carbon to predict crystalline metallic carbon as a postdiamond phase [9]. More recently, in the regime of 100–250 GPa, a six-fold coordinated postdiamond phase of carbon has been predicted [10], with similar characteristics as the simple-cubic high-pressure form of carbon known as SC4 [11]. The stability and equation of state of (transparent) rectangulated carbon has been reported, which is formed by the linking of buckled layers of graphite when subjected to high pressure at room temperature [12]. Other high-pressure forms of carbon have also been proposed, such as the fourfold coordinated body-centered-cubic BC8 [13] predicted to be stable over 1200 GPa [14].

At higher temperatures, it has been found that liquid carbon is metallic [15], although there is some conjecture regarding the exact structure of liquid carbon. High-pressure studies of first-order liquid–liquid phase transitions in carbon have been undertaken at temperatures of 4000–6500 K, reporting that liquid clusters are more likely to be graphite-like (threefold coordinated) than diamond-like (fourfold coordinated) [6]. Other studies, however, have predicted principally fourfold coordinated liquid clusters [15], such as a simple-cubic structure [16]. Even at more moderate pressures and temperatures, due to the high activation energies for solid-state transformations (and the specific effects of reaction paths), a wide spectrum of other metastable forms and complex hybrid carbon materials may be generated. These include the various specific types of graphite [17].

The currently accepted version [18] of the (thermodynamic) carbon phase diagram (up to 50 GPa and 6000 K) includes regions for the solid phase transformation of diamond to graphite, graphite to diamond, and hexagonal graphite to hexagonal diamond, and the shock compression of graphite to hexagonal or cubic diamond (as well as other experimentally observed phase transitions), as shown in Figure 1.1. Note that this diagram is distinct from the multicomponent (ternary) [19–22] and nonequilibrium phase diagrams that are constructed to describe the growth of

**FIGURE 1.1**

P – T phase and transition diagram for carbon. Solid lines represent equilibrium phase boundaries. A: commercial synthesis of diamond from graphite by catalysis; B: P – T threshold of very fast (<1 ms) solid–solid transformation of graphite to diamond; C: P – T threshold of very fast transformation of graphite to diamond; D: single crystal hexagonal graphite transforms to retrievable hexagonal-type diamond; E: upper ends of shock compression/quench cycles that convert hexagonal graphite particles to hexagonal diamond; F: upper ends of shock compression/quench cycles that convert hexagonal graphite to cubic diamond; B, F, G: threshold of fast P – T cycles, however generated, that convert either type of graphite or hexagonal diamond into cubic diamond; H, I, J: path along which a single crystal hexagonal graphite compressed in the c -direction at room temperature loses some graphite characteristics and acquires properties consistent with a diamond-like polytype but reverses to graphite upon release of pressure.

Source: Reproduced with permission from Ref. [18]. Copyright 1996, Elsevier.

diamond films from hydrocarbons [23], the phase of carbon under nonequilibrium conditions (such as under electron irradiation) [24,25], and the solvation of metals in carbon [26].

1.2 Nanocarbon phase diagrams

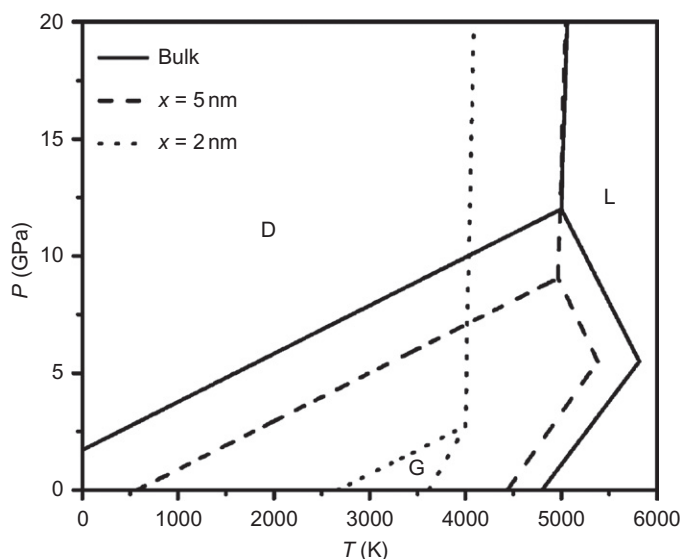
In general, the thermodynamic properties of nanoscale carbon particles may be calculated by considering the coexistence of several phases of gases, liquids, and solids in chemical equilibrium [27]. A number of equations of state for carbon in

detonation products (which promote a smooth transition from an effective graphite phase to an effective diamond phase) were compared by Charlet et al. [28] to determine their reliability in the consideration of the adiabatic gamma, defined by $\gamma = -(\partial \ln P / \partial \ln V)_S$, but such approaches fail to capture many of the important features of carbon nanostructures.

An alternative approach is to add a surface energy contribution to the bulk Gibbs free energy per atom of a particle of n atoms in a given phase [29] and define the phase equilibrium by equating the Gibbs energies for n -atom particles of each phase. A number of phase diagrams that include nanocarbon have been proposed using this approach, each exhibiting displacement of the phase equilibrium lines for small carbon particles containing from 10^2 to 10^4 atoms [29–31]. Along similar lines, Verechshagin [32] predicted a nanocarbon phase diagram based on the published properties of detonation diamond, predicting nanodiamond to be the most stable phase at particle sizes below 3 nm, but introducing a new transformation boundary (above the region for graphite) arising from observations of ~ 4 nm spherical diamond particles in the liquid state at a temperature of 3000 K (lower than that for bulk diamond) [33]. Another variant of the 3D phase diagram based on the results reported in Ref. [29] was suggested by Shenderova et al. [34], introducing a change of the slope of the diamond/graphite equilibrium line as particle size is decreased. This change reflects the higher stability of nanodiamond over nanographite observed experimentally under ambient conditions [34]. By considering the formation of nanodiamond and other allotropes under a range of nonequilibrium conditions (during the condensation of carbon in a detonation wave), a more sophisticated phase diagram was proposed by Danilenko, highlighting the appropriate synthesis conditions [35].

Most recently, a size-dependent temperature–pressure phase diagram of carbon was proposed by Yang and Li [36] that considered the contribution of surface stress to the internal pressure of diamond and graphite nanocrystals through a thermodynamic formalism. The model predicts that nanodiamond is more stable than nanographite when the crystal size is significantly reduced, in agreement with previous studies and observations, but provides some new insights. The theoretical work was combined with experimental data to produce a size-dependent temperature–pressure phase diagram, showing that the diamond/graphite/liquid triple point shifts toward lower temperature and pressure regions with decreasing nanocrystal size, as shown in Figure 1.2.

In general, a review of the literature regarding the structure of carbon nanoparticles [34] highlights that at sizes below ~ 1.8 nm, other carbon forms are abundant, such as fullerenes and onion-like carbon (OLC). Therefore, it was suggested by Kuznetsov et al. [37] to assign a corresponding region of the phase diagram to closed-shell sp^2 -bonded nanocarbons. This is shown schematically in Figure 1.3, where the regions of stability are specifically indicated for fullerenes and OLC for $n = 10$ to 10^3 atoms. The phase diagram for fullerenes was later revisited by other researchers, such as Sundqvist [38], who examined the polymetric phases of

**FIGURE 1.2**

T – P phase diagrams of bulk and nanocrystalline carbon presented in Ref. [36]. The solid, dashed, and dotted lines denote the bulk, $x = 5$ nm, and $x = 2$ nm, respectively. D indicates diamond, G represents graphite, and L represents liquid carbon.

Source: Reproduced with permission from Ref. [36]. Copyright 2008, American Chemical Society.

C_{60} and C_{70} fullerenes under pressure, and Korobov et al. [39], who constructed phase diagrams for pressure-induced solid–solid transformations in polymerized C_{60} . Later, Schöll-Paschinger and Kahl [40] extended the self-consistent Ornstein–Zernike approximation to model the coexistence of fullerenes ($C_{n \geq 60}$) with liquid carbon phases.

In addition to the particles mentioned above, the phase diagrams of other low-dimensional nanocarbon systems have also been examined. These include single-walled carbon nanotubes (SWNTs) [41] and bundles of SWNTs (often referred to as nanotube ropes or just “nanoropes”) [42]; and possibly the smallest nanoscale diamond units of all, the adamantane and diamantane hydrocarbon molecules [43]. These tiny members of the polymantane family are sometimes referred to as diamondoids [44]. The complete and thorough amalgamation of the phase diagrams of these nanoscale structures (described above) with the phase diagram of bulk “macroscopic” carbon has not yet been realized. There is still a great deal of work to be done in the construction of a complete $\langle P, T, n \rangle$ phase diagram of carbon. It is likely, however, that knowledge gained from theoretical and computational studies of nanocarbon stability [45] will play an important role in the conception of such a diagram, with thermodynamic treatments of phase equilibrium showing the way.

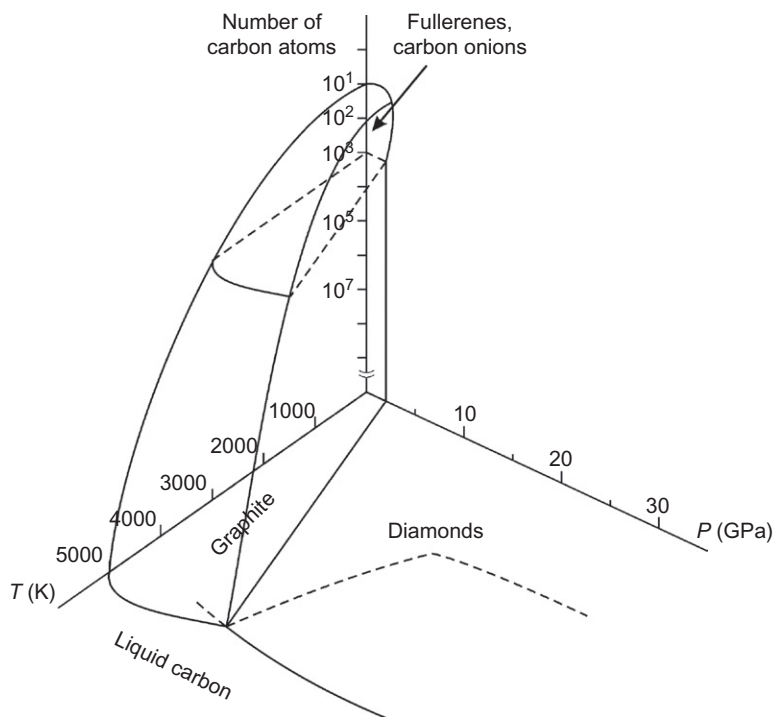


FIGURE 1.3

Schematic 3D phase diagram for carbon, including fullerenes and OLC.

Source: Reproduced with permission, courtesy of Professor V. L. Kuznetsov (2005).

1.3 Structure, stability, and morphology

In this section, a summary of the theoretical and computational studies of the relative stability of carbon nanoparticles is provided. The focus will be upon analytical theory and first-principles calculations, with complementary experimental results on this topic covered in other chapters of this book. In general, the models reviewed here are thermodynamically based and center around the relationship between graphitic (sp^2 -bonded) and diamond-like (sp^3 -bonded) carbon at the nanoscale.

To begin, the primary assumption common to most of the studies included here is that (although graphite is the thermodynamically stable phase of carbon macroscopically), because of the small molar volume of diamond compared to that of graphite (for a sufficiently small carbon particle), nanodiamond can be more stable than nanographite. It should be noted that in analyzing the stability between the particles of diamond and graphite, the number of carbon atoms in each particle should be the same, and thus the radius of the diamond particle is smaller than

that of a graphite particle for the same number of atoms. This is important because when a particle becomes smaller, the surface effects dominate over the bulk effects. As we will see, the effective surface area, the relative surface area, and the type of surface reconstructions or chemistry can all have an important influence on the stability of carbon at the nanoscale.

1.3.1 Computational modeling of diamond nanoparticles

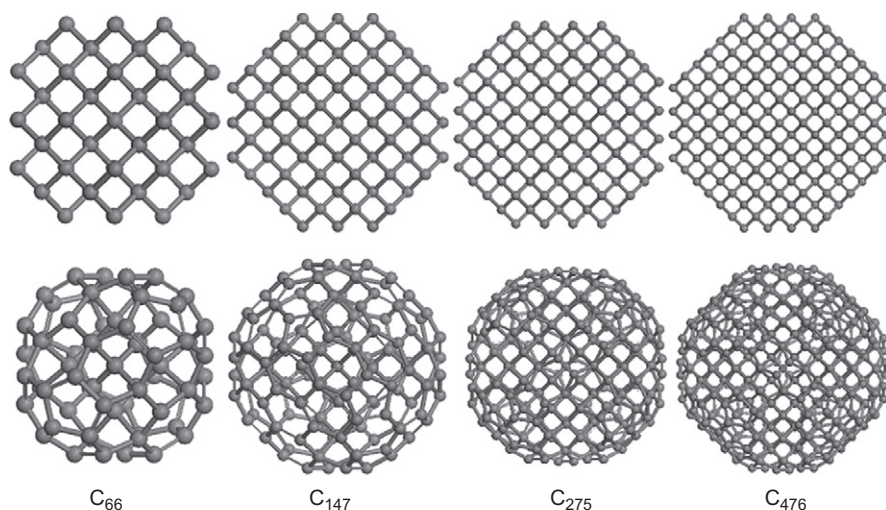
Although the phase diagrams are dominated by diamond-like and graphitic structures, still more interesting forms of carbon nanoparticles exist. Therefore, it is appropriate to mention here the relationship between these structures and fullerenes, below ~ 1.5 nm in diameter. Mass spectra data of molecular beams have shown that C_{11} , C_{15} , C_{19} , C_{23} , C_{28} , and C_{36} particles are in fact more abundant than particles in the range C_{29} – C_{35} [46]. In 1991, Tománek and Schluter [47] undertook a study of the stability of “small” carbon particles using tight-binding methods, examining the growth regimes of various configurations. Other more recent studies using a density function theory [48,49] have identified three regions for the stability of small clusters, including 1D ring clusters below 20 atoms, an assorted variety of geometries coexisting between 20 and 28 atoms, and fullerenes over 30 atoms. A study of the clusters in the range 24–32 atoms was also undertaken by Kent et al. [50] using Quantum Monte Carlo methods to compare the energetic stability of bowl, ring, sheet, and cage (fullerene) geometries [50].

In 1998, Winter and Ree [51] used the semiempirical modified neglect of diatomic overlap (MNDO) method to optimize the geometry of a range of small octahedral diamond nanoparticles. The results of the optimizations showed varying degree of structural distortion, including the separation of the outer layers of surface atoms from the interior core. This “exfoliation” of the outer layers results in the flattening of the surface corrugation to form π -bonds from the dangling orbitals [51]. This type of exfoliation of the diamond $\{111\}$ surface was explicitly examined by Kuznetsov et al. [52] via a two-layer particle model to represent the $\{111\}$ and $\{110\}$ surfaces using the MNDO method, within restricted Hartree–Fock (RHF) theory (including only the valence electrons). The graphitization energies for the $\{111\}$ and $\{110\}$ surfaces were calculated to be 0.003 and 0.24 eV/surface atom (respectively), clearly demonstrating that graphitization of a $\{111\}$ surface is preferred over that of a $\{110\}$ surface. It was also suggested that surface graphitization is initiated by a significant thermal displacement of a single carbon atom at temperatures close to the Debye temperature, and the surface delamination of the $\{111\}$ surface to form curved graphitic sheets proceeds by a “zipper”-like migration mechanism. A mechanism for the self-assembling formation of a mosaic surface structure on larger (micron size and up) diamond particles was also presented, where the initial diamond surface “blisters” under tensile stress, forming fullerene-like “bubbles” that appear as a partial fullerene-like cage structure (nonplanar, with five-membered rings) that is anchored to the remaining stable diamond surfaces around its edges [52].

Similar surface delamination and changes in structure are also observed in the relaxed “spherical” diamond nanoparticles considered by Raty et al. [53], who presented *ab initio* calculations on the effect of quantum confinement and surface reconstructions in nanodiamond, using the generalized gradient approximation (GGA), the time-dependent local density approximation (using a pseudopotential, plane-wave approach) and semiempirical tight binding. The GGA calculations were performed for the <1.4 nm particle sizes, and the tight-binding calculations for the 2–3 nm particle sizes, and the results were aligned [53]. Beginning with (ideal) bulk-diamond terminated “spherical” particles, the spontaneous low-temperature reconstruction dehydrogenated particles of 1.4, 2, and 3.0 nm resulted in graphitization of the first atomic layer of the {111} facets. The smaller particles (studied with GGA) exhibited surface delamination, followed by the formation of five-membered rings linking the delaminated graphene fragments with the remaining core atoms, producing a curved surface the same as the “bubbles” of Kuznetsov et al. [52]. The barrier between the ideal (bulk-diamond) surface structure and the reconstructed surface on a diamond nanocrystal was found to be size dependent (increasing as the size of the nanoparticle is increased). In the larger nanoparticles, the barrier was of the order of several tens of electronvolts [53].

To further investigate the importance of surface structure on the nanomorphology of diamond nanoparticles and the relationship between stability and *shape*, Barnard and coworkers [54–57] undertook a broad *ab initio* study of nanodiamond structures of octahedral, cuboctahedral, and cubic morphologies, up to ~2 nm in diameter. Three cubic nanodiamonds were included in the study (C_{28} , C_{54} , and C_{259} structures), and in each case the initial step of the relaxation process involved the reconstruction of the (100) surfaces to the (2×1) structure, characteristic of bulk diamond [57]. Three octahedral nanodiamonds were also investigated (C_{35} , C_{84} , and C_{165} structures) and were found to exhibit exfoliation of the {111} surfaces in agreement with the previous results of Winter and Ree [51]. Finally, three structures with cuboctahedral morphology were considered (C_{29} , C_{142} , and C_{323} structures), and it was found that both reconstructions could coexist on the one particle. The (100) surfaces reconstructed to the (2×1) structure, followed by the formation of the curved fullerene “cages” on the {111} surfaces [55]. This study confirmed that, although there is preferential exfoliation of the {111} surfaces over lower index surfaces on isolated particles, in the absence of {111} surfaces nanodiamond structures may be stable, without rehybridization of the C–C bonds at the surface [45,56].

Most recently, first-principles calculations using GGA were also carried out to study the geometric structure and electronic properties of dehydrogenated nanodiamonds with diameters varying from 0.8 to 1.6 nm by Wang et al. (Figure 1.4). The results confirmed that the structure of dehydrogenated nanodiamond is quite different from those of bulk diamond or hydrogenated nanodiamond and highlighted that surface atoms play an important role in the electronic structure, especially the states near the Fermi level. In addition, it was revealed that the size-dependent features in the electronic properties for dehydrogenated diamonds are also contributed by the surfaces, in addition to the quantum confinement effects [58].

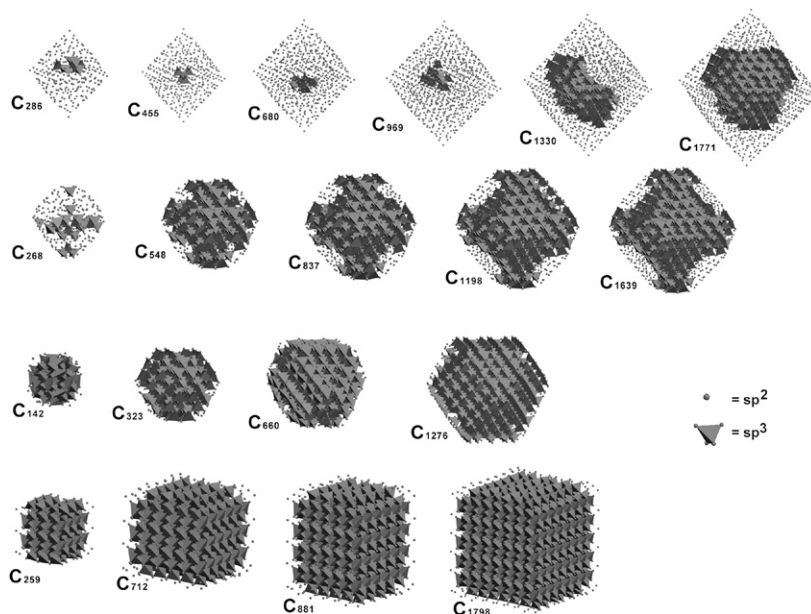
**FIGURE 1.4**

The structures of C₆₆, C₁₄₇, C₂₇₅, and C₄₇₆ nanoparticles from Ref. [58], viewed from the [100] direction, before (top) and after (bottom) the geometric optimization. The {111} facets transform to fullerene-like caps after the surface reconstruction, and the inner atoms keep the diamond-like structure.

Source: Reproduced with permission from Ref. [58]. Copyright 2004, Elsevier.

To extend the sizes previously treated using computational methods, and more closely approach sizes observed experimentally, Barnard and Sternberg [59] used the density functional based tight-binding method with self-consistent charges (SCC-DFTB) to simulate a set of 19 different diamond nanoparticle structures ranging from 1 to 3.3 nm in diameter (142–1798 atoms). This method was selected as it had previously been shown to provide good agreement with higher level quantum chemical methods for all-carbon systems and is capable of accommodating sizes much larger than those accessible to the purely first-principles methods (mentioned above). Within this structure set there were four subsets, consisting of octahedral, truncated octahedral, cuboctahedral, and cuboid shapes. The complete octahedral subset contains C₂₈₆, C₄₅₅, C₆₈₀, C₉₆₉, C₁₃₃₀, and C₁₇₇₁ structures enclosed entirely (100%) with {111} surfaces. The truncated octahedral subset contains C₂₆₈, C₅₄₈, C₈₃₇, C₁₁₆₉, and C₁₆₃₉ structures enclosed with ~76% {111} surfaces and ~24% {100} surfaces. The cuboctahedral subset contains C₁₄₂, C₃₂₃, C₆₆₀, and C₁₂₇₆ structures enclosed with ~36% {111} surfaces and ~64% {100} surfaces. The final subset of cuboid structures contains C₂₅₉, C₇₁₂, C₈₈₁, and C₁₇₉₈, with ~34% {100} surfaces and ~66% {110} surfaces. All of the structures were fully relaxed using the conjugate gradient scheme to minimize the total energy.

In this article the authors systematically modeled the evolution of the core-shell structure for octahedral, truncated octahedral, cuboctahedral, and cuboid shapes over

**FIGURE 1.5**

Optimized diamond nanoparticles reported in Ref. [59]. Top row: the octahedral subset: C_{286} , C_{455} , C_{680} , C_{969} , C_{1330} , and C_{1771} structures, enclosed entirely (100%) with $\{111\}$ surfaces. Second row: the truncated octahedral subset: C_{268} , C_{548} , C_{837} , C_{1198} , and C_{1639} structures, enclosed with $\sim 76\%$ $\{111\}$ surfaces. Third row: the cuboctahedral subset: C_{142} , C_{323} , C_{660} , and C_{1276} structures, enclosed with $\sim 36\%$ $\{111\}$ surfaces. Bottom row: the relaxed structures of the cuboid subset: C_{259} , C_{712} , C_{881} , and C_{1798} structures, with 0% $\{111\}$ surfaces. Tetrahedrally coordinated sp^3 hybridized atoms are indicated by surrounding (fourfold coordinated) polyhedra, and the sp^2 and sp^{2+x} hybridized atoms are indicated by simple balls without wire-frame connections.

Source: Reproduced with permission from Ref. [59]. Copyright 2007, Royal Society of Chemistry.

this size range, including explicit examination of the fraction of sp^3 , sp^{2+x} and sp^2 -bonded atoms, and their location. This can be seen in the figure plate provided in Figure 1.5 based on a combination of visualization modes, employing a simple ball method for the sp^2 and sp^{2+x} hybridized atoms (where $0 < x < 1$) and the polyhedron method for the tetrahedrally coordinated sp^3 hybridized atoms (each of which is surrounded by a coordination tetrahedron spanned by the four neighbors of the central atom). In this figure, the diamond-like regions will appear clearly as collections of interpenetrating tetrahedra, and sp^2 or sp^{2+x} atoms participating in the fullerene (or graphitic) regions can be seen as simple spheres decorating the outer surface of the diamond-like regions. This was designed to make the shape and extent of the diamond-like cores easily discernable [59], at the expense of detail in the shell region (which is more prevalently displayed in other works) [45,53,55,56,58,60].

Based on these results it was determined that there is a relationship between the size of the particle and the fraction of diamond-like and/or fullerenic carbon; but that it depended significantly on the overall shape. In shapes when there is $>76\%$ $\{111\}$ surface area, nanodiamonds are likely to prefer a core-shell (bucky-diamond) structure, and the core/shell ratio depends on the overall size. The author noted a distinct crossover between predominately sp^2 and predominantly sp^3 structures at ~ 1100 atoms, which coincides with the crossover predicted theoretically, as we will see in Section 1.3.2. If there is $<76\%$ $\{111\}$ surface area, particles are likely to be stable in the diamond structure with a thin (either single or double layer) shell down to ~ 600 atoms (which is discussed in Section 1.3.3). It was presumed that a type of confinement by multiple layers is responsible for inhibiting relaxation of sp^3 -bonded atoms into a sp^2 -bonded shell and promoting the stability of diamond-like cores at the center of the structures with a high fraction of $\{111\}$ surface area.

1.3.2 Theoretical modeling of nanocarbon particles

Due to the limitations imposed by computational resources, it is often convenient to undertake a limited set of explicit calculations to parameterize analytical theories to probe issues of stability, rather than a large number of explicit simulations on vast collections of model particles (particularly when one wants to use electronic structure methods). In the late 1980s, Almlöf and Lüthi [61] carried out *ab initio* RHF calculations on the phase stability of planar graphene sheets and cubic diamond particles. Neglecting the contribution from the particle zero-point energy, they defined the cohesive energy as the difference between the energy per carbon atom and the energy of the free carbon atom. Although the results for the cohesive energies of graphene and diamond were considerably higher than experiment, this was certainly a step in the right direction [61]. Later, Shaw and Johnson [62] used a diffusion-limited model that assumed that the difference in energy between small carbon particles and the macroscopic (bulk) carbon, ΔE , was related to the number of surface atoms. Their calculations estimated that $\Delta E \propto n^{1/3}$ (where n is the total number of atoms) [62].

Building on this foundation, Badziag et al. [63] compared the binding energy of carbon atoms in small sp^3 -bonded hydrocarbon molecules and sp^2 -bonded polycyclic aromatics (ranging from C_2 to C_{60}). They introduced a simple model to calculate the molecular energies of tetrahedral and hexagonal particles. In all cases, the C–C and C–H bond lengths were optimized prior to the energy calculation, although the geometry was restricted. The binding energy was plotted as a function of the hydrogen to carbon ratio, with the results forming two approximately linear trends corresponding to the hexagonal and tetrahedral particles, respectively. Overall, the sign and magnitude of the slopes (obtained from the linear fits) did agree with experimental observation, although explicit values were not reported. By examining the intersection point of the linear fits, the results showed that small hydrogenated nanodiamonds are more stable than graphite, although the actual crossover was found to be very sensitive to the type of particles included (i.e., the shape). The crossover of particle stability varied from ~ 300 atoms (or a diameter of ~ 1.3 nm) to 21,000 atoms (diameter of ~ 6.0 nm) [63].

In a different approach, Hwang et al. [64] outlined a chemical potential model to examine the low-pressure synthesis of nanodiamond, in terms of the surface energy of diamond and graphitic particles. The main advantage of their approach was its applicability to nonequilibrium conditions. They performed thermodynamic calculations using bulk diamond as the reference state and the deposition and its etching of carbon during synthesis was analyzed in terms of the activity of carbon. The driving forces for the precipitation of graphite and diamond were evaluated and it was predicted that, depending on the sign of the driving force, precipitation or etching would occur. These authors also suggested that the capillary effect (given by the Laplace–Young equation for a small carbon particle) is essential in approaching formation of diamond over graphite, and that the precipitation of diamond and graphite (from the gas phase) are kinetically equivalent. Assuming that the diamond and graphite particles are spherical, the crossover of phase stability was estimated to be 104 atoms for graphitic particles and 177–584 atoms for diamond particles, respectively. This study also went on to examine the nucleation on a substrate, and the model was elaborated to consider the conditions required for nucleation of diamond to dominant during chemical vapor deposition (CVD) growth [64].

Around the same time, Winter and Ree [29,51] outlined a method for investigating the relative stability of graphene sheets and hydrogenated nanodiamonds. They derived an expression for the heat of formation as a function of particle size and used it to predict the relative stability of the graphite and diamond phases of finite carbon particles. They assumed that each carbon atom in graphite forms three intralayer sp^2 bonds and experiences a weak interlayer dispersive interaction between graphene sheets; and in diamond, each carbon atom forms four identical sp^3 bonds with the neighbor carbons. Semiempirical and density functional theory (DFT) methods were used to determine the total energy of sp^2 and sp^3 isolated carbon particles. To account for the surface effects, the total energy per carbon atom was plotted as a linear function of the hydrogen to carbon ratio. The C–H bond energy was obtained from the coefficients of a least squares fit for both the graphite and diamond particles, respectively. In agreement with previous results, the model predicted that small nanodiamond particles are more stable than graphite below $\sim 33,000$ – $70,000$ atoms (depending upon the computational method used), corresponding to a particle size of 6–8 nm [29,51].

The question of the surface stress on the phase stability of smaller (<2.5 nm) particles has also been explicitly investigated by Barnard et al. [65] by extending this established thermodynamic theory to include fullerenes. By treating only dehydrogenated nanodiamonds (i.e., nanodiamond structures consisting of mostly sp^3 -bonded atoms, as opposed to bucky-diamond), a direct comparison with fullerenes was made [65]. The method was based on the enthalpy of formation as a function of size, expressed in terms of the bond energies for diamond-like and fullerenic particles, the surface dangling bond energy, the number of carbon atoms, the number of dangling bonds on the surface of the particle, and the standard heat of formation of carbon at $T = 298.15$ K. In the case of fullerenes, the closed shell eliminates the dependence on the effective surface-to-volume ratio and therefore the size

dependence. Therefore, a term for the strain energy that vanishes in the graphene limit was added, by first making the assumption that a fullerene may be approximated as a homogeneous and isotropic elastic sphere. This was derived by considering the bending and stretching of a suitable elastic sheet, in terms of the bending energy per unit area, the bending modulus of the sheet, and the mean radius of curvature. A spherical model was assumed and an expression for the strain energy per carbon atom for fullerenes is proportional to the inverse of the square of the radius of curvature. Using this model, the crossover in the enthalpy of formation of dehydrogenated (stable) nanodiamond crystals and fullerenes was found to be at ~ 1100 atoms, which is approximately equivalent to cubic nanodiamond crystals of 1.9 nm in diameter. An important point in this work was the selection of the chemical reservoir and the frame of reference. The model used a reservoir of free (isolated) C atoms and included the enthalpy of formation of a dangling bond so that the nanoparticles were assumed to be in mutual equilibrium with a continuous diamond or graphitic surface, not the bulk [65].

The phase transition between nanodiamond and OLC structures has also been previously addressed by Zaiser and Banhart [66], who presented a thermodynamic quasi-equilibrium theory to explain this irradiation-induced transformation of OLC to nanodiamond. The model was based on the premise that irradiation of OLC leading to the destabilization of the sp^2 structure was due to the large difference in the cross sections for irradiation-induced displacements of carbon atoms in diamond and graphite. A nonequilibrium phase diagram was calculated showing the stability of graphite and diamond (as a function of the displacement rate of atoms) and the results related to experimentally observed results [66]. In this approach the issue of nucleation was excluded in favor of considering the phase transformation as the motion of a phase boundary separating the two (solid) allotropes. The OLC-to-nanodiamond phase transition was attributed to ballistic displacements causing interstitial C atoms (predominantly from sp^2 lattice sites) and a net flux of atoms from the sp^2 to the sp^3 phase. It was shown, however, that if the temperature exceeds an (upper) critical temperature, the sp^2 bonding may be stable, even though phase transitions may still occur at lower temperatures [66].

In addition to these thermodynamic treatments, a small number of kinetic theories have been developed to describe the actual phase transitions that occur at the interface between the sp^2 fullerenic and sp^3 nanodiamond phases. For example, Butenko et al. [67] derived a model to determine a temperature-dependent isotropic rate of migration of the interface between the diamond and graphitic regions of spherical nanocarbon particles. They employed a reducing sphere model that assumed that phase conversion begins simultaneously at all interface surface points, and that (under isothermal conditions) the interface moves with a constant isotropic rate inside the nanoparticle. The reaction rate of the nanodiamond to bucky-diamond (or OLC) transition was treated as a migration rate of the interface between the exfoliated fullerenic shells and the diamond cores. Estimated kinetic parameters in an Arrhenius expression (such as the activation energy) then allowed for quantitative calculations of the diamond graphitization rates in (and around) the critical temperature range [67].

1.3.3 Coexistence of nanocarbon particles

To investigate the cases where carbon nanoparticles may contain both sp^2 and sp^3 bonding simultaneously, Barnard et al. [68] addressed the stability of multishell carbon nanoparticles by taking the model outlined above for comparing the phase stability of nanodiamonds and fullerenes, and applying it to bucky-diamond and OLC. The onions were treated as nested fullerenes by adding a term for the van der Waals attraction, 0.056 eV [69], to the expression used to describe fullerenes. The bucky-diamonds were treated in the same manner as nanodiamonds, although obviously the dangling bond to carbon atom ratio is different for nanodiamonds and bucky-diamonds (of similar diameter) due to the formation of the delaminated fullerene outer shells [68].

The enthalpy of formation (as a function of particle size) for bucky-diamond and OLC was calculated and extrapolated along with the nanodiamond and fullerene results mentioned in the previous section. There were three main points apparent from this comparison. First, the sp^2 -bonded OLC and fullerene results were indistinguishable (within uncertainties) below ~ 2000 atoms. Second, the enthalpy of formation of bucky-diamond is more akin to OLC than to nanodiamonds. Finally, in the region from ~ 500 to ~ 1850 atoms, the results predicted that a thermodynamic coexistence region was formed, within which bucky-diamond coexists (within uncertainties) with the other nanocarbon nanoparticles [68]. This region was then further broken into three subregions, as indicated in Figure 1.6. From ~ 1.4 to 1.7 nm, the

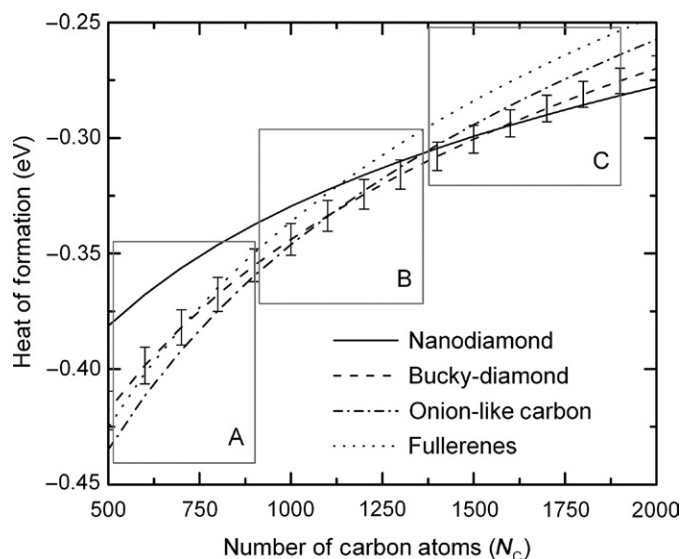


FIGURE 1.6

Atomic heat of formation of carbon nanoparticles, indicating the relative subregions of coexistence of bucky-diamond with other phases. Uncertainties indicated for bucky-diamond only.

Source: Reproduced with permission from Ref. [68]. Copyright 2003, American Physical Society.

enthalpy of formation of bucky-diamond was found to be indistinguishable from that of fullerenes (within uncertainties), although OLC represents the most stable form of nanocarbon. Between ~ 1.7 and 2.0 nm bucky-diamond and OLC coexist (within uncertainties), and bucky-diamond was found to coexist with nanodiamond (within uncertainties) between ~ 2.0 and 2.2 nm. Further, the intersection of bucky-diamond and OLC stability was found to be very close to the intersection for nanodiamonds and fullerenes at ~ 1100 atoms, suggesting that at ~ 1100 atoms, a sp^3 -bonded core becomes more favorable than a sp^2 -bonded core, irrespective of surface structure [68]. Once again, the model used in this study assumed a reservoir of free (isolated) C atoms, and that the nanoparticles were in mutual equilibrium with a continuous diamond or graphitic surface, not the bulk [65].

As we can see from the numerous studies outlined above, advances have been made in understanding the relative stability of sp^2 - and sp^3 -bonded particles at the nanoscale. These studies have clearly identified the two important size regimes, where (depending upon the phases under consideration) $sp^2 \rightarrow sp^3$ or $sp^3 \rightarrow sp^2$ phase transitions may be readily expected. In the case of larger particles, the crossover in stability between nanodiamond and nanographite may be expected at around 5 – 10 nm in diameter; and for smaller particles the crossover between nanodiamond and fullerene particles may be expected at 1.5 – 2 nm.

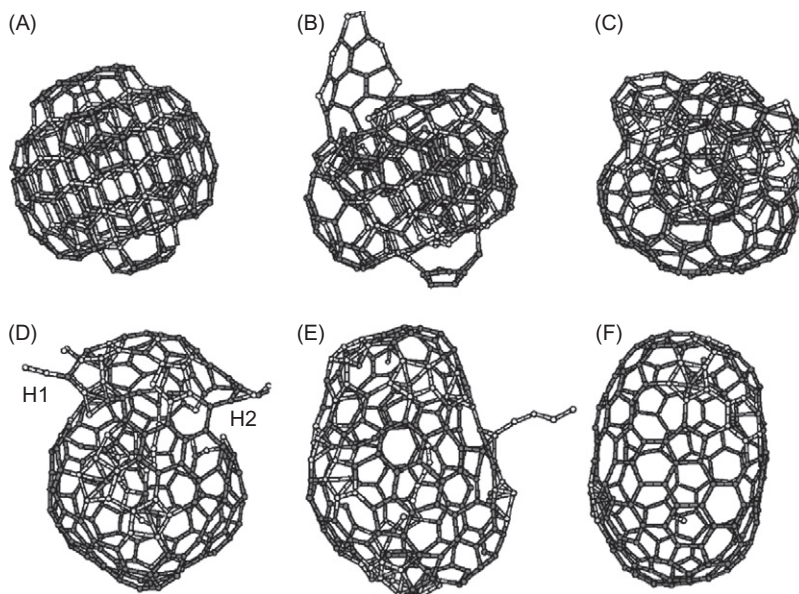
1.4 Stability in response to external stimuli

All of the studies described above have treated isolated structures, at low temperature, in a vacuum. In reality, carbon nanoparticles of all types will be exposed to a range of external stimuli, including variations in temperature, pressure, and electric fields. In this section, the role of these stimuli will be briefly discussed in relation to particle stability.

1.4.1 Annealing and thermal activation

There is no doubt that the existence of carbon nanoparticles with a diamond core (of a few nanometers) and a partial or complete fullerene outer shell (bucky-diamonds) represents a new level of complexity in the physics and chemistry of nanocarbons, as they possess more than one type of C–C hybridization. Transformations between the intermediary and limiting cases will be sensitive to thermal fluctuations, but how is this to be treated computationally or theoretically? Such core-shell structures are distinct from the more OLC-like particles obtained by Fugaciu et al. [70] in their study of the thermal stability and irradiation effects of spherical diamond nanoparticles. In this case, the authors reported that, under certain conditions, the nanodiamond particles of ~ 1.1 nm size underwent fragmentation and formed fullerene cages, but the nanodiamond particles > 1.2 nm transformed to form two-shell OLC structures [70].

This work was later repeated by Lee et al. [71], who also examined the heat-induced transformation of spherical nanodiamond particles into elongated fullerenes

**FIGURE 1.7**

Atomic processes of structural transformation of nanodiamond to tube-shaped fullerene by successive annealing. (A) 0 K (at time $t = 0$ ps), (B) ~ 2500 K ($t = 3$ ps), (C) ~ 2500 K ($t = 19$ ps), (D) ~ 2100 K ($t = 35$ ps), (E) ~ 1900 K ($t = 50$ ps), and (F) ~ 20 K ($t = 120$ ps). Simulated annealing with temperatures up to 3000 K were performed during the process (E)–(F). Note that two holes H1 and H2 are created in (D).

Source: Reproduced with permission from Ref. [71]. Copyright 2003, American Physical Society.

using tight-binding molecular dynamics, as shown in Figure 1.7. In this case, however, upon cooling ($T = 2500$ – 2000 K), the particle was found to completely transform to an elongated, tube-like fullerene via a “flow-out” mechanism where inner atoms exit the core region via holes and defects in the outer shell, a “direct absorption” mechanism where atoms within the shell are adsorbed into the shell structure, and a “push-out” mechanism where inner atoms replace the surface atoms that are pushed into the vacuum [71].

This issue has also been addressed theoretically, and in 1996 Gamarnik [72] reported on the boundaries of the stability regions of diamond and graphite nanoparticles using a model that began with a statement of the energy of carbon (at low pressure) in terms of the Helmholtz free energy. The lattice energy was determined by summation of the Born–Lande pair interaction potentials of all the charges in the crystals, and the kinetic energy for the bond electrons in diamond and graphite was derived by relating the Coulomb force acting on a bond electron with the bond electron centripetal force to the neighboring atom. A similar approach was used to calculate the kinetic energy of the graphite bond electron charges. The model also considered atoms located at the particle edges and corners and the conduction

electrons in the graphite model. By assuming that each inner atom relinquishes one electron charge value to establish a bond (although in the case of diamond this is distributed in four directions and in the case of graphite, three directions), the covalent bond charge value per atom and the conduction electron charge value were established. The results of this model showed that the energy per atom was dependent on the size of the nanodiamond and nanographite particles (as shown by other), as well as the temperature. At $T = 0$, the model predicted that nanodiamond was stable below the point of intersection with graphite at 15 nm, below 10.2 nm at room temperature, below 6.1 nm at 545°C, below 4.8 nm at 800°C, and below 4.3 nm at 1100°C [72].

1.4.2 Pressure- and irradiation-induced transformations

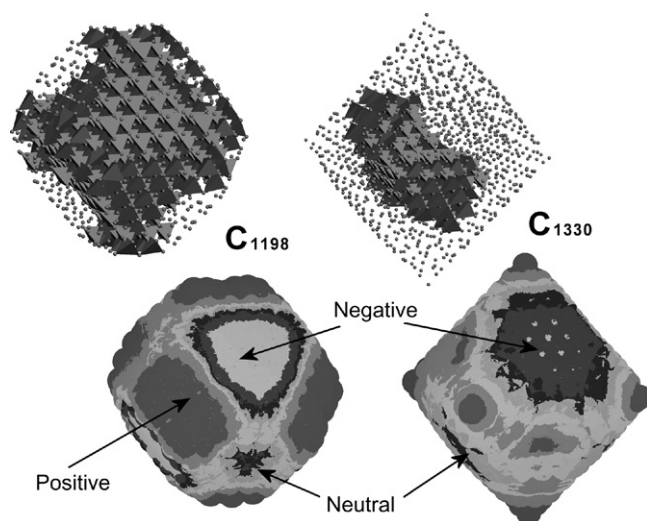
In all of the models mentioned above, the dependence of the nanodiamond/graphite phase stability on the pressure of the system has not been explicitly accounted for. This was first considered by Jiang et al. [73] using a model of the phase transition between nanodiamond and nanographite (as well as the corresponding thermodynamic functions) based on a pressure–temperature phase diagram of carbon, as a function of size. The contribution of the size-dependent internal pressure was estimated by assuming spherical, quasi-isotropic nanocrystals, with additional curvature-induced pressure given by the Laplace–Young equation, and using experimental values for the bulk phases. The thermodynamic functions for the diamond-to-graphite transition (in this case) were estimated via the Clausius–Clapeyron equation. The equilibrium size of diamond and graphite was equated (at equilibrium), neglecting the difference of pressure for nanocrystals as a first approximation, and it was shown that the transition size of nanodiamond decreases from ~8 nm at 0 K to 3 nm at 1500 K. The authors also point out that the diamond-to-graphite transition in each direction may follow different kinetics, and the model was used to explain why nanodiamonds are seen to graphitize at the surface, but direct conversion of graphite to nanodiamond is not observed. Such a transition requires a driving force such as that provided by electron irradiation [24,25].

This model was later extended to include the effects of surface stress on the internal pressure of the nanoparticle [74]. The melting enthalpy was described in terms of the Helmholtz function. The authors plotted the transition interface between nanodiamond {111} and nanographite {0001}, to find that the transition size of nanodiamond now appears at ~11 nm at 0 K to ~4 nm at 1500 K. Furthermore, the transition point at 1300 K was found to provide a transition size between diamond and the OLC, as the transformed product of OLC has a lower Gibbs free energy than the graphite. This indicated that the transition size between the nanodiamond and nanographite should be larger than 2 nm [74]. Although this study assumes the surface energy is equivalent to surface stress (an approximation that may not be valid in this case), the results clearly show that the effects of surface stress are very important in the description of the phase stability of nanocarbon, since the transition size of nanodiamond without surface stress (above) was ~8 nm at 0 K to ~3 nm at 1500 K, some 1–3 nm smaller than when surface stress was included [73,74].

Another approach to the crystalline stability of dehydrogenated nanodiamonds is to examine the stability and the coalescence of the cores, rather than the instability of the surfaces. As part of a study on the graphitization of diamond surfaces and the diamond/graphite interface using DFTB, Jungnickel et al. [75] examined the equilibrium structure of a sp^3 -bonded icosahedral structure of 300 atoms. The structure was found to be stable in a conjugate gradient relaxation, and although the energy was 0.30 eV/atom higher than a C_{300} two-shell carbon onion, the particle could not be induced to form the corresponding (lower energy) OLC, even at temperatures of 1200–2700 K [75]. In a later attempt to model the sp^2 to sp^3 nanocarbon phase transition, Astala et al. [76] reported results that used the DFTB method to model the collision-induced nucleation and growth of nanodiamond inside the same 300 atom OLC structure. The release of atoms due to “knock-on” displacements in outer shells and their transport to the core were simulated by a sequence of random atom additions with zero initial velocities. The evolution of the structures was found to be dependent upon the number of interstitial atoms during the *ad hoc* injection process. The inner C_{60} fullerene was seeded with a C_{10} particle, and the irradiation was simulated via the random introduction of varying numbers of additional interstitial carbon atoms. The growing structure was re-relaxed after each addition. These results were then compared with sets of complementary results that use different sampling regimes [76]. After each simulation, the sets were analyzed and the bonding geometries of the central cores of selected final relaxed systems were compared. The combined results indicated that a critical size for spherical atomic arrangements exists, below which sp^2 structures dominate, and above which sp^3 atoms bond into a diamond-like structure. The confinement by multilayer carbon fullerenes was suggested to lower this limit and to reduce the capabilities of sp^3 -bonded atoms to relax to a graphitic phase. The authors also described the transformation as the percolation of initially dispersed sp^3 -bonded regions fusing after a certain threshold, to form one sp^3 core particle [76].

1.4.3 Stability under induced anionic and cationic charge

As an extension of previous work (described above), Hwang et al. [77] also analyzed in detail the theoretical and experimental aspects of charge on the stability of small diamond and graphite particles. The charged particle model surmises that since graphite is conducting, the charge will be uniformly distributed over the conducting bulk and the interface; however, in the case of diamond, the charge on the diamond particle will be localized at the interface. Therefore, the surface energy of the diamond particle may be decreased by the presence of charges while that of the graphite particle cannot. Experimental evidence [77] suggested that the stability of diamond was favored by a positive bias on the substrate, and the stability of graphite carbon was favored by a negative bias. The implication that the stability of the charged nuclei was affected by the sign of the charge seemed closely related to the well-established fact that the nucleation behavior in the presence of charges depends on the sign of the charge. Unfortunately, the authors admit that the proposed

**FIGURE 1.8**

Examples of the anisotropic facet-dependent distribution of the surface electrostatic potential of diamond nanoparticles, calculated using DFTB in Ref. [59].

theory (and available data) was not sufficient to make any quantitative prediction on the sign dependence of the stability between diamond and graphite particles. An extensive and rigorous treatise of this model, outlining the theory and application to appropriate systems, is given in Ref. [78].

It has also been recently shown that stable interactions between nanodiamonds may also be affected by induced charges, due to multipolar variations in the surface electrostatic potential. Based on the relaxed structure of each of the particles presented at the end of Section 3.1 and in Figure 1.5, Barnard and Sternberg [59] also calculated the surface electrostatic potential (V) and found that the sign depended on the orientation of the surface facets and the underlying crystal structure. A sample of these results is shown in Figure 1.8. In general, the results show that the {100} surfaces consistently exhibit a strong positive electrostatic potential, and regions where the {111} surface graphitizes exhibit a strong negative electrostatic potential. Alternative {110} facets and {111} surfaces with incomplete (or inefficient) graphitization or a bulk-like surface reconstruction exhibit a neutral surface electrostatic potential. These results point to a preferred orientation for particle–particle interactions in nanodiamond aggregates [79], and the assembly of nanodiamond with polymers or biomolecules [80] is sensitive to changes in the core-shell structure and the different types of hybridization at the surface.

Based on these calculations, a number of preferred particle–particle orientations were subsequently identified by taking into account the crystallographic orientation of interfacing facets, the interfacial separation distance, and free particle rotations about the interfacial normal. This analysis gave rise to predictions of allowed and

forbidden interfaces, and a probability of observation of different types of nanodiamond assemblies [79]. These assemblies were later confirmed experimentally using high-resolution aberration-corrected transmission electron microscopy [81], which prompted further analysis of the effect of excess electrons on the electrostatic interactions and the ordering of diamond nanoparticles. It was determined that there was a charge-dependent change in the strength of the allowed interactions. Some interfaces become rapidly more unstable with increasing anionic charge and eventually become forbidden interactions, which will significantly destabilize the nanodiamond aggregates.

A detailed account of the effect of induced charge on the structure and stability of entire diamond nanoparticles has yet to be reported, but it has been found that significant anionic or cationic charge invokes important structural changes in graphene nanoflakes [82,83].

1.5 Surface passivation and functionalization

Although the shape-dependent surface electrostatic potential of nanodiamonds offers a range of new opportunities, the combination of diamond-like and fullerenic surface is not always desirable. The mechanism for the stabilization of bucky-diamond surfaces, however, appears to be appropriate passivation. As part of their 1998 study, Winter and Ree [51] also undertook semiempirical optimization of the geometry of diamond particles after capping the dangling bonds with hydrogen. In all cases, the surface instability observed following the relaxation of the dehydrogenated particles was eliminated, and the diamond structure was preserved throughout. The optimized (relaxed) diamond particles capped with hydrogen atoms gave sp^3 C–C bond lengths very close to the experimental value of 1.54 Å. This was confirmed using *ab initio* methods by Barnard et al. [56,84] via the direct comparison of relaxed dehydrogenated and hydrogenated versions of the same nanodiamonds that showed that the transformation to bucky-diamond eliminated and the passivated nanodiamonds recovered bulk-diamond-like properties (such as cohesive energy [84] and surface structure [57,84,85]).

In this size regime, Raty and Galli [60] used first-principles calculations to examine the relative stability of nanodiamond as a function of the *degree of surface hydrogenation*. Their results indicated that as the size of diamond is reduced to ~3 nm, bucky-diamonds are energetically preferred over hydrogenated nanodiamonds. The approach was also based on the formation energy, containing terms for the vibrational and the total energy of a nanoparticle obtained using DFT. By comparing various degrees of hydrogen coverage, the difference in formation energy between particles with hydrogenated surfaces and those with bare surfaces was found to decrease as the size of the nanoparticle increases but did not depend significantly on the hydrogen supersaturation. Although the calculations could not establish the exact size at which the crossover between hydrogenated and bare, reconstructed surfaces occurs, the numerical results contained within the paper were used to

suggest how varying the hydrogen pressure (and thus its supersaturation) during synthesis may promote different types of thin films. Two ranges for the hydrogen pressure corresponding to two different growth conditions of diamond were proposed: one that favors the formation of ultrananocrystalline diamond and the other that favors the formation of microcrystalline diamond thin films [60].

1.5.1 Passivation and functionalization in oxygen-rich environments

As there are a large number of unsatisfied covalent bonds on the surfaces of nanodiamonds, the surfaces are energetically unstable and will either spontaneously reconstruct to form sp^2 fullerene shells (as described above) or readily react with various adsorbates in the immediate environment in an attempt to find equilibrium. In the absence of deliberate hydrogenation, or exposure to hydrogen-rich environments, it is more likely that the surface of nanodiamond will suffer oxidation, rather than the homogeneous hydrogen coverages described in the last section.

The oxidation of nanodiamond surfaces occurs via several different mechanisms. Firstly, one may naturally expect the adsorption of oxygen and water molecules when nanodiamonds are exposed to air. Secondly, surface oxidation may be introduced from cooling media such as H_2O and CO_2 , which are commonly used during the synthesis of detonation nanodiamonds, or could be introduced during the purification process when detonation nanodiamonds are treated with strong liquid acids like HNO_3/H_2O_2 or CrO_3/H_2SO_4 to remove fullerene shell and metallic impurities [86]. Finally, surface oxidation may be deliberately applied with some specific chemical reactions in the post-treatment process. Experimentally, the surface chemistry of the nanodiamonds has been studied by using photoelectron [87], infrared (IR) [88], nuclear magnetic resonance (NMR) spectroscopy [89], or thermodesorption techniques [34]. The combination of these studies shows that the surfaces of the nanodiamonds after purification are mainly terminated with carboxyl, hydroxyl, and keto groups, with some additional anhydrides and lactones [90]. This makes it of great importance to examine the influence of these functional groups on the structures, properties, and stabilities of the nanodiamonds either in air or in liquid environments. Moreover, the different surface reactivity and surface reconstruction of the {100}, {110}, and {111} facets coexisting in a nanodiamond may give rise to different preference for specific terminated groups [91–97].

In a recent study, Lai and Barnard [98] used DFTB computer simulations and thermodynamic modeling to examine the thermodynamic stability of oxygen (O), hydroxyl (OH), and water (H_2O) on the surfaces of representative diamond nanoparticles. The thermodynamic modeling was performed with respect to temperature, and the environmental influence was probed through the use of different O-rich environments. The simulations compared O_2/H_2 and H_2O vapor reservoirs, which characterize the situation in air and in a hydrous environment, respectively [98].

Oxygen and hydroxyl terminations were shown to be thermodynamically favorable and form strong C–O covalent bonds on the nanodiamond surface in an O_2/H_2 gas reservoir, which confirmed previously reported experiments. Indeed, OH

functionalization was shown to be thermodynamically favorable up to 1500 K in an O_2/H_2 reservoir, which confirms the existence of detectable oxygen signals at 1050°C observed by x-ray photoelectron spectroscopy (XPS). Simple oxygen passivation was also energetically favored up to 1180 K in an O_2/H_2 reservoir, where the breaking of C–O bonds begins. In contrast, water molecules were found to prefer physisorption around the nanodiamonds, and forced chemical adsorption prompts H_2O to decompose into OH and H. It was also found that the thermodynamic stabilities of oxygen and hydroxyl functionalization dramatically decreased when calculations were performed with respect to a water vapor reservoir. In a water vapor reservoir, the OH desorption process begins between ~550 and ~560 K. Water is nearly unavoidable in these applications, which makes the stability of OH functionalized nanodiamonds of significant importance [98].

In addition to this, the functionalization efficiency of each stable species was found to be facet dependent. This facet selectivity is found to be largely dependent upon the environmental temperature, chemical reservoir, and morphology of the nanodiamonds. The oxygen functionalization prefers the {100} facets as opposed to alternative facets in an O_2/H_2 gas reservoir. The hydroxyl functionalization favors the {111} surfaces in an O_2/H_2 reservoir and the {100} facets in a water vapor reservoir, respectively. It was determined that the {111}: OH saturation in an O_2/H_2 reservoir is energetically more favorable up to ~1000 K. In addition, the {100} functionalization is always less sensitive to the temperature changes with either reservoir, which suggests a possible route for selective {100} oxidation by heating at high temperatures [98].

1.5.2 Passivation and functionalization in nitrogen-rich environments

In addition to this, the interactions of nitrogen groups with the surfaces of diamond nanoparticles is an important part of functionalization [99–101]. Proteins and other macromolecules often contain amide groups that can interact with carbon-based systems and aid in immobilization [102] and applications such as drug delivery [103]. It has previously been shown that, in the case of diamond, amine-terminations show an increased potential for acting as useful intermediaries for further functionalization, as well as serving as a substrate for self-assembly of other biomolecules [104,105]. For example, recently a new method was introduced using nanodiamonds as vectors for *in vitro* gene delivery via surface-immobilization with 800 Da polyethyleneimine (PEI800) and covalent conjugation with amine groups [106], as part of a rapid, scalable, and broadly applicable gene therapy strategy.

In a recent paper, Lai and Barnard [107] confirmed that stable functionalization of nanodiamond with amines is achievable by exploring the relative stability of the nanodiamond passivated by the primary (amidogen, NH_2), secondary (imidogen, NH), and tertiary (nitrogen, N) amines in N_2/H_2 and ammonia environments. The study was conducted using DFTB simulations, spanning a wide range of temperatures, and found that the efficiency of functionalization depends on the reaction environment. The different amines were selectively and systematically applied as monolayers to different

crystal facets on model nanodiamonds. The authors showed that passivation with nitrogen is thermodynamically unfavorable and spontaneous desorption from all low index facets may be expected, even at low temperature, but that amidogen and imidogen form stable chemical bonds with the surface, with the relative stability depending upon the facet orientation, the temperature, and the surrounding chemical environment. N adsorption is found to be energetically unfavorable on the nanodiamond surfaces up to 1500K. In contrast, NH and NH₂ adsorption are found to be thermodynamically stable at least around room temperature. By comparing different anisotropic (facet-dependent) adsorption configurations, it was also found that {100} facets of the nanodiamond are more preferred for NH adsorption in the entire temperature range considered, but are only favored at high temperature for NH₂ adsorption [107].

This information is inaccessible by Fourier transform infrared (FTIR) measurements, which cannot discriminate between primary and secondary amines. A detailed statistical analysis of the particle morphologies was also provided, along with the thermodynamic analysis of the different adsorption configurations and species. The study concluded that chemical functionalization with amines is more stable in the N₂/H₂ environment than in the ammonia environment, but (in general) its stability depends on the size, shape, and morphology of the nanodiamond as a whole [107].

1.6 Impurities, dopants, and functional defects

It is often convenient to think of nanodiamond as pure, and free of defects, but this is not necessarily realistic. Nanodiamonds can contain a variety of defects, whether we want them there or not. These include intrinsic point defects such as lattice vacancies and incidental impurities such as nitrogen that are a result of the synthesis and/or purification processes. In general, defects are always thermodynamically unstable, but the relative (in)stability of these defects, and hence the probability that they can be removed from the particle, can depend on the location of the defect within the particle. This is quite different than the case of bulk diamond, where all lattice sites are geometrically (and therefore, energetically) equivalent.

There are of course, types of defects that are very useful, and are deliberately introduced to provide some function. These include *p*-type or *n*-type dopants and optical centers. In this section, the stability of a range of different defects will be briefly reviewed, with a focus on how the stability of the host nanodiamond is affected by the defect, as well as how the stability of the defect is affected by the structure of the host.

1.6.1 Intrinsic defects

The concentration of vacancies (also known as GR1 defects) in bulk synthetic diamond has been estimated to be of the order of ~26ppm [108,109], and the concentration of monovacancies in polycrystalline diamond has been measured at ≤7ppm [110]. There is also evidence to suggest that the majority of these vacancies will be located in the vicinity of the diamond surface [111,112]. Previous studies have also

examined the diffusion barrier for individual vacancy defects in bulk diamond, both theoretically [113–115] and experimentally [112,116,117], and a study of the preferred location, concentration, and stability of these point defects in nanodiamond was recently reported [118].

In this study, Barnard and Sternberg used DFTB computer simulations to investigate the structural and energetic stability of vacancies in model diamond nanoparticles with clean and hydrogen passivated surfaces. Since there is currently no way of determining experimentally where a vacancy is likely to be located in a given particle, the authors sampled a range of possible substitution sites in the bucky-diamond and passivated nanodiamond structures. The particles used in this study are a C_{837} truncated octahedral bucky-diamond and a hydrogenated $C_{837}H_{252}$ truncated octahedral nanodiamond, each displaying six {100} facets and eight {111} facets. The vacancy defects were introduced individually at different lattice sites, so as to sample the full range of crystallographically and geometrically unique lattice sites within the particles.

Fully relaxed C_{837} and $C_{837}H_{252}$ nanoparticles were used as initial configurations, and the point defects were substituted for carbon atoms located along specific (albeit zig-zagged) substitution paths within the lattice, extending from the centro-symmetric atom to different points on the surface. The directions of these substitution paths are shown in Figure 1.9, and are denoted as A, B, C, D and E, for substitution paths terminating at the center of the {100} surface, {111} surface, {100}/{111} edge, {111}/{111} edge, and the {111}/{111}/{100} corner, respectively. If we consider the nanoparticle morphology as analogous to the shape of the diamond Brillouin zone, the substitution paths (A, B, C, D, and E) begin at the Γ point and extend along the X, L, U, K, and W directions, respectively. In all, the vacancy defects were introduced at over

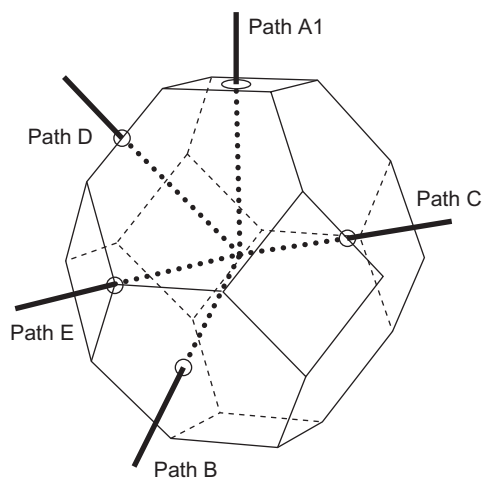


FIGURE 1.9

Substitution paths for the inclusion of a geometrically and crystallographically diverse range of point defects in a truncated octahedral diamond nanoparticle.

50 geometrically unique sites within the diamond nanoparticles, to effectively sample configuration space. Following inclusion of the defect, the entire structure has then been re-relaxed using the same method [118].

Figure 1.10 reproduces the site-dependent defect energies for the (a) hydrogen passivated nanodiamond and (b) bucky-diamond. In this study, the relative energy

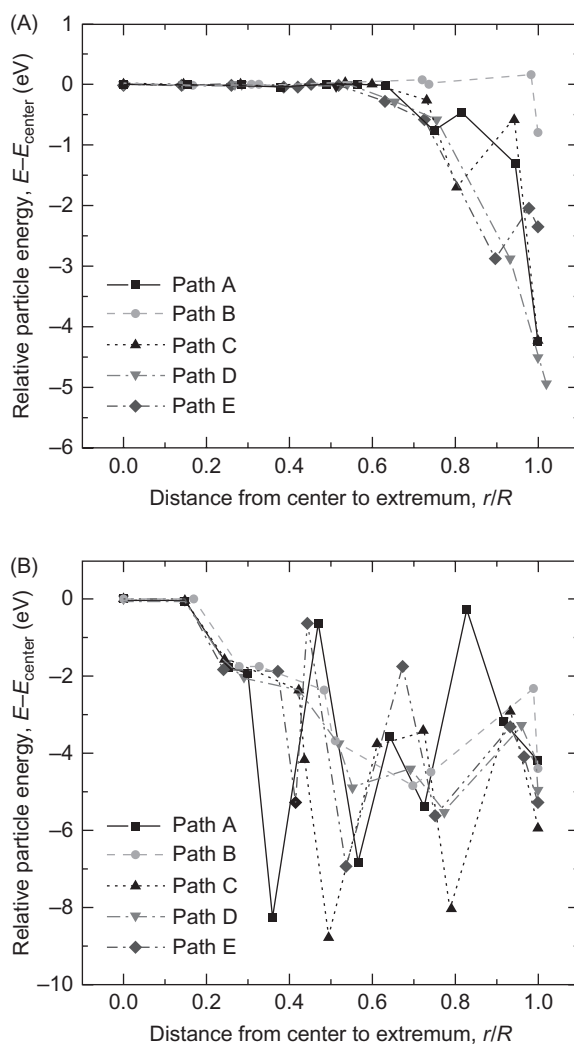


FIGURE 1.10

Stability of vacancy point defects (A) in a $\text{C}_{837}\text{H}_{252}$ nanodiamond and (B) C_{837} bucky-diamond, calculated with DFTB.

Source: Reproduced with permission from Ref. [118]. Copyright 2008, American Scientific Publishers.

$E - E_{\text{center}}$ was used, defined as the total energy of the nanoparticle with a given vacancy site relative to the energy of the nanoparticle with the vacancy in the centro-symmetric position. The x -axis represents a scaled (dimensionless) nanoparticle radius defined by dividing the distance from the center to the vacancy site (r_X) by the total distance from the center to the extremum (R_X) in each path (X). Hence $r/R = 0$ is the center and $r/R = 1$ is the outermost vacancy site located on a surface, edge, or corner. In Figure 1.10, the small site-to-site fluctuations in energy are due to redistribution of charge (electronic relaxations), whereas large energy variations are due to local changes in the structure of the lattice (ionic relaxations). In general, these site-to-site variations of the vacancy energy are comparable to (or larger than) the diffusion barrier for neutral vacancies in diamond [112–117]. As we will see in the following sections, the same technique has been used in other complementary studies on other functional defects, dopants, and impurities.

The results of this study showed that the (in)stability of the vacancy defect depends on the location of the defect within the nanoparticle and on the type of surface structure. Even when the surfaces are stabilized by hydrogen, the vacancy is thermodynamically unstable when the substitution site is within six atomic layers of the surface/edge/corner. At this point, there is a thermodynamic driving force for diffusion that increases. The study also showed that the stability of the nanodiamond itself is also affected by the presence of vacancies, particularly when they are close to the surface/edges/corners. This was particularly significant in the case of the bucky-diamond, where dramatic changes in energy were reported, due to subsurface graphitization of the “inner surface” of the bucky-diamond core. In these cases, the defect did not need to reside in (or near) the “shell” of the bucky-diamond, as the subsurface graphitization could be activated when the defect is up to as many as eight atomic layers away from the extrema. This resulted in structural asymmetry, where {111} facets in the vicinity of the defect exhibit a dual-shell (onion-like) structure, while the remaining {111} facets retain the single-shell surface structure [118].

These results suggested that diffusion is likely to occur spontaneously at temperatures used during synthesis, or possibly during irradiation, as there is a strong thermodynamic driving force for diffusion of vacancies in diamond nanoparticles toward the surface (escape) even when the surfaces are stabilized with hydrogen.

1.6.2 Incidental impurities

Nitrogen is ubiquitous in diamond nanoparticles. This is due, in part, to the fact that it is a primary constituent of the source explosive. Detonation-induced transformations of powerful explosives and their mixtures with the composition $C_aH_bN_cO_d$ with a negative oxygen balance in a nonoxidizing medium yield a number of condensed carbon phases, including diamond nanoparticles [86]. Therefore, commercial diamond nanoparticles contain a small fraction of nitrogen, usually between 1% and 4% [86,119], but it can sometimes be as high as 7–8% [120].

Using the same approach described above for vacancy point defects in Section 6.1 and the same model nanodiamond structures, Barnard and Sternberg [121]

also modeled the stability of substitutional nitrogen defects using the DFTB method. The study used the same sampling of substitution paths (and sites) and produced results that are directly comparable with the relative stability of vacancies, as shown in Figure 1.11. In the case of the relaxed hydrogenated nanodiamond (see Figure 1.11A), the results showed an interesting relation between the energy $E-E_{\text{center}}$ (given as the total energy of the nanoparticle relative to the energy of the

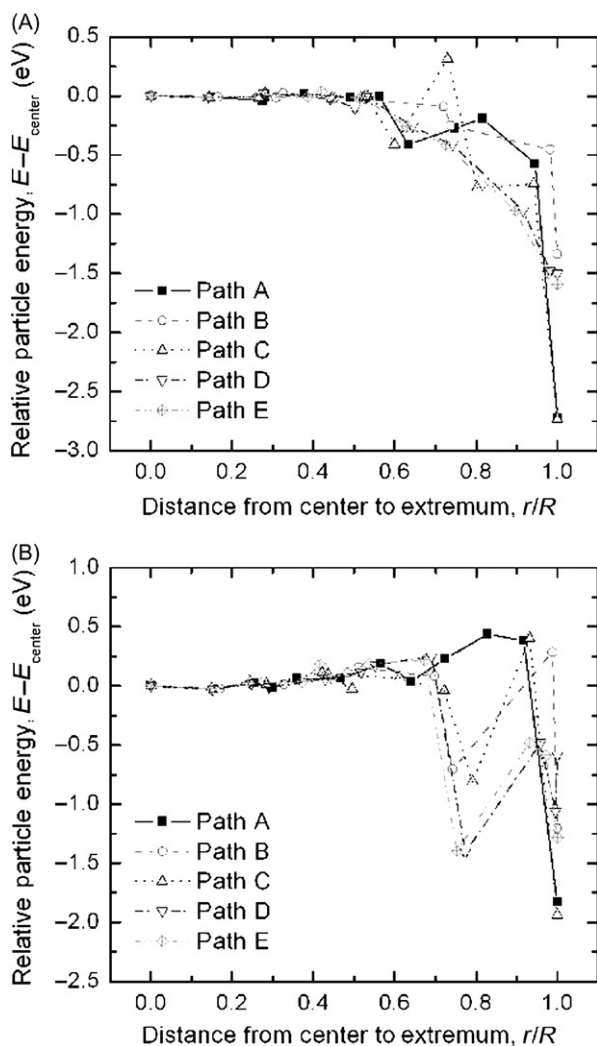


FIGURE 1.11

Stability of substitutional N defects (A) in a $\text{C}_{837}\text{H}_{252}$ nanodiamond and (B) C_{837} bucky-diamond, calculated with DFTB.

Source: Reproduced with permission from [121]. Copyright 2005, American Chemical Society.

nanoparticle with the impurity in the centro-symmetric position) and the location of the substitutional site. It was found that, while there is little energetic difference between the substitution paths in the core region of the particle (between 0% and ~50% of the distance from the center), beyond this distance the general trend is toward lower energies, indicating that it is energetically preferable for nitrogen to be located near the surface of the nanodiamond [121].

In the case of relaxed bucky-diamond, with the exception of the central region of the core, the results showed a gradual increase in energy for nitrogen substitution sites approaching the “inner surface” of the bucky-diamond core, as shown in Figure 1.11B. This was followed by a sharp decrease in energy for sites located on the “inner surface” (~75% of the distance from the center). These sites represent a “trap” if the nitrogen atoms were driven to diffuse. One path (A) did not follow this trend (and did not include a trap), since there is no surface graphitization (and therefore is no inner surface) in this direction. In addition to this, the *coordination* of N in the bucky-diamond was found to depend upon the distance from the center. Within the core, the dopants were found to be fourfold coordinated and threefold coordinated in the shell. This correlates with the general “flattening” of the atomic layers on the inner surface of the bucky-diamond core and all subsequent outer layers comprising the shell [121].

More detailed results for a variety of sizes and particles shapes were also reported, and it was confirmed that the stability of the defects were actually independent of particle size and related only to the location of the defect with respect to the extrema, regardless of shape [122]. In general, these results revealed that nitrogen atoms prefer to reside near the surfaces/edge/corners of diamond nanoparticle and not within the core, and there was an obvious thermodynamic incentive for diffusion. This fueled speculation that nitrogen, and hence it is more functional defect complexes (see Section 6.4), would not be stable with respect to diffusion, particularly in small particles.

1.6.3 Deliberate dopants

The search for a suitable *n*-type dopant of diamond has not been particularly successful. In theory, possible donors in diamond include lithium (interstitial) [123,124], sodium (interstitial) [123,124], nitrogen (substitutional) [125], phosphorus (substitutional), arsenic (substitutional), antimony (substitutional) [126,127], and sulfur [128–130]. Phosphorous [124,131–134] has been found to have donor level [129], but the electron mobility values achieved so far for CVD-grown P-containing diamond layers are still rather low. Limited donor level success has been reported with sulfur, but due to some B contamination found in the S-doped samples more work is required [135]. Lithium has been found to offer only very shallow donor levels [136]. Oxygen has also been introduced as an *n*-type donor [137] in diamond. There are indications that conduction due to the presence of the implanted O has been observed; however, the study [137] does not definitively prove *n*-type conductivity. A study has also been conducted on iodine doping of

amorphous carbon [138]. No experimental evidence has been found to support the *n*-type doping of diamond with As or Sb.

The search for a *p*-type dopant has been much more successful. Currently, boron (incorporated substitutionally) is the most successful *p*-type dopant, although potassium, sodium, and aluminum doping of diamond has been achieved by forced diffusion, with results showing shallow acceptor levels in the case of K and Na, and deep acceptor levels in the case of Al [136]. Boron may be introduced both during CVD diamond film growth [132] and by ion implantation [139], as well as via forced diffusion [140]. Hydrogen-acceptor level interactions have been investigated via deuterium diffusion in B-doped diamond [141]. More recently, with the advent of nanocrystalline diamond thin films [142–147], with grain sizes on the order of ~5–50 nm (depending upon growth conditions), there has been growing interest in this material for electronic purposes. The success of such doping will be largely dependent upon the positions of the dopants within the films and the nature of the bonding of the dopant atoms to the surrounding carbon atoms [148–151].

To address these issues, Barnard and Sternberg [152] repeated the DFTB calculations previously undertaken for nitrogen (described above) for the case of substitutional boron dopants, to determine the configuration and energetics of boron in model bucky-diamond particles. The results predicted that it is energetically preferable for boron to be positioned *just beneath* the surface of both structures. Near the core, at $\langle r/R \approx 0.5$, the results are insensitive to the defect location, but beyond this range (as the sites approach the “inner surface” of the bucky-diamond core), site-to-site differences begin to emerge. Small variations were also reported for particles of a different shape and when no surface delamination was present. In addition to this, the coordination of boron atoms was found to be largely insensitive to the location of the defect and readily adopted fourfold coordination, which is essential for ensuring *p*-type conductivity [152].

These studies superseded previous work using DFT to study the structure and stability of dopants in a diamond nanocrystal reported some years before [153]. Although the previous studies used a higher level of theoretical sophistication, much smaller structures were employed. A 29-atom dehydrogenated nanodiamond (C_{29}) with cuboctahedral morphology was used, along with a monohydrogenated nanodiamond ($C_{29}H_{24}$) of the same type. In the absence of the dopant, this little dehydrogenated particle shows a transition from the nanocrystal into the $C@C_{28}$ endohedral fullerene as the 28-atom “shell” separates from the central “core” atom [154]. When boron [155] (nitrogen, or any other potential dopants such as oxygen, aluminum, silicon, phosphorus, and sulfur [156]) was inserted substitutionally into the center of this structure an endofullerene was also produced (such as $B@C_{28}$). In some cases, the substitutional species shifted from the centro-symmetric position and attached to the surrounding carbon cage, which became distorted by the presence of the foreign atom. Many rigorous investigations have been undertaken on the properties of endohedral atoms in fullerenes (endofullerenes), including studies of the electronic structure and chemical stabilization of the tetravalent C_{28} fullerene with a variety of endohedral complexes [157] including carbon [154,158,159], boron [158], and nitrogen [158].

When identical relaxations were performed on the $C_{29}H_{24}$ nanodiamond, it was found that the tiny nanodiamond was stable. While the structure was perturbed, the central dopant remained bound to the outer carbon structure in a stable configuration [155,156].

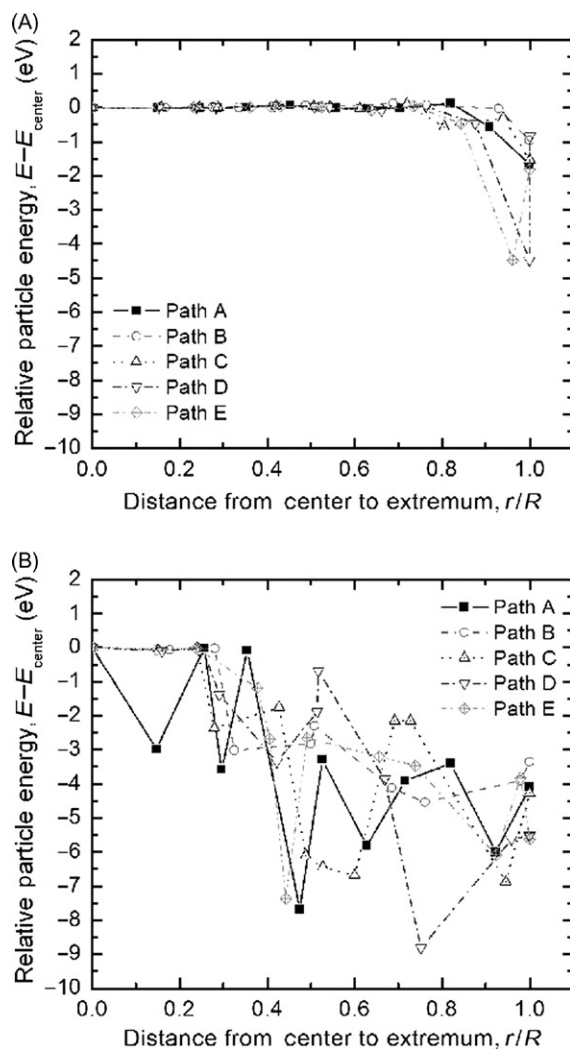
1.6.4 Optical centers and functional defects

Beyond the introduction of foreign species for electronic doping, there are a range of other types of point defects in diamond that can be useful. Collectively these are often referred to as “functional defects” (as they provide some functionality) and include the range of currently topical optically active defects and color centers [160].

Among the various types of optically active defects, the nitrogen–vacancy (N–V) complex is the most widely studied [161,162] and forms when a vacancy migrates to bind with a substitutional impurity [113,163]. The energy-level structure of the negatively charged $(N-V)^-$ defect results in emissions characterized by a narrow zero-phonon line (ZPL) at 637 nm, while the neutral $(N-V)^0$ center has a ZPL at 575 nm, both accompanied by a wide structured side band of lower energy due to transition from the same excited state, but with formation of phonons localized on the defect [161]. To date, all available data points to a strong dependence on crystal size and surface-to-volume ratio, and the optical emission from such defects is rarely seen in small diamond nanoparticles (≤ 40 nm in diameter) [162,164]. Photo-physical characteristics for 25 nm particles have been reported [164], and most recently N–V emission from 5 nm detonation nanodiamond agglomerates [165] and isolated 8 nm diamonds [166] were shown.

In order to realize any of the diverse applications for N–V centers in nanodiamonds, a clearer understanding of this dependence is imperative, so a series of simulations has also been reported, investigating the relationship between the location of the defect, the stability of the nanodiamond, and the probability of observation (akin to those described above). Once again, the computational work used DFTB and employed the 837 atom truncated octahedral model particle, and sampled the configuration-space of $(N-V)^0$ and $(N-V)^-$ defects by substituting individual defects at the familiar set of >50 geometrically unique sites along specific lattice directions [167]. The advantage of reusing the same method, model particle, and configurational sampling is that these results are directly comparable with the results of the intrinsic and incidental defects describe above. The relative energy results for $(N-V)^0$ and $(N-V)^-$ centers were found to be thermodynamically degenerate and will be termed N–V from this point on.

Presented in Figure 1.12 are the site-dependent defect energies for the (A) hydrogen passivated nanodiamond and (B) the bucky-diamond. In the case of the passivated $C_{837}H_{252}$ structure, the N–V defects were found to be relatively stable within the particle until the substitution site fell within three atomic layers of the surface/edge/corner. The small energy fluctuations for $r/R < 0.6$ are due to the redistribution of the excess charge from the donor electron that occurs when the

**FIGURE 1.12**

Stability of substitutional neutral N-V defects (A) in a $\text{C}_{837}\text{H}_{252}$ nanodiamond and (B) C_{837} bucky-diamond, calculated with DFTB.

Source: Reproduced with permission from Ref. [167]. Copyright 2009, American Chemical Society.

defect site is within the Bohr excitonic radius of the particle extremes [168]. In this region, the nitrogen atom is sp^3 hybridized and the configuration of the defect is constrained. Although the defect is thermodynamically unfavorable, the energetic barrier for a transformation to a lower energy configuration is too high. At $r/R > 0.7$, there is a $\sim 1.5\text{--}4.5\text{ eV}$ thermodynamic driving force for diffusion that increases as r/R approaches 1. [167].

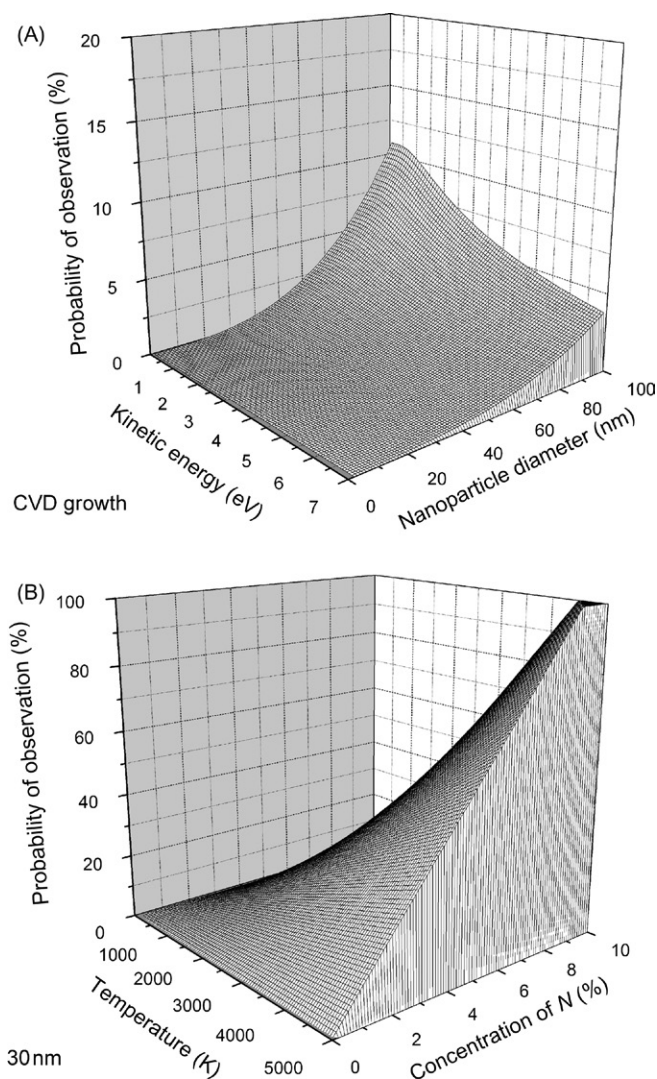
In the C_{837} bucky-diamond structure the defect was found to be highly unstable and with a substantial thermodynamic (up to ~ 6 to ~ 9 eV) driving force for diffusion within the particle core. In the bucky-diamond particles, where the sp^2 shell exists, the lattice parameter of the particle is different from the bulk, and a significant amount of strain already exists in the particle. This energy barrier for distortion of the N–V centers is lowered and depends on the position of the defect the structure of the defective region changes to reduce the total stress and the total energy. This was found to manifest as subsurface graphitization, since the defect energy for N–V was lower in sp^2 -bonded regions, and this provides a significant reduction in the site-dependent defect energy. These transformations are common near the surface of nanodiamonds, even when hydrogen terminated, and can be identified in the cores of bucky-diamonds by the large energy fluctuations in Figure 1.12, which appear as a series of local minima [167].

Based on these results, it was concluded that N–V centers will be stable deep within the core of diamond nanoparticles [169] but will only stay that way when the particles are sufficiently large so as to be predominantly bulk-diamond-like or they have stable passivated surfaces. Therefore, the authors estimated the probability P_{obs} for finding an N–V center in a stable hydrogen-terminated diamond nanoparticle of radius R . This quantity is a function of the probability P_{form} that an N–V center will be *formed* during synthesis and the probability of its *escape*, at a given kinetic energy E_K , such that

$$P_{\text{obs}}(R, E_K) = P_{\text{form}} \left(1 - \left[P_{\text{core}}(R) \exp\left(-\frac{E_{\text{barr,core}}}{E_K}\right) + P_{\text{shell}}(R) \exp\left(-\frac{E_{\text{barr,shell}}}{E_K}\right) \right] \right) \quad (1.1)$$

where $P_{\text{core}}(R)$ and $P_{\text{shell}}(R)$ are the probabilities of the N–V center occupying a lattice site in the core and shell, respectively. These were taken as proportional to the fraction of atoms occupying each region. Since even the stable hydrogen passivated diamond nanoparticles were found to consist of distinct *core* and *shell* regions, the escape probability was assumed to have different contributions from each region and that a defect escaping from the core will still pass through the shell (where trapping may occur depending upon the magnitude of the kinetic barriers in each). The escape probabilities were assumed dependent upon the kinetic energy $E_K = \frac{3}{2}k_B T$ and the diffusion barrier E_{barr} , where $E_{\text{barr}} = |E_{\text{diff}} - E_d|$. If $E_K \ll E_{\text{barr}}$, then the probability of escape will be zero, whereas when $E_K \approx E_{\text{barr}}$ the escape probability will become large.

This does not ensure that N–V defects will be observed in any great quantity, so the average values of $E_{d,\text{core}}$, $E_{\text{diff,core}}$, $E_{d,\text{shell}}$, and $E_{\text{diff,shell}}$ were explicitly calculated for use in Eq. (1.1). The diffusion of N–V defects is vacancy assisted and is dominated by the N–C exchange energy, but once again a defect diffusing out of the stable core region will be required to penetrate the shell in order to escape. Using the synthesis temperature of 800°C and nitrogen concentration of $C = 0.1\%$ from experiment [163], an estimate of the probability of observation of an N–V defect in H-terminated nanodiamond was predicted, as shown in Figure 1.13A. These

**FIGURE 1.13**

Probability of observation of a stable N–V defect in diamond nanoparticles: (A) over a range of particle diameters and kinetic energies during probing (using CVD growth conditions: $C = 0.1\%$ and $T_{\text{growth}} = 800\text{ K}$) and (B) for 30 nm particles over a range of synthesis temperatures and concentrations of nitrogen present in the precursor materials. Note the difference in vertical scales.

Source: Reproduced with permission from Ref. [167]. Copyright 2009, American Chemical Society.

results predict that nanodiamonds ≤ 22 nm in diameter will have a $< 1\%$ probability of containing a stable N–V defect, even under ambient conditions. In the case of bucky-diamond, the predicted probability of N–V defects being stable in 5 nm nanodiamonds at room temperature (with 300 ppm of nitrogen) was 0.0017% and only 0.00004% for 3 nm particles using the same conditions. However, by altering the synthesis temperature ($E_{K, \text{growth}}$) and C , this situation may be improved, as shown in Figure 1.13A. In general, increasing the synthesis temperature and quantity of N in the precursors increases the probability that N–V defects will be present in the lattice, assuming that diffusion occurs on the same timescale as observed in bulk diamond and graphite [167].

These results revealed that the stability of N–V centers is greatest within the core of nanodiamonds, and hence the probability of observation is greater for larger particles (where a greater number of lattice sites occupy the core region), but also showed how growth temperature and N concentration affect the incorporation of N–V centers, which can be used to engineer this material. Based on this model and technique, complementary predications were made for diamond nanoparticles produced with different synthesis techniques, including for detonation or ultradispersed diamond, CVD nanodiamond, and high-pressure/high-temperature diamond nanoparticles. These results were rigorously validated by explicitly measuring the emission for 3690 individual nanodiamonds and correlating the size (determined using atomic force microscopy) and single photon fluorescence. By measuring the second-order correlation function, it was possible to determine if the detected fluorescence was due to single or multiple N–V centers. In this case, the probability of detecting two simultaneous photons is normalized by the probability of detecting two photons at once for a random photon source, and an “antibunching” dip in the second-order correlation function indicates sub-Poissonian statistics of the emitted photons and reveals the presence of a single quantum system, which cannot simultaneously emit two photons. This was sufficient to confirm the predictions and provided additional identification of the critical dimension for which the probability of finding a single N–V defect is optimal (under the conditions employed) [167].

Subsequent work by the same researchers and their colleagues further confirmed the existence and behavior of N–V centers in isolated 5 nm nanodiamond and reported on the direct, room-temperature observation of a profound surface-controllable luminescence intermittency (blinking), which offered a fresh insight into color center behavior in isolated nanodiamonds [170]. Based on the DFTB simulations (described and shown above), it was determined that the blinking was related to the defects located in or near the shell of the particles, where the structural instability can alter the electronic states (such as the lowest unoccupied molecular orbital, LUMO) and extinguish the luminescence.

The study of impurities and defects within isolated diamond nanomaterials [86,171] and nanocrystalline diamond films [142,143,145,147] with grain sizes in the order of ~ 5 –100 nm is also receiving considerable attention. Some results have also been reported on other types of optically active defects, such as the analogous silicon-vacancy complex [172]. This defect has a much higher probability

of observation [173], but due to difficulties associated with Si introduction during synthesis, the N–V defect remains the firm favorite for the majority of relevant applications.

1.7 Stability of quasi-1D nanocarbon

In all of the previous sections, the focus has been on quasi-0D diamond nanoparticles, but nanodiamond can be produced with entirely different dimensionality. The thermodynamic phase stability of diamond nanowires was investigated by Barnard and Snook [174] in an attempt to ascertain if any diamond nanowires are energetically stable with respect to carbon nanotubes. They applied the same enthalpy of formation model outlined above for quasi-0D carbon nanoparticles [55,68] to the stable diamond nanowires [68,69] described in later sections. Both zigzag and armchair SWNT structures were investigated, for chiral indices $m = 3$ to 12.

Once again, the assumptions were made that the strain energy of a nanotube contains only two in-plane elastic constants and that the chiral graphene sheet is homogeneous and elastically isotropic. The nanotube strain was approximated as the bending and stretching of a suitable elastic sheet. Assuming a cylindrical model, the strain energy was obtained by applying a linear fit to the energy per ion versus the inverse square of the mean radius of curvature and extracting the strain energy and cohesive energy from the slope and intercept, respectively [174].

In similar fashion to their investigation of nanodiamond phase stability, the authors compared the energy of the C–C per atom versus the number of dangling surface bonds per atom. These values (along with those for SWNTs) were used to calculate the enthalpy of formation, which was plotted as a function of the number of carbon atoms per unit length (rather than just the number of carbon atoms) [65]. By extrapolating the fits, the intersection of diamond nanowires and carbon nanotubes was found to be ~ 450 atoms/nm. This corresponds to a diamond nanowire ~ 2.7 nm in diameter or an $m = 27$ armchair nanotube [174].

The intersection of diamond nanowires and nanotubes with graphite was also investigated, although the number of atoms in the graphite model was scaled (per unit length) in two chiral directions, equating to $\theta = 0^\circ$ and $\theta = 30^\circ$ (where θ is the chiral angle) to preserve the correct dimensionality. The intersection of the enthalpy of formation as a function of the number of atoms per unit length for diamond nanowire (averaged over morphologies) and carbon nanotubes with graphite was then obtained (for each “chiral scaling”) and found to be 870 and 930 atoms/nm for $\theta = 0^\circ$ and $\theta = 30^\circ$, respectively (~ 4 nm in diameter).

These results established that, although SWNT represents the most energetically preferred form for ultrafine 1D carbon nanostructures, a “window” of stability for diamond nanowires exists between ~ 450 and 870–930 atoms/nm (2.7 to ~ 4 nm in diameter), beyond which graphite is once again energetically preferred [174]. This simple model omitted the surface reconstructions and graphitization of the diamond nanowire surfaces and should be revisited in future work.

In addition to this, there are several studies that investigated the stability of nanotubes relative to graphene. For example, it was determined by Sinnott et al. [175] that graphene is the least stable sp^2 -bonded structure below ~ 6000 atoms. Beyond this size, graphene sheets become more stable than the (10,0) and (5,5) nanotubes [175]. This is in agreement with the modified heuristic “bond passivation model” outlined by Rotkin and Suris [176] and the results comparing nanotubes and nanographene sheets.

1.7.1 Morphology of diamond nanorods and nanowires

To accompany the theoretical prediction of 1D nanocarbon stability, the logical next step is to computationally simulate quasi-1D diamond nanostructures, such as diamond nanorods and nanowires, and explicitly examine the stability of the surface facets [177]. There have been far fewer studies regarding the stability of these types of materials than there have been regarding quasi-0D nanodiamond [85], leaving many important questions largely unresolved.

The stability of dehydrogenated $\{111\}$ surfaces on diamond nanowires has been considered by Barnard et al. [178] using two dehydrogenated nanowire morphologies with octahedral and cuboctahedral lateral forms. The computational technique used in this study is the same outlined above in the complementary study of diamond nanocrystals. Three octahedral nanowire structures were examined, bounded by $\{111\}$ surfaces in all lateral directions (with a rhombohedral cross section) and a principal axis in the $[110]$ direction. A very unusual relaxation was observed in these structures, involving the formation of three-membered rings at the acute edges. This was attributed to the formation of dimers in the $[100]$ direction (denoted as “[100]-dimers”) just below the acute nanowire edges, even in the absence of a $\{100\}$ surface facet [178]. The “larger” of the structures, measuring 0.69 nm and 0.90 nm in diameter, exhibited exfoliation of the $\{111\}$ surfaces to form nanotubular cages in addition to the formation of the unusual three-membered rings and $[100]$ -dimers. The nanotubular cages were oriented parallel to the nanowire principle axis, with chiral structure identical to that of an armchair carbon nanotube. They remained attached to the inner diamond-structured core of the nanowire at the $[100]$ -dimers and at the opposing corner [178].

Three cuboctahedral diamond nanowires were also examined, bounded by two $\{100\}$ surfaces and two $\{111\}$ surfaces in the lateral directions (with an almost circular cross section), and a principal axis in the $[110]$ direction. In each case, the first step of the relaxation involved reconstruction of the $\{100\}$ surfaces to the (2×1) structure, followed by the exfoliation of the $\{111\}$ surfaces. In the case of the smallest 0.42 nm cuboctahedral nanowire, this resulted in the entire nanowire transforming into a “nonclassical” nanotube, with the core atoms forming a sp -bonded linear chain along the axis. The authors denoted the final 0.42 nm cuboctahedral structure as a nonclassical nanotube, as the armchair structured sections (formed by the exfoliation of the $\{111\}$ surface) are separated by rows of eight-membered and five-membered rings, which are not present in classical nanotubes.

Similarly the $\{111\}$ surfaces of the larger 0.63 nm and 0.83 nm cuboctahedral nanowires were found to exfoliate following the $\{100\}$ reconstruction, forming nanotubular cages running the length of the nanowires (parallel to the principal axis). In these cases, however, the nanotubular cages remained bound to the inner core atoms at the $\{100\}$ (2×1) surfaces [178].

The structures resulting from this study, characterized by (armchair) nanotubular cages along the surface, and diamond-like cores, were denoted as “bucky-wires” (as they represented the 1D analog of the bucky-diamonds) [178]. The authors point out, however, that surface hydrogenation has a similar stabilizing effect on bucky-wires, eliminating the nanotubular cages [178]. An example is shown in Figure 1.14.

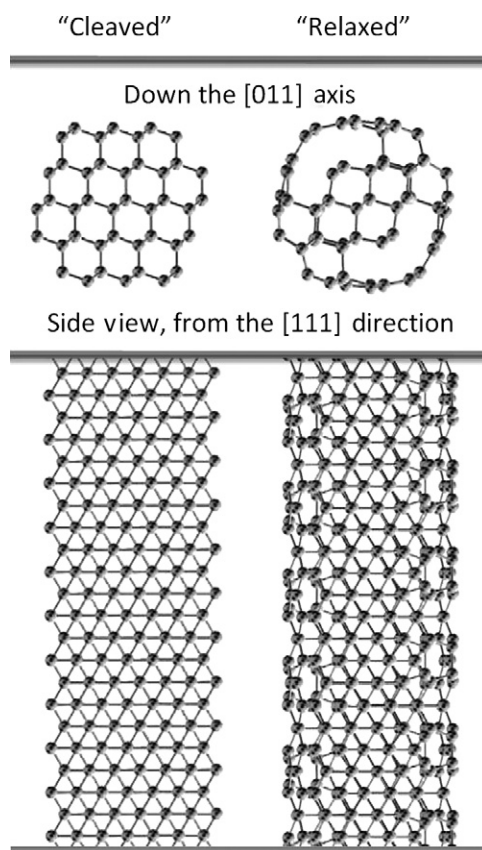


FIGURE 1.14

Example of unstable dehydrogenated diamond nanowires of Barnard et al. [178] with cuboctahedral morphology, showing the initial “cleaved” (bulk-like) configuration (left) and final “relaxed” (nanowire) configuration (right). The top images are viewed down the principle axis and the bottom images are perpendicular to the principle axis in the $[111]$ direction.

Source: Courtesy of Professor Ian. K. Snook (2004).

One-dimensional carbon nanostructures with a stable sp^3 -bonded core were first suggested by Menon et al. [179] who used a generalized tight-binding molecular dynamics scheme to study quasi-1D carbon nanorods. The structures proposed in this study consisted of fourfold coordinated atoms along the core and threefold coordinated atoms at the surface. The authors concluded that the fourfold coordinated (sp^3) atoms at the core were necessary to ensure structural stability following relaxation [179].

However, it has been found that (like diamond nanocrystals) clean surfaces on diamond nanowires or nanorods may be stable, given the appropriate orientation. In addition to the octahedral and cuboctahedral nanowires, Barnard et al. [180,181] also examined dehydrogenated nanowire morphologies characterized by dodecahedral and cubo-dodecahedral forms. The dodecahedral nanowires were bounded by $\{110\}$ surfaces in all lateral directions, with a square cross section and $[100]$ principal axis. One cubo-dodecahedral group (termed “cubic”) was bounded by two $\{100\}$ surfaces and two $\{110\}$ surfaces, with a square/rectangular cross section and a $[110]$ principal axis. The other cubo-dodecahedral group (termed “cylindrical”) was bounded by four $\{100\}$ surfaces and four $\{110\}$ surfaces, with an approximately circular cross section and a $[100]$ principal axis.

In the case of the dodecahedral nanowires, a mild contraction of the outermost atomic layer was reported, causing the $\{110\}$ surfaces of the nanowires to become slightly convex in shape [180]. In the case of the cubic nanowires, each structure underwent a two-stage relaxation involving the reconstruction of the $\{100\}$ surfaces to form the (2×1) surface structure, followed by further relaxation of the entire nanowire. Although the relaxation of the smallest cubic diamond nanowire (with a diameter of ~ 0.5 nm) resulted in a nonclassical SWNT (a transition that involved the dissociation of dicarbon molecules from the surface), the tetrahedral sp^3 structure was preserved throughout the “larger” 0.60 and 0.81 nm cubic nanowires, with (2×1) surface dimers comparable to bulk-diamond surfaces [182]. Finally, the relaxation of the three cylindrical nanowires also involved the reconstruction of the $\{100\}$ surfaces to form the (2×1) surface structure, followed by further relaxation of the entire nanowire. In this case, the authors described the final relaxed cylindrical nanowires as twisted rope-like structures, resulting from the (2×1) surface reconstruction and significant contraction of the outermost atomic layer [180].

Hence (with the exception of the smallest cubic nanowire), the diamond structure was preserved in all of the dodecahedral and cubo-dodecahedral nanowires upon relaxation. None of the surfaces exfoliated as observed in the octahedral and cuboctahedral diamond nanowires. Overall, the relative stability was found to be dependent on both the surface morphology and the crystallographic direction of the principal axis, and dodecahedral nanowires (with $[100]$ axes) were identified as the most structurally stable among all the nanowires considered [177].

It has also been shown by Shenderova et al. [183] that diamond nanowires with $[100]$ principal axes show increased structural stability and enhanced mechanical properties. The mechanical properties of SWNTs and multi-walled nanotubes (MWNTs) were compared to equivalent diamond nanowires with principal axes

oriented in the [111], [110], or [100] directions. The study found that at small diameters, SWNTs are stronger than nanowires because of the superior strength of single bonds in graphene over those in diamond. However, as the diameter increases, the load-bearing area increases linearly for SWNTs and as the square of the diameter for nanowires, leading to a larger fracture force for diamond nanowires above a critical diameter of ~ 1 nm to ~ 3 nm (depending on the direction of the axis) [183].

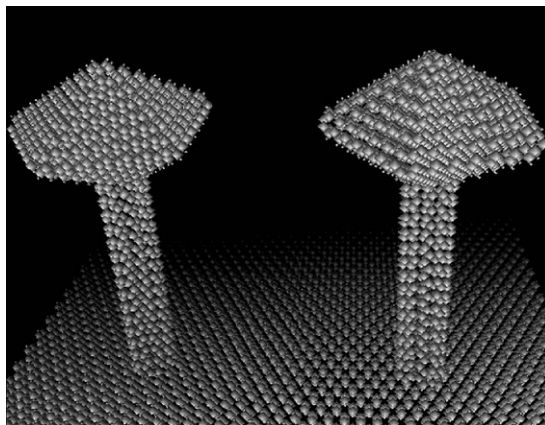
It was also found that with equal fracture force, the weight ratio nanowire/SWNT was a constant 1.47. However, with the requirement of equal weight, the ratio of related fracture forces of nanowire/SWNT was found to be 0.68, indicating that at larger diameters, nanowires are stronger but at the cost of a lower strength-to-weight ratio. The stiffness of diamond nanowires and SWNTs was also compared, using a relation for total force strain. A “nanostructure stiffness constant” was introduced as a coefficient of proportionality between the applied force and elongation, which was dependent on the diameter of the nanorod (or nanotube). By comparing this stiffness constant as a function of diameter, diamond nanowires were found to be stiffer than SWNTs at diameters exceeding ~ 1 nm. The study therefore concluded that diamond nanowires are mechanically viable nanostructures [183].

1.7.2 Hybrid 1D structures

Hybrid nanomaterials that couple nanodiamond and sp^2 -bonded nanocarbon are an attractive prospect for many applications. Currently there are two main synthesis routes in this direction, either the controlled, partial transformation of one phase of nanocarbon into another (as described above) or the consecutive growth or fabrication of respective phases to form one nanostructure. Such hybrid nanocarbon materials may be formed via the growth of carbon nanotubes onto nanodiamond or nanodiamond thin films, or the growth of nanodiamond onto carbon nanotubes. Although such materials are now being produced, the stability of such materials is largely unexplored.

The first study was undertaken by Shenderova et al. [184,185], who used many-body classic potential and environment-dependent self-consistent tight-binding approaches to examine the feasibility of designing composite architectures of nanodiamond and carbon nanotubes. Geometric considerations combined with detailed atomistic simulations were used to investigate the bonding and stability of general classes of diamond/carbon nanotube interface structures with low residual stresses and no unsatisfied bonding [184,185].

The hybrid nanocarbon structures under consideration were formed by bonding carbon nanotubes onto diamond substrates, bonding nanodiamond particles onto the ends of nanotubes, or both as shown in Figure 1.15. It was shown that, depending on nanotube size and morphology, certain chiralities of open nanotubes may be bonded with different facets of diamond particles or different orientations of diamond surfaces. Particular combinations of nanotubes and diamond surfaces were shown to form chemically and mechanically stable interfaces, since the significant lattice mismatches between a diamond surface and a nanotube may be accommodated due to

**FIGURE 1.15**

Schematic of two “mushroom” nanodiamond–nanotube hybrid structures, formed by attaching a pentagonal nanodiamond to the top of carbon nanotubes bound to a diamond surface.

Source: Courtesy of O. A. Shenderova (2005).

the high radial flexibility of carbon nanotubes. Possible applications of these systems include use as arrays of field emitters and as nanoscale diodes [184].

Another study undertaken by Barnard et al. [186] used *ab initio* simulations to investigate the role of atomic hydrogen in creating localized sp^3 hybridized defects on the outer wall of carbon nanotubes. The aim of the study was to elucidate the initial stages of nucleation in the formation of hybrid materials comprising SWNTs coated with faceted diamond nanocrystals all over the outer walls [187]. The results illustrate that certain absorption configurations of hydrogen may produce H-induced defects containing dangling carbon bonds. Such sites were then shown to be favorable adsorption sites for carbon adsorbates (lower in energy than for pristine sites away from the H-induced defect) [186]. Although a number of important problems remain to be addressed to fully understand the formation and growth of hybrid carbon nanomaterials (such as the kinetic processes at the surface and the structure at the nanotube–nanodiamond interface), these studies address some aspects that are critical to understanding the formation of more complicated carbon nanostructures.

1.8 Conclusions

The theoretical and computational studies outlined above have focused on the phase transitions between nanodiamond and graphitic and fullerenic forms of nanocarbon. Computationally, these transitions are well represented by quantum mechanical methods, and the transformations have been modeled using a variety of particle geometries and sizes.

The numerous analytical theories (the majority of which use thermodynamic arguments) appear to agree as to the upper limit of nanodiamond phase stability. These theories predict nanodiamond to be the stable phase of carbon in the range less than $\sim 5\text{--}6\text{ nm}$. The lower limit of nanodiamond stability has also been estimated to be $\sim 1.4\text{ nm}$ to $\sim 2.2\text{ nm}$ (again using a thermodynamic approach), along with the phase coexistence of nanodiamond and fullerene carbon at this lower limit, via the formation of bucky-diamonds. It is important to note that this range for nanodiamond stability does not by any means represent the only size regime in which nanocrystalline diamond may be formed; it simply indicates that outside of this range, the nanodiamonds will be metastable with respect to a transformation to graphitic or fullerene phases. Further, the identification of a coexistence region indicates that the phase transitions are not entirely thermodynamically driven, and that other factors such as surface energies, surface stress, and charge, as well as kinetic considerations, may be instrumental in inducing a change of phase. Therefore, a complete examination of nanocarbon phase stability should include not only the use of a sophisticated computational method and large particle sizes, but also theoretical terms to describe dependencies on a variety of experimentally relevant nanoparticle properties.

One such property, fundamental to the stability of nanodiamond, is the degree of surface passivation. The question of whether (experimentally) particulate nanodiamond can be expected to have passivated (and, hence, sp^3 -bonded) surfaces, or sp^2 -bonded “bucky” surfaces under ambient conditions, is currently unresolved. Theoretically it was shown by Raty and Galli [60] that a small bucky-diamond may be lower in energy than a hydrogenated nanodiamond, since the sp^2 fullerene shell is lower in energy than a hydrogenated diamond surface. Unfortunately, this study did not adequately account for the difference in chemical potential between “core” atoms and the reconstructed “bucky” surface atoms, and (according to the authors) is applicable to CVD synthesis conditions (far from equilibrium) [60]. However, working on the assumption that bucky-diamonds are energetically preferred, we are confronted with the computational studies that clearly show that suitably passivated nanodiamond surfaces are stable under ambient conditions.

Therefore, until a more rigorous study can be undertaken, we must proceed with the assumptions that (experimentally) most small nanodiamonds are in fact bucky-diamonds, but if purified properly (with the shell of a bucky-diamond completely removed) and the clean diamond surfaces are then suitably passivated or functionalized, they should remain that way until significantly perturbed.

Acknowledgments

This project has been supported by the Australian Research Council under grant number DP0986752. He would like to greatly acknowledge Ian Snook from RMIT University (Australia), Lin Lai from CSIRO (Australia), and O.A. Shenderova from the International Technology Center (USA).

References

- [1] D.A. Young, *Phase Diagrams of the Elements*, University of California Press, Berkeley, 1991.
- [2] R.C. De Vries, Synthesis of diamond under metastable conditions, *Annu. Rev. Mater. Sci.* 17 (1987) 161.
- [3] S. Prawer, D.N. Jamieson, R. Kalish, Investigation of carbon near the graphite–diamond–liquid triple point, *Phys. Rev. Lett.* 69 (1992) 2991.
- [4] J.B. Wang, G.W. Yang, Phase transformation between diamond and graphite in preparation of diamonds by pulsed-laser induced liquid–solid interface reaction, *J. Phys. Condens. Matter.* 11 (1999) 7089.
- [5] R. Berman, F.E. Simon, The graphite diamond equilibrium, *Z. Elektrochem.* 55 (1955) 333.
- [6] M. van Thiel, F.H. Ree, High-pressure liquid–liquid phase change in carbon, *Phys. Rev. B* 48 (1993) 3591.
- [7] L.E. Fried, W.M. Howard, Explicit Gibbs free energy equation of state applied to the carbon phase diagram, *Phys. Rev. B* 61 (2000) 8734.
- [8] W.J. Nellis, A.C. Mitchell, A.K. McMahan, Carbon at pressures in the range 0.1–1 TPa (10 Mbar), *J. Appl. Phys.* 90 (2001) 696.
- [9] R. Grover, Does diamond melt?, *J. Chem. Phys.* 71 (1979) 3824.
- [10] T. Sekine, Six-fold coordinated carbon as a postdiamond phase, *Appl. Phys. Lett.* 74 (1999) 350.
- [11] S. Scandolo, G.L. Chiarotti, E. Tosatti, SC4: a metallic phase of carbon at terapascal pressures, *Phys. Rev. B* 53 (1996) 5051.
- [12] J.V. Badding, T.J. Scheideman, FLAPW investigation of the stability and equation of state of rectangulated carbon, *Solid State Commun.* 122 (2002) 473.
- [13] M.T. Yin, Si-III (BC-8) crystal phase of Si and C: structural properties, phase stabilities, and phase transitions, *Phys. Rev. B* 30 (1984) 1773.
- [14] R. Biswas, R.M. Martin, R.J. Needs, O.H. Nielsen, Complex tetrahedral structures of silicon and carbon under pressure, *Phys. Rev. B* 30 (1984) 3210.
- [15] G. Galli, R.M. Martin, R. Carr, M. Parrinello, Structural and electronic properties of amorphous carbon, *Phys. Rev. Lett.* 62 (1989) 555.
- [16] M.P. Grumback, R.M. Martin, Phase diagram of carbon at high pressure: analogy to silicon, *Solid State Commun.* 100 (1996) 61.
- [17] W.H. Gust, Phase transitions and shock-compression parameters to 120 GPa for three types of graphite and for amorphous carbon, *Phys. Rev. B* 22 (1980) 4744.
- [18] F.P. Bundy, W.A. Bassett, M.S. Weathers, R.J. Hemley, H.K. Mao, A.F. Goncharov, The pressure–temperature phase and transformation diagram for carbon; updated through 1994, *Carbon* 34 (1996) 141.
- [19] E.G. Rakov, Calculation of diamond chemical vapor deposition region in C–H–O phase diagram, *Appl. Phys. Lett.* 69 (1996) 2370.
- [20] J.-T. Wang, Y.-Z. Wang, Z.-J. Liu, H. Wang, D.W. Zhang, Z.-Q. Huang, Phase diagrams for activated CVD diamond growth, *Mater. Lett.* 33 (1998) 311.
- [21] Y.-Z. Wan, H.-S. Shen, Z.-M. Zhang, X.-C. He, Ternary C–H–halogen phase diagram for CVD diamond, *Mater. Chem. Phys.* 63 (2000) 88.
- [22] Z.-J. Liu, D.W. Zhang, P.-F. Wang, S.-J. Ding, J.-Y. Zhang, J.-T. Wang, et al., Projective phase diagrams for CVD diamond growth from C–H and C–H–O systems, *Thin Solid Films* 368 (2000) 253.

- [23] F.H. Ree, Systematics of high-pressure and high-temperature behavior of hydrocarbons, *J. Chem. Phys.* 70 (1979) 974.
- [24] M. Zaiser, Y. Lyutovich, F. Banhart, Irradiation-induced transformation of graphite to diamond: a quantitative study, *Phys. Rev. B* 62 (2000) 3058.
- [25] F. Banhart, Structural transformations in carbon nanoparticles induced by electron irradiation, *Phys. Solid State* 44 (2002) 399.
- [26] A. Potemkin, V. Poliakov, The effect of metal-solvent properties on the alteration of specific zones on a carbon phase diagram, *Diamond Relat. Mater.* 10 (2001) 1597.
- [27] A.S. Barnard, Theory and modeling of nanocarbon phase stability, *Diamond Relat. Mater.* 15 (2006) 285.
- [28] F. Charlet, M.-L. Turkel, J.-F. Danel, L. Kazandjian, Evaluation of various theoretical equations of state used in calculation of detonation properties, *J. Appl. Phys.* 84 (1998) 4227.
- [29] F.H. Ree, N.W. Winter, J.N. Glosli, J.A. Viecelli, Kinetics and thermodynamic behavior of carbon clusters under high pressure and high temperature, *Physica. B* 265 (1999) 223.
- [30] J.A. Viecelli, F.H. Ree, Carbon particle phase transformation kinetics in detonation waves, *J. Appl. Phys.* 88 (2000) 683.
- [31] J.A. Viecelli, S. Bastea, J.N. Glosli, F.H. Ree, Phase transformations of nanometer size carbon particles in shocked hydrocarbons and explosives, *J. Chem. Phys.* 115 (2001) 2730.
- [32] A.L. Verechshagin, Phase diagram of ultrafine diamond, *Combust. Exp. Shock Waves* 38 (2002) 358.
- [33] A.M. Staver, N.M. Gubareva, A.I. Lyamkin, E.A. Petrov, Ultrafine diamond powders made by the use of explosion energy, *Fiz. Goreniya Vzriva* 20 (1984) 440.
- [34] O.A. Shenderova, V.V. Zhirnov, D.W. Brenner, Carbon nanostructures, *Crit. Rev. Solid State Mater. Sci.* 27 (2002) 227.
- [35] V.V. Danilenko, Features of carbon condensation in a detonation wave and the conditions for optimal synthesis of nanodiamond, *J. Superhard Mater.* 28 (2006) 7.
- [36] C.C. Yang, S. Li, Size-dependent temperature–pressure phase diagram of carbon, *J. Phys. Chem. C* 112 (2008) 1423.
- [37] V.L. Kuznetsov, A.L. Chuvilin, Yu. V. Butenko, I. Yu. Mal'kov, A.K. Gutakovskii, S.V. Stankus, et al., Science and technology of fullerene materials, in: P. Bernuer et al. (Eds.), *MRS Proceedings* 359, Pittsburgh, PA, 1995, p. 105.
- [38] B. Sundqvist, Buckyballs under pressure, *Phys. Status Solidi B* 223 (2001) 469.
- [39] M.V. Korobov, V.M. Senyavin, A.G. Bogachev, E.B. Stukalin, V.A. Davydov, L.S. Kashevarova, et al., Phase transformations in pressure polymerized C60, *Chem. Phys. Lett.* 381 (2003) 410.
- [40] E. Schöll-Paschinger, G. Kahl, Accurate determination of the phase diagrams of model fullerenes, *Europhys. Lett.* 63 (2003) 538.
- [41] M.H.F. Sluiter, Y. Kawazoe, Phase diagram of single-wall carbon nanotube crystals under hydrostatic pressure, *Phys. Rev. B* 69 (2004) 224111.
- [42] J. González, J.V. Alvarez, Phase diagram of carbon nanotube ropes, *Phys. Rev. B* 70 (2004) 045410.
- [43] J. Reiser, E. McGregor, J. Jones, R. Enick, G. Holder, Adamantane and diamantane: phase diagrams, solubilities and rates of dissolution, *Fluid Phase Equilib.* 117 (1996) 160.
- [44] J.E. Dahl, S.G. Liu, R.M.K. Carlson, Isolation and structure of higher diamondoid, nanometer-sized diamond molecules, *Science* 299 (2003) 96.

- [45] A.S. Barnard, S. Russo, I.K. Snook, Modeling of stability and phase transformations in 0 and 1 dimensional nanocarbon systems, in: M. Rieth, W. Schommers (Eds.), Handbook of Theoretical and Computational Nanotechnology, American Scientific Publishers, Stevenson Ranch, CA, 2005.
- [46] P. Harris, Carbon Nanotubes and Related Structures, Cambridge University Press, Cambridge, 1999.
- [47] D. Tománek, M.A. Schluter, Growth regimes of carbon clusters, Phys. Rev. Lett. 67 (1991) 2331.
- [48] R.O. Jones, Density functional study of carbon clusters C_2n ($2 < n < 16$). I. Structure and bonding in the neutral clusters, J. Chem. Phys. 110 (1999) 5189.
- [49] J.L. Martins, F.A. Reuse, S.N. Khanna, Growth and formation of fullerene clusters, J. Cluster Sci. 12 (2001) 513.
- [50] P.R.C. Kent, M.D. Towler, R.J. Needs, G. Rajagopal, Carbon clusters near the cross-over to fullerene stability, Phys. Rev. B 62 (2000) 15394.
- [51] N.W. Winter, F.H. Ree, Carbon particle phase stability as a function of size, J. Comput. Aided Mater. Des. 5 (1998) 279.
- [52] V.L. Kuznetsov, I.L. Zilberberg, Y.V. Butenko, A.L. Chuvilin, B. Seagall, Theoretical study of the formation of closed curved graphite-like structures during annealing of diamond surface, J. Appl. Phys. 86 (1999) 863.
- [53] J.Y. Raty, G. Galli, C. Bostedt, T.W. van Buuren, L.J. Terminello, Quantum confinement and fullerene-like surface reconstructions in nanodiamonds, Phys. Rev. Lett. 90 (2003) 37402.
- [54] A.S. Barnard, S.P. Russo, I.K. Snook, *Ab initio* modelling of stability of nanodiamond morphologies, Philos. Mag. Lett. 83 (2003) 39.
- [55] A.S. Barnard, S.P. Russo, I.K. Snook, Structural relaxation and relative stability of nanodiamond morphologies, Diamond Relat. Mater. 12 (2003) 1867.
- [56] A.S. Barnard, S.P. Russo, I.K. Snook, First principles investigations of diamond ultrananocrystals, Int. J. Mod. Phys. B 17 (2003) 3865.
- [57] S.P. Russo, A.S. Barnard, I.K. Snook, Hydrogenation of nanodiamond surfaces: structure and effects on crystalline stability, Surf. Rev. Lett. 10 (2003) 233.
- [58] C. Wang, B. Zheng, W.T. Zheng, Q. Jiang, Electronic properties of dehydrogenated nanodiamonds: a first-principles study, Diamond Relat. Mater. 17 (2008) 204.
- [59] A.S. Barnard, M. Sternberg, Crystallinity and surface electrostatics in diamond nanoparticles, J. Mater. Chem. 17 (2007) 4811.
- [60] J.-Y. Raty, G. Galli, Ultradispersity of diamond at the nanoscale, Nat. Mater. 2 (2003) 792.
- [61] J. Almlöf, H.P. Lüthi, Theoretical methods and results for electronic structure calculations on very large systems, in: K.F. Jensen, D.G. Truhlar (Eds.), Supercomputer Research in Chemistry and Chemical Engineering, ACS Symposium Series, vol. 353, 1987, pp. 35–48.
- [62] M.S. Shaw, J.D. Johnson, Carbon clustering in detonations, J. Appl. Phys. 62 (1987) 2080.
- [63] P. Badziag, W.S. Veowoerd, W.P. Ellis, N.R. Greiner, Nanometresized diamonds are more stable than graphite, Nature 343 (1990) 244.
- [64] N.M. Hwang, J.H. Hahn, D.Y. Yoon, Chemical potential of carbon in the low pressure synthesis of diamond, J. Cryst. Growth 160 (1996) 87.
- [65] A.S. Barnard, S.P. Russo, I.K. Snook, Size dependent phase stability of carbon nanoparticles: nanodiamond versus fullerenes, J. Chem. Phys. 118 (2003) 5094.

- [66] M. Zaiser, F. Banhart, Radiation-induced transformation of graphite to diamond, *Phys. Rev. Lett.* 79 (1997) 3680.
- [67] Y.V. Butenko, V.L. Kuznetsov, A.L. Chuvilin, V.N. Kolomiichuk, S.V. Stankus, R.A. Khairulin, et al., The kinetics of the graphitization of dispersed diamonds at low temperatures, *J. Appl. Phys.* 88 (2000) 4380.
- [68] A.S. Barnard, S.P. Russo, I.K. Snook, Coexistence of bucky diamond with nanodiamond and fullerene carbon phases, *Phys. Rev. B* 68 (2003) 73406.
- [69] Y. Guo, I. Molecular simulations of buckyball fullerenes. II. Quantum chemistry studies on high-Tc superconductors. Ph.D. Thesis, California Institute of Technology, 1992.
- [70] F. Fugaciu, H. Hermann, G. Seifert, Concentric-shell fullerenes and diamond particles: a molecular-dynamics study, *Phys. Rev. B* 60 (1999) 10711.
- [71] G.-D. Lee, C.Z. Wang, J. Yu, E. Yoon, K.M. Ho, Heat-induced transformation of nanodiamond into a tube-shaped fullerene: a molecular dynamics simulation, *Phys. Rev. Lett.* 91 (2003) 265701.
- [72] M.Y. Gamarnik, Size-related stabilization of diamond nanoparticles, *Nanostruct. Mater.* 7 (1996) 651: Energetical preference of diamond nanoparticles, *Phys. Rev. B*, 54 (1996), 2150.
- [73] Q. Jiang, J.C. Li, G. Wilde, The size dependence of the diamond–graphite transition, *J. Phys. Condes. Matter.* 12 (2000) 5623.
- [74] D. Zhao, M. Zhao, Q. Jiang, Size and temperature dependence of nanodiamond–nanographite transition related with surface stress, *Diamond Relat. Mater.* 11 (2002) 234.
- [75] G. Jungnickel, D. Porezag, Th. Frauenheim, M.I. Heggie, W.R.L. Lambrecht, B. Segall, et al., Graphitization effects on diamond surfaces and the diamond/graphite interface, *Phys. Status Solidi (a)* 154 (1996) 109.
- [76] R. Astala, M. Kaukonen, R.M. Nieminen, G. Jungnickel, Th. Frauenheim, Simulations of diamond nucleation in carbon fullerene cores, *Phys. Rev. B* 63 (2001) 81402.
- [77] N.M. Hwang, J.H. Hahn, D.Y. Yoon, Charged cluster model in the low pressure synthesis of diamond, *J. Cryst. Growth* 162 (1996) 55.
- [78] H.N. Jang, N.M. Hwang, Theory of the charged cluster formation in the low pressure synthesis of diamond: Part II. Free energy function and thermodynamic stability, *J. Mater. Res.* 13 (1998) 3536.
- [79] A.S. Barnard, Self-assembly in nanodiamond agglutinates, *J. Mater. Chem.* 18 (2008) 4038.
- [80] E. Ōsawa, D. Ho, H. Huang, M.V. Korobov, N.N. Rozhkova, Consequences of strong and diverse electrostatic potential fields on the surface of detonation nanodiamond particles, *Diamond Relat. Mater.* 18 (2009) 904.
- [81] L.Y. Chang, E. Ōsawa, A.S. Barnard, Confirmation of the electrostatic self-assembly of nanodiamonds, *Nanoscale* 3 (2011) 958.
- [82] A.S. Barnard, I.K. Snook, Transformation of graphene into graphane in the absence of hydrogen, *Carbon* 48 (2010) 981.
- [83] A.S. Barnard, I.K. Snook, Size- and shape-dependence of the graphene to graphane transformation in the absence of hydrogen, *J. Mater. Chem.* 20 (2010) 10459.
- [84] A.S. Barnard, N.A. Marks, S.P. Russo, I.K. Snook, Hydrogen stabilization of {111} nanodiamond, *MRS Symposium Proceedings*, 740 (2003) 69.
- [85] A.S. Barnard, S.P. Russo, I.K. Snook, Modeling of stability and phase transformations in quasi-zero dimensional nanocarbon systems, *J. Comput. Theor. Nanosci.* 2 (2005) 180.
- [86] V.Y. Dolmatov, Detonation synthesis ultradispersed diamonds: properties and applications, *Russ. Chem. Rev.* 70 (2001) 607.

- [87] P.I. Belobrov, L.A. Bursill, K.I. Maslakov, A.P. Dementjev, Electron spectroscopy of nanodiamond surface states, *Appl. Surf. Sci.* 215 (2003) 169.
- [88] T. Jiang, K. Xu, FTIR study of ultradispersed diamond powder synthesised by explosive detonation, *Carbon* 33 (1995) 1663.
- [89] J.B. Donnet, E. Fousson, L. Delmotte, M. Samirant, C. Baras, T.K. Wang, et al., ^{13}C NMR characterization of nanodiamonds, *C. R. Acad. Sci., Ser. IIc Chim.* 3 (2000) 831.
- [90] A. Krueger, New carbon materials: biological applications of functionalized nanodiamond materials, *Chem. Eur. J.* 14 (2008) 1382.
- [91] O. Manelli, S. Corni, M.C. Righi, Water adsorption on native and hydrogenated diamond (001) surfaces, *J. Phys. Chem. C* 114 (2010) 7045.
- [92] D. Petrini, K. Larsson, Electron-transfer doping on a (001) surface of diamond: quantum mechanical study, *J. Phys. Chem. B* 109 (2005) 22426.
- [93] D. Petrini, K. Larsson, Electron transfer from a diamond (100) surface to an atmospheric water adlayer: a quantum mechanical study, *J. Phys. Chem. C* 111 (2007) 13804.
- [94] D. Petrini, K. Larsson, A theoretical approach to the energetic stability and geometry of hydrogen and oxygen terminated diamond (100) surfaces, *J. Phys. Chem. C* 111 (2007) 795.
- [95] D. Petrini, K. Larsson, Theoretical study of the thermodynamic and kinetic aspects of terminated (111) diamond surfaces, *J. Phys. Chem. C* 112 (2008) 3018.
- [96] D. Petrini, K. Larsson, Origin of the reactivity on the nonterminated (100), (110), and (111) diamond surfaces: an electronic structure DFT study, *J. Phys. Chem. C* 112 (2008) 14367.
- [97] S.J. Sque, R. Jones, P.R. Briddon, Structure, electronics, and interaction of hydrogen and oxygen on diamond surfaces, *Phys. Rev. B* 73 (2006) 085313.
- [98] L. Lai, A.S. Barnard, Modeling the thermostability of surface functionalisation by oxygen, hydroxyl, and water on nanodiamonds, *J. Mater. Chem.* 3 (2011) 2566.
- [99] Y. Liu, Z. Gu, J.L. Margrave, V.N. Khabashesku, Functionalization of nanoscale diamond powder: fluoro-, alkyl-, amino-, and amino acid-nanodiamond derivatives, *Chem. Mater.* 16 (2004) 3924.
- [100] W.S. Yeap, Y.Y. Tan, K.P. Loh, Using detonation nanodiamond for the specific capture of glycoproteins, *Anal. Chem.* 80 (2008) 4659.
- [101] S.A. Dahoumane, M.N. Nguyen, A. Thorel, J.-P. Boudou, M.M. Chehimi, C. Mangeney, Protein-functionalized hairy diamond nanoparticles, *Langmuir* 25 (2009) 9633.
- [102] L.-C.L. Huang, H.-C. Chang, Adsorption and immobilization of cytochrome C on nanodiamonds, *Langmuir* 20 (2004) 5879.
- [103] K.V. Purtov, A.I. Petunin, A.E. Burov, A.P. Puzyr, V. Bondar, Nanodiamonds as carriers for address delivery of biologically active substances, *Nanoscale Res. Lett.* 5 (2010) 631.
- [104] J.B. Miller, D.W. Brown, Photochemical modification of diamond surfaces, *Langmuir* 12 (1996) 5809.
- [105] J.B. Miller, Amines and thiols on diamond surfaces, *Surf. Sci.* 439 (1999) 21.
- [106] X.-Q. Zhang, M. Chen, R. Lam, X. Xu, E. Ōsawa, D. Ho, Polymer-functionalized nanodiamond platforms as vehicles for gene delivery, *ACS Nano*. 3 (2009) 2609.
- [107] L. Lai, A.S. Barnard, Stability of nanodiamond surfaces exposed to N, NH, and NH_2 , *J. Phys. Chem. C* 115 (2011) 6218.
- [108] K. Iakoubovskii, I. Kiflawi, K. Johnston, A. Collins, G. Davies, A. Stesmans, Annealing of vacancies and interstitials in diamond, *Physica. B* 340 (2003) 67.

- [109] A.T. Collins, A. Dahwich, The production of vacancies in type Ib diamond, *J. Phys. Condens. Matter.* 15 (2003) L591.
- [110] S. Dannefaer, W. Zhu, T. Bretagnon, D. Kerr, Vacancies in polycrystalline diamond films, *Phys. Rev. B* 53 (1996) 1979.
- [111] L. Allers, A. Mainwood, Surface vacancies in CVD diamond, *Diamond Relat. Mater.* 7 (1998) 261.
- [112] F. Jelezko, J. Wrachtrup, Single defect centres in diamond: a review, *Phys. Stat. Sol. (a)* 203 (2006) 3207.
- [113] A. Mainwood, Nitrogen and nitrogen-vacancy complexes and their formation in diamond, *Phys. Rev. B* 49 (1994) 7934.
- [114] X.J. Hu, Y.B. Dai, R.B. Li, H.S. Shen, X.C. He, Molecular dynamics simulation on boron diffusion in diamond, *Solid State Commun.* 122 (2002) 45.
- [115] R.Q. Hood, P.R.C. Kent, R.J. Needs, P.R. Briddon, Quantum Monte Carlo study of the optical and diffusive properties of the vacancy defect in diamond, *Phys. Rev. Lett.* 91 (2003) 076403.
- [116] G. Davies, S.C. Lawson, A.T. Collins, A. Mainwood, S.J. Sharp, Vacancy-related centers in diamond, *Phys. Rev. B* 46 (1992) 13157.
- [117] D.C. Hunt, D.J. Twitchen, M.E. Newton, J.M. Baker, J.K. Kirui, J.A. van Wyk, et al., EPR data on the self-interstitial complex O_3 in diamond, *Phys. Rev. B* 62 (2000) 6587.
- [118] A.S. Barnard, M. Sternberg, Vacancy induced structural changes in diamond nanoparticles, *J. Comput. Theo. Nanosci.* 5 (2008) 2089.
- [119] G. Post, V.Y. Dolmatov, V.A. Marchukov, V.G. Sushchev, M.V. Veretennikova, A.E. Sal'ko, Industrial synthesis of ultradisperse detonation diamond and some fields of their use, *Rus. J. Appl. Chem.* 75 (2002) 755.
- [120] A.E. Aleksenski, V.Y. Osipov, A.Y. Vul', B.Y. Ber, A.B. Smirnov, V.G. Melekhin, et al., Optical properties of nanodiamond layers, *Phys. Solid State* 3 (2001) 145.
- [121] A.S. Barnard, M. Sternberg, Substitutional nitrogen in nanodiamond and bucky-diamond particles, *J. Phys. Chem. B* 109 (2005) 17107.
- [122] A.S. Barnard, M. Sternberg, Mapping the location of nitrogen in diamond nanoparticles, *Nanotech* 18 (2007) 025702.
- [123] S.A. Kajihara, A. Antonelli, J. Bernholc, R. Car, Nitrogen and potential *n*-type dopants in diamond, *Phys. Rev. Lett.* 66 (1991) 2010.
- [124] S.A. Kajihara, A. Antonelli, J. Bernholc, Impurity incorporation and doping of diamond, *Physica. B* 185 (1993) 144.
- [125] J.P. Goss, P.R. Briddon, R. Jones, S. Öberg, The lattice location of Ni in diamond: a theoretical study, *J. Phys. Condens. Matter.* 16 (2004) 4567.
- [126] V.S. Vavilov, Possibilities and limitations of ion implantation in diamond, and comparison with other doping methods, *Physics–Uspekhi* 37 (1994) 407.
- [127] V.S. Vavilov, Diamond in solid state electronics, *Physics–Uspekhi* 40 (1997) 15.
- [128] D. Saada, J. Adler, R. Kalish, Sulfur: a potential dopant for *n*-type diamond, *Appl. Phys. Lett.* 77 (2000) 878.
- [129] L.G. Wang, A. Zunger, Phosphorus and sulphur doping of diamond, *Phys. Rev. B* 66 (2002) 161202.
- [130] T. Miyazaki, H. Okushi, Theoretical modeling of sulfur–hydrogen complexes in diamond, *Diamond Relat. Mater.* 11 (2002) 323.
- [131] R. Jones, S. Öberg, Structure and dynamics of substitutional phosphorus in diamond, *Phil. Mag. Lett.* 64 (1991) 317.

- [132] E. Gheeraert, S. Koizumi, T. Teraji, H. Kanda, M. Nesladek, Electronic states of boron and phosphorus in diamond, *Phys. State Solid (a)* 174 (1999) 39.
- [133] E. Gheeraert, S. Koizumi, T. Teraji, H. Kanda, M. Nesladek, Electronic states of phosphorus in diamond, *Diamond Relat. Mater.* 2 (2000) 948.
- [134] E. Gheeraert, N. Casanova, S. Koizumi, T. Teraji, H. Kanda, *n*-Type doping of diamond by sulfur and phosphorus, *Diamond Relat. Mater.* 20 (2001) 444.
- [135] R. Kalish, The search for donors in diamond, *Diamond Relat. Mater.* 10 (2001) 1749.
- [136] G. Popovici, T. Sung, M.A. Prelas, Forced diffusion in diamond: a review, *J. Chem. Vapour. Depos.* 3 (1994) 115.
- [137] J.F. Prins, The nature of radiation damage in diamond: activation of oxygen donors, *Diamond Relat. Mater.* 9 (2000) 1275.
- [138] M. Allon-Alaluf, N. Croitoru, Nitrogen and iodine doping in amorphous diamond-like carbon films, *Diamond Relat. Mater.* 6 (1997) 555.
- [139] R. Kalish, Doping of diamond, *Carbon* 37 (1999) 781.
- [140] G. Popovici, R.G. Wilson, T. Sung, M.A. Prelas, S. Khasawinah, Diffusion of boron, lithium, oxygen, hydrogen, and nitrogen in Ila type natural diamond, *J. Appl. Phys.* 77 (1995) 5103.
- [141] J. Chevallier, A. Lussou, D. Ballutaud, B. Theys, F. Jomard, A. Deneuve, et al., Hydrogen-acceptor interactions in diamond, *Diamond Relat. Mater.* 10 (2001) 399.
- [142] S. Sattel, J. Robertson, Z. Tass, M. Scheib, D. Wiescher, H. Ehrhardt, Formation of nanocrystalline diamond by hydrocarbon plasma beam deposition, *Diamond Relat. Mater.* 6 (1997) 255.
- [143] D.M. Gruen, Ultrananocrystalline diamond films from fullerene precursors, *Annu. Rev. Mater. Sci.* 29 (1999) 211.
- [144] S.S. Proffitt, S.J. Probert, M.D. Whitfield, J.S. Foord, R.B. Jackman, Growth of nanocrystalline diamond films for low field electron emission, *Diamond Relat. Mater.* 8 (1999) 768.
- [145] T. Sharda, T. Soga, T. Jimbo, M. Umeno, Growth of nanocrystalline diamond films by biased enhanced microwave plasma chemical vapor deposition, *Diamond Relat. Mater.* 10 (2001) 1592.
- [146] T. Sharda, T. Soga, A different regime of nanostructured diamond film growth, *J. Nanosci. Nanotech.* 3 (2003) 521.
- [147] T. Wang, H.W. Xin, Z.M. Zhang, Y.B. Dai, H.S. Shen, The fabrication of nanocrystalline diamond films using hot filament CVD, *Diamond Relat. Mater.* 13 (2004) 6.
- [148] J.E. Yater, A. Shih, J.E. Butler, P.E. Pehrsson, Effect of material properties on low-energy electron transmission in thin chemical-vapor deposited diamond films, *J. Appl. Phys.* 93 (2003) 3082.
- [149] J.E. Yater, A. Shih, J.E. Butler, P.E. Pehrsson, Electron transport mechanisms in thin boron-doped diamond films, *J. Appl. Phys.* 96 (2004) 446.
- [150] G.W. Muna, N. Tasheva, G.M. Swain, Electrooxidation and amperometric detection of chlorinated phenols at boron-doped diamond electrodes: a comparison of microcrystalline and nanocrystalline thin films, *Env. Sci. Tech.* 38 (2004) 3674.
- [151] Y. Show, M.A. Witek, P. Sonthalia, G.M. Swain, Characterization and electrochemical responsiveness of boron-doped nanocrystalline diamond thin-film electrodes, *Chem. Mater.* 15 (2003) 879.
- [152] A.S. Barnard, M. Sternberg, Substitutional boron in nanodiamond, bucky-diamond and nanocrystalline diamond grain boundaries, *J. Phys. Chem. B* 110 (2006) 19307.

- [153] A.S. Barnard, S.P. Russo, I.K. Snook, Simulation and bonding of dopants in nanocrystalline diamond, *J. Nanosci. Nanotech.* 5 (2005) 1395.
- [154] K. Jackson, E. Kaxiras, M.R. Pederson, Electronic states of group-IV endohedral atoms in C₂₈, *Phys. Rev. B* 48 (1993) 17556.
- [155] A.S. Barnard, S.P. Russo, I.K. Snook, Ab initio modelling of B and N in C₂₉ and C₂₉H₂₄ nanodiamond, *J. Chem. Phys.* 118 (2003) 10725.
- [156] A.S. Barnard, S.P. Russo, I.K. Snook, First principles modelling of dopants in C₂₉ and C₂₉H₂₄ nanodiamond, *J. Phys. Chem. B* 109 (2005) 11991.
- [157] K. Jackson, E. Kaxiras, M.R. Pederson, Bonding of endohedral atoms in small carbon fullerenes, *J. Phys. Chem.* 98 (1994) 7805.
- [158] Y.N. Makurin, A.A. Sofronov, A.I. Gusev, A.L. Ivanovsky, Electronic structure and chemical stabilization of C₂₈ fullerene, *Chem. Phys. Lett.* 270 (2001) 293.
- [159] M.R. Pederson, N. Laouini, Covalent container compound: empty, endohedral, and exohedral C₂₈ complexes, *Phys. Rev. B* 48 (1993) 2733.
- [160] A.S. Barnard, Diamond standard in diagnostics: nanodiamond biolabels make their mark, *Analyst* 134 (2009) 1751.
- [161] A.T. Collins, G. Davies, H. Kanda, G.S. Woods, Spectroscopic studies of carbon-13 synthetic diamond, *J. Phys. C* 21 (1988) 1363.
- [162] J.R. Rabeau, A. Stacey, A. Rabeau, S. Praver, F. Jelezko, I. Mirza, et al., Single nitrogen vacancy centers in chemical vapor deposited diamond nanocrystals, *Nano. Lett.* 7 (2007) 3433.
- [163] K. Iakoubovskii, G.J. Adriaenssens, Trapping of vacancies by defects in diamond, *J. Phys. Condens. Matter* 13 (2001) 6015.
- [164] Y.-R. Chang, H.-Y. Lee, K. Chen, C.-C. Chang, D.-S. Tsai, C.-C. Fu, et al., Mass production and dynamic imaging of fluorescent nanodiamonds, *Nat. Nanotech.* 3 (2008) 284.
- [165] B.R. Smith, D. Inglis, B. Sandnes, J.R. Rabeau, A.V. Zvyagin, D. Gruber, et al., Lighting up 5-nm monocrystalline nanodiamond with luminescent nitrogen-vacancy defect centers, *Small* 5 (2009) 1649.
- [166] J. Tisler, G. Balasubramanian, B. Naydenov, R. Kolesov, B. Grotz, R. Reuter, et al., Fluorescence and spin properties of defects in single digit nanodiamonds, *ACS Nano.* 3 (2009) 1959.
- [167] C. Bradac, T. Gaebel, N. Naidoo, J.R. Rabeau, A.S. Barnard, Prediction and measurement of the size-dependent stability of fluorescence in diamond over the entire nanoscale, *Nano. Lett.* 9 (2009) 3555.
- [168] A.S. Barnard, M. Sternberg, Can we predict the location of impurities in diamond nanoparticles?, *Diamond Relat. Mater.* 16 (2007) 2078.
- [169] S. Turner, O.I. Lebedev, O. Shenderova, I.I. Vlasov, J. Verbeeck, G. Van Tendeloo, Determination of size, morphology, and nitrogen impurity location in treated detonation nanodiamond by transmission electron microscopy, *Adv. Funct. Mater.* 19 (2009) 2116.
- [170] C. Bradac, T. Gaebel, N.N. Naidoo, M.J. Sellars, J. Twamley, L. Brown, et al., Observation and control of blinking nitrogen vacancy centres in discrete nanodiamonds, *Nat. Nanotechnol.* 5 (2010) 345.
- [171] V.V. Danilenko, On the history of detonation nanodiamond discovery, *Phys. Solid State* 6 (2004) 595.
- [172] I.I. Vlasov, A.S. Barnard, V.G. Ralchenko, O.I. Lebedev, M.V. Kanzuba, A.V. Saveliev, et al., Nanodiamond photo emitters based on strong luminescence from silicon-vacancy defects, *Adv. Mater.* 21 (2008) 808.

- [173] A.S. Barnard, I.I. Vlasov, V.G. Ralchenko, Predicting the distribution and stability of photoactive defect centers in nanodiamond biomarkers, *J. Mater. Chem.* 19 (2009) 360.
- [174] A.S. Barnard, I.K. Snook, Phase stability of nanocarbon in one-dimension: nanotubes versus diamond nanowires, *J. Chem. Phys.* 120 (2004) 3817.
- [175] S.B. Sinnott, R. Andrews, D. Qian, A.M. Rao, Z. Mao, E.C. Dickey, et al., Model of carbon nanotube growth through chemical vapor deposition, *Chem. Phys. Lett.* 315 (1999) 25.
- [176] S.V. Rotkin, R.A. Suris, Bond passivation model: diagram of carbon nanoparticle stability, *Phys. Lett. A* 261 (1999) 98.
- [177] A.S. Barnard, Structural properties of diamond nanowires: theoretical predications and experimental progress, *Rev. Adv. Mater. Sci.* 6 (2004) 94.
- [178] A.S. Barnard, S.P. Russo, I.K. Snook, Bucky-wires and the instability of diamond (111) surfaces in one-dimension, *J. Nanosci. Nanotech.* 4 (2004) 151.
- [179] M. Menon, E. Richter, P. Raghavan, K. Teranishi, Large-scale quantum mechanical simulations of carbon nanowires, *Superlattices Microstruct.* 27 (2000) 577.
- [180] A.S. Barnard, S.P. Russo, I.K. Snook, *Ab initio* modelling of diamond nanowire structures, *Nano. Lett.* 3 (2003) 1323.
- [181] A.S. Barnard, S.P. Russo, I.K. Snook, From nanodiamond to diamond nanowires: structural properties affected by dimension, *Philos. Mag.* 84 (2004) 899.
- [182] A.S. Barnard, S.P. Russo, I.K. Snook, Surface structure of cubic diamond nanowires, *Surf. Sci.* 538 (2003) 204.
- [183] O.A. Shenderova, D.W. Brenner, R.S. Ruoff, Would diamond nanorods be stronger than fullerene nanotubes?, *Nano. Lett.* 3 (2003) 805.
- [184] O.A. Shenderova, D. Areshkin, D.W. Brenner, Carbon based nanostructures: diamond clusters structured with nanotubes, *Mater. Res.* 6 (2002) 11.
- [185] O.A. Shenderova, D. Areshkin, D.W. Brenner, Bonding and stability of hybrid diamond/nanotube structures, *Mol. Simulat.* 29 (2003) 259.
- [186] A.S. Barnard, M.L. Terranova, M. Rossi, Density functional study of H-induced defects as nucleation sites in hybrid carbon nanomaterials, *Chem. Mater.* 17 (2005) 527.
- [187] M.L. Terranova, S. Orlanducci, A. Fiori, E. Tamburri, V. Sessa, M. Rossi, et al., Controlled evolution of carbon nanotubes coated by nanodiamond: the realization of a new class of hybrid nanomaterials, *Chem. Mater.* 17 (2005) 3214.

Advances in Plasma Synthesis of UNCD Films

2

Jes Asmussen^{a, b}, Timothy A. Grotjohn^a, and Thomas Schuelke^b

^aMichigan State University, Department of Electrical and Computer Engineering, East Lansing, MI,

^bFraunhofer USA, Center for Coatings and Laser Applications, East Lansing, MI

CHAPTER OUTLINE

2.1 Introduction and historical development of UNCD films.....	53
2.2 UNCD growth: theory, modeling, and diagnostics	55
2.2.1 Plasma discharge region	56
2.2.2 Species arriving at the growth surface	60
2.2.3 Growth at the surface: high renucleation rate for UNCD	62
2.3 Scaling up the MPACVD process: large-area UNCD synthesis	
using a floating substrate holder	63
2.3.1 Background	63
2.3.2 Experimental description and methodologies	64
2.3.3 Reactor operating road maps.....	68
2.3.4 Experimental procedures and results.....	70
2.4 Hot-filament CVD UNCD synthesis.....	75
2.4.1 First report and principle of HFCVD diamond synthesis.....	75
2.4.2 Scaling and current reactor technology.....	76
2.4.3 Nanocrystalline diamond versus UNCD	77
2.4.4 HFCVD (U)NCD synthesis	77
2.5 Summary	78
Acknowledgments.....	80
References	80

2.1 Introduction and historical development of UNCD films

Research activities concerned with the synthesis of nanocrystalline diamond (NCD) films, or what is now known as ultrananocrystalline diamond (UNCD) films, began at Argonne National Laboratory in the early 1990s with the pioneering experimental work of Gruen et al. [1–9]. The early experiments used fullerene vapors as the carbon source [1]. The fullerenes were injected into a hydrogen-poor and argon-rich plasma, such as a microwave discharge, and were further broken into

fragments by an energy source such as the microwave discharge itself. Under the appropriate conditions, very fine grain diamond films were deposited on a substrate. This diamond synthesis method was later modified and generalized (1) to allow any noble input gases [2] and (2) to allow the carbon input source to include not only fullerene vapors but also many carbonaceous vapor input process gases such as CH_4 and C_2H_2 [3]. Additionally, the inputs of small amounts of H_2 gas were also allowed, and diamond synthesis could also be controlled via a temperature-adjustable substrate holder [3–6]. The deposited diamond films were originally referred to as NCD, had average grain diameters of 15 nm, and were very smooth, i.e., the films had a root mean square flatness of less than 50 nm [4–7].

It was observed even in the earliest investigations as well as the later reported work [1–8] that as the fullerenes fragmented the associated plasma discharges turned green, thereby indicating the presence of carbon dimers, i.e., C_2 , in the plasma gas phase. This also led to the suggestion that the observed C_2 groups may be ultimately involved in the growth of the observed diamond films [1,9].

In order to differentiate UNCD films that are discussed in this chapter from other NCD films, the term UNCD must be defined. The UNCD films that are discussed in this chapter are identified as small grain diamond films that are synthesized in argon-rich and hydrogen-poor gas environments. Typically, the gas mixtures of argon, hydrogen, and methane vary around 99–95%, 1–4%, and 1–2%, respectively. These films have a distribution of crystal sizes ranging from a few nm to 15 nm and contain up to several percent sp^2 bonded carbon. The resulting continuous films are very smooth with surface roughnesses, depending on the thickness,

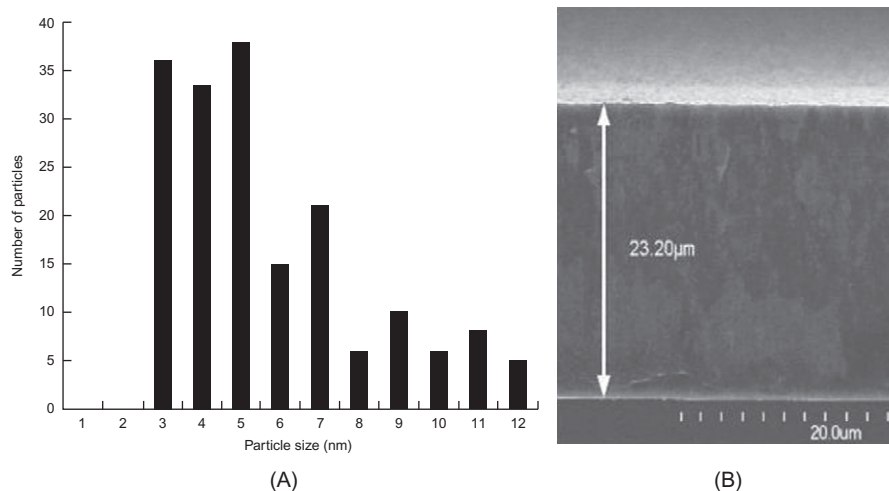


FIGURE 2.1

(A) Grain size distribution of Michigan State University (MSU)-synthesized UNCD film and (B) cross-sectional SEM image of UNCD grown on a silicon substrate [10].

of less than 50–70 nm. An example of such a UNCD distribution of crystal sizes and a thick cross section of a smooth film are displayed in [Figure 2.1](#) [10].

Since the early work by Gruen et al., interest in UNCD films has dramatically increased. Many research groups around the world, driven by the many potential applications of UNCD, have devoted considerable effort toward improving and understanding UNCD synthesis, characterizing the UNCD films, modeling and diagnosing the synthesis process [11,12], and then applying the UNCD films to specific applications. Many of these developments have been discussed and summarized in recent review articles [13,14].

In this chapter, the recent progress on several important issues related to the synthesis of UNCD are reviewed: (1) the theory, modeling, and diagnosis of UNCD growth, (2) large-area microwave plasma-assisted chemical vapor deposition (MPACVD) of UNCD, and (3) the potential for hot-filament chemical vapor deposition (HFCVD) to synthesize UNCD. Large-area commercial UNCD reactors are also briefly identified and discussed in the sections below.

2.2 UNCD growth: theory, modeling, and diagnostics

The basic understanding of microcrystalline diamond (MCD) growth with a methane/hydrogen mixture is that the growth occurs on a one-atom-at-a-time mechanism. The “standard model” as described in the review article by Butler et al. [15] is that the gaseous discharge dissociates the hydrogen that reacts with the hydrocarbon feed gas creating radicals that supply carbon to the growth surface. The atomic hydrogen also serves to cover much of the diamond growth surface with C–H bonds, i.e., terminating the surface with hydrogen. The influx of atomic hydrogen also opens sites on the diamond surface. The atomic hydrogen from the gas phase reacts with the surface-bonded hydrogen, creating molecular hydrogen. This leaves the surface, producing an open surface site. This open site can be reoccupied with either another hydrogen atom or a carbon-containing radical. The mixture of atomic hydrogen and carbon-containing radical fluxes to the surface can for a range of conditions produce sp^3 bonded carbon yielding diamond growth. The species that is believed to be the dominant carbon growth radical for diamond growth conditions is CH_3 .

UNCD growth typically occurs in microwave plasma reactors under argon-rich plasma conditions containing less than a few percent of methane and hydrogen. UNCD material consists of small diamond crystals with sizes of less than 15 nm and a common size distribution ranging from 3 to 5 nm (see [Figure 2.1A](#)). UNCD growth requires that renucleation events occur frequently so that individual crystal sizes remain small.

In general, diamond growth will be considered in this section by thinking of the processes in three regions:

1. The bulk plasma region (the hot central part of the plasma and surrounding cooler regions).
2. The plasma species that arrive at the growth surface.
3. The surface reaction processes that produce renucleation.

The sections below describe the processes in each of the three regions as well as focus on the unique aspects important for UNCD growth.

2.2.1 Plasma discharge region

The behavior of the plasma discharge depends primarily on the plasma gas temperature and hydrogen concentration. In a microwave plasma deposition system, the microwave energy heats the electron gas that then transfers energy to the hydrogen- and carbon-containing species via elastic and inelastic collision processes, thereby creating radicals, ions, and gas heating. In a hydrogen-based plasma discharge at pressure conditions where diamond deposition is performed, the microwave energy is first transferred to the electron gas and then heats the hydrogen gas, dissociating it and creating ions. At moderate pressures above a few tens of torrs, the dominant hydrogen dissociation mechanism is thermal dissociation due to the high neutral gas temperature. Since the neutral gas temperature ranges from the discharge wall temperatures (approximately room temperature to a few hundred °C) up to the plasma core gas temperature that is often ~3000 K, some insight into diamond plasma discharge characteristics can be obtained by considering the discharge species of a hydrogen/methane mixture in thermal equilibrium. In Figure 2.2A, the thermal equilibrium concentration of carbon species versus neutral gas temperature is shown [16].

Higher temperatures tend to create more C_2 species, especially C_2H_2 . The gas temperature in plasma discharges for diamond deposition in microwave systems is often measured in the 2000–3500 K range. Therefore, the central hot part of the plasma discharge is dominated by C_2 species. The behavior at cooler temperatures is also important, as the outer regions of the discharge are cooler, especially at the substrate growth surface. There is a steep temperature gradient from 2000–3000 K

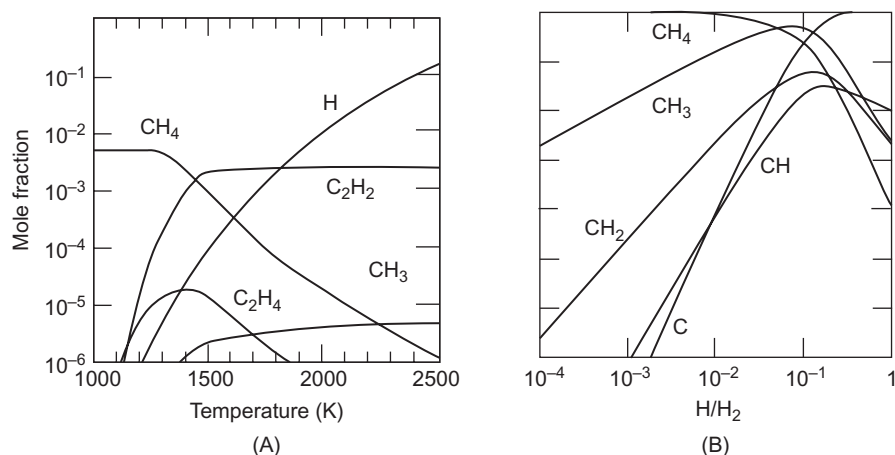
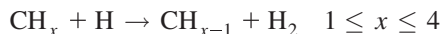


FIGURE 2.2

(A) Thermal equilibrium H_2 and CH_4 mixture and (B) atomic hydrogen influence [16].

in the core plasma to 900–1300 K on the growth substrate surface. The carbon species change across this boundary layer following the mole fraction versus temperature graph shown in Figure 2.2A.

The thermal equilibrium approach is instructive, but it is inadequate because of the large amount of atomic hydrogen present in the discharge. Typically, in the hotter regions, reactions of atomic hydrogen with carbon species tend to shift the carbon species to having lower H content:

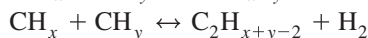
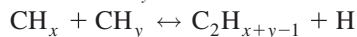
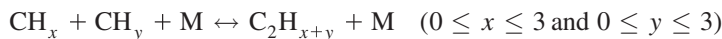


The opposite reaction tends to occur in cooler regions, which shift the carbon species to having more H content:



where M is any molecule or atom in the discharge. The atomic hydrogen concentration has an influence as shown in Figure 2.2B. The higher the atomic hydrogen mole fractions are relative to H_2 , the fewer hydrogen atoms are attached to the carbon species. Figure 2.2B represents data at a temperature of 2500 K [16] and similar behavior occurs for C_2H_y and C_3H_z species.

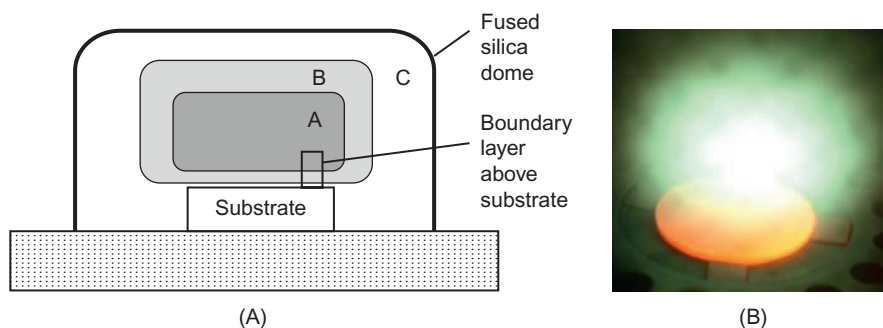
The gas-phase reactions that produce the C_2H_y species when methane is the feed gas consist of CH_x radical recombination reactions such as



As mentioned above and shown in Figure 2.2A, at higher temperatures these reactions shift the discharge concentration from the C_1 to the C_2 species.

The plasma discharge for UNCD deposition formed in a microwave plasma-assisted deposition reactor is spatially nonuniform with a temperature in the center of the discharge (core region) that has been measured and modeled in the range from 2500 to 3500 K. At the outer edges of the discharge region, the discharge gases touch the metal or dielectric (fused silica) surface, which is much cooler (>300 up to 600 K), or the substrate for diamond deposition, which is 700–1300 K. Because of the wide temperature range, it is useful as shown in Figure 2.3 to define three regions as hot central region A with $T > 2200$ K, region B with $1400 \text{ K} < T < 2000$ K, and region C with $T < 1400$ K [17].

The overall chemical dynamics occurring in each region was described by Mankelevich et al. [17]. Typical feed gases for single crystal and polycrystalline diamond deposition are hydrogen and methane. For such a feed gas mixture, in region B the input CH_4 gas is reformed into C_2H_2 . Other dominant reactions include (1) in region C the C_2 species are reformed into C_1 species (mostly C_2H_2 to CH_4) and (2) in region A an equilibrium-like situation exists with mixtures of C_1 and C_2 species and possibly some higher C_z species ($z > 2$). Specifically, due to the high temperature and abundant atomic hydrogen in region A, a range of CH_x ($0 \leq x \leq 4$), C_2H_y ($0 \leq y \leq 6$), and some possible higher carbon species (e.g., C_3H_z ($0 \leq z \leq 8$)) exist.

**FIGURE 2.3**

(A) Regions A, B, and C shown for a typical deposition reactor and (B) photograph of diamond deposition discharge at ~ 200 Torr.

In the case of microwave UNCD deposition, the dominant specie in the plasma is argon. The argon-dominated discharge has a higher electron temperature and more dissociation of the hydrogen occurs because of electron impact dissociation of hydrogen. Comparing two plasmas, a hydrogen-dominated discharge and an argon-dominated discharge, provides insight into the difference in the H_2/CH_4 and $\text{Ar}/\text{H}_2(\text{small})/\text{CH}_4$ plasmas. In a study done by Richley et al. [11] at 150 Torr, a plasma with 4.4% $\text{CH}_4/88.6\%$ $\text{H}_2/7\%$ Ar had a $[\text{H}]/[\text{H}_2]$ ratio of 0.09, while a UNCD plasma (0.5% $\text{CH}_4/1\%$ $\text{H}_2/98.5\%$ Ar) had a $[\text{H}]/[\text{H}_2]$ ratio of 2.5 in the central part of the plasma. In their work, they conclude that UNCD plasma produces atomic hydrogen through electron impact excitation of H_2 in an amount comparable to thermal dissociation. For comparison, in a hydrogen-dominated discharge, the atomic hydrogen for pressures of 50 Torr and above is produced by thermal dissociation of molecular hydrogen. Other observations or conclusions in Ref. [11] relate to the power density of the discharge. Hydrogen-dominated discharges have a large fraction ($>90\%$) of the input microwave power go into rotational and vibrational excitation of molecular hydrogen. However, with less molecular hydrogen in UNCD discharges, the argon plasma is bigger in size for a given input power and the power density in the discharge is substantially less by an order of magnitude. The power required per unit volume is less to excite the argon-dominated discharge because it contains less molecular hydrogen in the feed gas. In fact, Richley et al. [11] note that the limit for a 0.5% $\text{CH}_4/1\%$ H_2/Ar plasma is a power density of less than 2 W/cm^3 , whereas the power densities for hydrogen-dominated discharges are $10\text{--}50\text{ W/cm}^3$ at the pressure considered.

Richley et al. [11] also note that overall the electron temperature and electron density increase and the fraction of dissociated hydrogen is higher in the UNCD deposition discharges that have high argon concentrations in the feed gas. Of course, the higher fraction of atomic hydrogen shifts the reactions in Figure 2.2 to

carbon species with fewer hydrogen attached. Richley et al. [11] found that for both the hydrogen-dominated (88.6%) discharge and the argon-dominated discharge (88.5%), the gas temperature is in the range 2900 to 3100 K for the 150 Torr pressure studied. This is due to the thermal dissociation of hydrogen becoming a major source of hydrogen atoms for $T_{\text{gas}} > 2800$ K, where T_{gas} is the plasma discharge gas temperature.

A critical point is that in a H_2/CH_4 plasma, the dominant species is C_2H_2 in the hot part of the plasma, whereas in a UNCD (argon-rich) plasma, the species composition is shifted by the higher relative concentrations of atomic hydrogen with respect to H_2 to be more C_2 because of the higher atomic hydrogen mole fraction. This shift to less hydrogen on the carbon species explains the observed increase in the Swan band emission (green light) from the UNCD plasma discharges. The observation of the bright C_2 Swan band emissions from the UNCD plasma led to a number of plasma diagnostics studies to understand the C_2 concentration, as well as other species in the UNCD deposition discharge.

Early work by Goyette et al. [18] measured the C_2 species using white light absorption spectroscopy. The plasma conditions included a pressure of 100 Torr and hydrogen from 0% to 20% and methane of 1%. The C_2 species concentration measured 1.5 cm above the substrate was 10^{10} – 10^{12} cm^{-3} .

The work of Rabreau et al. [19] measured the C_2 species concentration using cavity ring down spectroscopy and reports values of 2 – 4×10^{12} cm^{-3} for deposition conditions of 90 Torr and 0–14% H_2 . It is interesting that when the argon in the discharge was replaced with helium, the C_2 was below the detection limit, but the UNCD was still deposited. Since similar diamond was deposited with both the argon-dominated plasma and the helium-dominated plasma, it was concluded that C_2 may not play a significant role in the main UNCD deposition process.

Work by Lombardi et al. [20] used UV–visible emission and absorption spectroscopy to measure the gas temperature and the absolute C_2 concentration in plasma discharges for UNCD deposition. The deposition conditions were a pressure of 170 Torr, a hydrogen percentage of 2–7%, and a methane percentage of 1%. The investigation showed temperature measurements of 3000–4000 K and C_2 concentrations of 10^{13} – 10^{14} cm^{-3} in the plasma discharge. The work of Ma et al. [21] used cavity ring down spectroscopy to measure the gas temperature of ~ 3000 K for pressures of 100–150 Torr. Their work also looked at the relative variation in the C_2 concentration versus vertical position above the substrate. Typical variations include that the C_2 density was largest for positions 10 mm or more above the substrate. Also, the density at 2 mm above the substrate decreased to 10% or less of the higher C_2 concentration at 10 mm or more above the substrate. The experimental measurements showed that the C_2 density decreases near the substrate, as presented in Figure 2.4. The plasma conditions included gas flows of 40 sccm argon, 500 sccm hydrogen, and 25 sccm methane. Note that the relative concentration of other species, such as excited state H ($n = 2$), was much stronger for the region from 0 to 2 mm above the deposition substrate.

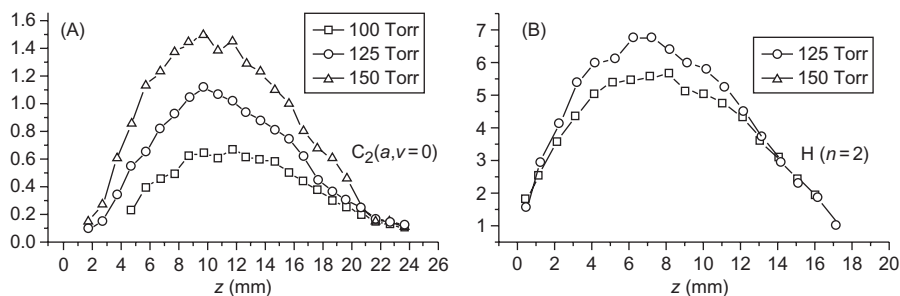


FIGURE 2.4

(A) Relative C_2 concentration and (B) $H(n=2)$ signal versus distance above the substrate located at $z = 0$ mm [21].

2.2.2 Species arriving at the growth surface

It is the species flux at the growth surface that is a determining factor for the growth process. A key concept is that the gas temperature cools from the higher temperature of ~ 2500 – 3100 K in the central part of the plasma to a value that is near the substrate temperature (~ 700 – 1300 K) at the growth surface. The plasma temperature near the surface is close to that of the surface for the pressures of UNCD deposition (50–200 Torr) due to the high collision frequency of the gaseous species with the surface and each other [16]. As the growth surface is approached, the gas temperature cools causing a shift from C_2 and C_3 species to C species as described above in Figure 2.2A. Even though the core part of the plasma discharge has many C_2 and C_3 species, the cooling of the gas temperature approaching the substrate causes the species distribution to be dominated by C, CH, CH_2 , CH_3 , and CH_4 species near the substrate. The most abundant reactive C or CH_x species is CH_3 . The CH_3 species has generally been concluded to be the primary growth species for diamond deposition.

It is illustrative to comment on the flux of species to the diamond growth surface [15]. It is a dynamic environment with a continuous flux of species arriving at the surface. Some of the species hitting the surface have little effect such as neutral and ground-state/low-energy-state H_2 and Ar. They collide with the surface and exchange some thermal energy that maintains the gas temperature near the substrate close to the temperature of the substrate. A more important species for reactions is the atomic hydrogen, which arrives at the growth surface with a flux on the order of 10^{20} – 10^{22} cm^{-2}/s . For an individual carbon site on the diamond growth surface, this is a flux of 10^4 – 10^7 collisions/s. The atomic hydrogen that arrives at the surface has a probability ($\sim 10\%$) of abstracting a hydrogen atom from the surface, resulting in an open radical site and a hydrogen molecule leaving the surface. The open radical site can either accept another atomic hydrogen or, if a carbon species arrives at the surface, it can be attached to this open radical site. It is this attachment of the C_1 species (primarily CH_3) that is supported by experimental evidence and

computations to be the primary growth species. It has also been described that, in general, when species with two or more carbons arrive at the surface, they will be short lived on the surface. In particular, because of the high flux of atomic hydrogen to the surface, C_2 and large carbon species will be quickly attacked leaving no or single carbon species (C_1H_x) behind on the surface. These reactions that limit the incorporation of C_2 and higher hydrocarbons on the surface are called beta-scission reactions [16].

The different species flux to the surface created in argon-dominated UNCD plasmas has been studied by a number of researchers. The work of May et al. [22] looked at the concentration of species both 0.5 mm above the surface and also developed two fitting models for the concentration at the surface. Model A fits the concentration data from 0.5–5 mm above the substrate and extrapolated the data to the substrate surface. Model B used the concentration data from measurements and computations for the top of the plasma discharge and from the region of the plasma discharge where the gas temperature approaches the substrate temperature. Table 2.1 shows the data for both a hydrogen-dominated discharge and an argon-dominated (UNCD) discharge.

Several observations can be made from Table 2.1 including that the highest concentration radical at the surface is CH_3 for both the hydrogen-dominated and the argon-dominated discharges. The CH_3 concentration for the hydrogen-dominated discharge is higher in comparison to argon-dominated discharge, which is consistent with the higher growth rate of single crystalline and microcrystalline diamond (SCD, MCD) as compared to UNCD. It is also noted that the other C_1 species including C, CH, and CH_2 are higher for the UNCD discharge. The C_2 species concentration is higher at the surface in the UNCD discharge.

Table 2.1 Species Concentrations Near ($z = 0.5$ mm) and at ($z = 0$ mm) the Substrate in a Hydrogen-Dominated Discharge and an Argon-Dominated (UNCD) Discharge

Discharge Type	$CH_4:H_2 = 10\%:90\%$ and 180 Torr			$CH_4:H_2:Ar = 1\%:1\%:98\%$ and 170 Torr		
T_s (K)	973	973	973	873	873	873
z (mm)	0.5	0,A	0,B	0.5	0,A	0,B
H (cm^{-3})	3.38×10^{16}	3.38×10^{16}	3.38×10^{16}	4.31×10^{14}	4.31×10^{14}	4.31×10^{14}
CH_3	3.24×10^{13}	1.0×10^{13}	2.86×10^{13}	5.60×10^{11}	1.0×10^{12}	8.48×10^{12}
CH_2	1.06×10^{12}	1.0×10^{10}	5.65×10^6	2.31×10^9	1.0×10^8	6.13×10^9
CH	1.60×10^{11}	5.0×10^8	2.36×10^3	7.05×10^8	1.0×10^7	1.10×10^9
C	1.41×10^{12}	1.0×10^{10}	1.29×10^4	1.47×10^{11}	5.0×10^9	8.14×10^9
$C_2(X) + C_2(a)$	5.31×10^{10}	1.1×10^6	~ 0	1.65×10^{11}	1.5×10^{10}	9.98×10^6
C_2H_2	2.96×10^{16}	4.0×10^{17}	1.41×10^{16}	2.35×10^{15}	2.7×10^{15}	3.42×10^{15}
Ar				1.21×10^{18}		

T_s , substrate temperature.

2.2.3 Growth at the surface: high renucleation rate for UNCD

The reactive species believed to be critical for diamond growth is CH_3 for both UNCD and MCD. As described above, there is believed to be higher quantities of C, CH, CH_2 , C_2 , C_2H_x , C_3 , and C_3H_y species arriving at the surface in UNCD growth than discharges with hydrogen-dominated diamond growth. The key question for UNCD growth is why are the crystals so small? Or phrased differently the question is what is the cause of the high renucleation rate needed for UNCD growth? Two basic explanations offered in the literature include (1) that nanoparticles are created in the gas phase that cause renucleation when they end up on the diamond growth surface and (2) the different species fluxes to the surface produce defects or renucleation on the surface. The number of such renucleation events can be estimated from the number of carbon atoms in small grains of diamond. In Ref. [23], it is noted that a 5 nm diameter diamond grain contains 10000+ carbon atoms. Subsequently, a renucleation event needs to occur only after 10000+ carbon atoms are added. It needs to be noted that the reason that UNCD diamond growth has a high renucleation rate is still a matter of investigation. Three explanations found in the recent literature are described in the following paragraphs.

Richley et al. [24] looked at reactions of various carbon radicals on the hydrogen-terminated diamond surface. They calculated that the species C, CH, CH_2 , and C_2 can not only react with an open surface site but can also undergo an insertion reaction into a C–H bond at the surface, i.e., these species do not need an open surface site to be incorporated since they can directly insert at a hydrogen-terminated location. This is in contrast to a CH_3 species that can just attach to the diamond surface at an open carbon site on the surface created when a hydrogen atom is removed. One possible explanation for the higher renucleation rate during UNCD growth conditions is due to the higher C and C_2 concentrations in the flux to the growth surface. The increased flux of non- CH_3 reactive carbon species, especially C and C_2 , causes surface insertion of carbon that may both add a carbon and cause a renucleation event.

The explanation of the higher renucleation rate in UNCD films given by Eckert et al. [25,26] looks at the growth process of diamond on the surface. The growth mechanism of well-faceted diamond is believed to occur by a “step-flow growth mechanism.” In this growth process, the diamond surface is quite smooth during growth but terraces exist that are the primary sites where new carbon atoms are added. The growth occurs primarily by the carbon filling in at the terrace edge to complete the diamond layer. The explanation offered by the investigations of Eckert et al. is that the species more abundant in UNCD diamond growth “suppress the extension of terrace step edges through defect formation.” Whereas in hydrogen-dominated discharges, the species arriving at the surface “enhance the extension of diamond terraces, which is believed to result in well-faceted diamond films.”

Another explanation of renucleation in the UNCD discharges is the observation of particulates in the gas phase. In a recent paper by May et al. [22], the previous

works related to particulates in UNCD discharges were cited, and it was noted that UNCD discharges can generate hydrocarbons with many carbons and even particulates in the cool plasma region (region C in Figure 2.3). In fact, it has been noted by us and others that, under some conditions, the particulates (soot, nanoparticles) on the outer edges of the discharge appear to the naked eye as an orange glow or flames due to the hot particulates. The speculation is that these larger hydrocarbons and/or particulates form defect/nucleation sites on the UNCD growth surface. It is noted that the conditions in the regions where these particulates are observed are replicated in the thin layer above the substrate, which indicates particulate formation in the region just above the substrate is a possibility.

2.3 Scaling up the MPACVD process: large-area UNCD synthesis using a floating substrate holder

2.3.1 Background

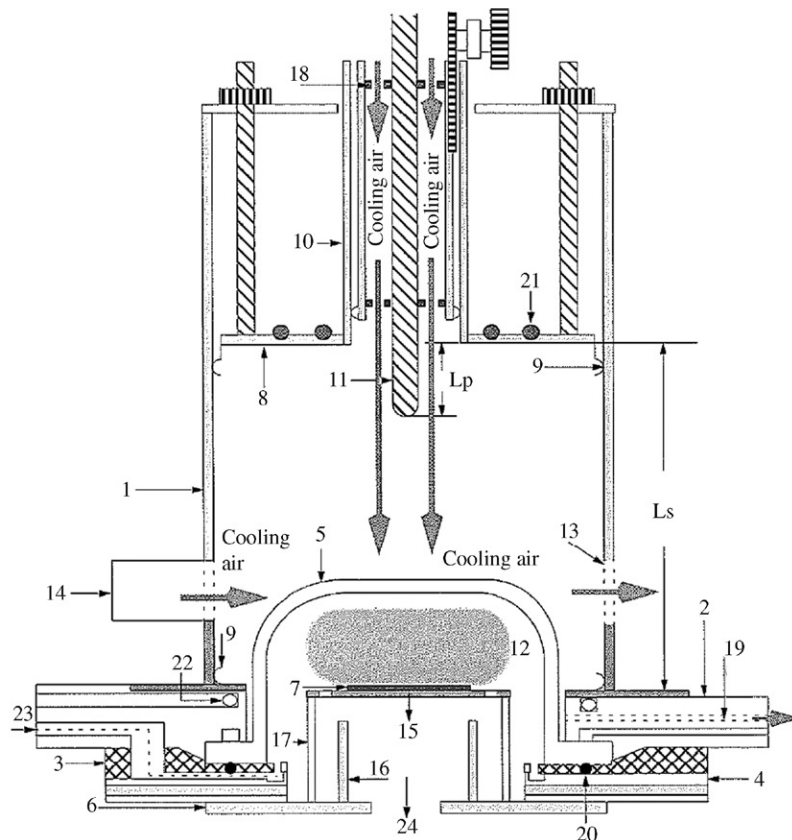
During the past 10 years, the ability of MPACVD to synthesize UNCD over large areas has greatly improved. Previous to the late 1990s, MPACVD UNCD synthesis was limited to low growth rates and to substrates of less than 5 cm in diameter. However, in the late 1990s, a number of research groups attempted to increase the synthesis rates and to enlarge the MPACVD synthesis areas of all forms of CVD diamond. They first improved the conventional 2.45 GHz reactor designs [27–29] and then scaled up the reactor size by decreasing the excitation frequency to 915 MHz [30–33]. These reactor configurations were then employed to investigate UNCD synthesis.

Here, we report on one such UNCD synthesis effort carried out at Michigan State University (MSU) using a microwave cavity plasma reactor (MCPR). Work was started with 2.45 GHz excitation by Huang and coworkers [10,34] and Tran and coworkers [35,36] during the 1997–2005 period. During the 2005–2007 period, UNCD process development was continued at the MSU and Fraunhofer CCL Laboratories and, as a result, the UNCD deposition area was scaled up using an excitation frequency of 915 MHz [37].

These experiments were unique in that instead of using an electrically grounded and heated substrate holder they employed a “warm reactor” and an adjustable substrate holder stage that was both electrically and thermally floating. This floating substrate MCPR configuration allowed the electromagnetic fields that created and maintained the discharge to be varied and modified and thereby enabled the shaping and the positioning of the discharge to optimize uniform deposition over large-area substrates. These experiments successfully deposited uniform UNCD over 7.5 cm diameter silicon substrates with 2.45 GHz excitation and over 15–20 cm diameter silicon substrates using 915 MHz excitation. The experimental methodologies and synthesis recipes that were developed to deposit large-area UNCD over a wide range of pressures and plasma conditions are summarized below.

2.3.2 Experimental description and methodologies

Large-area UNCD synthesis experiments were performed with two different MCPRs. The first reactor was a 2.45 GHz excited system [28,38] connected to a 6 kW variable input power supply. The second reactor was a scaled up 915 MHz MCPR system [37], which was connected to a variable 30 kW power supply. Figure 2.5 shows the



Legend

- | | | |
|-----------------------------|----------------------------|--------------------------|
| (1) Cavity side wall | (2) Baseplate | (3) Annular plate |
| (4) Distribution plate | (5) Quartz dome | (6) Holder-baseplate |
| (7) Substrate | (8) Sliding short | (9) Finger stock |
| (10) Coaxial waveguide | (11) Excitation probe | (12) Plasma discharge |
| (13) View window (grid) | (13) Air blower outlet | (14) Air blower inlet |
| (15) Flow pattern regulator | (15) Substrate holder | (16) Metal tube |
| (17) Quartz tube | (18) Teflon pieces | (19) Optical access port |
| (20) Seal O-ring | (21) Cooling sliding short | (22) Cooling baseplate |
| (23) Gas inlet | (24) Gas outlet | |

FIGURE 2.5

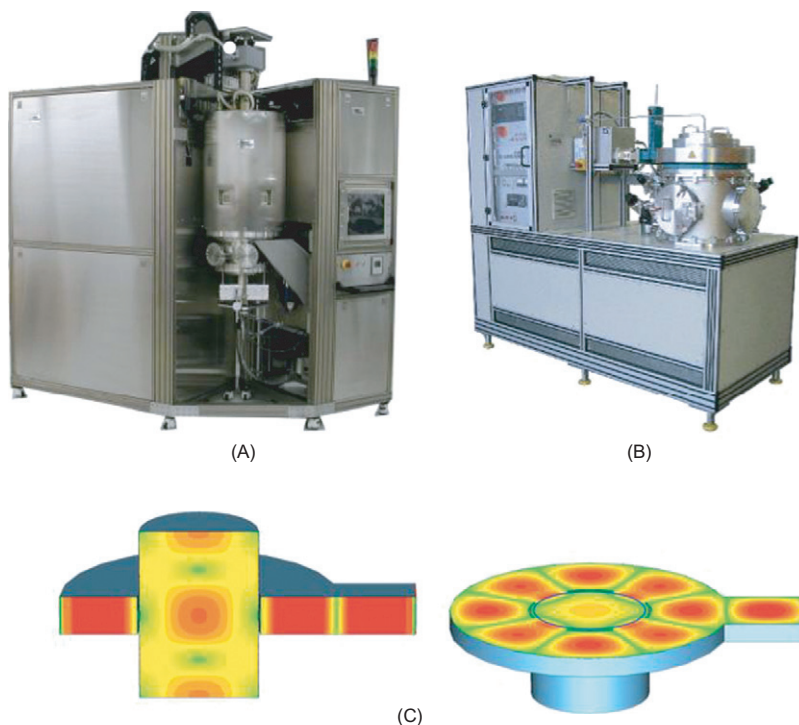
Cross-sectional view of the MCPR [10].

cross-sectional view of a generic system that describes both MCPs [36]. The major difference between the two systems is the excitation frequency and the associated adjustments in the size of the connecting waveguides, and MCP dimensions that were required to enable operation at either of the excitation frequencies.

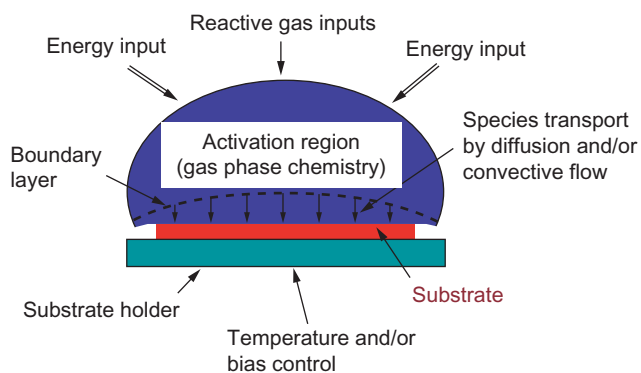
Using Figure 2.5 as a reference, the 2.45 GHz system consists of a microwave power supply that is connected to a 17.8 cm diameter cylindrical MCP [10,28] via a coaxial coupling input waveguide (10). As is discussed elsewhere [38], the MCP has a variable short (8) and a variable-depth coupling probe (11), i.e., the reactor system is tunable allowing for internal cavity matching of the incident microwave power. Microwave energy is coupled into the MCP through the mechanically tunable coaxial excitation probe shown at the top of the reactor in Figure 2.5. When the MCP's sliding short position L_p is adjusted to ~ 21.6 cm, the TM_{013} cavity mode is excited and a hemispherical discharge (12) is created and confined inside the 12.5 cm diameter cylindrical quartz dome (5) that is located on the fixed base plate (2) at the bottom of the applicator. A molybdenum substrate holder (15) is electrically and thermally floating because it is placed on a quartz tube (17) located on the holder base plate. Process gases are introduced upward into the discharge region via a gas distribution ring located at the bottom flange of the quartz dome. The input gases then flow through the discharge and out of the reactor via an annular ring of holes located on the outer rim of the substrate holder.

The larger "scaled up" system consists of a 915 MHz microwave power supply that is connected to a 46 cm inside diameter MCP via the coaxial coupling port located at the top of the reactor. The cross section of the reactor is the same as shown in Figure 2.5. All the dimensions of the scaled up 915 MHz reactor are larger, approximately by a factor of 2.7 compared to the corresponding dimensions of the 2.45 GHz reactor. Similar to the 2.45 GHz system, the TM_{013} mode is excited and a hemispherical discharge is created inside a 32.5 cm diameter cylindrical quartz dome. The discharge is adjusted to be in good contact with the 24 cm diameter molybdenum substrate holder that is placed on the cylindrical quartz tube located and centered on the holder base plate. Examples of scaled up commercially available 915 MHz UNCD MPACVD reactors are shown in Figure 2.6. Two systems are displayed, a Lambda Technologies system and an IPLAS system. Both of these systems have demonstrated large-area UNCD synthesis. Note that the IPLAS system is a different reactor design. Two cross sectional views of this reactor are shown in Figure 2.6C.

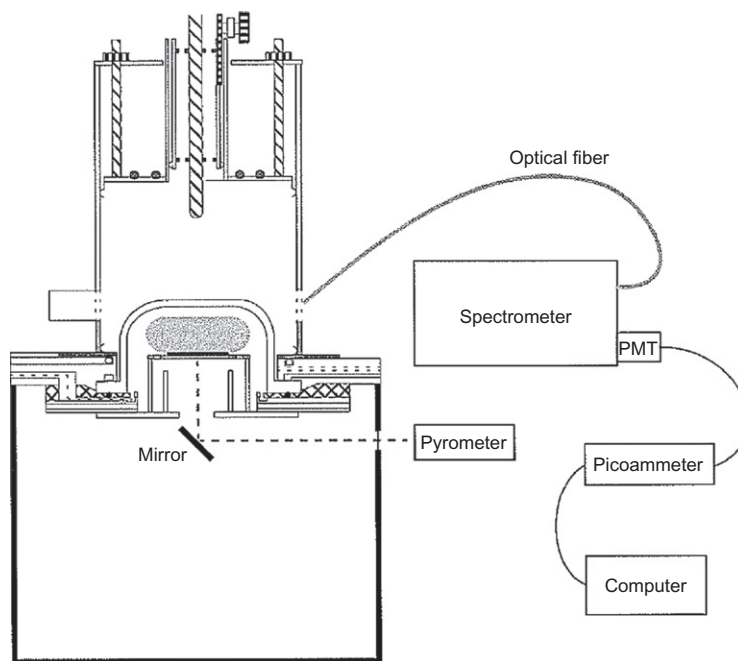
Silicon substrates (7) are placed on the molybdenum holder as shown in Figure 2.5. The 2.45 GHz system employed 7.5 cm diameter silicon substrates, while the 915 MHz system employed 15–20 cm diameter silicon wafers. At each experimental operating pressure, the stage height and the cavity sliding short tuning were adjusted to position the substrate in direct contact with the microwave discharge as shown in Figure 2.7. The discharge then assumes an intense, hemispherical shape hovering over and in direct contact with the substrate. The backside substrate temperature was measured with an optical pyrometer that viewed the backside of the substrate through several 3 mm diameter holes that were located radially across the substrate holder. This setup is displayed in Figure 2.8. A topside

**FIGURE 2.6**

Commercially available large-area 915 MHz UNCD synthesis machines offered by (A) Lambda Technologies Inc. [39] and (B) IPLAS GmbH [40]. The cross section of the Lambda reactor is shown in Figure 2.5 and the cross sections of the IPLAS CYRANNUS machine along with its electromagnetic field patterns are shown in (C) [41].

**FIGURE 2.7**

Generic CVD diamond growth process.

**FIGURE 2.8**

Experimental setup for substrate temperature and OES measurements [10].

substrate temperature measurement was also made and was about 200°C higher than the backside substrate temperature measurements. It was believed that the intense emission from the discharge influenced the topside measurement. Thus, as shown in Figure 2.8, only the backside substrate temperature measurements are reported here.

As indicated in Figure 2.5, the reactor base plate was water cooled and the quartz dome was air cooled. The air and water cooling temperatures were monitored and controlled so that process repeatability could be achieved. Additionally, the reactor was operated in a warm/hot condition, i.e., quartz dome walls were held at 250–350°C to efficiently produce a thermally uniform deposition environment inside the quartz dome.

It is useful to note here that the substrate holder shown in Figure 2.5 is supported and is positioned into contact with the microwave discharge by a cylindrical quartz tube and thus is also electrically floating. Subsequently, the molybdenum holder is held at the plasma floating potential since the molybdenum is not electrically grounded and, hence, there is no conducting path for direct current to flow. Other UNCD MPACVD process configurations used by other investigators employ a substrate heater or cooler that is grounded and, as a result there may be a current flow from the holder. Thus, the direct current (DC) and radio frequency (RF) fields

in the plasma sheaths adjacent to a grounded holder may be different from the associated sheath electric fields next to the floating holder configuration described here.

Initial UNCD experiments demonstrated that in order to routinely synthesize high-quality, smooth, and uniform UNCD films, the deposition must be performed in a high-purity input gas environment [10, 34]. Thus, experiments were carried out using a leak-free vacuum system with mixtures of (1) argon or helium, (2) hydrogen, and (3) methane source gases. The Ar and H₂ gases had purities of 99.999%, while CH₄ had a purity level of 99.99%.

The initial nucleation density of diamond on the substrate surface greatly influences the CVD synthesis of UNCD films. Recent advances in high-density seeding have been discussed elsewhere [14] and have led to the improved synthesis of very thin UNCD films including the low-temperature deposition of UNCD on glass. However, in the experimental data discussed here, a simple mechanical method of seeding is employed. Substrate pretreatment involved mechanical scratch seeding with 0.1 μm diamond powder followed by an ultrasonic bath cleaning and acetone and deionized water rinse [10]. The deposited films were characterized using high-resolution transmission electron microscopy (TEM) to determine crystal size distribution, atomic force microscopy to determine the surface roughness, and scanning electron microscopy (SEM) images of the film cross section to determine the film thickness and uniformity. The average film thickness and, consequently, the deposition rate were obtained by measuring the weight gain of the substrate after deposition.

There are two experimental issues that arise and must be overcome when working in argon-rich hydrogen and methane-poor gas mixtures: (1) argon discharge filamentation as pressure is increased to over 100 Torr and (2) the formation of carbon particulates or soot in the gas phase. Argon discharge filamentation was avoided by igniting the discharge at low pressures of 10–20 Torr. Then, the pressure is allowed to slowly rise to the deposition pressure as the reactor heats up and becomes a warm-wall reactor. The formation of carbon particulates in the gas phase is observed as an orange glow or “flames” around the green discharge and also by the formation of soot that under some conditions settles onto the substrate. At times, these particulates are large enough to be observed as black particles moving around in and out of the plasma. The soot forming operating conditions must be avoided since the associated synthesized UNCD film is of poor quality. The formation of these flames is a function of gas pressure, input power, gas residence time, and the ratio of H₂/CH₄. In the MCPRs that are described here, the formation of flames was avoided over a wide range of pressures even with the low H₂ (0–4 sccm) and CH₄ (1–2 sccm) and with the high Ar (100 sccm) input gas mixtures.

2.3.3 Reactor operating road maps

As described briefly above and in detail elsewhere [34,36,38], all experiments were performed using a thermally floating substrate configuration. In this configuration, the substrate holder and the substrate are not actively cooled or heated, and thus all the energy supplied to the substrate originates from the microwave discharge. The heat

flow from the discharge to the substrate and the loss of heat due to conduction, radiation, and convection determine the steady-state substrate temperature. When operating in this configuration, the substrate temperature is a function of both the pressure and the absorbed microwave power. That is, given a constant input chemistry, the major independent experimental variables, i.e., absorbed microwave power, P_{abs} , and pressure, p , have an experimentally repeatable, single-valued nonlinear relationship with the experimentally measured substrate temperature. Given a specific reactor configuration, gas input chemistry, and flow rate, this nonlinear relationship can be measured. The resulting set of curves represents important data describing the useful experimental operating UNCD deposition regions of the reactor system. Such a set of curves is identified here as the “operating road map” of the reactor, which provides acceptable operating regimes for power and pressure parameters to obtain a desired substrate temperature at uniform substrate coverage with the plasma discharge. Figure 2.9 displays an example of the operating road map for the 2.45 GHz reactor system when operating with the specific 100:4:1 sccm Ar:H₂:CH₄ input gas chemistries.

As shown in Figure 2.9, the operation of the reactor at a given specific absorbed input power and operating pressure results in a unique and repeatable substrate temperature. When the pressure is held constant, the input power is independently

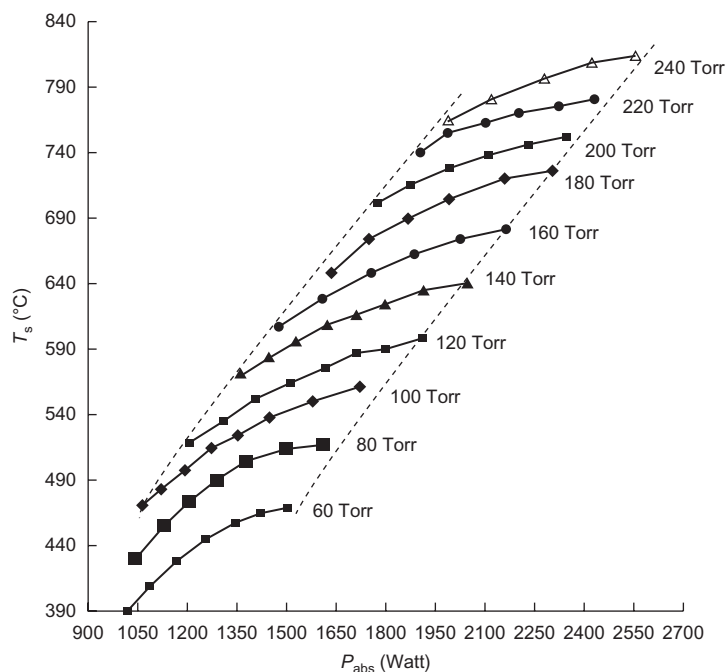


FIGURE 2.9

The experimentally measured 2.45 GHz MPACVD operating road map for Ar:H₂:CH₄ = 100:4:1 [36].

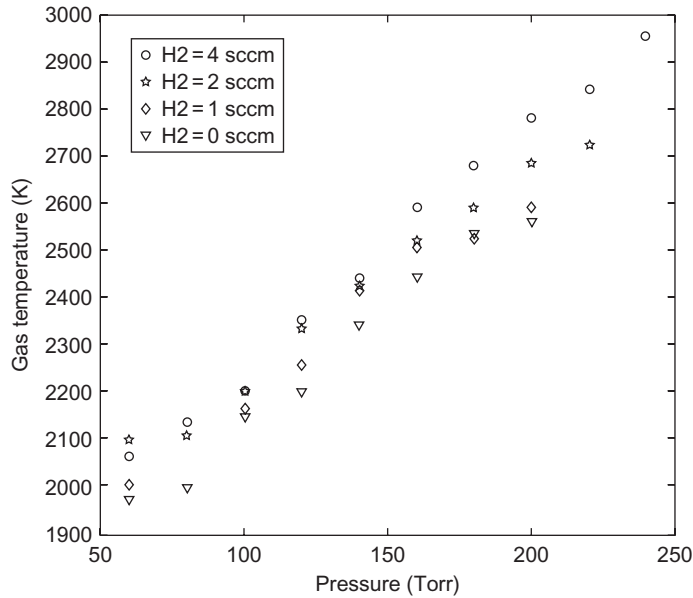
increased or decreased, the discharge size is also correspondingly increased and decreased, and the substrate temperature traces out the curves as shown in Figure 2.9. The left and right dashed lines in each figure represent for each pressure the allowable operating input power levels that yield useful UNCD deposition over a 3 inch diameter (7.5 cm) silicon substrate. The left dashed line represents the minimum power required to form a 7.5 cm diameter hemispherical discharge over the 7.5 cm diameter wafer. If the input power level is less than indicated by the left dashed line, the plasma discharge will not be sufficient in size to produce uniform UNCD deposition over 3 inch diameter substrates. The right dashed line represents the input power at which the plasma expands to touch the quartz dome walls. Greater input powers cause excessive dome heating and possibly undesirable plasma dome wall interactions. Thus, the road map curves in Figure 2.9 define the reactor operating regimes within which optimum, uniform UNCD synthesis can be achieved. Within this operating regime, the discharge is sufficiently large to cover the 7.5 cm diameter substrate, but it is small enough to not touch the walls of the 12.5 cm diameter quartz dome.

Note that if the input gas chemistry varies, i.e., the hydrogen concentration is changed from 0% to 4%, then the road map curves shift slightly. In particular, if the hydrogen concentration increases from 1% to 2%, the substrate temperature increases in the range of 10–25°C and as it increases from 2% to 4%, the substrate temperature increases by another 10–25°C. Thus, as the hydrogen chemistry is varied, another dimension related to the percentage of input hydrogen gas can be added to produce a road map defining the three-dimensional volume in which UNCD synthesis can be achieved. The experimental optimization of the process for a given application will take place within this road map volume. A similar operating road map was constructed for the 915 MHz MPCR [37].

The operating field map displayed in Figure 2.9 shows that as the pressure increases the substrate backside temperature also increases from about 450–500°C (725–775K) at 60–80Torr to 740–820°C (1010–1090K) at 200–240Torr. Since the deposition process is sensitive to the gas temperature, it is interesting to compare the discharge gas temperature as measured by observing the Swan band (0,0) emission intensity via optical emission spectroscopy (OES) [10]. Figure 2.10 displays the results of these measurements. The gas temperature also increases as the pressure increases, i.e., the temperature increases from about 2000–2150 K at 80Torr to 2550–2800 K at 200Torr. Thus, there is a temperature difference between the substrate backside and the gas of 1300 K at the low pressures of 80Torr, and this difference increases to 1600 K at the higher pressures of 200Torr. Thus, as the pressure increases, the temperature gradient between the main discharge body and the silicon wafer increases as well. Figure 2.10 also indicates that at a constant operating pressure, the gas temperature increases by about 100–200 K as the amount of H₂ increases from 0% to 4%.

2.3.4 Experimental procedures and results

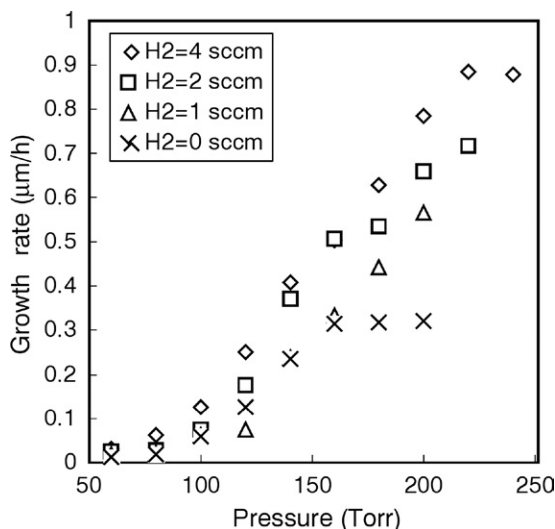
A wide range of experimental conditions, i.e., pressure, input power, and flow rate, were explored to identify the optimal conditions that enabled the repeatable

**FIGURE 2.10**

Gas temperature versus pressure [10].

deposition of a uniform and smooth UNCD film over 7.5 cm diameter silicon wafer substrates. The pressure range was varied from 60 to 180 Torr, and the feed gases investigated included mixtures of argon–hydrogen–methane (99–95%, 1–4%, 1–2%). Input 2.45 GHz microwave power was varied between 600 and 3000 W. Experimental road map curves such as those shown in Figure 2.9 provided the operating substrate/pressure/power multidimensional road map for this experimental investigation. At each operating pressure, optimal discharge uniformity, substrate temperature uniformity and, hence, deposition uniformity were achieved over the substrate diameter by the careful adjustment of (1) microwave input power, (2) cavity tuning, and (3) stage height. A set of more than 50 individual experimental 8-hour runs were performed to obtain the data.

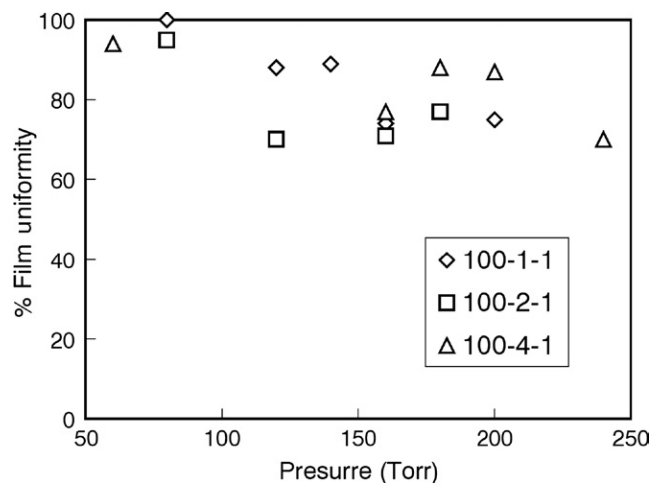
A large, useful UNCD experimental uniform deposition window (60–240 Torr, 400–1650 W, total gas flow rate 100–110 sccm, H₂ 0–4%, CH₄ 1–3%) was identified. Figures 2.11–2.13 summarize the experimental results within this window. Using 0–1% H₂, i.e. hydrogen-deficient conditions, discharges were sustained in contact with the 7.5 cm substrates over a 60–200 Torr pressure regime. High-quality UNCD film deposition was extended to 240 Torr when H₂ concentrations were increased to 1–4%. Figures 2.11–2.13 show that within the 7.5 cm diameter UNCD synthesis window, there are process trade-offs between growth rate, uniformity, and surface roughness.

**FIGURE 2.11**

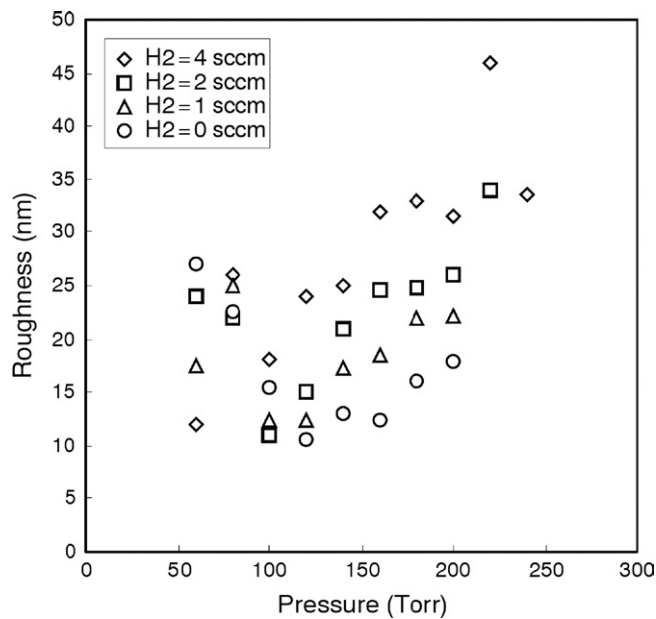
Linear deposition rates versus pressure for Ar/CH₄/H₂ where 100/1/0–4 sccm [34].

Data given in Figure 2.11 show that for a constant CH₄ input of 1 sccm, the deposition rate increases as both pressure and the H₂ percentage increase. Growth rates vary from <0.1 μm/h at 60 Torr to the highest growth rates of about 0.9 μm/h, which occurs at 200 Torr with an H₂ input of 4 sccm. It is useful to note that at the low pressures the substrate temperature is about 760 K and the gas temperature is about 2100 K, and both of these temperatures increase with pressure reaching 1070 and 2800 K, respectively, at 200 Torr. Both of these temperature increases favor higher growth rates. Data given in Figure 2.12 show that across the entire experimental parameter space, film uniformities were better than 70% (where uniformity is defined as the thinnest region divided by the thickest region). Uniformities across 7.5 cm diameters were >95% at pressures of less than 80 Torr. Film roughness, which is shown in Figure 2.13, generally decreases as the hydrogen flow rate decreases at the higher pressures of 100–120 Torr. The surface roughness has a minimum of 10 nm at 120 Torr for 0 sccm of H₂. These experimental results indicate that UNCD films can be grown at 120–150 Torr over 7.5 cm diameter substrates with uniformities of 75–90%, growth rates of 0.4 μm/h, and surface roughnesses of <20 nm using the gas input argon:hydrogen:methane chemistries of 100:0–1:1 sccm. Thus, a process window was identified that allows the growth of uniform UNCD films over a 7.5 cm diameter at reasonable growth rates of ~0.4 μm/h. A typical example of the distribution of the diamond crystal sizes in these films as measured by high-resolution TEM is displayed in Figure 2.1.

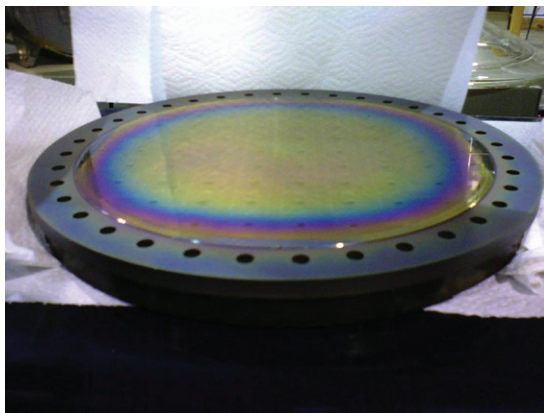
Using a similar set of process methodologies, the process was scaled up to 150–200 mm diameter substrates using the 915 MHz MCPR operating in the 50–120 Torr pressure and the 2–6.5 kW input power regimes. The results have been summarized in more detail elsewhere [37]. The discharge absorbed power

**FIGURE 2.12**

Film uniformity across a 7.5 cm diameter silicon wafer versus deposition pressure. The argon/hydrogen/hydrogen flow rates are given in the legend [34].

**FIGURE 2.13**

Surface roughness versus pressure. Ar:CH₄:H₂ = 100:1:0-4 [34].

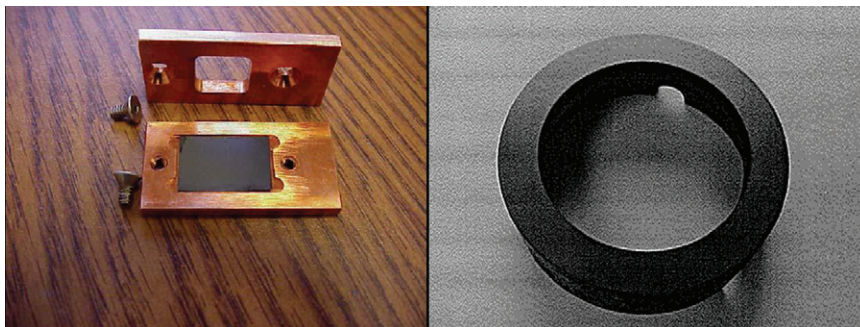
**FIGURE 2.14**

915 MHz MPACVD UNCD film synthesis over 8-inch silicon wafer.

density was 0.3 W/cm^3 at 50 Torr and increased as pressure increased to 1.1 W/cm^3 at 120 Torr. The comparable discharge power densities for the 2.45 GHz MCPR are 2.7 W/cm^3 at 50 Torr and 5.3 W/cm^3 at 120 Torr. Thus, the experimentally observed discharge absorbed power density in the 915 MHz reactor was lower by approximately a factor of 9 at low pressures (40–100 Torr) and approximately a factor of 5 at higher pressures (>100 Torr) when compared to the 2.45 GHz reactor. Given the same input operating conditions of pressures and gas mixtures, the floating substrate temperatures were similar for both reactors, which led to similar deposition rates. Within the 75–110 Torr pressure regime, growth rates ranged from 30 to 460 nm/h and the uniformity varied from excellent at the low pressure to good at the higher pressures. The thickness variation ranged from 4% to 15% for the 150 mm diameter substrates and 6–21% for the 200 mm diameter substrates. Figure 2.14 displays a UNCD film that was deposited in the 915 MHz reactor. These experimental results can be further improved by additional optimization of input power, substrate temperature uniformity, adjustment of the substrate position reactor tuning, etc.

It is interesting to compare the discharge absorbed power densities of UNCD argon-rich hydrogen-poor microwave discharges with the hydrogen-rich microwave discharges that are used to grow MCD [37]. Over the 50–120 Torr pressure regime, the hydrogen-rich discharge absorbed power densities for 2.45 GHz excited MCPRs range from 12.5 W/cm^3 at 50 Torr to 40 W/cm^3 at 150 Torr and with 915 MHz excitation they vary from 1.4 W/cm^3 at 50 Torr to 5.2 W/cm^3 at 120 Torr. Thus, in a similar fashion to the UNCD discharges, the discharge absorbed power densities are much lower in the 915 MHz reactor than the 2.45 GHz reactor. However, the discharge absorbed power densities are much lower for the argon-rich hydrogen-poor UNCD discharges.

After each MCPR's performance was initially explored and characterized using the above experimental methodologies, UNCD was synthesized for a number of applications. For example, uniform thick 10–80 μm UNCD films were deposited

**FIGURE 2.15**

UNCD freestanding foil and SiC pump seal application [10,34].

over 75 mm diameter silicon wafers and were applied (1) to fabricate very smooth UNCD (see Figure 2.1B) for surface acoustic wave (SAW) devices [42], (2) to create stress-free, freestanding UNCD films for electron stripping foil applications for heavy ion beams [34], and were also deposited (3) as coatings for pump seals [10] (Figure 2.15).

2.4 Hot-filament CVD UNCD synthesis

2.4.1 First report and principle of HFCVD diamond synthesis

Low-pressure HFCVD of diamond was first reported in Ref. [43]. In this work, MCD particles were grown on diamond and nondiamond substrates including molybdenum, silicon wafers, and glass plates. The reactor consisted of an electrically heated and evacuated furnace, a stabilized direct current powered tungsten filament (0.15 mm diameter, 30 mm length, 20 turn coil), and a feed gas system for methane and hydrogen. Both the tungsten filament and the feed gas delivery were placed in close proximity to the substrate with the filament being ~10 mm above the surface. Typical diamond deposition was achieved at reactor pressures from 10 to 100 Torr and substrate temperatures from 700 to 1000°C. Additional reactor temperature control was exercised to keep the substrate temperature constant when the filament was operated at 2000°C and thus contributed to the substrate surface heating due to radiation and heat conduction. The methane-to-hydrogen ratio was between 0.5% and 5%. Increasing the methane concentration increased the formation of disordered graphite on the crystallites and ultimately led to the deposition of black carbon films. The experiments were limited to 3 hours and formed particles up to about 4 μm in diameter.

HFCVD of diamond relies on the hot surface of a refractory wire to activate the process gases and to perform hydrocarbon dissociation in close proximity to the substrate surface. Many parameters influence the flux of activated particles that reach the substrate surface. Just the filament-related parameters alone include its

material prior to and after carburization, geometry, temperature, filament–substrate distance, and electrical bias voltage between substrate and filament. Since diamond growth depends on the substrate surface temperature and the filament is operated at high temperatures, heat radiation from the filament is an important factor when optimizing process conditions. This thermal radiation and the catalytic efficiency of the filament to form hydrogen are functions of material, temperature, and total surface area. Similar to other multiparameter processes, the optimization of HFCVD is challenging due to the strong interdependence of the many process variables where a variation of a single parameter often causes the simultaneous change of multiple other conditions [44]. For example, while a higher filament temperature will improve the effectiveness of gas activation and increase deposition rate, it will also lead to more impurities in the diamond film and it may simultaneously deteriorate the film thickness uniformity. The incorporation of filament material impurities into the diamond films is a principle disadvantage of HFCVD technology. However, for many applications (e.g., wear parts), these impurities do not prove detrimental to performance [45].

2.4.2 Scaling and current reactor technology

A commercially demonstrated advantage of HFCVD technology is the capability to uniformly coat large-area substrates. Scaling the HFCVD reactor to larger sizes involves using more than one filament. The filament arrangement requires optimization to achieve uniform deposition over large substrate areas. In principle, a group of parallel filaments can be arranged in single or multiple parallel planes and in horizontal or vertical orientation. Placing substrates on both sides of a single plane of parallel filaments greatly improves the energy efficiency of the diamond deposition process [44]. Complex arrangements such as using multiple filament planes and positioning the substrates in between them also requires gas flow optimization to achieve uniform coatings. Even though it may initially appear to be a relatively simple task, it is important to point out that the optimization and scaling of HFCVD reactors is a complex process, in particular because the hot-filament surface also contributes to the decomposition of methyl radicals, which is essential for diamond formation [45].

The company Seki Technotron USA offers the HFCVD reactor “Model 650” with a coatable substrate area of $350 \times 375 \text{ mm}^2$ capable of depositing NCD films [46]. The system can simultaneously coat nine 100 mm diameter wafers with a diamond film thickness uniformity of $\pm 5\%$ across the 90 mm center and a thickness variation from wafer to wafer of $\pm 3\%$. Growth rates for NCD (smallest grain size 10 nm) were as high as $0.7 \mu\text{m/h}$ [47,48]. An even larger substrate size of $500 \times 1000 \text{ mm}^2$ can be accommodated with the “CVDiamond XXL” reactor developed by Fraunhofer Laboratories in Germany [49]. The company CONDIAS GmbH commercialized this reactor technology for the manufacturing of boron-doped diamond electrodes [50]. More recently, the company Advanced Diamond Technologies Inc. entered the electrochemical electrode market, specifically

offering HFCVD-grown boron-doped UNCD electrodes of dimensions up to $150 \times 180 \text{ mm}^2$ for water treatment [51]. HFCVD-grown NCD coatings were also successfully commercialized for advanced cutting tool applications. One of the industry leaders in this field is Diamond Tool Coating [52].

2.4.3 Nanocrystalline diamond versus UNCD

For application selection and diamond growth chemistry considerations, it is important to distinguish ultrananocrystalline from nanocrystalline materials. UNCD according to today's terminology was first synthesized using carbon-containing noble gas plasmas excited by microwave energy [5,6]. However, a hydrogen–methane chemistry with microwave plasma as well as hot-filament excitation will, with increasing carbon supersaturation, also lead to the deposition of a wide variety of nanostructured materials, which are sometimes referred to as “ballas diamond,” “cauliflower diamond,” or “ball-shaped diamond” [53].

Original works on diamond materials with grain sizes of less than 10 nm referred to “nanodiamond” or “nanocrystalline diamond” films [5,6,54–56]. A grain size distribution of 2–5 nm was measured with high-resolution electron microscopy and first shown in Ref. [54]. Early processes used fullerenes as the carbon source and a high percentage of argon with about 20% hydrogen in microwave plasma-assisted deposition [6]. In 1998, a 1% methane and 99% argon process was also demonstrated [55]. UNCD was first distinguished from nanocrystalline materials in around 2001. By then, materials with grain sizes from 2 to 5 nm and 0.3–0.4 nm wide grain boundaries were explicitly termed “ultrananocrystalline” [36,57], whereas grain sizes from 30 to 100 nm were referred to as “nanocrystalline” [58]. However, the usefulness of the term UNCD as a subclass of NCD materials is still questioned by some researchers today [59].

2.4.4 HFCVD (U)NCD synthesis

The explicit search for HFCVD process chemistries similar to microwave plasma-assisted deposition leading to NCD film growth was first reported in Ref. [60]. Inspired by successful experiments growing nanocrystalline phases with MPACVD using carbon-containing noble gas chemistries [5,6,55], Lin et al. varied the feed gas composition through the argon–methane–hydrogen parameter space in search for NCD deposition using a conventional HFCVD system. NCD deposition was found at process conditions of 60 Torr pressure and 875°C substrate surface temperature in a narrow process window of 95.5–98% argon concentration. The films were purely NCD with grain sizes of about 50 nm and no graphitic phases. Based on the similarity of the observed very narrow deposition window for nanocrystalline films with that of MPACVD reports, the authors concluded that the gas-phase chemistry responsible for the transition from MCD to NCD growth may be similar for both MPACVD and HFCVD diamond synthesis techniques. However, the argon–methane-based MPACVD work reported in Ref. [55] indicated the formation of

crystalline diamond films with grain sizes ranging from 3 to 20 nm, which is substantially smaller than the grain sizes of 50 nm observed in Ref. [60]. A 2001 paper by Zhang et al. studies the influence of argon in the hot filament synthesis of NCD using an argon-to-hydrogen ratio of 1:1 at 2% methane content which is substantially more hydrogen as compared to typical microwave plasma-based UNCD synthesis processes) based hot-filament synthesis of NCD films with grain sizes ranging from 4 to 30 nm, which would likely be referred to as “ultrananocrystalline” in today’s terminology. Zhang et al. [61] point out that the argon concentration in their experiments is too low to show a substantial C_2 dimer concentration and thus conclude that C_2 dimers may not be the main growth species.

May et al. [62,63] extended the compositional map for HFCVD growth of NCD in the argon–methane–hydrogen space as originally explored in Ref. [60]. They confirmed the existence of a very narrow process window and found that MPACVD typical gas mixtures of 1% methane in argon and 1–2% hydrogen would only yield graphitic films in their HFCVD experiments. Some NCD was grown in a very narrow process window at about 1% methane at a growth rate of 0.1 $\mu\text{m}/\text{h}$. However, May et al. argue that HFCVD cannot efficiently synthesize UNCD material using argon-dominated chemistries as they are used in MPACVD processes. HFCVD reactors operate at lower power levels and rely on thermal energy for hydrogen dissociation at the filament surface. The very localized heat source (i.e., the filament) also leads to a rapidly decreasing gas temperature toward the substrate. Subsequently, it is difficult for the HFCVD process to maintain sufficient dissociation of molecular hydrogen near the substrate where atomic hydrogen is needed for diamond growth. Conventional hydrogen-dominated chemistries still work for diamond synthesis in HFCVD since there is more hydrogen available near the filament heat source to begin with, and it is also easier for atomic hydrogen to diffuse toward the substrate compared to diffusing in an argon-dominated gas phase [62,63].

Recent HFCVD work using hydrogen–methane chemistries (no argon) in a bias-enhanced process demonstrated the synthesis of nanocrystalline materials with crystal sizes of 7 nm measured by X-ray diffraction [64]. The authors refer to the synthesized material as UNCD as well. Here lies a general difficulty of nomenclature, which is evidenced throughout the literature on UNCD and NCD. So far, there has not been a report published on UNCD synthesis with HFCVD using any process chemistry that actually provides a grain size distribution comparable to those published for argon-dominated MPACVD processes. However, the closest experiment showing HFCVD synthesis of UNCD material is perhaps the one reported in Ref. [61], which not only shows grains as small as 4 nm in high-resolution electron microscopy images but also used substantially less argon in the process feed gas (~50%).

2.5 Summary

Modeling and experimental diagnostics of UNCD microwave discharges have been used to understand the deposition environment. Argon is generally added as

an inert gas for the UNCD deposition process and the small amount of hydrogen, either from the methane or from added hydrogen, is dissociated to a significant extent in UNCD discharges. This atomic hydrogen is important for creating surface conditions that maintain and promote diamond growth. The microwave discharge formed with methane, hydrogen, and predominantly argon shows a characteristic green color from the C_2 Swan band emission. The dominant reactive species for both UNCD and MCD deposition is considered by many researchers to be CH_3 , which bonds to the diamond surface at open sites. However, the CH_3 concentration is lower in UNCD processes leading to a slower deposition rate than for MCD processes. The species fluxes to the surface in UNCD deposition as compared to MCD deposition are modeled to include higher fluxes of such reactive species as C and C_2 . It is the increased flux of species, such as C, C_2 , and other non- CH_3 reactive species, that is one explanation for the high renucleation rate that occurs for the growth of UNCD. These non- CH_3 reactive species are also believed to have some contribution toward the UNCD growth since some species such as C and C_2 can insert easily into the CH bonds at the diamond surface without needing an open surface site. An alternative explanation for the high renucleation rate occurring in UNCD growth is that nanoparticles are formed in the plasma discharge and then they are deposited on the growth surface causing renucleation.

During the past 20 years, the synthesis of MPACVD UNCD has evolved to where large areas can now be coated routinely. New high-density seeding techniques have been developed, and they have enhanced the deposition of thin UNCD films and enabled low substrate temperature ($<500^\circ\text{C}$) synthesis on glass substrates [14]. Using 915 MHz excitation, the synthesis of large area and uniform UNCD films has been expanded to 200 mm diameter substrates. However, there is a trade-off between film uniformity and growth rates. Uniform films are readily grown at lower pressures resulting in lower growth rates. Higher growth rates favor higher pressure, i.e., 120–220 Torr, synthesis. However, they are not as uniform. This issue may be resolved with reactor designs where the discharge position and shape are varied and controlled and reactor walls and the substrate are heated. This approach would lead to a more uniform gas temperature within the reactor volume and also allow substrate temperature control for high growth rates. New reactor designs should focus on concepts where the discharge is positioned into good contact with the substrate and away from all of the other reactor walls.

Additional reactor scale up is possible. Using reactor design techniques that have already been implemented and tested with 2.45 GHz excitation, it is expected that deposition areas in the 915 MHz excited reactors can be expanded further to 300 mm diameter substrates. Even larger deposition areas appear to be possible by further scale up of reactor designs via 400 MHz excitation. Thus, there does not appear any major roadblocks to further increasing MPACVD UNCD synthesis areas.

So far, HFCVD synthesis of UNCD has not been convincingly demonstrated with respect to the applied criteria of using argon-rich deposition chemistries and sub-15 nm grain size distributions. However, HFCVD processes have clearly

produced NCD materials. HFCVD is a capable and scalable deposition technology, which is industrially deployed for the production of diamond materials including MCD, NCD, and their boron-doped variations.

Acknowledgments

The authors would like to acknowledge the National science Foundation, MRSEC program grant DMR- 9809688 (1995–2000) for the support of the initial MPACVD UNCD synthesis activities at Michigan State University. We also acknowledge support from the Fraunhofer USA Center for Coatings and Laser Applications and the Richard M. Hong Chaired Professorship.

References

- [1] D.M. Gruen, Conversion of fullerenes to diamond, US Patents 5,370,855 (1994) and 5,462,776 (1995).
- [2] D.M. Gruen, S.Z. Liu, A.R. Kraus, X.Z. Pan, Diamond film growth from fullerene precursors, US Patent 5,620,512 (1997).
- [3] D.M. Gruen, A.R. Kraus, S.Z. Liu, X.Z. Pan, C.D. Zuiker, Diamond film growth from argon–carbon plasmas, US Patent 5,849,079 (1998).
- [4] D.M. Gruen, X.Z. Pan, A.R. Krauss, S.Z. Liu, J.S. Luo, C.M. Foster, Deposition and characterization of nanocrystalline diamond films, *J. Vac. Sci. Technol. A* 12 (1994) 1491.
- [5] D.M. Gruen, S.Z. Liu, A.R. Krauss, J.S. Luo, X.Z. Pan, Fullerenes as precursors for diamond film growth without hydrogen or oxygen additions, *Appl. Phys. Lett.* 64 (1994) 1502.
- [6] D.M. Gruen, S.Z. Liu, A.R. Krauss, X.Z. Pan, Buckyball microwave plasmas: fragmentation and diamond film growth, *J. Appl. Phys.* 75 (1994) 1758.
- [7] D.M. Gruen, A.R. Krauss, A. Erdemir, C. Bindal, C.D. Zuiker, Smooth diamond films as low friction, long wear surfaces, US Patent 5,989,511 (1999).
- [8] D.M. Gruen, Conversion of fullerenes to diamond, US Patents 5,209,916 (1993) and 5,328,676 (1994).
- [9] D.M. Gruen, C.D. Zuiker, A.R. Krauss, X.Z. Pan, Carbon dimer, C₂, as a growth species for diamond films from methane/hydrogen/argon microwave plasmas, *J. Vac. Sci. Technol. A* 13 (1995) 1628.
- [10] W.S. Huang, Microwave Plasma Assisted Chemical Vapor Deposition of Ultra-Nanocrystalline Diamond Films, Ph.D. Thesis, Michigan State University, Michigan, 2004.
- [11] J.C. Richley, O.J.L. Fox, M.N.R. Ashfold, Y.A. Mankelevich, Combined experimental and modeling studies of microwave activated CH₄/H₂/Ar plasmas for microcrystalline, nanocrystalline and ultrananocrystalline diamond deposition, *J. Appl. Phys.* 109 (2011) 063307.
- [12] F. Bénédic, G. Lombardi, K. Hassouni, F. Mohasseb, A. Gicquel, Plasma-assisted synthesis: plasma experimental diagnostics and modeling, in: O.A. Shenderova, D.M. Gruen (Eds.), *Ultrananocrystalline Diamond: Synthesis, Properties, and Applications*, 2006, p. 185 (Chapter 6), William Andrew Publishing, Norwich, New York USA.

- [13] J.E. Butler, A.V. Sumant, The CVD of nanodiamond materials, *Chem. Vap. Deposition* 14 (2008) 145.
- [14] O. Auciello, A.V. Sumant, Status and review of the science and technology of ultra-nanocrystalline diamond (UNCD™) films and application to multifunctional devices, *Diamond Relat. Mater.* 19 (2010) 699.
- [15] J.E. Butler, Y.A. Mankelevich, A. Cheesman, J. Ma, M.N.R. Ashfold, Understanding the chemical vapor deposition of diamond: recent progress, *J. Phys. Condens. Mater.* 21 (2009) 364201.
- [16] D.G. Goodwin, J.E. Butler, Theory of diamond chemical vapor deposition, in: M.A. Prelas, G. Popovici, L.K. Bigelow (Eds.), *Handbook of Industrial Diamonds and Diamond Films*, Dekker, New York, NY, 1997, pp. 527–581.
- [17] Y.A. Mankelevich, M.N.R. Ashfold, J. Ma, Plasma-chemical processes in microwave plasma-enhanced chemical vapor deposition reactors operating with C/H/Ar gas mixtures, *J. Appl. Phys.* 104 (2008) 113304.
- [18] A.N. Goyette, J.E. Lawler, L.W. Anderson, D.M. Gruen, T.G. McCauley, D. Zhou, et al., C₂ swan band emission intensity as a function of C₂ density, *Plasma Sources Sci. Technol.* 7 (1998) 149.
- [19] J.R. Rabeau, P. John, J.I.B. Wilson, Y. Fan, The role of C₂ in nanocrystalline diamond growth, *J. Appl. Phys.* 96 (2004) 6724.
- [20] G. Lombardi, K. Hassouni, F. Bénédic, F. Mohasseb, J. Ropcke, A. Gicquel, Spectroscopic diagnostics and modeling of Ar/H₂/CH₄ microwave discharges used for nanocrystalline diamond deposition, *J. Appl. Phys.* 96 (2004) 6739.
- [21] J. Ma, J.C. Richley, M.N.R. Ashfold, Y.A. Mankelevich, Probing the plasma chemistry in a microwave reactor used for diamond chemical vapor deposition by cavity ring down spectroscopy, *J. Appl. Phys.* 104 (2008) 103305.
- [22] P.W. May, J.N. Harvey, N.L. Allan, J.C. Richley, Y.A. Mankelevich, Simulations of chemical vapor deposition diamond film growth using a kinetic Monte Carlo model and two-dimensional model of microwave plasma and hot filament chemical vapor deposition reactors, *J. Appl. Phys.* 108 (2010) 114909.
- [23] P.W. May, J.N. Harvey, J.A. Smith, Y.A. Mankelevich, Reevaluation of the mechanism for ultrananocrystalline diamond deposition from Ar/CH₄/H₂ gas mixtures, *J. Appl. Phys.* 99 (2006) 104907.
- [24] J.C. Richley, J.N. Harvey, M.N.R. Ashfold, On the role of carbon radical insertion reactions in the growth of diamond by chemical vapor deposition methods, *J. Phys. Chem. A* 113 (2009) 11416.
- [25] M. Eckert, E. Neyts, A. Bogaerts, Differences between ultrananocrystalline and nanocrystalline diamond growth: theoretical investigations of C_xH_y species at diamond step edges, *Cryst. Growth Des.* 10 (2010) 4123.
- [26] M. Eckert, E. Neyts, A. Bogaerts, Insights into the growth of (ultra)nanocrystalline diamond by combined molecular dynamics and Monte Carlo simulations, *Cryst. Growth Des.* 10 (2010) 3005.
- [27] Y. Ando, T. Tachibana, K. Kobashi, Growth of diamond films by a 5-kW microwave plasma CVD reactor, *Diamond Relat. Mater.* 10 (2001) 312.
- [28] K.P. Kuo, J. Asmussen, An experimental study of high pressure synthesis of diamond films using a microwave cavity plasma reactor, *Diamond Relat. Mater.* 6 (1997) 1097.
- [29] S.S. Zuo, M.K. Yaran, T.A. Grotjohn, D.K. Reinhard, J. Asmussen, Investigation of diamond deposition uniformity and quality for freestanding film and substrate applications, *Diamond Relat. Mater.* 17 (2008) 300.

- [30] J. Asmussen, J. Hopwood, F.C. Sze, A 915MHz/2.45GHz ECR plasma source for large area ion beam and plasma processing, *Rev. Sci. Instrum.* 61 (1990) 250.
- [31] F.C. Sze, J. Asmussen, Experimental scaling laws for ECR plasma sources, *J. Vac. Sci. Technol. A* 11 (1993) 1289.
- [32] Y. Ando, Y. Yokota, T. Tachibana, A. Watanabe, Y. Nishibayashi, K. Kobashi, et al., Large area deposition of <100>-textured diamond films by a 60-kW microwave plasma CVD reactor, *Diamond Relat. Mater.* 17 (2008) 1055.
- [33] E. Woerner, C. Wild, W. Mueller-Sebert, P. Koidl, CVD-diamond optical lenses, *Diamond Relat. Mater.* 5 (1996) 688.
- [34] W.S. Huang, D.T. Tran, J. Asmussen, T.A. Grotjohn, D. Reinhard, Synthesis of thick, uniform, smooth ultrananocrystalline diamond films by microwave plasma-assisted chemical vapor deposition, *Diamond Relat. Mater.* 15 (2006) 341.
- [35] D.T. Tran, Synthesis of Thin and Thick Ultra-Nanocrystalline Diamond Films by Microwave Plasma CVD System, M.Sc. Dissertation, Michigan State University, Michigan, 2005.
- [36] D.T. Tran, W.S. Huang, J. Asmussen, T.A. Grotjohn, D. Reinhard, Synthesis of ultrananocrystalline diamond films by microwave plasma-assisted chemical vapor deposition, *New Diamond Front. Carbon Technol.* 16 (2006) 281.
- [37] D. King, M.K. Yaran, T. Schuelke, T.A. Grotjohn, D.K. Reinhard, J. Asmussen, Scaling the microwave plasma-assisted chemical vapor deposition of diamond over 150–200 mm wafer substrates, *Diamond Relat. Mater.* 17 (2008) 520.
- [38] T.A. Grotjohn, J. Asmussen, In: J. Asmussen, D.K. Reinhard (Eds.), *Diamond Films Handbook*, Dekker, New York, NY, 2002, pp. 211–302 (Chapter 7 - Microwave-Plasma Assisted Diamond Deposition, particularly pp. 217–219).
- [39] <<http://www.microcure.com>>
- [40] <<http://www.cyrannus.com>>
- [41] F. Silva, K. Hassouni, X. Bonin, A. Gicquel, Microwave engineering of plasma-assisted CVD reactors for diamond deposition, *J. Phys. Condens. Matter* 21 (2009) 364303.
- [42] B. Bi, W.S. Huang, J. Asmussen, B. Golding, Surface acoustic waves on nanocrystalline diamond, *Diamond Relat. Mater.* 11 (2002) 677.
- [43] S. Matsumoto, Y. Sato, M. Tsutsumi, N. Setaka, Growth of diamond particles from methane–hydrogen gas, *J. Mater. Sci.* 17 (1982) 3106.
- [44] R. Haubner, B. Lux, Diamond growth by hot-filament chemical vapor deposition: state of the art, *Diamond Relat. Mater.* 2 (1993) 1277.
- [45] C.-P. Klages, L. Schäfer, Hot-filament deposition of diamond, low-pressure synthetic diamond: manufacturing and applications, in: B. Dischler, C. Wild (Eds.), *Springer Series in Materials Processing*, 1998, p. 85, Springer-Verlag, Berlin/Heidelberg.
- [46] <<http://www.sekicvdsolutions.com/hot-filament/reactors.html>>
- [47] J. Zhang, J.W. Zimmer, R.T. Howe, R. Maboudian, Characterization of boron-doped micro- and nanocrystalline diamond films deposited by wafer-scale hot filament chemical vapor deposition for MEMS applications, *Diamond Relat. Mater.* 17 (2008) 23.
- [48] S. Porro, G. De Temmerman, S. Lisgo, P. John, I. Villalpando, J.W. Zimmer, et al., Nanocrystalline diamond coating of fusion plasma facing components, *Diamond Relat. Mater.* 18 (2009) 740.
- [49] <<http://www.ist.fhg.de>>
- [50] <<http://www.condias.de>>
- [51] <<http://www.thindiamond.com>>

- [52] <<http://www.diamondtc.com>>
- [53] R. Haubner, B. Lux, Deposition of ballas diamond and nano-crystalline diamond, *Int. J. Refract. Met. Hard Mater.* 20 (2002) 93.
- [54] L.C. Quint, D. Zhoutt, A.R. Krauss, D.M. Gruen, The characterization of nanodiamond thin films, *Nanostruct. Mater.* 10 (1998) 649.
- [55] D. Zhou, T.G. McCauley, L.C. Qin, A.R. Krauss, D.M. Gruen, Synthesis of nanocrystalline diamond thin films from an Ar-CH₄ microwave plasma, *J. Appl. Phys.* 83 (1998) 540.
- [56] D.M. Gruen, Nanocrystalline diamond films, *Annu. Rev. Mater. Sci.* 29 (1999) 211.
- [57] S. Bhattacharyya, O. Auciello, J. Birrell, J.A. Carlisle, L.A. Curtiss, A.N. Goyette, et al., Synthesis and characterization of highly-conducting nitrogen-doped ultrananocrystalline diamond films, *Appl. Phys. Lett.* 79 (2001) 1441.
- [58] H.D. Espinosa, B. Peng, B.C. Prorok, N. Moldovan, O. Auciello, J.A. Carlisle, et al., Fracture strength of ultrananocrystalline diamond thin films—identification of Weibull parameters, *J. Appl. Phys.* 94 (2003) 6076.
- [59] O.A. Williams, Nanocrystalline diamond, *Diamond Relat. Mater.* 20 (2011) 621.
- [60] T. Lin, G.Y. Yu, A.T.S. Wee, Z.X. Shen, K.P. Loh, Compositional mapping of the argon-methane-hydrogen system for polycrystalline to nanocrystalline diamond film growth in a hot-filament chemical vapor deposition system, *Appl. Phys. Lett.* 77 (2000) 2692.
- [61] Y.F. Zhang, F. Zhang, Q.J. Gao, X.F. Peng, Z.D. Lin, The roles of argon addition in the hot filament chemical vapor deposition system, *Diamond Relat. Mater.* 10 (2001) 1523.
- [62] P.W. May, J.A. Smith, Y.A. Mankelevich, Deposition of NCD films using hot filament CVD and Ar/CH₄/H₂ gas mixtures, *Diamond Relat. Mater.* 15 (2006) 345.
- [63] P.W. May, Y.A. Mankelevich, Experiment and modeling of the deposition of ultrananocrystalline diamond films using hot filament chemical vapor deposition and Ar/CH/H gas mixtures: a generalized mechanism for ultrananocrystalline diamond growth, *J. Appl. Phys.* 100 (2006) 024301.
- [64] F. Klauser, D. Steinmüller-Nethl, R. Kaendl, E. Bertel, N. Memmel, Raman studies of nano and ultra-nanocrystalline diamond films grown by hot-filament CVD, *Chem. Vap. Deposition* 16 (2010) 127.

Theoretical Studies of UNCD Properties

3

Shashishekar P. Adiga^a, Peter Zapol^b, and Larry A. Curtiss^b

^aKodak Research Laboratories, Eastman Kodak Company, Rochester, NY,

^bMaterials Science Division, Argonne National Laboratory, Argonne, IL

CHAPTER OUTLINE

3.1 Introduction	85
3.2 Computational methodologies	86
3.2.1 Classical MD simulations	86
3.2.2 DFTB calculations	86
3.3 Bulk properties of UNCD	87
3.3.1 UNCD model generation	87
3.3.2 Structure of GBs	89
3.3.3 Vibrational spectra	91
3.3.4 Specific heat and Debye temperature	92
3.3.5 Thermal stability and the effect of annealing on sp^2/sp^3 composition	95
3.4 Surface properties: CNT-diamond hybrid nanomaterials	97
3.5 Concluding remarks	99
Acknowledgment	100
References	100

3.1 Introduction

Ultrananocrystalline diamond (UNCD) films are characterized by a microstructure of crystallites with an average size of up to about 10 nm [1]. The properties of the films are significantly different from those that have larger grain sizes, such as nanocrystalline or microcrystalline diamond, which are grown in hydrogen-rich plasma and have distinctly different growth mechanisms [2]. The unique electrical and mechanical properties of UNCD films open numerous opportunities for specific applications in tribology, microelectromechanical systems (MEMS), electrochemistry, and electronics. These properties have been the subject of many studies and have been reviewed in the previous book on this subject [3]. Since then there has been further exploration of the properties of UNCD that continue to reveal interesting new aspects of this novel material.

In this chapter, we describe research carried out to understand various aspects of the physical properties of UNCD from a computational perspective. This chapter reviews recent computational studies of bulk mechanical and thermodynamic properties of UNCD. This includes molecular dynamics (MD) studies to elucidate the structure of grain boundaries of UNCD, predictions of its vibrational spectra, calculations of its specific heat and Debye temperatures, and thermal stability. In addition, we also review recent work on the hybrid materials formed from carbon nanotubes (CNTs) on diamond surfaces. In Section 3.2 we review the computational methodologies that have been used to study the properties of UNCD including density functional based tight-binding (DFTB) and MD simulations. In Section 3.3 we discuss computational studies of the bulk properties of UNCD, while in Section 3.4 we review some surface properties of diamond hybrid materials, which was motivated by UNCD studies. Concluding remarks appear in Section 3.5.

3.2 Computational methodologies

The presentation in this chapter is based on classical MD and DFTB calculations. While the DFT-based methods have the advantage of providing information regarding electronic properties, classical MD simulations present a computationally efficient means of probing mechanical and phonon properties when the system size is large. The DFT-based methods, using the current state-of-the-art high performance computers, are suitable for simulating systems comprising up to a few thousand atoms or approximately one nanodiamond (ND) particle of 2–3 nm size; whereas, using the classical MD simulations systems with thousands of nanoscale grains may be computed. We briefly discuss the details of these methods in the following sub-sections.

3.2.1 Classical MD simulations

The force field we have used in these simulations is the second-generation reactive empirical bond-order (REBO-II) potential [4]. This potential, which is fitted to the experimental values of cohesive energy, lattice parameters, and elastic constants, has been successfully applied in many works concerning a wide variety of carbon systems including diamond [5,6], amorphous carbon [7], ND [8,9], and nanotubes [10,11]. This potential considers local coordination and the degree of conjugation and has been successful in describing both sp^2 and sp^3 hybridized bonds. Classical equations of motion for each atom were numerically integrated using a third-order Nordsieck predictor–corrector algorithm with a time step size 0.5 fs. Prior to calculating the properties, the system was equilibrated at a given temperature using a Langevin thermostat. The microcanonical (NVE) ensemble was used for production runs.

3.2.2 DFTB calculations

The modeling of structures and properties of nanostructured carbon materials, such as diamond-nanotube hybrid systems considered in this chapter, requires a

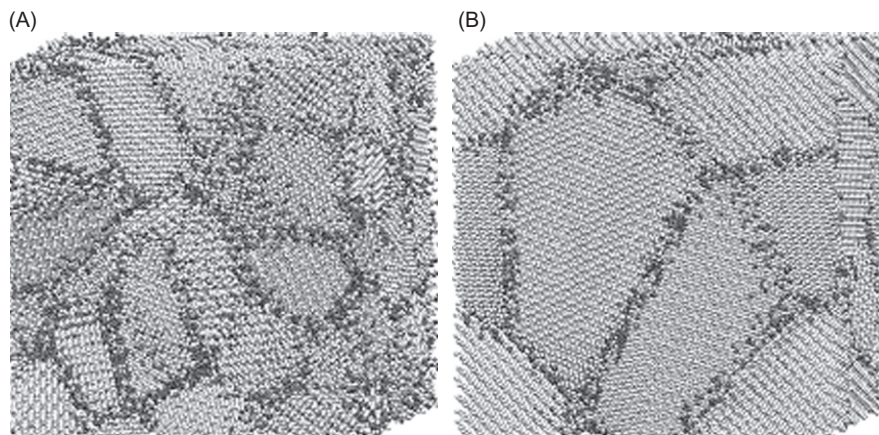
compromise between the number of atoms and the level of theoretical approximations in the calculations. In some of the work discussed in this chapter, the tight-binding methodology has been employed to study carbon nanotunnels on diamond surfaces. The method includes quantum mechanics in an approximate way so that a sufficiently large number of atoms can be handled, yet it includes electronic structure. The tight-binding approach that is used is a self-consistent charge DFTB (SCC-DFTB, denoted as DFTB in short) method that is parameterized by fitting to density functional results for appropriate systems as developed by Frauenheim and coworkers [12,13].

3.3 Bulk properties of UNCD

3.3.1 UNCD model generation

The grain size of a UNCD film determines the sp^2 and hydrogen content. It follows that smaller grains result in higher grain-boundary (GB) areas, which in turn leads to higher sp^2 and hydrogen content. Additionally, grain boundaries contain carbon atoms with the sp^1 and noninteger hybridization states. During the plasma-assisted chemical vapor deposition (CVD) process, increasing carbon/hydrogen ratio leads to higher re-nucleation rates and the grains become smaller [1,14]. The structure of grain boundaries in UNCD continued to receive significant attention in recent years as it plays an important role in determining the mechanical, thermal, and electronic properties of UNCD films. High resolution transmission electron microscopy (HRTEM) images have provided evidence for randomly oriented crystallites and an atomically sharp GB region [15]. Because the grains sizes are extremely small and the grains are randomly oriented [15,16], there are numerous possibilities for two crystallographic planes to meet at a GB in UNCD. Thus, in addition to the fact that carbon can form both sp^2 and sp^3 hybridized electronic states, the structure and bonding at the UNCD grain boundaries is complex and not completely known [17]. The use of an appropriate atomic model with a realistic GB structure is critically important. A majority of the previous theoretical descriptions of UNCD grain boundaries have considered “special” GB planes [17–19]; for example, the high-angle (100) plane or the $\Sigma 13$ twist (100) GB.

Keblinski et al. [17] used Monte Carlo simulations and the Tersoff potential to obtain high-temperature equilibrated GB atomic structures and energies for a set of twist boundaries with different degrees of misorientation between the two grains in a bicrystal. They considered the high-angle twist boundaries to represent the mostly incommensurate grain boundaries between randomly oriented grains in UNCD. They observed that in diamond, because of its greater bond stiffness and carbon’s ability to change hybridization, the structural disorder is energetically much more costly as compared to small bond distortions that lead to local sp^2 -type bonding. The competition between structural disordering and local coordination disordering translates into considerably more ordered GB structures than in silicon GBs, where atoms tend to retain sp^3 hybridization at the cost of structural disorder. This results in very narrow GB regions with as many as 80% of the GB atoms

**FIGURE 3.1**

The model systems used in this work: (A) UNCD (2nm) and (B) UNCD (4nm). Under-coordinated atoms are colored dark to indicate the grain boundaries.

being only threefold-coordinated in diamond [17]. A tight-binding MD study of the $\Sigma 29$ twist GB of diamond by Cleri et al. [18] indicated that about 40% of the GB atoms are threefold-coordinated. DFTB MD simulations by Zapol et al. [19] on the $\Sigma 5$, $\Sigma 13$, and $\Sigma 29$ twist (100) grain boundaries in diamond found about 50% of the atoms in the interface fourfold-coordinated, with the rest having lower coordination.

Remediakis et al. [20] have studied mechanical properties of UNCD models that consisted of random grain orientations, using the Tersoff potential. Their simulations of UNCD models with random grain orientations led them to conclude that the local bulk moduli of sp^1 and sp^2 atoms in the GBs, derived from decomposition by dimensional fitting of the second energy derivatives over volume, could be significantly lower than the bulk moduli of sp^3 atoms that resulted in the softening of UNCD as the grain size decreased. The vibrational properties of UNCD discussed in the next section are based on UNCD models constructed using the Voronoi method [21]. In this method, a set of grain centers in a periodic simulation box are chosen at random but with average spacing corresponding to the desired grain size. The region of space closer to a given center than to any other center is filled with atoms in the diamond lattice with a randomly selected crystallographic orientation. While inserting atoms near the Voronoi lines, an insertion is rejected if the atom being inserted is within 2\AA of any existing atom in other grains. This way, no two atoms belonging to two different grains are closer than 2\AA initially (during the course of the simulation they may arrange and rebond to closer spacings). We used a cubic, 3D periodic simulation box. Before performing production runs, the systems were annealed for 50ps at 1000K, allowing unfavorable configurations in the grain boundaries to relax. Here, we have considered UNCD models with 2 and

Table 3.1 Properties of the Model Systems Simulated

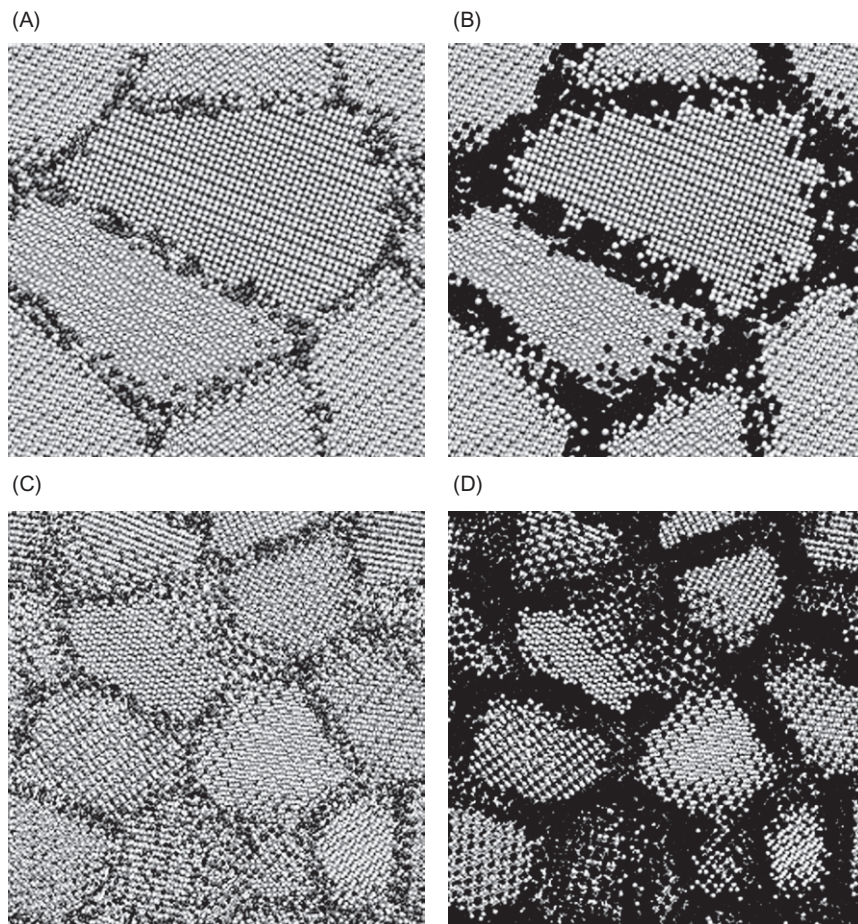
	Diamond	UNCD (4 nm)	UNCD (2 nm)
Number of atoms	64,000	82,696	81,769
Number of grains/particles	–	8	66
sp ¹ content (%)	0	0.9	4
sp ² content (%)	0	11.6	23.7
sp ³ content (%)	100	87.5	72.3
Box dimension (Å)	70.89	78.56	80.51

4 nm average grain sizes as illustrated in [Figure 3.1](#). For comparison, we have also simulated a bulk diamond system. The properties of the UNCD models presented in this work are summarized in [Table 3.1](#).

3.3.2 Structure of GBs

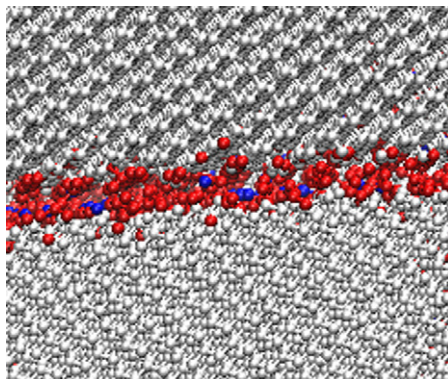
In [Figure 3.2A and C](#), we have depicted a cross section of the periodic simulation box to show atoms based on their coordination number for 4 and 2 nm models, respectively. The coordination number is calculated by counting all the bonding neighbors of an atom. Two atoms are considered bonded if the distance between them is less than 2 Å, the value corresponding to the minimum between the first two peaks in the radial distribution function. The under-coordinated atoms are shown in darker colors and are mostly confined to very narrow regions where the grains meet. They terminate individual crystallites at the grain boundaries.

To further examine the structure at the atomic level, we classify atoms according to the local crystalline order using common neighbor analysis (CNA) [22] with the visualization tool, OVITO [23]. The CNA determines if the local structure around an atom corresponds to the diamond lattice based on the connections it make to the nearest neighbors. In [Figure 3.2B](#), the same cross-sectional view of the model UNCD (4 nm) system as [Figure 3.2A](#) is shown with atoms colored based on their local crystalline order. Similarly, in [Figure 3.2D](#), the cross section of the 2 nm system shown in [Figure 3.2C](#) is illustrated based on local crystalline order. The light colored atoms are in local diamond crystal order and hence considered core atoms that are “inside” the grains; all other atoms, colored dark, are considered as belonging to the grain boundaries as they lack local diamond crystal order. The under-coordinated atoms in [Figure 3.2A](#), for example, are confined to a narrower region near the grain boundaries as compared to the atoms that deviate from diamond lattice in [Figure 3.2B](#). This is because the sp³ hybridized atoms near the grain boundaries are often bonded to sp² or sp¹ hybridized atoms, hence altering their local environment. To determine the width of the GB region we defined a cut-off distance d_{GB} and counted the number of atoms classified as not in diamond lattice by the CNA. The distance d_{GB} is the distance from an under-coordinated atom; we use this criterion because the under-coordinated atom determines the position of

**FIGURE 3.2**

The cross sections of 4 nm (A and C) and 2 nm (B and D) grain-sized UNCD models. The atoms are colored according to (A and B) coordination number: silver, gray, and black colors indicate 4-, 3-, and 2-coordinated C atoms, respectively; (C and D) local crystalline order based on the CNA: lighter colored atoms are in diamond crystalline order.

the grain's edge. Approximately 80% of all the atoms classified as not belonging to the core by the CNA are within a distance of $d_{GB} = 3.0 \text{ \AA}$ from the nearest under-coordinated atoms. It is important to note that, based on this analysis 80% of all the atoms that deviate from a diamond lattice are at most the third nearest neighbor of an under-coordinated atom. Thus, beyond the third neighbor of an under-coordinated atom, or within 3.0 \AA from the interface, the structure is bulk diamond like. Thus the total width of the GB region is $\sim 6\text{--}8 \text{ \AA}$. A close-up view of a GB is shown in Figure 3.3, with 3- and 2-coordinated atoms in red and blue, respectively. The

**FIGURE 3.3**

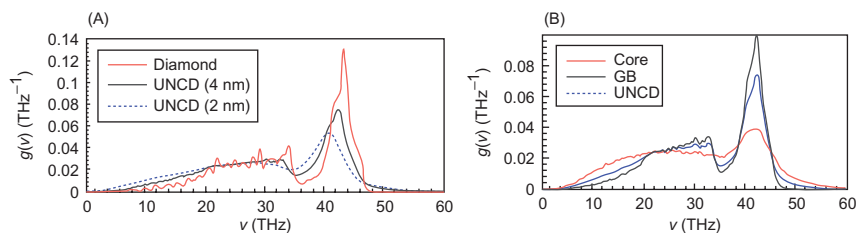
Snapshot from a GB region. 3- and 2-coordinated atoms are colored red and blue, respectively.

grain boundaries are characterized by void regions interspersed with bonds formed between C atoms across the boundary.

3.3.3 Vibrational spectra

Phonons directly influence several material properties including, for example, the specific heat capacity, the thermal expansion coefficient, the thermal conductivity (specifically at low temperatures), and the temperature dependence of the elastic constants [24]. In addition, they may play an important role in determining electrical and optical properties as well. The vibrational properties depend on the local atomic structure and it is important to analyze the vibrational spectra of UNCD as the nanocrystallinity implies that there is a considerable fraction of GB atoms, and it differs from the vibrational properties of CVD diamond composed of larger grain sizes. In addition to causing a reduction in the phonon mean free path, the GBs, as noted before, have under-coordinated atoms and local crystalline order different from the interior of the grains.

In Figure 3.4A, we have presented the computed vibrational spectra at $T = 300$ K for the two UNCD model systems (2 and 4 nm grain sizes) and the single crystal diamond. Before comparing the spectra of the model systems, it is important to point out that simulated vibrational spectra have, in general, features shifted to higher energies compared to experiment. This shift lies within the range of deviations observed in previous calculations using bond-order potentials [25]. Nonetheless, the calculated power spectrum bears a reasonably good agreement with the experimental vibrational spectrum of diamond [26]. The main feature of the spectrum for single crystal diamond is a strong peak at ~ 43.2 THz (1425 cm^{-1}) with two shoulders around 41.5 THz (1384 cm^{-1}) and 45 THz (1501 cm^{-1}). This peak is followed by a

**FIGURE 3.4**

(A) The calculated vibrational spectra of UNCD (4 nm), UNCD (2 nm), and single crystal diamond (solid line) at $T = 300 \text{ K}$. (B) The partial spectra due to GB and core atoms for the UNCD (4 nm) system at $T = 300 \text{ K}$.

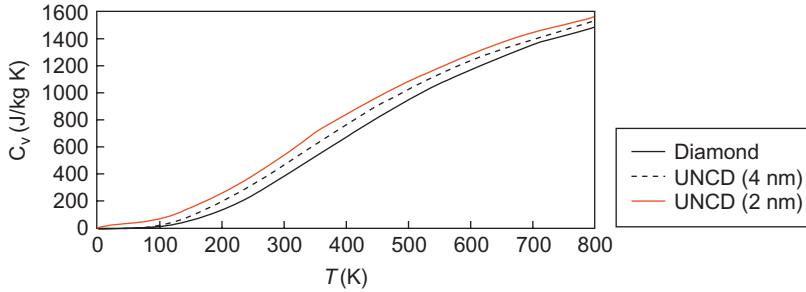
smaller peak at 33.7 THz (1128 cm^{-1}) and a relatively flat region at intermediate frequencies. The overall features of the vibrational spectra of UNCD systems are similar to that of single crystal diamond. However, there are significant differences, most notably, the whole spectrum in each UNCD model is redshifted in comparison to diamond. For example, in the case of UNCD (4 nm) the main peak around 43 THz is redshifted to 42 THz , an effect of phonon confinement that is common to nanocrystalline materials. In addition, this peak is broader and smaller for UNCD. The redshift for the UNCD (2 nm) system is larger owing to smaller crystallite size. For UNCD systems, a high-frequency tail extends beyond 47 THz . The high-frequency tail is attributed to strained bonds involving under-coordinated atoms in the grain boundaries/surfaces that have enhanced force constants.

In Figure 3.4B we show normalized partial spectra of GB and core atoms for the UNCD (4 nm) system at 300 K . The GB atoms are defined as all the under-coordinated atoms (sp^2 and sp^1 hybridized) and atoms that are within a distance of 3 \AA from them. The remaining atoms are defined as core (interior) atoms. For comparison the total spectrum of the UNCD (4 nm) system is also plotted. The spectrum of GB atoms is clearly disordered as it shows signatures of both under-coordinated and sp^3 atoms. The optical peak due to sp^3 atoms in the core region is redshifted to 42 THz as compared to single crystalline diamond (43.2 THz) due to the phonon confinement effect. Based on the comparison of the spectra of GB and core atoms with the total spectra of the UNCD system, the enhancement of the acoustical modes at lower frequency can be directly attributed to the GB atoms.

3.3.4 Specific heat and Debye temperature

To study the effect of temperature on the specific heat of UNCD, the phonon specific heats of UNCD and diamond are computed from the temperature-dependent vibrational spectra using the following equation:

$$C_V = \frac{h^2}{k_B T^2} \int_0^\infty \frac{\nu^2 \exp(h\nu / k_B T)}{(\exp(h\nu / k_B T) - 1)^2} g(\nu) d\nu \quad (3.1)$$

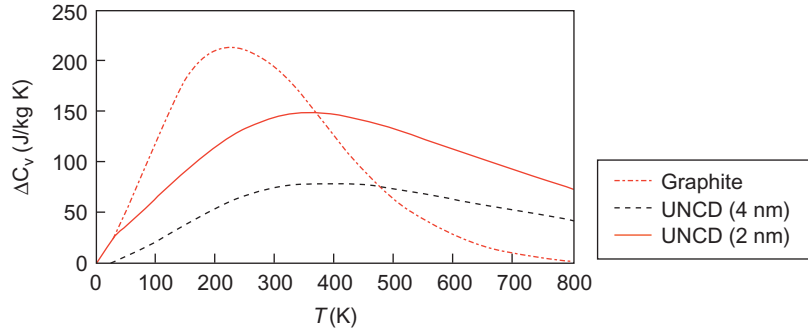
**FIGURE 3.5**

Temperature dependence of the specific heat at constant volume for UNCD (4 nm), UNCD (2 nm), ND particle, and diamond systems.

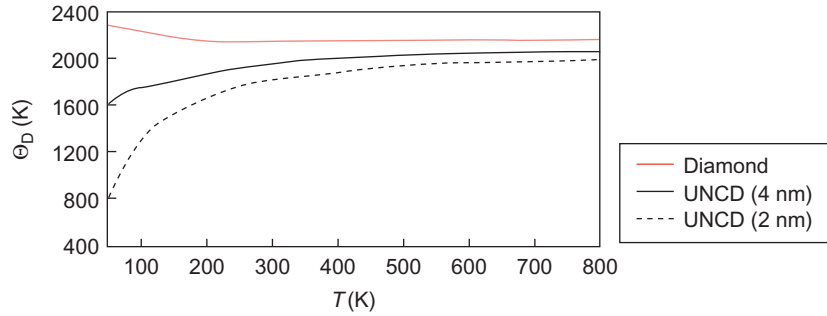
The plot in [Figure 3.5](#) shows the specific heat of UNCD (4 nm), UNCD (2 nm), ND particle, and single crystal diamond as a function of temperature. We note that our computed value C_v of diamond is lower than that of experimental values, for example, the computed C_v is 380 J/kg K at 300 K as compared to the experimental value of 502 J/kg K. This discrepancy is due to many factors including (i) the absence of defects such as vacancies, impurities, and isotopes in our model and (ii) the interatomic potential. For example, previous calculations [27] of C_v of diamond employing the REBO-II have reported similar deviations in the computed C_v from experimental values.

The specific heats of all three ND models are enhanced as compared to single crystal diamond over the whole range of the temperature we have considered. The excess specific heat as a function of temperature is plotted in [Figure 3.6](#). For comparison, the excess specific heat of graphite compared against diamond as obtained from Ref. [28] is also plotted. The excess specific heat of UNCD systems go through a maximum value at ~ 350 K and the C_v values for UNCD (4 nm) and UNCD (2 nm) models are 15% and 33% greater, respectively, than single crystal diamond.

The relative importance of contributions from frequencies < 20 THz occurs mostly at low temperatures. As the temperature increases, the relative contribution of excess states in the low to medium frequency region in UNCD becomes less important. Therefore, the excess C_v goes through a maximum around 350 K. In comparison, the maximal excess for bulk graphite in relation to bulk single crystal diamond ([Figure 3.6](#)) occurs around 200 K. Note that in UNCD excess specific heat is due to the contributions from atoms at grain boundaries (under-coordinated sp^2 and sp^1 atoms, sp^3 atoms bonded to under-coordinated atoms, or sp^3 atoms very close to grain boundaries) which have slightly different bonding energies in contrast to the perfect order of sp^3 bonded diamond or sp^2 bonded graphite. We note that the sharp sp^3 features of single crystal diamond or sp^2 bonded graphite visible in the vibrational spectra are broadened by the different energy landscapes due to

**FIGURE 3.6**

The excess specific heat of UNCD models and ND particle as compared to single crystal diamond. For comparison, the excess specific heat for graphite as reported in Ref. [28] is also plotted.

**FIGURE 3.7**

The Debye temperature as a function of temperature for UNCD (4 nm) and UNCD (2 nm) models and diamond.

the disorder at the grain boundaries. This broadening of the vibrational spectra features results in excess specific heat.

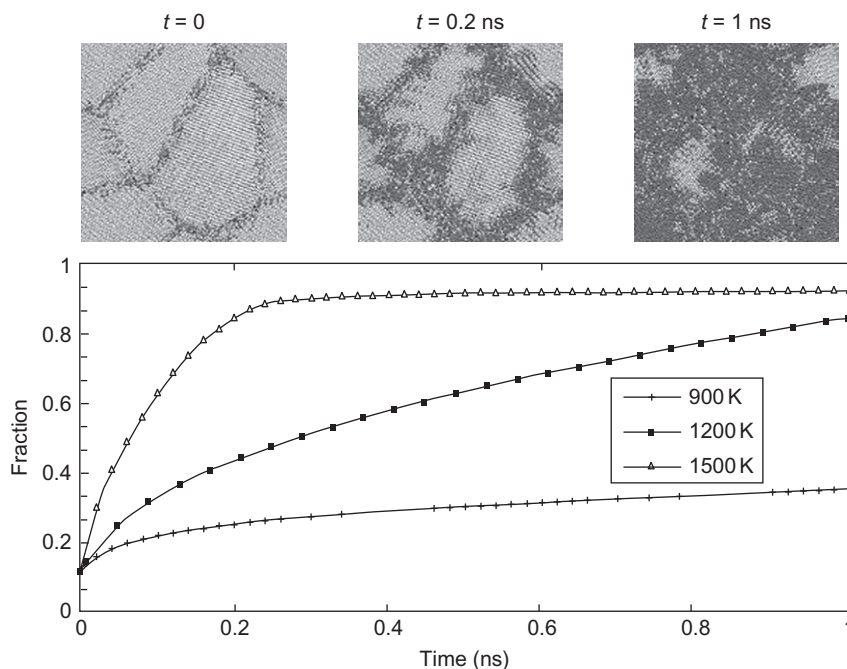
We now turn to the Debye temperature of UNCD. It is proportional to the Debye frequency and within the harmonic approximation relates to the stiffness of the material. The GB atoms are expected to cause reduced stiffness in UNCD as compared to the diamond model. From the simulated C_v versus temperature behavior we calculated the Debye temperature as a function of temperature as detailed elsewhere [9,27]. We plotted the Debye temperatures for the two UNCD systems and diamond models as a function of temperature in Figure 3.7. The Debye

temperature of diamond is overestimated in our calculations [29] because the simulated C_v values in our work are lower than the experimental values as discussed previously. However, the relative values of diamond and UNCD models provide useful information about the stiffness of the material. The Debye temperatures of UNCD (2nm) and UNCD (4nm) systems are $\sim 15\%$ and 9% lower, respectively, than that of diamond at 300 K. The softening of UNCD can be explained on the basis of GB atoms leading to an enhancement of soft modes in the vibrational spectra compared to diamond.

3.3.5 Thermal stability and the effect of annealing on sp^2/sp^3 composition

The thermal stability of UNCD films is important for many applications. It is well known that ND particles undergo graphitization when heated above 1200 K, and the graphitization process begins at the surface and proceeds towards the center of the particles [8]. The grains in UNCD are somewhat different from ND particles as they are terminated by GBs instead of free surfaces and it is expected that UNCD is more stable than ND. While there has not been extensive work on the thermal stability of UNCD, in a recent work Michaelson et al. [30] investigated bulk and surface thermal stability of UNCD films with 10–20 nm grain size. They showed that annealing at temperatures up to 1200°C caused considerable surface graphitization, whereas the bulk remained relatively stable. However, the thermal stability of UNCD films with smaller grain sizes and hence larger GB volumes remains to be investigated. Many properties, most notably electronic properties, are dependent on the sp^2/sp^3 composition in UNCD films. An increase in the fraction of sp^2 bonded carbon due to annealing-induced conversion of sp^3 to sp^2 hybridized atoms in UNCD is expected to lead to an increase in electrical conductivity. An intriguing possibility is to anneal UNCD in a controlled fashion to yield a desired sp^2/sp^3 composition and electrical conductivity. For this purpose, it is important to probe the annealing-induced transformation of UNCD to determine the temperature and extent of transformation.

Here, we present results from classical MD simulations of annealing-induced sp^3 – sp^2 transformation in the 4 nm grain size UNCD model annealed at $T = 900$, 1200, and 1500 K in an isobaric–isothermal ensemble (NPT). In Figure 3.8 the time evolution of sp^3 – sp^2 is illustrated with a series of snapshots of a cross section, the UNCD system after $t = 0$, 0.2, and 1 ns of annealing at $T = 1200$ K. The 2-, 3-, and 4-coordinated carbon atoms are colored black, gray, and silver, respectively. The transformation begins at the GBs and progresses toward the center of the grains. The plot of the fraction of sp^2 hybridized atoms further illustrates the progression of the transformation in terms of fraction of sp^2 and sp^3 atoms as a function of annealing time. The fractions of sp^2 atoms in the resulting structures obtained after annealing for 1 ns at 900, 1200, and 1500 K are 0.35, 0.84, and 0.92, respectively. The transformation appears to be near completion after about

**FIGURE 3.8**

Progression of sp^3 - sp^2 conversion during the initial stages of annealing. The fraction of sp^2 hybridized carbon atoms in the 4 nm grain-sized UNCD model is plotted as a function of annealing time at $T = 900$, 1200, and 1500 K. The transformation at $T = 1200$ K is also depicted in the form of snapshots of a cross section of the simulation box after $t = 0$, 0.2, and 1 ns of annealing. The 2-, 3-, and 4-coordinated carbon atoms are colored black, gray, and silver, respectively. The sp^3 - sp^2 transformation begins at grain boundaries and proceeds toward the interior of the grains.

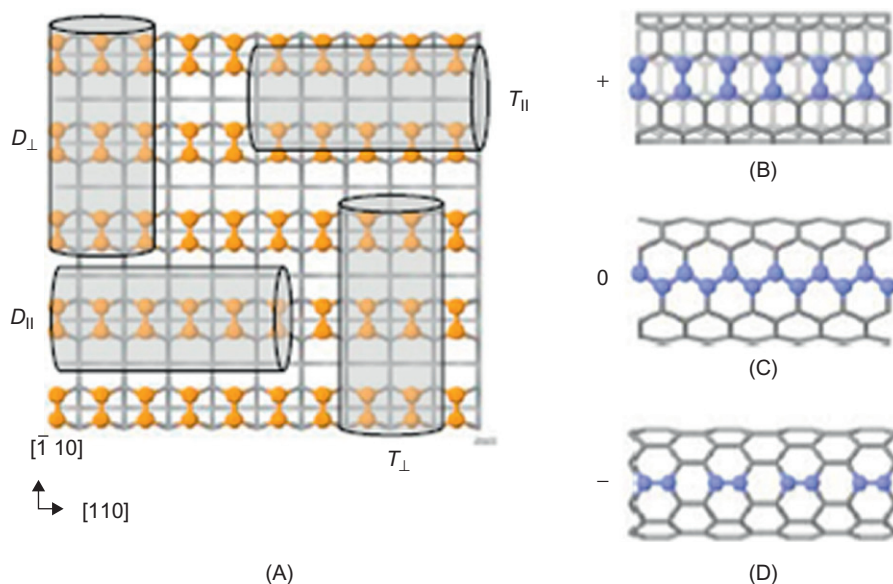
0.3 ns of annealing at 1500 K. Conversely, the transformation at 1200 K appears to be incomplete even after 1 ns. It is interesting to note that the transformation in UNCD is slower than an isolated ND particle of the size same as the UNCD grain size. For example, in our work on ND graphitization, the transformation is complete by 0.2 ns and very little or no change occurred after that for annealing at $T = 1200$ K. This difference stems from the absence of free surfaces in the UNCD system and hence the structural relaxation occurs at a slower rate. At 900 K, however, the UNCD appears to be more stable and the sp^3 - sp^2 is limited to regions near grain boundaries. It is expected that UNCD is stable with respect to sp^2 conversion below 900 K. Obviously, many factors such as grain size, hydrogen content, and annealing atmosphere will ultimately affect the nature of sp^3 - sp^2 transformation in UNCD.

3.4 Surface properties: CNT-diamond hybrid nanomaterials

With electrical properties of UNCD arising to a large extent due to the presence of sp^2 bonding at the grain boundaries, it is interesting to see at how they compare to the properties of hybrid materials composed of nanostructured sp^2 carbons at the surfaces of diamond. In particular, we consider single-walled CNTs (SWCNTs), which have electrical properties of interest due to their potential use as building blocks in hybrid nanomaterials for electronics [31]. An important aspect of the use of CNTs in any electronic nanodevice is the formation of organized arrangements on relevant substrates. Consequently, the interaction of CNTs with semiconductor substrates, including diamond, has been of recent interest, including the bonding at the interface and the electronic properties of the resulting composites. Using plane wave local-density approximation (LDA)-DFT calculations, Sque et al. [32] carried out calculations on (7,7) and (8,8) CNTs oriented parallel to a hydrogen-terminated diamond (100) surface. Due to the hydrogen termination, they found physisorbed nanotubes that can dope the diamond surface. In another study, they also investigated some physisorbed structures of a (7,7) nanotube on a diamond (100) surface. [33]. Yan et al. [34] carried out density functional calculations of interactions of diamond (100) surfaces with (3,3) and (4,4) CNTs lying parallel to the surfaces. They reported the existence of chemisorbed nanotube-diamond structures for each tube, with binding. Shenderova et al. [35] carried out MD studies of CNT-diamond hybrids having zigzag SWCNTs oriented perpendicular to diamond (111) and (100) surfaces. These hybrids have covalent C–C bonds formed at the interfaces. Horner et al. [36] carried out DFTB (see Section 3.2) investigations of the interaction of CNTs of various orientations with an unhydrided (100) diamond surface with covalent interfaces and structures that resemble nanotunnels. These structures showed varying degrees of distortion of the CNT and significant modification of the electronic structure of the nanotubes. In this section the structures and properties of the carbon nanotunnels from the work of Horner et al. on a diamond surface are reviewed.

In the DFTB study of hybrids comprising CNTs covalently bonded with a diamond surface, various SWCNT sizes and chiralities as well as various orientations with respect to the surface were explored. Stable structures of (5,5), (7,7), (9,9) armchair and (8,0) zigzag SWCNTs were found to have covalent bonds at the interface on the reconstructed (100) surface. The possible conformations of (5,5) and (8,0) CNTs with respect to a reconstructed (100) diamond surface are shown in Figure 3.9.

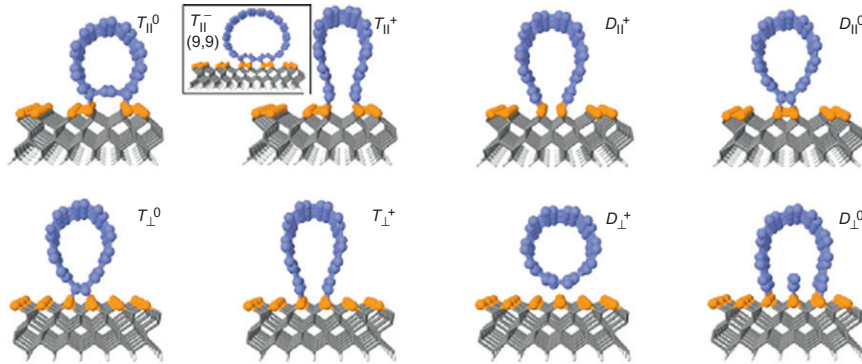
The DFTB optimized structures of the eight conformations of the (5,5) nanotube on the (100) surface are shown in Figure 3.10. The binding energies per unit length of these conformations are given in Table 3.2. Based on the calculations, the most stable (5,5) nanotube-diamond structure has the orientation $D_{||}^+$ and a binding energy of 1.7 eV/Å, and is characterized by strong covalent bonds formed between the CNT and the diamond surface. As illustrated in

**FIGURE 3.9**

(A) Top view of adsorption configurations of CNTs on a reconstructed diamond (100)–(2 × 1) surface. Carbon dimers on the surface are highlighted in orange, and CNTs are shown as shaded cylinders. Site D_{\parallel} : tube axis lies above and parallel to a dimer row; site T_{\parallel} : tube axis lies above a trough between and parallel to dimer rows; site D_{\perp} : tube axis is perpendicular to dimer rows and lies above dimers; site T_{\perp} : tube axis is perpendicular to dimer rows and lies above the shallow trough between dimers. (B – D) Top view of rotational orientations of CNTs. Atoms on top of tube are highlighted in blue: (B) (5,0) nanotube in “+” orientation; (C) (5,0) nanotube in “0” orientation; (D) (8,0) nanotube in “–” orientation.

Source: Reprinted with permission from Ref. [36].

Figure 3.10, it has a nanotunnel-like structure in which the nanotube is distorted by adsorption on the surface. The interaction between the nanotube and the diamond surface results in a 0.6 eV band gap. Two other nanotunnel structures that were found for the (5,5) nanotube had large binding energies. These are structures T_{\parallel}^{+} and T_{\perp}^{+} illustrated in Figure 3.10 and they have binding energies of 1.39 and 1.09 eV/Å, respectively. In each of these structures, the metallic character of the nanotube is maintained, probably because they are less strongly bound than the D_{\parallel}^{+} structure. The electron states of these three structures were examined and no charge transfer was found to occur between the diamond surface and the nanotunnels. In calculations on larger CNTs, (7,7) and (9,9), the nanotube-diamond binding energies are found to decrease with an increase in tube diameter.

**FIGURE 3.10**

Optimized geometries of (5,5) CNTs adsorbed onto a diamond (100)–(2 × 1) surface. The T_{\parallel}^{+} structure formed from a (9,9) CNT is shown in the inset. Carbon dimers on the surface are highlighted in orange, and nanotube atoms in blue.

Source: Reprinted with permission from Ref. [36].

Table 3.2 Binding Energies per Unit Length (eV/Å) of (5,5) SWCNTs Adsorbed on a Diamond (100)–(2 × 1) Surface

T_{\parallel}^0	T_{\parallel}^{+}	D_{\parallel}^0	D_{\parallel}^{+}	T_{\perp}^0	T_{\perp}^{+}	D_{\perp}^0	D_{\perp}^{+}
−0.23	1.09	0.09	1.74	0.45	1.39	0.90	0.03

The orientations are as described in Figure 3.9.

3.5 Concluding remarks

This chapter has described research that has been carried out to understand various aspects of the physical properties of UNCD from a computational perspective, including studies of bulk mechanical and thermodynamic properties of UNCD. This includes MD studies of the structure of GBs of UNCD, predictions of its vibrational spectra, calculations of its specific heat and Debye temperatures, and thermal stability. The sp^2 hybridized atoms in the GBs and the relative misorientations of grains lead to UNCD exhibiting some very interesting properties. These include, for example, enhanced spectral density, and a reduction in the Debye stiffness as compared to single crystal diamond. In addition, the GB atoms assist the annealing-induced sp^2 transformation of UNCD and present an important way to introduce controlled amounts of sp^2 atoms in an sp^3 matrix.

In the last section, we reviewed our recent theoretical work on the hybrid materials formed from CNTs and diamond surfaces. Based on DFTB simulations, we have

identified the possible ways in which CNTs adsorb onto a diamond (100)-(2 × 1) surface. These investigations have revealed unique nanotunnel structures that are energetically stable. These results provide a the theoretical basis for experimental investigation of hybrid CNT-diamond structures for applications in nanoelectronics.

Acknowledgment

This work was supported by the US Department of Energy, Office of Basic Energy Science, Division of Materials Science and Engineering under contract DE-AC02-06CH11357.

References

- [1] D.M. Gruen, Nanocrystalline diamond films, *Annu. Rev. Mater. Sci.* 29 (1999) 211.
- [2] D. Zhou, D.M. Gruen, L.-C. Qin, T.G. McCauley, A.R. Krauss, Control of diamond film microstructure by Ar additions to CH₄/H₂ microwave plasmas, *J. Appl. Phys.* 84 (1998) 1981.
- [3] M. Sternberg, P. Zapol, L.A. Curtiss, Theoretical studies of UNCD synthesis and properties, in: O.A. Shenderova, D.M. Gruen (Eds.), *Ultrananocrystalline Diamond: Synthesis, Properties, and Applications*, William Andrew, New York, NY, 2006.
- [4] D.W. Brenner, O.A. Shenderova, J.A. Harrison, S.J. Stuart, B. Ni, S.B. Sinnott, A second-generation reactive empirical bond order (REBO) potential energy expression for hydrocarbons, *J. Phys. Cond. Matt.* 14 (2002) 783–802.
- [5] O.A. Shenderova, D.W. Brenner, A. Omeltchenko, X. Su, L.H. Yang, Atomistic modeling of the fracture of polycrystalline diamond, *Phys. Rev. B* 61 (2000) 3877–3888.
- [6] G. Gao, K.V. Workum, J.D. Schall, J.A. Harrison, Elastic constants of diamond from molecular dynamics simulations, *J. Phys. Cond. Matt.* 18 (2006) S1737–S1750.
- [7] G.T. Gao, P.T. Mikulski, G.M. Chateaufneuf, J.A. Harrison, The effects of film structure and surface hydrogen on the properties of amorphous carbon films, *J. Phys. Chem. B* 107 (2003) 11082–11090.
- [8] S.P. Adiga, L.A. Curtiss, D.M. Gruen, in: D. Ho (Ed.), *Nanodiamonds: Applications in Biology and Nanoscale Medicine*, first ed., Springer, New York, NY, 2010.
- [9] (a) S.P. Adiga, V.P. Adiga, R.W. Carpick, D.W. Brenner, The vibrational properties and specific heat of ultrananocrystalline diamond: molecular dynamics simulations, *J. Phys. Chem. C* 115 (2011) 21691. (b) S.P. Adiga, V.P. Adiga, R.W. Carpick, D.W. Brenner, The vibrational properties of ultrananocrystalline diamond based on molecular dynamics simulations, *MRS Proceedings* 1404 (2012) mrsf11-1404-w01-03, doi:10.1557/opl.2012.268.
- [10] A. Garg, S.B. Sinnott, Effect of chemical functionalization on the mechanical properties of carbon nanotubes, *Chem. Phys. Lett.* 295 (1998) 273–278.
- [11] B. Ni, S.B. Sinnott, P. Mikulski, J.A. Harrison, Compression of carbon nanotubes filled with C₆₀, CH₄, or Ne: predictions from molecular dynamics simulations, *Phys. Rev. Lett.* 88 (205505) (2002) 1–4.
- [12] Th. Frauenheim, G. Seifert, M. Elstner, Z. Hajnal, G. Jungnickel, D. Porezag, et al., Self-consistent charge density-functional based tight-binding method for predictive materials simulations in physics, chemistry and biology, *Phys. Stat. Sol. B* 217 (2000) 41.

- [13] D. Porezag, Th. Frauenheim, Th. Kohler, G. Seifert, R. Kaschner, Construction of tight-binding-like potentials on the basis of density-functional theory: application to carbon, *Phys. Rev. B* 51 (1995) 12947.
- [14] O.A. Williams, A. Kriele, J. Hees, M. Wolfer, W. Muller-Sebert, C.E. Nebel, High Young's modulus in ultra thin nanocrystalline diamond, *Chem. Phys. Lett.* 495 (2010) 84–89.
- [15] J. Birrell, J.A. Carlisle, O. Auciello, D.M. Gruen, J.M. Gibson, Morphology and electronic structure of nitrogen-doped ultrananocrystalline diamond, *App. Phys. Lett.* 81 (2002) 2235–2237.
- [16] P.W. May, Y.A. Mankelevich, From ultrananocrystalline diamond to single crystal diamond growth in hot filament and microwave plasma-enhanced CVD reactors: a unified model for growth rates and grain sizes, *J. Phys. Chem. C* 112 (2008) 12432–12441.
- [17] P. Keblinski, D. Wolf, S.R. Phillpot, H. Gleiter, Role of bonding and coordination in the atomic structure and energy of diamond and silicon grain boundaries, *J. Mater. Res.* 13 (1998) 2077–2100.
- [18] F. Cleri, Atomic and electronic structure of high-energy grain boundaries in silicon and carbon, *Comput. Mater. Sci.* 20 (2001) 351.
- [19] P. Zapol, M. Sternberg, L.A. Curtiss, Th. Frauenheim, D.M. Gruen, Tight-binding molecular dynamics simulation of impurities in ultrananocrystalline diamond grain boundaries, *Phys. Rev. B* 65 (2001) 045403.
- [20] I.N. Remediakis, I.G. Kopidakis, P.C. Kelires, Softening of ultra-nanocrystalline diamond at low grain sizes, *Acta Mater.* 56 (2008) 5340–5344.
- [21] J. Schiotz, F.D. Di Tolla, K.W. Jacobsen, Softening of nanocrystalline metals at very small grain sizes, *Nature* 391 (1998) 561–563.
- [22] J.D. Honeycutt, H.C. Anderson, Molecular dynamics study of melting and freezing of small Lennard-Jones clusters, *J. Phys. Chem.* 91 (1987) 4950–4963.
- [23] A. Stukowski, Visualization and analysis of atomistic simulation data with OVITO—the open visualization tool, *Modell. Simul. Mater. Sci. Eng.* 18 (015012) (2010) 1–7.
- [24] O.L. Anderson, *Equations of State for Solids in Geophysics and Ceramic Science*, first ed., Oxford University Press, New York, NY, 1995.
- [25] I. Rosenblum, J. Adler, S. Brandon, Calculation of thermal properties of diamond from simulated phonon spectra, *Comput. Mater. Sci.* 12 (1998) 9–25.
- [26] J. Walker, Optical absorption and luminescence in diamond, *Rep. Prog. Phys.* 42 (1987) 1605.
- [27] T. Tohei, A. Kuwabara, F. Oba, I. Tanaka, Debye temperature and stiffness of carbon and boron nitride polymorphs from first principles calculations, *Phys. Rev. B* 73 (064304) (2006) 1–7.
- [28] N. Mounet, N. Marzari, First-principles determination of the structural, vibrational and thermodynamic properties of diamond, graphite, and derivatives, *Phys. Rev. B* 71 (205214) (2005) 1–14.
- [29] H. Jiang, Y. Huang, K.C. Hwang, A finite-temperature continuum theory based on interatomic potentials, *J. Eng. Mat. Tech.* 127 (2005) 408–416.
- [30] Sh. Michaelson, A. Stacey, J. Orwa, A. Cimmino, S. Prawer, B.C.C. Cowie, et al., Bulk and surface thermal stability of ultrananocrystalline diamond films with 10–30 nm grain size prepared by chemical vapor deposition, *J. App. Phys.* 107 (093521) (2010) 1–7.
- [31] P.L. McEuen, M.S. Fuhrer, H. Park, Single-walled carbon nanotube electronics, *IEEE Trans. Nanotechnol.* 1 (2002) 78.
- [32] S.J. Sque, R. Jones, S. Öberg, P.R. Briddon, *Theoretical study on the adsorption of armchair carbon nanotubes on the hydrogenated surface of diamond*, *Phys. Stat. Sol. A*

- 203 (2006) 3107; S.J. Sque, C.P. Ewels, R. Jones, P.R. Briddon, *Modelling the effect of doping metallic carbon nanotubes on their ability to transfer-dope diamond*, Phys. Stat. Sol. A. 204 (2007) 2898.
- [33] S.J. Sque, R. Jones, S. Öberg, P.R. Briddon, *Carbon nanotubes and their interaction with the surface of diamond*, Phys. Rev. B 75 (2007) 115328.
- [34] L. Yan, Q. Sun, Y. Jia, First-principles calculations of carbon nanotubes adsorbed on diamond (100) surfaces, J. Phys. Condens. Matter. 20 (2008) 225016.
- [35] O.A. Shenderova, D. Areshkin, D.W. Brenner, *Bonding and stability of hybrid diamond/nanotube structures*, Mol. Simulat. 29 (2003) 259.
- [36] D.A. Horner, M. Sternberg, P. Zapol, L.A. Curtiss, Carbon nanotunnels form from single-walled carbon nanotubes interacting with a diamond (100)-(2×1) surface, Diamond Relat. Mater. 20 (2011) 1103.

n-Type Nanocrystalline Diamond Films: Synthesis, Structure, Composition, Properties, and Applications

Raul Arenal^{a,b}

^a*Laboratorio de Microscopías Avanzadas (LMA), Instituto de Nanociencia de Aragón (INA), Universidad de Zaragoza, Zaragoza, Spain,*

^b*Fundacion ARAID, Zaragoza, Spain*

CHAPTER OUTLINE

4.1 Introduction	103
4.2 <i>n</i>-type (nitrogen) carbon materials	104
4.3 Synthesis of <i>n</i>-type NCD films	106
4.3.1 Synthesis and growth mechanism	106
4.4 Structural and compositional analysis of <i>n</i>-type NCD/UNCD	108
4.5 Physical and chemical properties of <i>n</i>-type NCD/UNCD	114
4.5.1 Electronic properties (transport, FE, and thermal conductivity)	115
<i>Transport properties</i>	115
<i>Electron field emission</i>	117
<i>Thermal conductivity</i>	119
4.5.2 Optical properties	119
4.5.3 Vibrational properties	121
4.5.4 Mechanical properties	124
4.5.5 Chemical properties	125
4.6 Applications	125
4.7 Conclusions	127
Acknowledgment	127
References	127

4.1 Introduction

Nanostructured carbon materials such as carbon nanotubes, nanodiamond, fullerenes, nanofibers, and more recently graphene, have gained heightened interest because they serve as potential building blocks for field emission (FE), electronic and

optoelectronic devices, gas and energy storage media, biosensing/biotechnology, and medicine [1–3]. Thus, under this context nanocrystalline diamond (NCD) materials, ultrananocrystalline diamond (UNCD) films, are excellent candidates for some of those mechanical and electronic applications due to their outstanding properties [4–6].

However, the presence of defects and dopants within carbon materials is of great importance for new emerging technologies [7–9]. It is well known that one route for modifying the solid state properties of materials is the addition of electron acceptors or donors. Therefore, nitrogen incorporation to the gas chemistry during the growth of NCD/UNCD films has opened new and very attractive perspectives in the field of diamond research and applications. Actually, the progressive substitution of nitrogen for argon in the synthesis gas renders UNCD films increasingly electrically conducting with conductivities reaching several hundreds S/cm for 20% by volume of N₂ added to the synthesis gas. A strong correlation between the N₂ addition and the morphology/structure of these films is observed and discussed in almost all related publications and it will be deeply discussed in this chapter, along with the consequences of the properties of these films.

In this chapter, we will review all the aspects related to these *n*-type or nitrogenated NCD/UNCD films, including their synthesis, characterization, physical and chemical properties, and applications.

4.2 *n*-type (nitrogen) carbon materials

It is well known that the addition of foreign atoms as dopants in a material modifies and, in a certain way, allows control over their electronic, optical, and mechanical properties. In this chapter, we are interested in the particular case of *n*-type carbon nanomaterials. In this sense, due to the proximity of nitrogen to carbon in the periodic table, this element will be, in principle, the most evident candidate for achieving this goal. Thus, keeping in mind that there are different carbon materials, as a function of the atomic hybridization of the C atoms (sp¹, sp², sp³), the nitrogen incorporation could also be different for each of them. Significant efforts have been devoted to study this aspect on different carbon materials such as diamond, graphite, graphene, nanotubes, and diamond-like carbon (DLC) [7–10]. Of course, bulk carbons drastically differ from nitrogen-doped carbon-based nanostructures, mainly due to their reduced dimensions and confinement effects.

The most active field of research in this area probably concerns the study of carbon nanotubes. Actually, the incorporation of nitrogen atoms into the honeycomb lattice leads to chemical activation of the rather passive surface of a carbon nanotube and adds additional electronic states around the Fermi level [8,9]. Furthermore, it should be mentioned that these nanomaterials, and in particular single-walled carbon nanotubes (SWCNTs), are extremely sensitive to the localization of incorporated nitrogen. This is the reason why completely new possibilities, but also difficulties arise when we study these new molecular systems. However, it is important to note that the doping regimes required for different applications are

vastly different. To date, nitrogen-doping concentrations in SWCNTs are limited to around 2% [9], whereas in multiwalled nanotubes average concentrations can reach ~15–20 at. %, with local concentrations up to 25–30% [11]. These values are much higher than those of doping in classical semiconductors, which is of low concentration (typically 10^{-9} at. %).

However, it has been shown that nitrogen atoms tend to introduce disorder in the graphene planes. Very recent theoretical studies have shown how nitrogen substitution within the carbon lattice tends to introduce curvature effects on the graphitic sheets [12].

Extensive works have been developed in the case of CN_x films and in the study, theoretically and experimentally, of different structural phases. That is the case of the quest for C_3N_4 . Two different phases (α - C_3N_4 or β - C_3N_4), by structural analogy with Si_3N_4 , could be “ultra-hard” phases and may even be harder than diamond as postulated by Cohen, who calculated a semiempirical bulk modulus between 461 and 483 GPa [13]. However, even though C_3N_4 has been predicted to be a superhard material, little has been achieved in synthesizing it in the form of a thin film [14].

Another active research field is that of *n*-type DLCs. Different attempts have been made to obtain *n*-type doped DLC via nitrogen [15] and phosphorous addition [16]. For instance, Anita et al. [17] obtained this kind of *n*-type DLC film and found that nitrogen incorporation reduced its electrical resistivity. However, Robertson [18] pointed out that the successful *n*-type doping of DLC films is difficult because of the high density of midgap states, wide-band tail, low carrier mobility, and poor doping response.

Concerning diamond materials, a controllable doping mechanism is needed to produce *n*-type material in order to have a significant number of electrons in the conduction band. Potential *n*-type dopants in diamond may be found in the group V elements, as substitutional donors. However, *n*-type doping appears to be extremely difficult. Substitutional nitrogen, which is naturally the first candidate, is not a good option because atoms move spontaneously to an undoped lone pair configuration [19]. In fact, the activation energy of the nitrogen donors is measured to be 1.7 eV in type Ib diamond, and 4 eV in type Ia diamond. These deep levels below the conduction band make the nitrogen-doped diamond electrically inactive at room temperature. One way that has been successfully employed for introducing nitrogen in diamond has been by implantation followed by annealing at high temperature [20]. These authors showed that even following this treatment, nitrogen-doped diamonds are useless in electronic devices, including at high temperature. However, recently Panda et al. [21] have successfully achieved N implantation in UNCD films grown by microwave plasma enhanced chemical vapor deposition (MWPECVD). These authors have studied the influence this N implantation has in the FE properties of these films. These results will be discussed in Section 4.5.1 devoted to their electronic properties.

Phosphorus is then the next potential dopant in the type V elements. Thus, Koizumi et al. [22] introduced phosphorus during the growth process by CVD and obtained a donor level at 0.5 eV below the bottom of the conduction band.

However, this successful *n*-type doping has not been reproduced by any other group. One difficulty is that the phosphorus incorporation is obtained only on (111) oriented surfaces of diamond crystals.

Another dopant is sulfur. The number of works in this field is very low. Gupta et al. [23] and Koeck et al. [24] achieved to manipulate and to work on these films.

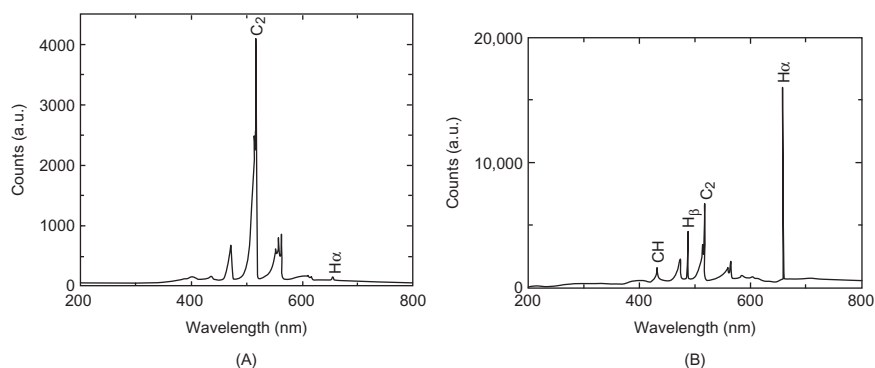
4.3 Synthesis of *n*-type NCD films

4.3.1 Synthesis and growth mechanism

Nanodiamond is a term including a vast number of diamond structures smaller than 100 nm. In the case of crystalline nanodiamond films, two different kinds of structures have been classified: a generic one for NCDs that include all these materials <100 nm, and a second one, UNCDs, where the diamond grains, smaller than 10 nm, are bound together by grain boundaries (GBs) of 1–2 nm wide. The morphological differences between these two kinds of nanostructures are related to their respective growth mechanisms [25,26].

Many efforts have been devoted to produce such exciting materials. In this sense, CVD is a very appropriate technique for the synthesis of these films because (1) diamond can be grown on numerous substrate materials, (2) dopants and crystal size can be carefully controlled, (3) parallel fabrication strategies can be implemented, and (4) scale-up production can be reached. Several CVD techniques that are already employed for conventional diamond production have been used to synthesize both kinds of films (NCD and UNCD): MWPECVD [27–29], hot-filament CVD (HFCVD) [30], and direct current plasma CVD (DCCVD) [31]. Furthermore, the synthesis conditions can be modulated to obtain a specific kind of UNCD/NCD film depending on the application: more transparency, increasing or reducing the roughness, etc.

In order to improve the quality and performance of any material, a very significant aspect that should be also considered is the understanding of its growth mechanism and formation. In this sense, some works on NCD/UNCD films have been dedicated to investigating this aspect. Thus, several studies have shown the importance of the carbon dimer (C_2) for the growth of both kind of films, in particular UNCD ones. In fact, optical emission spectroscopy (OES), a well-known method for plasma diagnostics, has demonstrated that the plasmas under UNCD growth show intense C_2 emission, which is not the case for NCD films where the C_2 contribution is much less [4,32,33]. Figure 4.1 corresponds to OES measurements carried out during the formation of UNCD and NCD films, respectively [33]. This figure shows the differences between them in terms of C_2 deposition. Thus, this indicates that the plasma processes between those systems are significantly different. Furthermore, it has been evoked that C_2 could play a very important role in the re-nucleation process. Actually, the intense C_2 signal observed for UNCD growth (Figure 4.1) could indicate that the re-nucleation rate should be very high.

**FIGURE 4.1**

Optical emission spectra of plasma processes: (A) UNCD hydrogen-poor plasma and (B) NCD conventional hydrogen plasma.

Source: Reprinted from Williams et al. [33].

In the case of NCD films, there is no evidence for a re-nucleation process, and their growth takes place within a columnar structure following a van der Drift model [25,26], which is different from the random grains in UNCD films [28,29]. Actually, these differences have a consequence in the roughness of each kind of film.

To sum up, there is a criterion to discern the growth mechanism of these two systems (NCD and UNCD films), which is the suppression or enhancement of the re-nucleation process.

Now we turn to the case of nitrogen addition to the plasma gas. Nitrogen has, for a long time, been known to play an important role in determining growth behavior and therefore, as already mentioned in this chapter, strongly influencing the microstructure of CVD diamond films [34,35]. This is also the case for UNCD films. In fact, when N_2 is added to the gas synthesis during the growth of UNCD films, OES studies have shown that both the CN/C_2 ratios and the number of nitrogen atoms per cubic centimeter incorporated in the GBs strongly increase in the region 0–5% by volume of added nitrogen. This enables the controlled variation of synthesis conditions so as to produce ambient conducting *n*-type diamond films showing the entire range from insulating to semiconducting behavior [29]. As we will see more in detail in the following section, this drastic changes in conductivity that accompany the nitrogen into UNCD films are related to the growth of highly elongated diamond crystallites (80–100 nm long) replacing the 3–5 nm randomly oriented diamond crystallites of non-nitrogen containing UNCD films and the presence of a carbon sp^2 sheath covering these elongated structures. These structures become particularly pronounced when nitrogen contents of 10% and above are combined with deposition temperatures of about 800°C and above [29]. Furthermore, Arenal et al. [29] have shown that these elongated structures are

composed of 10–20 nm long diamond crystallite segments which are linked together. Thus, even if the chemistry of the synthesis gas becomes considerably more complex with N₂ addition, a plausible growth mechanism should involve the formation of a copolymer: polymeric HCN species from the combination of methane and N₂. This polymeric HCN is thermally unstable and decomposes into a copolymer of polymethineimine (polynitrile) and polyacetylene with the liberation of nitrogen. It is worth mentioning that polyacetylene already plays a very important role in the case of non-nitrogen-added UNCD films [4]. Thus, it seems very reasonable to assume that these copolymer-like structures form the sp² carbon sheath and they could be involved in the formation of these segments composing the core elongated structures [29,36].

Another interesting point to consider is the comparison of these results coming from MWPECVD syntheses with those coming from the synthesis of *n*-type NCD films from HFCVD. Indeed, Rakha et al. [37] found that the length of diamond nanocrystallites produced by HFCVD was not as long as reported by using MPCVD system. It might be because of less energetic species in HFCVD as compared to energetic species produced in a high power plasma field. In fact, in the case of MWPECVD, the formation of this copolymer mentioned above during NCD synthesis is likely because the microwave plasma strongly enhances polymerization reactions. Excitation processes due to collisions with Ar⁺ and Ar* [38] lead to the formation of a complex mixture of organic molecules, including *trans*-polyacetylene and polycyclic aromatic hydrocarbons, even in the absence of added nitrogen. Thus, this can be the reason for the differences between these two synthesis methods.

4.4 Structural and compositional analysis of *n*-type NCD/UNCD

Since the beginning of the 2000s, a large quantity of works has been devoted to investigate the effects of nitrogen addition in the synthesis gas during the production of UNCD and NCD films. All these works have shown that this addition has a strong influence in the morphology, structure, and composition of these films which will be also reflected in their physical and chemical properties. Actually, these properties are mainly governed by the presence of GBs in these films, and, as we will discuss below, the main effect of N₂ addition is the modification of the size, the chemical nature, and the crystal quality of these GBs [25,26,28,29,36].

It is worth mentioning that the complexity of these materials, where different phases (amorphous and crystalline) and atomic bonding configurations coexist in a few nanometers, requires the combination of different characterization techniques, some of them pushed to the limit of their present resolutions/capabilities. These techniques are mainly scanning electron microscopy (SEM), Raman and infrared (IR, or Fourier-transformed IR (FTIR)) spectroscopies, X-ray photoelectron spectroscopy (XPS), transmission electron microscopy (TEM; high-resolution TEM (HRTEM)), electron diffraction, and electron energy loss spectroscopy (EELS)),

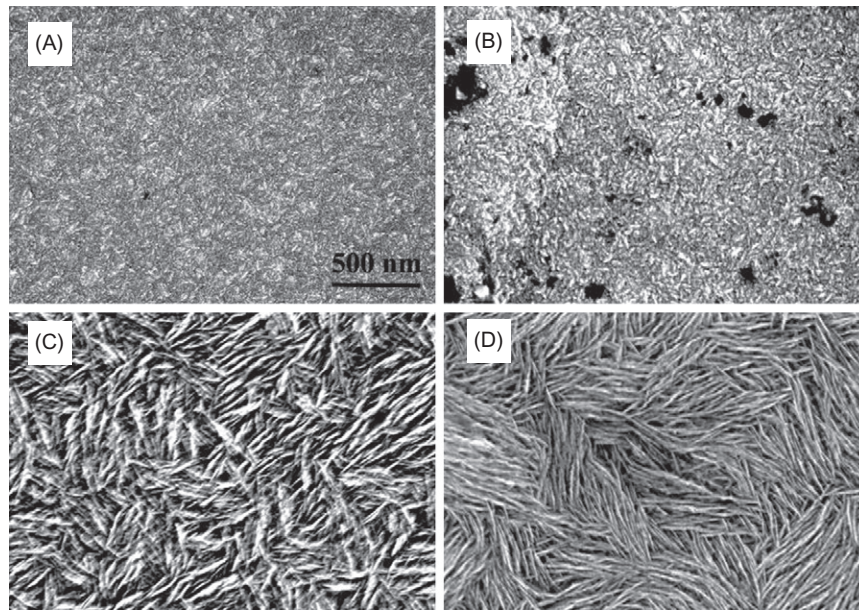
and X-ray diffraction. Most of these techniques are complementary and provide morphological, structural, and/or compositional information. In this section we will present an overview of the characterization techniques developed on these *n*-type NCD films, showing the present knowledge of these materials (*n*-type UNCD and NCD films), including the aspects that should be addressed in the near future and the limitations of the characterization techniques employed to investigate them.

Concerning *n*-type UNCD films, we have already mentioned that nitrogen addition in the synthesis gas provokes drastic modifications in the morphology of the films, among other very significant effects related to their properties, which will be discussed latter.

The pioneer works of Bhattacharyya et al. [39] and Birrell et al. [28] at Argonne National Laboratory showed these modifications when nitrogen was added in the gas mixture during CH₄/Ar or C₆₀/Ar syntheses. These authors demonstrated that the size of the diamond grains and the width of the GBs increase with N₂ addition in the synthesis gas. Furthermore, they proposed that these GBs were responsible for the changes in the electronic transport of these films, when N₂ was incorporated to the synthesis atmosphere. This result has been confirmed by other authors [40,41]. More recently, Arenal et al. [29], working in similar *n*-type UNCD films, showed for the first time that the abrupt changes in the morphology of the films were related to a new configuration/arrangement of the diamond crystallites (Figure 4.2). Actually, these authors observed that elongated nanostructures appeared along with diamond nanograins, whereas a granular structure is typical for the film grown without nitrogen.

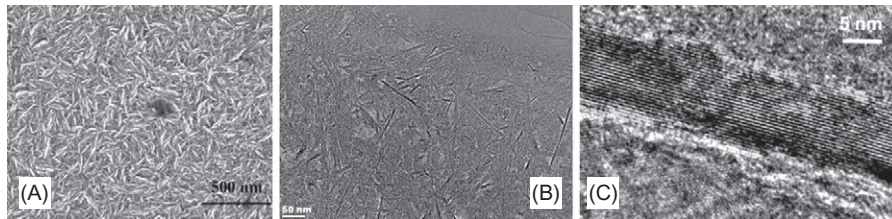
These elongated nanocrystals were called nanowires (NWs) due to their role in increasing the performance of the electronic transport of these films. Figure 4.3 corresponds to SEM, low-magnification, and HRTEM plane view micrographs, respectively. These images show the presence of these elongated NWs embedded in a matrix composed by randomly oriented 3–5 nm crystallites of UNCD. The formation of these NWs starts to appear when the N₂ content in the gas phase reaches about 10% in volume. They are ~100 nm in length and about 5 nm in width as shown in the TEM image (Figure 4.2 and more precisely in Figure 4.3). This HRTEM micrograph shows the presence of the lattice fringes with a spacing of ~0.21 nm, which corresponds to the *d*-spacing of the (111) planes of diamond. The NWs are enveloped by a layer about 1 nm thick. This layer is likely formed during the growth of the NWs. Furthermore, as mentioned above these diamond NWs are composed by segments 10–20 nm long (Figure 4.4). Vlasov et al. [42] also investigated the effects of N₂ additions in the synthesis gas, and observed as well as very analogous elongated structures.

In a certain way, similar findings to these ones presented above concerning the GBs and the size of the diamond grains have been observed in the case of *n*-type NCD films. For instance, Rakha et al. [43] found that the addition of up to 20% of N₂ during the synthesis (MWPECVD) increases the size of the grains and the formation of elongated crystallites. This result has been also observed by other researchers working on *n*-type NCD films [44,45]; it was even, as mentioned above, observed before in UNCD films [29]. Furthermore, these authors propose that the increase in crystallite size could be due to the reduction of C₂ species

**FIGURE 4.2**

SEM showing morphology changes of the UNCD films as a function of nitrogen content ((A) 5%, (B) 10%, (C) 15%, and (D) 20%) at a substrate temperature of 800°C. The scale bar is the same for all the micrographs (A).

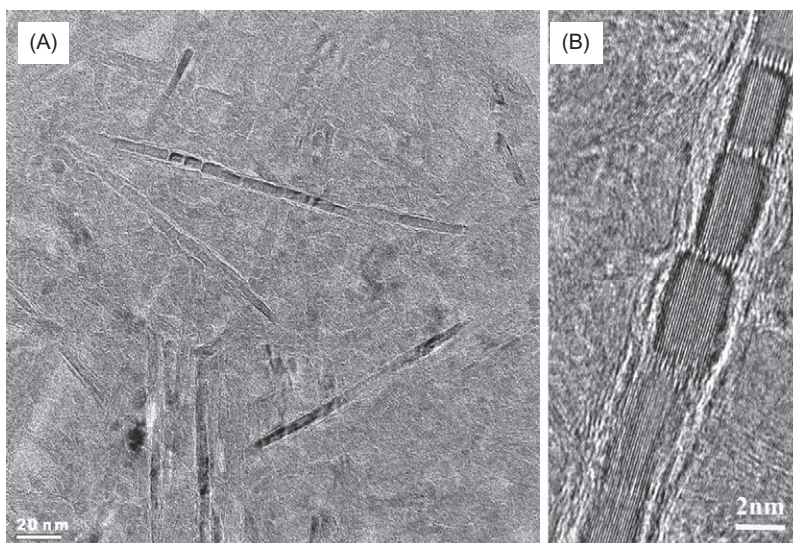
Source: Reproduced from Arenal et al. [29].

**FIGURE 4.3**

(A) SEM and (B) low-magnification TEM images of the samples showing the presence of NWs. (C) HRTEM image of one of these elongated structures to show the (111) diamond planes.

Source: Adapted from Arenal et al. [29].

during the formation of C_xN_y species [43]. However, Ping et al. [46] have observed that, in the case of low amounts of nitrogen addition (0.24%) in a CH_4/H_2 plasma (MWPECVD), this N_2 addition induces the reduction of the grain size. It is worth noting that this is the only work where this opposite behavior has been observed. Furthermore, these authors also showed that the N_2 addition induces changes in the

**FIGURE 4.4**

(A) Low-magnification TEM image showing the UNCD NWs. (B) HRTEM micrograph displaying the segments composing these NWs.

Source: Reprinted from Arenal et al. [29].

morphology of the films as well as in the quality and growth rate of large-grained NCD films. Another aspect pointed out by most of these authors is the reduction of crystallinity or deterioration and the increasing of graphitization of the films when N_2 is added [43–45].

Until now we have showed and discussed the morphology and structure of these films and their modifications related to nitrogen addition in the synthesis gas. However, there are several important points related to this nitrogen incorporation to take into account, as the distribution of these nitrogen atoms, their atomic configuration and their quantification. Nevertheless, it is worth mentioning that mainly because of the low amounts of N incorporated, these studies are not trivial. In this respect, there are three main analytical techniques that can shed some light on this problem/aspect: EELS, near-edge X-ray absorption fine structures (NEXAFS), and XPS. The effectiveness of using one or other technique is not only related to the doping amounts in the sample but also to the sensitivity and resolution of the instruments. For instance, EELS can be used as a local probing method when it is developed in a TEM. Actually, EELS performed in a TEM permits the correlation of spectroscopic information to morphological and structural features of the specimen, allowing an accurate characterization of the materials at the nanometer (even atomic) scale. However, when working in the very low doping regime of NCD/UNCD films, it is very complicated to probe the incorporation of atoms at the local scale via TEM-EELS [7,47,48]. Impurity doping in classical semiconductors is, at low concentrations (typically 10^{-9} at. %), below the detection limit for

many of these spectroscopic techniques. Thus, in some cases, the detection of N in UNCD/NCD structures contributes to these difficulties. However, XPS is a meso/macroscopic probing method that cannot be used in a straightforward manner with samples “as produced,” without any previous characterization. However, if a careful sample preparation is taken into account and not very local measurements are required, XPS and NEXAFS represent very sensitive methods to estimate doping levels and bonding environments.

Before discussing the works devoted to the study of the atomic configuration/bonding and spatial distribution of N in *n*-type UNCD/NCD films, it is worth mentioning again the pioneer works of Bhattacharyya et al. [39]. These authors employed secondary ion mass spectrometry (SIMS) to evaluate the nitrogen-doping level in UNCD films. Actually, SIMS is a nondestructive and complementary technique to the previous ones, which is usually employed to precisely measure dopant concentration with low concentration levels (down to ppb levels). These authors found that the nitrogen content in the films saturates at $\sim 2 \times 10^{20}$ atoms/cm³ for 5–10% of N₂ in the plasma. These values are visible in Figure 4.8 in the section devoted to the transport properties of UNCD/NCD films.

XPS and NEXAFS techniques have been employed by several groups to measure for instance the sp² and sp³ ratio in UNCD/NCD films [44], to investigate the C_xN_y phases [49], and to elucidate the nitrogen bonding environments. Furthermore, Teng et al. [49] observed the formation and disorder of sp²-bonded carbon due to incorporation of N₂ in the synthesis gas. Figure 4.5 corresponds to XPS UNCD and *n*-type UNCD films. Concerning NCD films, Ma et al. [44] estimated the nitrogen concentration to be about 1%.

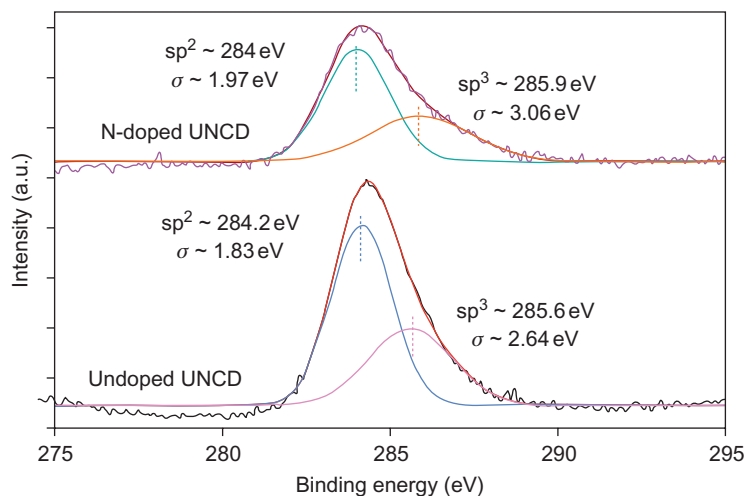


FIGURE 4.5

XPS spectra C 1s of undoped and nitrogenated UNCD films synthesized using CVD.

Source: Reprinted from Teng et al. [49].

As mentioned above, EELS performed in a TEM is a complementary technique to XPS and NEXAFS. Thus, several EELS–TEM works have been developed by Birrell et al. [28], Arenal et al. [29], and Vlasov et al. [42] to investigate the modifications due to N incorporation in UNCD films, including the analysis of the sp^2 and sp^3 phases, N detection, etc. It is then easy to understand that not only these morphological and structural changes or the amount of N incorporated in the films, but also the bonding environments of the N atoms and their distribution must compulsorily be analyzed. However, the small size of the crystal structures, the presence of amorphous material, and the inhomogeneity of the material make the characterization of these films highly difficult. A technique at the nanometer scale, like EELS–TEM, which also provides information about the chemical and bonding configuration of the elements, is needed. In this sense, Arenal et al. [36] carried out spatial-resolved EELS (SR-EELS) measurements in *n*-type UNCD films. They confirmed the presence of elongated structures with a diamond core and a sp^2 -bonded carbon sheath surrounding the core (Figures 4.6 and 4.7). However, the most significant result of these works was to show that the nitrogen was incorporated in the sp^2 carbon sheath. The amount of this nitrogen is ~ 1.5 at. % and is situated in

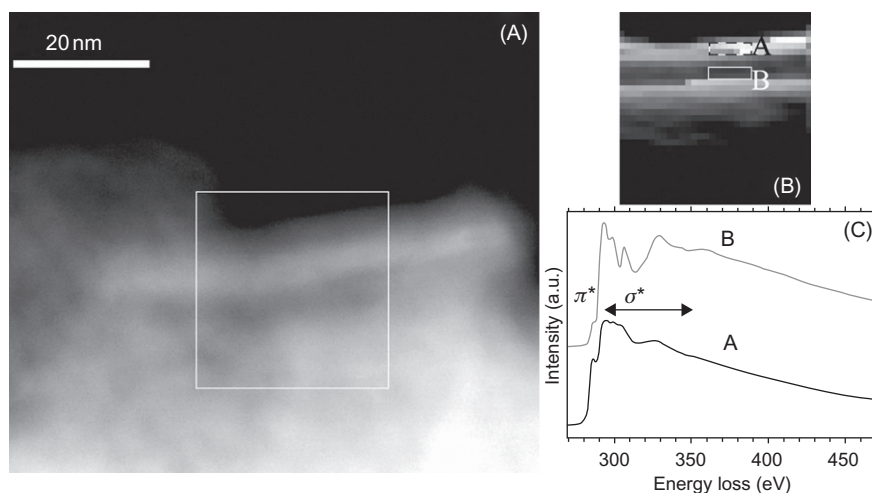
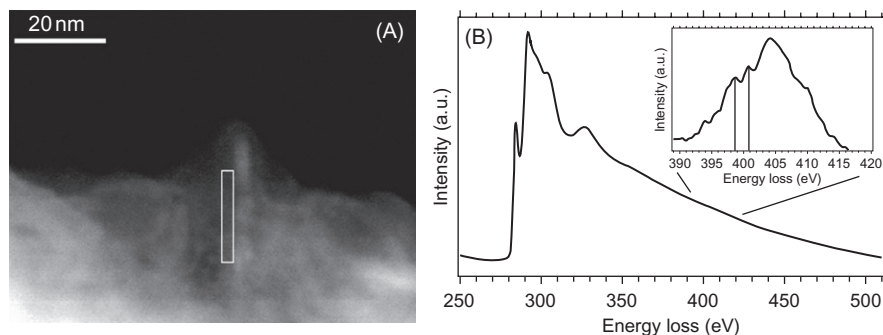


FIGURE 4.6

(A) STEM high angular annular dark field (HAADF) image of an UNCD film where several diamond NWs can be observed. The white box shows the region from which an EELS spectrum-image (SPIM) was acquired. (B) EELS C–K π peak intensity map extracted from the SPIM (A). (C) Two different EEL spectra showing the C–K edge, recorded in the areas A and B as marked in (B). Spectra from area A (dotted area in (B) at the edge of the NW) corresponds to sp^2 -bonded carbon. Spectrum from area B (middle of the NW) is assigned to sp^3 carbon with a small contribution of sp^2 -bonded carbon from the surface of the NW.

Source: Reprinted from Arenal et al. [36].

**FIGURE 4.7**

(A) STEM HAADF image of a different area of the sample. (B) EEL spectra recorded in the white area marked in (A). In this spectrum, C- and N-K edges are visible at ~284 and 397 eV, respectively. The inset is a magnification of the N-K edge, after background subtraction.

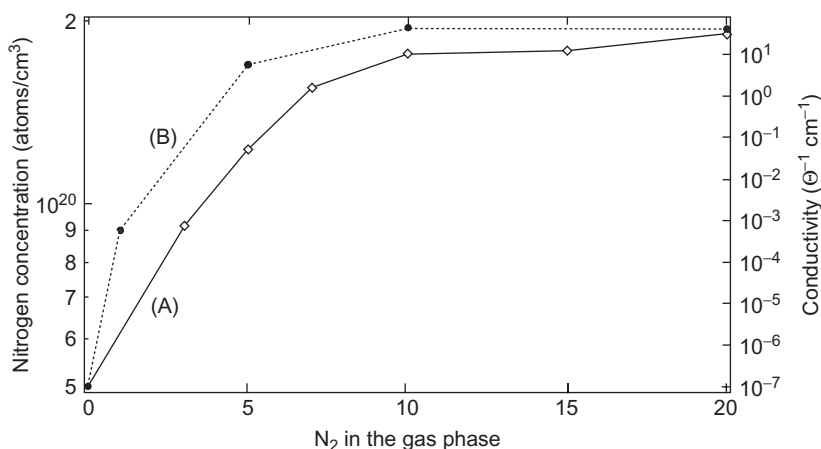
Source: Reprinted from Arenal et al. [36].

pyridine-like and graphitic configurations (Figure 4.7). Nevertheless, pyrrole-like atomic arrangement cannot be excluded in less graphitized carbon sheaths. These results confirmed that the addition of large amounts of nitrogen to the synthesis gas is crucial for the formation of diamond NWs, as well as for the promotion of sp^2 aromatic clustering, for the enhancement of the ordering of these clusters, and for increasing their size. Thus, a better understanding of the conditions leading to the unusual *n*-type electrically conducting UNCD films has been achieved, even if some aspects, such as the understanding of the nitrogen's influence on the formation of nanodiamond segments composing the NWs, are still not fully achieved.

In summary, it has to be stressed that the characterization of the effects of nitrogen incorporation in these NCD/UNCD films is difficult to qualitatively and quantitatively determine. These problems arise mainly because of sample complexity and low level dopant concentrations. The nature of the nitrogen atoms in nitrogen-doped carbon materials, and whether they are really the active catalytic sites, is still controversial. In this sense, another important point that should be considered is that from semiconductor physics, the doping concept is related to a doping level in the order of parts per million. However, the cases in which higher impurity incorporation occurs must also be taken into account as they have been. Thus, in this context the concept of a C_xN_y heterostructure must also be considered.

4.5 Physical and chemical properties of *n*-type NCD/UNCD

In this section, we shall review the state of the art of the main physical and chemical properties of *n*-type UNCD/NCD films. It is worth mentioning that despite the efforts devoted to understanding how these properties have been modified due to

**FIGURE 4.8**

(A) Conductivity and (B) SIMS of UNCD films (Ref. [39]) as a function of nitrogen concentration within the gas phase.

Source: Reprinted from Arenal et al. [29].

the nitrogen addition in the synthesis gas, further studies are required, in particular theoretical ones.

4.5.1 Electronic properties (transport, FE, and thermal conductivity)

As we have already mentioned several times in this chapter, nitrogen addition in the synthesis gas has drastic effects on the electronic properties of NCD/UNCD films. In this section, these properties, including electron transport, FE, and thermal conductivity, will be reviewed.

Transport properties

Both NCD and UNCD films, even if as a single crystal of diamond, are originally insulators; they can have a metallic behavior. Nevertheless, the metallic conductivity of these two kinds of films is very different. In the case of NCD films it is *p*-type, via substitutional boron doping [50]. However, substitutional nitrogen (*n*-type) in the diamond lattice does not contribute at all, or at best only minimally, to conductivity because nitrogen occupies a doping level that lies at 1.7 eV below the conduction band [4]. The progressive substitution of nitrogen for argon in the synthesis gas renders UNCD films increasingly electrically conducting with conductivities reaching several hundred S/cm for 20% by volume of N₂ added to the synthesis gas, which makes it the only currently available *n*-type diamond material that is electrically conducting at ambient temperatures. As shown in Figure 4.8, the electrical conductivity of these UNCD films is strongly correlated with the amount of incorporated nitrogen. This figure displays, in logarithmic scale, the

conductivity, together with the number of nitrogen atoms per cubic centimeter incorporated in the GBs as determined by SIMS measurements [29,39], which is plotted as a function of nitrogen concentration within the gas phase.

Hall-effect measurements have determined the carriers in these films to be *n*-type with concentrations of $(10^{19}\text{--}10^{21})/\text{cm}^3$ and mobilities of several $\text{cm}^2/\text{V}\cdot\text{s}$, as measured by Achatz et al. and Williams et al. [51,52].

Since the discovery of these *n*-type UNCD films around 10 years ago, the mechanism of electron transport has attracted considerable interest [25,26,29,32,33,36,42,53]. However, even considerable efforts have been devoted to understand this complex conductivity behavior, and further studies are required, in particular to detail the mechanism underlying the insulator–metal transition. This mechanism occurs presumably by electron transport through the ubiquitous GBs characteristic of nanocrystalline materials. In this sense, the most stable configuration in the GB turns out to have energy of formation of -0.64eV compared to a substitutional site in the diamond crystal lattice of 4.9eV . This large energy difference essentially dictates that nitrogen incorporation occurs by incorporation into the GBs. However, for more than 10% by volume of N_2 added to the synthesis gas, Arenal et al. [29,36] and Vlasov et al. [42] have observed the formation of diamond fibers. Arenal et al. [36] called them NWs because their presence is related to the increasing electrical conductivity of the UNCD films. In addition, they also showed that the remarkable increase in conductivity is associated with the fact that each NW is enveloped by a sheath that is composed of largely sp^2 -bonded carbon as assessed by EELS measurements. Furthermore, this sp^2 -bonded carbon sheath provides a plausible transport mechanism for electronic conductivity to occur.

The application of density-functional-based tight-binding (DFTB) theory to this problem has given considerable insight into the changes in the electronic structure of the band gap of diamond due to the incorporation of nitrogen. The finding that GB nitrogen enhances π bonding and electron delocalization is particularly relevant to electron transport mechanisms [54]. In this sense, nitrogen lone pairs hybridized with carbon dangling bond states are situated above the Fermi level and can donate electrons to carbon defect states near the Fermi level causing it to shift upward toward a delocalized π^* band. In part, based on these ideas, conductivity mechanisms involving nitrogen-vacancy complexes as shallow donors and GB nitrogen dangling bond or nitrogen–p bond complexes as compensation centers have been proposed based on DFTB cluster calculations [55]. Another approach using a combination of hopping and delocalized state conduction for low and high nitrogen content UNCD, respectively, comes to the conclusion that the experimental data are in accord with the DFTB predictions that the Fermi level shifts toward the conduction band with increasing nitrogen incorporation [56]. Recently, giant negative magnetoresistance has been found in *n*-type UNCD at very low temperatures, which was interpreted on the basis of GB conduction having the character of a low-dimensional disordered metal in weakly localized orbits that extend over the entire crystallite [50,57]. An input confirming these aspects has been obtained by Arenal et al. [58] who found sp^2 rings formed and promoted in the GBs, via

multiwavelength Raman experiments carried out, provided very rich information about the delocalization of the π bonds in these rings.

Another approach is by Joseph et al. [59] who investigated the doping with lithium of freestanding UNCD films. They found low-resistivity values ($1.2 \Omega \text{ cm}$) with carrier concentration of $-2 \times 10^{20} \text{ cm}^{-3}$, which is related to Li incorporation.

Concerning *n*-type NCD films, Jeedigunta et al. [60] showed that hydrogen plasma treatments of the surface of these films, which have metal contacts Ti/Au, modified their electrical properties. In fact, these treatments seem to promote sp^2 formation/transformation and the amount of defects. However, Teii and Ikeda [61] also showed that the presence of amorphous nondiamond phases in nitrogen-generated NCD films is responsible for their transition from resistive to conductor. Furthermore, they observed that the resistivity of these films increased considerably by adding a small amount of O_2 . Similar results concerning the effects of nitrogen addition in NCD films were observed by Ma et al. [62]. These authors found that the resistivity of these films is reduced by six orders of magnitude. Finally, Zimmermann et al. [63] grew a rectifying NCD pn-structure by HFCVD on Si substrates. This device showed a diode behavior with an ideality factor of $\sim n = 10$ and a barrier height for current injection of $\sim 0.76 \text{ eV}$.

Electron field emission

Electron sources have an essential role in information display. They mostly use the thermionic emission mechanism, where electrons are emitted from heated filaments (hot cathodes). However, there is an alternative mechanism to extract electrons, FE (EFE for electron FE). It is a quantum effect where by applying a sufficiently high external electric field, electrons near the Fermi level can tunnel through the energy barrier and escape to the vacuum level. Compared to thermionic emission, this is a preferred mechanism for certain applications because no heating is required (cold cathodes). Nevertheless, practical application of the presently available cold cathode materials is limited due to their irregularity and lack of reproducibility [64]. In this sense, the negative electron affinity of the diamond surface has attracted much attention because of the potential use of diamond for the fabrication of cold-cathode field emitters for application in flat panel displays and other electro-vacuum devices for the generation of an intense electron beam [65]. However, the use, as a cold cathode, of wide-band-gap insulating diamond is still a challenge because it requires a rather high concentration of free electrons at its conduction band for effectively supplying electrons to its emitting surface. The typical problem can be the energy barrier between substrate and insulating diamond film, which may hinder the efficient supply of electrons to the top surface emission sites.

UNCD/NCD materials, maybe due to decrease of crystalline size and mainly due to the addition of conduction channels from the GBs, show superior EFE behavior than that of micrometer diamond films. In this sense, *n*-type UNCD/NCD are ideal materials to enhance the EFE properties of diamond as has been demonstrated from the pioneer EFE studies of *n*-type NCD by Wu et al. [66]. These authors found an emission threshold of $1 \text{ V}/\mu\text{m}$ and an emission current of $10 \text{ mA}/\text{cm}^2$ for NCD films

grown by CVD using a mixture of N_2 and CH_4 as precursors. They considered that the graphite present in the films explain the EFE properties of these films. Since these works, other groups have studied the EFE properties of *n*-type UNCD/NCD films [67,68]. Thomas et al. [67] worked on freestanding UNCD films *n*-doped by Li species from $LiNbO_3$ substrates. These authors demonstrated that the EFE of these films could be turned on at a low field of $E_0 = 10.0\text{ V}/\mu\text{m}$, attaining EFE current density of $0.2\text{ mA}/\text{cm}^2$ at an applied field of $18.0\text{ V}/\mu\text{m}$, which is superior to the EFE properties of UNCD films grown on Si substrates with the same CVD process. They considered that diffusion of Li into the films is presumed to promote *n*-type conductivity, the formation of disordered carbon nanochannels, and GB incorporation of Li. However, they observed that the formation of a homojunction interface between conducting and insulating UNCD layers facilitated the tunneling of electrons, the injection of conduction band electrons from conducting side to the insulating UNCD layer, and their direct transport to emitting sites that are possibly the major reasons for their high EFE properties (Figure 4.9).

Concerning the study of the EFE characteristics of more standard (using silicon and silicon nitride substrates) nitrogenated UNCD films, Chen et al. [69] investigated the effects of the substrate temperature on the EFE properties of such films. They observed a clear improvement of the EFE properties of these films when the substrate temperature increased from 600°C to 830°C . In fact, the turn-on field decreased from $20\text{ V}/\mu\text{m}$ to $10\text{ V}/\mu\text{m}$ and the EFE current density increased from less than 0.05 to $15\text{ mA}/\text{cm}^2$. Again, the role of nitrogen additions in the gas, which modify the GB regions promoting the formation of sp^2 -bonded carbons, is

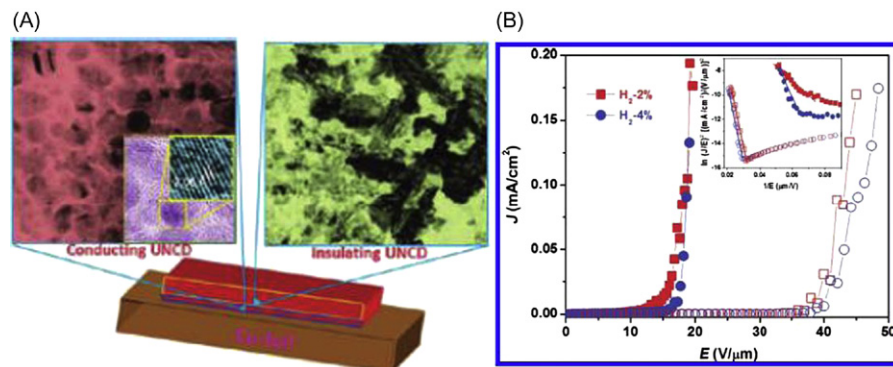


FIGURE 4.9

(A) Schematic representations of fabrication and bonding processes of freestanding UNCD films and typical photograph of the film bonded to Cu-foil substrate, including TEM low-magnification micrographs of the UNCD films. (B) Comparison between the EFE properties of insulating surfaces of freestanding UNCD films (solid symbols) and UNCD films grown on Si substrates (open symbols) with different $H_2\%$ in the CH_4/Ar plasma (inset is Fowler-Nordheim plot of the corresponding data).

Source: Reprinted from Thomas et al. [67].

presumed to be behind the possible mechanism that could explain these improvements. Singh et al. [70] have also observed an increase of around 20 times the current density at 10V/ μm with 20% N_2 added in the synthesis gas. However in this case, they synthesized diamond nanorods decorating a SiO_2 NWs.

Among these studies, other groups have investigated sulfur-doped NCD/UNCD films, which are another kind of *n*-type material [24,71]. All these works showed an effective enhancement of the EFE properties due to the doping.

Thermionic emission has been also studied. Indeed, Suzuki et al. [72] carried out these studies on *n*-type NCD films grown on Si substrates. Low threshold temperature ($\sim 260^\circ\text{C}$) and low threshold electric field ($\sim 5 \times 10^{-5} \text{V}/\mu\text{m}$) were observed. The saturation current obtained was as high as 1.4mA at $5.6 \times 10^{-3} \text{V}/\mu\text{m}$ and they found a low value for the effective work function (1.99eV). These results suggest that nitrogen doped NCD has an excellent possibility of being a highly efficient thermionic emitter material.

Thermal conductivity

Some forms of carbon (diamond and nanotubes) are the best known heat conductors at room temperature, around 20 times better than pure copper. There are a few recent works on the thermal conductivity of *n*-type UNCD films, showing the interest of this kind of sample for different applications. Ralchenko et al. [73] have measured the thermal conductivity of UNCD films as well as of nitrogen added in plasma (up to 25%) UNCD films and compared them to those of polycrystalline diamond films. They found that the thermal conductivity of the UNCD films is two orders of magnitude lower than the polycrystalline diamond ones. Furthermore, in the case of nitrogenated UNCD films the thermal conductivity decreases from 10 to 6W/mK. They assumed that this modification is related to the structural changes due to the nitrogen incorporation. Almost simultaneously Shamsa et al. [74] have published some studies of thermal conductivity measurements carried out on samples coming from the same reactor and produced at similar conditions. These results are consistent with the previous ones, confirming these low values compared to those of single crystal diamond ($\sim 1000 \text{W/mK}$; [73]). These authors explained the lower values of thermal conductivity of *n*-type UNCD films as due to the stronger phonon scattering on point defects (as in the case of bulk crystalline semiconductors; [75]) or to the structural modifications of nitrogen addition.

4.5.2 Optical properties

The unique optical properties of diamond play an important role in its investigation and application, including for industrial use. Actually, after mechanical hardness, optical properties are the second best property of diamond. Indeed, diamond has the widest optical transparency band of all known solids: diamond is transparent in the ultraviolet, visible, and IR spectral regions (ranging from 220nm (fundamental absorption edge) to the far-IR). Thus, the high mechanical hardness and thermal conductivity of diamond greatly support its optical applications making diamond optics very stable and resistant in many respects.

However, the incorporation of impurities in diamond, creating optical centers, offers very interesting properties/applications. In this sense, nitrogen is responsible for the vast majority of impurity-related optical centers of diamond throughout their whole optical range. Furthermore, they are among the most intense and most interesting optical centers of diamond for practical applications. There are several ways for nitrogen to form optically active defects: single isolated nitrogen atoms, multiatom nitrogen complexes, and complexes of nitrogen atoms with intrinsic lattice defects and other impurities.

The optical properties of UNCD/NCD films strongly depend on the sp^2 content and their morphology and structure/crystallinity. The optical absorption spectra of the nonnitrogenated UNCD films have a sharp onset at about 0.8 eV. Which is introduced into the band gap by the high amount of sp^2 carbon at the GBs. This onset is attributed to transitions from π and π^* states. Nitrogen incorporation in the plasma gas causes a significant increase and broadening of the π and π^* bands, and the onset of optical absorption is shifted to lower energies. Thus, the incorporation of nitrogen leads to a strong absorption in the whole energy spectrum, as a result of the increasing number of sp^2 carbon atoms [51].

Ralchenko et al. [73] have also investigated the effects of nitrogen addition to the optical properties of UNCD films. They found a strong absorption, $\alpha = 4.5 \times 10^3$, 2.2×10^4 , and $7.3 \times 10^4 \text{ cm}^{-1}$ at $\lambda = 400 \text{ nm}$ for 0%, 5%, and 25% N_2 samples, respectively. They suggest that these bands can be related to an intergrain mixed phase located in between nanodiamond crystallites being the sp^2 -bonded GBs treated as a separate phase.

Ralchenko et al. [73] have also measured the Tauc optical gap (see Figure 4.10). They observed that the optical gap decreases with N_2 addition to the plasma from 2.2 to 0.2 eV. Thus, this result could be related to the growing of sp^2 clusters as has also been observed by Arenal et al. [54] via Raman spectroscopy (see Section 4.5.3).

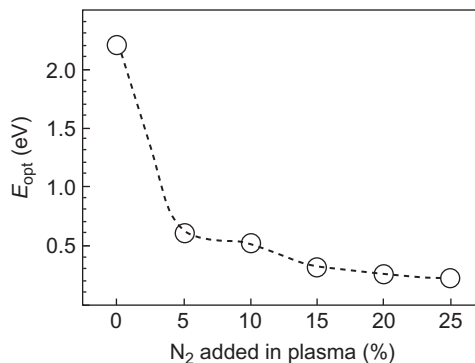


FIGURE 4.10

Tauc optical band gap for UNCD films grown at different N_2 amounts added in plasma.

Source: Reprinted from Ralchenko et al. [73].

4.5.3 Vibrational properties

Particular efforts are always devoted to study the vibrational properties of a material because they are responsible for elastic and thermodynamic properties such as heat capacity and thermal expansion [76]. Furthermore, in the case of carbon materials, the study of lattice dynamics via Raman spectroscopy is widely employed because it is a quick and nondestructive tool, and because structural and electronic properties can also be probed [1,77]. Actually, Raman spectroscopy used in carbon materials provides useful information, such as sp^2/sp^3 ratio, density, and sp^2 site ordering [77–80]. That is why we will deeply review the characteristics of the different Raman signals that can be observed when working on *n*-type NCD/UNCD materials and the kind of information to be extracted.

The Raman spectrum of C materials is divided into first- and second-order regions [81]. In the first-order region ($1100\text{--}1800\text{cm}^{-1}$) are two peaks, denoted as *D* and *G*, corresponding to breathing and stretching modes in sp^2 -bonded carbon clusters, respectively. The *D* peak at $\sim 1350\text{cm}^{-1}$ implies whole aromatic rings with delocalization of the π -bonds and this mode is activated by disorder through a double resonance process involving the elastic scattering of electrons by defects [77,82], while the *G* peak at $\sim 1580\text{cm}^{-1}$ is produced by modes in either olefinic chains or aromatic rings. A third peak related to sp^3 sites may also be present in this region at 1332cm^{-1} , corresponding to the T_{2g} mode. However, as the Raman scattering cross section is resonantly enhanced for sp^2 sites, in practice this peak may be hard to observe and the first-order region will be dominated by the structural configurations of the sp^2 -bonded carbon. Features due to second-order Raman processes are observed in the $2100\text{--}3400\text{cm}^{-1}$ spectral region and correspond to overtones and possible combinations of the modes described above.

In the particular case of nanodiamonds, there are other specific modes corresponding to the *trans*-polyacetylene (TPA) segments that are added to the previous ones. The TPA (poly- CH_x) is an alternate chain of sp^2 carbon atoms, with a single hydrogen bonded to each carbon atom and this TPA lying in the GB of UNCD crystallites [42,79,81]. In the first-order region, these peaks of the TPA are centered at 1140 and $\sim 1480\text{cm}^{-1}$. They correspond, respectively, to the CH bending and to the CC stretching Raman modes of TPA [98]. A weak band at $\sim 2275\text{cm}^{-1}$ is visible at the second-order region; in addition to this line other combinations and overtones of other modes from the TPA could be present in the broad band between 2500 and 3200cm^{-1} described previously, but they are masked or overlapped with the other modes from the overtones of the sp^2 -bonded carbons. It is worth mentioning that these peaks disappear with increasing temperature due to the release of hydrogen.

When working on these NCD/UNCD materials, the development of Raman spectroscopy with multiple excitation wavelengths (UV and visible) is required. Actually, visible Raman scattering from carbons is mainly sensible to the sp^2 sites and less to the sp^3 bonding ones. That is due to the proximity of the visible laser wavelength to the band gap of sp^2 carbon atoms that leads to resonance enhancement in the corresponding Raman cross section [78]. In fact, sp^2 sites have a cross

section for visible Raman more than 50 times larger than sp^3 sites [79]. To overcome this problem and to increase the sensitivity to sp^3 -bonded carbon (through resonance enhancement of these atomic sites), UV Raman spectroscopy, in addition to visible Raman, should be carried out.

We turn now to the study of Raman spectroscopy of *n*-type NCD/UNCD materials. Several works have been developed in this area, including studies by Vlasov et al. [42], Arenal et al. [58], and Ikeda et al. [83]. Figure 4.11 corresponds to the works of Arenal et al. conducted on different UNCD films where the percentage of N_2 in the gas during the synthesis is varies from 0% to 20%. Figure 4.11A shows the Raman spectra recorded at 514.5 nm. Typical UNCD Raman features can be seen for all these samples that consist of four distinctive peaks at 1140 (marked as

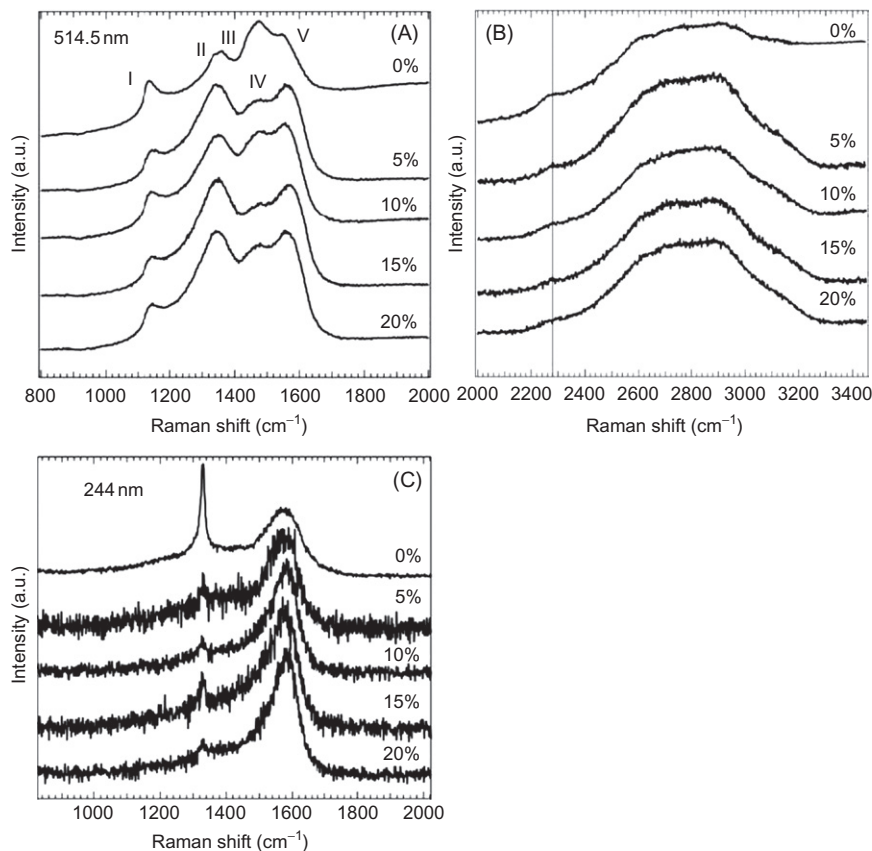


FIGURE 4.11

Raman spectra at two different wavelengths of different UNCD films where the nitrogen addition in the synthesis gas increases from 0% until 20% (substrate temperature of 800°C during deposition): (A and B) 514.5 nm (first and second order) and (C) 244 nm.

Source: Adapted from Arenal et al. [58].

I in this figure), 1345 (marked as III), ~ 1480 (marked as IV), and $1550\text{--}1580\text{ cm}^{-1}$ (marked as V). The pair of peaks at $1550\text{--}1580$ and 1345 cm^{-1} are assigned to the *G* and *D* peaks. In addition to these features, there is a peak corresponding to the sp^3 sites at 1332 cm^{-1} (marked as II in Figure 4.11A).

The most significant changes in the spectra related to the nitrogen addition are those of the sp^2 features. For instance, the fact that the peak of the sp^3 sites is clearly visible for the samples with 0% and 5% of N_2 but not for the rest of the samples indicates that the quantity of the sp^2 -bonded carbon increases with the amount of nitrogen added to the synthesis gas. A similar result has been observed by Vlasov et al. [42]. In the same way, we observe an increase in the Raman scattering with the increase of nitrogen in the synthesis gas. This result confirms the increase of the sp^2 fraction for these samples as Achatz et al. pointed out by optical absorption measurements [51].

The second-order Raman spectra recorded on these samples is shown in Figure 4.12B. The different overtones of the 1350 and 1550 cm^{-1} modes described before are visible, as well as the peak at $\sim 2275\text{ cm}^{-1}$ associated to the TPA. It is interesting to note that the intensity of this peak at 2275 cm^{-1} decreases with the addition of N_2 to the synthesis gas.

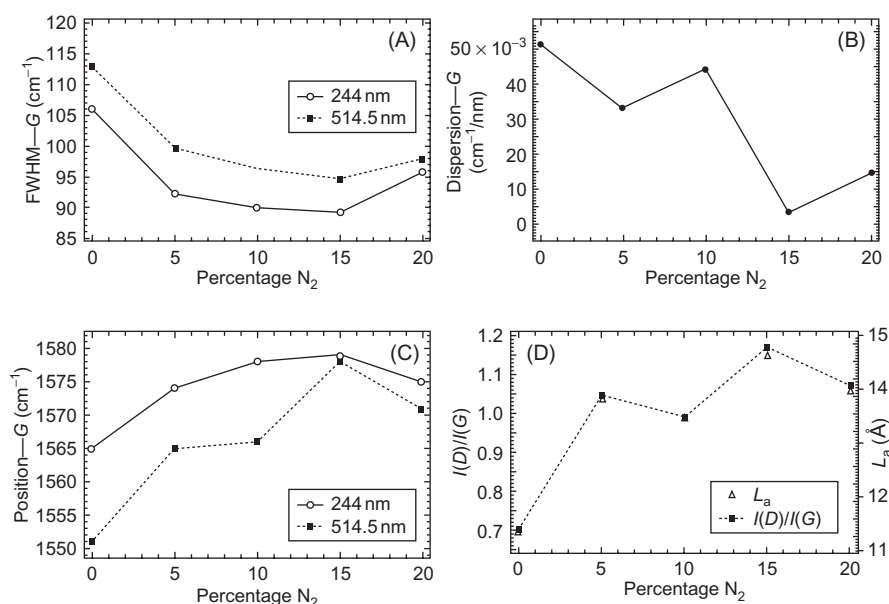


FIGURE 4.12

(A) Variation of the *G* peak position with nitrogen addition in the synthesis gas of UNCD films. (B) Variation of the *D* to *G* peaks intensity ratio ($I(D)/I(G)$) for these UNCD films. (C) FWHM of the *G* peak for UNCD films as a function of nitrogen addition in the synthesis gas. (D) Dispersion of the *G* peak for these UNCD films.

Source: Adapted from Arenal et al. [58].

Monitoring different parameters from the peaks in the first-order region of Raman spectra (as the position, the width (full width at half-maximum (FWHM)) and the dispersion (variation of the position of the peak in function of the excitation energy, Disp (*G*)) of the *G* peak, as well as the intensity ratio of the *D* and *G* peaks, $I(D)/I(G)$) can give insights into the proportion and clustering of the sp^2 phase, as well as their ordering [58,78,79,84] (Figure 4.12). The behavior of these parameters as a function of the increasing of nitrogen in the NCD samples gives very rich information. From this kind of analysis Arenal et al. deduced that the addition of nitrogen to the synthesis gas during the formation of UNCD films, besides the formation of the diamond NWs, promotes sp^2 aromatic clustering, the increase of the size of these clusters, and enhancement of their ordering [58]. Furthermore, these Raman studies confirmed the electronic weak localization for these films as well as the existence of a carbon sheath covering the diamond grains/crystallites. Vlasov et al. [42] showed, via similar experiments on *n*-type UNCD films, the shrinkage of the optical Tauc gap from 2 to 0.25 eV. They deduced that this narrowing of the optical gap is promoted by the addition of nitrogen that stimulates the transformation of amorphous carbon into a graphite-like structure.

Thus, all these Raman spectroscopy works on *n*-type nanodiamond show that very detailed and valuable information (structural, electronic, optical, mechanical, etc.) can be obtained, which has been, for instance, crucial to understanding the high conductivity values showed by *n*-type NCD materials.

It is worth mentioning, as described in the above structural and composition section, that FTIR (or IR) spectroscopy is a complementary technique to Raman spectroscopy for studying the lattice dynamics of a material. In particular, the FTIR spectral analyses of vibrational modes, such as CH stretching ($2750\text{--}3300\text{ cm}^{-1}$), provide the chemical bonding structure of *n*-type UNCD [85].

4.5.4 Mechanical properties

The mechanical properties of *n*-type NCDs, as any other material, are very important and often are critical in engineering potential applications, but usually it is a unique combination of properties that lead to the selection of these nanomaterials for a particular application. These other characteristics are, in the case of UNCD/NCD films, high stiffness and hardness, flat surface, chemical and electrochemical inertness, electrical conductivity, etc., which result in exceptional materials for applications such as nano/microelectromechanical systems (NEMS/MEMS). However, even if the mechanical properties are very important for potential applications, it is worth mentioning that only a few works have been devoted to the study of those of *n*-type UNCD/NCD films. One of these works is by Shen and Chen [86]. These authors calculated using molecular dynamics the mechanical response of a polycrystalline UNCD block with an artificial GB and some incorporated nitrogen atoms. This model may be too simple but they extracted some important information. They studied the compression of this system considering different sizes of the grains. They concluded that elastic moduli is independent of the size of the grains and found a value around 940 GPa.

Recently, Tanei et al. [87] determined the elastic constants of *n*-type NCD films by resonant ultrasound spectroscopy coupled with laser-Doppler interferometry. They found that as N_2 gas increases, the diagonal elastic constants C_{11} , C_{33} , and C_{66} decrease, while the off-diagonal elastic constants C_{12} and C_{13} increase. They concluded that such results could be due to the presence of graphitic GBs.

4.5.5 Chemical properties

In addition to the other very interesting properties of nitrogenated NCD/UNCD films which have been already presented and discussed above, another remarkable characteristic of these films is their chemical inertness. Actually, Ostrovskaya et al. [88] investigated the wetting of *n*-type NCD films and found that they are super-inert. These authors observed that nitrogenated (up to 5% N_2 addition) NCD films exhibited the largest contact angle for tin among all carbon materials. Thus, these films are the most inert coating for this metal. However, it is worth mentioning that they also observed a decrease of the contact angle when nitrogen addition increased. They suggest that such behavior (decrease of the contact angle) could be due to an increase of the sp^2 contribution in the films for high amounts of N_2 addition in the plasma gas as well as the presence of diamond NWs [29] having a sharp relief. This latter result could be very interesting because it could be possible to tune the wetting properties by adjusting the N_2 addition.

However, as we have just mentioned, pure diamond is chemically inert. Thus, the functionalization or the modification of its surface could make them chemically active. Doping these materials with foreign atoms, which are able to create superficial defects and break out the chemical inertness of diamond, represents a feasible path to reactivity and toward a number of applications.

4.6 Applications

In this section the applications of *n*-type NCD/UNCD films are presented taking into account the properties covered in previous sections. It is worth mentioning that from the beginning of this document it has been emphasized that the type of nano-carbon materials (NCD or UNCD films) and the amount of N_2 added to the plasma gas should be pursued first keeping in mind the applications. Thus, of particular significance is the fact that while the sp^3 phase of the diamond grains influences its mechanical properties, the sp^2 -bonded carbon atoms in the GBs control the films' electronic and optical properties.

The outstanding properties of diamond have been already mentioned, in particular those concerning its hardness, thermal conductivity, optical transparency in a wide range of wavelength, and chemical stability. Furthermore, as a semiconducting material, it has excellent dielectric breakdown and mobility. Thus, diamond may be ideally suitable for power-control devices, offering high performances in the form of high-temperature noncooled devices associated with high-voltage and

high-current density. In this sense, Zimmermann et al. [63] have successfully processed a highly rectifying heterostructural diode composed of a single crystal diamond (*p*-type doped part) and a layer of *n*-type UNCD. They showed that the IV behavior of the diode is rather complex. This behavior was explained on the basis of the concept of a “merged diode.” This concept is based on the hypothesis of a heterogeneous interface related to the UNCD grains and GB characteristics, respectively; therefore it corresponds to two junctions acting in parallel. It is proposed that the individual nitrogen-doped grains form a diamond pn-junction with ~ 3.8 eV built-in potential. In parallel, the GB network acts as a distributed parallel diode with a built-in potential of 0.7 eV. Thus, in this structure low forward losses can be combined with high breakdown strength.

Attention up to now has been focused on the biological applications of *n*-type NCD/UNCD films due to, for instance and apart from the other properties mentioned above, their low biocytotoxicity [89] and good photo-stability. Recently, Villalba et al. [90] have functionalized nitrogenated NCD films with enzyme glucose oxidase. They demonstrated the high and fast performance of these films for sensing glucose.

These *n*-type NCD/UNCD films are also very promising in the field of electrochemistry, as is already the case of diamond for water purification. For instance, Furuta et al. [91] have used diamond cells to disinfect potable water contaminated with *Legionella*. Due to similar characteristics of diamond, UNCD films are a very effective electrochemical electrode [92]. Recently, Pleskov et al. [93] studied the effects of nitrogenation on the electrochemical properties of UNCD films. They confirmed the acceptable electrochemical properties of these materials. In fact they have a wide potential window, low background current, and stable electrochemical characteristics, and thus they are very promising for use as electrodes.

Another area where *n*-type UNCD films (highly conductive) play an important role is in their use in FE, as we have already discussed, due to the very interesting characteristics that they possess, such as emission thresholds as low as $2\text{ V}/\mu\text{m}$ [94,95]. It is worth mentioning that the main effect of nitrogen is to increase the density of states associated with sp^2 -bonded carbon atoms. Thus, this higher density of states within the band gap significantly reduces the potential barrier for field-emitted electrons. Furthermore, these GB regions also provide a conductive path to the UNCD/vacuum interface, which is surrounded by nonconductive sp^3 regions. As these GBs are rather narrow, they provide strong field enhancement in the local electric field at the interface. This behavior is similar to that reported in amorphous carbon films, where it was found that the EFE originated from small sp^2 regions in a sp^3 matrix [96].

Finally, these nanomaterials (NCD/UNCD) could have a very significant role in nano/micromechanical systems (NEMS/MEMS) where robust, reliable, and long-endurance materials are required. Indeed, diamond is one of the most promising materials in this area because of its superior physical, tribomechanical, and chemical properties. Thus, *n*-type NCD and/or UNCD films are very promising candidates for NEMS/MEMS applications, including high-frequency resonators, radio frequency, and photonic devices [25,97].

4.7 Conclusions

Here we have summarized the key experimental and theoretical findings and understanding of *n*-type NCD and UNCD films. These are the two most studied forms of diamond films in the last decade. Their growth processes and nanostructures are different, but they have complementary (in some cases similar) properties. We have presented an overview of the changes in the physical and chemical properties upon nitrogen incorporation in these films. The applications for these kinds of new structures have also been pointed out. We have drawn attention to the ongoing theoretical discussions and experimental attempts. Despite tremendous efforts in the different areas that we have presented that have been developed only in the last decade, different aspects such as the growth mechanism and some of the properties require a better understanding. In any case, it is worth mentioning that all the present works are very encouraging and that, in the future, a significant outcome is expected for these materials.

Acknowledgment

R.A. acknowledges the support of the INA—U. Zaragoza (Spain). He also wishes to thank Dr. D.M. Gruen for introducing him to this fascinating research field of nanodiamonds and for rich and stimulating discussions.

References

- [1] M. Dresselhaus, G. Dresselhaus, P. Avouris, Carbon Nanotubes: Synthesis, Structure, Properties, and Applications, Springer, Germany, 2001.
- [2] A. Loiseau, Understanding carbon nanotubes: Lectures Notes in Physics, Springer, Berlin Heidelberg, 2006.
- [3] Y.K. Yap (Ed.), B-C-N Nanotubes and Related Nanostructures, Springer, New York, NY, 2008.
- [4] D.M. Gruen, Nanocrystalline diamond films, Annu. Rev. Mater. Sci. 29 (1999) 211.
- [5] O. Shenderova, D.M. Gruen, Ultrananocrystalline Diamond: Synthesis, Properties, and Applications, William Andrew, New York, NY, 2006.
- [6] O. Williams, Nanocrystalline diamond, Diamond Relat. Mater. 20 (2011) 621–640.
- [7] R. Arenal, X. Blase, A. Loiseau, Boron-nitride and boron-carbonitride nanotubes: synthesis, characterization and theory, Adv. Phys. 59 (2010) 101.
- [8] P. Ayala, R. Arenal, A. Loiseau, A. Rubio, T. Pichler, The physical and chemical properties of heteronanotubes, Rev. Mod. Phys. 82 (2010) 1843–1885.
- [9] P. Ayala, R. Arenal, M. Rummeli, A. Rubio, T. Pichler, The doping of carbon nanotubes with nitrogen and their potential applications, Carbon 48 (2010) 575.
- [10] J. Robertson, Diamond-like amorphous carbon, Mater. Sci. Eng. R Rep. 37 (2002) 129.
- [11] M. Castignolles, PhD Thesis, Etudes de la synthèse et de la structure par microscopie et spectroscopie électroniques de nanotubes de carbone purs et dopés à l'azote U. Montpellier 2, France, 2004.

- [12] X. Liu, T. Pichler, M. Knupfer, J. Fink, Electronic and optical properties of alkali-metal-intercalated single-wall carbon nanotubes, *Phys. Rev. B* 67 (2003) 125403.
- [13] A.Y. Liu, M.L. Cohen, Prediction of new low compressibility solids, *Science* 245 (1989) 841–842.
- [14] P. Sitch, Th. Köhler, G. Jungnickel, D. Porezag, Th. Frauenheim, A theoretical study of boron and nitrogen doping in tetrahedral amorphous carbon, *Solid State Commun.* 100 (1996) 549.
- [15] M.-T. Kuo, P.W. May, A. Gunn, M.N.R. Ashfold, R.K. Wild, Studies of phosphorus doped diamond-like carbon films, *Diamond Relat. Mater.* 9 (2000) 1222.
- [16] S.C.H. Kwok, J. Wang, P.K. Chu, Surface energy, wettability, and blood compatibility phosphorus doped diamond-like carbon films, *Diamond Relat. Mater.* 14 (2005) 78–85.
- [17] V. Anita, T. Butuda, T. Maeda, K. Takizawa, N. Saito, O. Takai, Effect of N doping on properties of diamond-like carbon thin films produced by RF capacitively coupled chemical vapor deposition from different precursors, *Diamond Relat. Mater.* 13 (2004) 1993.
- [18] J. Robertson, Improving the properties of diamond-like carbon, *Diamond Relat. Mater.* 12 (2003) 79–84.
- [19] S.A. Kajihara, A. Antonelli, J. Bernholc, R. Car, Nitrogen and potential *n*-type dopants in diamond, *Phys. Rev. Lett.* 66 (1991) 2010.
- [20] R. Kalish, C. Uzan-Saguy, B. Philosoph, V. Richter, J.P. Lagrange, E. Gheeraert, et al., Nitrogen doping of diamond by ion implantation, *Diamond Relat. Mater.* 6 (1997) 516.
- [21] K. Panda, B. Sundaravel, B.K. Panigrahi, P. Magudapathy, D. Nandagopala Krishna, K.G.M. Nair, et al., Structural and electronic properties of nitrogen ion implanted ultra nanocrystalline diamond surfaces, *J. Appl. Phys.* 110 (2011) 044304.
- [22] S. Koizumi, M. Kamo, Y. Sato, S. Mita, A. Sawabe, A. Reznik, et al., Growth and characterization of phosphorus doped *n*-type diamond thin films, *Diamond Relat. Mater.* 7 (1998) 540.
- [23] S. Gupta, B.R. Weiner, G. Morell, Investigations of the electron field emission properties and microstructure correlation in sulfur-incorporated nanocrystalline carbon thin films, *J. Appl. Phys.* 110 (2005) 044304.
- [24] F.A.M. Koeck, M. Zumer, V. Nemanic, R.J. Nemanich, Photo and field electron emission microscopy, from sulfur doped nanocrystalline diamond films, *Diamond Relat. Mater.* 15 (2006) 880–883.
- [25] O.A. Williams, Growth, electronic properties and applications of nanodiamond, *Diamond Relat. Mater.* 17 (2008) 1080–1088.
- [26] O.A. Williams, Ultrananocrystalline diamond for electronic applications, *Semicond. Sci. Technol.* 21 (2006) 49–56.
- [27] J. Philip, P. Hess, T. Feygelson, J.E. Butler, S. Chattopadhyay, K.H. Chen, et al., Elastic, mechanical, and thermal properties of nanocrystalline diamond films, *J. Appl. Phys.* 93 (4) (2003) 2164–2171.
- [28] J. Birrell, J.A. Carlisle, O. Auciello, D.M. Gruen, J.M. Gibson, Morphology and electronic structure in nitrogen-doped ultrananocrystalline diamond, *Appl. Phys. Lett.* 81 (2002) 2235.
- [29] R. Arenal, P. Bruno, D.J. Miller, M. Bleuel, J. Lal, D.M. Gruen, Diamond nanowires and the insulator-metal transition in ultrananocrystalline diamond films, *Phys. Rev. B* 75 (2007) 195431.
- [30] R. Haubner, B. Lux, Diamond growth by hot-filament chemical vapor deposition: state of the art, *Diamond Relat. Mater.* 2 (9) (1993) 1277–1294.

- [31] L.C. Nistor, J. Van Landuyt, V.G. Ralchenko, E.D. Obraztsova, A.A. Smolin, Nanocrystalline diamond films: transmission electron microscopy and Raman spectroscopy characterization, *Diamond Relat. Mater.* 6 (1) (1997) 159–168.
- [32] D.M. Gruen, X. Pan, A.R. Krauss, A. Liuy, J. Luo, C.M. Foster, Deposition and characterization of nanocrystalline diamond films, *J. Vac. Sci. Technol. A* 12 (1994) 1491.
- [33] O.A. Williams, M. Daenen, J. D'Haena, K. Haenen, J. Maes, V.V. Moshchalkov, et al., Comparison of the growth and properties of ultrananocrystalline diamond and nanocrystalline diamond, *Diamond Relat. Mater.* 15 (2006) 654–658.
- [34] P. Koblinski, D. Wolf, S.R. Phillpot, H. Gleiter, Role of bonding and coordination in the atomic structure and energy of diamond and silicon grain boundaries, *J. Mater. Res.* 13 (1998) 2077.
- [35] F. Cleri, P. Koblinski, L. Colombo, D. Wolf, S.R. Phillpot, On the electrical activity of sp^2 -bonded grain boundaries in nanocrystalline diamond, *Europhys. Lett.* 46 (1999) 671.
- [36] R. Arenal, O. Stephan, P. Bruno, D.M. Gruen, Spatially resolved electron energy loss spectroscopy on *n*-type ultrananocrystalline diamond films, *Appl. Phys. Lett.* 94 (2009) 111905.
- [37] S. Rakha, Z. Xintai, D. Zhu, Y. Guojun, Effects of N_2 addition on nanocrystalline diamond films by HFCVD in Ar/CH_4 gas mixture, *Current Appl. Phys.* 10 (2010) 171–175.
- [38] S.C. Lind, D.C. Bordwell, J.H. Perry, The chemical action of gaseous ions produced by alpha particles. VII. Unsaturated compounds, *J. Am. Chem. Soc.* 48 (1926) 1556.
- [39] S. Bhattacharyya, O. Auciello, J. Birrell, J.A. Carlisle, L.A. Curtiss, A.N. Goyette, et al., Synthesis and characterization of highly-conducting nitrogen-doped ultrananocrystalline diamond films, *Appl. Phys. Lett.* 79 (2002) 1441.
- [40] C.S. Wang, G.H. Tong, H.C. Chen, W.C. Shih, I.N. Lin, Effect of N_2 addition in Ar plasma on the development of microstructure of ultra-nanocrystalline diamond films, *Diamond Relat. Mater.* 19 (2010) 147–152.
- [41] C.R. Lin, W.H. Liao, D.H. Wei, J.S. Tsai, C.K. Chang, W.C. Fang, Formation of ultrananocrystalline diamond films with nitrogen addition, *Diamond Relat. Mater.* 20 (2011) 380–384.
- [42] I.I. Vlasov, O. Lebedev, V.G. Ralchenko, E. Goovaerts, G. Bertoni, G. Van Tendeloo, et al., Hybrid diamond-graphite nanowires produced by microwave plasma chemical vapor deposition, *Adv. Mater.* 19 (2007) 4058–4062.
- [43] S.A. Rakha, Y. Guojun, C. Jianqin, H. Suixia, Z. Xingtai, Influence of CH_4 on the morphology of nanocrystalline diamond films deposited by Ar rich microwave plasma, *J. Appl. Phys.* 107 (2010) 114324.
- [44] K.L. Ma, J.X. Tang, Y.S. Zou, Q. Ye, W.J. Zhang, S.T. Lee, Photoemission spectroscopic study of nitrogen-incorporated nanocrystalline diamond films, *Appl. Phys. Lett.* 90 (2007) 092105.
- [45] Y.K. Liu, P.L. Tso, D. Pradhan, I.N. Lin, M. Clark, Y. Tzeng, Structural and electrical properties of nanocrystalline diamond (NCD) heavily doped by nitrogen, *Diamond Relat. Mater.* 14 (2005) 2059–2063.
- [46] Gu Li-Ping, Tang Chun-Jiu, Jiang Xue-Fan, J.L. Pinto, Impact of nitrogen doping on growth and hydrogen impurity incorporation of thick nanocrystalline diamond films, *Chin. Phys. B* 20 (2011) 058104.

- [47] R. Egerton, *Electron Energy-Loss Spectroscopy in the Electron Microscope*, second ed., Plenum, New York, NY, 1996.
- [48] H. Lin, R. Arenal, S. Enouz, O. Stephan, A. Loiseau, Nitrogen configuration in individual CN_x -SWNTs synthesized by laser vaporization technique, *J. Phys. Chem. C* 113 (2009) 9509.
- [49] C.C. Teng, S.M. Song, C.-M. Sung, C.T. Lin, Structural transformation upon nitrogen doping of ultrananocrystalline diamond films by microwave plasma CVD, *J. Nanomater.* 621208 (2009) 7.
- [50] M. Nesladek, D. Tromson, C. Mer, P. Bergonzo, P. Hubik, J.J. Mares, Superconductive B-doped nanocrystalline diamond thin films: electrical transport and Raman spectra, *Appl. Phys. Lett.* 88 (2006) 232111.
- [51] P. Achatz, J.A. Garrido, M. Stutzmann, O.A. Williams, D.M. Gruen, A. Kromka, et al., Optical properties of nanocrystalline diamond thin films, *Appl. Phys. Lett.* 88 (2006) 101908.
- [52] O.A. Williams, S. Curat, J.E. Gerbi, D.M. Gruen, R.B. Jackman, *n*-Type conductivity in ultrananocrystalline diamond films, *Appl. Phys. Lett.* 85 (2004) 1680.
- [53] J.E. Gerbi, O. Auciello, J.M. Gibson, D.M. Gruen, J.A. Carlisle, Bonding structure in nitrogen doped ultrananocrystalline diamond, *J. Appl. Phys.* 93 (2003) 5606.
- [54] P. Zapol, M. Sternberg, L.A. Curtiss, T. Frauenheim, D.M. Gruen, Tight-binding molecular-dynamics simulation of impurities in ultrananocrystalline diamond grain boundaries, *Phys. Rev. B* 65 (2002) 045403.
- [55] Y. Dai, D. Dai, C. Yan, B. Huang, S. Han, *n*-Type electric conductivity of nitrogen-doped ultrananocrystalline diamond films, *Phys. Rev. B* 71 (2005) 075421.
- [56] S. Bhattacharyya, Mechanism of high *n*-type conduction in nitrogen-doped nanocrystalline diamond, *Phys. Rev. B* 70 (2004) 125412.
- [57] J.J. Mares, P. Hubik, J. Kristofik, D. Kindl, M. Fanta, M. Nesladek, et al., Weak localization in ultrananocrystalline diamond, *Appl. Phys. Lett.* 88 (2006) 092107.
- [58] R. Arenal, G. Montagnac, P. Bruno, D.M. Gruen, Diamond nanowires and the insulator-metal transition in ultrananocrystalline diamond films, *Phys. Rev. B* 76 (2007) 245316.
- [59] P.T. Joseph, N.H. Tai, I.N. Lin, Monolithic *n*-type conductivity on low temperature grown freestanding ultrananocrystalline diamond films, *Appl. Phys. Lett.* 97 (2010) 042107.
- [60] S. Jeedigunta, P. Spagnol, J. Bumgarner, A. Kumar, Electrical contacts to nitrogen incorporated nanocrystalline diamond films, *Diamond Relat. Mater.* 17 (2008) 2037–2040.
- [61] K. Teii, T. Ikeda, Conductive and resistive nanocrystalline diamond films studied by Raman spectroscopy, *Diamond Relat. Mater.* 16 (2007) 753–756.
- [62] K.L. Ma, W.J. Zhang, Y.S. Zou, Y.M. Chong, K.M. Leung, I. Bello, et al., Electrical properties of nitrogen incorporated nanocrystalline diamond films, *Diamond Relat. Mater.* 15 (2006) 626–630.
- [63] T. Zimmermann, M. Kubovic, A. Denisenko, K. Janischowsky, O.A. Williams, D.M. Gruen, et al., Ultra-nano-crystalline/single crystal diamond heterostructure diode, *Diamond Relat. Mater.* 14 (2005) 416–420.
- [64] W. Zhu, G.P. Kochanski, S. Jin, Low-field electron emission from undoped nanostructured diamond, *Science* 282 (1998) 1471–1473.
- [65] G.R. Brandes, C.P. Beetz, C.A. Feger, R.L. Wright, Diamond junction cold cathode, *Diamond Relat. Mater.* 4 (1995) 586.

- [66] K. Wu, E.G. Wang, Z.X. Cao, Z.L. Wang, X. Jiang, Microstructure and its effect on field electron emission of grain-size-controlled nanocrystalline diamond films, *J. Appl. Phys.* 88 (2000) 2967–2974.
- [67] J.P. Thomas, H.-C. Chen, N.-H. Tai, I.-N. Lin, Freestanding ultrananocrystalline diamond films with homojunction insulating layer on conducting layer and their high electron field emission properties, *ACS Appl. Mater. Interfaces* 3 (2011) 4007–4013.
- [68] Y.C. Lin, K.J. Sankaran, Y.C. Chen, C.Y. Lee, I.-N. Lin, N.-H. Tai, Enhancing electron field emission properties of UNCD films through nitrogen incorporation at high substrate temperature, *Diamond Relat. Mater.* 20 (2011) 191–195.
- [69] Y.C. Chen, N.-H. Tai, I.-N. Lin, Substrate temperature effects on the electron field emission properties of nitrogen doped ultrananocrystalline diamond, *Diamond Relat. Mater.* 17 (2007) 457–461.
- [70] M.K. Singh, E. Titus, M.G. Willinger, J.C. Madaleno, J. Grácioa, Microstructure and electron field emission study of diamond nanorod decorated a-SiO₂ nanowires by microwave Ar-CH₄/H₂ plasma chemical vapor deposition with addition of N₂, *Diamond Relat. Mater.* 18 (2009) 865–869.
- [71] S. Gupta, B.R. Weiner, G. Morell, Investigations of the electron field emission properties and microstructure correlation in sulfur-incorporated nanocrystalline carbon thin films, *J. Appl. Phys.* 91 (2002) 10088–10097.
- [72] M. Suzuki, T. Ono, N. Sakuma, T. Sakai, Low-temperature thermionic emission from nitrogen-doped nanocrystalline diamond films on *n*-type Si grown by MPCVD, *Diamond Relat. Mater.* 18 (2009) 1274–1277.
- [73] V. Ralchenko, S. Pimenov, V. Konov, A. Khomich, A. Saveliev, A. Popovich, et al., Nitrogenated nanocrystalline diamond films: thermal and optical properties, *Diamond Relat. Mater.* 16 (2007) 2067–2073.
- [74] M. Shamsa, S. Ghosh, I. Calizo, V. Ralchenko, A. Popovich, A.A. Balandin, Thermal conductivity of nitrogenated ultrananocrystalline diamond films on silicon, *J. Appl. Phys.* 103 (2008) 083538.
- [75] M. Shamsa, W.L. Liu, A.A. Balandin, J.L. Liu, Phonon-hopping thermal conduction in quantum dot superlattices, *Appl. Phys. Lett.* 87 (2005) 202105.
- [76] M. Cardona, G. Guntherodt, *Light Scattering in Solids*, Springer, New York, NY, 1982.
- [77] S. Reich, C. Thomsen, J. Maultzsch, *Carbon Nanotubes: Basic Concepts and Physical Properties*, Wiley-VCH, Berlin, 2004.
- [78] A.C. Ferrari, J. Robertson, Interpretation of Raman spectra of disordered and amorphous carbon, *Phys. Rev. B* 61 (2000) 14095.
- [79] A.C. Ferrari, J. Robertson, Resonant Raman spectroscopy of disordered, amorphous, and diamondlike carbon, *Phys. Rev. B* 64 (2001) 075414.
- [80] R. Arenal, A.C.Y. Liu, Clustering of aromatic rings in near-frictionless hydrogenated amorphous carbon films probed using multiwavelength Raman spectroscopy, *Appl. Phys. Lett.* 91 (2007) 211903.
- [81] F. Tuinstra, J.L. Koenig, Raman spectrum of graphite, *J. Chem. Phys.* 53 (1970) 1126–1130.
- [82] C. Thomsen, S. Reich, Double resonant Raman scattering in graphite, *Phys. Rev. Lett.* 85 (2000) 5214.
- [83] R. Ikeda, H. Tanei, N. Nakamura, H. Ogi, M. Hirao, A. Sawabe, et al., Elastic constant of nanocrystalline diamond film, *Diamond Relat. Mater.* 15 (2006) 729.

- [84] C. Casiraghi, A.C. Ferrari, J. Robertson, Raman spectroscopy of hydrogenated amorphous carbons, *Phys. Rev. B* 72 (2005) 085401.
- [85] S. Al-Riyami, S. Ohmagari, T. Yoshitake, Fourier transform infrared spectroscopic study of nitrogen-doped ultrananocrystalline diamond/hydrogenated amorphous carbon composite films prepared by pulsed laser deposition, *Diamond Relat. Mater.* 20 (2011) 1072.
- [86] L. Shen, Z. Chen, An investigation of grain size and nitrogen-doping effects on the mechanical properties of ultrananocrystalline diamond films, *Int. J. Solids Struct.* 44 (2007) 3379–3392.
- [87] H. Tanei, N. Nakamura, H. Ogi, M. Hirao, Unusual elastic behavior of nanocrystalline diamond thin films, *Phys. Rev. Lett.* 100 (2008) 016804.
- [88] L. Ostrovskaya, V. Perevertailo, V. Ralchenko, A. Dementjev, O. Loginova, Wettability and surface energy of oxidized and hydrogen plasma-treated diamond films, *Diamond Relat. Mater.* 11 (2002) 845.
- [89] C. Popov, W. Kulisch, M. Jelinek, A. Bock, J. Strnad, Nanocrystalline diamond/amorphous carbon composite films for applications in tribology, optics and biomedicine, *Thin Solid Films* 297 (2006) 506–507.
- [90] P. Villalba, M.K. Ram, H. Gomez, A. Kumar, V. Bhethanabotla, A. Kumar, GOX-functionalized nanodiamond films for electrochemical biosensor, *Mater. Sci. Eng. C* 31 (2011) 1115–1120.
- [91] T. Furuta, H. Tanaka, Y. Nishiki, L. Pupunat, W. Haenni, P. Rychen, *Legionella* inactivation with diamond electrodes, *Diamond Relat. Mater.* 13 (2004) 2016–2019.
- [92] B. Fausett, M.C. Granger, M.L. Hupert, J. Wang, G.M. Swain, D.M. Gruen, The electrochemical properties of nanocrystalline diamond thin-films deposited from C-60/argon and methane/nitrogen gas mixtures, *Electroanalysis* 12 (2000) 7–15.
- [93] Y.V. Pleskov, M.D. Krotova, A.V. Saveliev, V.G. Ralchenko, The effects of nitrogenation on the electrochemical properties of nanocrystalline diamond films, *Diamond Relat. Mater.* 16 (2007) 2114–2117.
- [94] A.R. Krauss, O. Auciello, M.Q. Ding, D.M. Gruen, Y. Huang, V.V. Zhirnov, et al., Electron field emission for ultrananocrystalline diamond films, *J. Appl. Phys.* 89 (2001) 2958–2967.
- [95] T.D. Corrigan, D.M. Gruen, A.R. Krauss, P. Zapol, R.P. Chang, The effect of nitrogen addition to Ar/CH₄ plasmas on the growth, morphology and field emission of ultrananocrystalline diamond, *Diamond Relat. Mater.* 11 (2002) 43–48.
- [96] A. Ilie, A.C. Ferrari, T. Yagi, S.E. Rodil, J. Robertson, E. Barborini, et al., Role of sp² phase in field emission from nanostructured carbons, *J. Appl. Phys.* 90 (2001) 2024–2032.
- [97] A.V. Sumant, O. Auciello, R.W. Carpick, S. Srinivasan, J.E. Butler, Ultrananocrystalline and nanocrystalline diamond thin films for MEMS/NEMS applications, *MRS Bull.* 35 (2010) 281–288.
- [98] H. Kuzmany, R. Pfeiffer, N. Salk, B. Gunther, The mystery of the 1140 cm⁻¹ Raman line in nanocrystalline diamond films, *Carbon* 42 (2004) 911.

Advances in Synthesis of Nanodiamond Particles

5

Vycheslav Danilenko^a and Olga A. Shenderova^b

^a*Novogorsk, Chimki, Moscow region, Russia*

^b*Nanodiamond Laboratory, International Technology Center, Raleigh, NC*

CHAPTER OUTLINE

5.1 Introduction	133
5.2 Brief history of DND discovery.....	135
5.3 Types of NDs and methods of ND synthesis	141
5.3.1 ND particles produced by detonation shock-wave-assisted synthesis ...	144
<i>ND produced from carbon and carbon/explosive mixture</i>	<i>145</i>
<i>ND produced from high-energy explosives</i>	<i>145</i>
<i>Structure of different types of dynamically synthesized NDs.....</i>	<i>149</i>
5.3.2 NDs from HPHT diamond	152
5.3.3 Laser-assisted synthesis of ND	154
5.3.4 Cavitation-assisted synthesis of ND.....	155
5.3.5 ND particles synthesis based upon the CVD technique.....	156
5.3.6 Methods using irradiation with high energetic particles.....	157
5.3.7 Carbide-derived diamond.....	158
5.3.8 Other recent methods of ND synthesis	158
5.4 Conclusion and future outlook	159
Acknowledgment	159
References	160

5.1 Introduction

Today there is a wide variety of nanostructured diamond particles available for research. They have been synthesized by the detonation technique [1], laser ablation [2], high-energy ball milling of high-pressure high-temperature (HPHT) diamond microcrystals [3], plasma-assisted chemical vapor deposition (CVD) [4], autoclave synthesis from supercritical fluids [5], chlorination of carbides [6], ion irradiation of graphite [7], electron irradiation of carbon onions [8], and ultrasound cavitation [9],

with the first three of these methods being used commercially. Astronomical observations suggest that nanodiamonds (NDs) are present in the protoplanetary disks of certain types of stars [10,11], although the origins of these cosmic sources are still under investigation. The most popular in the research laboratories are so-called detonation nanodiamonds (DNDs), produced by detonation of carbon-containing explosives and HPHT ND particles. The reason for this is twofold. First, colloidal suspensions of individual ND particles of only 4–5 nm in size (so-called single-digit ND) recently became available [12]. Before that, due to the high tendency of DND to aggregate, typical commercial suspensions of DND contained large aggregates, up to several hundred nanometers in size (which can withstand ultrasonic treatment). Second, the production of ND particles containing specific impurity defects that allow for photoluminescent particles seems poised to revolutionize biological imaging and quantum optics applications [13,14]. Bright photoluminescent NDs were produced using HPHT diamond, containing 10–300 ppm of native substitutional nitrogen defects, by grinding them to nanosized particles [15,16] followed by irradiation with energetic particles (e.g., electrons and protons) to create vacancies.

The availability of single-digit ND particles produced by detonation of explosives in kilogram quantities has opened broad prospective applications of NDs in composites, lubricants, and as drug delivery vehicles. Indeed, the specific surface areas of ND particles 4 and 30 nm in diameter are 428 and 57 m²/g, respectively, making a noticeable 7× difference in the adsorption and load capacity of the nanoparticles. The availability of single-digit ND particles is also important for biomedical applications for delivery of biologically active molecules, for example, through the blood–brain barrier [17]. A central focus of many research groups remains the controlled production of nitrogen-vacancy (NV) centers in nanoscale diamond. Due to the strong optical transition, single defects can be detected using a fluorescence microscope. The spin state of the negatively charged NV centers can be polarized by optical pumping and can be manipulated using electron paramagnetic resonance (EPR), permitting the implementation of efficient single photon emitters for quantum information processing [13] or a magnetic sensor with nanoscale resolution [14]. Single color centers show outstandingly high photo stability, even at room temperature [15]. The two major breakthroughs, the production of ND particles 4–5 nm in size and ND particles containing impurity defects exhibiting stable luminescence and unique spin properties, are related to ND particles synthesized by different techniques (detonation of explosives and grinding of HPHT diamond, respectively). Thus these two important characteristics are not currently available through a single synthesis route. Synthesis of NDs a few nanometers in size with specific color centers remain an important goal. New methods of ND particle synthesis are possibly needed to address this goal.

Another important class of nanostructured diamond particles is a class of micron-sized single particles with nanocrystalline structure produced using shock-wave compression of carbon materials (graphite, carbon black) [18]. This so-called polycrystalline diamond (known with its earlier trade name as Mypolox), has been commercially available since the 1970s and is widely used in the polishing industry.

A central goal of this chapter is to present a brief survey of the different classes of ND particles and provide a comparison of their structure and physical properties. Another purpose of this chapter is to review the well-established and novel methods of synthesis of ND particles. We start the chapter with a brief historical outline of the discoveries of methods of nanostructured diamond synthesis using explosives with a major emphasis on DND.

5.2 Brief history of DND discovery

Nanostructured diamond particles were first produced by direct phase transformation of graphite induced by an explosive shock wave by De Carli at Poulter Laboratories, CA, in 1961 [19]. Yield of diamond phase was low due to excessive graphitization of diamond during release of the shock pressure, while the temperature was still high. Soon after the work by De Carli, researchers from I.E. Du Pont De Nemours & Company suggested the use of a mixture of starting carbon phases with cooling media (metals) in the shock-wave synthesis of diamond [18]. The yield of diamond phase was significantly increased and the product has been commercially available since that time under the trade name *Mypolex* primarily for use in the polishing industry. In 1999 the Mypolex polycrystalline diamond business was acquired from DuPont by Microdiamant AG, Switzerland, a company specializing in the micron and submicron diamond market. Polycrystalline diamond from Microdiamant is available in grades ranging from submicron up to 30 micron particles, consisting of 10–20 nm grains.

The general history of the development of dynamic methods for diamond synthesis is outlined in Table 5.1. The history of the discovery of DND synthesis is unique as has been described in detail by Danilenko [20]. DND (or ultradispersed diamond (UDD), as the material was called in the USSR) was discovered four times over the period of 25 years by scientists from different research centers. Specialists from the All-Union Research Institute of Technical Physics (VNIITF), a research institute where nuclear weapons were developed, were the first in the USSR, starting studies on UDD synthesis in 1960 by an initiative of Zababakhin, who headed the VNIITF (later the institute was named after him). Owing to his initiative and support, scientists from the gas dynamics group, including Volkov, Danilenko, and Elin, carried out the following pioneering developments regarding dynamic synthesis in the time period 1960–1965 [1,21]: (i) diamonds were obtained by shock compression of graphite and carbon black in spherical and cylindrical storage ampoules (1962); (ii) compression of a graphite-metallic coolant mixture was used, which made it possible to increase the diamond yield by an order of magnitude (1963); (iii) the superhard wurtzite modification of boron nitride was obtained using explosion (1963); and (iv) detonation synthesis of NDs from carbon molecules of explosives was discovered and investigated (1963).

To simplify the diamond synthesis, Danilenko proposed and implemented (in 1962) ampoule-free synthesis with explosions in an explosion chamber. Graphite

Table 5.1 Historical Outline of Dynamic Diamond Synthesis

Authors	Year	Subject of Research
B.I. Zababakhin (VNIITP)	1960	Justification of the possibility of diamond synthesis via shock compression of graphite; beginning of experimental research
B.J. Alder and R.H. Christian (USA) M.N. Pavlovskii (VNIIEF), K.K. Krupnikov (VNIITP), A.N. Dremin, and S.V. Pershin (IchP)	1961 1963 1968	Derivation of the shock adiabat for graphite and confirmation of its conversion into diamond
P.J. De Carli and A.C. Jamisson (USA)	1961	Diamond synthesis with preservation of shock-compressed graphite in a plane ampoule
K.V. Volkov, V.V. Danilenko, and V.I. Elin (VNIITP)	1962 1963 1963	The same, but in spherical and cylindrical ampoules (diamond yield—2%) Diamond synthesis by compression of graphite+Me and carbon black+Me mixtures (diamond yield—20%) UDD synthesis from carbon of explosion products (diamond yield 8–12% of the charge mass)
G.A. Adadurov (IchP)	1965	Diamond synthesis from graphite
Du Pont de Nemours and Co. (USA)	1964 1976	Diamond synthesis from graphite mixed with metal Commercial production of diamond micropowder <i>Mypolex</i> by compressing graphite–copper mixture with a charge mass of 5 tons in cylindrical enclosures
G.I. Savvakín (IPM)	1982	UDD synthesis
A.M. Staver, E.A. Petrov, and A.I. Lyamkin (IG)	1982	UDD synthesis
O.N. Breusov, V.N. Drobyshev, G.A. Adadurov, and A.N. Dremin (IchP)	1983	Pilot-scale production of diamond micropowders by explosion of pressed 100g charges of graphite or carbon black mixture with RDX in an explosion chamber
G.V. Sakovich and coworkers (NPO “Altay,” Biisk)	1984 1985	Industrial production of UDD (0.6kg charges from RDX/TNT 40/60%, “dry” cooling) Applications of UDD in wear-resistive coating, production of lubricant additives with UDD for motor oils
N.R. Greiner, P.S. Philips, and J.D. Johnson (USA) F. Volk (Germany)	1988	UDD synthesis

Table 5.1 Historical Outline of Dynamic Diamond Synthesis (*Continued*)

Authors	Year	Subject of Research
Collaborators of the VNIITP and PGUP “Elektrokhimpribor,” ZAO “Almazny center,” NPO “Sinta” (Minsk), ZAO “ALIT”	1991– 1995	Pilot-scale production of UDD
V.V. Danilenko, I.A. Petrusha and A.A. Bothethka (ISM) V.V. Danilenko (ZAO “ALIT”)	1994 1995	Beginning of studies on UDD sintering under static conditions Ampoule-free sintering of high-density UDD grains by explosion, obtaining of diamond single crystals
V.V. Danilenko, P.P. Tolochko, B.A. Vyskubenko, and E.E. Lin (ZAO “ALIT,” VNIITF, VNIIEF)	1986– 1992	Experiments on UDD synthesis by explosion of large-mass charges (10–140 kg)
V.Y. Dolmatov	2008	UDD synthesis in the presence of reducing agents in the cooling media

was placed directly into a cylindrical charge made from the RDX/TNT (60/40%) mixture. The charge was enveloped in a water jacket to suppress graphitization of the synthesized diamond and to reduce the unloading rate of detonation products (DPs). Even the first experiment with such a setup resulted in a significant diamond yield. A control experiment, carried out with a graphite-free charge in July 1963, confirmed the hypothesis that diamond was synthesized from the carbon contained in the DP.

Simultaneously, a comparison of the phase diagram for carbon and the parameters at the Jouguet point for the detonation of high-density charges of powerful explosives (the values of pressure and temperature obtained in DP as a result of detonation-induced decomposition of explosive molecules) proved that the free carbon of DP condenses in the form of diamond [22]. It was also concluded that, in order to obtain free carbon in DP, an explosive with a negative oxygen balance must be used. Such explosive compounds simultaneously serve as sources of energy and carbon. As compared to diamond synthesis from graphite, the advantage of condensation of the atomic carbon of DP into diamond is that neither energy nor time expenditures are required for the destruction or rearrangement of the initial crystal lattice of graphite. Thus, the main problem is not in the formation of DND but in its preservation (i.e., in creating conditions in the detonation chamber that prevent oxidation and graphitization of the DNDs obtained). Despite convincing theoretical predictions (Table 5.1), only the experiment carried out in 1963 proved for the first time that diamond is indeed formed in a detonation wave and that it can be preserved.

In 1963–1965, about 100 successful experiments were carried out to analyze the effect of explosion conditions, as well as the composition and configuration of charges, on DND synthesis and the properties of the DND produced [1,21,23]. It was shown that DP cooling as a result of conversion of the potential energy of DP into kinetic energy of the envelope surrounding the charge plays a decisive role in DND synthesis. It was found that an elongated cylinder is the best shape for charges; the explosion of such a charge from RDX/TNT 60/40% in a water jacket gives a DND yield of 8–12% of the charge mass and DND concentration in the detonation soot of up to 75%. Unfortunately, nanometer-sized diamond with low abrasion effect as compared to diamond particles of static synthesis was considered a research topic of low priority at that time by the Soviet government. In addition, the first discovery of DND synthesis took place at the VNIITF, which specialized in topics far from diamond production. The results of the experiments were highly classified and were not published until late 1980s [1,21], when this research topic became very popular. Only in 1986 were the largest part of the reports of 1963 provided by VNIITF to other research centers working on the synthesis of diamond and, particularly, on DND.

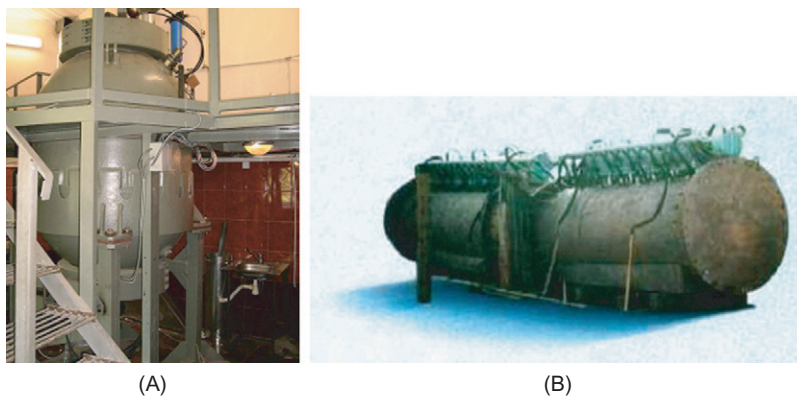
DND synthesis was rediscovered by Staver and coworkers at the Institute of Hydrodynamics, Siberian Division, Academy of Sciences of the USSR (Novosibirsk) [24–26], and by Savvakín at the Institute of Problems of Materials Science, Ukraine Academy of Sciences (Kiev) [27–29]. In the experiments initiated by Staver and coworkers in 1982 [30], the cooling of the DP to preserve the DND formed during detonation was implemented using a gaseous medium inert toward carbon, the so-called “dry” cooling. The patent [27] filed by Savvakín and colleagues in 1979 indicates that the research on synthesis of UDD directly from carbon-containing explosives during their detonation was started even earlier—in the late 1970s. In the USA, DND synthesis was reported for the first time in 1988 [31]. This serendipitous fourth DND discovery took place as a result of investigation of the DPs (gases, soot, etc.) of different explosives during detonation in an argon atmosphere in a chamber volume 1.5 m³. Experiments were conducted at the Fraunhofer Institute of Chemical Technology, Germany, by Fred Volk (Division Head of the Institute) and by Roy Greiner (from Los Alamos National Laboratory, USA). Detailed investigation of the soot produced by explosion of RDX mixtures conducted by Greiner and coworkers at Los Alamos Laboratory revealed the presence of DND in the soot.

NDs produced by another dynamic method, detonation of a mixture of a carbon precursor (graphite or carbon black) and explosives, is much less known in the community. This approach was invented in the Institute of Problems of Chemical Physics, Russian Academy of Sciences, Chernogolovka, by Adadurov et al. in the late 1970s [32,33] and registered under the trademark DALAN (Russian acronym for detonation diamonds of the Academy of Sciences). A pilot-scale production of diamond micropowders by explosion of graphite mixture with RDX is still taking place in Dzerzhinsk, providing nanostructured polycrystalline diamond powder (similar to Mypolex) for polishing applications.

In the early 1980s, scientists from the Institute of Hydrodynamics of AN SSSR began a collaboration with researchers from the Research and Production Center Altai on industrialization of DND synthesis with Sakovich leading the research. In 1984, a DND pilot-scale production facility was established at Altai (charges 0.6 kg from RDX/TNT 40/60%, “dry” cooling by inert gases in chamber, DND yield 4–6%, DND concentration in soot 40–50%) [34]. In 2011, Sakovich received a prestigious award from Rusnano, Russian Corporation of Nanotechnologies, for “developing a technology of production of functionally nanosized synthetic diamonds from carbon atoms of molecules of explosive substances during their detonation.” In 1989, the USSR government issued a decree to increase the production scale at Altai from 10 million to 75, and ultimately up to 250 million carats of DND per year [34]. By 1993 Altai produced more than 25 million carats (more than 5 tons). By the end of the 1980s, the DND produced at Altai had been widely used in various technical applications [34]. According to Vereshchagin [34], the major consumer of DND was the machine-building industry, where DND was used for co-deposition in chrome galvanic coatings. This process had been utilized at more than 200 machine-building factories in the former USSR. According to Savvakina [29], by the beginning of the 1990s, DND had been also reduced to practice in Ukraine in such applications as lubricants, metallic coating composites, DND compacts, polymer composites, and others. In the 1980s, several research centers in the USSR were working on dynamic methods for DND production: VNIITF (Snezhinsk, Chelyabinsk region); Institute of Chemical Physics, Academy of Sciences (ICHF, Chernogolovka, Moscow region); Institute of Hydrodynamics, Siberian Academy of Sciences of the USSR (IG, Novosibirsk); Institute of Superhard Materials, Ukraine Academy of Sciences (ISM, Kiev); Institute of Problems of Materials Science, Ukraine Academy of Sciences (IPM, Kiev); Dnepropetrovsk Institute of Mines (DGI, Dnepropetrovsk, Ukraine), and Krasnoyarsk Polytechnic Institute.

In the late 1980s and mid-1990s, extensive studies of carbon condensation in the form of DND during detonation were performed by Staver, Lyamkin, Anisichkin, Mal'kov, Petrov, Ershov, and Titov [25,26,35]. Staver, who was a leader of the DND discovery at the Institute of Hydrodynamics, continued DND research at Krasnoyarsk Polytechnic Institute from 1983, where the pilot-scale production of DND was organized in 1991.

In 1986–1988 at VNIITF, Danilenko investigated DND synthesis using large-mass charges (with a mass of up to 20 kg) of various explosives in large explosion chambers with a purpose to generate large-scale production of inexpensive, high-quality DND, which is essential for DND application on an industrial scale. It was shown that an increase in the mass of charges using a RDX/TNT 60/40% mixture does not change the DND yield, but DND grains become coarser (the specific surface area of DND grains is reduced by half, from 400 to 200 m²/g), and macroscopic lonsdaleite crystals are also formed [23]. In 1991 at VNIIEF (Sarov, Russia), a unique experiment on DND synthesis was carried out by exploding a charge with a mass of 140 kg in a water jacket in a chamber 300 m³ in volume [36]. Danilenko

**FIGURE 5.1**

Photographs of detonation camera: (A) camera with volume 6 m^3 for detonation of 1 kg charge and (B) camera at Alit, 100 m^3 for detonation of 10 kg charges.

Source: Photograph (A) is courtesy of Dolmatov, Diamond Center, Russia, and photograph (B) is courtesy of ALIT Inc., Ukraine.

left VNIITF, Snezhinsk, in 1989 and continued his carrier at the Institute for Material Science Problems, Ukraine. In 1992, he developed a large-scale technology for producing DND (charges 10kg of RDX/TNT 60/40%, water cooling, DND yield 8–10% and DND concentration in soot 60–75%, DND-specific surface area $200\text{ m}^3/\text{g}$, and average particle size 4–6 nm) and implemented it at the commercial plant of the “ALIT” company (Zhitomir, Ukraine). The main part of the plant was an explosion chamber 100 m^3 in volume with water cooling of the DND [37] (Figure 5.1). At present all other manufacturers use small explosion chambers ($2\text{--}5\text{ m}^3$) and small charges (0.5–2 kg).

Since the market for polycrystalline micron-sized diamond is well established, there are several approaches used to produce similar products using DND as a starting material. The technology of DND sintering under moderate high-pressure, high-temperature conditions at “ALIT” provided unique “soft” diamond sub-micropowders with polycrystal particles for superfinish polishing of some electronic devices (produced at “ALITEX,” Kiev) [23,38]. In 1995, experiments using the big “ALIT” chamber for shock-wave-based sintering of DND resulted in high-density DND grains and diamond single crystals (up to 0.6 mm) [23,39].

As can be seen from the above review, detonation synthesis of ND was a very advanced topic in the research community of the former USSR, with a very well-developed scientific infrastructure. Along with numerous pilot-scale production centers, industrial-scale producers also emerged. However, production of NDs in small batches was unprofitable and resulted in the shutting down of a number of research centers and decreasing or termination of DND production in Russia, Ukraine, and Belorussia by the mid-2000s. There was a short spike of interest in

DND for magnetic disks texturing applications in the mid-2000s, but that quickly declined after the texturing technology was changed.

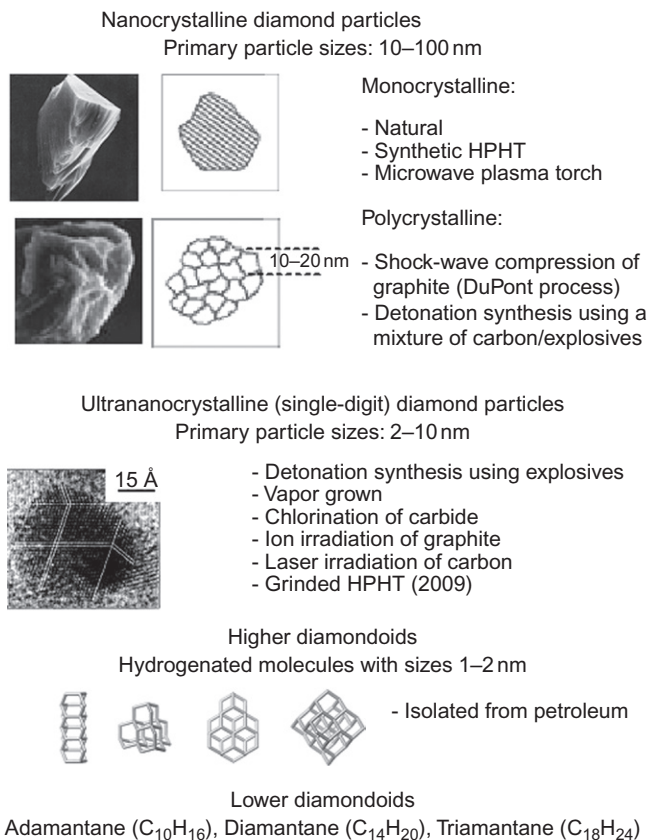
At the beginning of the second decade of the twenty-first century, the interest in DND within the world scientific community has significantly increased [40] due to the availability of single-digit NDs and newly developed methods of ND surface functionalization. These achievements allowed exploitation of DND's true "nano" properties. If a real commercial demand for DND will take place as a result of the scientific activity in the near future, industrial production of this material will be in order. However, additional innovations in DND synthesis and processing will be needed to satisfy modern requirements for material with specific properties and at reasonable cost, and in light of competition with other nanomaterials.

5.3 Types of NDs and methods of ND synthesis

ND particles can be conveniently categorized into three groups according to the size of their primary particles (Figure 5.2): nanocrystalline particles, ultrananocrystalline particles, and diamondoids. Characteristic sizes of nanocrystalline particles encompass the size range of tens of nanometers, while sizes of primary particles of ultrananocrystalline diamond are within several nanometers [41]. Diamondoids are well-defined hydrogen-terminated molecular forms consisting of several tens of carbon atoms with characteristic sizes of $\sim 1\text{--}2\text{ nm}$ [42]. While a choice of 10 nm as the margin between two classes of NDs seems arbitrary, however, it reflects a difference in properties of the resulting products using diamond nanoparticles of different sizes. As was pointed out in the introduction, the specific surface areas of ND particles 4 and 30 nm in diameter make a noticeable $7\times$ difference in the adsorption and load capacity of the nanoparticles. The term "single-digit ND" coined by Osawa [43] seems to be gaining broader acceptance in the community for sub- 10 nm ND particles, rather than "ultrananocrystalline" ND particle.

The class of nanocrystalline diamond particles includes subgroups of monocrystalline and polycrystalline particles (Figure 5.2). Monocrystalline nanoparticles include ND particles processed from HPHT synthetic diamond as well as from natural diamond powders, commercially available with smallest average particle size around 20 nm (produced, for example, by Microdiamant AG). Polycrystalline ND powder is processed from micron-sized polycrystalline diamond particles obtained by shock compression of graphite mixed with metals [19] (method developed by DuPont de Nemours) or by detonation of a mixture of graphite and explosives [32,44]. Polycrystalline particles consist of nanometer-sized diamond grains ($\sim 10\text{--}20\text{ nm}$). The finest diamond fraction produced by micronizing followed by grading has an average size of an individual particle of $\sim 25\text{ nm}$ (available at Microdiamant AG).

Of the several types of ultrananocrystalline diamond particles (Figure 5.2), only detonation ND, obtained by the detonation of solid explosives in an inert atmosphere, has been commercialized on a large scale (e.g., by ALIT, Ukraine). The average size of primary detonation ND particles produced by most vendors lies in

**FIGURE 5.2**

Summary of the types of nanoscale diamond particles and molecular forms (diamondoids) according to primary particle size. Examples of higher diamondoids from petroleum, 1–2 nm hydrogen-terminated diamond molecules (left to right): rod-shaped [1212] pentamantane C₂₆H₃₂, pyramid-shaped [1(2,3)4] pentamantane C₂₆H₃₂, irregular disk-shaped [121321] heptamantane C₃₀H₃₄, and octahedral [1231241(2)3] decamantane C₃₅H₃₆.

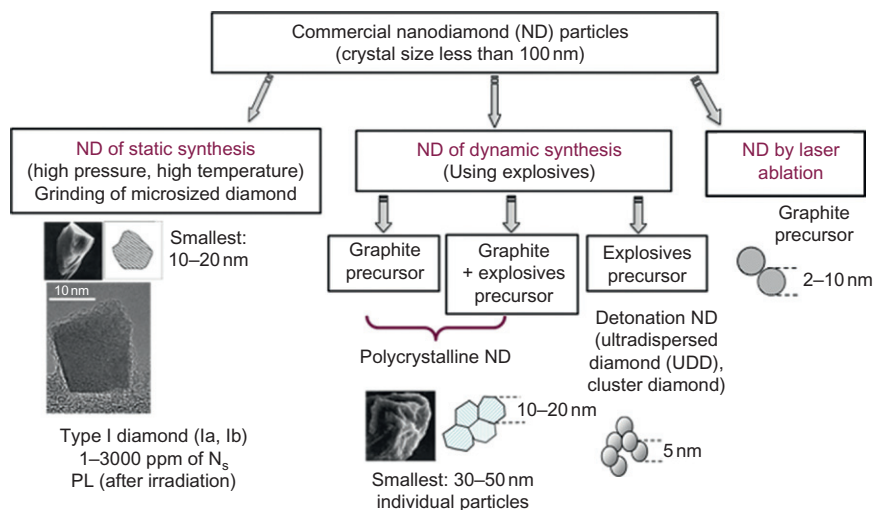
Source: Pictures of nanocrystalline diamond are courtesy of Microdiamant AG, Switzerland.

Pictures of UNCD single particles are courtesy of T.L. Daulton, Naval Research Laboratory.

Pictures of higher diamondoids are courtesy of ChevronTexaco MolecularDiamond Technologies.

the range of 3.5–6 nm. Recently, single-digit ND produced by laser ablation of carbon precursors has become commercially available (Ray Techniques Ltd, Israel). Details on the methods of synthesis of other single-digit ND particles are provided in the next sections.

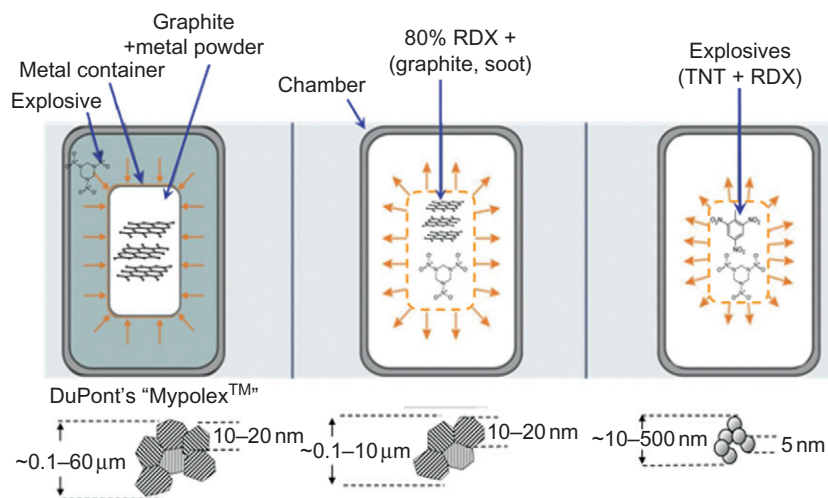
Higher diamondoids (Figure 5.2) are highly rigid, well-defined hydrogen-terminated diamond species [42,45,46]. With more than three crystal diamond cages,

**FIGURE 5.3**

Summary of types of commercial NDs.

higher diamondoids are intermediate in size to the adamantane molecule, the smallest species of H-terminated cubic diamond containing only 10 carbon atoms, and ultrananocrystalline diamond particles with sizes more than 3 nm as described above. Higher diamondoids are extracted from petroleum as diamond molecules in the form of nanometer-sized rods, helices, disks, pyramids, etc. [42,46]. So far it has not been possible to synthesize higher diamondoids except anti-tetramantane, a tetramantane isomer [45]. By comparison, lower diamondoids (adamantane, diadamantane, and triadamantane), extracted from crude oil much earlier than larger members of the diamondoid series, are currently available in kilograms quantities [45] and can be synthesized.

Figure 5.3 summarizes commercially available ND particles based on their method of synthesis. Major classes of commercial ND are of static and dynamic synthesis. ND of static synthesis is one to two orders of magnitude more expensive than ND of dynamic synthesis; this material is a primary material for production of photoluminescent ND particles. ND of static synthesis can be HPHT ND type Ib, with a substitutional nitrogen (N_s) concentration 1–300 ppm. ND produced from natural diamond type Ia (N_s concentration up to 3000 ppm) is also available. High-energy particle irradiation of type Ib ND causes formation of NV centers with red emission, while ND from diamond Ia demonstrates green luminescence originating from formation of N-V-N centers after irradiation and annealing. A large subgroup of ND is produced via dynamic synthesis, harnessing the energy of explosives and different carbon-containing precursor materials. Three classes of dynamically synthesized NDs manufactured on an industrial scale are summarized in Figure 5.4 and are as follows: (i) NDs produced by direct phase transformation of graphite induced by an external shock wave (the DuPont method); (ii) NDs produced from a mixture

**FIGURE 5.4**

Classes of NDs produced by detonation shock-wave-assisted synthesis on an industrial scale.

of a carbon precursor and explosives; and (iii) NDs produced from the carbon contained in high-energy explosives (DND), or UDD.

Depending on the precursor material used in the dynamic synthesis, NDs with primary crystal sizes between 4 and 25 nm can be synthesized. Slurries of 4 nm individual DND particles or slurries of polycrystalline NDs synthesized from graphite and graphite/RDX precursors with average aggregate size of 20–30 nm are commercially available.

While the first publications on laser irradiation of graphite precursors in liquids appeared a decade ago [47], ND produced using a laser became commercially available (in small quantities) only recently (Ray Techniques Ltd). Primary particle size, as reported by the vendor, ranges between 2 and 10 nm. Aggregate size in water suspensions is about 100 nm. At the moment, this type of ND is two orders of magnitude more expensive than detonation ND. Appealing features of the ND produced by laser-assisted synthesis is their high purity and the possibility of varying primary particle size by varying laser radiation parameters.

Sections below provide more details on manufacturing of ND of dynamic synthesis, followed by a brief survey of methods of synthesis of ND particles produced at a laboratory scale.

5.3.1 ND particles produced by detonation shock-wave-assisted synthesis

Below we briefly survey methods of synthesis and characteristics (crystal size, morphology) of the three classes of dynamically synthesized NDs manufactured on an industrial scale (Figure 5.4).

ND produced from carbon and carbon/explosive mixture

Under suitable conditions, explosively produced shock waves can create high pressure ($\sim 20\text{--}200\text{ GPa}$) and high temperature ($>2000\text{ K}$) in confined volumes (Figure 5.4) for a sufficient duration that will result in partial conversion of graphite into nanometer-sized diamond grains ($\sim 20\text{ nm}$); these grains compact into micron-sized, polycrystalline particles. Copper is mixed with graphite in this process to provide fast heat dissipation at the high temperatures reached during the explosion, which will avoid transformation of the diamond back to graphite [18]. It was shown that by mixing graphite with metals, yield of polycrystalline diamond (as a fraction of the mass of graphite) can be increased from 2–2.5% up to 19–20% [21]. Yield of diamond increasing as the thermal conductivity of a metal in the mixture is increased: Pb, Mn, Cu, and Ag [21]. The diamond powder with characteristic sizes of particles in the submicron range can be processed from micron-sized polycrystalline diamond particles obtained by shock synthesis. Polycrystalline diamond particles are more tough than monocrystalline diamond microparticles (natural or produced by HPHT) and are widely used in fine polishing applications. It is important to note that agglomerate-free suspensions of nanocrystalline diamond in water and oil are commercially available (Microdiamant AG, Lengwil, Switzerland).

NDs produced by another dynamic method, detonation of a mixture of a carbon precursor (graphite or carbon black) and explosives, is much less known in the community. Tatsii [44] recently summarized the data on the production of DALAN ND from three types of precursors: mixture of RDX and carbon black (charge density $1.34\text{--}1.39\text{ g/cm}^3$), RDX and graphite (charge density $1.61\text{--}1.67\text{ g/cm}^3$), and gunpowder/carbon/RDX (charge density $1.67\text{--}1.75\text{ g/cm}^3$). The concentration of carbon precursor materials can be varied between 5% and 35%. The detonation pressure measured by dynamic methods (in the Chapman–Jouguet plane) was about $27.5\text{--}14.5\text{ GPa}$. It was concluded that the diamond powders synthesized from graphite consists of $1\text{--}3\text{ }\mu\text{m}$ particles of lamellar shape with different phase compositions (diamond, lonsdaleite, graphite) and different grain sizes. The particles of diamond powder synthesized from carbon black are aggregates consisting of $20\text{--}80\text{ nm}$ grains of cubic phase diamond exhibiting either a round or polyhedral shape. The particles of diamond extracted from the solid DPs of the gunpowder/carbon black/RDX mixture are single-phase particles having a homogeneous grain structure with a grain size of mainly $1\text{--}3\text{ nm}$. These smaller grains form spherule-shaped aggregates. These findings demonstrate the key role of the carbon precursor material in the phase composition and the primary particle size of the resulting products. Currently, polycrystalline diamond produced from graphite/RDX mixture is a valuable commercial product for polishing applications. While micron-sized particles ($1\text{--}10\text{ }\mu\text{m}$) with narrow size distribution are of most demand, the fractions of polycrystalline diamond with sub- 100 nm particle sizes are also utilized.

ND produced from high-energy explosives

An in-depth elaboration of the mechanism of detonation ND synthesis was provided by Danilenko in several recent publications [23,48,49]. The approach is based

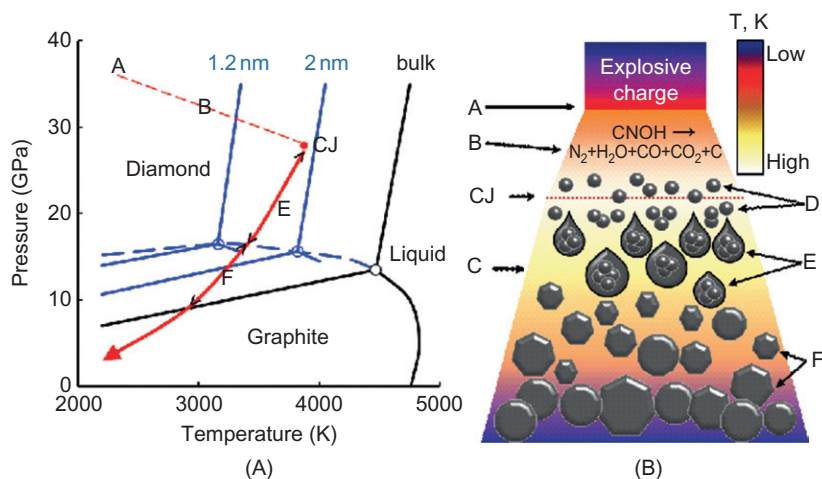


FIGURE 5.5

Detonation synthesis of ND. (A) The phase diagrams for bulk and nanoscale (blue lines) carbon. Red lines demonstrate a pressure–temperature trajectory in a detonation wave during synthesis of DND (for the composition B, RDX/TNT 64/36%). (B) Schematic of the detonation wave propagation showing zone A, the front of the shock wave caused by the explosion; zone B, the zone of chemical reaction; CJ, the Chapman–Jouguet plane; zone C, the expanding DPs; D, the formation of carbon nanoclusters; E, the coagulation into liquid nanodroplets; and F, the crystallization, growth, and agglomeration of NDs.

Source: The figures are adapted from Ref. [40] with permission.

on the analysis of the *nanocarbon* phase diagram in combination with detonation parameters for high-energy explosives. At the nanoscale, the carbon phase diagram must also include cluster size as a third parameter (in addition to pressure and temperature) because the Gibbs free energy depends on the surface energy, which leads to changes in the phase diagram [48–50] (Figure 5.5A). The region of liquid carbon is shifted to lower temperatures for nanocarbon and the region of ND stability is slightly shifted to higher pressures (Figure 5.5A). Viecelli et al. [50] report that including small carbon particle surface energies in hydrocarbon Hugoniot calculations provide better agreement with shock experiments. The results also suggest that carbon particles, of the order of 10^3 – 10^4 atoms, can exist in the liquid state at lower temperatures than bulk carbon [48–50] (Figure 5.5A).

The mechanism of DND formation is as follows [48,49]. The initial shock wave created by a detonator compresses the high-explosive material, heating it and causing chemical decomposition, thereby releasing enormous amounts of energy in a fraction of a microsecond. The detonation wave includes (Figure 5.5B) the front of the shock wave caused by the explosion (plane A in Figure 5.5B and point A in

Figure 5.5A); a zone of detonation-induced decomposition of explosive molecules (a zone of chemical reaction, zone B); the Chapman–Jouguet (CJ) plane (where P and T correspond to point CJ in Figure 5.5, indicating the conditions when reaction and energy release are essentially complete); and a zone of expanding DPs (zone C). The zones of chemical reaction and expanding DPs are shown for the so-called composition B explosive at the corresponding phase diagram (Figure 5.5A, red lines). Decomposition of explosive molecules with the formation of free carbon (for an explosive with a negative oxygen balance) schematically proceeds according to the formula



It can be seen in Figure 5.5A that P–T values in the CJ point do not reach a region of liquid carbon for a bulk carbon phase diagram, while conditions for the existence of liquid carbon can be achieved on the phase diagram for nanoscale carbon. Importantly, the CJ point of several powerful explosives is located in the region of liquid carbon in the nanocarbon phase diagrams, as confirmed by calculations of two different groups [48–51]. Pressures at temperatures at the CJ point are not high enough to produce liquid bulk carbon, but they are high enough to produce liquid carbon at the nanoscale. Thus, it is suggested that ND is formed by homogeneous nucleation in the volume of the supersaturated carbon vapor via condensation and crystallization of liquid carbon (Figure 5.5B). First, after decomposition of the explosive molecules (during ~ 1 ns), primary carbon clusters (< 2 nm in size) are formed in the zone of a chemical reaction (during ~ 10 ns) (zone D, Figure 5.5B), followed by their coagulation into carbon droplets > 2 nm in size along the isentrope of expanding DPs above 16.5 GPa (this stage lasts $\sim 10^2$ – 10^3 ns) (zone E in Figure 5.5A and B). Finally, ND particles are formed by crystallization of the liquid carbon droplets along the isentrope of expanding DPs in the region 9–16.5 GPa (zone F in Figure 5.5A (outlined by arrows) and Figure 5.5B). Duration of this stage is longer than 10^3 ns. When the pressure drops below the diamond–graphite equilibrium line (at pressure ~ 9 GPa), the growth of diamond is replaced by the formation of graphite.

From a practical viewpoint, the conversion of the carbon-containing explosive compounds into diamond occurs by firing the explosives in a detonation chamber of typical volume 2 – 5 m³ (for 0.1 – 1 kg charges) [23,52]. The resultant product is a mixture of diamond particles with a primary particle size of 4 – 5 nm, other carbon allotropes, and metallic impurities. A wide variety of explosive materials may be used. A typical explosive mixture is TNT (2-methyl-1,3,5-trinitrobenzene) and RDX (1,3,5-trinitroperhydro-1,3,5-triazine) in the proportion from 40% to 60% of TNT. The explosion takes place in an inert medium of either gas (N_2 , CO_2 , Ar, or other gases) or water (ice), called “dry” or “wet” synthesis, respectively. The medium acts as a coolant.

The product of detonation synthesis, called detonation soot or diamond blend, contains 40–80 wt% diamond phase depending on the detonation conditions [23,52]. The carbon yield is 4–10% of the weight of the explosive charge, depending on the cooling media where 10% correspond to the wet synthesis.

Further details on the synthesis of DND can be found in books [23,24,53,54], and reviews [52–59]. Recently, DND synthesis was revisited by several groups with a purpose to address new demands to this material. Major focuses for novel approaches for DND synthesis are as follows:

1. Further reduction of the primary particle size
2. Control of the level of aggregation of DND at the stage of synthesis
3. Increased sp^3 carbon content in detonation soot (in terms of reduction of non-carbon elements and sp^2 carbon on DND particle surfaces)
4. Doping of DND during synthesis, including control of the amount of substitutional nitrogen in the diamond core

Reducing the DND primary particle size down to the range of 1–3 nm may further increase their capability for penetrating cells and organelle membranes including nucleus pores. ND particles with sizes ~ 2 nm and smaller show quantum confinement effects [60]. Thus, synthesis of small particles would open perspectives for the development of diamond quantum dots. An increase of the ND-specific surface area to a level, compared to that for carbon nanotubes, would bring ND to the stage of perspective materials for hydrogen storage, catalyst support, fuel cells, and other applications.

In principle, the X-ray diffraction (XRD) data on the size distribution of primary DND particles within detonation soot, which were reported in a limited number of publications [23,61], include 2 nm peaks. It was reported by Dolmatov [61] that his novel method of using reducing agents (e.g., urea, ammonia) in water cooling media allows the preservation of the DND fraction with a primary particle size less than 3 nm along with a “typical” fraction of 5 nm primary particles. In general, production of several classes of DND with average primary particle sizes from the 2 to 10 nm size range (e.g., classes with 2–3, 4–5, and 10 nm average sizes) would be beneficial for various applications.

Also, a method reported by Dolmatov [61] of using reducing agents provides the benefits of increased DND yield from soot (by 2–5 wt%) as well as overall yield of soot itself (by 100%) as well as an increased carbon content (up to 96 mass%) within DND particle composition, where the total content of C, H, N, and O corresponds to 100 mass%. A possible mechanism of action of the reducing agents in the cooling media is as follows. In the presence of reducing agents, the oxidants (the DPs CO_2 , H_2O , O_2 , NO_2 , N_2O_3) interact primarily with the reducing agents, instead of oxidizing the carbon and particularly DND. This increases the yield of detonation soot and DND and quantitatively changes their elemental composition, including carbon. Besides, the presence of readily oxidizable reducing agents among the DPs helps to reduce graphitization of DND. It is also reported that the smallest amount of incombustible impurities (0.1–0.3 wt%) was found in the DND synthesized in the presence of urotropine. This is due to the fact that urotropine is a strong complexing agent and captures impurities (metals Fe, Ni, Cr, Cu, Ti, etc.) to form soluble complexes that are easy to remove by subsequent chemical purification, i.e., treatment with nitric acid.

Another question is related to the possibility of optimizing the detonation process to produce mostly isolated primary particles and only small size aggregates in the detonation soot. This would significantly reduce the cost of the final DND product. In fact, it has been recognized that the dry DND synthesis results in smaller primary DND particle sizes and smaller average aggregate sizes as compared to wet synthesis. Other factors that influence the aggregation of DNDs during synthesis are the mass of the charge and the ratio between the mass of the charge and wet cooling media used [62].

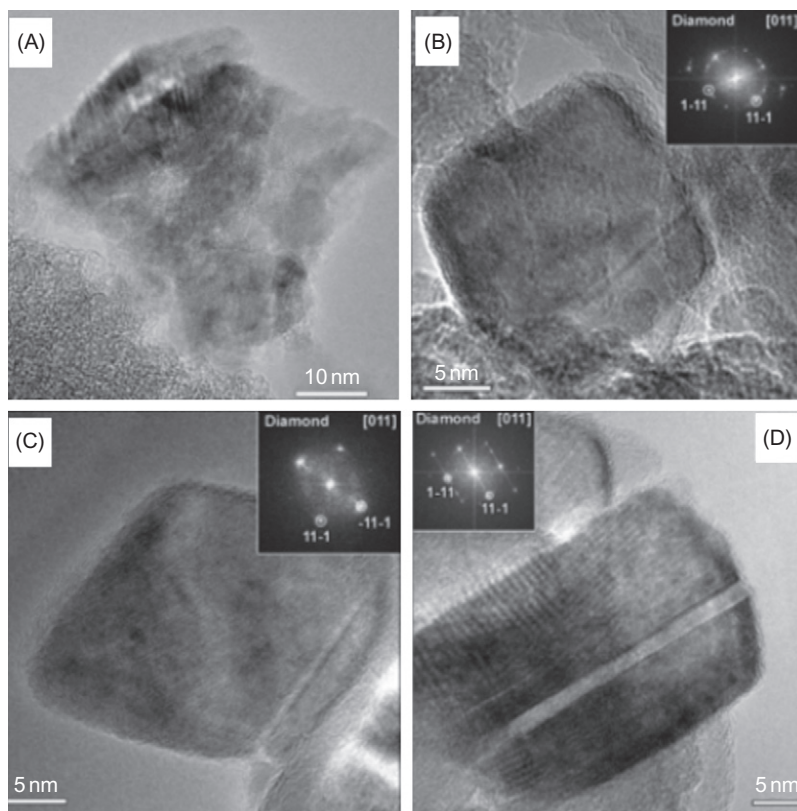
Tailoring of DND electronic and optical properties for specific applications can possibly be done at the stage of synthesis by development of different combinations of explosive materials with possible solid dopants, as well as using the nontraditional cooling media (both gaseous and liquid) with possible additives to alter DND composition (both bulk defects/doping content and surface groups). The possibility to control N content by a proper choice of the precursor material [63] is discussed in the next section. Of particular importance would be synthesis of boron-doped NDs, which are conducting and therefore can be used in electroanalysis, electrochemical double-layer capacitors, and batteries [64,65].

Finally, high cost of DND material is one of the major restricting factors for its commercialization. As was shown by Danilenko [66], use of the current pilot-scale small charge detonation chambers is not profitable and a new industrial-level approach utilizing larger charges is required.

Structure of different types of dynamically synthesized NDs

Recently, Shenderova et al. [63] carried out a thorough comparative analysis of the structure and composition of ND of dynamic synthesis produced by the three major methods described above. Polycrystalline diamond from Microdiamant (produced by shock-wave conversion of graphite) and from Real-Dzerzhinsk (obtained from a graphite/RDX mixture), as well as detonation ND synthesized from different explosives, was studied. Aggregates with sizes below 100 nm were chosen for the investigation. The phase composition and size distribution of the ND crystallites in the ND powders were analyzed by X-ray diffraction and small-angle X-ray scattering (SAXS). For all samples the diamond phase in the XRD patterns dominated. However, the presence of various amounts of graphitic carbon was also observed (peak at $\sim 26.9^\circ$), most pronounced in ND from Microdiamant. The diamond 111 diffraction peak was nonsymmetric due to overlap of the diamond 111 and graphite 101 peaks. The dimensions of the diamond crystallites were estimated from the Debye–Scherrer formula and were ~ 13.6 nm for the 111 reflection and 9.6 nm for the 110 peak for the ND produced from graphite/RDX; 8 nm for the ND obtained from graphite; and 4 nm for DNDs produced from explosives. A very rough estimation of the possible lonsdaleite grain size in the Microdiamant's ND gives ~ 2.4 nm.

For all samples, the crystal size of the dominant fraction determined by SAXS was larger than the size determined from the broadening of the Bragg peaks. The discrepancy in the crystal size determined by both techniques reflects the fact that diamond particles consist of several crystallites within a single grain.

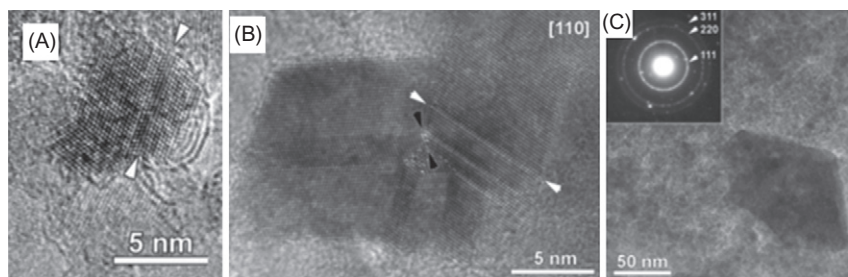
**FIGURE 5.6**

HRTEM images of ND synthesized by (A) shock compression of graphite and (B–D) by detonation of graphite/RDX mixture.

Source: Courtesy of S. Turner, University of Antwerp, Antwerp, Belgium.

The SAXS data for the ND sample from graphite showed a bimodal size distribution of the particles with peaks (diameters) at ~ 6 nm (possibly graphite or lonsdaleite) and at ~ 23 nm. The size distribution for the ND from the graphite/RDX mixture possessed a relatively broad size distribution centered at ~ 34 nm. The size distribution of the NDs produced from explosives (TNT/RDX and TNT/HNS) was typical for DNDs: the main peak shows diameters around 6 nm and a broad tail stretching out to larger sizes.

Figure 5.6 shows high-resolution transmission electron microscope (HRTEM) images of the different ND samples. ND produced from graphite contained only abundant, large, rounded, or elongated diamond particles without a clear morphology (Figure 5.6A). These structures often consist of agglomerates of smaller particles and show the presence of large amounts of defects in the diamond lattice. These particles can also be found in ND produced from a graphite/RDX mixture,

**FIGURE 5.7**

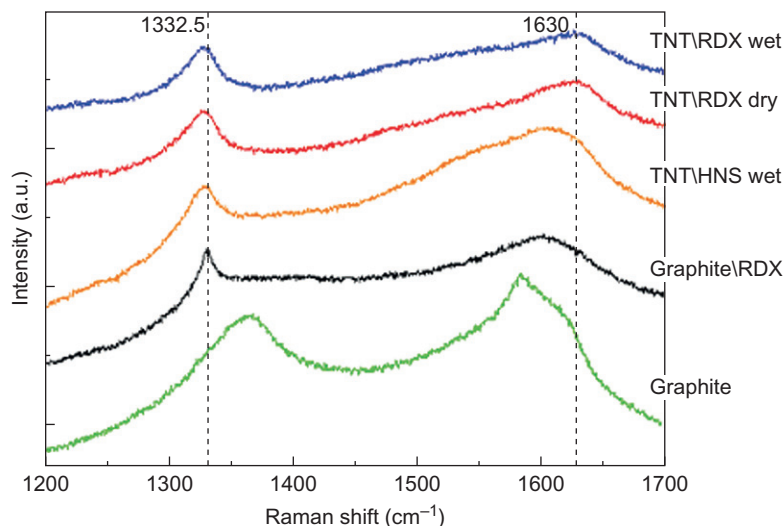
HRTEM images of ND synthesized by detonation of TNT/RDX explosives. (A) The main fraction of DND particles has a particle size close to 6 nm. Twinning is frequently observed in these small particles, with all visible twinning occurring along a (111) twin plane (examples of twin planes are indicated by white arrows in (A) and (B)). (B) Larger, multiple-twinned ND particle. An incoherent region is indicated by black arrows. (C) A rarely observed 100 nm octahedral particle. The inset electron diffraction ring pattern is typical for all DND samples and clearly evidences the cubic diamond crystal structure of all of the nanoparticles.

Source: Courtesy of S. Turner, University of Antwerp, Antwerp, Belgium.

but in combination with rounded or well-faceted polyhedral and truncated octahedral particles with low-index facets (Figure 5.6B–D). The smaller DND particles below 6 nm in diameter show mainly (111) and (100) facets typical for small DND particles (Figure 5.7A); larger particles also show higher index facets (Figure 5.7B). These particles show the presence of coherent $\Sigma = 3$ (111) twinning, common for detonation ND. Large, multiple-twinned particles with diameters up to 100 nm can be found occasionally in DND samples (Figure 5.7C).

Raman spectra of the samples are demonstrated in Figure 5.8. Typically, the first-order Raman spectrum of highly purified DND consists of two peaks. The first one is located in the vicinity of 1332.5 cm^{-1} and corresponds to the vibrational mode of a diamond lattice from the center of its Brillouin zone. The origin of the second one observed at 1630 cm^{-1} is still a subject of debate. When an abundance of sp^2 -bonded carbon clusters is present in ND, another two peaks characteristic for sp^2 carbon appear between 1350 and 1380 cm^{-1} (the D-band) and 1580 – 1610 cm^{-1} (the G-band). The G- and D-band, obscuring the diamond peak in the ND produced from graphite, indicate a high content of sp^2 -bonded carbon in this sample. Large primary particles of the ND produced from graphite/RDX are not influenced by the phonon confinement effect and the diamond line position is actually not shifted from the 1332.5 cm^{-1} position characteristic for the bulk material. All samples of detonation-type synthesis demonstrate a shift in the diamond Raman line down to 1328.5 cm^{-1} which is explained by the phonon confinement effect observed for small nanocrystals [67].

Besides the morphological characteristics, of particular interest is the investigation of the effect of the type of synthesis on N content, N location in the ND core, and its ability to form optically active centers through the creation of complexes

**FIGURE 5.8**

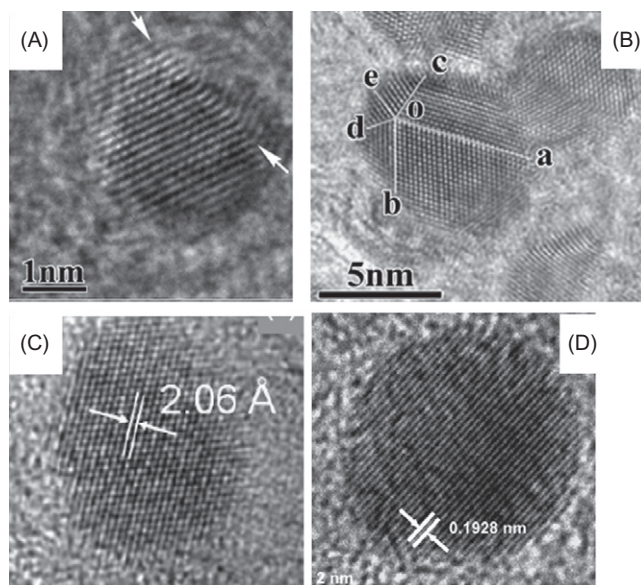
Raman spectra of the dynamically synthesized ND samples.

Source: Figure courtesy of I. Vlasov, General Institute of Physics, Moscow.

with vacancies [63]. In ND synthesis using explosives, N is an integral part of the high-energy explosive compounds. It can also be present as an impurity or an on-purpose dopant in graphite (or other carbon-containing materials) in the methods of the dynamic synthesis involving bulk carbon precursors for ND production. The nitrogen content in the ND samples measured using combustion analysis indicated that the N concentration in the ND produced from a mixture of TNT/RDX explosives is higher than 2–2.5 wt%, from TNT/HNS lower than 1% and in ND from graphite and graphite/RDX mixture—lower than 0.5%. Thus, variations in the type of explosives can provide variation in the N content in the final ND product. It is possible that the NN units of RDX molecule contribute to enhanced N aggregation in the ND core, if they are not completely destroyed during detonation and are incorporated into the ND core as neighboring nitrogen atoms. Substituting RDX with HNS significantly reduces the N content [63]. These issues require further study. On the contrary, Pichot et al. [68] demonstrated that the incorporation of melamine leads to a further increase by a factor of two or three in the nitrogen content in the DND core. Thus, variations in the types of explosives can be used together with the addition of other carbon precursor materials (for example, a combination of graphite and HNS) to achieve the desired N content.

5.3.2 NDs from HPHT diamond

As was discussed above, monocrystalline ND particles processed from HPHT synthetic diamond as well as from natural diamond powders are commercially available

**FIGURE 5.9**

HRTEM images of NDs synthesized by different methods: (A) a single crystal structure; (B) multiple-twinning structure produced by pulsed-laser irradiation [70]; (C) a spherical HPHT ND particle obtained by high-energy ball milling [3]; and (D) a spherical diamond in a carbide matrix synthesized by carbide chlorination process [6].

Source: Figures are reproduced with permission.

with the smallest average particle size around 20 nm (produced, for example, by Microdiamant AG) [69]. The shape of diamond nanoparticles obtained by ball milling of micron-sized HPHT or natural diamond particles typically have sharp edges and look in HRTEM-like shattered glass particles. Remarkably, ND particles with rounded shapes and particle sizes below 10 nm were recently obtained by a group of researches starting with HPHT diamond (Figure 5.9C) [3]. The reported method is an important breakthrough in the production of single-digit ND containing NV centers, as it was demonstrated by the authors through processing of Ib-type diamond. The initial raw material was a highly crystalline synthetic micron diamond powder (from Element Six) containing 80–100 mesh (150–190 μm) blocky, very uniformly shaped cubooctahedral diamond crystals. The first step included nitrogen jet milling micronization resulting in a powder with 97% of particles having sizes below 2 μm . Then an aliquot was ball milled under argon using a planetary ball mill (Vario-Planetary Mill, Pulverisette 4, Fritsch, Germany), with 10 mm balls made of WC–Co cemented carbide for 24 h of effective grinding time. NDs appear as deformed polygons with a quasispherical shape and an aspect ratio varying from 1.13 to 1.75. The overall yield of this method is about 15 wt% of the microdiamond mass converted into sub-10 nm diamond nanoparticles. The authors attribute the success of the

production of the quasispherical particles to complex loading regimes of the Vario-Planetary Mill as compared to regular planetary mills [71].

While a particular class of NDs is obtained as a commercial by-product of HPHT synthesis, there are laboratory studies of HPHT conversion of exotic carbon forms to ND. The HPHT process requires ~ 6 GPa pressure and 1500°C to convert graphite powder into diamond in the presence of a catalyst. The use of exotic precursor materials such as fullerenes [72] as well as carbon nanotubes [73] allows much lower temperatures and externally applied pressures as compared to the use of graphite in order to synthesize diamond. For example, the transformation of buckyballs to diamond at high static pressure can be done at room temperature and does not require a catalyst at all [72]. Another group of authors reported the conversion of fullerenes to diamond under “moderate” conditions 5.0–5.5 GPa and 1400°C [74]. Carbon nanotubes have been converted to diamond at 4.5 GPa and 1300°C using NiMnCo catalyst [73]. Based upon HRTEM observations, the authors suggest that under HPHT conditions the tubular structures collapse and broken graphitic shells curl up and close into spheroidal networks to eliminate the dangling bonds at the edges.

Multiwalled carbon nanotubes (MWNT) were heated by a laser in a diamond anvil cell to above 17 GPa and 2500 K [75]. The recovered product consisted of nanosized octahedral crystals (diamond) of less than 50 nm. The tubular structure completely changed to granular and the grain sizes corresponded to the diameter of the nanotubes. The grain size of the diamond suggests that the transformation took place by direct conversion of nanotubes, which might provide a means to control diamond size by the choice of the MWNT size.

An interesting implementation of HPHT treatment was reported by Soltamova et al. [76]. Sintering experiments were carried out on detonation ND with average particle sizes 4.5 nm at temperatures 1500 – 1700°C and pressure 6–7 GPa. According to the results of the XRD, the average size of the primary particles became 8.5 nm after sintering. When the sintering temperature is above 800°C vacancies start to diffuse. The presence of a significant amount of NV centers was detected in 10 micron aggregates using pulsed EPR. Formation of the NV centers can be possibly attributed to the combination of elimination of surface paramagnetic centers and for vacancy diffusion from the high temperature of the process.

5.3.3 Laser-assisted synthesis of ND

Generation of nanoparticles by laser ablation in liquids is a relatively new approach that has been actively explored during the last decade [77]. It has a number of important advantages over conventional multistep chemical synthesis methods that introduce contamination from the intermediate reactants and/or produce agglomerated structures with degraded functionality. The direct laser ablation eliminates the need for chemical precursors and enables generation of “clean” nanoparticles. Due to the highly nonequilibrium nature of laser ablation process, the structure and composition of nanoparticles produced in laser ablation can be very far from the equilibrium ones, opening an exciting range of opportunities for generation of novel nanostructures with unique properties.

The first studies on the formation of ND by pulsed-laser ablation (PLA) using a nanosecond laser irradiation focused on the surface of a graphite target immersed in benzene were reported by Ogale et al. [78] in 1992. Later, in 1998, Polo et al. [79] demonstrated formation of ND by laser ablation of graphite in a hydrogen atmosphere, in a liquid-free environment. However, ablation of graphite immersed in different liquids is more effective and the most popular approach [2,70,80–86]. Yang et al. [80] demonstrated synthesis of nanocrystalline diamond from graphite in combination with water as a liquid media, and later in combination with acetone [82]. The authors reported the presence of both cubic and hexagonal phases of diamond [80–82]. Later, same authors detected the presence of hydrogen in the ablation plume [77] and concluded that hydrogen is necessary for ND formation. Piers et al. [86] obtained similar diamond structures using water and cyclohexane as liquid media. Jiang et al. used a low-power laser with 1.2 μ s pulses and produced individual (not agglomerated) ND particles only 3–6 nm in size [70,83] (Figure 5.9A). HRTEM studies demonstrated that ND contained large number of twins (Figure 5.9B) [70]. Based on thermodynamic calculations, the authors concluded that twinning is energetically favorable for ND stability in a certain size range of ND particles. One more interesting observation was high luminescence of synthesized NDs terminated with polyethylene glycol molecules.

It is possible that the diamond phase can be obtained by PLA without using a graphite precursor [84]. The authors used an iron substrate (as a catalyst) immersed in a hydrocarbon liquid (source of carbon) irradiated with femtosecond laser. As a result, a mixture of cubic and hexagonal diamond species on iron nanoparticles was produced.

The above references indicate that a wide variety of experimental conditions (laser parameters, target, type of liquid) are favorable for ND formation by PLA. The mechanism of ND formation by PLA can be explained as follows [85]. The sequence of processes in pulse laser ablation is likely to include an explosive decomposition of the overheated surface region of the absorbing target, ejection of clusters, and vapor into the surrounding liquid, mixing of the ejected ablation plume with the liquid and bringing the liquid to boiling or supercritical states and bubbles formation. The bubbles collapse, which results in nucleation, growth, and solidification of the nanoparticles under conditions of fast quenching. The formation of a diamond phase is attributed to the extreme temperature/pressure conditions created by collapse of the bubbles. During collapse of the cavitation bubbles, the temperature can reach more than a thousand degrees, while the pressure can reach several gigapascals [86]. The final size, structure, and composition of the produced nanoparticles are defined by the heat and mass transfer occurring under highly nonequilibrium, quickly evolving conditions that are poorly understood at this time.

5.3.4 Cavitation-assisted synthesis of ND

Temperatures and pressures required for synthesis of diamond material can be achieved by different means, including ultrasound cavitation as a result of the rapid collapse of cavitation bubbles generated in a suitable liquid medium. Depending

upon the cavitation conditions, the pressure and temperature inside the cavity at the moment of collapse may reach extremely high instantaneous values of $\sim 10^5$ – 10^6 bar and 1000 K, correspondingly [87]. Galimov hypothesized in 1973 that natural diamond can be formed in kimberlitic pipes as a result of magma cavitation [88]. Cavitation occurs in fluids containing gases and kimberlitic magma is known to be saturated with carbon dioxide. Kimberlitic pipes have different cross sections, where pressure can be abruptly decreased and cavitation bubbles formed. This idea of cavitation-assisted diamond synthesis recently was reduced to practice by Galimov et al. [9]. The system for creation of hydrodynamic cavitation bubbles was based on the so-called Venturi tube (a tube consisting of sections with different diameters) connecting two reservoirs and a series of shock waves produced in the system. The first shock wave is produced in a reservoir connected with the narrow side of the Venturi tube, so that bubbles are formed in the wider side of the Venturi tube and collected in the adjusting reservoir. Then, another shock wave is formed in the reservoir containing the formed bubbles for the efficient bubbles implosion. Benzene is used as a source of carbon and the cavitation media. Cavitation destruction of benzene results in production of particles consisting of aggregates of nanocrystallites 10–30 nm in size. Besides diamond and graphite electron diffraction patterns, the samples contained unidentified lines. Later, a group of researchers from the same research center (Vernadsky Institute of Geochemistry and Analytical Chemistry, Moscow) concluded that the product of synthesis also contains n-diamond [89,90]. New diamond (n-diamond) was proposed as a new carbon allotrope in 1991 by Hirai and Kondo [91], who developed a procedure involving rapid cooling during the shock compression of graphite sheets. n-diamond's electron diffraction pattern matches that of cubic diamond (space group $Fd\bar{3}m$) apart from additional reflections that are forbidden for diamond, indexed as {200}, {222}, and {420}. Based on the electron diffraction data, it was suggested that n-diamond has a face-centered cubic (fcc) structure with space group $Fm\bar{3}m$ and lattice parameter 0.357 nm, however, first principle calculations led to controversy about the stability of fcc carbon [92]. One of the recent models of n-diamond suggests that it is a hydrogen-doped diamond [93]. Thus, at the present, the structure of n-diamond is not unambiguously resolved, and some controversies still exist [92].

Khachatryan et al. [94] reported the formation of monocrystalline micron-sized diamond particles using a combination of two ultrasonic horns aligned toward each other. Micron-sized diamond crystals (5–10 μm) were produced by this ultrasonic cavitation synthesis method from a suspension of powdered graphite (100–200 μm) in an organic liquid. The major factor influencing the diamond yield in the cavitation process was the composition of the cavitation medium. The diamond yield was about 10% of the initial graphite weight. As cavitation fluids, a series of aromatic C–H–O oligomers with low saturated vapor pressure and high boiling temperatures were used.

5.3.5 ND particles synthesis based upon the CVD technique

Frenklach and coworkers [95] studied the nucleation and growth of ND powder directly from the vapor phase in a substrate-free low-pressure microwave-plasma

CVD reactor. The particles were collected downstream of the reaction zone on a filter within the tubular flow reactor and were subjected to wet oxidation to remove nondiamond carbon. The homogeneous diamond nucleation took place when the dichloromethane- and trichloroethylene-oxygen mixtures were used as source material. The particles formed had crystalline shapes with an average particle size around 50 nm. A mixture of diamond polytypes were observed in the powder.

Frenklach et al. [4] also studied the effects of heteroatom addition on the nucleation of solid carbon in a low-pressure plasma reactor. The addition of diborane (B_2H_6) resulted in substantial production of diamond particles, 5–450 nm in diameter, under the same conditions that show no diamond formation without the presence of diborane. The observed yield of the oxidation-resistant powder produced in boron-containing mixtures reached 1.3 mg/h. It was found that NDs in the CVD residue have an abundance of linear twins and star-twin microstructures consistent with radial (isotropic) gas phase growth conditions. Studies of diamond nucleation directly from an activated gas phase have important implications in revealing mechanisms of interstellar dust formation.

Another example of homogeneous diamond nucleation in the gas phase is laser-induced decomposition of C_2H_4 at low pressures and temperatures that result in diamond powder formation with grain diameters of 6 nm to 18 μm [96]. According to the authors, the high purity homogeneously nucleated diamond nanoparticles had spherical and faceted morphology.

Ting et al. [97] developed a method of ND particle synthesis with 25–50 nm diameters using a microwave-plasma torch system operating at near atmospheric pressure. Gas mixtures of CH_4 with Ar or N_2 were used for ND particles synthesis, with Ar or N_2 serving as catalysts. The larger flow rate of Ar and N_2 or the greater pressure in the reaction chamber produced larger nanoparticles.

The CVD technique was recently used for the production of electrically conductive ND in particulate form by CVD growth of boron-doped ND films around a dielectric core of diamond nanoparticles [64]. Production of electroconductive boron-doped ND particles can be very beneficial and can find broad applications in high surface area carbon electrode materials in electroanalysis, electrochemical double-layer capacitors, storage materials for batteries, as a possible electrocatalyst support material for fuel cells, stationary support for liquid chromatography, and other applications.

5.3.6 Methods using irradiation with high energetic particles

Another group of methods of ND formation include direct transformation of carbon solids to ND. Recent experiments have shown that heavy ion or electron irradiation induces the nucleation of diamond crystallites inside concentric nested carbon fullerenes [8,98]. High-energy electron irradiation (1.2 MeV, $>10^{24} e/cm^2$; ~ 100 dpa) was successfully used to convert the cores of concentric-shell graphitic onions into nanometer-sized diamonds at irradiation temperatures above 900 K [8]. These experiments were performed *in situ* in an electron microscope, which allowed continuous observation of the formation process. A strong compression in the interior of the

onion was inferred by the observed reduction in the spacing between adjacent concentric shells during irradiation. Ion beam irradiation of carbon solids also resulted in formation of ND [98]. Irradiation with Ne⁺ (3 MeV, $4 \times 10^{19} \text{ cm}^{-2}$; $\sim 600 \text{ dpa}$) at temperatures between 700°C and 1100°C converted graphitic carbon soot into nanometer-sized diamonds [98]. Again the diamonds were found to nucleate in the cores of graphitic onions that developed under irradiation. The increased diamond yield as compared to e-beam irradiation is explained by the higher displacement cross section, the higher energy transfer, and the higher total beam current on the specimen. Other carbon materials can also be transformed to ND by using a MeV electron or ion beams. ND nucleation occurs inside graphite under ion irradiation at ambient temperature when implanted with Kr⁺ ions (350 MeV, $6 \times 10^{12} \text{ cm}^{-2}$) [7]. The residue of the ion-irradiated graphite was found to contain NDs with an average diameter of 7.5 nm. Another example of ND formation includes irradiation of highly oriented pyrolytic graphite surfaces using a highly charged ion (HCl) [99].

5.3.7 Carbide-derived diamond

Selective etching of carbides is an attractive technique for the synthesis of various carbon structures including nanocrystalline diamond [5,6,100]. Carbon produced by extraction of metals from carbides is called carbide-derived carbon [100]. As summarized by Nikitin [100], leaching in supercritical water, high-temperature treatment in halogens, vacuum decomposition, and other methods can be used to remove metals from carbides to produce carbon coatings or bulk and powdered carbon. In principle, chlorination of carbides for the production of carbon-based materials and, particularly, nanoporous carbon, is a relatively mature technology that has been commercialized (see, for example, <http://www.skeletontech.com/>). However, the synthesis of nanocrystalline diamond by this technique [5] is a recent achievement. Particularly, during extraction of silicon from silicon carbide or metal carbide using chlorine-containing gases at ambient pressure and temperatures not exceeding 1000°C [6], nanocrystalline diamond with an average crystallite size of 5 nm was formed (Figure 5.9D). The nanocrystalline diamond formed by this method is usually surrounded by amorphous carbon.

5.3.8 Other recent methods of ND synthesis

New methods of ND synthesis constantly appear and will continue to be invented since carbonaceous materials are a very popular topic of research. In this section, two recent examples are provided. Rud et al. [101] reported a new electric discharge technique for production of a wide range of carbon nanomaterials, including fullerene-like clusters, nanotubes, amorphous carbon and nanosized graphite, and NDs, using the methods of electrical wire explosion of graphite rods and electric breakdown of organic liquids. The phase composition of the carbon nanomaterials could be effectively controlled by variation of the time-energy parameters of the synthesis process and type of the surrounding medium. According to the authors, if the specific energy injected into samples is substantially smaller than the graphite sublimation energy, carbon nanotubes and fullerenes are formed from the fragments

of graphene obtained from explosive fractured graphite. NDs are formed by phase transformation of graphite–liquid–diamond, if the injected specific energy is substantially greater than the graphite sublimation energy. In another approach, West et al. [102] reported a method for producing nanoparticles of n-diamond, p-diamond, and i-carbon, which are diamond-like materials with not well-identified properties and structures [92]. The authors found these structures in the activated carbon produced by carbonizing and/or activating a carbonaceous feedstock while restricting the presence of oxygen during treatment.

5.4 Conclusion and future outlook

Compared to many other nanomaterials, ND produced by detonation of explosives (also called DND) is relatively expensive since it has not experienced scale-up to large volume production. As in any market, price is a factor that influences expansion of the material's use. Even at the current purity and particle size, the demand for DND will increase dramatically with even a factor of two reduction of price. Advances in the methods of separation and fractionation of DND have led to the availability of 50, 20, and 5 nm particle sizes (average agglomerate size) versus typical 200–300 nm agglomerates, which were not readily available even 5 years ago. Production volumes of these smaller size fractions opens up new markets and expands existing ones as the material meets the demand for specific uses. New technologies are providing the means to increase the production of small size fractions in larger volumes. However, the method of production of the initial soot has largely remained the same for the past 30 years. Use of larger detonation charges will significantly increase production of DND [66]. Other methods of ND synthesis, such as laser-assisted synthesis, are intended to be brought up to a large-scale production.

The availability of single-digit ND particles produced by detonation of explosives by Osawa [12] has opened broad perspectives for the application of ND in composites and nanolubricants. Breaking of HPHT diamond to sub-10 nm particles is an important breakthrough for quantum optics and luminescent markers applications. Both approaches (DND deagglomeration and HPHT ND milling) require further development of inexpensive methods of processing to be affordable for large-scale production and applications.

Production of electroconductive (for example, boron-doped) ND particles during their synthesis can be very beneficial and can find broad applications in high surface area carbon electrode materials in electroanalysis and energy storage applications. If inexpensive methods of HPHT ND milling will be developed, grinding of electrically conductive HPHT diamond will also be advantageous.

Acknowledgment

Gary McGuire, International Technology Center, is acknowledged for his valuable comments.

References

- [1] K.V. Volkov, V.V. Danilenko, V.I. Elin, Diamond synthesis from detonation carbon, *Fiz. Goren. Vzryva*. 26 (3) (1990) 123–125.
- [2] G.W. Yang, J.B. Wang, Q.X. Liu, Preparation of nano-crystalline diamonds using pulsed laser induced reactive quenching, *J. Phys. Condens. Matter*. 10 (1998) 7923–7927.
- [3] J.P. Boudou, P. Curmi, F. Jelezko, J. Wrachtrup, P. Aubert, M. Sennour, High yield fabrication of fluorescent nanodiamonds, *Nanotechnology* 20 (2009) 235602.
- [4] M. Frenklach, W. Howard, D. Huang, J. Yuan, K.E. Spear, R. Koba, Induced nucleation of diamond powder, *Appl. Phys. Lett.* 59 (1991) 546–548.
- [5] Y.G. Gogotsi, K.G. Nickel, D. Bahloul-Hourlier, T. Merle-Mejean, G.E. Khomenko, K.P. Skjerlie, Structure of carbon produced by hydrothermal treatment of beta-SiC powder, *J. Mater. Chem.* 6 (1996) 595–604.
- [6] S. Welz, Y. Gogotsi, M.J. McNallan, Nucleation, growth, and graphitization of diamond nanocrystals during chlorination of carbides, *J. Appl. Phys.* 93 (2003) 4207–4214.
- [7] T.L. Daulton, M.A. Kirk, R.S. Lewis, L.E. Rehn, Production of nanodiamonds by high-energy ion irradiation of graphite at room temperature, *Nucl. Instrum. Methods Phys. Res. B* 175 (2001) 12–20.
- [8] F. Banhart, P.M. Ajayan, Carbon onions as nanoscopic pressure cells for diamond formation, *Nature* 382 (1996) 433–435.
- [9] É.M. Galimov, A.M. Kudin, V.N. Skorobogatskii, V.G. Plotnichenko, O.L. Bondarev, B.G. Zarubin, et al., Experimental corroboration of the synthesis of diamond in the cavitation process, *Dokl. Phys.* 49 (2004) 150–153.
- [10] O. Guillois, G. Ledoux, C. Reynaud, Diamond infrared emission bands in circumstellar media, *Astrophys. J.* 521 (1999) L133–L136.
- [11] M. Goto, Th. Henning, A. Kouchi, H. Takami, Y. Hayano, T. Usuda, et al., Spatially resolved 3 μ m spectroscopy of Elias 1: origin of diamonds in protoplanetary disks, *Astrophys. J.* 693 (2009) 610–616.
- [12] E. Osawa, Recent progress and perspectives in single-digit nanodiamond, *Diamond Relat. Mater.* 16 (12) (2007) 2018–2022.
- [13] F. Jelezko, T. Gaebel, I. Popa, A. Gruber, J. Wrachtrup, Observation of coherent oscillations in a single electron spin, *Phys. Rev. Lett.* 92 (7) (2004) 76401–76405.
- [14] G. Balasubramanian, I.Y. Chan, R. Kolesov, M. Al-Hmoud, J. Tisler, C. Shin, et al., Nanoscale imaging magnetometry with diamond spins under ambient conditions, *Nature* 455 (2008) 648–651.
- [15] Y.-R. Chang, H.-Y. Lee, K. Chen, C. Chang, D. Tsai, C. Fu, et al., Mass production and dynamic imaging of fluorescent nanodiamonds, *Nat. Nanotechnol.* 3 (2008) 284–288.
- [16] J.-P. Boudou, P. Curmi, F. Jelezko, J. Wrachtrup, P. Aubert, M. Sennour, et al., High yield fabrication of fluorescent nanodiamonds, *Nanotechnology* 20 (2009) 235602.
- [17] J.A. Chang, Y. Jallouli, A. Barras, N. Dupont, D. Betbeder, Drug delivery to the brain using colloidal carriers, *Prog. Brain Res.* 180 (2009) 3–17.
- [18] G.R. Cowan, N.J. Woodbury, B.W. Dunnington, P. Wood, W. Chester, A. Holtzman, Process for synthesizing diamond, US Patent 3,401,019 (1968).
- [19] P.S. DeCarli, J.C. Jamieson, Formation of diamond by explosive shock, *Science* 133 (346) (1961) 1821.
- [20] V.V. Danilenko, On the discovery of detonation nanodiamond, in: O.A. Shenderova, D.M. Gruen (Eds.), *Ultrananocrystalline Diamond*, William Andrew, Norwich, NY, 2006, pp. 335–344.

- [21] K.V. Volkov, V.V. Danilenko, V.I. Elin, S.E. Sanina, T.P. Timofeeva, K.K. Krupnikov, et al., Synthesis of diamond and dense modifications of boron nitride by dynamic method, *Explosion, Shock, Protection. Inform. Bull. No. 17, Inst. Geofiz. Sib. Otd. Acad. Nauk USSR, Novosibirsk*, 1987.
- [22] B.J. Alder, R.H. Christian, Behavior of strongly shocked carbon, *Phys. Rev. Lett.* 7 (10) (1961) 367.
- [23] V.V. Danilenko, *Explosion. Physics. Technique. Technology*, Energoatomizdat, Moscow (in Russian) 2010.
- [24] A.M. Staver, A.I. Lyamkin, N.A. Gubareva, E.A. Petrov, Ultradisperse diamond powders produced by explosion, *Fiz. Goren. Vzryva.* 20 (5) (1984) 100–103.
- [25] A.I. Lyamkin, E.A. Petrov, A.P. Ershov, G.V. Sakovich, A.M. Staver, V.M. Titov, Production of diamond from explosives, *Dokl. Akad. Nauk* 302 (3) (1988) 611–613.
- [26] V.M. Titov, V.P. Anisichkin, I.Y. Mal'kov, A study of ultradispersed diamond synthesis by detonation waves, *Fiz. Goren. Vzryva.* 25 (3) (1989) 117–126.
- [27] G.I. Savvakín, V.I. Trefilov, N.I. Zaika, Method of manufacturing of ultradispersed diamond and boron nitride powders, Institute for Material Science Problems, Ukraine, Patent SU 845378 (1979) filed 05.10.1979.
- [28] M.V. Vlasova, N.G. Kakazei, G.I. Savvakín, Some properties of ultradispersed diamond obtained by high-temperature explosive synthesis, *Inorg. Mater.* 15 (7) (1979) 1020–1021.
- [29] G.I. Savvakín, V.I. Trefilov, Formation of the structure and properties of ultradispersed diamonds during detonation of condensed carbon-containing explosives with negative oxygen balance in various media, *Lecture Books Acad. Sci. USSR* 321 (1) (1991) 99–103.
- [30] A.M. Staver, A.I. Lyamkin, N.I. Gubareva, E.A. Petrov, Method of diamond synthesis, Patent SU 1165007 (1982), filed 01.07.1982.
- [31] N. Roy Greiner, P.S. Philips, J.D. Johnson, Diamond in detonation soot, *Nature* 333 (1988) 6172.
- [32] G.A. Adadurov, A.V. Baluev, O.N. Breusov, et al., Some properties of diamonds produced by an explosive method, *Izv. Akad. Nauk SSSR, Ser. Neorg. Mater.* 13 (4) (1977) 649–653.
- [33] G.A. Adadurov, T.V. Bavina, O.N. Breusov, V. Drobyshch, M. Messinev, A. Rogacheva, et al., Method of producing diamond and/or diamond-like modifications of boron nitride, US Patent 4483836 (1984), from 20.11.1984.
- [34] A.L. Vereshchagin, *Detonation Nanodiamonds*, Altai State Technical University, Barnaul, 2001.
- [35] E.A. Petrov, G.V. Sakovich, P.M. Brylykov, Conditions for preserving diamonds when produced by explosion, *Dokl. Acad. Nauk* 313 (1990) 862.
- [36] A. Vyskubenko, V.V. Danilenko, E.E. Lin, V.A. Mazanov, T.V. Serova, V.I. Suharenko, et al., The influence of scale factors on the size and yield of diamond in detonation synthesis, *Fiz. Goren. Vzryva.* 28 (2) (1992) 108–109.
- [37] V.V. Danilenko, V. Trefilov, V.N. Danilenko, USSR Patent No. SU 181329 A3 (1991), priority 12.06.1991.
- [38] K.V. Kirilin, V.V. Padalko, Diamond powder and method for its production, Priority Patent 38541A Ukraine, MPK7 CO1V 31/06 (2001), 21.07.2001—Publ. 15.05.2001, Byul. No. 4.
- [39] V.V. Danilenko, Shock-wave sintering of nanodiamonds, *Phys. Solid State* 46 (4) (2004) 711–715.
- [40] V.N. Mochalin, O. Shenderova, D. Ho, Y. Gogotsi, The properties and applications of nanodiamonds, *Nat. Nanotechnol.* 7 (1) (2012) 11–23.
- [41] O. Shenderova, G. McGuire, Types of nanocrystalline diamond, in: O. Shenderova, D. Gruen (Eds.), *Ultrananocrystalline Diamond*, William Andrew, 2006, pp. 79–109.

- [42] J.E. Dahl, S.G. Liu, R.M.K. Carlson, Isolation and structure of higher diamondoids, nanometer-sized diamond molecules, *Science* 299 (2003) 96–102.
- [43] E. Osawa, Single-nano buckydiamond particles, in: D. Ho (Ed.), *Nanodiamond. Applications in Biology and Nanoscale Medicine*, Springer, New York/Dordrecht/Heidelberg/London, 2010, pp. 55–79.
- [44] V.F. Tatsii, A.V. Bochko, G.S. Oleinik, Structure and properties of DALAN detonation diamonds, *Combust. Explos. Shock Waves* 45 (1) (2009) 95–103.
- [45] H. Schwertfeger, A.A. Fokin, P.R. Schreiner, Diamonds are a chemist's best friend: diamondoid chemistry beyond adamantane, *Angew. Chem. Int. Ed. Engl.* 47 (2008) 1022–1036.
- [46] R.M.K. Carlson, J.E.P. Dahl, S.G. Liu, Diamond molecules found in petroleum, in: D.M. Gruen, A. Vul, O.A. Shenderova (Eds.), *Synthesis, Properties, and Applications of Ultrananocrystalline Diamond*, Springer, Dordrecht, The Netherlands, 2005.
- [47] G.W. Yang, J.B. Wang, Q.X. Liu, Preparation of nano-crystalline diamonds using pulsed laser induced reactive quenching, *J. Phys. Condens. Matter.* 10 (1998) 7923–7928.
- [48] V.V. Danilenko, Features of carbon condensation in a detonation wave and the conditions for optimal synthesis of nanodiamond, *J. Superhard Mater.* 28 (5) (2006) 7–22.
- [49] V.V. Danilenko, in: D.M. Gruen, O.A. Shenderova, A.Y. Vul (Eds.), *Proceedings of the NATO Advanced Research Workshop on Synthesis, Properties and Applications of Ultrananocrystalline Diamond*, 7–10 June 2004, St. Petersburg, Russia, Springer, Netherlands, 2005, pp. 181–198.
- [50] J.A. Viecelli, S. Bastea, J.N. Glosli, F.H. Ree, Phase transformations of nanometer size carbon particles in shocked hydrocarbons and explosives, *J. Chem. Phys.* 115 (2001) 2730.
- [51] J.A. Viecelli, F.H. Ree, Carbon particle phase transformation kinetics in detonation waves, *J. Appl. Phys.* 88 (2) (2000) 683.
- [52] V.Y. Dolmatov, Detonation nanodiamonds: synthesis, structure, properties and applications, *Usp. Khim.* 76 (4) (2007) 375–397.
- [53] V.Y. Dolmatov, *Detonation Nanodiamonds*, St. Petersburg: Publisher SPbSPU, 2003 (in Russian).
- [54] O.A. Shenderova, D.M. Gruen (Eds.), *Ultrananocrystalline Diamond*, William Andrew, Norwich, NY, 2006.
- [55] O.A. Shenderova, V.V. Zhirnov, D.W. Brenner, Carbon nanostructures, *Crit. Rev. Solid State* 27 (2002) 227–356.
- [56] K.B. Holt, Diamond at the nanoscale: applications of diamond nanoparticles from cellular biomarkers to quantum computing, *Philos. Transact. A Math. Phys. Eng. Sci.* 365 (2007) 2845–2861.
- [57] A. Krueger, Diamond nanoparticles: jewels for chemistry and physics, *Adv. Mater.* 20 (12) (2008) 2445–2449.
- [58] A.M. Schrand, S.A. Hens, O.A. Shenderova, Nanodiamond particles: properties and perspectives for bioapplications, *Crit. Rev. Solid State Mater. Sci.* 34 (1) (2009) 18–74.
- [59] M. Baidakova, A. Vul, New prospects and frontiers of nanodiamond clusters, *J. Phys. D Appl. Phys.* 40 (20) (2007) 6300–6311.
- [60] J.Y. Raty, G. Galli, C. Bostedt, T.W. Van Buuren, L.J. Terminello, Quantum confinement and fullerene-like surface reconstructions in nanodiamonds, *Phys. Rev. Lett.* 90 (2003) 37401.
- [61] G.S. Yur'ev, V.Y. Dolmatov, X-ray diffraction study of detonation nanodiamonds, *J. Superhard Mater.* 32 (5) (2010) 29–50.
- [62] V.V. Danilenko, Assessment of the influence of particle size and degree of cohesion on their thermal stability, *J. Superhard Mater.* 31 (4) (2009) 218–225.

- [63] O. Shenderova, I. Vlasov, S. Turner, G. Van Tendeloo, S. Orlinskii, A. Shiryayev, et al., Nitrogen control in nanodiamond produced by detonation shock-wave-assisted synthesis, *J. Phys. Chem. C* 115 (2011) 14014–14024.
- [64] A. Ay, V.M. Swope, G.M. Swain, The physicochemical and electrochemical properties of 100 and 500 nm diameter diamond powders coated with boron-doped nanocrystalline diamond, *J. Electrochem. Soc.* 155 (10) (2008) B1013–B1022.
- [65] A. Cunci, C. Cabrera, Preparation and electrochemistry of boron-doped diamond nanoparticles on glassy carbon electrodes, *Electrochem. Solid State Lett.* 14 (3) (2011) K17–K19.
- [66] V.V. Danilenko, Nanodiamonds: problems and prospects, *J. Superhard. Mater.* 32 (5) (2009) 301–310.
- [67] J.W. Ager, D.K. Veirs, G.M. Rosenblatt, Spatially resolved Raman studies of diamond films grown by chemical vapor deposition, *Phys. Rev. B* 43 (1991) 6491.
- [68] V. Pichot, O. Stephan, M. Comet, E. Fousson, J. Mory, K. March, et al., High nitrogen doping of detonation nanodiamonds, *J. Phys. Chem. C* 114 (2010) 10082–10087.
- [69] Microdiamant AG, Switzerland. <<http://www.microdiamant.com/products/micron-diamond-powders/msy/>>.
- [70] S. Hu, J. Sun, X. Du, F. Tian, L. Jiang, The formation of multiply twinning structure and photoluminescence of well-dispersed nanodiamonds produced by pulsed-laser irradiation, *Diamond Relat. Mater.* 17 (2008) 142–146.
- [71] E. Gaffet, F. Bernard, J. Niepce, F. Charlot, C. Gras, G. Caër, et al., Some recent developments in mechanical activation and mechanosynthesis, *J. Mater. Chem.* 9 (1999) 305–314.
- [72] M. Núñez-Regueiro, P. Monceau, J.-L. Hodeau, Crushing C60 to diamond at room temperature, *Nature* 355 (1992) 237–239.
- [73] L.M. Cao, C.X. Gao, H.P. Sun, G.T. Zou, Z. Zhang, Synthesis of diamond from carbon nanotubes under high pressure and high temperature, *Carbon* 39 (2001) 311–317.
- [74] Y.Z. Ma, G.T. Zou, H.B. Yang, J.F. Meng, Conversion of fullerenes to diamond under high pressure and high temperature, *Appl. Phys. Lett.* 65 (1994) 822–826.
- [75] H. Yusa, Nanocrystalline diamond directly transformed from carbon nanotubes under high pressure, *Diamond Relat. Mater.* 11 (2002) 87–91.
- [76] A.A. Soltamova, I.V. Ilyin, F.M. Shakhov, Electron paramagnetic resonance detection of the giant concentration of nitrogen vacancy defects in sintered detonation nanodiamonds, *JETP Lett.* 92 (2) (2010) 106–110.
- [77] L. Yang, P.W. May, L. Yin, J.A. Smith, K.N. Rosser, Growth of diamond nanocrystals by pulsed laser ablation of graphite in liquid, *Diamond Relat. Mater.* 16 (2007) 725–729.
- [78] S.B. Ogale, A.P. Malshe, A.R.S.M. Kanetkar, S.T. Kshirsagar, Formation of diamond particulate by pulsed ruby irradiation of graphite, *Solid State Commun.* 84 (1992) 371.
- [79] M.C. Polo, J. Cifre, G. Sanchez, R. Aguiar, M. Varela, J. Esteve, Pulsed laser deposition of diamond from graphite targets, *Appl. Phys. Lett.* 67 (1995) 485.
- [80] G.W. Yang, J.-B. Wang, Q.-X. Liu, Preparation of nano-crystalline diamonds using pulsed laser induced reactive quenching, *J. Phys. Condens. Mater.* 10 (1998) 7923–7927.
- [81] G.W. Yang, J.B. Wang, Pulsed-laser-induced transformation path of graphite to diamond via an intermediate rhombohedral graphite, *Appl. Phys. A* 72 (2001) 475–479.
- [82] J.B. Wang, C.Y. Zhang, X.L. Zhong, G.W. Yang, Cubic and hexagonal structures of diamond nanocrystals formed upon pulsed laser induced liquid–solid interfacial reaction, *Chem. Phys. Lett.* 361 (2002) 86–90.
- [83] J. Sun, S.-L. Hu, X.-W. Du, Y.-W. Lei, L. Jiang, Ultrafine diamond synthesized by long-pulse-width laser, *Appl. Phys. Lett.* 89 (2006) 183115.

- [84] A. Hu, J. Sanderson, Y. Zhou, W.W. Duley, Formation of diamond-like carbon by fs laser irradiation of organic liquids, *Diamond Relat. Mater.* 18 (2009) 999–1001.
- [85] S.R.J. Pearce, S.J. Henley, F. Claeysens, P.W. May, K.R. Hallam, J.A. Smith, et al., Production of nanocrystalline diamond by laser ablation at the solid–liquid interface, *Diamond Relat. Mater.* 13 (2004) 661–665.
- [86] S.J. Shaw, W.P. Schiffrers, T.P. Gentry, D.C. Emmony, *J. Phys. D. Appl. Phys.* 32 (1999) 1612.
- [87] C.E. Brennen, *Cavitation and Bubble Dynamics*, Oxford University Press, Oxford, 1995.
- [88] E.M. Galimov, On possibility of natural diamond synthesis under conditions of cavitation, occurring in a fast-moving magmatic melt, *Nature* 243 (1973) 389.
- [89] S. Voropaev, Cavitations synthesis of carbon nanostructures, *J. Phys. Conf. Ser.* 291 (2011) 12028.
- [90] S.A. Voropaev, A.Y. Dnestrovskii, V.N. Skorobogatskii, A.S. Aronin, V.M. Shkinev, O.L. Bondarev, et al., Face-centered cubic carbon synthesis under cavitation compression, *Dokl. Phys.* 56 (9) (2011) 463.
- [91] H. Hirai, K.I. Kondo, Modified phases of diamond under shock compression and rapid quenching, *Science* 253 (1991) 772.
- [92] B. Wen, J.J. Zhao, T.J. Li, Synthesis and crystal structure of n-diamond, *Int. Mater. Rev.* 52 (3) (2007) 131.
- [93] B. Wen, R. Melnik, S. Yao, T. Li, Hydrogen-doped cubic diamond and the crystal structure of n-diamond, *Chem. Phys. Lett.* 516 (2011) 230–232.
- [94] A.K. Khachatryan, S.G. Aloyan, P.W. May, R. Sargsyan, V.A. Khachatryan, V.S. Baghdasaryan, Graphite-to-diamond transformation induced by ultrasonic cavitation, *Diamond Relat. Mater.* 17 (2008) 931–937.
- [95] M. Frenklach, R. Kematich, D. Huang, W. Howard, K.E. Spear, A.W. Phelps, et al., Homogeneous nucleation of diamond powder in the gas phase, *J. Appl. Phys.* 66 (1989) 395–399.
- [96] P.R. Buerki, S. Leutwyler, Homogeneous nucleation of diamond powder by CO₂ laser-driven reactions, *J. Appl. Phys.* 69 (1991) 3739–3745.
- [97] C.C. Ting, T. Young, C.S. Jwo, Fabrication of diamond nanopowder using microwave plasma torch technique, *Int. J. Adv. Manuf. Technol.* 34 (2007) 316–322.
- [98] P. Wesolowski, Y. Lyutovich, F. Banhart, H.D. Carstanjen, H. Kronmüller, Formation of diamond in carbon onions under MeV ion irradiation, *Appl. Phys. Lett.* 71 (1997) 1948–1951.
- [99] T. Meguro, A. Hida, M. Suzuki, Y. Koguchi, H. Takai, Y. Yamamoto, et al., Creation of nanodiamonds by single impacts of highly charged ions upon graphite, *Appl. Phys. Lett.* 79 (2001) 3866–3870.
- [100] A. Nikitin, Y. Gogotsi, Nanostructured carbide-derived carbon, *Encycl. Nanosci. Nanotechnol.* 7 (2004) 553–574.
- [101] A.D. Rud, N.I. Kuskova, L.I. Ivaschuk, G.M. Zelinskaya, N.M. Biliy, Structure state of carbon nanomaterials produced by high-energy electric discharge techniques, *Fuller. Nanotub. Carb. Nanostr.* 19 (2011) 120–126.
- [102] A. West, J. Kennett, Nanodiamonds and diamond-like particles from carbonaceous material, US Patent Application 20110020646 (2008).

Deagglomeration of Detonation Nanodiamond

6

Eiji Osawa^a, Shuichi Sasaki^b, and Ryoko Yamanoi^a

^a*NanoCarbon Research Institute, AREC, Shinshu University, Ueda, Nagano, Japan,*

^b*Bravus Co. Ltd, Arakawa-ku, Tokyo, Japan*

CHAPTER OUTLINE

6.1 Introduction	165
6.2 Why are the agglutinates useful?	166
6.3 Methods of deagglomeration.....	170
6.4 Beads-milling	172
6.5 Primary particles	175
6.6 Conclusion	176
Acknowledgments.....	177
References	177

6.1 Introduction

Unusually strong agglomeration, or “agglutination” as we designated it [1], among primary particles in as-produced detonation nanodiamond must have been noticed by many scientists who encountered with this novel artificial diamond after its discovery in 1963 by Danilenko, Volkov, and Elin in Soviet Russia [2,3]. However, to our knowledge, the novel phenomenon of agglutination was never mentioned nor discussed in any publications on detonation nanodiamond till long after Perestroika. The first clear statement on the necessity of breaking up agglutination was made in the first edition of this book by its editors [4]. Unfortunately, the warning seems to have been largely ignored and still now many people use agglutinates without paying much attention to dispersity [5]. To make the situation more complicated, agglutinates sometimes proved useful to some extent for applications like heavy-duty lubrication and as additives to galvanization baths, and actually small production of about 10 tons per year of agglutinates began in the 90th while almost all the products are consumed as they are. In view of persistent failure in most of the attempts to disintegrate, it is totally incomprehensible that the agglutinates worked at all in the applications mentioned above. The only success in finding good application of agglutinates has been for abraser in the final scratching process of hard

disk production. It seems likely that the very rare attributes of the agglutinates (fluffy and voluminous with a small, hard core) incidentally were found fit to this particular application. However, the life of this usage will be short, only until multi-channel vertical recording technology is put into practice.

For these reasons, we will first give an in-depth interpretation on the structure of agglutinated single-nano diamond (SND) and the mechanism of its response to perturbations like sonication. This Section 6.2 should help further understanding of the mechanisms in the known methods of deagglomeration of detonation nanodiamond. Among them, attrition milling will be mentioned in some detail. A few properties of dispersed SND particles will be given at the end. Excellent reviews are available on the properties and prospects of dispersed SND particles [6,7].

6.2 Why are the agglutinates useful?

Interactions in the agglutinates of SND particles are dominated by the Coulombic force of facet–facet type between SND, as first proposed by Barnard in 2008 on the basis of Mulliken charge distribution obtained by Self-consistent charge-density functional tight binding (SCC-DFTB) calculations on polyhedral models [8] (Figure 6.1). Such an extensive electron migration might appear less likely to occur on a stable and inactive material like diamond, but can be readily understood by invoking the presence of graphitic layers on the surface (111) layers. Graphitic layers are formed as the result of spontaneous diamond–graphite phase transition and have been often observed in the transmission electron microscopy (TEM) images on the nano-scale of detonation nanodiamond [9]. This transition was also occurred

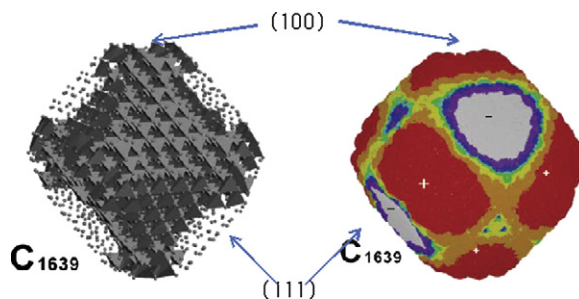


FIGURE 6.1

Geometric (left) and electronic (right) structures calculated for C_{1639} truncated octahedral models of a primary particle of detonation nanodiamond crystal. Geometry is given by semi-perspective drawing with graphitic shells by means of dots and diamond core by 3D tetrahedra, both at the positions of carbon nuclei. Positive charges are distributed over (100) and (110) facets, and negative charges over (111) facets. Charge densities range between large positive through neutral to large negative values depending on the size of the particle and type of models.

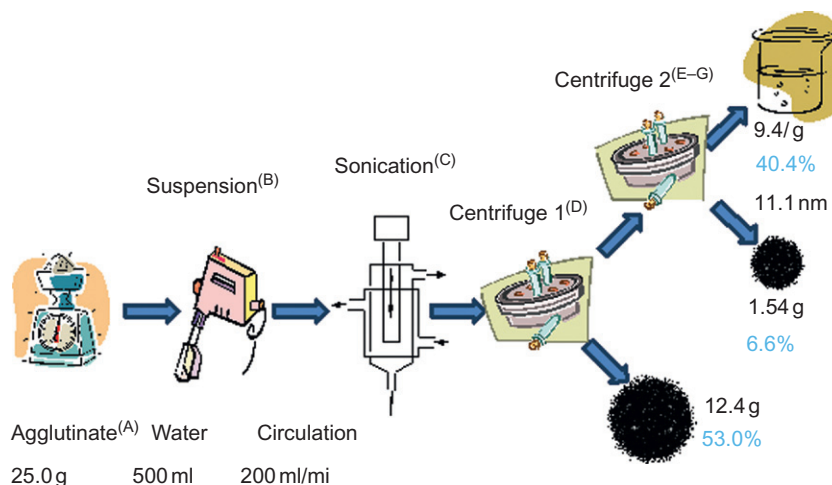
during the geometry optimization of the all-diamond polyhedral inputs to considerable depths beneath the surface [10]. The transition produces a number of free spins on the new surface of diamond, which migrate from electropositive diamond core to electronegative graphitic shell, thus creating positive holes as well as negative electrostatic fields on the surface. Intraparticle migration of electrons leads to novel multipole electronic structure in the otherwise neutral diamond crystal [11].

All these intraparticle phenomena occur immediately after the shock wave of detonation passes the diamond crystal growth region at ultrasonic speed within the detonation chamber but temperature still remains high. As a consequence, interparticle facet–facet Coulombic interactions start, generating attraction between oppositely charged facets of neighboring particles and repulsion between similarly charged facets. Assisted by vigorous thermal vibration of atoms, extensive displacements of particles will occur and lead to the formation of highly complex core agglutinates including a large number of nanopores [8]. Some of the facet–facet bonding pairs have enough time to anneal and reach optimum configuration by adjusting facet–facet orientation, vertical distance, and rotational angle around a common axis passing through the centers of interacting facets, achieving extremely strong bonding comparable in strength to the dissociation energy of covalent CC bonds. Barnard named them coherent interfacial Coulombic interaction (CICI), which Chang confirmed experimentally by analyzing TEM images of agglutinates [9].

The annealing period does not last long enough for all the SND particles to find optimum interparticle configurations, so there will be almost continuous distribution of bonding intensities in the incoherent interfacial Coulombic interactions (IICIs) in nonoptimum facet–facet configurations. Some of the weaker interparticle bonds of IICI may be destroyed by conventional means of disintegration like sonication and decompose into smaller fragments. It seemed interesting to study the effects of sonication upon the suspension of commercial agglutinates in order to see the extent of disintegration and the smallest possible size of the particles attainable by this process.

Scheme 6.1 summarizes one of our preliminary experiments, which involves irradiation of high-power supersonic wave to circulating aqueous suspension of commercial agglutinate powder, followed by repeated centrifugal separation of supernatant liquid from sedimented solid. To our surprise, 40% of the starting powder dissolved in water, and Dynamic light scattering (DLS) analysis of the size-distribution of particles in the final supernatant liquid revealed 11 nm as the reliable average diameter for colloidal particles. This experiment was repeated and almost perfectly reproduced as shown in the second line of **Table 6.1**. The first line is a separate experiment performed under much weaker sonication. In the latter, only the weakest interfacial Coulombic bonds (ICBs) were broken to give an average diameter of 100 nm. Combined with the third line, which was taken from one of the attrition millings mentioned below, a differential disintegration sequence in the agglutinates is shown to occur, suggesting random distribution of CICI and IICI in the agglutinate.

Going back to the average diameter of 11–12 nm obtained by intense sonication, we realize that this size corresponds to a trimeric assembly of SND particles. In view of the poor resolution of DLS method, especially for single-nano particles,

**SCHEME 6.1**

(A) Imported from Gansu Goldstone Nano Material Co. in 2010. Product No. 59. Grayish fine powder. (B) Stirred at 5000rpm for 30 min in a multifunction emulsifier T.K. Robomix f-Model from Primix Co. to a homogeneous and viscous aqueous suspension. (C) Suspension circulated for 1 h at a flow rate of 193 ml/min through Ultrasonic Processor (Dr. Hielscher GmbH, Teltow, Type UP400S, 400W) equipped with a vertically pulsing sonorod H22D, emitting acoustic power density of 68W/cm² in an amplitude of 80 μ m. (D) The first stage of ultracentrifugal separation carried out on a tabletop centrifuge (Kubota Mfg. Co., Type 5200) at 2380xg relative centrifugal field (RCF) for 1 h. (E) Supernatant from the first centrifuge subjected to the second ultracentrifugal separation on a refrigerating microcentrifuge (Kubota Mfg. Co., Type 3700) at 5867 \times g RCF for 20 min. (F) Particle-size distribution in the final supernatant was determined on a DLS Particle Analyzer (Otsuka Electronic Co., Type FPAR1000 + Autosampler FP3000) in 1.4–1.7% solution to give a representative value of 11.1 \pm 0.8 nm (99.91 vol%). For the reproducible DLS measurements, see E. Osawa, Tech. Bull. NCRI, No. 2 (2007) (<http://nano-carbon.jp>). (G) The second run gave the following results: solid composition of the supernatant versus sediments = 37.4:58.1, particle size in the final supernatant 12.0 \pm 1.0 nm (99.92 vol%). Rather poor recovery of solid material in both experiments is due to the loss from sampling for analysis.

Table 6.1 Results of Applying Various Disintegration Methods to the Colloidal Solutions of SND Particles

Disintegration Methods	Particle Size in Supernatant (nm)	Approximate Composition (wt%)	
		Supernatant	Sediments
100W supersonic washing bath	100.00 \pm 22.8	~90	~10
400W sonorod-type ultrasonic processor	12.0 \pm 1.0	37.4	58.1
Beads-milling	3.7 \pm 0.6	97.9	0.6

it may be more reasonable to think that all sizes of soluble oligomeric aggregates, e.g., 3–20 nm in diameters, are involved in the observed peak. However, in order to simplify the argument, we will hypothesize here that only the trimers exist in supernatant liquid and all the higher aggregates were precipitated by centrifugation. We proceed to interpret the experimental results as follows:

1. An interesting consequence of invoking the interfacial Coulombic bonding as the cause of agglomeration of the polyhedral single crystals of SND is the high number of coordination that one can expect. The highest possible number is equal to the total number of crystal facets. For the most popular model of diamond, truncated octahedron, the number is 14. Although the higher coordination numbers are unlikely due to steric congestion, 4–6 bindings of neighboring crystals to one central crystal may occur frequently. Such ease of multiple bonding leads to the formation of a large number of ICBs. An agglutinate will consist of a tight 3D network of ICBs. The large number of ICBs should be a reason for the difficulty in breaking up the agglomeration.
2. Coordination angles are rigorously fixed to isometric. This characteristic leads to a rigid packing of SND particles containing a large number of nanovoids, which could be the reason for the low bulk density of agglutinates observed (0.2–0.7 g/ml; [5]). We can also argue that the most likely configuration of trimer will be linear.
3. One more characteristic in the agglutinate of nanodiamond is nonuniformity in the strengths of ICBs, ranging from very strong CICI to a variety of weaker and weaker IICIs. The latter offers weak points in the destruction of agglutinate.
4. Deagglomeration of core agglutinates by sonication starts from the surface, first at the sites of the weakest IICI bonds, then proceeding to the stronger and stronger IICIs. With the progress of cleavage in the ICB network, small pieces of aggregate will be detached from the surface, and quickly fragmented in solution, eventually reaching the levels of soluble sizes like trimers. In these small oligomers, the weaker IICI bonds have been exhaustively broken, and CICI bonds remain and prevail.
5. Trimers appear to be the last and tough intermediates before reaching complete dispersion, and accumulating as we have seen. The two remaining ICBs in trimers are due to CICI or very strong IICI.

Thus, our model of agglutinates, consisting of a large number of primary particles multiply bonded to each other by ICBs in isometric directions, mainly in terms of IICIs but interspersed with CICIs, fits the result of our experiments as given in [Scheme 6.1](#) and [Table 6.1](#). This means that in the past when a large excess of agglomerates were used, perturbations like high-speed mixing and supersonic irradiation would have released tiny amounts of very small fragments of aggregates, e.g., those having 10–20 nm in diameter.

We are now in the last stage of answering the question “Why were agglutinates somehow useful in the past?” The answer is that the tiny amounts of very small aggregates like trimer of SND crystals are enough to show noticeable effects.

Table 6.2 Number Density of the SND as Calculated by Spherical Approximation

Average diameter of an SND ($D = 2r$, nm)	3.7
Average volume of an SND ($v = 4\pi r^3/3$, cm ³)	2.65×10^{-20}
Mass of one particle of SND ^a ($w = \rho v$, g)	7.74×10^{-20}
Particulate weight ^{b,c} (PW = wN)	46,583
Total number of carbon atoms in an SND ($n = PW/12$) ^d	3,882
Number of particles/g SND ^e ($\delta_n = 1/w$)	1.29×10^{19}
Number of particles in 1 μ l of 0.001 wt% colloid of SND (δ'_n)	1.29×10^{11}

^a $\rho = 2.92(\text{obs})$. Compare ρ of natural diamond = 3.52.

^bPW is a conceptual weight proper to nanotechnology and corresponds to the molecular weight in chemistry.

^cAvogadro number is 6.023×10^{23} .

^d100% diamond assumed.

^eNumber density. Note that 10^{19} is equal to ten quintillion, and 10^{10} ten billion.

Then, one would ask “Why is a small amount enough?” The answer is, “This is because even a very small amount of dispersed (or almost dispersed) SND contains a surprisingly large number of particles.” If the performance of individual nanoparticle counts, then enough particles are there because nanoparticles are surprisingly small. The number density of SND having an average diameter of 3.7 ± 0.6 nm per unit weight is equal to 1.29×10^{19} particles/gram, according to simple calculations shown in Table 6.2 [12]. For example, 1 μ l (=1 mm³, a fraction of one drop) of 0.001% dispersion of SND contains 1.29×10^{11} or about 100 billion particles. This is an unbelievably large number, but one needs to recognize the surprising *smallness* of SND. This recognition is called the “number density effect,” and provides the outstanding advantage of nanoparticles [12].

6.3 Methods of deagglomeration

It was a tragic misfortune that such an interesting and potentially useful material like SND was left practically unattended for nearly 40 years. The reason cannot be totally political, but the major cause is simply that the discovery of SND was premature.

Taking advantage of the highest toughness property of diamond, we began testing all the known brute force methods one by one, and encountered with wet attrition milling with ceramic microbeads as the crushing media, which proved right [1]. The result was announced on the occasion of the First International Symposium on Detonation Nanodiamonds in July 2003 [13].

Almost 10 years after this breakthrough, beads-milling is still the most convenient and only reliable method for dispersing agglomerates of detonation nanodiamond into the primary particles at a rate of 100 g output in a day, even by our equipment, which is the smallest available. The process should be readily scalable. However, the operation of beads-milling is not easy, and considerable experience is required to obtain sizable amounts of well-dispersed primary particles in economically feasible time. The beads-milling technique will be mentioned in some more detail in Section 6.4.

A few other methods of deagglomeration have been reported thereafter, which include intensive sonication under agitation with ceramic beads [14], low-temperature combustion [15], milling with inorganic salts [16], chemical reactions like hydrogenation [17], and the other partial deagglomeration methods like oxidation (by supercritical water, unpublished results), ozonization [18], perfluorination (H. Touhara, personal communication), removal of metal impurities followed by annealing and centrifugation [19], and electrophoresis [20]. Among these, only reductive dispersion [17] will be briefly mentioned here. Reductive removal of graphitic by-products by hydrogen flow at high temperatures of up to 1000°C has been practiced for a long time, since the discovery of chemical vapor deposition (CVD) method [21]; hence the know-how on the safe operation of heated hydrogen gas may be considered established. On the laboratory scale it would be most convenient to use the CVD set-up for diamond thin films. This technique is being used extensively for purification of carbon nanotubes [22]. When applied to disperse agglutinates of detonation nanodiamond, hydrogen will remove the surface graphitic layers and cover the exposed bare surface of diamond with CH bonds to give diamond hydrocarbons as the product, which may be regarded as higher members of the diamondoid hydrocarbons recently under development [23]. The nanodiamond hydrocarbons are literally small pieces of bulk diamond, should be regarded as the basic models of nanodiamonds, and are useful for many applications including derivatization and the nuclei for the CVD growth of diamond crystals [24]. On the other hand, this reductive treatment destroys the paths of electron migration that gave the novel multipolar core-shell structure in detonation nanodiamond. Thereupon the surface Mulliken charges will disappear and the ICB is lost, eventually leading to disintegration of agglutinates. Hydrogenated SND will not generate ICB but will be agglomerated by interparticle van der Waals attractions, which is actually an interatomic phenomenon. Facet–facet van der Waals attractions should certainly be stronger than simple atom–atom or molecule–molecule attractions, but as strong as ICBs. In view of the fact that computational geometry optimization of nanodiamond led to spontaneous graphitization on the surface, the nanodiamond hydrocarbon may not be stable and may turn itself into “bucky diamond” with a graphitic shell after standing for a long time under normal conditions.

The mechanism of agglutination in the primary particles of detonation nanodiamond has been discussed above. Additional remarks are due here. First, ICB is primarily influenced by the areas of interacting facets. If the surface asperities,

edges, and apexes of a crystal are removed by etching or erosion, new smaller facets are produced and the areas of old facets decreased. While the number of ICBs increases, not all of them cannot form ICBs due to steric reasons, hence the overall effect will decrease in the attractive bonding per particle. There will be an optimum combination between the number of facets and the interparticle bonding. Conversely, agglomeration will decrease by making more and more facets on the crystal surface. In the extreme end of truncation of edges and apexes, namely a sphere, ICB disappears. Nanodiamond having high sphericity would be an interesting new material that never aggregates even in the smallest size.

6.4 Beads-milling

A mill is essentially a type of grinding equipment, wherein a source material is crushed by means of head-on collision with a hard ball or by shearing attrition with a rotating hard ball. In the present case, the source material is gross agglomerate powder of detonation nanodiamond. Agglomerates are considered to have a hierarchical structure, wherein the outer portions are bound by soft nonbonding van der Waals forces common to other micron-sized powders and easy to destroy by any conventional methods like fast agitation and mild sonication. However, the core portion having diameter of below 100–200 nm (Table 6.1) is hard and dominated by CICI-bonding. We want to destroy these bonds in order to achieve dispersion. For this purpose, we used an attrition mill called Ultra Apex Mill (type UAM-150 from Kotobuki Industries Co., Tokyo), with 30 μm beads made of zirconia (30 μm , Toso Co., Tokyo) as the crusher (Figure 6.2). Note that the inside of the mill including the inner wall, rotation axis, agitating blades, and centrifugal separator (to separate beads from the diamond mixture and return the former to the mill) are all lined with zirconia. In order to earn attrition, impact beads are moved at very high speed by rotating agitation blades at, e.g., 4500 rpm.

When we began to disintegrate agglomerates of detonation nanodiamond in early 2002, the difficulty was tremendous, partly because there was no precedence and also because the nature of agglomerating interactions were unknown. One right thing we did was to purchase DLS equipment (Type FPAR1000, Otsuka Electronic Co., Tokyo) and monitor particle-size distribution as frequently as possible. Fortunately, we soon found that some fragments of agglomerates below a hundred nanometers in diameter *dissolved* in water to allow determination of their size by DLS. Later we even noticed that the primary particles with 4–5 nm in size are soluble in water up to 10%, although we learned the reason for unexpected solubility of nanodiamond only after the seminal publication of Barnard and Sternberg [8,10]. Actually, the high solubility of nanodiamond in water was crucial to the successful disintegration of agglomerates by beads-milling. No less important was the fact that one of the commercial agglutinates from China gave fairly stable suspension in water even at high concentration like 10%, stable enough to stay suspended

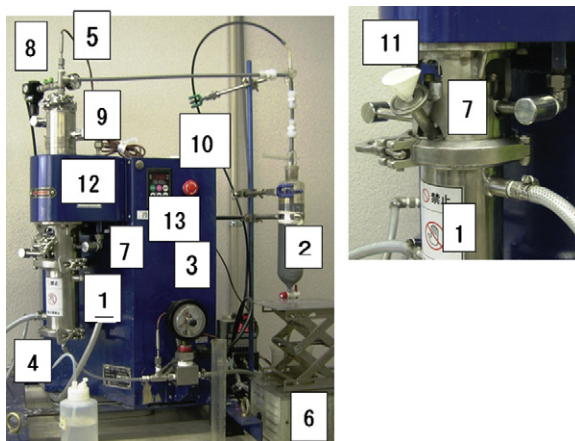


FIGURE 6.2

The attrition mill used in our laboratory for disintegration of nanodiamond agglutinate. Ultra Apex Mill Type UAM-015, Kotobuki Ind. Co., Tokyo. (1) Mill covered with coolant jacket, (2) suspension reservoir, (3) pressure sensor, (4) suspension inlet, (5) suspension outlet, (6) suspension circulation drive, (7) mechanical seal, (8) to nitrogen tank, (9) sealant tank, (10) emergency stop, (11) inlet for beads, (12) rotor drive inside, and (13) switch board.

during the circulation cycle. As the disintegration proceeds during beads-milling, the suspension-colloidal solution acquires high zeta-potential to keep the intermediate particles in good suspension in water, despite considerable increase in viscosity.

When we thought of using beads-milling to destroy agglomerates, we were afraid that reverse attrition by the freed diamond nanoparticles against crusher beads of zirconia would contaminate the product with nanoparticles of zirconia. The contamination, if any, will start from the moment when the surface of nanodiamond began to appear on the surface of agglutinate, and continue until all the agglomerating bonds have been destroyed, thus creating a considerable length of contact time between the zirconia and diamond. However, the fear proved not as formidable as we first thought for the following reason. In a collision or attrition between zirconia and diamond particles, the reaction energy D_z that a zirconia bead receives is given by

$$D_z = c_d m_d v_d$$

where c_d is a collisional constant dependent primarily upon the elastic modulus of diamond, m_d is the mass of the diamond particle and is equal to $(4/3)\pi r_d^3 \rho_d$, where ρ_d is the density of diamond, and v_d the velocity of the diamond particle. Similar

derivation of D_d , the reaction energy of diamond, and combination of the two relations gives the ratio of reactions:

$$D_z/D_d = (c_d/c_z)(r_d/r_z)^3(\rho_d/\rho_z)(v_d/v_z) = 10 \cdot 10^{-4} \cdot 0.5 \cdot 1 = 0.0005$$

We may conclude that it is diamond rather than zirconia that may be damaged by the hetero-attrition. This means that we should be able to find conditions where no contamination by zirconia will occur and that prolonged contact of zirconia beads with diamond under beads-milling conditions will even remove the surface graphitic layers and eventually round up the sharp edges and apexes of diamond particles.

There was another concern on the design of the Ultra Apex Mill, which is the only vertical type among commercial attrition mills wherein horizontal types prevail. A vertical mill has a distinguished advantage at least for our present purpose: a simple centrifugal separator can be installed at the top of mill. However, the separator is fixed *coaxially* with the agitator, and this coaxial design forces the separator and the mill to rotate at an identical speed, despite the fact that the optimum speed of the separator and that of the agitator do not need to coincide. In addition to this limitation, quite a few other critical pitfalls exist in the operation conditions, but we will not discuss all the small points here.

In spite of all these anxieties, we somehow found a workable set of operational conditions, based only on a trial-and-error strategy. The CICI hypothesis explains the remarkable effectiveness of beads-milling to disintegrate the agglomerates of detonation nanodiamond as well. As shown by Barnard, the binding energy of CICI changes sensitively with the relative rotation angle of a facet against the other. Therefore, any external force that affects the interfacial rotation angle (around the common central vertical axis perpendicular to the binding facets disposed parallel at a distance of $\sim 1.8 \text{ \AA}$) or even slight displacements of the binding facets against each other effectively decrease the binding force. Attrition with beads is a good way to cause such perturbations at the interfacial bonds. In beads-milling, pinching or shearing action is given to the bonding sites in the agglomerates by means of fast moving microbeads packed in astronomical number in the mill (70–80% of the mill space is occupied by beads). In contrast, conventional measures to disperse molecular aggregates like vigorous agitation and cavitation from sonication are ineffective in causing these actions as we saw above (Scheme 6.1).

During the initial few years of operation, the contamination level of zirconia was quite high, despite the optimistic estimation given above. The contamination level often reached 2%. This unfavorable level could be reduced to 0.2%, then to 0.02%, by manually adjusting the operational conditions of the beads-milling. However, increasing demands for using our nanodiamond dispersion for biomedical uses [6,7] prompted us to reduce contamination with zirconia to nearly zero. Chemical aftertreatment is ineffective due to the chemical inertness of zirconia. We recently performed optimization of beads-milling conditions by using Taguchi's

Table 6.3 Geometrical Features of Truncated Octahedral Models for Variously Sized All-Carbon Primary Crystals of Detonation Nanodiamond

Computational Method	Diam (nm)	Number of Carbon Atoms			Surface/Bulk Ratio (%)
		Total	Surface	Bulk	
MM3 ^a	4.8 ^b	7000	1000	6000	15
	3.7 ^c	3700	800	2900	19
	2.7	1600	500	1100	23
SCC-DFTB	2.7 ^d	1639	–	–	–

^aCalculated by Mr. A. Otake. Surface carbon atoms are saturated with one or two hydrogen atoms.
^bOur previous experiment value.
^cOur present experiment value.
^dThe largest model used in Ref. [10].

quality engineering method [25], hoping that the contamination level will be further reduced by using the shortest possible milling time. A total of eight variables (including axis rotational rate, total volume of zirconia, and concentration of agglomerate) were adopted in two or three levels and 18 combinations of experimental conditions were created according to the L_{18} orthogonal table. For each set, aliquot samples were taken out in short time intervals, and DLS particle-size and zeta-potentials were recorded. Results were analyzed in terms of S/N ratios in the observed sizes. Optimum levels could be unambiguously determined for all the variables to give the best S/N ratio. The optimum condition determined in this way not only produced stable operation but also produced two major improvements in the quality of the primary particles obtained: particle-size distribution changed from 4.8 ± 0.7 to 3.7 ± 0.6 nm, while contamination of ZrO_2 decreased from 0.02% or 20 to 2 ppm. The change in diameter is dramatic (23%), but the direction of change is as expected and favorable for many applications (Table 6.3). The estimated number of carbon atoms (3700) in a particle decreased to about one half of the previous value (7000) (unpublished results from our laboratory). It is hoped that the new size can now be amenable to SCC-DFTB calculations. Other confirming experiments on the new particle size are in progress.

The ultimate beads material for producing pure SND particles by attrition milling will undoubtedly be spherical microdiamond. A project of *diamond beads-milling* is going on in our laboratories and the progress will be disclosed in the near future.

6.5 Primary particles

Nanoparticles (definition: 1–100 nm in diameter) are very special in their behavior among small particles, in that only in this size-range does surface play a dominant role (see the rightmost column of Table 6.3). The importance of surface, especially

Table 6.4 Dramatic Difference in Behaviors and Properties between Agglomerates and Primary Particles of Detonation Nanodiamond

Terms	Primary Particle	Agglomerate
Origin	Gansu Nanodiamond Powder Co., Gansu, China	
Product forms	1. Colloidal solutions in water and a few organic solvents 2. Hard hydrogel (water content 20%)	Dry, fine powder
Outlook	1. Clear solution 2. Heavy, compact, and brown powder	Light, fluffy, fine, and gray powder
Particle size by DLS (nm)	3.7 ± 0.6	60–200 ^a
Number of primary crystals in one particle	1	1,000–100,000 (est.)
Apparent density (g/cm ³)	2.99	Undetermined
In water	<0.01%: Brown to colorless colloidal solution 0.1–8%: Clear but black colloidal solution	Forms unstable suspension, which precipitates within 30 min
DSC of gel	Contains aqueous phase freezing at -8°C	No gelation

^aAfter light sonication.

in the single-nano range, cannot be overemphasized. However, information was lacking in the past, because no other stable nanoparticle was known and the dispersed nanodiamond that we obtained by deagglomeration of crude detonation product in 2002 was virtually the first typical nanocarbon particle to appear in science. C_{60} is generally considered as the forerunner in nanotechnology, but this one is actually too small to be regarded as nanoparticle (0.7 nm in internuclei diameter) and even can be readily dissolved in quite a few other organic solvents to give a *molecularly* dispersed solution quite easily. C_{60} is better classified as a molecule.

Here, we would like to show the big difference between primary particles and commercial agglutinates (Table 6.4). It may be all too clear that the primary particles of SND in a perfectly dispersed state qualify to the methodology of scientific research. Nevertheless, a number of basic characteristic quantities like solubilities in various solvents, purity in terms of diamond carbon, elementary analysis, elemental compositions, and shape analysis, are still not available.

6.6 Conclusion

In this chapter the reason for the certain usefulness of agglomerated detonation nanodiamond was given, there was in-depth speculation about the structure and bonding in

agglutinates of detonation nanodiamond, the state of the art in beads-milling was mentioned, the behaviors and properties of detonation nanodiamond were presented, and finally perspectives on developing diamond milling were touched upon.

A perspective on dispersed single-nano diamond (DSND) particles in comparison with other nanocarbon apexes is briefly included here for the sake of those who seek positive views on the future of nanocarbons as essential materials for nanotechnology. DSND satisfies all conceivable requirements for the fundamental material of nanotechnology: material supply (wartime explosive, hence cheap by definition), materials cost (negative), production cost (low cost technology), dispersion cost (should be improved), cytotoxicity (none, no chemical reactivity in diamond core) [26], genotoxicity (slightly positive, like most other chemical entities) [27], major applications (two already discovered and being explored, many more to come) [28], popularity (diamond is forever), excellent properties (inherited from bulk diamond), chemically active but controllable surface (unprecedented in the history of materials science), and research possibilities (inexhaustible).

Acknowledgments

We thank Japan Science and Technology Bureau for partial financial support of the work described above through a grant A-STEP, No. AS2321334C. Experimental results presented in Section 6.2 are taken from M. Eng. Thesis of Mr. K. Kakinuma submitted to the Faculty of Textile Science and Technology, Shinshu University, in 2011.

References

- [1] A. Krüger, F. Kataoka, M. Ozawa, A. Aleksenskii, A.Y. Vul', Y. Fujino, et al., Unusually tight aggregation in detonation nanodiamond: identification and disintegration, *Carbon* 43 (6) (2005) 1722–1730.
- [2] V.V. Danilenko, Discovery of detonation nanodiamond, *Phys. Solid State* 46 (2004) 595–599.
- [3] E. Osawa, Monodisperse single-nano diamond particulates, *Pure Appl. Chem.* 80 (7) (2008) 1365–1379.
- [4] O. Shenderova, V. Zhirnov, D. Brenner, Carbon materials and nanostructures, *Crit. Rev. Solid State Mater. Sci.* 27 (2002) 227–356.
- [5] Typical advertisement of commercial agglutinate of detonation nanodiamond reads like “Diamond nanopowder, particle size <10 nm, >97%, spherical, bulk density 0.2–0.7 g/ml, glass bottle, ¥13,000/g.” June, 2012, <http://www.sigmaaldrich.com/catalog/product/aldrich/636428?lang=ja®ion=JP>.
- [6] V. Mochalin, O. Shenderova, D. Ho, Y. Gogotsi, The properties and applications of nanodiamonds, *Nat. Nanotechnol.* 7 (2012) 11–23.
- [7] A. Krüger, Beyond the shine: recent progress in applications of nanodiamond, *J. Mater. Chem* 21 (2011) 12571–12578.
- [8] A.S. Barnard, Self-assembly in nanodiamond agglutinates, *J. Mater. Chem.* 18 (2008) 4038–4041.

- [9] L.-Y. Chang, E. Ōsawa, A.S. Barnard, Confirmation of the electrostatic self-assembly of nanodiamonds, *Nanoscale* (2011). doi: 10.1039/c0nr00883d.
- [10] A.S. Barnard, M. Sternberg, Crystallinity and surface electrostatics of diamond nanocrystals, *J. Mater. Chem.* 17 (2007) 4811–4819.
- [11] E. Ōsawa, D. Ho, H. Huang, M.V. Korobov, N.N. Rozhkova, Consequences of strong and diverse electrostatic potential field on the surface of detonation nanodiamond particles, *Diamond Relat. Mater.* 18 (2009) 904–909.
- [12] E. Ōsawa, Chemistry of single-nano diamond particles, in: F. Wudl, S. Nagase, K. Akasaka, (Eds.), *Chemistry of Nanocarbons*, John Wiley & Sons, Oxford, 2010, pp. 413–432 (Chapter 17).
- [13] E. Ōsawa, Nanodiamond agglutinates: characterization and disintegration, in: *A Lecture Presented Before the First International Symposium of Detonation Nanodiamonds: Technology, Properties and Applications*, 7–9 July 2003, St. Petersburg, Russia, p. 17 (Book of Abstracts).
- [14] M. Ozawa, M. Inaguma, M. Takahashi, F. Kataoka, A. Krüger, E. Ōsawa, Preparation and behavior of brownish, clear nanodiamond colloids, *Adv. Mater.* 19 (2007) 1201–1206.
- [15] S. Osswald, G. Yushin, V. Mochalin, S.O. Kucheyev, Y. Gogotsi, Control of sp^2/sp^3 carbon ratio and surface chemistry of nanodiamond powders by selective oxidation in air, *J. Am. Chem. Soc.* 128 (2006) 11635–11642.
- [16] A. Pentecost, S. Gour, V. Mochalin, I. Knoke, Y. Gogotsi, Deaggregation of nanodiamond powders using salt- and sugar-assisted milling, *Appl. Mater. Interf.* 2 (2010) 3289–3294.
- [17] O.A. Williams, J. Hees, C. Dieker, W. Jaeger, L. Kirste, C.E. Nebel, Size-dependent reactivity of diamond nanoparticles, *ACS Nano*. 4 (2010) 4824–4830.
- [18] N.N. Rozhkova, L.E. Gorlenko, G.I. Yemel'yanava, A. Jankowska, M. Korobov, V.V. Lunin, et al., Effect of ozone on the structure and physicochemical properties of ultradisperse diamond and shungite nanocarbon elements, *Pure Appl. Chem.* 81 (2009) 2093–2105.
- [19] A.E. Aleksenskiy, E.D. Eydelman, A.Y. Vul', Deagglomeration of detonation nanodiamond, *Nanosci. Nanotechnol. Lett.* 3 (2011) 68–74 F-13058.
- [20] A.M. Affoune, B.L.V. Prasad, H. Sato, T. Enoki, Electrophoretic deposition of nano-sized diamond particles, *Langmuir* 17 (2001) 547–551 F-12095.
- [21] S. Koizumi, C. Nebel, M. Nesladek, (Eds.), *Physics and Applications of CVD Diamond*, Wiley-VCH, Weinheim, 2008, 362 pp.
- [22] A.V. Talyzin, Hydrogenation, purification, and unzipping of carbon nanotubes by reaction with molecular hydrogen: road to graphane nanoribbons, *ACS Nano* 5 (2011) 5132–5140.
- [23] H. Schwertfeger, A.A. Fokin, P.R. Schreiner, Diamonds are a chemist's best friend: diamondoid chemistry beyond adamantane, *Angew. Chem. Int. Ed.* 47 (2008) 1022–1036.
- [24] O.A. Williams, O. Douheret, M. Daenen, K. Haenen, E. Ōsawa, M. Takahashi, Enhanced diamond nucleation on monodispersed nanocrystalline diamond, *Chem. Phys. Lett.* 445 (2007) 255–258.
- [25] G. Taguchi, S. Chowdhury, Y. Wu, *Taguchi's Quality Engineering Handbook*, Wiley-Interscience, New York, NY, 2004, 1696 pp.

- [26] A.M. Schrand, J. Johnson, L. Dai, S.M. Hussain, J.J. Schlager, L. Zhu, et al., Cytotoxicity and genotoxicity of carbon nanomaterials, in: T.J. Webster (Ed.), *Safety of Nanoparticles: From Manufacturing to Medical Applications*, Springer Science+Business Media, New York, NY, 2008, pp. 159–188 (Chapter 8).
- [27] Y. Xing, W. Xiong, L. Zhu, E. Osawa, S. Hussain, L. Dai, DNA damage in embryonic stem cells caused by nanodiamonds, *ACS Nano* 5 (2011) 2376–2384.
- [28] E. Osawa, 5-nm Bucky diamond: an emerging nanocarbon, in: D.K. Aswal, A.K. Debnath (Eds.), *International Conference on Physical Emerging Functional Materials (PEFM-2010)*, 22–24 September 2010, Bhaba Atomic Research Center, Mumbai, India, AIP Proceedings, No. 1313, 2010, pp. 3–7.

Diamond Phase Transitions at Nanoscale

7

Vladimir L. Kuznetsov^a and Yuriy V. Butenko^b

^a*Boriskov Institute of Catalysis, Novosibirsk, Russia,*

^b*European Space Agency, ESTEC, Noordwijk, the Netherlands*

CHAPTER OUTLINE

7.1 Introduction	182
7.2 Stability of nanocarbons	184
7.3 Surface chemistry: stability of surface species	186
7.3.1 Surface groups of NDs.....	187
7.3.2 Thermal stability of ND surface groups.....	189
7.3.3 Critical view of the formation of sp ² -bonded carbon in pristine NDs	193
7.3.4 The onset temperature of ND graphitization.....	196
7.4 Kinetics of diamond graphitization	198
7.4.1 Experimental approaches for the study of ND graphitization	198
<i>Estimation of the diamond fraction in the intermediates of</i>	
<i>ND graphitization.....</i>	<i>198</i>
<i>The kinetic model—the reducing sphere model</i>	<i>199</i>
7.4.2 Kinetic parameters of ND graphitization for the temperature range	
of 1370–1860 K	200
<i>Two temperature regions for diamond graphitization (1370–1860 K</i>	
<i>and above 1900 K).....</i>	<i>200</i>
<i>Absolute rates of ND graphitization</i>	<i>203</i>
7.5 Mechanism of diamond graphitization	205
7.5.1 Diamond surface reconstruction	205
7.5.2 Cleavage energies of diamond planes.....	206
7.5.3 Shape of diamond particles	207
7.5.4 Graphite–diamond interfaces	209
7.5.5 Formation of nanocarbon species via “low”-temperature diamond	
graphitization	211
<i>Model of ND annealing and formation of OLC structure with holes.....</i>	<i>212</i>
7.5.6 The formation of CCGS on the surface of micron-size diamond	217
7.6 Catalytic graphitization of NDs in the presence of metal clusters	221
7.7 Graphitization of NDs in the presence of oxygen- and hydrogen-containing	
gases	225

7.8 Properties of ND annealing products: OLC, sp^2/sp^3 nanocomposites	226
7.9 Conclusion	232
Acknowledgments	233
References	233

7.1 Introduction

The graphitization and oxidation of diamond is a crucial issue for practical applications. These processes limit the performance of diamond used in cutting tools, optical windows, and electronic devices when the diamond surface is exposed to high temperatures and reactive gases (O_2 , CO_2 , H_2O , etc.) [1–4]. Graphitization of diamond crystals occurs through several steps that lead to different final structures depending on a number of atoms in the diamond crystals. The first step includes the diamond structure transformation into graphene-like fragments, while further steps include the transformation of these primary fragments via joining and rearrangement and defect annealing into final products. In some cases, the significant difference in the rates of these elementary steps allows us to distinguish them very clearly. At the same time, this difference in the rates of elementary steps result in a rather diverse family of nanocarbon materials.

Experimental data analysis available in the scientific literature leads to the conclusion that the mechanism of diamond graphitization depends on reaction conditions and factors causing graphitization. Thus, one can distinguish several principal independent processes resulting in diamond graphitization, namely:

1. Thermal graphitization under vacuum, which occurs due to thermally activated movements of carbon atoms
2. Reactive graphitization caused by reactive gases in ambient atmosphere [5–7]
3. Graphitization catalyzed by metals [1]
4. Irradiation-induced graphitization (caused by laser or gamma-ray irradiation and by particle (electron, neutron, ion) beams) [8–10]

Recently, diamond graphitization under high contact compression was observed as a result of pressing a sharp diamond indenter against its surface [11].

In this chapter, we consider the first three types of graphitization leading to nanoscale objects while the basic mechanisms of radiation effects in carbon nanostructures with particular emphasis on atom displacements by knock-on collisions-induced diamond graphitization was described in detail by Banhart [10]. Furthermore, Banhart et al. [12–15] have observed an interesting aspect of carbon transformation at nanoscale concerning the mutual transformation of onion-like carbon (OLC) to diamond and vice versa under electron or ion irradiation of dispersed carbon materials. Using the assumption that changes of atomic positions in irradiated phases are governed by thermally activated jumps (equilibrium diffusion) on the one hand, and, on the other hand, by ballistic knock-out displacements

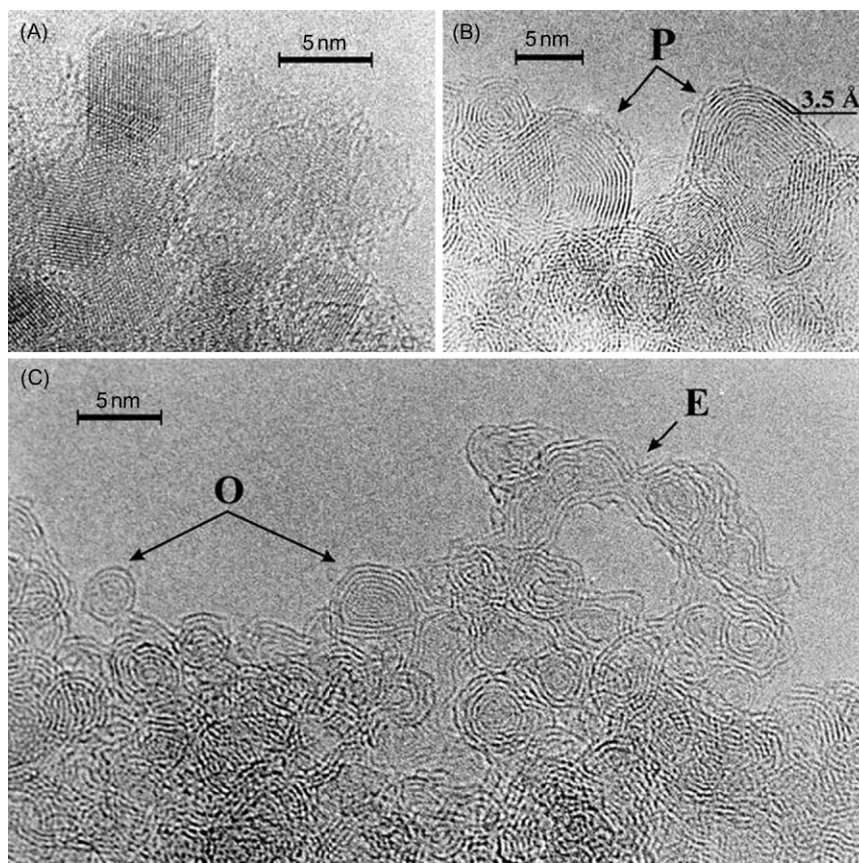
(nonequilibrium contribution), Zaiser and Banhart [16] developed a nonequilibrium phase diagram showing the stability of the phases (dynamical phase equilibrium) as a function of atom displacement rate and temperature.

The surface of atomically pure diamond is very active both physically and chemically, providing the chemical modification of the diamond surface with oxygen- and hydrogen-containing surface groups [17]. Decreasing diamond particle size leads to an increase in the ratio of surface and bulk carbon atoms. It determines the higher concentration of surface atoms and the higher concentration of surface defects. Finally, it provides higher reactivity and some specific properties of small diamond particles.

Synthesis of nanodiamonds (NDs) of average size 3–5 nm by the detonation of explosives was developed over the last four decades. The history of the discovery of detonation NDs, the development of the detonation synthesis method and purification procedures of NDs, properties, and application fields of NDs are described in detail in recent books and reviews [18–24] and in this book as well. The technology is based on the detonation transformation of carbon-containing explosives with negative oxygen balance [25–33]. Knowledge of the reactivity of NDs to graphitization and oxidation can be even more important than that for bulk diamond crystals. At the same time, the small size of NDs provides additional features of the structure of graphitization products and a new approach in the production of new types of nanocarbons: OLC consisting of closed graphene shells enclosed in each other; closed polygonized nanographite particles; and sp^2/sp^3 nanocomposites with diamond cores (bucky diamonds). We demonstrated that high-temperature annealing (1200–1800 K) of NDs in vacuum produces OLC [34,35]. Figure 7.1 shows the annealing products produced by ND annealing at these temperatures. One can clearly see the formation of OLC and polyhedral particles with closed graphitic shells.

While one could predict the formation of nanosized products of ND annealing because of the low self-diffusion of carbon atoms up to high temperatures (2000–2200 K), it was rather surprising to observe the self-organized formation of closed, curved graphite nanostructures (multilayer nanotubes and nanofolds) during annealing of micron-sized diamond [36]. Thus, Figure 7.2 demonstrates the initial stage of surface transformation of micron-sized diamond particles after heating in vacuum at 1890 K [36]. One can see the formation of fullerene-like semi-spheres bonded with the diamond surface. The same results were obtained in experiments with synthetic and natural diamonds.

The detection of intermediate products of the annealing of the diamond surfaces [34–36] provides the most informative features of these studies. In this chapter, we attempt to provide explanations of these and other observations concerning diamond graphitization using experimental and theoretical data available in the literature. We present the data concerning features of nanoscale diamond transformation, and discuss the mechanism of graphitization and properties of diamond annealing products.

**FIGURE 7.1**

(A) High-resolution TEM (HRTEM) images of pristine NDs and (B and C) their annealing products produced at 1200–1800 K. (A) Dark contrast lines and (B and C) curves correspond to diamond crystal planes and graphite-like shells, respectively. The distances between lines correspond to the $\{111\}$ lattice parameter of ND (A) ($d_m = 0.2063$ nm) and those between rings (B and C) to the distance between the graphite-like shells, 0.34–0.35 nm ($d_{002} = 0.3354$ nm for hexagonal graphite). OLC particles are marked **O** (C), polyhedron particles (B) are marked **P**, elongated particles with linked external graphite-like layers and closed quasi-spherical internal shells (C) are marked **E** [34].

7.2 Stability of nanocarbons

The relative stability of nanocarbons became a major issue following the discovery of NDs in detonation soot, fullerenes, and nanotubes, nanocarbons in interstellar dust, etc. This problem was carefully considered in numerous articles and reviews [19,37]. Here, we present main conclusions of these considerations.

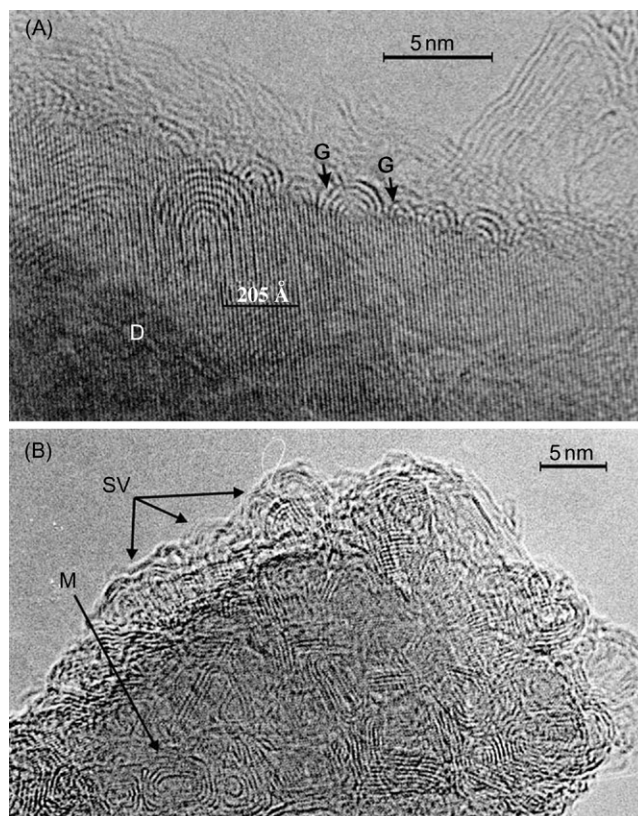


FIGURE 7.2

HRTEM images of the surface intermediates of micron-sized diamond transformation to nanosized curved graphite-like carbon; diamond heated at 1890 K for 1 h. (A) One can see the formation of two graphitic sheets (**G**) from three diamond planes {111} (**D**) on the interface of diamond with growing graphitic species (arrows show 3–2 transformation). (B) Mosaic (**M**) of CCGSs on diamond core (dark region). A variation of focus gave the possibility of seeing {111} diamond planes of the core. **SV** indicates the side view of the closed curved graphite-like structures [36].

First, we refer to the traditional P–T phase diagram of carbon [38], which contains two allotropic forms of carbon: graphite and diamond. Diamond at the atmospheric pressure is an unstable form of carbon at all temperatures, despite the rather small energy difference between the two phases (~ 0.02 eV/atom). Existence of NDs at temperatures up to 1200 K can be explained in terms of the high activation barrier for the phase transition of diamond to graphite. High temperatures (>1200 K), radiation, and/or the use of a catalyst are required to realize this phase transformation. It is obvious that when dealing with nanoscale objects the traditional phase

diagrams should be modified. The downsizing of a material particle increases its surface energy and inflects an aspect of the phase diagrams of disperse systems in comparison with those for bulk single crystals. Thus, the boundaries of a liquid phase and pressure-dependent regions of polymorphic transformations are inflected.

Independently, Viecelli et al. [39] and Danilenko [40] demonstrated that coordinates of triple points on the phase diagram for NDs shift to lower temperatures and higher pressures in comparison with those of bulk diamond crystals. This means that the region of thermodynamically stable diamond particles shifts to higher pressures. These data allow us to propose a three-dimensional phase diagram of carbon, where the number of carbon atoms in a particle is an additional parameter besides pressure and temperature [19,41].

However, traditional thermodynamic considerations can hardly be used for the estimation of the stability of particles consisting of a few hundred atoms, because significant changes occur in the macroscopic parameters, which had been traditionally used for the description of nanoscale objects. Computational methods can provide data on the relative stability of carbon systems with a limited number of carbon atoms. Summarizing the results on the stability of different carbon clusters [42–45], one can conclude that three regions for the stability of small carbon clusters can be distinguished: below 20 atoms the most stable geometries are one-dimensional ring clusters; between 20 and 28 atoms, clusters with quite different types of geometry have similar energies; and for larger clusters fullerenes would be more stable. OLC seems to be the most stable structure for carbon clusters containing up to 1000–2000 atoms. At least the OLC is a final product of ND annealing when carbon atoms cannot migrate from one OLC particle to another. The conversion of diamond clusters containing up to 275 atoms into concentric-shell fullerene structures with cross-links between the two concentric shells was observed by means of molecular dynamics (MD) simulations (at temperatures from 1400 to 2800 K) based on approximate Kohn–Sham equations [46].

Stability of small carbon clusters also depends on their surface group composition and charge of the cluster. It was demonstrated that hydrogenated carbon diamond clusters are more stable than graphitic clusters with the same number of carbon atoms and possess negative enthalpy of formation in respect to bulk graphite used as the standard state [47,48]. This coincides with the discovery of higher diamondoids, hydrocarbons resembling hydrogenated nanometer-sized diamond molecules, which demonstrate exceptional thermal stability [49,50]. Furthermore, it was mentioned [2] that in a hydrogen atmosphere, diamond is stable up to 2000°C. Therefore, it is essential to consider the composition and thermal stability of surface groups to eliminate diamond dangling bonds and stabilize the diamond structure.

7.3 Surface chemistry: stability of surface species

The earlier work devoted to the surface states and surface chemistry of macroscopic diamonds was reviewed by Evans [51]. It was noted that the hydrogen-containing

groups ($\geq\text{CH}$, $>\text{CH}_2$, $-\text{CH}_3$) are formed on oil-polishing diamond surfaces or treated by hydrogen; oxygen-containing groups such as $>\text{C}=\text{O}$, $-\text{COOH}$, $\geq\text{C}-\text{OH}$, $\geq\text{C}-\text{O}-\text{C}\leq$ can be formed on diamond surfaces polished in an aqueous media or oxidized by heating in an oxygen atmosphere; and the fluorination of diamond results in the formation of $\geq\text{CF}$, $>\text{CF}_2$, CF_3 groups. In contrast to macroscopic diamonds, due to the high surface-to-volume ratio of carbon atoms in a nanoparticle, the influence of surface structures and surface groups on the physical and chemical properties of ND particles becomes crucial. In this chapter, we consider the thermal stability of surface groups of detonation NDs. It is considered that the decomposition of surface groups is followed by the surface graphitization of NDs. The fields of applications of detonation NDs and methods of investigation of ND surface chemistry are briefly reviewed.

7.3.1 Surface groups of NDs

Detonation ND particles as produced are encapsulated in amorphous carbon and mixed with other nondiamond forms of carbon. Partial graphitization of ND particles during detonation synthesis results in the formation of graphite-like curved layers on the surfaces of diamond particles [36]. ND content in explosive soot can be up to 80% depending on the synthesis conditions [20,35]. The average size of ND particles is 4–5 nm while the majority of particles are within the size range 2 to 20 nm [18,19,35].

To isolate NDs from explosive soot, purification techniques based on chemical treatments with different oxidative agents (HClO_4 , HNO_3 , nitrogen oxides, H_2O_2 , O_3 , CrO_3 , $\text{K}_2\text{Cr}_2\text{O}_7$, etc.) are applied [18,19,21]. The purification procedure results in the oxidation of nondiamond forms of carbon and leaves more stable ND particles. However, the surfaces of ND particles that are exposed to strong oxidative agents also undergo oxidation. Depending on the temperature of the purification process and the oxidizing agent, various chemical groups are formed on diamond surfaces. Investigations of the surface chemistry of NDs started in the early 1980s with the development of synthesis techniques and the purification of detonation NDs in the USSR. This work is widely reviewed in the recent monographs of Vereschagin [18] and Dolmatov [21].

Diamond nanoparticles of size 4–5 nm have a significant number of surface atoms (~15%) [19]. The chemical groups of ND bonded to its surfaces eliminate the highly reactive dangling bonds of these surface atoms. This provides a relatively high content of surface groups in ND considered as a material. Thus, the elemental analysis of the as-prepared ND revealed the following elemental composition of detonation ND: 85–87% of carbon, 0.1–2.5% nitrogen, and 0.5–2.5% hydrogen; the rest is oxygen [18–21,52–54]. All oxygen and hydrogen atoms belong to surface groups of ND [18,52,53,55,56]. Nitrogen is incorporated in nitrogen-containing groups such as amide groups [53] and nitro-groups [55,57]. It is also incorporated in the diamond lattice. An X-ray photoelectron spectroscopy (XPS) study of a partially graphitized ND sample at 1100°C showed the presence of nitrogen; thus it was concluded that

nitrogen is included within the diamond structure [58]. However, the nature of nitrogen centers in detonation NDs is still under discussion [18,53,57,59].

One can see that the contribution to the total weight of surface groups in diamond nanoparticles is 10–14% [18]. The estimations given in Ref. [18] showed that each surface carbon atom of an ND particle forms a bond to at least one heteroatom (H, O, N); the authors of Ref. [55] concluded that one oxygen atom present in oxygen-containing surface groups falls on two surface carbon atoms of ND treated in strong oxidative reagents (HClO_4 or a mixture of HNO_3 and H_2SO_4). It can be concluded that the chemical surface groups of ND form a dense “coat” on its surface.

The surface groups of ND are important not just from the point of view concerning diamond particle stability and graphitization. They also have attracted great interest from different research groups as a way to the controlled functionalization of the ND surface. It was proposed that surface groups of ND are responsible for some of the infrared (IR) absorption features observed in spectra of the interstellar medium [60–63] (see also Chapter 2). ND surfaces can be rendered as either hydrophobic or hydrophilic by adjusting the surface chemistry and, thus, ND particles can be prepared in the form of stable colloidal solutions in different media, which is necessary for different applications [18,19,21,64–67]. It was shown that ND particles suspended in a solution can be electrophoretically deposited on a substrate [18,19,21,68–74]. The high surface area of ND particles ($250\text{--}420\text{ m}^2/\text{g}$) provides improved integration in composite materials with metal and polymers [18–21]. This also opens up possibilities for chemical reactions on ND surfaces [75] and the wide potential for surface functionalization of ND [52,53,55,56,76,77]. Specific surface functionalization of ND powders enables a variety of biomedical applications of ND derivatives: for example, for the separation, purification, and immobilization of nucleic acids and proteins [21,64,78–83], application as a luminescent biochip [80,84], biosensors [19], and as antigen delivery vehicles [85]. The influence of NDs on human blood cells was studied in Refs. [86,87]. Oxidized ND can generate interest as an efficient support for different catalysts as was found for larger diamond crystals [88–94].

The surface chemistry of detonation NDs has been intensively investigated in a number of articles: IR spectroscopy [53,55–57,60–63,66,76,77,82,95–99], temperature-programmed desorption (TPD) [55,100,101], chemical titration [18,98], polarography [18], and XPS [77]. It was found that oxygen-containing groups, such as $\geq\text{C}\text{--}\text{OH}$ (hydroxyl), $\geq\text{C}\text{--}\text{O}\text{--}\text{C}\leq$ (ether group or bridge oxygen), $>\text{C}=\text{O}$ (ketonic group), --COOH (carboxyl), $\text{--C(O)--O--C}\leq$ (ester or lactone group), and --C(O)--O--(O)C-- (cyclic acid anhydride group) are formed on the surfaces of the ND starting material during oxidative treatments. The relative concentration of these groups depends on the type of oxidative agent used [52,53,55,56]. Table 7.1 summarizes the main characteristic frequencies of surface groups observed in IR adsorption spectra of NDs. The spectral features of ND surface groups mainly correspond to those for larger diamond crystals or graphite materials [103]. For their primary identification, one can also use the spectral characteristic of functional

Table 7.1 Infrared Assignments of Main Bands for Surface Groups Observed on NDs

Frequency Range (cm ⁻¹)	Assignment	References
3200–3600	ν O–H in water, hydroxyl groups in carboxylic or tertiary alcohol	[53,56,57,82,95,99,103]
3360–3320	ν N–H amide groups	[53]
2800–3000	ν -as and ν -s C–H vibrations in hydrogen-containing groups: $>\text{CH}$, $>\text{CH}_2$, $-\text{CH}_3$	[53,57,66,77,95,103]
1700–1865	ν C=O in ketonic, carboxylic, acid anhydrides groups, ester (lactones)	[53,56,57,66,77,82,95,103]
1620–1640	δ O–H in absorbed water	[53,56,66,95]
1460 (weak)	δ -as C–H in $\geq\text{CH}$, $>\text{CH}_2$, $-\text{CH}_3$ groups	[53]
1458 (weak)		[95]
1300–1400		[57]
1300–1450	δ C–H for sp^3 -bonded carbon	[102]
–1260	ν C–C, ν C–N N-induced one-phonon process and/or defect structure in diamonds	[53,57]
1100–1370	ν C–O–C in ether, acid anhydride, lactones, epoxy groups	[53,56,57,82,103]
1120–1200	δ O–H in carboxylic groups	[53,56,103]
1100–1350	ν -as and ν -s C–F vibrations	[77]
1000–1100	ν -s C–F in C–F group	[102]
1200–1350	ν -as C–F in CF_2 and CF_3 groups	
1100–1200	ν -s C–F in CF_2 and CF_3 groups	

Some frequencies were related to characteristics for functional groups found in Ref. [102]. Abbreviations as in Ref. [102]: as, antisymmetric; s, symmetric; ν , stretch; δ , bend or deformation.

groups found, for example, in Ref. [102]. It should be noted that besides the spectral features of surface groups, lattice vibrations of diamond are also observed in IR spectra. Jiang and Xu [53] proposed that the presence of impurities such as nitrogen and/or defects in the structure of NDs cause the forbidden single phonon modes to become IR active. This makes a partial contribution to the broad bands at $1500\text{--}1000\text{ cm}^{-1}$, which are greatly superimposed on the functional group modes.

7.3.2 Thermal stability of ND surface groups

The thermal stability of ND surface groups has been studied in Refs. [53,56,95]. Thermal decomposition of the oxygen-containing groups results in the formation mainly of CO and CO_2 . Both these gases are normally detected by a mass spectrometer or a chromatograph in TPD spectra upon heating a sample. However, it is difficult to unequivocally identify the surface groups from which the desorbing

species originate. The combination of Fourier transform infrared (FTIR) spectroscopy, XPS, and TPD is useful in the identification of the surface groups and gives additional information about their decomposition temperatures.

Dandekar et al. [103] combined TPD and diffuse reflectance Fourier transform infrared spectroscopy (DRIFTS) to study the nature of surface groups of differently treated carbon materials including diamond powder with an average size of 1 μm . The authors of this work reviewed work devoted to applications of the TPD technique for the characterization of carbon surface groups. It was shown that CO_2 -yielding complexes like carboxylic acids, anhydrides, and lactones are mainly responsible for the acidic character of carbon rather than CO -yielding complexes like the phenolic and quinonic groups [103,104]. For sp^3 -bonded carbon, these groups correspond to hydroxyl groups in tertiary alcohol (weak acid) and ketonic groups (nonacidic group). The CO_2 -yielding complexes were shown to decompose typically over a temperature range starting at 500 K and exhibited desorption maxima at 600 and 900 K [103,104]. It was also proposed that carboxylic groups are responsible for the low-temperature peak; the high-temperature CO_2 evolution was attributed to acid anhydride groups. The CO -yielding groups were divided into distinct groups, which have CO evolution maxima at 900 and 1100 K.

Cataldo and Koscheev [56] studied the thermal stability of ND samples treated with ozone using thermogravimetric analysis (TGA-DTG) combined with differential thermal analysis (DTA). They found that an ND sample treated with ozone loses 3% of its weight at 550°C (in an inert atmosphere); in contrast to this behavior, the weight loss of bulk diamond was zero at this temperature. It was proposed that, due to the large concentration of oxygen-containing groups on ND surfaces and high surface area of ND powder, the weight loss was related to the desorption of different absorbed molecules, and to the condensation processes of adjacent chemical groups: for example, two neighboring carboxylic groups form an anhydride group; carboxylic and hydroxyl groups form a lactone group [56]. This process results in the release of water molecules. Raising the temperature to 900°C in an inert atmosphere resulted in the decomposition of all oxygen-containing groups and in a total weight loss of 11.5% (for bulk diamond the weight loss was found to be only 1% at the same temperature) [56]. This result agrees well with the values of 10–14% for the weight of ND surface groups found in other work [18].

Figure 7.3 presents the FTIR spectra of an ND sample annealed in a vacuum at different temperatures. Figure 7.4 presents the TPD spectra of ND and submicron diamond (ASM1 0.1/0) [97]. All diamond samples were treated in similar conditions with a mixture of HClO_4 and H_2SO_4 (1:1) at 200°C [35,95]. One can see that there is a correspondence between features in the spectra of ND and submicron diamond. However, the spectrum of submicron diamond is better resolved, while the peaks of the TPD spectrum of ND are broad and overlap each other. This can be understood if we take into account that a chemical group on defective surfaces of ND particles has a larger number of possible locations. Therefore, the temperature range of the thermal decomposition of a surface group depends on its surrounding and the crystallographic plane on which this group is attached.

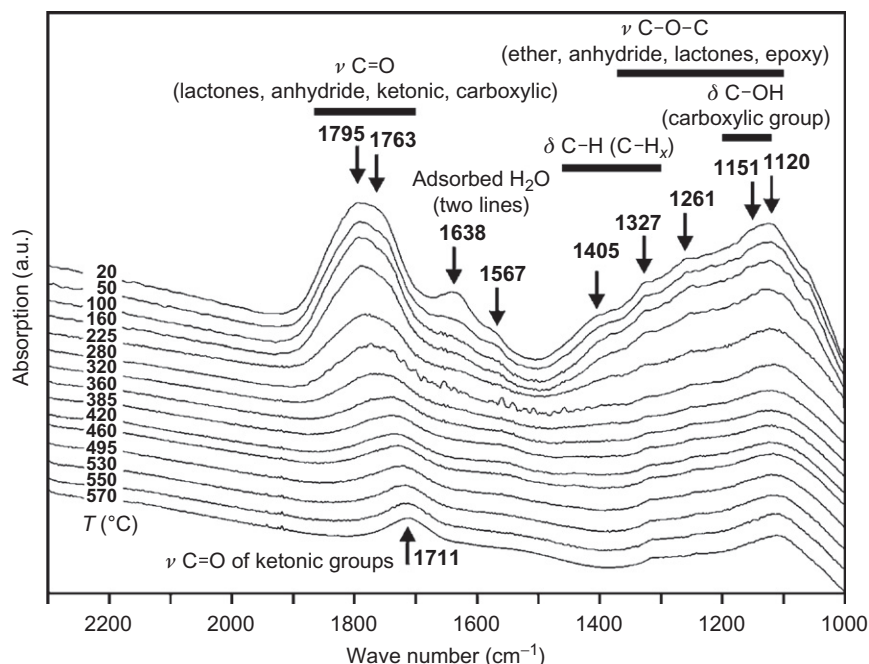
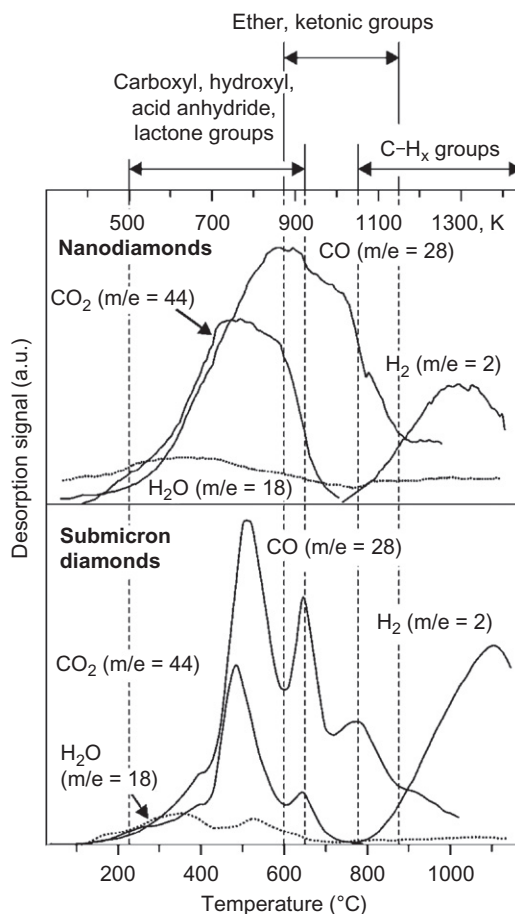


FIGURE 7.3

FTIR spectra of surface groups of an ND sample heated at different temperatures (as shown in the figure). The initial ND sample was purified in a mixture of HClO_4 and H_2SO_4 (1:1) at 200°C. The characteristic ranges of vibrations of the surface groups are presented (FTIR spectra were recorded by Prof. E.A. Paukshtis.) [100].

The decomposition of oxygen-containing surface groups of an ND sample treated in a mixture of HClO_4 and H_2SO_4 starts at ~500 K and finishes at a temperature of 1150 K. Hydrogen-containing groups decompose in a temperature range of 1050–1400 K releasing hydrogen (Figure 7.4). We believe that at a low-temperature region of 500–920 K two processes occur: (1) the condensation of different oxygen-containing groups releasing water molecules and corresponding oxygen-containing groups [56] and (2) the decomposition of acidic groups (carboxyl, anhydride, and lactone groups) releasing CO_2 and CO gases. It should be noted that partial decomposition of CO_2 resulting in CO formation occurs in the electron ionizer of our mass spectrometer, which could be a reason for the observed correspondence in the positions of CO_2 and CO peaks. We registered the maximum of gas evolution of all gases (pressure abruptly increased) from the diamond samples over a temperature range of 720–850 K. We attribute the evolution of CO at the temperature region of 870–1150 K to the decomposition of ether (bridging oxygen) and ketonic groups. The TPD data allow us to attribute observed changes in the FTIR spectra of the ND sample (Figure 7.3) at a temperature range of 290–840 K.

**FIGURE 7.4**

TPD curves of CO, CO₂, H₂O, and H₂ gases originating from decomposition of the surface functional groups of pristine ND and submicron diamonds purified in a mixture of HClO₄ and H₂SO₄ (1:1) at 200°C. The temperature regions of decomposition of different oxygen- and hydrogen-containing surface groups of diamonds are presented [100].

Thus, decreasing the bands at 1700–1865 cm⁻¹ corresponds to the disappearance of C=O stretching modes in carboxylic groups, anhydrides, lactones, while the remaining peak at maximum heating temperature with a maximum at 1711 cm⁻¹ (Figure 7.3) belongs to C=O stretches in ketonic groups of the ND sample.

The thermal decomposition of surface groups provides an additional way for the regulation of their composition and modification of surface properties [53,97,105]. The full decomposition of surface groups in a vacuum or inert atmosphere results in the formation of bare diamond surfaces, which can reconstruct decreasing surface energy due to the closing of dangling bonds of surface atoms (see Section 7.5.1).

However, for ND particles the situation can be different. Barnard et al. [106] and Raty et al. [107] showed theoretically that bare {111} surfaces of an ND particle undergo deeper graphitization. A bare ND particle transforms to a more stable bucky-diamond particle that appears as an ND particle covered with nanometer-sized fullerene-like shells [106,107]. It was shown that further graphitization progresses from the surfaces of ND particles and leads to the formation of OLC [34,41,108–112]. The bucky diamonds appear as intermediates of the ND transformation to OLC.

7.3.3 Critical view of the formation of sp^2 -bonded carbon in pristine NDs

There is not a commonly accepted view on the nature of sp^2 -bonded carbon on the surface of ND particles. Since different authors used NDs from different vendors using different purification procedures and no uniform standard method of purification exists, experimental results on the presence of sp^2 carbon in pristine NDs differ significantly. Here, we briefly demonstrate the results obtained by different research techniques, which can be found in the literature:

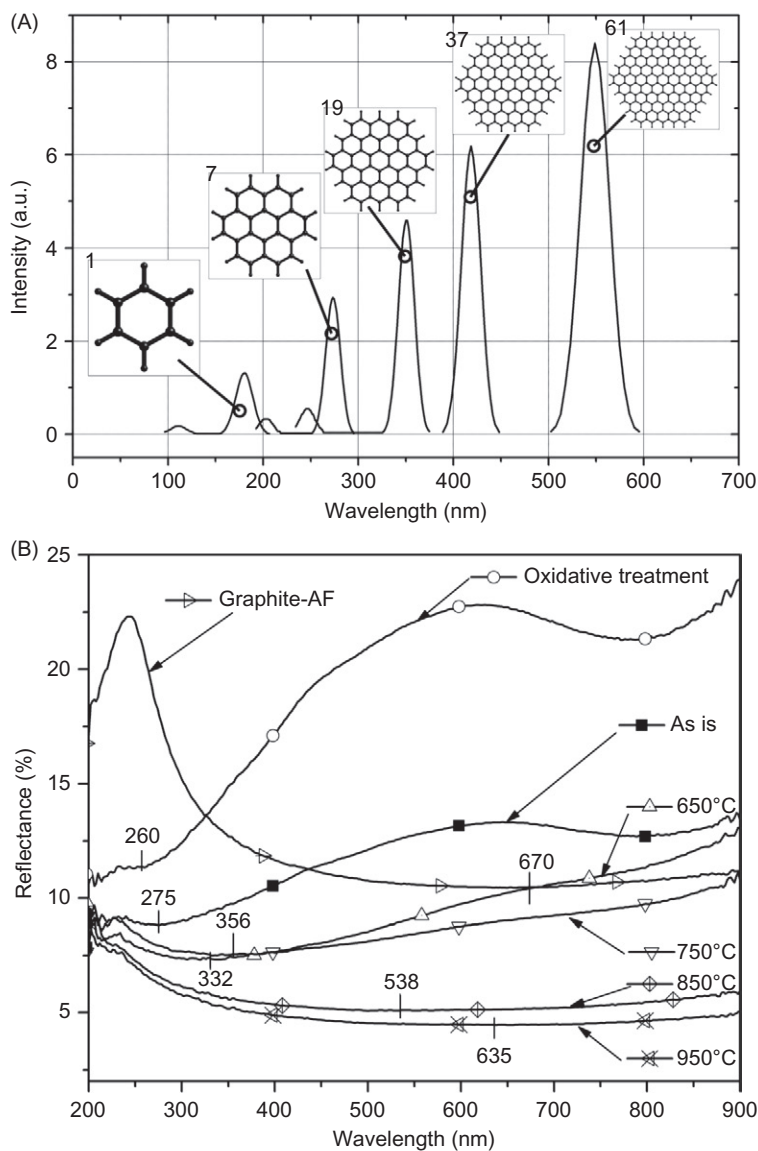
- *X-ray diffraction (XRD)*. The XRD analysis of ND samples performed in Refs. [111,113–115] revealed the presence of a small amount of disordered carbon. Tomita et al. [111] and Xu et al. [113] clearly showed in an XRD spectrum of an initial ND sample the presence of the {002} peak of graphite corresponding to small quantities of sp^2 -bonded carbon in pristine samples. However, Prasad et al. [116], Mykhaylyk et al. [112], and Qian et al. [117] did not observe features belonging to sp^2 -bonded carbon in XRD spectra of pristine ND samples.
- *Raman spectroscopy*. The sp^2 -bonded carbon in initial ND samples was observed by Yoshikawa et al. [118] (excitation at 514.5 nm); Tabata et al. [75] (excitation at 514.5 nm); Mykhaylyk et al. [112] (excitation at 244 nm); Aleksenskii et al. [114] (excitation at 488 nm); and Prasad et al. [116] (excitation at 514.5 nm). Obraztsova et al. [119] found no graphite features in the Raman spectrum of an ND sample (excitation at 457.9 nm).
- *Electron energy-loss spectroscopy (EELS), small-angle X-ray scattering (SAXS), and high-resolution transmission electron microscopy (HRTEM)*. An EELS study undertaken in Ref. [112] revealed about 40% of sp^2 -bonded carbon in an initial ND sample. SAXS modeling performed in this work also confirmed the presence of outer, less dense shells surrounding ND particles, which were attributed to amorphous carbon with mixed sp^2/sp^3 bonding. The presence of disordered graphite-like species on ND surfaces can also be observed by HRTEM [109,112,113,116].

These contradictory results can be understood if we consider limitations of these methods:

1. XRD is more sensitive to the presence of well-ordered materials (with a particle size more than 2–3 nm) and less sensitive to amorphous materials; thus the disordered sp^2 -bonded carbon cannot be observed if its concentration is less than 5–7%.

2. The Raman scattering cross section of diamond and graphite carbon strongly depends on the excitation wavelength used [118,120]. The Raman scattering cross section of diamond is about one-sixtieth that of graphite at an excitation wavelength of 514.5 nm [118]; therefore, the presence of even a negligible amount of sp^2 -bonded carbon significantly contributes to the Raman bands of graphite-like species. If Raman spectra of a carbon sample are measured by a shorter excitation wavelength close to the band gap of diamond (~ 5.5 eV, 225.8 nm), the detection sensitivity for the Raman band of diamond might become higher than that for graphite. It should also be considered that the laser radiation in a Raman spectrometer can result in local overheating of a specimen and can cause oxidation (in air) and even graphitization of an ND sample.
3. As mentioned above, the surfaces of ND particles after a purification procedure with oxidative agents are covered by a dense “coat” composed of various chemical groups. These groups stabilize ND surfaces and prevent them from graphitization. However, under electron bombardment (EELS, HRTEM) the decomposition of surface groups occurs [121–124] resulting in surface graphitization. The transformation of diamond particles to carbon onions under electron irradiation was demonstrated by Qin and Iijima [125]. Later, Roddatis et al. [126] also demonstrated that OLC formation from NDs can be activated by high-energy electron irradiation. Zaiser and Banhart [16] showed that irradiation at low temperatures (<580 K) and high temperatures (>1100 K) promotes the transformation from diamond to graphite, but at intermediate temperatures the reverse process can occur. Thus, conclusions from TEM data concerning the nature of graphite-like carbon on the surface of NDs should be accepted with care.

At the same time, diffuse reflectance UV–VIS spectroscopy (DRS) is one of the most sensitive methods of detection of sp^2 impurities on the ND surface. This technique, because of the possibility of collecting and measuring specular and/or diffuse reflectance, does not have the limitations typical of transmission spectroscopy when the latter is used for the characterization of powder samples. DRS was recently applied to characterize ND annealing at low temperatures at 300–950°C [127]. ND annealing at these temperatures was accompanied by the decomposition of surface group which stabilizes diamond surface [58] that caused the spontaneous transformation of unstable diamond surface into graphene flakes of the size 1–5 nm. Initially, these primary graphene flakes do not form conductive network. Thus, ND annealed at T below 900–1000°C are low conductive (bulk resistivity $>10^{12} \Omega\text{cm}$). Figure 7.5A(1) presents DRS of ND annealed at temperatures below 950°C. Pristine ND oxidized at 420°C to remove traces of sp^2 carbon demonstrates relatively high reflectivity. However, the increase of annealing temperature leads to systematic decrease of the reflectance accompanying with shift of absorption maximum into a low frequency spectrum range. Thus, the absorption maximum of ND annealed at 300–950°C shows a significant bathochromic shift from 250 nm, which is characteristic of pristine samples, up to 635 nm for ND annealed at 950°C.

**FIGURE 7.5**

(A) Absorbance spectra of polyaromatic molecules of different size calculated with semiempirical method ZINDO/S. [218]. (B) Diffuse reflectance spectra of ND (series DD) heated at 300–950°C in vacuum. DRS spectra of graphite AF is presented for the comparison [127].

This observation can be explained in terms of systematic growth of the size of graphene flakes up to the size comparative with the size of ND crystal planes of ND primary particles. In accordance with this observation, HRTEM data demonstrate the appearance of growing graphene planes of 1–5 nm (TITAN TEM with low accelerating voltage 80 kV was used to diminish graphitization diamond surface under electron beam). Absorbance spectra of condensed aromatic compounds with increasing number of aromatic rings are characterized by bathochromic shift (because of the π band's optical transition). Thus, Figure 7.5B demonstrates calculated absorbance spectra of polyaromatic flakes of different size. However, absorbance is growing in a wide region because of coexistence in sample of small graphene flakes of very different sizes. Thus, DRS may be used to develop a quality control method for sp^2 -carbon impurities in explosive NDs.

It can be concluded that the disordered sp^2 -bonded carbon can appear on surfaces of initial ND particles, but its presence and quantity evidently depend on the conditions of synthesis and purification of ND samples. The formation of sp^2 species on ND surfaces can be avoided by the hydrogenation of ND particles [128–130].

7.3.4 The onset temperature of ND graphitization

The thermal graphitization of detonation NDs has been studied by a number of authors. It has been carried out in vacuum [34,41,108–112], argon [73,113–116,131,132] and hydrogen ambient [133], and under high pressure [117]. The registered low-temperature onset of ND graphitization differs in different articles depending on experimental conditions and the research technique used. Thus, when graphitization was performed in argon ambient the changes in XRD spectra related to the appearance of sp^2 carbon were observed between 800°C and 1000°C [113,131]. Raman spectroscopy used in these two articles revealed that features originating from graphitic carbon become significant after annealing at 800°C. Xu et al. [113] used differential scanning calorimetry (DSC) in argon to find the temperature onset of ND graphitization. The onset of an exothermic peak at 670°C on a DSC curve was related to the initiation of ND graphitization. Qian et al. [117] studied the graphitization of diamond powders of different sizes at high pressures from 2 to 8 GPa. The onset temperature of 730°C for graphitization of 5 nm ND powder was estimated at 2 GPa with Raman spectroscopy data. However, Prasad et al. [116] did not observe features belonging to sp^2 -bonded carbon in the XRD spectra of an ND sample annealed at 900°C in argon.

It is difficult to explain the variation of the onset temperature of ND graphitization from 670°C to 1000°C found in these works. However, we should emphasize the removal of oxygen-containing reactive gases (O_2 , H_2O , CO_2 , CO , etc.) from a reaction vessel (reactor). The decomposition of oxygen-containing groups at a temperature range of 500–923 K results in a large evolution of CO and CO_2 (Figure 7.4) [95], which can affect the graphitization process. Thus, even small concentrations of these reactive gases can cause a decrease in the graphitization onset

temperature, increase the graphitization rate, and affect the structure of graphitization products (see Section 7.8).

Pristine ND nanoparticles often have a gray color. It should be noted that the color of a pristine ND sample can vary depending on the size of ND particles and their aggregates. Osawa [134] has observed the change of color of an ND colloidal solution (from gray to black) during milling of ND suspensions in water or organic solvents, which leads to a decrease in the size of ND particle aggregates. We observed a change of color of ND particles from gray color to the black color of pristine ND particles after heating at 900°C in a vacuum of 10^{-5} Torr for 1 h. HRTEM studies of this sample did not reveal the presence of well-ordered graphitic structures on its surfaces (see Section 7.5.5 and Ref. [108]). The surfaces of annealed ND particles mostly look uncovered after annealing in vacuum at this temperature. Note that TEM irradiation promotes ND graphitization (see Section 7.3.3); however, a short time registration can help to avoid significant surface graphitization of diamond. Prasad et al. [116] observed the change of color of an ND sample from the brownish to black appearance of the pristine particles after heating at 900°C in argon ambient for 3 h. However, these authors mentioned that HRTEM images after this heat treatment show large portions of unconverted diamond particles, while the surface seems to have been covered with portions of amorphous carbon with no clear long-range order. Thus, it can be concluded that the black color of ND samples does not necessarily portray their significant graphitization while the presence of small no interacting graphene-like flakes can be proposed after DRS study [127].

The absence of a pronounced sp^2 component at lower binding energy in the C1s photoemission spectrum (see Ref. [135]) of an ND sample annealed at 900°C in vacuum for 1 h also indicates that the annealing of NDs at these conditions is insufficient to produce appreciable graphitization. The sample remains as an insulator [136]. Partial graphitization of the sample, nevertheless, according to Raman spectroscopy and XRD data, [137] occurs. The graphitization can proceed only on bare ND surfaces. As the annealing temperature increases up to 1150°C (for 1 h), the HRTEM images reveal the formation of 2–4 curved graphite layers on surfaces of ND particles with sizes more than 2 nm [41,108] (see Section 7.8). The images demonstrate well-resolved interfaces between diamond cores and curved graphite layers adjacent to the diamond surfaces [41,108] (see Section 7.8). The HRTEM images show that the full graphitization of ND particles with sizes less than 2 nm occurs at these conditions, indicating significantly higher graphitization rates for small ND particles.

The experimental data discussed above allow us to conclude that the temperature of full decomposition of oxygen-containing groups (about 900°C) results in the reconstruction and only partial graphitization of ND surfaces in vacuum; however, at this temperature no well-ordered graphite-like structures can be formed on ND surfaces. The full unveiling of ND surfaces occurs at 900–1150°C with decomposition of hydrogen-containing groups resulting in the formation of several curved graphite-like shells on the surfaces of large ND particles (>2 nm), and full graphitization of small ND particles (<2 nm) with the formation of OLC particles

containing 2–3 fullerene-like shells (see Section 7.5.5). We believe that surface groups of NDs stabilize the ND particles. Upon complete removal of the surface groups, the surface carbon atoms become more mobile, which inevitably leads to the graphitization of NDs.

7.4 Kinetics of diamond graphitization

As mentioned earlier, in general, large diamond transforms into graphite at appreciable rates only at high temperatures ($T > 2000\text{ K}$). Classic quantitative studies of the graphitization of macroscopic size diamonds by Davies and Evans (hereafter DE) [138] were carried out in the temperature range 2150–2300 K. These researchers determined the rates of graphitization for the {111} and {110} faces as well as the kinetic parameters describing the rates. Under high vacuum conditions, the first steps of diamond graphitization are preceded by a rearrangement of diamond surfaces [139]. Because of the relatively low graphitization rates involved, Hoffman et al. [140] obtained quantitative data for the range 1500–1800 K only for a {100} surface exposed to ion etching. In this chapter, we consider the kinetics of ND graphitization in a low-temperature region (1370–2150 K). A detailed explanation of the experimental procedure and calculations can be found elsewhere [108]. In this section, we outline some of the main steps and results of this work in comparison with the results of other work devoted to diamond graphitization.

7.4.1 Experimental approaches for the study of ND graphitization

It is essential to note that investigations of the graphitization of diamond nanoparticles with sizes of 2–20 nm allowed us to carefully examine the structure of the starting material and products of their graphitization by HRTEM. A study of macroscopic objects (more than 1 μm in size) demands a special preparation procedure for the samples, while HRTEM was successfully applied for study of the graphitization of NDs [34,41,108] and submicron diamonds [36,141]. Another advantage of the use of nanoparticles is their high surface area compared to the surface area of macroscopic particles. Thus, graphitization starts from the surface of diamond particles, and even slight graphitization can be quantitatively measured, though it is difficult to perform in the case of macroscopic diamond crystals due to their low surface area. This allowed us to investigate ND graphitization in the lower temperature region (1370–1870 K) and to register directly the extent of graphitization.

Estimation of the diamond fraction in the intermediates of ND graphitization

The estimation of diamond fractions was performed by determining the densities of pristine NDs, partially graphitized samples, and fully graphitized samples [108]. Rather, this is facilitated by the large difference in the density of carbon in its diamond and graphite forms. Since, as noted earlier, graphitization proceeds from the

surface to the bulk, larger percentage changes in the density are observed in smaller particles than in larger ones. In small ND samples, a significant conversion from diamond to graphite-like carbon occurs within experimentally reasonable times in the temperature range of interest. The intermediates of ND graphitization are composed of two phases (sp^3 - and sp^2 -bonded carbon), in which both have the same molecular weight. Thus, the ratios of sp^3/sp^2 carbon can be calculated as

$$\frac{1}{\rho} = \frac{x_1}{\rho_1} + \frac{x_2}{\rho_2}, \quad (7.1)$$

where x_1 and x_2 are the weight fractions of the diamond and graphite-like carbon, respectively, ρ_1 and ρ_2 are their densities, and ρ is the average density of a sample, which is defined from the values of the volume and weight of the sample. The volume of samples was measured by a helium pycnometer (the measured ND density (ρ_1) was $3.07 \pm 0.02 \text{ g/cm}^3$ and the density of OLC (ρ_2) was $2.03 \pm 0.02 \text{ g/cm}^3$) [108]. The weight fractions x_1 and x_2 are related as

$$x_1 = 1 - x_2. \quad (7.2)$$

Taking into account experimental errors arising from density measurements, one can only estimate the sp^3/sp^2 ratio within the experimental error. However, according to the literature, the estimation of this ratio based on the density of a carbon material is often used and becomes useful when compared with results of other methods. For example, the authors of Refs. [142,143] used the following relation between the diamond fraction in amorphous carbon films and the sample's density:

$$x_{\text{diamond}}(\%) = (\rho \text{ g/cm}^3 - 1.92) / 0.0137, \quad (7.3)$$

where ρ is determined by EELS.

A comparison of the results obtained by Eqs. (7.3) and (7.1) is given in Table 7.2. The small difference in the values obtained by different approaches can be explained by the differences of carbon materials, namely, amorphous carbon in Refs. [142,143] and OLC ND in Ref. [108].

The kinetic model—the reducing sphere model

Since the graphitization of diamond starts from its surface and proceeds to the bulk, one goal was to determine a temperature-dependent isotropic rate of migration of the interface between the diamond and graphite regions of the particles [108].

Table 7.2 Comparison of Values of Diamond Fractions in Partially Graphitized ND Samples Obtained by Different Approaches

Annealing Temperature (K)	1420	1600	1800
Density (g/cm^3) (Ref. [108] and this work)	2.90 ± 0.02	2.53 ± 0.02	2.14 ± 0.02
Diamond fraction (Ref. [108] and Eq. (7.1))	0.86 ± 0.05	0.57 ± 0.05	0.15 ± 0.05
Diamond fraction (Refs. [141,142]; Eq. (7.3))	0.72 ± 0.02	0.45 ± 0.02	0.16 ± 0.02

For the study of ND particle graphitization the orientational effects of diamond graphitization were averaged. To achieve the goal we employed the reducing sphere model. The model assumes that the phase conversion begins simultaneously at all surface points and that under isothermal conditions the interface moves with a *constant isotropic rate (k) inside the bulk of the particle*. We also made the simplifying assumption that the particles are spherical. In the simplest case the initial diamond particles all have the same radius r_0 and weight M_0 . Then the graphitization of the surface diamond layers leads to a change in the diamond core radius, Δr , and a new weight of diamond M . The weight fraction x of the nongraphitized diamond can be expressed as

$$x_{\text{diamond}} = \frac{M}{M_0} = \frac{(r_0 - \Delta r)^3}{r_0^3}. \quad (7.4)$$

Thus, if the weight fraction x of the diamond at the end of the heating is known, the change in radius can be calculated. Further, to the extent that the sample was heated isothermally, one could relate the corresponding Δr to the rate of interface motion k and the time interval Δt by $\Delta r/k\Delta t$, and thereby determine k .

Finally, the size distribution of initial ND particles (determined by SAXS) was taken into account. The detailed calculations of the graphitization rates for this realistic case are presented elsewhere [108].

7.4.2 Kinetic parameters of ND graphitization for the temperature range of 1370–1860 K

Two temperature regions for diamond graphitization (1370–1860 K and above 1900 K)

Figure 7.6 presents an Arrhenius plot of the obtained ND graphitization rates (triangles in the figure) as a function of $1/T$, where T is the annealing temperature. We found the activation energy, 45 kcal/mol, in the lower temperature region (1370–1860 K), to be only roughly one-half the energy of one C–C bond in diamond, 87.3 kcal/mol. That suggests a graphitization mechanism in which the atoms do not completely separate from the surface but in which the outer diamond planes transform progressively into graphite planes. Our estimate of the graphitization activation energy is very close to that found for a {100} face that had been amorphitized by Ar ions (42 kcal/mol) [140]. The obtained activation energy for NDs agrees well with results presented in Ref. [117], which are 202, 206, and 214 kJ/mol (48.3, 49.2, and 51.2 kcal/mol, respectively) for diamond powders of average grain sizes of 5, 50, and 250 nm, respectively, for the temperature range of 1073–1673 K at a pressure of 2 GPa.

It was interesting to compare our data with those obtained by DE for temperatures ranging from 2150 to 2300 K [5,138]. DE determined the rates of graphitization of the {110} and {111} faces of macroscopic samples of diamond (mass ~0.02 g). Fitting those rates to the Arrhenius expression, DE found the activation energies for the {110} and {111} faces to be 176 kcal/mol (736 kJ/mol or 7.6 eV/atom) and

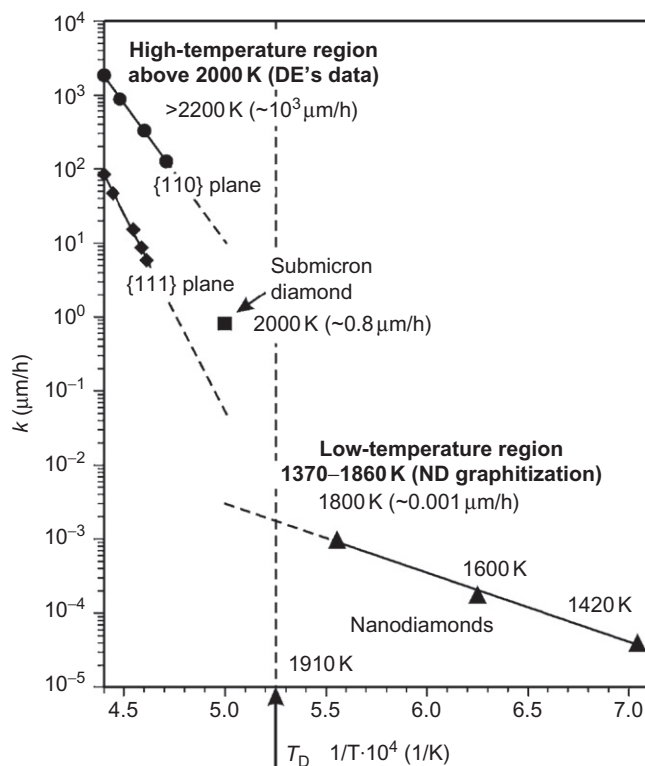
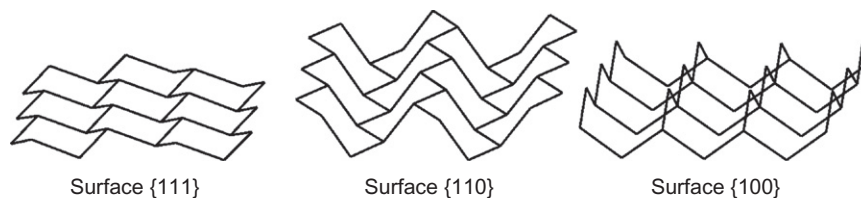


FIGURE 7.6

The rates of interface migration for the ND and submicron-sized particles (see Ref. [108]) and for the {111} and {110} faces of macroscopic diamonds determined by DE (DE's data; see Refs. [5,138]). The dashed lines are extrapolations of the Arrhenius expression fits to the low- and high-temperature rates. The Debye temperature for diamond, $T_D = 1910\text{ K}$, appears to serve as the boundary between the low- and high-temperature regions of diamond graphitization where the graphitization occurs by different mechanisms.

252 kcal/mol (1054 kJ/mol or 10.9 eV/atom), respectively. From measurements of the rates at elevated pressures, DE determined that the “activation volumes” for both surfaces are about $10\text{ cm}^3/\text{mol}$. In the DE model, it is taken in the account that the activation energies are high (close to the energy for the vaporization of diamond) and correspond to the breaking of the two C=C bonds for the {110} surface and the three C—C bonds for the {111} surface (see Figure 7.7), and that the activation volume is approximately equal to that for a single carbon atom in diamond. Based on these assumptions it was concluded that the process defining the rate of graphitization is the detachment of a single atom from the diamond surface.

We estimated the rate of the migration of the diamond–graphite interface to be $0.8 \pm 0.4\text{ }\mu\text{m/h}$ at 2000 K for submicron diamonds [108]. To relate our results for the

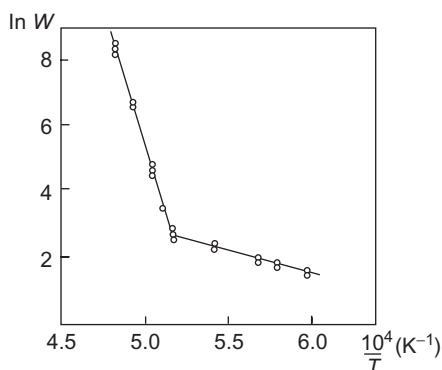
**FIGURE 7.7**

Fragments of different diamond surfaces.

rates, k , for the ND and submicron-sized particles to those of the DE model [5,138], we display both sets of results in Figure 7.6 over the extended temperature range of 1400–2400 K. The results of both models have been extrapolated up to temperatures around 2000 K using the Arrhenius fits at higher and lower T , respectively. It is seen that while the rate for the submicron diamonds lies well above the extrapolated rate for the NDs, it is within the range of values extrapolated from DE's rates for the {110} and {111} surfaces. This supports the conclusion that different graphitization mechanisms are operative at and above 2000 K and below 1800 K. The Debye temperature, $T_D = 1910$ K, can be taken as the boundary between the two regimes. We recall that at and above T_D , all modes of vibrations are excited [108].

Fedoseev et al. [7] studied graphitization kinetics on synthetic and natural diamond powders with particle size in the range 0.5–120 μm in a vacuum of 10^{-4} Torr. The authors found the existence of two temperature regions for graphitization, which have substantially different activation energies. It was shown that in the low-temperature region, up to 1900 K, the graphitization activation energy is 200 kJ/mol (47.8 kcal/mol), whereas in the high-temperature region it is 1200 kJ/mol (287 kcal/mol). Therefore, the mechanisms of the graphitization process in these regions are expected to be different [7]. Figure 7.8 shows the dependence of the specific graphitization rate on temperature in Arrhenius coordinates found in Ref. [7]. The temperature boundary of 1900 K between the two regions coincides fairly well with that found by us for NDs [108]. The graphitization activation energy for the high-temperature region approximately coincides with the activation energies found using the DE model. For the low-temperature region (below 1900 K), the activation energy of 200 kJ/mol (47.8 kcal/mol) is close to that of 230 kJ/mol (55 kcal/mol) for the oxidation of diamond found by Evans [5] and Uspenskaya et al. [6] (see Section 7.7). Therefore, Fedoseev et al. [7] concluded that there seems to be an influence of oxygen-containing compounds on the graphitization process in the low-temperature region.

Such an influence is discussed in Section 7.7. It is shown that oxygen- and hydrogen-containing gases participate in the carbon redistribution processes. These processes influence not only the observed graphitization rates but also the graphitization products. Enoki et al. [73,116,131] conducted graphitization of NDs in argon flow and found the formation of graphite nanoparticles, while graphitization of NDs at the same conditions but in a vacuum of 10^{-5} Torr resulted in the formation of

**FIGURE 7.8**

Dependence of the specific graphitization rate (l/l_0) on temperature in Arrhenius coordinates for diamond powder with a mean particle size of about $4\text{ }\mu\text{m}$. The specific graphitization rate was determined from the dependence of the amount of the graphite formed on time.

Reprinted from Ref. [7]. Copyright (1986) with permission from Elsevier.

OLC [34,41,108–112]. It is likely that argon, which was used in Refs. [73,116,131], could contain some impurities of oxygen-containing gases, causing graphitization to occur by a different mechanism (see Section 7.7). HRTEM images of ND graphitization products produced at different temperatures in vacuum [41,108,136] (see Section 7.8) with clearly observed intermediates of the ND transformation allow us to conclude that the derived activation energy of $E = 45 \pm 4\text{ kcal/mol}$ (188 kJ/mol) for the low-temperature region ($1370\text{--}1870\text{ K}$) corresponds to the activation energy of the graphitization process occurring through the direct transformation of sp^3 -bonded carbon to graphite-like carbon.

Absolute rates of ND graphitization

Rates of the diamond–graphite interface movement calculated from the derived kinetic parameters for various temperatures are presented in Table 7.3. One can see that at the onset of the low-temperature region ($1370\text{--}1860\text{ K}$) the rates of graphitization are very low, while small diamond particles $1\text{--}2\text{ nm}$ in size are easily graphitized even at 1420 K by 1 h treatment to produce $3\text{--}4$ curved defective graphite shells, whereas only $1\text{--}2$ graphite layers are formed on the surface of larger diamond particles. However, the contribution of the small particles to the kinetic results is negligible because, according to the SAXS data [108], the amount of small particles with radii below 1.0 nm in the ultradispersed diamond sample is about 0.5% by weight. Thus, the estimated rates of graphitization are also average rates. Obviously, there is a dependence of graphitization rates on sizes of diamond particles, and smaller ND particles graphitize at significantly higher rates. Qian et al. [117] observed differences in graphitization rates among nano, submicron, and micron diamonds.

Table 7.3 Migration Rates of the Diamond–Graphite Interface at Various Temperatures Calculated from the Kinetic Parameters for the Temperature Range of 1370–1860 K (Activation Energy of $E = 45 \pm 4$ kcal/mol and Pre-exponential Factor $A = 74 \pm 5$ nm/s) in Ref. [108]

TT (°C)	1373	1473	1573	1673	1773	1873
k (Å/h)	0.2	0.6	1.6	3.8	8.2	16.2

Raising the annealing temperature to 1800 K for about 1 h results in almost full graphitization of ND. The XPS study revealed the absence of sp^3 carbon in the sample and is consistent with our previous HRTEM data, which showed the absence of diamond structures in samples heated above 1800 K [135]. However, the data on the true densities and, thus, calculated graphitization rates of the ND annealing products indicate that this sample still consists of 15% diamond [108]. This discrepancy is explained by the presence of sp^3 -bonded carbon only in the core of the largest particles (of size up to 20 nm). The “screening” of these diamond cores by the surrounding graphite-like shells is the reason for the absence of the sp^3 -bonded carbon component in the C1s XPS spectra of the sample annealed at 1800 K (photoelectrons from the cores have a mean free path shorter than the thickness of the outer graphitic shells). Some particles may contain a small diamond core, which cannot be seen in the HRTEM micrographs because of their low contrast. It is probable that such cores are retained as a result of the high pressures existing inside the OLC particles. The existence of high pressure inside a graphitized particle at temperatures below the Debye temperature can be explained in the following way. As the graphitization proceeds from the surface and the outer graphite shells close, the OLC particle formed retains an excess of carbon atoms that could ultimately convert into graphite-like structures. Since at this temperature the external carbon layers cannot easily be rearranged and thus relieve stress, a pressure develops that is capable of stabilizing the diamond core. Banhart and Ajayan [12] reported on the formation of a diamond core inside the OLC when their samples were heated to 1270 K and radiated with an electron beam. Even annealing at higher temperature is sometimes not enough to convert all ND particles to OLC; Tomita et al. [111], using the XRD technique, revealed the presence of traces of sp^3 -bonded carbon in an ND sample annealed at 1700°C for 30 min at a pressure less than 2×10^{-3} Pa [110].

The HRTEM data indicate that the annealing of synthetic micron-size diamonds at 1890 K (see Figure 7.2B) in a vacuum for 1 h results in the formation of a graphite-like carbon layer 30–50 Å thick. This corresponds to the graphitization of a diamond surface layer 17–30 Å thick. The thickness of the diamond layer calculated with the kinetic parameters is equal to 18 Å (Table 7.3). The experimental and calculated rates of graphitization thus agree within the experimental error.

The direct measurement of sample density appears to be a reliable method for estimating the diamond fraction in a sample composed from two phases: sp^2 - and sp^3 -bonded carbon. This method allows estimation only of an average value of the

diamond fraction; therefore, derived values of graphitization rates do not reflect the dependence of the rates on sizes of diamond particles. However, the determined kinetic parameters yield graphitization rates that agree well with the HRTEM data related to the graphitization of submicron diamond. This suggests that the kinetic parameters of the ND graphitization can be used to estimate rates for the graphitization of larger diamonds. These parameters can help one control the modification of the diamond surface by the formation of fullerene-like carbon states on this surface.

7.5 Mechanism of diamond graphitization

7.5.1 Diamond surface reconstruction

The reconstruction of diamond surfaces has been the subject of numerous theoretical and experimental studies [3]. Surface reconstruction starts after the decomposition of surface groups. The motive force for the reconstruction of diamond surfaces is the saturation of the dangling bonds, which is induced by partial rehybridization of the surface atoms toward sp^2 [139]. The simple crystallographic planes {100}, {110}, and {111} correspond to the faces of the three major crystal forms of diamond: the {100} cubic, the {110} dodecahedral, and the {111} octahedral (see Figure 7.9). Both cubic and octahedral surfaces are predominant in high-pressure synthetic diamond and in CVDUNCD films. Twinning occurs frequently on the {111} planes. The diamond planes with different crystallographic indexes have different abilities for further transformation after surface group elimination. Among the ideal dehydrogenated and reconstructed diamond {100} surfaces, the most energetically favorable are dimers in two principal arrangements, namely, row and zigzag. The energies of the two are close to each other. The row dimer reconstruction has been observed experimentally [128,144–146] as well as zigzag steps [147], and confirmed theoretically [148].

There are some differences in the descriptions of the nature of C–C bonds of the reconstructed {100} surface. On the one hand, the minimum energy of a dehydrogenated {100} diamond surface was found to consist of dimers having biradical

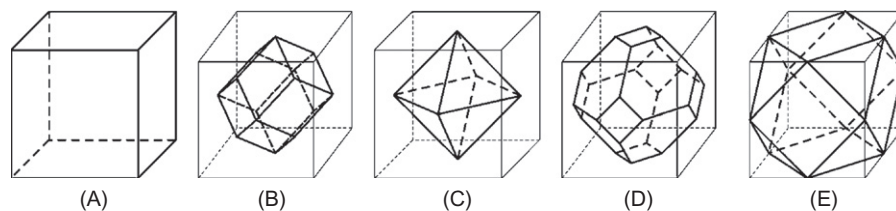


FIGURE 7.9

Shapes of diamond crystals and their surface planes: (A) cubic form {100}; (B) dodecahedral form {110}; (C) octahedral form {111}; (D and E) mixed forms with surface planes {111} and {100}.

structures (2×1 reconstruction). The reason the dimers have a single C—C bond as opposed to a double bond is the strain characteristic to other C—C bonds of the surface [148]. On the other hand, the $\{100\}$ surface reconstruction, as was proposed, is achieved by the formation of rows of π -bonded dimers giving a 2×1 reconstruction [149] with a bond length of $d = 1.37 \text{ \AA}$ comparable to that of a C=C double bond in a hydrocarbon molecule [150].

It is known that clean reconstructed diamond $\{111\}$ surface has an n-bonded chain structure, denoted as 2×1 [149,151–153]. Unlike Si or Ge, long-range reconstruction is absent in diamond $\{111\}$ [139]. Pate [128] confirmed the results of other researchers that upon annealing (up to -1270 K) a diamond $\{111\}$ surface reconstructs to a $2 \times 2/2 \times 1$ surface structure, which is accompanied by the formation of intrinsic surface states. Photon-stimulated ion desorption and EELS results indicate that very little, if any, hydrogen-bonded carbon exists on this reconstructed surface. The $2 \times 2/2 \times 1$ surface is therefore thought to be hydrogen free [128]. At complete or near-complete monolayer hydrogen coverage, the diamond $\{111\}$ surface transforms to a bulk-like structure [154–156], denoted as 1×1 . The hydrogen coverage has been found to control the transition between the two distinct structures [157]. The 1×1 structure readily reconstructs back to the 2×1 structure after complete removal of hydrogen by thermal desorption [128,158]. At intermediate hydrogen coverage, a transition state exists [156].

On the $\{110\}$ and $\{111\}$ surfaces, reconstructions lead to the formation of π -bonded chains with bond lengths of $d \sim 1.43 \text{ \AA}$ comparable to those in graphite. This requires a 2×1 reconstruction on $\{111\}$, while no reconstruction on $\{110\}$ is necessary [149]. The important difference is that for the $\{110\}$ surface, chain formation is compatible with the topology of the underlying lattice, whereas on the C $\{111\}$ surface the six-ring topology of the ideal diamond structure has to be replaced by alternating five- and seven-membered rings [159,160].

7.5.2 Cleavage energies of diamond planes

To consider the graphitization ability of different diamond surfaces it is reasonable to compare it to the cleavage energy of different planes because of the similarities of these processes. Theoretical cleavage energies along different planes were calculated using the fixed energy of a single C—C bond and a number of C—C bonds per square of specific plane necessary to cleave along this plane [161]. This provides a rather small energetic difference for the planes. However, cleavage of diamond occurs mostly along $\{111\}$ planes and significantly less frequently along the other planes. Quantum chemistry calculations allow better understanding of the preferential cleavage of diamond along $\{111\}$ diamond planes.

Kern et al. [162] and Shenderova et al. [163] estimated the cleavage energies of the low-index surfaces of diamond. It was found that the $\{110\}$ surface has the lowest cleavage energy. On the $\{111\}$ surface with one dangling bond (1db), where also only one bond per surface atom has to be broken, the cleavage energy is

0.66 eV higher. However, these authors showed that, as already emphasized in Ref. [159], simple bond-scission arguments are not appropriate for a reliable estimation of the cleavage energies. For the {111} and {110} 1 db surfaces, even a simple relaxation of the surface layer reduces the surface energy by an important amount, whereas for the multiple dangling surfaces a relaxation is energetically quite ineffective [162]. A reconstruction reduces the energies of the {100} and {111} surfaces by almost 50% so that finally the reconstructed {111} 1 db surface has the lowest energy and the {100} 2 db surface is only 0.46 eV/atom higher in energy than the {110} surface (which is stable in an unreconstructed state), in spite of a much larger cleavage energy.

Kuznetsov et al. [141], using the standard semiempirical method (MNDO), demonstrated that the binding energy between two layers in the {111} cluster is lower than that in {110} clusters (2.83 eV for the {111} surface and 3.93 eV for the {110} surface, respectively). They also studied the effect of surface relaxation on the interlayer binding energy. For this the top layers were allowed to relax during optimization of the geometry. For both the {111} and {110} surfaces, some flattening of the surface layer takes place. Despite the latter, the 1×1 periodicity of the top {111} layer remains unchanged. These authors [141] obtained a relaxation energy of 0.20 eV/surface atom for the {111} surface and 0.27 eV/surface atom for the {110} surface. The relaxation energy for {111} is gratifyingly close to the value of 0.17 eV/surface atom obtained by Jungnickel et al. [164] in a first-principles MD study. The very small difference between the two relaxation energies indicates that relaxation does not significantly alter the previously calculated difference between the binding energies for the {111} and {110} surfaces.

A difference between interlayer binding energies along the [111] and [110] directions seems to arise from the different “packing” of the interlayer bonds in the volume between the “parallel” planes [141]. For the {111} planes all such bonds are parallel, in contrast to those of the {110} planes. Thus, despite the fact that each “isolated” sp^3 C—C bond has the same energy in all diamond lattice directions, the interbond interactions depend on the orientations of the bonds with respect to each other. This interaction should be mainly repulsive in character, taking into account the relatively small average distances of about 0.25 nm between bonds and the fact that each bond is occupied by two electrons.

7.5.3 Shape of diamond particles

The shape of a diamond crystal is inherently related to the ability of different crystallographic planes to reconstruct, to graphitize, and to react with the environmental gases. As was observed by Evans [5], the graphitization rates of diamond crystallographic planes (GR_{hkl}) depend on the reaction conditions. For the high-temperature range (higher than 2000 K) [5] $\text{GR}_{110} > \text{GR}_{111} > \text{GR}_{100}$, while for the low-temperature range (1370–1860 K; see Section 7.5.2)

$$\text{GR}_{111} > \text{GR}_{110} > \text{GR}_{100}.$$

It is necessary to mention that the oxidation rates of diamond planes also differ significantly and decrease in the following sequence [5]:

$$OR_{111} > OR_{110} > OR_{100}.$$

In the case of detonation ND, due to the possibility of partial graphitization of primary diamond particles in such explosions during decreasing pressure and temperature, the faceting of the primary particles can occur. Furthermore, oxidative treatments used for ND elimination from explosive soot usually partially oxidize the diamond particles and lead to additional faceting of the particles with the most reactive faces in these conditions. Figure 7.10 illustrates the shape of ND crystals

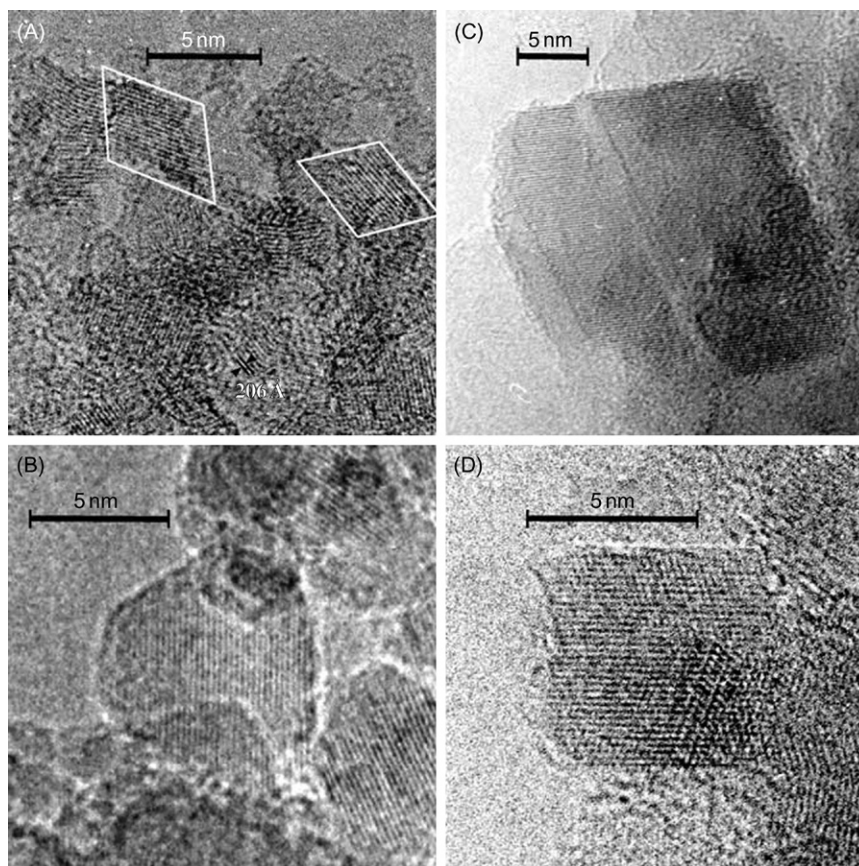


FIGURE 7.10

(A–D) HRTEM micrographs of initial ND particles with different shapes and sizes. The straight dark contrast lines in the micrographs correspond to the {111} crystallographic diamond planes. The distance between these lines is 2.06 Å. The frames in micrograph (A) outline the forms of two ND particles.

produced in explosive conditions. This shape is similar to that of microscopically sized diamond particles formed in the gas phase during a CVD process, as was first described in Ref. [165]. The typical habit of these clusters was regularly shaped cuboctahedral and twinned crystals, that is, a twinned cuboctahedron, an icosahedron, and a decahedral Wulff polyhedron.

7.5.4 Graphite–diamond interfaces

Two different types of graphite–diamond interfaces were registered by HRTEM [34,36]. The first type occurs when the diamond surface contains $\{111\}$ faces. It is well known that a $\{111\}$ layer of diamond consists of buckled hexagons and that their projected size on a $\{111\}$ plane is very close to that of the hexagons in graphite. The resemblance of the $\{111\}$ diamond planes to $\{0001\}$ graphite planes and, as noted earlier, the low cleavage energy of the $\{111\}$ surface lead to exfoliation of graphitic layers during graphitization from diamond $\{111\}$ surfaces. Figure 7.11 presents the exfoliated graphitic scales oriented parallel to $\{111\}$ diamond planes, while their edges merge to the diamond surface.

Another type of graphite–diamond interface occurs if less reactive planes facet diamond surfaces. In this case, the transformation of $\{111\}$ diamond planes is nevertheless the most reactive to graphitization. Using multibody potential

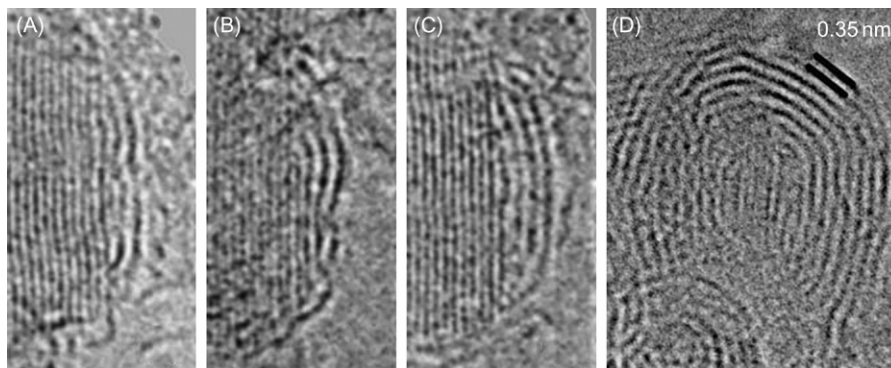
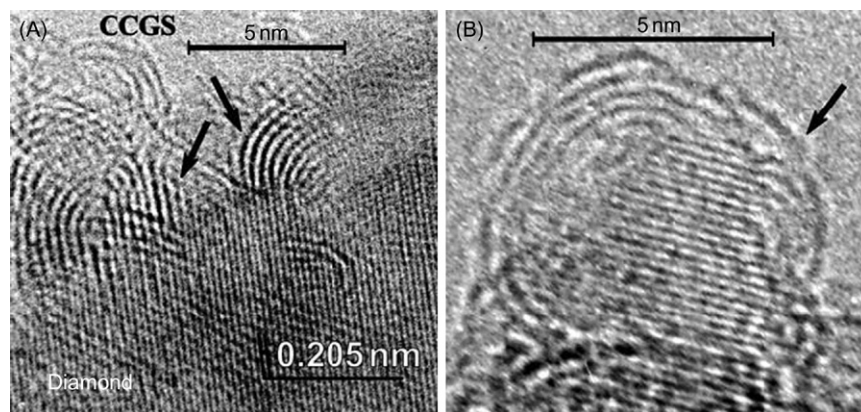


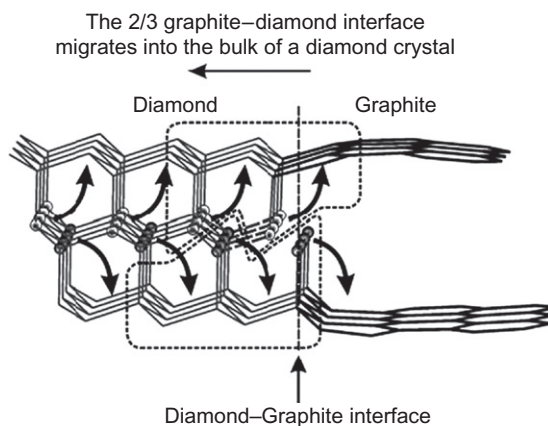
FIGURE 7.11

(A–C) HRTEM micrographs of three different ND particles at a very early stage of the transformation. Dark contrast parallel lines correspond to diamond $\{111\}$ crystal planes (the distance between the lines is 0.206 nm). Other curved lines correspond to graphite-like shells with the distance between them equal to 0.34–0.35 nm ($d_{002} = 0.3354$ nm for hexagonal graphite). The exfoliation occurs preferentially from the diamond $\{111\}$ surfaces. The exfoliated planes are seen to merge with the diamond surface and sometimes with each other to avoid dangling bond formation. (D) The formation of semi-closed graphite-like shells; a diamond core (4–5 diamond $\{111\}$ planes) is seen within nested nearly spherical shells [141].

**FIGURE 7.12**

HRTEM micrographs of the “diamond–graphite-like species” interfaces of diamond annealing products (vacuum of 10^{-5} Torr) on (A) a submicron diamond particle annealed at 1890 K for 1 h [141] and (B) an ND particle annealed at 1420 K for 1.44 h [41,108]. The formation of two graphitic sheets (arrows) from three {111} diamond planes are clearly seen.

calculations, Lambrecht et al. [166] demonstrated that the interface strain energy is minimized when three {111} diamond planes match up with two {0001} planes of graphite. A key idea behind this graphite–diamond interface model is that there is a 2/3 correspondence between the density of graphite and diamond. This points to a 2/3 relationship between the number of layers that meet at the interface between a {1100} graphite and a {121} diamond surface [164]. We have in fact found direct experimental evidence for the formation of the 2/3 interface [36,141] during the graphitization of micron-size diamond and ND (see Figures 7.2A and 7.12). Detailed quantum mechanical or MD calculations of the migration of the graphite–diamond interface into a diamond crystal for a cluster of adequate size are difficult. Consequently, we restrict our considerations here to geometrical aspects alone. As shown in Figure 7.13, we propose that as the 2/3 graphite–diamond interfaces migrate into the bulk of a diamond crystal, the atoms of the inner diamond layer should take part equally in the formation of both graphite sheets. Only in this way can one obtain the same lengths for the two growing graphitic sheets. Figure 7.13 shows that the process somewhat resembles the opening of a zipper. Each of the marked groups of atoms provides for the formation of an additional row of graphite sixfold rings. The process probably proceeds via successive insertion of two carbon atoms per 2 sixfold rings of a growing sheet with the intermediate formation and subsequent reconstruction of eightfold rings. However, this simple consideration does not take into account the shrinkage of graphene sheets along the 3/2 interface line as compared to the projection of a {111} diamond plane. It results in the

**FIGURE 7.13**

Zipper-like scheme in which three $\{111\}$ diamond planes transform into two graphitic sheets (2/3 interface) as the graphite–diamond interface migrates into the bulk of the diamond crystal. Each of the groups of atoms marked contains two rows of sixfold rings and one additional carbon atom per ring provides for the formation of an additional row of graphite sixfold rings [141].

formation of a rounded interface line, which could avoid the structural strain along the interface line.

It should be mentioned that the 2/3 graphite–diamond interface can be developed via primary exfoliation of several $\{111\}$ planes with the formation of fullerene-like caps because the bonds of the edges of their exfoliated graphene sheets merge with the diamond surface. Thus, successive exfoliations of several $\{111\}$ planes lead to the progressive decrease of the diameter of the internal contacting $\{111\}$ diamond plane and the formation of multicap structures. Further development of these structures produces mosaic-like structures consisting of multiwall carbon nanotubes (see Section 7.5.6).

7.5.5 Formation of nanocarbon species via “low”-temperature diamond graphitization

Previously, we have demonstrated that thermal diamond graphitization is initiated after the removal of oxygen- and hydrogen-containing surface groups stabilizing the diamond surface. Surface reconstructions follow the elimination of the surface groups. Further graphitization depends on the diamond particle size and indexes of a surface crystallographic plane. Thus, the formation of OLC is observed from the NDs with a size less than 5–6 nm; closed polyhedral particles can be produced from the NDs with a size of 7–15 nm, while closed curved graphite-like structures form on the surface of micron-sized diamond.

Initially, we consider the graphitization of NDs leading to the formation of OLC and then the formation of closed curved graphitic structure (CCGS) on the surface of micron-sized diamond.

Model of ND annealing and formation of OLC structure with holes

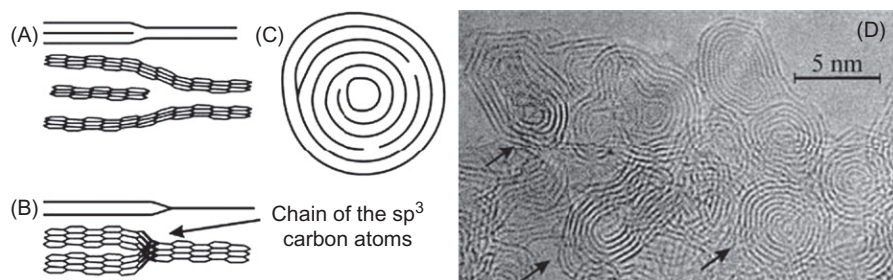
Figures 7.1 and 7.11 present HRTEM images of intermediates of ND annealing products, providing the following conclusions on the most significant features of ND annealing:

- ND graphitization under annealing moves from the surface toward the crystal bulk.
- The transformation rate of the {111} diamond planes to graphite-like sheets is higher than that of other planes.
- The edges of exfoliated graphite-like sheets merge with the upper untransformed diamond planes.
- The distance between the inner graphite-like sheet and the upper untransformed diamond layer does not exceed 0.35 nm, indicating an interaction between the diamond and graphite layers.
- Closure of the fullerene-like shell occurs generally after complete transformation of the diamond core of the particle (Figure 7.11D).

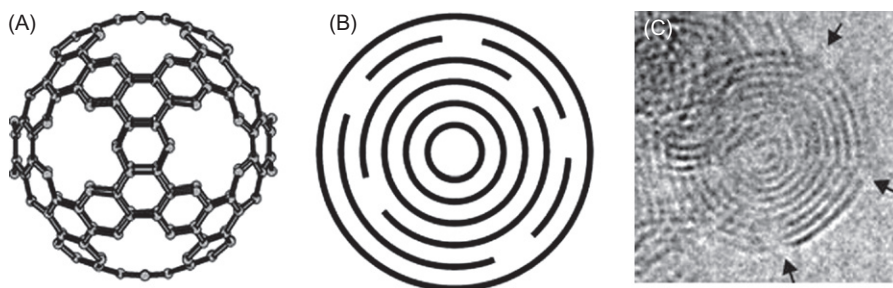
The graphitization of diamond particles depends on the size of the particles. Specifically, the graphitization of very small particles ($d \sim 2$ nm), which have a higher surface energy and contain many surface defects, starts at lower temperatures (1150–1300 K) than those for larger particles. In the case of the annealing of NDs ($d \sim 5$ nm), the curling and closure of nanometric graphite shells and the formation of OLC are explained in terms of elimination of dangling bonds (relating to the difference in the surface energies of the graphite basal plane, 0.135 J/m^2 , and of the high-index {101} and {112} planes located on the edges of the basal planes, 4.8 J/m^2) [167]. Closure of the graphite shells thus provides a significant decrease in the surface energy of the carbon particles. It is necessary to mention that ND graphitization at relatively low temperatures (1400–1600 K) results in a highly defective OLC structure. This means that ND graphitization and the closure of graphite-like shells proceed independently. Several examples of possible defects in the OLC structure are presented in Figure 7.14.

Another principal fact concerns the formation of holes in fullerene-like shells (confirmed by X-ray emission spectroscopic characterization of NDs produced at temperatures lower than 1900 K [168]; see Figure 7.15). At the same time, Raman spectroscopy studies allow us to conclude that some portion of the OLC has the structure of ideal carbon onions [119]. Using higher annealing temperatures (higher than 1900–2000 K) leads to the formation of material consisting of closed, polyhedral, hollow nanographite particles, which have no hole defects and do not contain ideal onion-like structures.

Based on these results, a mechanism of OLC formation via ND annealing can be suggested as follows. At the first steps of ND annealing, curved graphite-like

**FIGURE 7.14**

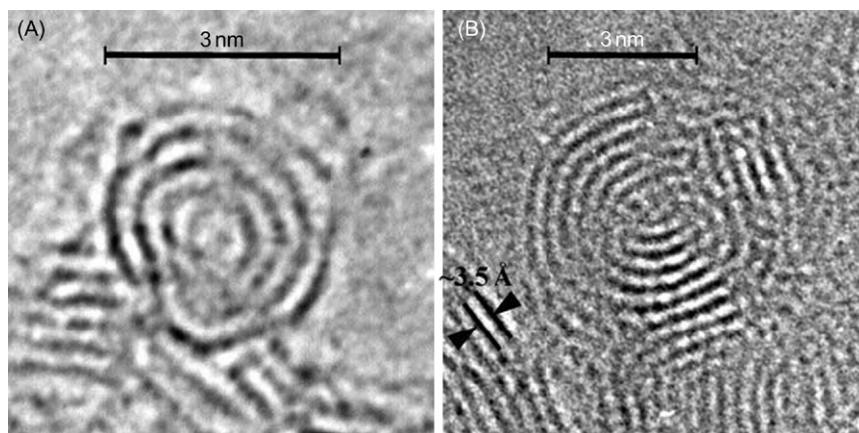
Defects in OLC particles produced by annealing of ND: (A) an interstitial plane between two basal planes [10]; (B) “Y” junction of two basal planes into one plane; (C) a schematic of a spiral-like structure having an interstitial plane between two basal planes; and (D) an HRTEM image of OLC produced from ND [34]; curved lines correspond to graphite-like shells with the distance between them equal to 0.34–0.35 nm. The arrows on the figure show the proposed locations of the “Y” junctions. The interstitial planes and holes are difficult to observe due to their low contrast on HRTEM images.

**FIGURE 7.15**

(A) Spherical cage C_{180} with holes obtained by removing 12 pentagons from C_{240} [168]; (B) scheme of a holed-OLC particle [168]; (C) an HRTEM image of an OLC particle produced by annealing of ND at 1900 K for 1 h in vacuum of 10^{-5} Torr; curved lines correspond to graphite-like shells with the distance between them equal to 0.34–0.35 nm. Irregularities in the micrograph of the OLC particle (shown by the arrows) are likely caused by holes in the fullerene-like shells or spiral-like structure of the OLC particle.

sheets are formed and exfoliated from the diamond particles (Figure 7.10). Merging of these sheets leads to the formation of spiral-like multishell particles (Figure 7.16) and finally OLC forms.

Preliminary consideration provides an understanding that the transformation of the most tightly packed diamond {111} plane to the {0001} graphite one is accomplished by shrinkage along the graphitic network. At the same time, transformation of ND to OLC leads to a dramatic increase in particle volume (compare the

**FIGURE 7.16**

(A and B) HRTEM micrographs of spiral graphite-like particles produced by the annealing of ND. The dark lines in the micrographs correspond to the {0002} crystallographic graphite planes. The distance between these lines is $\sim 3.5 \text{ \AA}$.

densities of graphite and diamonds, 2.265 and 3.515 g/cm^3 , respectively). Thus, one can conclude that the number of surface carbon atoms of the pristine diamond particle is not sufficient to form the perfect closed fullerene-like shell. Thus, the cuboctahedral diamond crystal (2.14 nm between $\{n00\}$ planes), composed of 1683 carbon atoms, has 530 surface atoms. The cubic diamond particle of the same size, having 1963 atoms, has 434 surface atoms. At the same time, a perfect OLC particle (of size 2.814 nm) composed of four fullerene shells, containing 1800 carbon atoms, has 960 surface atoms. Thus, the lack of carbon atoms should be compensated by the capture of carbon atoms from the edges of the inner layers or lead to the formation of hole defects in the graphite-like shells.

To elucidate the reasons leading to the formation of holed-OLC structure, modeling of ND annealing has been performed. A DFT study of annealing small ND clusters has been undertaken [46,107]. However, in these articles, due to the limitation on the numbers of atoms in a model, the size of diamond clusters was not large enough to understand the mechanism of defect formation. We have used a combination of MD calculations, which use forces computed by standard semiempirical quantum mechanics (MNDO, AM1, PM3), to model the surface reconstruction of small diamond clusters followed by molecular mechanics (MM) modeling of intermediate products of annealing large diamond clusters. In the latter case, the initial ND cuboctahedral cluster contained 4490 carbon atoms. Figure 7.17 shows the principal results of the MD study of the annealing of bare $\{100\}$ and $\{111\}$ diamond planes. One can see that annealing of the $\{100\}$ plane results in a 2×1 surface reconstruction stable up to very high temperatures (1500 K), while in the case of a cluster with $\{111\}$ planes, graphitization occurs at low temperatures. This is in good agreement with

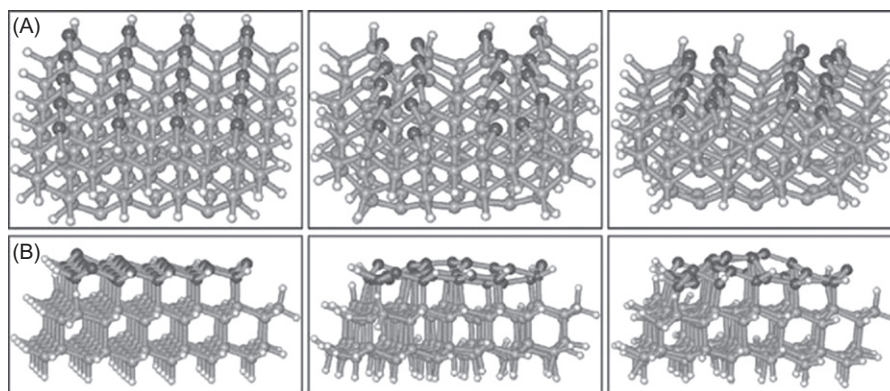


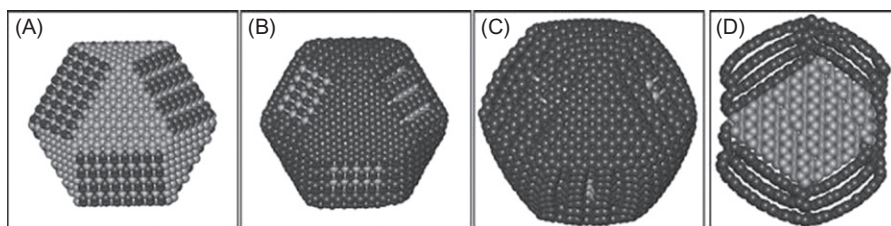
FIGURE 7.17

Results of MD simulations using standard semiempirical method PM3 for the study of annealing of diamond clusters with bare surfaces of different crystallographic planes [96]. Surface carbon atoms are marked in black, and white atoms are hydrogens stabilizing the diamond framework: (A) reconstruction of {100} planes (2×1 structure observed even at 0 K, stable up to 1500 K); (B) successive graphitization of {111} planes with exfoliation of {0002} graphitic planes (graphitization begins after 0.4 ps and 150 K).

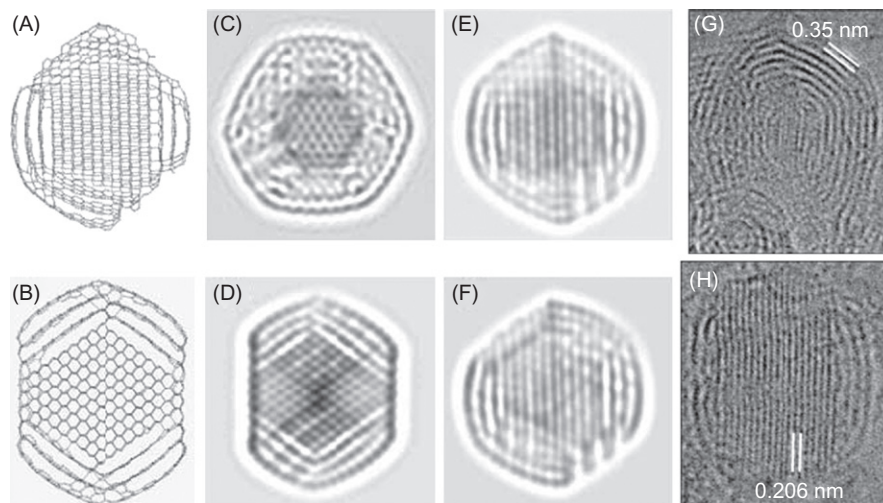
experimental results [128] and computer simulations of diamond cluster annealing. Thus, for the cuboctahedral cluster surface the reconstruction of the {100} surface and “buckification” of the {111} surfaces was proposed [169].

We have used results on the relative stability of different diamond planes to construct a sequence of MM models reflecting the successive steps of graphitization of an ND particle. In agreement with our experimental data and MD simulation, the diamond transformation occurs mainly via graphitization of {111} planes. At the same time, reconstructed {100} planes graphitize only at the cross sections with transformed {111} planes (see Figure 7.17). One can see the deficit of carbon atoms required for the formation of perfect closed fullerene-like shells at the interface of reconstructed {100} planes where the produced graphene shells merged with each other (Figure 7.18).

The comparison of the model electron microscopy images calculated using the MM model provide very reasonable agreement with experimental ones (see Figure 7.19). Thus, one can see that graphene-like sheets initially form after transformation of {111} planes. The merging of graphene sheets leading to OLC formation experiences a high deficit of carbon atoms in the regions of pristine {100} planes and likely leads to the formation of hole defects in OLC shells. Annealing of these holes starts only at temperature higher than 1800–2000 K due to the higher mobility of carbon atoms at these temperatures. In fact, we have observed the formation of hollow onions and annealing defects after heating OLC at temperatures higher than 1900–2000 K. Thus, the origin of defects accompanying OLC formation can be explained in terms of the deficit of diamond carbon atoms

**FIGURE 7.18**

MM models of the successive graphitization of a cuboctahedral diamond cluster [96]. Black atoms correspond to carbon atoms involved in graphitic shells and reconstructed diamond planes. (A) {100} planes only reconstructed into 2×1 structures; (B and C) graphitization occurs via the transformation of {111} planes: one in case (B) and three in case (C), respectively; (D) a cross section of the particles in (C): one can see three graphitic layers around the diamond core. The particle volume is increased due to formation of graphitic scales with decreased density.

**FIGURE 7.19**

The comparison of the MM models (A and B) of the partially graphitized diamond particle previously presented in Figure 7.17 and their electron microscopy images (C–F) calculated after the orientation of the model at different angles of the electronic beam. (G and H) HRTEM micrographs of intermediates of ND annealing products [96]. (The electron microscopy images were obtained and calculated by Dr. A.L. Chuvilin.)

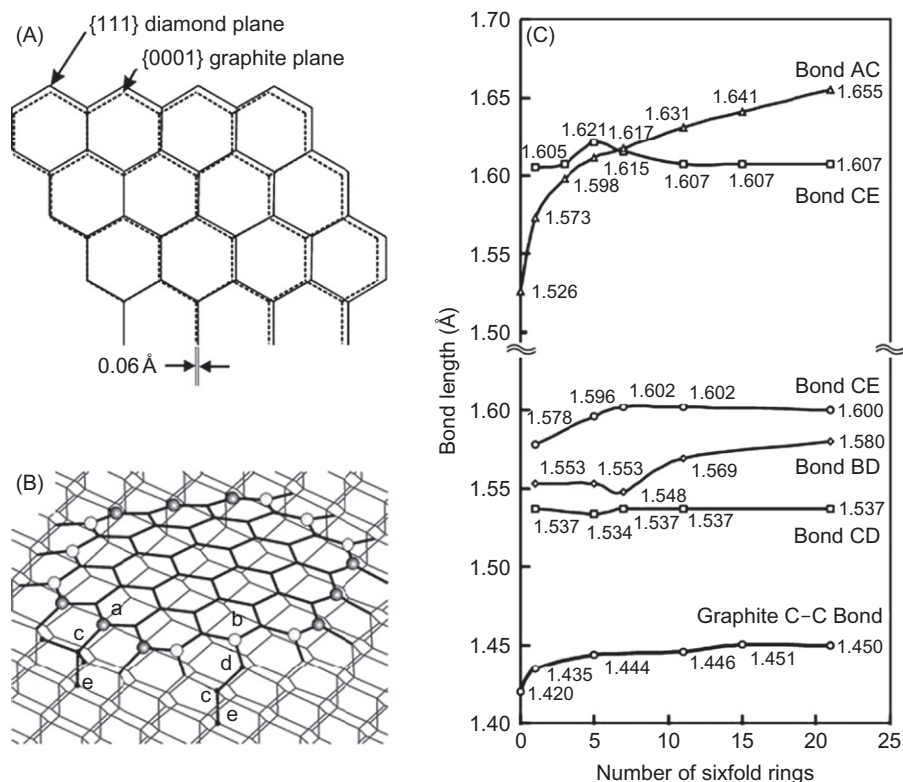
in the graphite–diamond interface to form perfect fullerene-like shells. However, it should be mentioned that a detailed mechanism of merging local graphitic flakes into closed fullerene-like shells is not clear. It can be assumed that such a mechanism would be similar to that of defect annealing in graphitic materials. So far two

mechanisms of defect annealing have been discussed in the literature [10], namely a migration of carbon interstitials and a vacancy healing through the dangling bond saturation effect resulting in the formation of nonhexagonal rings and Stone–Wales defects [170].

7.5.6 The formation of CCGS on the surface of micron-size diamond

By varying the temperature of the annealing process of submicron diamonds (synthetic submicron diamond ASM 0/1) [36], we have succeeded in preparing samples in which the intermediates of the diamond to graphite transformation are detectable [36,141]. Figures 7.2A and 7.11 show the interface between the diamond and the growing graphite-like structures. One can see that the direction of {0002} graphite planes coincides with that of the {001} diamond plane with the 2/3 relationship between the number of layers of graphite and diamond, respectively. At the interface between the diamond and the evolving graphite, the formation of two curved graphitic sheets from three diamond planes occurs. Sometimes, on the edges of the diamond particles, we could observe that the images of the closed graphite-like structures overlap each other (Figure 7.2A). The latter indicates that these structures have a limited thickness. So the observed curved graphitic sheets presumably form closed structures, e.g., caps, folds. Actually, a top view of the closed structures shows that they form a mosaic structure (MS) on the diamond core (Figure 7.2B). The lengths of the growing folds do not exceed 5–7 nm and short folds appear to form closed multilayered caps. The annealing of diamond in the multicap regions can lead to splitting of the particle surface and the formation of divergent tubular-like or fold structures.

Graphitization can be initiated at the surface defects. It was found that stepped {111} surfaces are graphitized spontaneously [171]. Spontaneous graphitization near a twin core has also been proposed in Ref. [164]. MD studies [164,166] lead to the conclusion that graphitization is strongly facilitated by any kind of surface perturbation or roughness such as step-like adsorbates. We found that diamond annealing leads to the formation of CCGS such as OLC (for ND) [34,41,108], nanofolds, and nanotubes (for micron-sized diamond) [36,141]. A partial explanation of the self-assembling formation of these structures is discussed below. The most difficult problem concerns the formation of CCGS on samples with dimensions larger than 20–40 nm. Additional factors rather than those for the small particles are involved. We first consider how the “blistering” of a single graphitic segment leads to a saucer-like structure on a diamond surface. As noted above, graphitization is expected to be initiated at a surface imperfection (e.g., at a step or defect). One essential point to note is that the graphite segment is in a state of tension. This is because the width of the sixfold graphite ring is 0.006 nm less than the projection of a diamond sixfold ring on the graphite basal surface (Figure 7.20A). Thus, 10 graphite rings are characterized by a 0.06 nm “shrinkage,” an amount which, if concentrated in a single bond, is more than enough to break it. Additional stretching is produced by the formation of curvature at the contacts between the diamond surface and the exfoliated graphite sheet due

**FIGURE 7.20**

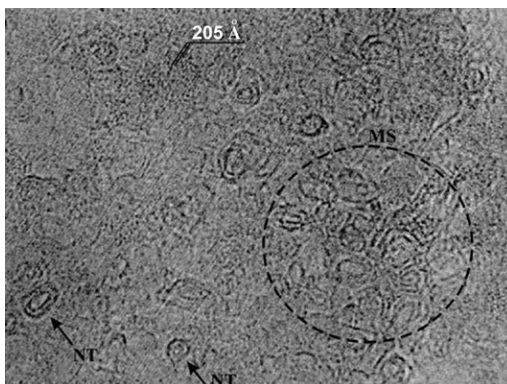
MM (MM⁺ force field) modeling of the initial stage of the formation of a graphitic structure on a diamond surface: (A) comparison of the projections of the {111} diamond and {0001} graphite planes; (B) model of an exfoliated {111} plane as a symmetric six-angle sheet. There are two different types of bonding of the sheet to the diamond surface as indicated by the bondings of the atoms labeled a and b on the edges of the sheet; (C) dependence of the lengths of the relevant bonds indicated in (B) on the size of the exfoliated graphite sheet (number of sixfold rings across). The lowest curve is a typical bond length well within the free graphene sheets of different size [141].

to the increased distance between the diamond surface and the delaminated graphite shell. To obtain fairly detailed and quantitative information about the exfoliation of a graphite sheet from a diamond surface, we have performed MM simulations (MM force field) [141] on several model structures. The results for one of them are presented in Figure 7.20B. It is found that the average carbon–carbon bond length along the exfoliated network is 0.146 nm. This should be compared to the 0.140 nm bond length given by a MM simulation of a relaxed separated graphite sheet, the value of which is somewhat lower than the measured value of 0.142 nm. At the same time, the calculated distance between the diamond surface and the graphite sheet is found to

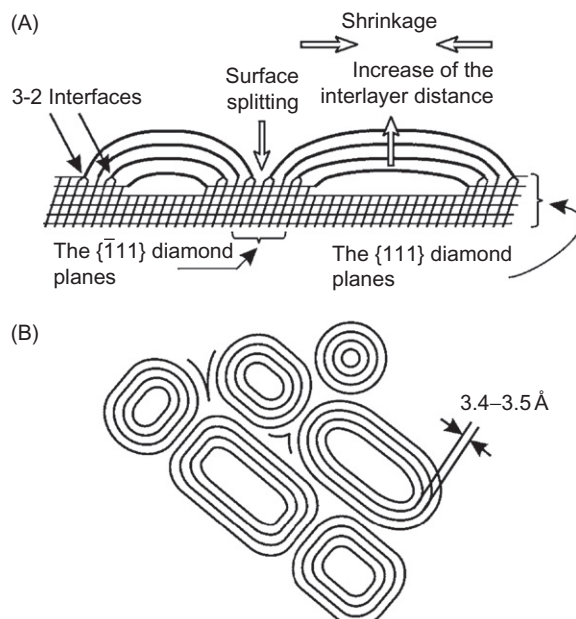
be -0.32 nm, which is slightly lower than (but still reasonably close to) that found experimentally (0.34 – 0.35 nm) [34]. We note also that when the tension is reduced by detaching one side of the graphite sheet, the calculated distance between the sheet and the diamond surface rose to a value of 0.34 – 0.35 nm. These results together show that an attached exfoliated graphite network is appreciably stretched. As we will see, this stretching can lead to the breaking of a bond between neighboring surface carbon atoms (not the breaking of a bond between the surface layer and diamond bulk) and to the formation of a saucer-like structure. These breaks tend to create mono-atomic steps on the diamond surface. Graphitization is then initiated at these steps. This process ultimately leads to the formation of a mosaic of plates separated by interatomic distances.

To provide more detailed insight into the behavior of the exfoliated graphitic sheets, we focus on the nature of the CC bonds at the edges of the sheets. In our model, in accordance with our experimental data, we keep the graphitic sheet merged with the diamond surface. In our simulations, we consider a symmetric six-angle sheet (Figure 7.20B). It turns out to have two different types of interfaces. In the first, each edge graphite atom (A) is directly bonded to a surface diamond atom (C), which in turn is attached to the internal diamond atom (E). In the second type, each edge graphite atom (B) is attached to a border atom (D), which is bonded with two surface diamond atoms (C), which in turn are attached to the internal diamond layer. We have carried out MM studies of a number of such sheets of various sizes, which are characterized by the number of sixfold rings across the structure at its widest extent. In Figure 7.20B, for example, the number of rings across the structure is five. These calculations yielded the lengths of the various bonds involved as a function of the size of the sheet. The results are displayed in Figure 7.20C, where the results for the bonds along the edges in the *A* and *B* “directions” are separated for clarity. Also shown, for reference, is the bond length for a sixfold ring well within the sheet. The most relevant feature of these results for our purpose is the monotonic growth of the “*ac*” bond and the fact that for *eight or more rings* this bond becomes significantly longer than the others. This indicates that the bond is clearly the one most likely to rupture. Breaking of the bond will be followed by the bonding of the “*a*” graphite atom to an internal diamond atom under the graphitic sheet to eliminate its dangling bond. This process will lead to the formation of a closed plate-like structure and, in addition, to a mono-atomic step. It seems reasonable that the rupture of the atomic surface layer will occur roughly around 8–10 rings or so, i.e., for sizes of about 2.0–2.5 nm. This is in reasonable accord with our experimental work, where structures ranging from 1 to 4 nm have been observed [36,141]. This agreement, along with that for the distance between the graphitic sheet and the diamond, suggests that the model and calculations are reasonable.

Above, only the initiation of CCGS formation has been simulated. The HRTEM results in Figures 7.2B and 7.21 show that the structures are generally multiwalled (or “multicapped”) and grow to heights significantly greater than -0.3 nm. Further surface graphitization results in the formation of mosaic-like structures consisting of tightly packed multiwalled nanotubes. This is shown schematically in Figure 7.22.

**FIGURE 7.21**

HRTEM micrograph of annealing products on a $\sim 1\text{ }\mu\text{m}$ diamond particle ($T = 1500\text{ K}$, 3 h , $P = 10^{-5}\text{ Torr}$). Top view of several surface carbon nanotubes (NT) and the MS of carbon nanotubes. The straight dark contrast lines, which can be seen in the micrograph, correspond to the $\{111\}$ crystallographic diamond planes with a distance between them of $2.05\text{ }\text{\AA}$ [141].

**FIGURE 7.22**

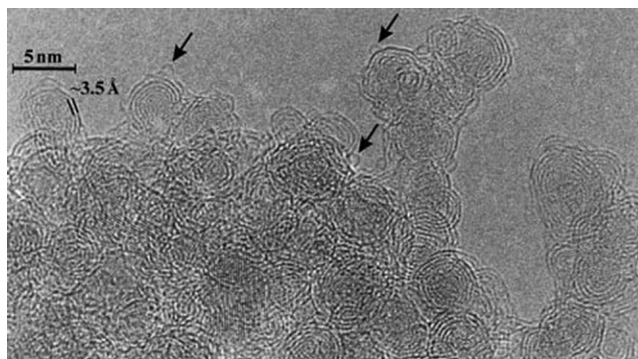
(A) The scheme of closed, curved graphite structure formation. The shrinkage along the graphite network and simultaneous increase of the distance between graphite sheets results in the surface splitting and formation of nanotubes. The arrows show the 2/3 graphite–diamond interfaces migrating into the bulk of a diamond crystal. (B) Top view of nanotubes. The closed packing of nanotubes results in the formation of MS [36].

The exfoliation of succeeding layers is expected to proceed with the formation of the 2/3 graphite–diamond interface discussed above. The “extra” atoms provided to the two graphitic layers by the third diamond layer allow for the extension of the caps. Ultimately, the multicap structures can, in turn, grow into nanotubes attached to the diamond surface.

7.6 Catalytic graphitization of NDs in the presence of metal clusters

It is not surprising that metals interact with carbon presenting in diamonds. Earlier work devoted to the interactions of macroscopic diamond with metal and metal oxides was reviewed by Evans [51]. Characterization structure and electron properties of diamond–metal interfaces are important, since differently doped diamond substrates are p- and n-type semiconductors and are of interest for diamond-based electronics [172]. Evans distinguished the following types of chemical interactions of diamond with metals: carbide formation, redox processes involving diamond carbon, and catalytic graphitization. We believe that metal–carbon interactions can be generally described in terms of metal–carbon phase diagrams, which reflect the principal possibility of a specific metal dissolving carbon in its volume with the formation of metal–carbon solid solutions or metal carbides. Thus, chemical interaction of metals with diamond occurs at sufficiently high temperature, so that carbon from diamond can migrate into the metal and, according to the metal–carbon phase diagram, form metal carbide phases (e.g., with the following metals: Al, Fe, Mo, Ta, Cr, Ti, Mn, V) [51] or metal–carbon solid solutions (Ni, Co) [4]. Carbon presenting in diamond reduces partially or completely metal oxide films deposited on its surfaces [51]. Evans described the catalytic graphitization of diamonds involving first detachment of carbon atoms from diamond surfaces, then their transport through the metal film in interstitial sites, and finally their re-precipitation at the interface with a vacuum as the thermodynamically more stable graphite. The temperature of the onset of catalytic graphitization decreases compared to one of uncatalyzed graphitization [51]. Thus, catalytic graphitization in internal diamond surfaces surrounding nickel inclusions in synthetic diamond was described [51]. Onset of this process occurred at about 800°C. Other interesting examples of catalytic diamond graphitization were reported by Pantea et al. [173] who observed internal graphitization of synthetic diamonds also caused by metal inclusions. Another example of the interaction of metals with condensed carbon was manifested by the Ni- and Fe-catalyzed hydrogen etching of the diamond. These reactions can be used for different kinds of diamond treatment such as polishing and drilling [174].

In this chapter, we consider the catalytic graphitization of NDs in the presence of metal nanoparticles of iron and cobalt. The purpose of this work was to explore the influence of the metal particles on the ND graphitization process, especially in those cases when the sizes of metal particles were less than, comparable to, or more than the sizes of ND particles.

**FIGURE 7.23**

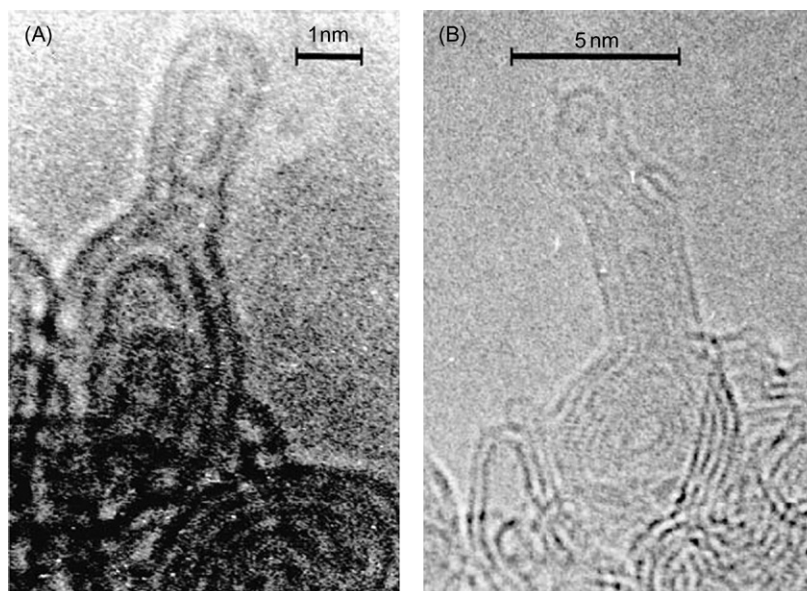
HRTEM images of ND particles annealed at 1420K for 1 h in a vacuum of 10^{-5} Torr in the presence of iron nanoparticles (1–1.5 nm, mass% 12) [175]. Iron nanoparticles are not seen on the image due to their small size and, therefore, low contrast. Dark contrast parallel lines and curved lines correspond to diamond crystal planes and graphite-like shells, respectively. The distance between lines corresponds to the {111} lattice parameter of ND ($d_{111} = 0.2063$ nm) and between curved lines to the distance between the graphite-like shells (0.34–0.35 nm). The arrows demonstrate small graphitic “caps” appearing only during annealing in the presence of the iron nanoparticles.

A detailed explanation of the experimental procedure for the preparation of metal particles on ND surfaces and the investigation of the catalytic graphitization effect can be found elsewhere [175]. In this section, we describe only the main results of this work. The iron particles were deposited on ND particles from the vaporization of iron pentacarbonyl ($\text{Fe}(\text{CO})_5$); cobalt particles were also deposited on diamond surfaces from solutions of cobalt acetates. These approaches allowed us to deposit metal particles with a variety of sizes on ND surfaces.

Figure 7.23 presents the HRTEM images of products of the ND annealing in the presence of the deposited iron nanoparticles. The formation of small “caps” (less than 1 nm) (marked by arrows on Figure 7.23) on the surfaces of OLC is clearly seen. We also observed the formation of short multiwall carbon nanotubes presented in Figure 7.24.

Figure 7.25 illustrates the HRTEM images of the ND graphitization products in the presence of cobalt particles with sizes up to 100 nm. The products are presented only for the cobalt particles with sizes less than 5 nm. One can see the formation of curved graphite-like shells (A) and cones (B and C in the marked region).

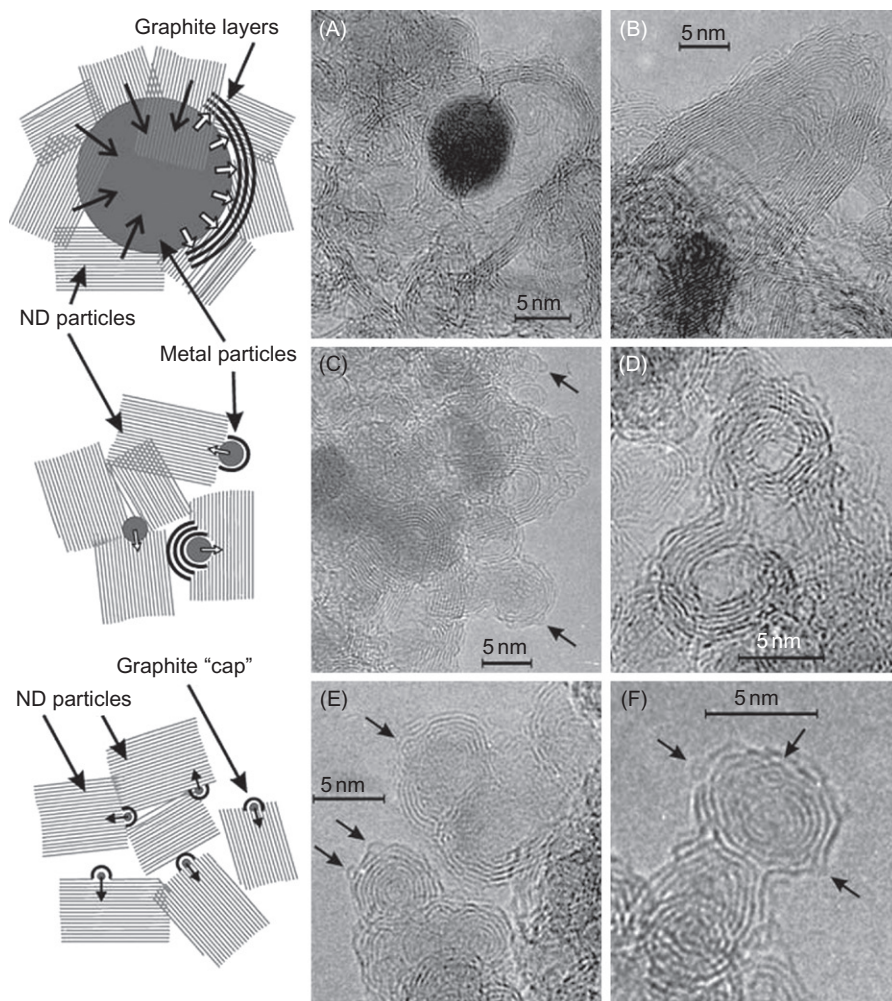
Such carbon structures are not formed under the same conditions of ND graphitization in the absence of metal particles. Therefore, metal particles catalyze the ND graphitization and formation of these products. The mechanism for the catalytic graphitization of ND probably consists of successive stages: dissolving of carbon in the metal particles; diffusion of carbon through these particles from the carbon/metal

**FIGURE 7.24**

HRTEM images of short multiwall nanotubes (1–2 nm) produced by ND annealing at 1420 K for 1 h in a vacuum of 10^{-5} Torr in the presence of iron nanoparticles (A and B) [175]. Iron nanoparticles are not seen on the image due to their small size and, therefore, low contrast. Dark curved lines correspond to diamond crystal planes and graphite-like shells. The distance between lines corresponds to the distance between the graphite-like shells, 0.34–0.35 nm ($d_{002} = 0.3354$ nm for hexagonal graphite).

contact regions to the opposite side of the metal particles; and then precipitation of carbon resulting in the formation of different graphitic forms of carbon. At high temperature, this process results in the metal particles melting and starting to move in a direction opposite to the formation of graphite-like deposits. The process of catalytic graphitization is schematically presented in the left part of Figure 7.24. Krivoruchko et al. [176] observed *in situ* a similar catalytic graphitization of amorphous carbon caused by moving liquid-like iron particles with sizes mainly ranging from 20 to 40 nm at 920–1170 K in a TEM microscope.

One can also see the similarities between the catalytic ND graphitization and the catalytic formation of carbon filaments and nanotubes [177–182]. The diameter of carbon nanotubes produced by the catalytic decomposition of carbon-containing gases is believed to be determined by the size of the catalyst particles [177,179]. The types of carbon deposits presented in Figure 7.24 also depend on the sizes of metal particles. The movement of large metal particles (dark spots on Figure 7.25A and B) results in the formation of prolonged graphite shells consisting of several curved graphite layers. The cooling down to room temperature of these particles

**FIGURE 7.25**

HRTEM images (right side of the figure) of the ND graphitization products in the presence of cobalt particles at 1500K for 3h in a vacuum of 10^{-6} Torr [177]. Curved solid lines correspond to {0002} graphite-like layers with an interplanar distance of $\sim 3.4\text{--}3.6\text{ \AA}$. Structures of these products depend on the metal particle size: large metal particles (dark spots on images (A) and (B)) participate in the formation of curved graphite shells and cones, images (A–D). The interaction of small metal clusters consisting of only several metal atoms with diamond surfaces initiates the graphitization leading to the formation of graphite “caps” with sizes less than 1 nm on surfaces of larger graphitization products. On images (C), (E), and (F), these “caps” are marked by short arrows. Schemes (left side) illustrate the interaction of metal particles having different sizes of ND particles. Metal particle size influences the type of graphitization products.

leads to their cessation of movement and encapsulation in graphite layers. One such encapsulated cobalt particle surrounded by graphite layers can be clearly seen in Figure 7.25A. The observed graphite cones and shells (Figure 7.25B–D) are formed by metal particles which left the graphitization products and are not seen on the images. The interaction of small metal clusters consisting of only several metal atoms with diamond surfaces initiates graphitization leading to the formation of graphite “caps” with sizes less than 1 nm on the surfaces of large carbon particles (see Figure 7.25C and F).

Thus, we can summarize that metal particles catalyze the ND graphitization. The mechanism of this graphitization consists of successive stages: dissolving of carbon in the metal particles; diffusion of carbon through these particles from the carbon/metal contact regions to the opposite side of the metal particles; and precipitation of carbon resulting in the formation of different graphite forms of carbon. At high temperature, this process results in the movement of metal particles leading to the formation of different forms of graphite-like deposits. Structures of these products depend on the metal particle size. Large metal particles participate in the formation of curved graphite shells and cones. Metal clusters consisting of several atoms are inserted into diamond particles. This results in the formation of carbon “caps” (less than 1 nm in sizes) on the surfaces of larger graphitization products.

7.7 Graphitization of NDs in the presence of oxygen- and hydrogen-containing gases

Evans [5] showed that oxidation of macroscopic diamond crystals in oxygen (0.4 Torr) promotes the production of a black graphite layer on diamond surfaces. Specifically, it was found that the {111} and {110} faces start to graphitize at a temperature of 970 K, whereas the appearance of a graphite layer on the {100} face was registered at 1120 K. The activation energy of 230 ± 10 kJ/mol was found for all diamond surfaces at temperatures where no graphitization was detected. Later, Uspenskaya et al. [6] also observed the formation of graphite layers on the surfaces of diamond powders (5–7 μm) at a temperature of 1120 K and above in the presence of oxygen (0.05–0.5 Torr). These authors recorded an activation energy of 230 ± 30 kJ/mol for diamond oxidation, which coincides with the one found by Evans [5].

Evans also demonstrated that a surface graphite layer is formed on the surfaces of diamond by oxidation in oxygen, while no graphitization occurs under the same conditions, but in a good vacuum or in the atmosphere of a purified inert gas. It was shown that diamond heating at 1700 K with a pressure of 10^{-4} Torr for 1 h results in a black surface coating, whereas doing the same experiment at 10^{-6} Torr results in the diamond remaining clear and unchanged [5]. It was concluded that a study of true graphitization should be done at conditions preventing oxidation [5]. Thus, it was shown that even negligible concentrations of oxygen-containing gases can

accelerate the diamond graphitization process, decrease the temperature of graphitization, and, as shown in Ref. [183], effect the structure of graphitization products. The catalytic effect on diamond graphitization of oxygen-containing gases was mentioned by Palosz et al. [184] and Qian et al. [185].

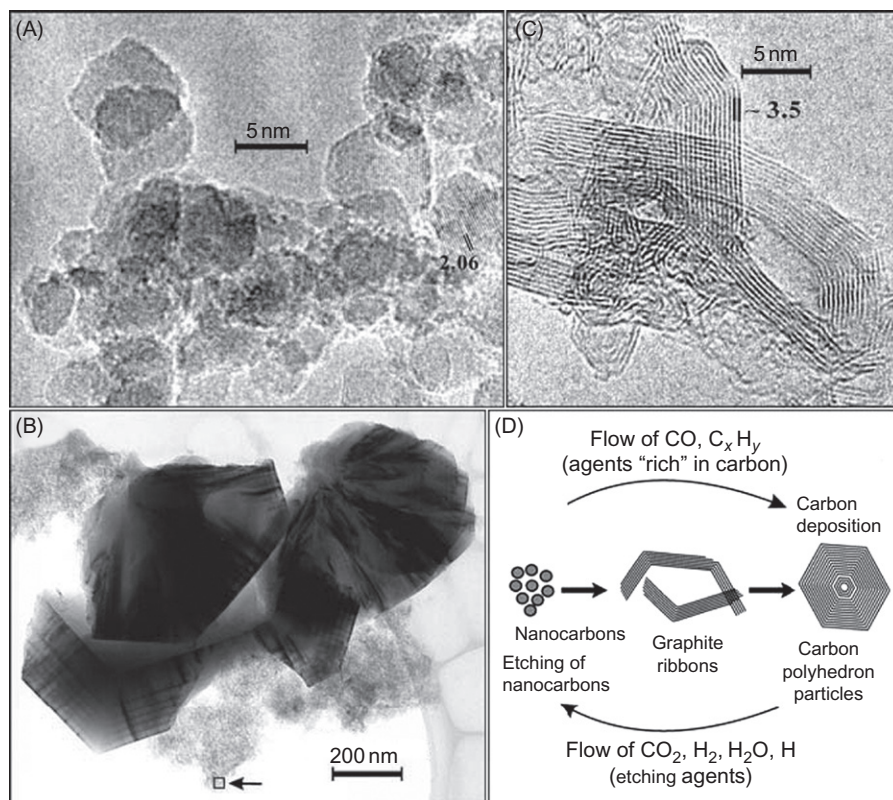
The catalytic effect of oxygen on diamond graphitization can be explained by the emergence of a new pathway for the reaction of the conversion of diamond to graphitic forms of carbon. We believe that carbon redistribution processes [183] underlie the mechanism of formation of graphite layers on diamond surfaces in hydrogen- and/or oxygen-containing media. As shown in Ref. [183], the carbon redistribution processes result in the formation of macroscopic graphitic carbon particles from initial nanosized diamond particles when graphitization was performed in a closed chamber filled with argon at 1870°C for 1 h (Figure 7.26); however, the graphitization of the ND sample under the same conditions, but in a vacuum of 10^{-5} Torr, resulted in the formation of OLC [34,41,108–112]. The thermal decomposition of surface groups provides (see Section 7.3) evolution of CO, CO₂, H₂O, and H₂, which are involved in reversible reactions with carbon:



Thus, the presence of oxygen- and hydrogen-containing gases results in carbon atom redistribution processes, which occur via etching and deposition steps due to the reversible reactions (7.1) to (7.3) of carbon with the reactive gases. These reactions can be considered as carbon transport reactions. These processes result in the etching of carbon nanostructures (ND, OLC, etc.) with a high surface energy and the formation of large-scale graphitic structures. The redistribution process is schematically shown in Figure 7.26D. The thermodynamic calculations suggest that at temperatures exceeding 1500 K, redistribution of carbon is mostly caused by the reactions that involve hydrogen and hydrogen-containing gases, while at temperatures below 1500 K the carbon redistribution processes mainly involve oxygen-containing gases (CO₂, CO, H₂O).

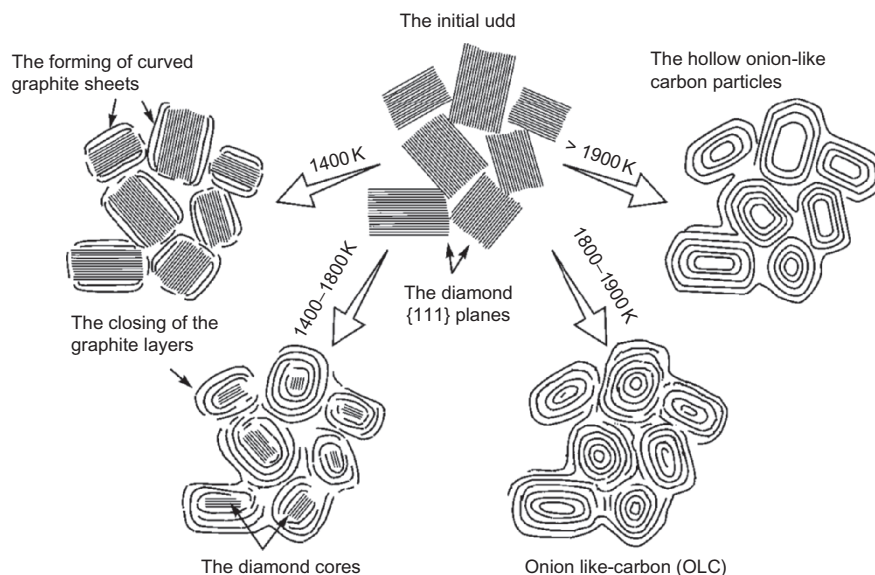
7.8 Properties of ND annealing products: OLC, sp²/sp³ nanocomposites

Knowledge of the kinetics of ND graphitization provides one with the opportunity of producing diamond/nanographite nanocomposites with variable ratios of diamond carbon (diamond cores) and defective curved graphitic shells. A desirable extent of graphitization can be achieved at different annealing temperatures by using corresponding heating durations. However, due to the different rates of defect annealing, the defect concentration and their nature can be significantly different.

**FIGURE 7.26**

HRTEM images of (A) pristine ND before thermal treatment, (B) graphite ribbons, and (C) polyhedron graphite particles observed in the sample prepared by annealing at 2140 K of the pristine ND in a closed chamber filled by argon-containing admixtures of CO , CO_2 , H_2O , and H_2 gases [183]. Image (C) is a higher resolution image of the marked region of micrograph (B). (D) Scheme of the carbon redistribution process via carbon transport reactions leading to etching of nanocarbons characterized by high surface area and formation of low surface graphitic particles. The graphite ribbons are most likely the primary structures. Carbon deposition preferentially occurs on their surface. A further growth of the ribbons leads to the formation of graphitic polyhedron particles [183].

Figure 7.27 presents a general scheme of production of OLC and nanocomposites with different fractions of diamond and nanosized graphitic sheets [136]. The scheme demonstrates that ND annealing at moderate temperatures of 1400–1800 K makes it possible to produce carbon nanocomposites with a controlled ratio of sp^2/sp^3 states in which ND particles are covered with nanosized fullerene-like shells, which are similar to bucky diamonds [106,107]. Figure 7.28 presents the HRTEM images of the ND annealing products at different temperatures. It should

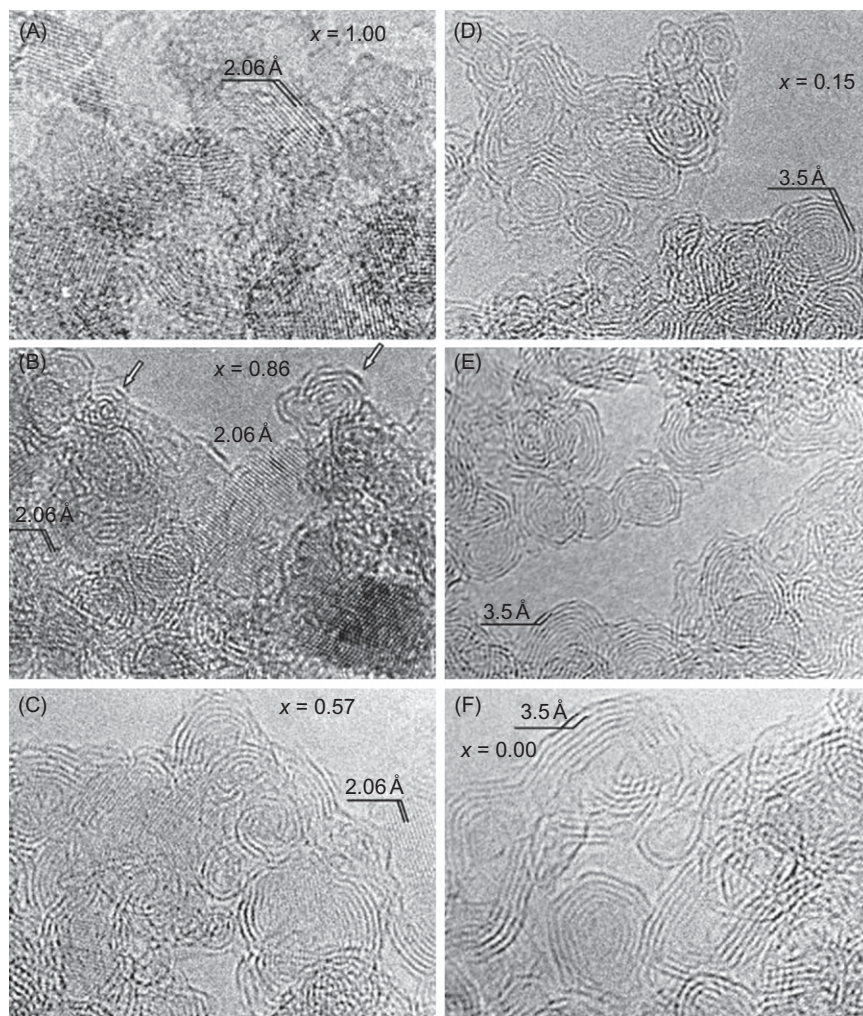
**FIGURE 7.27**

Scheme of sp^2/sp^3 nanocomposites and OLC formation [136].

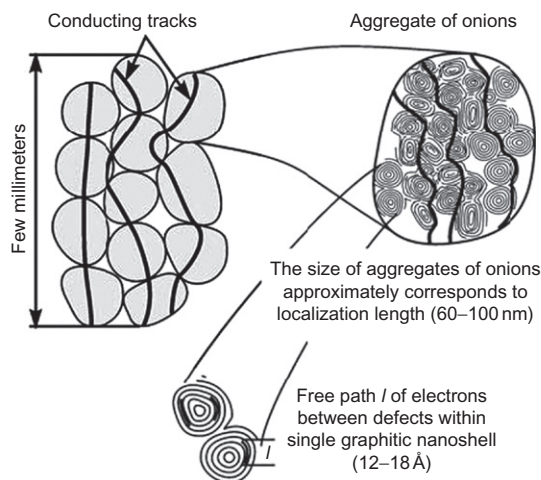
be mentioned that the durations of annealing experiments did not exceed 1.5 h; therefore, more prolonged heating can result in full graphitization of all ND particles even at low temperatures of 1400–1600 K (see Section 7.4). Annealing at 1800–1900 K leads to the formation of OLC containing the carbon onions with 3–8 fullerene-like spherical shells and aggregates of onions. Heating at higher temperatures leads to the formation of hollow OLC with a structure similar to that which was observed when fullerene-containing soot was annealed at temperatures above 2300 K [186,187].

Products of ND graphitization were characterized with HRTEM [34,35, 108–112,141], Raman spectroscopy [110,119,137], XRD [111,112,114,115,133, 137,188], XPS [135,189], EELS [109,112,126], electron spin resonance (ESR) [110], X-ray emission spectroscopy [168], ultraviolet-visible absorption spectroscopy [190,191], and electro- and magnetoresistivity measurements [136,192,193].

Raman spectroscopy data show that some portion of OLC exists as almost ideal fullerene-like shells enclosed in each other (up to 6–7 shells) [119]. However, the results of other characterization methods demonstrate the presence of various types of defects, which resemble the defects in graphite materials [2,10]. Figure 7.14 shows possible defects in OLC structures. The X-ray emission study of OLC combined with quantum chemical simulation for the characterization of their electronic structure led to the conclusion that the onions produced by ND annealing at the intermediate temperature (1400–1900 K) have holes in the internal shells [168]. The origin of such defects accompanying OLC formation can be explained in terms

**FIGURE 7.28**

HRTEM micrographs of ND samples annealed under a vacuum of 10^{-5} Torr for 1–1.5 h at (A) 1170, (B) 1420, (C) 1600, (D) 1800, (E) 1900, and (F) 2140 K [108,135]. The straight dark contrast lines in micrographs (A–C) correspond to the {111} crystallographic diamond planes. The distance between these lines is 2.06 Å. The curved dark lines in (D–F) correspond to the {0002} crystallographic graphite planes. The distance between these lines is 3.5 Å. The diamond weight fractions (x) of the samples are also presented within each image. The arrows in (B) show OLC particles containing 2–3 graphite-like shells that were produced by the graphitization of small ND particles (<2 nm) at 1420 K.

**FIGURE 7.29**

Scheme of three scales of OLC particle organization [193]. The heavy solid lines correspond to current conduction tracks.

of the deficit of diamond carbon atoms in the diamond–graphite interface to form perfect fullerene-like shells during ND annealing (see Section 7.5.5). The radicals in the inner cores of OLC are well shielded by outer defect-free shells from the adsorption of reactive gases. The proposed formation of OLC with a holed structure is in a good agreement with the ESR study [110] of similar samples. The accumulation of different types of defects in the curved graphite layers during ND graphitization was proposed to cause an increase in the density of states near the Fermi level of OLC produced from NDs at 1600, 1800, and 1900 K (Ultraviolet Photoelectron Spectroscopy (UPS) study) [135]. The defects present in carbon onions can be annealed at temperatures higher than 2100 K. This annealing of defects is accompanied with the formation of bigger polygonized hollow onions. A photoemission study of potassium-intercalated polygonal hollow onions produced at 2140 K showed that these carbon onions behave as small graphite crystals [189].

Data on the structure of OLC correlate with its electrical properties. Figure 7.29 summarizes the data on the conductivity of OLC. The electroresistivity of the samples demonstrates the temperature dependence typical of systems with variable hopping-length conductivity. The dimensionality of the space for current carrier movement varies between $1/2$, 1 , and $3/2$ depending on the annealing temperature [136]. Figure 7.29 illustrates the scheme of a hierarchical arrangement of OLC forming aggregates that results in their unique electrical characteristics. OLC aggregates are obtained by annealing ND aggregates. Within the aggregates, onions are linked to each other by defect graphite-like sheets and CC bonds. Some part of the onions is represented by elongated particles with linked external graphitic layers

and closed quasi-spherical shells. The conduction carrier concentration n for OLC samples was estimated within the framework of the theory of negative magnetoresistance in semiconductors in the hopping-conduction region (with the proposition $n \sim nc$, where nc is the critical concentration). The parameter is estimated as $n \sim 8 \cdot 10^{21} \text{ cm}^{-3}$ for OLC prepared at 1800 K and $n \sim 3 \cdot 10^{21} \text{ cm}^{-3}$ for OLC prepared at 2140 K [192,193]. The free path length of electrons within OLC particles is comparable to the size of graphitic fragments within the hollow structure of a single onion ($l \sim 12 \pm 2 \text{ \AA}$). When their hollow structure is annealed with the formation of hollow polygonized structures, the free path length of the electron increases to $18 \pm 2 \text{ \AA}$. The size localization length of current carriers is comparable to the size aggregates of OLC particles.

At present, ND high-temperature annealing is the most productive method of OLC preparation. Unusual OLC properties can be used in a variety of applications. We just mention some of them. OLC is potentially a perfect solid lubricant similar to hollow WS₂ nanoparticles. Recently, Hirata et al. [194] showed that carbon onions produced by the heat treatment of diamond clusters exhibit stable low-friction coefficients both in air and in vacuum at room temperature. Different important features of tribological applications are considered in number of forthcoming articles [195–197].

OLC is an interesting candidate for electromagnetic compatibility material applications in a wide electromagnetic (EM) frequency range [198–204]. EM characteristics of OLC based composites in microwaves were found to be sensitive to the OLC type and synthesis conditions. It is proved that EM response of the OLC fillers in composite materials can be tailored through the alternation of the electrical conductivity within OLC aggregate via variation of the annealing temperature and use of OLC aggregates with smaller or larger sizes. The latter can be controlled through the fractionation of initial ND material and selection of the fraction with the largest aggregate sizes used for OLC production [205].

It has been shown that due to an efficient optical limiting action of OLC, it is a good candidate for photonic applications [196,206–208]. These structures are related to the interstellar dust problem, and can contribute to the large UV adsorption band at 217.5 nm wavelength [188,189,197,209].

It was demonstrated that ultrahigh-power micrometer-sized supercapacitors based on OLC can be developed [210–213]. Although OLC offers a moderate specific surface area compared to that of activated carbons, this surface is fully accessible to ions, whereas with some other materials, the size or shape of the pores or of the particles themselves would slow down the charging or discharging process.

OLC can be used as a model system in carbon-based catalysts studies. OLC can be used as a support [214] and can directly take part in chemical reactions as catalysts [215]. OLC also demonstrates high selectivity and catalytic activity in the oxidative dehydrogenation of ethyl benzene to styrene [199,216,217]. The properties of sp²/sp³ nanocomposites and bucky diamonds have not yet been properly investigated and are topics of future research.

7.9 Conclusion

Diamond graphitization is important from both theoretical and practical points of view. Graphitization of diamond may be induced by thermal treatment and reactive gases, and promoted by metal catalysts and irradiation from different sources. On the one hand, graphitization limits the temperature range and conditions where diamond can be effectively used; on the other hand, it provides the possibility to produce new nanosized carbon materials. We found that thermal annealing of NDs of the sizes 2–5 nm produces OLC, while the annealing of micron-sized diamond produces closed curved graphite-like structures, namely, nanotubes, nanofolds, and so on. Theoretical considerations based on molecular modeling using combinations of MM, MD, and Hartree–Fock methods allow us to propose that the formation of OLC and closed curved graphite species on a diamond surface have features of self-assembling processes, which proceed via several steps.

Due to the high surface-to-volume ratio of ND particles and their high surface area, the surface groups of ND play an important role in its physical and chemical properties. Controlled functionalization presents a powerful tool for the specific modification of properties of ND particles; promotes ND participation in various chemical reactions; improves the interaction of ND particles with a solvent, components of a composite material, a polymer, a catalyst; and allows design of new types of biocompatible sorbents and materials. Surface groups stabilize ND surfaces and prevent ND particles from graphitization. Decomposition of surface groups results in graphitization of ND and the formation of bucky diamonds (intermediates in the ND to OLC transformation) and eventually OLC. Due to the high stability of surface hydrogen-containing groups, the most thermally stable ND can be prepared via its surface hydrogenation.

The large difference between the rates and the kinetic parameters obtained by us (1370–1860 K) and those estimated by G. Davies and T. Evans for the temperature range 2150–2300 K indicates that there are different graphitization mechanisms operating in the “low” and “high” temperature regions. Within the high-temperature region the graphitization rate-determining step in the process is detachment of a single atom from the diamond surface. Within the low-temperature region the graphitization mechanism involves a process in which carbon atoms do not completely separate from the diamond surfaces and the outer diamond planes transform progressively into graphite planes. The Debye temperature for diamond, 1910 K, appears to serve as the boundary between these regions. At and above this temperature all oscillating degrees of freedom of the diamond are excited.

Knowledge of the kinetics of ND graphitization provides the possibility to produce diamond/nanographite composites with variable ratios of diamond core and defective curved graphitic shells (sp^2/sp^3 nanocomposites) decreasing in size. The small size of curved graphitic shells, the presence of an interface between nanosized diamond cores and graphitic shells, and probably the high concentration of open graphitic edges can produce the unusual electronic properties of these composites and OLC.

The properties of OLC are poorly studied, mainly due to its low availability for experiments. Nevertheless, this material stimulates great interest. It is related to the interstellar dust problem. Due to a very efficient optical limiting action of OLC, it is a good candidate for photonic applications. OLC is a perfect solid lubricant. OLC also demonstrates high selectivity and catalytic activity in the oxidative dehydrogenation of ethyl benzene to styrene. This last example shows that OLC, like ND, can participate in chemical reactions. The onions' surface can be functionalized allowing further incorporation into biosystems. However, extensive experiments on the preparation of narrow fractions of onions and their functionalization are still required.

Acknowledgments

This work was supported in part by the Russian Foundation for Basic Research Grants No. 05-03-32995; the NATO project CBP.NR.SFPP 981051; and the cooperative grant of the Department of Education of Russian Federation and CRDF NO-008-X1. The authors would like to thank Dr. A.L. Chuvilin for fruitful discussions and assistance on HRTEM experiments.

References

- [1] J.E. Field (Ed.), *The Properties of Natural and Synthetic Diamonds*, Academic Press, London, 1977.
- [2] H.O. Pierson, *Handbook of Carbon, Graphite, Diamond and Fullerenes: Properties, Processing and Applications*, Noyes Publications, Park Ridge, NJ, 1993.
- [3] J.E. Field, *The Properties of Natural and Synthetic Diamond*, Academic Press, London, 1992.
- [4] N.V. Novikov, A.S. Vishnevsky, P.S. Kisly, G.V. Kurdyumov, V.S. Lisanov, V.F. Romanov, et al., (Ed.), *Physical Properties of Diamond*, Handbook, Naukova Dumka, Kiev, 1987.
- [5] T. Evans, Changes produced by high temperature treatment of diamond, in: J.E. Field (Ed.), *The Properties of Diamond*, Academic Press, London, 1979, pp. 403–425.
- [6] K.S. Uspenskaya, Y.N. Tolmachev, D.V. Fedoseev, Oxidation and graphitization of diamond at low pressures, *Zh. Fiz. Khim.* 56 (1982) 495 (in Russian).
- [7] D.V. Fedoseev, S.P. Vnukov, V.L. Bukhovets, B.A. Anikin, Surface graphitization of diamond at high temperatures, *Surf. Coat. Technol.* 28 (1986) 207–214.
- [8] G. Davies, *Properties and Growth of Diamond*, INSPEC, London, 1994.
- [9] J.F. Prins, Ion implantation of diamond for electronic applications, *Semicond. Sci. Technol.* 18 (3) (2003) S27.
- [10] F. Banhart, Irradiation effects in carbon nanostructures, *Rep. Prog. Phys.* 62 (1999) 1181.
- [11] Y.G. Gogotsi, A. Kailer, K.G. Nickel, Transformation of diamond to graphite, *Nature* 401 (1999) 663.
- [12] F. Banhart, P.M. Ajayan, Carbon onions as nanoscopic pressure cells for diamond formation, *Nature* 382 (1996) 433.
- [13] F. Banhart, The transformation of graphitic onions to diamond under electron irradiation, *J. Appl. Phys.* 81 (1997) 15.

- [14] P. Wesolowski, Y. Lyutovich, F. Banhart, H.D. Carstanjen, H. Kronmüller, Formation of diamond in carbon onions under MeV ion irradiation, *Appl. Phys. Lett.* 71 (1997) 1948.
- [15] Y. Lyutovich, F. Banhart, Low-pressure transformation of graphite to diamond under irradiation, *Appl. Phys. Lett.* 74 (1999) 659.
- [16] M. Zaiser, F. Banhart, Radiation-induced transformation of graphite to diamond, *Phys. Rev. Lett.* 79 (1997) 3680.
- [17] S. Evans, Surface properties of diamond, in: J.E. Field (Ed.), *The Properties of Natural and Synthetic Diamond*, Academic Press, London, 1992.
- [18] A.L. Vereschagin, *Detonation Nanodiamonds*, Altai State Technical University, Barnaul, Russian Federation, 2001.
- [19] O.A. Shenderova, V.V. Zhirnov, D.W. Brenner, Carbon nanostructures, *Crit. Rev. Solid State Mater. Sci.* 27 (3/4) (2002) 227.
- [20] V.V. Danilenko, *Synthesis and Sintering of Diamond by Detonation*, Energoatomizdat, Moscow, 2003.
- [21] V.Y. Dolmatov, *Detonation Synthesis Ultra-dispersed Diamond*, St. Petersburg Government University, St. Petersburg, 2003.
- [22] *Proceedings of the International Symposium on Detonation Nanodiamonds: Technology, Properties and Applications*, St Petersburg, Russia, 7–9 July, 2003, *Phys. Solid. State* 46 (4) (2004).
- [23] D.M. Gruen, O.A. Shenderova, A.Y. Vul' (Eds.), in: *Proceedings of the NATO ARW on Synthesis, Properties and Applications of Ultrananocrystalline Diamond*, 7–10 June 2004, St. Petersburg, Russia, *Synthesis, Properties and Applications of Ultrananocrystalline Diamond*, Kluwer Academic, Dordrecht, 2005, XI.
- [24] V.Y. Dolmatov, Detonation synthesis ultradispersed diamonds: properties and applications, *Usp. Khim.* 70 (2001) 687 (in Russian).
- [25] V.I. Trefilov, G.I. Savvakina, V.V. Skorokhod, Y.M. Solonin, A. Khrienko, Specific features of ultradispersed diamond produced by the high temperature synthesis under conditions of explosion, *Dokl. Akad. Nauk SSSR* 239 (1978) 838.
- [26] G.I. Savvakina, Y.M. Solonin, V.I. Trefilov, Formation possibility and nonstoichiometric cubic phase of molybdenum carbide under high pressure shock compression, *Dokl. Akad. Nauk SSSR* 270 (1983) 92.
- [27] G.I. Savvakina, V.A. Serdyuk, V.I. Trefilov, Influence of the crystallization conditions of diamonds under high-temperature shock compression on their optical-properties, *Dokl. Akad. Nauk SSSR* 270 (1983) 329.
- [28] A.M. Staver, A.I. Lyamkin, N.A. Gubareva, E.A. Petrov, Ultradispersed diamond powders obtained with the use of explosion energy, *Fiz. Gorenya Vzryva* 20 (5) (1984) 101.
- [29] A.M. Staver, N.V. Gubareva, A.I. Lyamkin, E.A. Petrov, Ultra-disperse diamond powders made by the use of explosion energy, *Combust. Explos. Shock Waves* 20 (5) (1984) 567.
- [30] A.I. Lyamkin, E.A. Petrov, A.P. Ershov, et al., Production of diamonds from high explosives, *Dokl. Akad. Nauk SSSR* 302 (3) (1988) 611.
- [31] N.R. Greiner, D.S. Phillips, J.D. Johnson, F. Volk, Diamonds in detonation soot, *Nature* 333 (1988) 440.
- [32] V.M. Titov, V.F. Anisichkin, I.Y. Malkov, Synthesis of ultradispersed diamond in detonation-waves, *Combust. Explos. Shock Waves* 25 (3) (1989) 372.
- [33] A.L. Vereschagin, G.V. Sakovich, V.F. Komarov, E.A. Petrov, Properties of ultrafine diamond clusters from detonation synthesis, *Diamond Relat. Mater.* 3 (1993) 160.
- [34] V.L. Kuznetsov, A.L. Chuvilin, Y.V. Butenko, I.L. Malkov, V.M. Titov, Onion-like carbon from ultradisperse diamond, *Chem. Phys. Lett.* 222 (1994) 343.

- [35] V.L. Kuznetsov, A.L. Chuvilin, E.M. Moroz, V.N. Kolomiichuk, S.K. Shaichutdinov, Y.V. Butenko, et al., Effect of explosions on the structure of detonation soots: ultradisperse diamond and onion carbon, *Carbon* 32 (1994) 873.
- [36] V.L. Kuznetsov, A.L. Chuvilin, Y.V. Butenko, A.K. Gutakovskii, S.V. Stankus, R.A. Khairulin, Closed curved graphite-like structures formation on micron-size diamond, *Chem. Phys. Lett.* 289 (1998) 353.
- [37] O.A. Shenderova, Z. Hu, D. Brenner, Carbon family in nanoscale, in: D.M. Gruen, O.A. Shenderova, A.Y. Vul (Eds.), *Synthesis, Properties and Applications of Ultrananocrystalline Diamond*, Springer, Berlin, 2005, pp. 1–14.
- [38] F.P. Bundy, W.A. Bassett, M.S. Weathers, R.J. Hemley, H.K. Mao, A.F. Goncharov, The pressure–temperature phase and transformation diagram for carbon; updated through 1994, *Carbon* 34 (1996) 141.
- [39] J.A. Viecelli, S. Bastea, J.N. Glosli, F.H. Ree, Phase transformations of nanometer size carbon particles in shocked hydrocarbons and explosives, *J. Chem. Phys.* 115 (2001) 2730.
- [40] V.V. Danilenko, Nanocarbon phase diagram and conditions for detonation nanodiamond formation, in: D.M. Gruen, O.A. Shenderova, A.Y. Vul (Eds.), *Synthesis, Properties and Applications of Ultrananocrystalline Diamond*, Springer, Berlin, 2005, pp. 181–198.
- [41] V.L. Kuznetsov, A.L. Chuvilin, Y.V. Butenko, I.Y. Malkov, A.K. Gutakovskii, S.V. Stankus, et al., Study of onion-like carbon (OLC) formation from ultra disperse diamond, in: P. Bernuer, et al.(Ed.), *Science and Technology of Fullerene Materials*, vol. 359, MRS Proceedings. Material Research Society, Pittsburgh, 1995, pp. 105–110.
- [42] D. Tomanek, M.A. Schluter, Growth regimes of carbon clusters, *Phys. Rev. Lett.* 67 (1991) 2331.
- [43] J.L. Martins, F.A. Reuse, S.N. Khanna, Growth and formation of fullerene clusters, *J. Cluster Sci.* 12 (2001) 513.
- [44] R.O. Jones, Density functional study of carbon clusters C_{2n} ($2 < n < 16$). I. Structure and bonding in the neutral clusters, *J. Chem. Phys.* 110 (1999) 5189.
- [45] G.N. Churilov, P.V. Novikov, V.E. Tarabanko, V.A. Lopatin, N.G. Vnukova, N.V. Bulina, On the mechanism of fullerene formation in a carbon plasma, *Carbon* 40 (2002) 891.
- [46] F. Fugaciu, H. Hermann, G. Seifert, Concentric-shell fullerenes and diamond particles: a molecular-dynamics study, *Phys. Rev. B* 60 (1999) 10711.
- [47] N.W. Winter, F.H. Ree, Carbon particle phase stability as a function of size, *J. Comput. Aided Mater. Des.* 5 (1998) 279.
- [48] F.H. Ree, N.W. Winter, J.N. Glosli, J.A. Viecelli, Kinetics and thermodynamic behavior of carbon clusters under high pressure and high temperature, *Physica B* 265 (1999) 223.
- [49] J.E. Dahl, S.G. Liu, R.M.K. Carlson, Isolation and structure of higher diamondoids, nanometer-sized diamond molecules, *Science* 299 (2003) 96.
- [50] R.M.K. Carlson, J.E.P. Dahl, S.G. Liu, M.M. Olmstead, P.R. Buerki, R. Cat, Diamond molecules found in petroleum. New members of the H-terminated diamond series, in: D.M. Gruen, O.A. Shenderova, A.Y. Vul (Eds.), *Synthesis, Properties and Applications of Ultrananocrystalline Diamond*, Springer, Berlin, 2005, pp. 63–78.
- [51] S. Evans, Surface properties of diamond, in: J.E. Field (Ed.), *The Properties of Natural and Synthetic Diamond*, Academic Press, London, 1992.
- [52] V.F. Loktev, V.I. Makal'skii, I.V. Stoyanova, A.V. Kalinkin, V.A. Likholobov, V.N. Mit'kin, Surface modification of ultradispersed diamonds, *Carbon* 29 (1991) 817.

- [53] T. Jiang, K. Xu, FTIR study of ultradispersed diamond power synthesized by explosive detonation, *Carbon* 33 (1995) 1663.
- [54] E. Mironov, E. Petrov, A. Koretz, Chemical aspect of ultradispersed diamond formation, *Diamond Relat. Mater.* 12 (2003) 1472.
- [55] V.L. Kuznetsov, M.N. Aleksandrov, I.V. Zagoruiko, A.L. Chuvilin, E.M. Moroz, V.N. Kolomiichuk, et al., Study of ultra disperse diamond obtained using explosion energy, *Carbon* 29 (1991) 665.
- [56] F. Cataldo, A.P. Koscheev, A study on the action of ozone and on the thermal stability of nanodiamond, Fullerenes, Nanotubes, *Carbon Nanostruct.* 11 (3) (2003) 201.
- [57] E. Mironov, A. Koretz, E. Petrov, Detonation synthesis ultradispersed diamond structural properties investigation by infrared absorption, *Diamond Relat. Mater.* 11 (2002) 872.
- [58] Y.V. Butenko, V.L. Kuznetsov, E.A. Paukshtis, A.I. Stadnichenko, I.N. Mazov, S.I. Moseenkov, et al., The thermal stability of nanodiamond surface groups and onset of nanodiamond graphitization, Fullerenes, Nanotubes, *Carbon Nanostruct.* 14 (2006) 557–564.
- [59] K. Iakoubovskii, M.V. Baidakova, B.H. Wouters, A. Stesmans, G.J. Adriaenssens, A.Y. Vul, et al., Structure and defects of detonation synthesis nanodiamond, *Diamond Relat. Mater.* 9 (2000) 861.
- [60] H. Mutschke, J. Dorschner, Th. Henning, C. Jäger, U. Ott, Facts and artifacts in interstellar diamond spectra, *Astrophys. J.* 454 (1995) L157.
- [61] W.W. Duley, V.I. Grishko, Evolution of carbon dust in aromatic infrared emission sources: formation of nanodiamonds, *Astrophys. J.* 554 (2001) L209.
- [62] A.P. Koscheev, A.E. Serzhantov, S. Merchel, U. Ott, O. Guillois, C. Reynaud, Surface chemistry of chemically treated diamond nanograins, 34th Lunar and Planetary Science Conference, Houston, TX, The Lunar and Planetary Institute, 17–21 March, 2003, p. 1287.
- [63] A.P. Jones, L.B. d'Hendecourt, S.Y. Sheu, H.C. Chang, C.L. Cheng, H.G.M. Hill, Surface CH stretching features on meteoritic nanodiamonds, *Astron. Astrophys.* 416 (2004) 235.
- [64] V.S. Bondar, A.P. Puzyr, Nanodiamonds for biological investigations, *Phys. Solid State* 46 (2004) 716.
- [65] X.Y. Xu, Y.W. Zhu, B.C. Wang, X.Q. Shen, Surface modification of nanodiamond in aqueous medium, *Trans. Nonferrous Met. Soc. China* 13 (2003) 1415.
- [66] X. Xua, Z. Yua, Y. Zhuh, B. Wang, Effect of sodium oleate adsorption on the colloidal stability and zeta potential of detonation synthesized diamond particles in aqueous solutions, *Diamond Relat. Mater.* 14 (2005) 206.
- [67] T. Xu, J.Z. Zhao, K. Xu, The ball-bearing effect of diamond nanoparticles as an oil additive, *J. Phys. D Appl. Phys.* 29 (1996) 2932.
- [68] G.A. Chiganova, V.A. Bondar, A.S. Chiganov, Electrophoresis of ultradispersed diamond hydrosols of and modification of its surface, *Colloid J.* 55 (1993) 182 (in Russian).
- [69] A.N. Alimova, N.N. Chubun, P.I. Belobrov, V.V. Zhirnov, Electrophoresis of nanodiamond powder for cold cathode fabrication, *J. Vac. Sci. Technol. B* 17 (1999) 715.
- [70] E. Maillard-Schaller, O.M. Kuettel, L. Diederich, L. Schlappbach, V.V. Zhirnov, P.I. Belobrov, Surface properties of nanodiamond films deposited by electrophoresis on Si(100), *Diamond Relat. Mater.* 8 (1999) 805.
- [71] T. Tyler, V.V. Zhirnov, A.V. Kvit, D. Kang, J.J. Hren, Electron emission from diamond nanoparticles on metal tips, *Appl. Phys. Lett.* 82 (2003) 2904.

- [72] A.M. Affoune, B.L.V. Prasad, H. Sato, T. Enoki, Electrophoretic deposition of nano-sized diamond particles, *Langmuir* 17 (2001) 547.
- [73] T. Enoki, Diamond-to-graphite conversion in nanodiamond and the electronic properties of nanodiamond-derived carbon system, *Phys. Solid State* 46 (4) (2004) 651.
- [74] G.L. Bilbro, Theory of electrodeposition of diamond nanoparticles, *Diamond Relat. Mater.* 11 (2002) 1572.
- [75] H. Tabata, M. Fujii, S. Hayashi, Laser ablation of diamond nanoparticles suspended in solvent: synthesis of polyynes, *Chem. Phys. Lett.* 395 (2004) 138.
- [76] X. Xu, Z. Yu, Y. Zhu, B. Wang, Influence of surface modification adopting thermal treatments on dispersion of detonation nanodiamond, *J. Solid State Chem.* 178 (2005) 688.
- [77] Y. Liu, Z. Gu, J.L. Margrave, V.N. Khabashesku, Functionalization of nanoscale diamond powder: fluoro-, alkyl-, amino-, and amino acid-nanodiamond derivatives, *Chem. Mater.* 16 (2004) 3924.
- [78] V.S. Bondar, A.P. Puzyr, Use of nanodiamond particles for rapid isolation of recombinant apoobelin from *Escherichia coli*, *Dokl. Biochem.* 373 (1–6) (2000) 129.
- [79] A.P. Puzyr, V.S. Bondar, P.I. Belobrov, A.A. Bukaemskii, Preparation of nanodiamond-protein- δ -aluminum oxide complex, *Dokl. Russ. Acad. Sci.* 373 (2000) 408 (in Russian).
- [80] K.V. Purtov, V.S. Bondar, A.P. Puzyr, Supramolecular structure of nanodiamond particles and obelin built up on a two-dimensional plate, *Dokl. Biochem. Biophys.* 380 (2001) 339.
- [81] V.S. Bondar, I.O. Pozdnyakova, A.P. Puzyr, Applications of nanodiamonds for separation and purification of proteins, *Phys. Solid State* 46 (4) (2004) 758.
- [82] L.-C. Lora Huang, H.-C. Chang, Adsorption and immobilization of cytochrome c on nanodiamonds, *Langmuir* 20 (2004) 5879.
- [83] X.L. Kong, L.C.L. Huang, C.-M. Hsu, W.-H. Chen, C.-C. Han, H.-C. Chang, High-affinity capture of proteins by diamond nanoparticles for mass spectrometric analysis, *Anal. Chem.* 77 (2005) 259.
- [84] A.P. Puzyr, I.O. Pozdnyakova, V.S. Bondar, Design of a luminescent biochip with nanodiamonds and bacterial luciferase, *Phys. Solid State* 46 (2004) 761.
- [85] N. Kossovsky, A. Gelman, H.J. Hnatyszyn, S. Rajguru, R.L. Garrell, S. Torbati, et al., Surface-modified diamond nanoparticles as antigen delivery vehicles, *Bioconjugate Chem.* 6 (5) (1995) 507.
- [86] A.P. Puzyr, S.V. Tarskikh, G.V. Makarskaya, G.A. Chiganova, I.S. Larionova, P.Y. Detkov, et al., Damaging effect of detonation diamonds on human white and red blood cells *in vitro* translated, *Dokl. Biochem.* 385 (2002) 201.
- [87] A.P. Puzyr, D.A. Neshumayev, S.V. Tarskikh, G.V. Makarskaya, V.Y. Dolmatov, V.S. Bondar, Destruction of human blood cells in interaction with detonation nanodiamonds in experiments *in vitro*, *Diamond Relat. Mater.* 13 (2004) 2020.
- [88] K. Nakagawa, K. Okumura, T. Shimamura, N. Ikenaga, T. Suzuki, T. Kobayashi, et al., Novel selective oxidation of light alkanes using carbon dioxide. Oxidized diamond as a novel catalytic medium, *Chem. Lett.* 32 (2003) 866.
- [89] K. Okumura, K. Nakagawa, T. Shimamura, N.O. Ikenaga, M. Nishitani-Gamo, T. Ando, et al., Direct formation of acetaldehyde from ethane using carbon dioxide as a novel oxidant over oxidized diamond-supported catalysts, *J. Phys. Chem. B* 107 (2003) 13419.
- [90] K. Nakagawa, C. Kajita, N. Ikenaga, T. Suzuki, T. Kobayashi, M. Nishitani-Gamo, et al., The role of chemisorbed oxygen on diamond surfaces for the dehydrogenation of ethane in the presence of carbon dioxide, *J. Phys. Chem. B* 107 (2003) 4048.

- [91] K. Nakagawa, H. Nishimoto, M. Kikuchi, S. Egashira, Y. Enoki, N. Ikenaga, et al., Synthesis gas production from methane using oxidized-diamond-supported group VIII metal catalysts, *Energy Fuels* 17 (2003) 971.
- [92] S.B. Wang, Z.H. Zhu, Catalytic conversion of alkanes to olefins by carbon dioxide oxidative dehydrogenation—a review, *Energy Fuels* 18 (2004) 1126.
- [93] K. Nakagawa, M. Nishitani-Gamo, T. Ando, Hydrogen production from methane for fuel cell using oxidized diamond-supported catalysts, *Int. J. Hydrogen Energy* 30 (2005) 201.
- [94] H. Nishimoto, K. Nakagawa, N. Ikenaga, M. Nishitani-Gamo, T. Ando, T. Suzuki, Partial oxidation of methane to synthesis gas over oxidized diamond catalysts, *Appl. Catal. A* 264 (2004) 65.
- [95] B.V. Spitsyn, M.N. Gradoboev, T.B. Galushko, T.A. Karpukhina, N.V. Serebryakova, I.I. Kulakova, et al., Purification and functionalization of nanodiamond, in: D.M. Gruen, O.A. Shenderova, A.Y. Vul, (Eds.), *Synthesis, Properties and Applications of Ultrananocrystalline Diamond*, Springer, Berlin, 2005, pp. 241.
- [96] V.L. Kuznetsov, Y.V. Butenko, Nanodiamond graphitization and properties of onion-like carbon, in: D.M. Gruen, O.A. Shenderova, A.Y. Vul (Eds.), *Synthesis, Properties and Applications of Ultrananocrystalline Diamond*, Springer, Berlin, 2005, pp. 199–216.
- [97] N.V. Novikov, G.P. Bogatyreva, M.N. Voloshin, Detonation diamonds in Ukraine, *Phys. Solid State* 46 (2004) 600.
- [98] I.I. Kulakova, Surface chemistry of nanodiamonds, *Phys. Solid State* 46 (2004) 636.
- [99] S. Ji, T. Jiang, K. Xu, S. Li, FTIR study of the adsorption of water on ultradispersed diamond powder surface, *Appl. Surf. Sci.* 133 (1998) 231.
- [100] V.L. Kuznetsov, Y.V. Butenko, Synthesis and properties of nanostructured carbon materials: nanodiamond, onion-like carbon and carbon nanotubes, in: Y.G. Gogotsi, I.V. Uvarova (Eds.), *Nanostructured Materials and Coating for Biomedical and Sensor Applications*, NATO Science Series 102, Kluwer Academic, Dordrecht, 2003, pp. 187.
- [101] A.P. Koscheev, N.V. Zaripov, U. Ott, Diamond nanograins in carbon soot: does the chemistry of extracted diamonds depend on the properties of pristine soot?, 36th Lunar and Planetary Science Conference, League City, TX, The Lunar and Planetary Institute, 14–18 March, 2005, p. 1406.
- [102] A.J. Gordon, R.A. Ford, *The Chemist's Companion. A Handbook of Practical Data, Techniques, and References*, John Wiley & Sons, New York, NY, 1972.
- [103] A. Dandekar, R.T.K. Baker, M.A. Vannice, Characterization of activated carbon, graphitized carbon fibers and synthetic diamond powder using TPD and DRIFTS, *Carbon* 36 (1998) 1821.
- [104] Y. Otake, R.G. Jenkins, Characterization of oxygen-containing surface complexes created on macroscopic carbon by air and nitric acid treatment, *Carbon* 31 (1993) 109.
- [105] G.P. Bogatyreva, M.M. Voloshin, V.G. Malogolovets, V.L. Gvyazdovskaya, G.D. Ilnitskaya, The effect of heat treatment on the surface condition of nanodiamond, *J. Optoelectron. Adv. Mater.* 2 (2000) 469.
- [106] A.S. Barnard, S.P. Russo, I.K. Snook, Coexistence of bucky diamond with nanodiamond and fullerene carbon phases, *Phys. Rev. B* 68 (2003) 073406.
- [107] J.-Y. Raty, G. Galli, C. Bostedt, T.W. van Buuren, L.J. Terminello, Quantum confinement and fullerene-like surface reconstructions in nanodiamonds, *Phys. Rev. Lett.* 90 (2003) 037401.

- [108] Y.V. Butenko, V.L. Kuznetsov, A.L. Chuvilin, V.N. Kolomiichuk, S.V. Stankus, R.A. Khairulin, et al., The kinetics of the graphitization of dispersed diamonds at “low” temperatures, *J. Appl. Phys.* 88 (2000) 4380.
- [109] S. Tomita, M. Fujii, S. Hayashi, K. Yamamoto, Electron energy-loss spectroscopy of carbon onions, *Chem. Phys. Lett.* 305 (1999) 225.
- [110] S. Tomita, T. Sakurai, H. Ohta, M. Fujii, S. Hayashi, Structure and electronic properties of carbon onions, *J. Chem. Phys.* 114 (2001) 17.
- [111] S. Tomita, A. Burian, J.C. Dore, D. LeBolloch, M. Fujii, S. Hayashi, Diamond nanoparticles to carbon onions transformation: X-ray diffraction studies, *Carbon* 40 (2002) 1469.
- [112] O.O. Mykhaylyk, Y.M. Solonin, D.N. Batchelder, R. Brydson, Transformation of nanodiamond into carbon onions: a comparative study by high-resolution transmission electron microscopy, electron energy-loss spectroscopy, X-ray diffraction, small-angle X-ray scattering, and ultraviolet Raman spectroscopy, *J. Appl. Phys.* 97 (2005) 074302.
- [113] N.S. Xu, J. Chen, S.Z. Deng, Effect of heat treatment on the properties of nanodiamond under oxygen and argon ambient, *Diamond Relat. Mater.* 11 (2002) 249.
- [114] A.E. Aleksenskii, M.V. Baidakova, A.Y. Vul, V.Y. Davydov, Y.A. Pevtsova, Diamond-graphite phase transition in ultradisperse-diamond clusters, *Phys. Solid State* 39 (6) (1997) 1007.
- [115] M.V. Baidakova, V.I. Siklitsky, A.Y. Vul, Ultradisperse-diamond nanoclusters. Fractal structure and diamond-graphite phase transition, *Chaos Solitons Fractals* 10 (1999) 2153.
- [116] B.L.V. Prasad, H. Sato, T. Enoki, Y. Hishiyama, Y. Kaburagi, A.M. Rao, et al., Heat-treatment effect on the nanosized graphite pi-electron system during diamond to graphite conversion, *Phys. Rev. B* 62 (2000) 11209.
- [117] J. Qian, C. Pantea, J. Huang, T.W. Zerda, Y. Zhao, Graphitization of diamond powders of different sizes at high pressure-high temperature, *Carbon* 42 (2004) 2691.
- [118] M. Yoshikawa, Y. Mori, H. Obata, M. Maegawa, G. Katagiri, H. Ishida, et al., Raman scattering from nanometer-sized diamond, *Appl. Phys. Lett.* 67 (1995) 694.
- [119] E.D. Obraztsova, M. Fujii, S. Hayashi, V.L. Kuznetsov, Y.V. Butenko, A.L. Chuvilin, Raman identification of onion-like carbon, *Carbon* 36 (1998) 821.
- [120] N. Wada, S.A. Solin, Raman efficiency measurements of graphite, *Physica B* 105 (1981) 353.
- [121] R. Azria, Y.L. Coat, M.H. Hamou, M.N. Hedhili, S. Ustaze, M. Tronc, et al., Dissociative electron attachment in H^- electron stimulated desorption from hydrogenated diamond surfaces, *Surf. Sci.* 482 (2001) 324.
- [122] C. Goeden, G. Dollinger, Electron stimulated desorption of negative ions: a time-of-flight experiment, *Rev. Sci. Instrum* 73 (2002) 3058.
- [123] C. Goeden, G. Dollinger, Electron-stimulated hydrogen desorption from diamond surfaces and its influence on the low-pressure synthesis of diamond, *Appl. Phys. Lett.* 81 (2002) 5027.
- [124] A. Laikhtman, A. Lafosse, Y. Le Coat, R. Azria, A. Hoffman, Clarification of oxygen bonding on diamond surfaces by low energy electron stimulated desorption and high resolution electron energy loss spectroscopy, *J. Chem. Phys.* 119 (2003) 1794.
- [125] L.-C. Qin, S. Iijima, Onion-like graphitic particles produced from diamond, *Chem. Phys. Lett.* 262 (1996) 252.
- [126] V.V. Roddatis, V.L. Kuznetsov, Y.V. Butenko, D.S. Su, R. Schloegl, Transformation of diamond nanoparticles into carbon onions under electron irradiation, *Phys. Chem. Chem. Phys.* 4 (2002) 1964.

- [127] V.L. Kuznetsov, S.I. Moseenkov, K.V. Elumeeva, T.V. Larina, V.F. Anufrienko, A.I. Romanenko, et al., Comparative study of reflectance properties of nanodiamonds, onion-like carbon and multiwalled carbon nanotubes, *Phys. Status Solidi B* 248 (11) (2011) 2572–2576.
- [128] B.B. Pate, The diamond surface: atomic and electronic structure, *Surf. Sci.* 165 (1986) 83.
- [129] A.P. Dementjev, K.I. Maslakov, A.V. Naumkin, Interaction of carbon atoms with nanodiamond surface, in: D.M. Gruen, O.A. Shenderova, A.Y. Vul (Eds.), *Synthesis, Properties and Applications of Ultrananocrystalline Diamond*, Springer, Berlin, 2005, pp. 253.
- [130] A.S. Barnard, N.A. Marks, S.P. Russo, I.K. Snook, Hydrogen stabilization of {111} nanodiamond, *MRS Symp. Proc.* 740 (2003) 69.
- [131] O.E. Anderson, B.L.V. Prasad, H. Sato, T. Enoki, Y. Hishiyama, Y. Kaburagi, et al., Structure and electronic properties of graphite nanoparticles, *Phys. Rev. B* 58 (1998) 16387.
- [132] J. Chen, S.Z. Deng, J. Chen, Z.X. Yu, N.S. Xu, Graphitization of nanodiamond powder annealed in argon ambient, *Appl. Phys. Lett.* 74 (1999) 3651.
- [133] A.E. Aleksenskii, M.V. Baidakova, A.Y. Vul, A.T. Dideikin, V.I. Siklitskii, Effect of hydrogen on the structure of ultradisperse diamond, *Phys. Solid State* 42 (2000) 1575.
- [134] E. Osawa, Disintegration and purification of crude aggregates of detonation nanodiamond, in: D.M. Gruen, O.A. Shenderova, A.Y. Vul (Eds.), *Synthesis, Properties and Applications of Ultrananocrystalline Diamond*, Springer, Berlin, 2005, pp. 231–240.
- [135] Y.V. Butenko, S. Krishnamurthy, A.K. Chakraborty, V.L. Kuznetsov, V.R. Dhanak, M.R.C. Hunt, et al., Photoemission study of onion-like carbons produced by annealing nanodiamonds, *Phys. Rev. B* 71 (2005) 075420.
- [136] V.L. Kuznetsov, Y.V. Butenko, A.L. Chuvilin, A.I. Romanenko, A.V. Okotrub, Electrical resistivity of graphitized ultra-disperse diamond and onion-like carbon, *Chem. Phys. Lett.* 336 (2001) 397.
- [137] E.D. Obraztsova, S.M. Pimenov, V.I. Konov, M. Fujii, S. Hayashi, V.L. Kuznetsov, et al., Raman investigation of onion-like carbon, *Mol. Mater.* 10 (1–4) (1998) 249.
- [138] G. Davies, T. Evans, Graphitization of diamond at zero pressure and a high pressure, *Proc. R. Soc.* 328 (1972) 413.
- [139] F. Bechstedt, A.A. Stekolnikov, J. Furthmuller, P. Käckell, Origin of the different reconstructions of diamond, Si, and Ge(111) surfaces, *Phys. Rev. Lett.* 87 (2001) 016103.
- [140] A. Hoffman, K. Bobrov, B. Fisgeer, H. Shechter, M. Folman, Annealing of ion beam amorphized diamond surfaces studied by *in situ* electron spectroscopy, *Diamond Relat. Mater.* 5 (1996) 76.
- [141] V.L. Kuznetsov, I.L. Zilberberg, Y.V. Butenko, A.L. Chuvilin, B. Segall, Theoretical study of the formation of closed curved graphite-like structures during annealing of diamond surface, *J. Appl. Phys.* 86 (1999) 863.
- [142] A.C. Ferrari, A. Libassi, B.K. Tanner, V. Stolojan, J. Yuan, L.M. Brown, et al., Density, sp^3 fraction, and cross-sectional structure of amorphous carbon films determined by X-ray reflectivity and electron energy-loss spectroscopy, *Phys. Rev. B* 62 (2000) 11089.
- [143] R. Haerle, E. Riedo, A. Pasquarello, A. Baldereschi, sp^2/sp^3 hybridization ratio in amorphous carbon from C1s core-level shifts: X-ray photoelectron spectroscopy and first-principles calculation, *Phys. Rev. B* 65 (2002) 045101.

- [144] P.C. Lurie, J.M. Wilson, The diamond surface. I. The structure of clean surface and the interaction with gases and metals, *Surf. Sci.* 65 (1977) 453.
- [145] A.V. Hamza, G.D. Kubiak, R.H. Stulen, Hydrogen chemisorption and the structure of the diamond C(100)-(2 × 1) surface, *Surf. Sci.* 237 (1990) 35.
- [146] R.E. Thomas, R.A. Rudder, R.J. Markunas, D. Huang, M. Frenklach, Atomic hydrogen adsorption on the reconstructed diamond (100)-(2 × 1) surface, *J. Chem. Vapor Depos.* 1 (1992) 6.
- [147] L.F. Sutcu, C.J. Chu, M.S. Thompson, R.H. Hauge, J.L. Margrave, M.P. D'Evelin, Atomic force microscopy of (100), (110) and (111) homoepitaxial diamond films, *J. Appl. Phys.* 71 (1992) 5930.
- [148] S. Scocov, C.S. Carmer, B. Weiner, M. Frenklach, Reconstruction of (100) diamond surface using molecular dynamics with combined quantum and empirical forces, *Phys. Rev. B* 49 (1994) 5662.
- [149] J. Ristein, Electronic properties of diamond surfaces—blessing or curse for devices? *Diamond Relat. Mater.* 9 (2000) 1129.
- [150] G. Kern, J. Hafner, J. Furthmüller, G. Kresse, (2 × 1) reconstruction and hydrogen-induced de-reconstruction of the diamond (100) and (111) surfaces, *Surf. Sci.* 352–354 (1996) 745.
- [151] K.C. Pandey, New π -bonded chain model for Si(111)-(2 × 1) surface, *Phys. Rev. Lett.* 47 (1981) 1913.
- [152] G.D. Kubiak, K.W. Kolasinski, Normally unoccupied states on C(111) (diamond) (2 × 1)-support for a relaxed n-bonded chain model, *Phys. Rev. B* 39 (1989) 1381.
- [153] S. Iarlori, G. Galli, F. Gygi, M. Parrinello, E. Tosatti, Reconstruction of the diamond (111) surface, *Phys. Rev. Lett.* 69 (1992) 2947.
- [154] R.P. Chin, J.Y. Huang, Y.R. Shen, T.J. Chuang, H. Seki, M. Buck, Vibrational spectra of hydrogen on diamond C(111)-(1 × 1), *Phys. Rev. B* 45 (1992) 1522.
- [155] R. Stumpf, P.M. Marcus, Relaxation of the clean and H-covered C(111) and clean Si(111)-1 × 1 surfaces, *Phys. Rev. B* 47 (1993) 16016.
- [156] C. Su, K.-J. Song, Y.L. Wang, H.-L. Lu, T.J. Chuang, J.-C. Lin, Hydrogen chemisorption and thermal desorption on the diamond C(111) surface, *J. Chem. Phys.* 107 (1997) 7543.
- [157] C. Su, J.-C. Lin, Structural instability of the diamond C(111) surface induced by hydrogen chemisorption, *J. Chem. Phys.* 109 (1998) 9549.
- [158] T. Schaich, J. Braun, J.P. Toennies, M. Buck, C. Woll, Structural changes accompanying the hydrogen desorption from the diamond C(111):H(1 × 1)-surface revisited by helium atom scattering, *Surf. Sci.* 385 (1997) L958.
- [159] G. Kern, J. Hafner, G. Kresse, Atomic and electronic structure of diamond (111) surfaces: I. Reconstruction and hydrogen-induced de-reconstruction of the one dangling-bond surface, *Surf. Sci.* 366 (1996) 445.
- [160] G. Kern, J. Hafner, G. Kresse, Atomic and electronic structure of diamond (111) surfaces: II. (2 × 1) and ($\sqrt{3} \times \sqrt{3}$) reconstructions of the clean and hydrogen-covered three dangling-bond surfaces, *Surf. Sci.* 366 (1996) 464.
- [161] G.N. Ramachandran, Crystal structure of diamond, *Nature* 156 (1945) 83.
- [162] G. Kern, J. Hafner, *Ab-initio* calculations of the atomic and electronic structure of clean and hydrogenated diamond (110) surfaces, *Phys. Rev. B* 56 (1997) 4203.
- [163] O.A. Shenderova, D.W. Brenner, A. Omeltchenko, X. Su, L.H. Yang, Atomistic modeling of the fracture of polycrystalline diamond, *Phys. Rev. B* 61 (2000) 3877.
- [164] G. Jungnickel, D. Porezag, Th. Frauenheim, M.I. Heggie, W.R.L. Lambrecht, B. Segall, et al., Graphitization effects on diamond surfaces, *Phys. Status Solidi A* 154 (1996) 109.

- [165] S. Matsumoto, Y. Matsui, Electron microscopic observation of diamond particles grown from the vapour phase, *J. Mater. Sci.* 18 (1983) 1785.
- [166] W.R.L. Lambrecht, C.H. Lee, B. Segall, J.C. Angus, Z. Li, M. Sunkara, Diamond nucleation by hydrogenation of the edges of graphitic precursors, *Nature* 364 (1993) 607.
- [167] J. Abrahamson, The surface energies of graphite, *Carbon* 11 (1973) 337.
- [168] A.V. Okotrub, L.G. Bulusheva, V.L. Kuznetsov, Y.V. Butenko, A.L. Chuvilin, M.I. Heggie, X-ray emission studies of valence band of nanodiamonds annealed at different temperatures, *J. Chem. Phys. A* 105 (2001) 9781.
- [169] A.S. Barnard, S.P. Russo, I.K. Snook, Structural relaxation and relative stability of nanodiamond morphologies, *Diamond Relat. Mater.* 12 (2003) 1867.
- [170] A.J. Stone, D.J. Wales, Theoretical studies of icosahedral C₆₀ and some related species, *Chem. Phys. Lett.* 128 (1986) 501.
- [171] B.N. Davison, W. Picket, Graphite-layer formation at a diamond (111) surface step, *Phys. Rev. B* 49 (1994) 14770.
- [172] C. Nebel, J. Ristein (Eds.), *Thin Film Diamond: Semiconductors and Semimetals*, Academic Press, London, 2003.
- [173] C. Pantea, J. Qian, G.A. Voronin, T.W. Zerda, High pressure study of graphitization of diamond crystals, *J. Appl. Phys.* 91 (2002) 4.
- [174] A.P. Grigoriev, S.K. Lifshits, P.P. Shamaev, Method of treating diamond, US Patent 4,339,304 (1980).
- [175] Y.V. Butenko, Low temperature diamond graphitization, Ph.D. Thesis, Boreskov Institute of Catalysis, Novosibirsk, 2001 (in Russian).
- [176] O.P. Krivoruchko, V.I. Zaikovskii, K.I. Zamaraev, Formation of unusual liquid-like FeC particles and dynamics of their behavior on amorphous carbon surface at 920–1170 K, *Dokl. Akad. Nauk* 329 (1993) 744.
- [177] M.S. Dresselhaus, G. Dresselhaus, P.C. Eklund, *Science of Fullerenes and Carbon Nanotubes*, Academic Press, San Diego, CA, 1996.
- [178] T.W. Ebbesen (Ed.), *Carbon Nanotubes: Preparation and Properties*, CRC Press, Boca Raton, FL, 1997.
- [179] M.S. Dresselhaus, G. Dresselhaus, P. Avouris, *Carbon nanotubes: synthesis, structure, properties, and applications. Topics in Applied Physics*, vol. 80, Springer, New York, NY, 2001.
- [180] P. Harris, *Carbon Nanotubes and Related Structures: New Materials for the Twenty-First Century*, Cambridge University Press, Cambridge, 2001.
- [181] R. Saito, G. Dresselhaus, M.S. Dresselhaus, *Physical Properties of Carbon Nanotubes*, Imperial College Press, London, 1998.
- [182] J. Liu, S. Fan, H. Dai, Recent advances in methods of forming carbon nanotubes, *MRS Bull.* 29 (4) (2004) 244.
- [183] V.L. Kuznetsov, Y.V. Butenko, V.I. Zaikovskii, A.L. Chuvilin, Carbon redistribution processes in nanocarbons, *Carbon* 42 (2004) 1057.
- [184] B. Palosz, E. Grzanka, C. Pantea, T.W. Zerda, Y. Wang, J. Gubicza, et al., Microstructure of nanocrystalline diamond powders studied by powder diffractometry, *J. Appl. Phys.* 97 (2005) 064316.
- [185] C. Jiang Qian, G. Pantea, Voronin, T.W. Zerda, Partial graphitization of diamond crystals under high-pressure and high-temperature conditions, *J. Appl. Phys.* 90 (2001) 1632.
- [186] W.A. de Heer, D. Ugarte, Carbon onions produced by heat treatment of carbon soot and their relation to the 217.5 nm interstellar absorption feature, *Chem. Phys. Lett.* 207 (1993) 480.

- [187] D. Ugarte, High-temperature behavior of fullerene black, *Carbon* 32 (1994) 1245.
- [188] M.V. Baidakova, Y.V. Butenko, V.L. Kuznetsov, A.Y. Vul', M.A. Yagovkina, X-ray diffraction study of low temperature graphitization of diamond, *International Symposium, Detonation Nanodiamonds: Technology, Properties and Applications*, St. Petersburg, Russia, 7–9 July 2003, p. 77.
- [189] M. Montalti, S. Krishnamurthy, Y. Chao, Y.V. Butenko, V.L. Kuznetsov, V.R. Dhanak, et al., Photoemission spectroscopy of clean and potassium-intercalated carbon onions, *Phys. Rev. B* 67 (2003) 113401.
- [190] S. Tomita, M. Fujii, S. Hayashi, Optical extinction properties of carbon onions prepared from diamond nanoparticles, *Phys. Rev. B* 66 (2002) 245424.
- [191] S. Tomita, S. Hayashi, Y. Tsukuda, M. Fujii, Ultraviolet-visible absorption spectroscopy of carbon onions, *Phys. Solid State* 44 (2002) 450.
- [192] A.I. Romanenko, O.B. Anikeeva, A.V. Okotrub, L.G. Bulusheva, V.L. Kuznetsov, Y.V. Butenko, et al., The temperature dependence of the electrical resistivity and the negative magnetoresistance of carbon nanoparticles, *Phys. Solid State* 44 (2002) 487.
- [193] A.I. Romanenko, O.B. Anikeeva, A.V. Okotrub, V.L. Kuznetsov, Y.V. Butenko, A.L. Chuvilin, et al., Temperature dependence of electroresistivity, negative and positive magnetoresistivity of carbon nanoparticles, in: S. Komarneni, et al. (Eds.), *Nanophase and Nanocomposite Materials*, MRS Proceedings. Material Research Society, Pittsburgh, 2002, 703, 259.
- [194] A. Hirata, M. Igarashi, T. Kaito, Study on solid lubricant properties of carbon onions produced by heat treatment of diamond clusters or particles, *Tribol. Int.* 37 (2004) 899.
- [195] N. Matsumoto, L. Joly-Pottuz, H. Kinoshita, N. Ohmae, *Diamond Relat. Mater.* 16 (2007) 1227–1230.
- [196] L. Joly-Pottuz, B. Vacher, N. Ohmae, J.M. Martin, T. Epicier, Anti-wear and friction reducing mechanisms of carbon nano-onions as lubricant additives, *Tribol. Lett.* 30 (2008) 69–80.
- [197] E.W. Bucholz, N. Matsumoto, S.R. Phillpot, S.B. Sinnott, N. Ohmae, J.M. Martin, Friction properties of carbon nano-onions from experimental and computer simulations, *Tribol. Lett.* 37 (2010) 75–81.
- [198] S.A. Maksimenko, V.N. Rodionova, G.Y. Slepyan, V.A. Karpovich, O. Shenderova, J. Walsh, et al., Attenuation of electromagnetic waves in onion-like carbon composites, *Diamond Relat. Mater.* 16 (2007) 1231–1235.
- [199] V. Kuznetsov, S. Moseenkov, A. Ischenko, A. Romanenko, T. Buryakov, S. Olga Anikeeva, et al., Controllable electromagnetic response of onion-like carbon based materials, *Phys. Status Solidi B* 245 (10) (2008) 2051–2054.
- [200] O. Shenderova, V. Grishko, G. Cunningham, S. Moseenkov, G. McGuire, V. Kuznetsov, Onion-like carbon for terahertz electromagnetic shielding, *Diamond Relat. Mater.* 17 (2008) 462–466.
- [201] J. Macutkevicius, R. Adomavicius, A. Krotkus, D. Seliuta, G. Valusis, S. Maksimenko, et al., Terahertz probing of onion-like carbon-PMMA composite films, *Diamond Relat. Mater.* 17 (2008) 1608–1612.
- [202] I. Mazov, V. Kuznetsov, S. Moseenkov, A. Usoltseva, A. Romanenko, O. Anikeeva, et al., Electromagnetic shielding properties of MWCNT/PMMA composites in Ka-band, *Phys. Status Solidi B* 246 (2009) 2662–2666.
- [203] J. Macutkevicius, D. Seliuta, G. Valusis, J. Banys, V. Kuznetsov, S. Moseenkov, et al., High dielectric permittivity of percolative composites based on onion-like carbon, *Appl. Phys. Lett.* 95 (2009) 112901-1–112901-3.

- [204] J. Macutkevicius, D. Seliuta, G. Valusis, J. Banys, P. Kuzhir, S. Maksimenko, et al., Dielectric properties of onion-like carbon based polymer films: experiment and modeling, *Solid State Sci.* 11 (2009) 1828–1832.
- [205] P. Kuzhir, A. Paddubskaya, S. Maksimenko, V. Kuznetsov, S. Moseenkov, A. Romanenko, et al., Carbon onion composites for EMC applications, *IEEE Trans. Electromagn. Compat.* 54 (2012) 6–16.
- [206] E. Koudoumas, O. Kokkinaki, M. Konstantaki, S. Couris, S. Korovin, P. Detkov, et al., Onion-like carbon and diamond nanoparticles for optical limiting, *Chem. Phys. Lett.* 357 (2002) 336.
- [207] G.M. Mikheev, V.L. Kuznetsov, D.L. Bulatov, T.N. Mogileva, S.I. Moseenkov, A.V. Ishchenko, Photoinduced transparency of a suspension of onion-like carbon nanoparticles, *Tech. Phys. Lett.* 35 (2009) 162–165.
- [208] G.M. Mikheev, V.L. Kuznetsov, D.L. Bulatov, T.N. Mogileva, S.I. Moseenkov, A.V. Ishchenko, Optical limiting and bleaching effect in a suspension of onion-like carbon, *Quantum Electron.* 39 (2009) 342–346.
- [209] P. Lambin, L. Henrard, A.A. Lucas, T. Cabioc'h, Optical properties of the carbon onions, in: G. Benedek, P. Milani, V.G. Ralchenko (Eds.), *Nanostructured Carbon for Advanced Applications*, Kluwer Academic, Dordrecht, 2001, pp. 273–284.
- [210] C. Portet, G. Yushin, Y. Gogotsi, Electrochemical performance of carbon onions, nanodiamonds, carbon black and multiwalled nanotubes in electrical double layer capacitors, *Carbon* 45 (2007) 2511–2518.
- [211] E.G. Bushueva, P.S. Galkin, A.V. Okotrub, L.G. Bulusheva, N.N. Gavrilov, V.L. Kuznetsov, et al., Double layer supercapacitor properties of onion-like carbon materials, *Phys. Status Solidi B* 245 (10) (2008) 2296–2299.
- [212] D. Pech, M. Brunet, H. Durou, P. Huang, V. Mochalin, Y. Gogotsi, et al., Ultrahigh power electrochemical micro-capacitors based on onion-like carbon, *Nat. Nanotechnol.* 5 (2010) 651–654.
- [213] J.K. McDonough, A.I. Frolov, V. Presser, J. Niu, C.H. Miller, T. Ubieta, et al., Influence of the structure of carbon onions on their electrochemical performance in supercapacitor electrodes, *Carbon* (2012).
- [214] G.A. Kovalenko, L.V. Perminova, N.A. Rudina, I.N. Mazov, S.I. Moseenkov, V.L. Kuznetsov, Immobilization of enzymatic active substances by immuring inside nano-carbon-in-silica composites, *J. Mol. Catal. B Enzym.* 76 (2012) 116–124.
- [215] O. Taran, E. Polyanskaya, O. Ogorodnikova, V.L. Kuznetsov, V. Parmon, M. Besson, et al., Influence of the morphology and the surface chemistry of carbons on their catalytic performances in the catalytic wet peroxide oxidation of organic contaminants, *Appl. Catal. A* 387 (2010) 55–66.
- [216] N. Keller, N.I. Maksimova, V.V. Roddatis, M. Schur, G. Mestl, V.L. Kuznetsov, et al., The catalytic use of onion-like carbon materials for styrene synthesis by oxidative dehydrogenation of ethylbenzene, *Angew. Chem. Int. Ed.* 41 (2002) 1885.
- [217] D.S. Su, N.I. Maksimova, G. Mestl, V.L. Kuznetsov, V. Keller, R. Schlogl, Oxidative dehydrogenation of ethylbenzene to styrene over ultra-dispersed diamond and onion-like carbon, *Carbon* 45 (2007) 2145–2151.
- [218] S.I. Moseenkov, Synthesis and study of onion-like carbon and composites on their base. Ph.D. Thesis, Boreskov Institute of Catalysis, Novosibirsk, RF, 2011, p. 58 (in Russian).

Bonding and Concentration of Hydrogen and Thermal Stability of Nanocrystalline Diamond Films

8

Shaul Michaelson and Alon Hoffman

Schulich Faculty of Chemistry, Technion—Israel Institute of Technology, Haifa, Israel

CHAPTER OUTLINE

8.1 Introduction	248
8.2 The polycrystalline diamond films: brief description of deposition methods and microstructure of the films	250
8.3 Hydrogen atom concentrations in polycrystalline diamond films as a function of grain size studied by SIMS	252
8.4 Hydrogen bonding configuration in diamond film bulk studied by Raman spectroscopy	254
8.4.1 Clarification of the hydrogen-associated Raman peaks through modifications induced by isotopic exchange	255
8.4.2 The impact of diamond grain size and hydrogen concentration on the shape of the Raman spectra	258
8.5 Hydrogen bonding configuration on diamond film surface studied by HR-EELS	261
8.5.1 The hydrogen and carbon bonding configuration of nanoscale-defined hydrogenated polycrystalline diamond surface: the assignment of HR-EELS peaks	261
8.5.2 The impact of diamond grain size on the shape of HR-EEL spectra	265
8.6 Bulk and surface thermal stability of UNC diamond films with 10–30 nm grain size	274
8.6.1 Nanodiamond <i>bulk</i> thermal stability study	274
8.6.2 Nanodiamond <i>surface</i> thermal stability study	278
8.6.3 Discussion of nanodiamond bulk versus surface thermal stability	279
8.7 Computational study	282
8.8 Summary	283
References	284

8.1 Introduction

Carbon science and technology has developed extensively in the last few decades due to discoveries of various polycrystalline and nanocrystalline diamond film deposition methods, synthesis of nanotubes, fullerenes, and carbon fibers. Nanocrystalline diamond films represent a new remarkable material that attracts a lot of attention of the scientific world due to its promising potential in many possible applications, such as tribology [1,2], field emission [3,4], electrochemistry [5,6], protective optical windows [7,8], and its unique ability to incorporate n-type dopants [9] compared to polycrystalline and single crystal diamond.

The microstructure and properties of carbon-based thin films depend on the deposition process and conditions used, including pressure, gas phase composition, and substrate temperature, as well as the energy of the reactive species (atoms or ions). Nanodiamond films may be deposited by a number of deposition processes, which differ in the growth species and deposition parameters. In fact, each method results in different types of nanodiamond films. These may differ in terms of the diamond particle size, grain boundary nature, hydrogen content, defect density, amorphous or graphitic component of the films, morphological properties of the films, and different chemical and physical properties. Also, the formation mechanisms of the different films are dissimilar. For example, the growth of nanodiamond films deposited by microwave (MW) chemical vapor deposition (CVD) from Ar-rich plasma was suggested to occur from C_2 dimers on the film surface [10], whereas deposition from hydrogen-rich direct current (dc) energetic plasma is a subsurface or subplantation process [11].

The ability to deposit diamond films with well-defined crystalline size and nanoscale-ordered surfaces is crucial for possible practical applications. The well-known negative electron affinity and high conductivity of diamond surfaces are properties of fully hydrogenated diamond surfaces [12–14]. Similarly, diamond grain size may influence the electronic and optical properties of the films [15–18]. The properties and associated practical applications of diamond films are significantly modified by their surface structure and chemical composition. However, the chemical and physical characterization of the uppermost surface atomic layers of diamond films present a great challenge. Common surface sensitive techniques (X-ray photoelectron spectroscopy (XPS), Auger electron spectroscopy, electron energy-loss spectroscopy (EELS), etc.) usually deal with a few nanometer surface region rather than with atomic monolayer coverage. Similarly, the characterization of diamond grain size (especially in nanometric scale) requires the use of complicated transmission electron microscopy (TEM) usually combined with X-ray diffraction (XRD) analysis. Therefore, the quest for additional complementary techniques providing information about the grain size and surface properties is of high importance.

In this chapter, we summarize our recent studies related to hydrogen concentration and bonding configuration on the surface and within diamond films as a

function of grain size in the tens to hundreds of nanometer range [19,20] Hydrogen is the major component of the gas mixture usually used for diamond nucleation and growth by CVD methods. It is thus involved in many different processes related to diamond nucleation and growth including (1) formation of clusters necessary for growth (CH_x or C_2H_x), (2) stabilization of diamond clusters and surfaces, (3) preferential etching and removal of nondiamond constituents, and (4) abstraction of hydrogen from the diamond surface to allow incorporation of additional carbon-containing growth species. It is no wonder that hydrogen must be incorporated in some quantity in diamond CVD films and the questions to be asked are (1) in what quantities, (2) in what locations (in the grains as interstitials, forming defect-H clusters in the grains, on the diamond surfaces, in grain boundaries, and in a non-diamond constituent between the grains (e.g., when nanodiamond crystallites are embedded in an a-C-graphitic matrix)), and (3) in what bonding configuration (e.g., bonded to C or as nonbonded H or H_2).

The presence of H in diamond lattice has serious repercussions on its characteristics [21]. While hydrogen incorporation and effects in hydrogenated amorphous carbon films, which may contain up to 45 at% hydrogen [22] are relatively well studied [22–27], only a little information is available on hydrogen distribution, concentration, and location in diamond films [21,28–31]. TEM and a combination of Fourier-transformed infrared (FTIR) absorption and elastic recoil detection analysis (ERDA) were used to evaluate the location of hydrogen in diamond. It has been found that hydrogen in CVD diamond is incorporated on diamond surfaces and in nondiamond regions (graphitic and amorphous carbon). Hydrogen was claimed to be found both in grain boundaries [21,30] and also trapped in grain defects [31].

Diamond polycrystalline films with varying grain size and thickness were extensively investigated by us over the last few years [11,15,16,32,33]. The films consist of diamond crystallites of sizes from ~ 5 to ~ 300 nm depending on deposition methods and conditions [11,33]. The thickness of continuous films varies from ~ 70 to ~ 1000 nm depending on deposition time. The investigated diamond films were grown by three different kinds of CVD methods: (1) hot filament (HF) CVD; (2) dc glow-discharge (dc GD) CVD, and (3) MW CVD. The first two methods utilize hydrogen-rich gas mixtures (CH_4/H_2 ratios were 1/99 and 9/91 correspondingly), while the third one uses a plasma mostly comprised of Ar gas ($>95\%$) while hydrogen atoms originate mainly from methane species. Although the three investigated kinds of diamond films were grown by different techniques resulting in different growth mechanisms, we believe that the final properties of these diamond films should be associated with diamond microstructure and phase composition rather than with a particular deposition method.

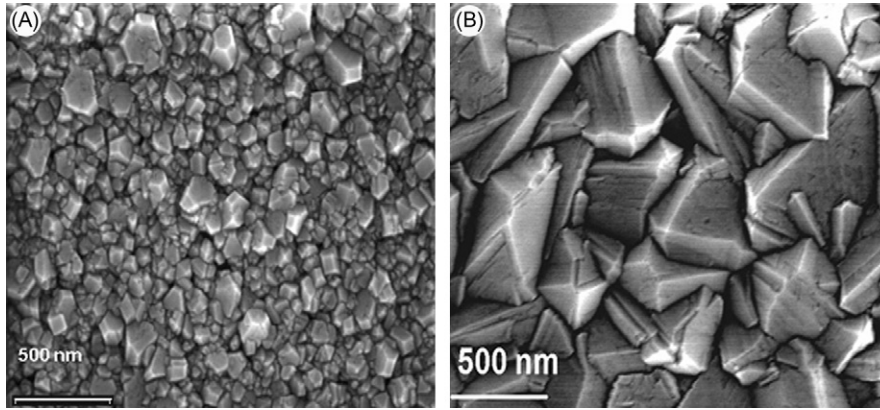
The general structure of this chapter is as follows. First, we discuss the study of hydrogen concentration by secondary ion mass spectroscopy (SIMS) as a function of diamond grain size. Then, we correlate the hydrogen retention with the appearance of Raman peaks and clarify the hydrogen bonding configuration within the film bulk. Subsequently, we review the study of hydrogen bonding configuration

on well-defined film surfaces by high-resolution electron energy-loss spectroscopy (HR-EELS). The assignment of the peaks was done by means of isotopic exchange. Then we report on the thermal stability of nanocrystalline diamond films with 10–30 nm grain size deposited by MW-enhanced CVD as a function of annealing temperature up to 1200°C. It was found that the surface of the film undergoes nearly complete graphitization at 1000°C, while the bulk region is stable beyond 1200°C. These conclusions are supported by computer simulation results where we show that hydrogen atoms at the boundary between a nanodiamond particle and an amorphous shell have lower energy than hydrogen atoms within either the nanodiamond or the amorphous region. These results suggest that hydrogen is expected to be localized at the nanodiamond/amorphous carbon interface, as experimentally found.

8.2 The polycrystalline diamond films: brief description of deposition methods and microstructure of the films

Three kinds of CVD diamond films were grown on silicon substrates by different methods. Below, the main differences in the underlying mechanism and film microstructure are briefly discussed.

1. MW CVD nanodiamond films were grown from a hydrogen-poor gas mixture. The mechanism of the film formation was investigated to a great extent [10] and is considered as a surface process occurring from C_2 molecule as the main growth species. The growth of nanodiamond films from C_2 species requires a surface pretreatment aimed to introduce diamond growth centers onto which the film grows. The as-deposited films are characterized by a high sp^3 content of $\sim 95\%$ [10] and nanometric grain size (in the present study, in the range 3–30 nm), homogeneously distributed over the whole thickness.
2. HF CVD diamond films were grown from a hydrogen-rich gas mixture (CH_4/H_2 ratio was 1/99). The evolution of the film occurs on nucleation centers immersed into the substrate by ultrasonic abrasion with polydispersed mixed diamond slurry [33]. This pretreatment results in an initial diamond particle density (DPD) of $\sim 5 \times 10^{10} \text{ cm}^{-2}$. This high DPD value allows deposition of continuous films with a minimal thickness of $\sim 70\text{--}100 \text{ nm}$ [15,33]. The nucleation is a surface process while the main growth species are CH_x and hydrogen radicals. The deposited films are characterized by high diamond quality ($>98\% \text{ } sp^3$) and well-defined diamond facets. The diamond growth occurs on nucleation centers that gradually merge and coalesce into continuous film. The crystal size evolves from $\sim 50\text{--}70 \text{ nm}$ in the nearly coalescent film ($\sim 100 \text{ nm}$ film thickness, $\sim 10 \text{ min}$ deposition) (Figure 8.1A) and reaches nearly constant value of $300\text{--}400 \text{ nm}$ in micron thick films (deposition time $\sim 1 \text{ h}$) (Figure 8.1B). The increased crystalline size observed in the high-resolution scanning electron microscopy (HR-SEM) images (Figure 8.1) is a result of the suppression of small crystallites by fast growing crystallites that comprise the faceted surface.

**FIGURE 8.1**

HR-SEM micrographs of as-deposited HF CVD diamond films: (A) film deposited from $\text{CH}_4 + \text{H}_2$ gas mixture for 10 min (thickness ~ 100 nm, grain size ~ 50 – 70 nm) and (B) film deposited from $\text{CH}_4 + \text{H}_2$ gas mixture for 60 min (thickness ~ 700 nm, grain size ~ 300 nm).

Table 8.1 Summary of Grain Size and Deposition Methods of the Investigated Diamond Films

Film Name	Grain Size (nm)	Deposition Method	Gas Composition ($\text{CH}_4/\text{H}_2/\text{Ar}$)
dc-GD-CVD-5 nm [32]	~ 5	dc GD CVD	9/91/0
HF-CVD-300 nm [33]	300	HF CVD	1/99/0
MW-CVD-3-20 nm [34]	3–20	MW CVD	1.4/0/98.6
MW-CVD-10-30 nm [34]	10–30	MW CVD	1.4/1/97.6

- dc GD CVD films were grown from hydrogen-rich plasma (CH_4/H_2 ratio was 9/91) by means of continuous substrate bombardment by positive hydrocarbon and hydrogen ions of ~ 100 – 200 eV kinetic energy. No pretreatment procedure is needed to induce diamond nucleation. The nanodiamond nucleation and growth occur in the subsurface region of the film resulting in the upper surface region consisting of hydrogenated amorphous carbon. The film evolves on top of a hydrogenated carbonaceous precursor containing a mixture of an amorphous and graphitic carbon formed during the first ~ 20 min of deposition (~ 300 nm thickness). When the precursor density reaches ~ 3 g/cm³, nanodiamond particles precipitate and grow to a final size of ~ 5 nm by means of preferential displacement of loosely bonded carbon atoms by energetic ions [11,32]. The sp^3 content of the film grown for 1 h reaches $\sim 80\%$. The nanodiamond particles are embedded in hydrogenated amorphous carbon matrix. Table 8.1 summarizes the deposition methods and the resulting grain size of all the investigated diamond films.

8.3 Hydrogen atom concentrations in polycrystalline diamond films as a function of grain size studied by SIMS

The hydrogen concentration within the three different kinds of polycrystalline diamond films described above were analyzed by SIMS technique [28,35]. SIMS analysis was carried out in a dynamic mode in a Cameca IMS4f ion microscope using a 14.5 keV Cs^+ ion beam. The sampling area was about $64\mu\text{m}^2$. The basic chamber pressure was 8×10^{-10} Torr, while the ion current was about 1×10^{-8} A.

SIMS depth profiles of hydrogen concentration within the different diamond films are shown in Figure 8.2. Profile A in Figure 8.2 is taken from a $\sim 1.6\mu\text{m}$ thick HF CVD sample grown for 2h from $\text{CH}_4 + \text{H}_2$ gas mixture. Its initial grain size (close to the film-Si substrate interface) is $\sim 50\text{nm}$ and develops during the deposition to a final grain size of $\sim 300\text{nm}$, thus allowing a direct measurement of the correlation between the hydrogen trapping and the crystalline size [28,35]. Notice that the sampling depth given in Figure 8.2 represents the film surface at a depth of

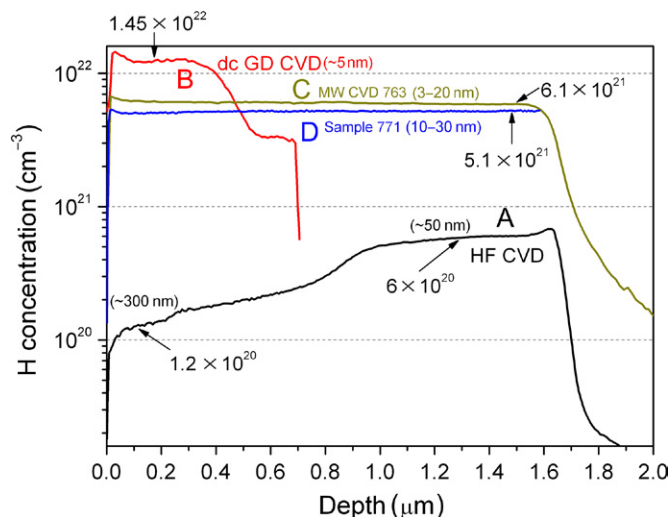


FIGURE 8.2

SIMS profile of hydrogen atoms within three different types of diamond films. (A) HF CVD film deposited from $\text{CH}_4 + \text{H}_2$ gas mixture for 2h. Notice the decrease of H concentration from 6×10^{20} atoms/ cm^3 at the initial growth region (grain size $\sim 50\text{nm}$) to 1.2×10^{20} atoms/ cm^3 for thicker film (grain size $\sim 300\text{nm}$). (B) 700nm thick nanodiamond film deposited by dc GD CVD. The hydrogen concentration increases from 3.3×10^{21} atoms/ cm^3 at the initial stage of film evolution (predominantly graphitic precursor) up to 1.45×10^{22} atoms/ cm^3 in the region where $\sim 5\text{nm}$ sized nanodiamond grains are embedded in an amorphous carbon matrix. (C) MW CVD diamond film with grain size 3–20nm. (D) MW CVD diamond film with grain size in the range of 10–30nm.

0 and the Si substrate region at a depth of 1.6 μm . It is very clear that the hydrogen concentration of this film decreases from 6×10^{20} atoms/ cm^3 at the region close to the Si substrate (50 nm grain size) to 1.2×10^{20} atoms/ cm^3 in the region close to the film's surface formed after a deposition time of ~ 2 h (~ 300 nm grain size) [19,33].

The profile of hydrogen atoms in dc GD CVD film grown for 1 h is shown in Profile B in Figure 8.2. In our previous works [11,32], we showed that the growth of the dc GD CVD film advances through the following stages: (1) graphitic film with its basal plane perpendicular to the substrate, a low H concentration, and low (~ 2.2 g/ cm^3) density; (2) an increase in density followed by incorporation of hydrogen; (3) the formation of a dense (~ 3 g/ cm^3), hydrogen-rich layer in which diamond nucleates and grows. The hydrogen concentration (Profile B in Figure 8.2) in the nanodiamond film deposited by dc GD CVD increases from 3.3×10^{21} at the nanographitic precursor region to 1.45×10^{22} atoms/ cm^3 in the ~ 5 nm sized nanodiamond crystallites region [28]. The hydrogen concentration depth profile of the dc GD film reflects the evolution of its structure from an initial low density, low hydrogen concentration graphitic film through a medium density, hydrogen-containing film until a dense, hydrogen-containing matrix evolves, in which ~ 5 nm sized nanodiamond crystallites precipitate. Our previous measurements of absolute hydrogen concentration within these films by means of ERDA revealed hydrogen concentration of 15–20 at% [28], which confirms the present SIMS measurements.

Profiles C and D in Figure 8.2 show hydrogen concentration in two nanodiamond films deposited by MW CVD with grain size of 3–20 and 10–30 nm, respectively. The measured hydrogen concentration for samples MW-CVD-3-20 nm and MW-CVD-10-30 nm were 6.1×10^{21} and 5.1×10^{21} atoms/ cm^3 , correspondingly. Note the slightly larger hydrogen concentration for MW-CVD-3-20 nm (CH_4/Ar ratio of 1.4/98.6, grain size 3–20 nm) than for MW-CVD-10-30 nm ($\text{CH}_4/\text{H}_2/\text{Ar}$ ratio of 1.4/1/97.6, grain size 10–30 nm), e.g., despite the higher hydrogen concentration in the gas phase its retention within the film is lower for the last sample. Moreover, the hydrogen concentration of MW CVD films (grown from hydrogen-poor gas mixture) largely exceeds that measured for the HF CVD grown films (carried out in a hydrogen-rich atmosphere). Therefore, one may suggest that the hydrogen incorporation within the diamond film is governed by another factor beyond gas mixture composition. The most evident factor that influences the retention of hydrogen atoms within the films is diamond grain size. Our results clearly show that the smaller the diamond crystallites are, the higher the hydrogen concentration is within the films. Notice that all samples were mounted at the same time in the SIMS chamber and measured at the same conditions. Therefore, while the absolute hydrogen concentration values within the films may depend on the correct relative sensitivity factor (RSF), the relative measured concentrations can be compared.

Table 8.2 summarizes the H concentrations in the different films, the atomic percentage of the H (assuming a C density of 10^{23} atoms/ cm^3), the crystalline size deduced from HR-SEM and HR-TEM, and the surface to volume atom ratio of face centered cubic (FCC) crystallites with the same crystalline size. It is very clear that the hydrogen concentration in the diamond films increases with decreasing crystalline

Table 8.2 Hydrogen Concentration versus Crystalline Size and the Surface to Volume Atom Ratio

Film Type	H Concentration (atoms/cm ³)	H Concentration (at%) ^a	Crystalline Size (nm)	Surface to Volume Atom Ratio (%) ^b
HF CVD (1 h)	1.2×10^{20}	0.12	300	0.5
HF CVD (10 min)	6×10^{20}	0.6	50	3
MW-CVD-3-20 nm	6.1×10^{21}	6.1	3–20	50–7.5
MW-CVD-10-30 nm	5.1×10^{21}	5.1	10–30	15–5
dc-GD-CVD-5 nm	1.45×10^{22}	14.5	5	28

^aAssuming a C concentration of 1×10^{23} atoms/cm³.
^bSurface to volume atom ratio of FCC crystallite with the same crystalline size.

size. This result strongly suggests that hydrogen atoms are bonded within the diamond film's bulk to the grains *surfaces*. The trapping of hydrogen in grain boundaries is a natural consequence of the accepted diamond growth mechanism, which involves adsorption of a CH_x growth species first and then abstraction of one hydrogen atom from the surface by atomic hydrogen in the gas phase, allowing the diamond carbon atom to be bonded to another CH_x radical. Coalescence of adjacent diamond crystallites most likely does not result in complete hydrogen desorption from touching surfaces leading to the incorporation of hydrogen on the touching crystallites surfaces (grain boundaries).

8.4 Hydrogen bonding configuration in diamond film bulk studied by Raman spectroscopy

Raman spectroscopy has a lot to offer as a nondestructive characterization tool. Backscattering geometry, especially with micro-focus instruments, allows small regions in the heterogeneous films to be easily examined. Raman spectroscopy is a very powerful technique for the identification of crystalline phases, and for studies of defects, structural disorder, and stresses in thin films. However, due to quantum size effects, the use of Raman spectroscopy for the unambiguous phase characterization of films composed of nanosized crystalline particles is complicated [36,37]. The Raman measurements were carried out using a DILOR XY system. The measurements were performed using the Ar line at 514.5 nm in a backscattering geometry. The laser beam spot size was $\sim 1 \mu\text{m}$ in diameter and the incident power was 10 mW [20].

The Raman spectrum of diamond consists of a single peak at 1332 cm^{-1} , whereas for graphite a single peak is observed at 1580 cm^{-1} (usually labeled the G peak) [37,38]. The diamond peak may be broadened by several wave numbers by defects, stresses, and/or small crystalline size. Usually, in the case of the CVD diamond films, this peak is accompanied by a broad band centered around $1500\text{--}1550 \text{ cm}^{-1}$ believed to be due to the sp²-bonded carbon, possibly in the grain

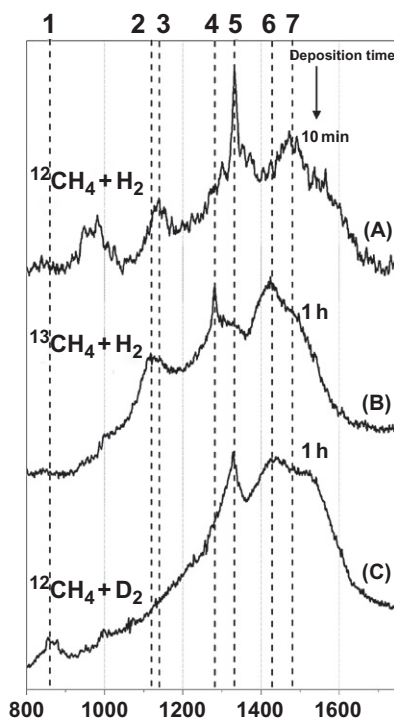
boundaries [37]. The Raman spectra of polycrystalline graphite and glassy carbon consist of two peaks. The first, located at $1580\text{--}1590\text{cm}^{-1}$ (G peak), originates from lattice vibrations in the plane of the graphite-like rings [38]. The second peak is located at about 1350cm^{-1} (the D peak) and occurs in graphitic materials with small crystalline size. This disordered-induced band corresponds to a peak in the vibrational density of states of graphite. In amorphous materials, the lack of long-range order leads to a relaxation of the selection rules governing the Raman scattering process, and all vibrational modes can contribute to the Raman spectra.

Because of the very much larger Raman cross section for graphite sp^2 bonds ($5 \times 10^{-5}\text{cm}^{-1}/\text{sr}$) relative to diamond sp^3 bonds ($9 \times 10^{-7}\text{cm}^{-1}/\text{sr}$), it is very difficult to observe any spectral Raman features associated with a small amount of sp^3 bonding in the presence of sp^2 -bonded material [37,39]. By the same token, the high sensitivity of the Raman spectra to sp^2 bonding allows sensitive detection of small concentrations of sp^2 bonding in a diamond film.

In this section, we clarify the Raman peaks associated with diamond grain boundary vibrations by means of reduced mass change via isotopic modification of the growth mixture. Then, we correlate the shape of the Raman spectrum with hydrogen retention studied by SIMS for the films possessing different grain size.

8.4.1 Clarification of the hydrogen-associated Raman peaks through modifications induced by isotopic exchange

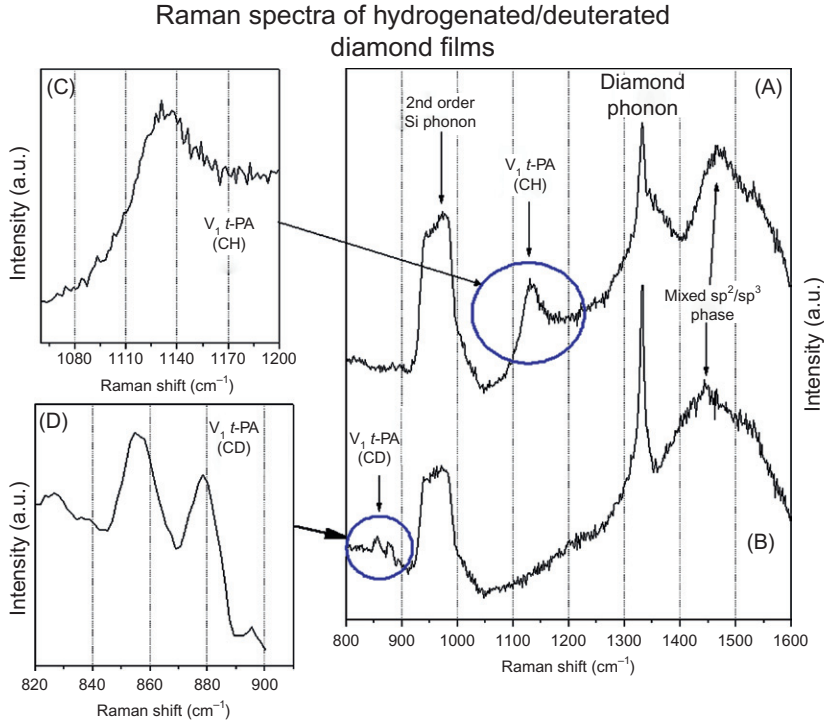
Raman spectra of diamond films display the diamond optical phonon line at 1332cm^{-1} and other contributions originated in sp^2 -carbon-related features (e.g., the 1350cm^{-1} D line and the 1580cm^{-1} G line); the relative intensity depends on diamond crystal size, grain quality, etc. [36–38]. An additional feature around 1140cm^{-1} , commonly observed in nanodiamond films, was initially assigned to sp^3 -bonded carbon [40] and often taken as a simple criterion for a nanocrystalline diamond phase [41,42]. Later, it was revealed that the 1140cm^{-1} peak usually appears together with the broad band at 1480cm^{-1} and shows significant dispersion, while the diamond mode does not [36]; therefore, its association with sp^3 -bonded carbon was questioned. It was shown by Raman [37,43] and surface-enhanced Raman spectroscopy [44] that these peaks are associated with the ν_1 and ν_3 vibration modes of *trans*-polyacetylene (*t*-PA) co-deposited with diamond phase. This assignment was supported by (1) the disappearance of the peak upon annealing to 1200°C (due to hydrogen release) keeping the diamond 1332cm^{-1} peak intact, (2) the shift of the peak position with increasing excitation energy and its disappearance for UV Raman, (3) its absence in the Raman spectra of nanodiamond powders made by detonation, and (4) the peak shift from 1140 to $\sim 860\text{cm}^{-1}$ upon full hydrogen exchange by deuterium in the CVD plasma used for growth. We confirmed this suggestion by deposition of diamond films from different isotopic gas mixtures, where hydrogen was replaced by deuterium fully ($\text{CD}_4 + \text{D}_2$) and partially ($\text{CD}_4 + \text{H}_2$ and $\text{CH}_4 + \text{D}_2$) as well as when ^{12}C was replaced by ^{13}C ($^{13}\text{CH}_4 + \text{H}_2$) [20]. Here, we shortly summarize our findings. Figure 8.3 presents the Raman spectra of HF CVD diamond films deposited from ($^{12}\text{CH}_4 + \text{H}_2$), ($^{13}\text{CH}_4 + \text{H}_2$), and ($^{12}\text{CD}_4 + \text{D}_2$) gas mixtures.

**FIGURE 8.3**

Raman spectra of submicron diamond films prepared by the HF CVD for different isotopic compositions of methane/hydrogen species (1/99) indicated on the plot. The deposition time was 1 h except for the sample corresponding to the upper line (A), which was grown for 10 min.

Raman spectrum A in Figure 8.3 of $\sim 100\text{nm}$ (crystalline size $< 50\text{nm}$) film, deposited from $^{12}\text{CH}_4 + \text{H}_2$ gas mixture, exhibits the 1332cm^{-1} diamond peak, the broad contribution centered at 1480cm^{-1} and the peak at 1140cm^{-1} . The additional broad peak around 1000cm^{-1} is attributed to the second overtone of Si optical phonon. Exchange of ^{12}C by ^{13}C (spectrum B in Figure 8.3) shifts the 1332cm^{-1} peak to 1280cm^{-1} but does not significantly shift the 1140cm^{-1} peak. In addition, the peak at 1480cm^{-1} (spectrum A) is shifted to 1420cm^{-1} (spectrum B) when ^{12}C is replaced by ^{13}C . The decrease of the 1332cm^{-1} diamond peak in the Raman spectra of the HF CVD diamond films due to isotopic exchange of H by D indicates that the crystalline quality of these films was affected by the isotopic replacement, which modified the deposition conditions, even though the growth parameters were kept intact. This explains why the 1140cm^{-1} peak of the high-quality diamond film (highest 1332cm^{-1} peak) is very weak. The same modifications of the Raman spectra were observed when dc GD CVD nanodiamond films were grown from similar isotopic gas mixtures [20].

In Figure 8.4 a detailed view of the Raman spectra is shown of $\sim 100\text{nm}$ thick HF CVD polycrystalline diamond film deposited from hydrogenated (spectra A and C)

**FIGURE 8.4**

Raman spectra of poly-Di film deposited from hydrogenated (A) and deuterated (B) gas mixture. The well-established shift of the C–H t -PA peak is observed. Spectra (C) and (D) show detailed spectra of relevant regions that were recorded separately for long acquisition time.

and deuterated (spectra B and D) species. The presented data clearly show that the 1140cm^{-1} peak is associated with C–H mode. This peak is shifted and split into two peaks at ~ 860 and $\sim 880\text{cm}^{-1}$ by isotopic exchange of H in the growth plasma, suggesting at least two different bonding configurations of hydrocarbon that are indistinguishable in hydrogenated mode. The possible explanation of this phenomenon may be found in Ref. [45].

In contrast, C–C modes are not affected by isotopic substitution of H and are shifted by isotopic substitution of C. The 1480cm^{-1} peak is shifted to 1420cm^{-1} position and is associated with C–C mode. The experimental isotopic shifts of the Raman peaks closely match the calculated shifts for the specific C–H or C–C modes. Indeed, the carbon 1480cm^{-1} peak shifts to 1420cm^{-1} in perfect agreement with ^{12}C and ^{13}C reduced mass difference:

$$\omega_{^{13}\text{C}-^{13}\text{C}} = \frac{\omega_{^{12}\text{C}-^{12}\text{C}}}{\sqrt{\frac{\mu_{^{13}\text{C}-^{13}\text{C}}}{\mu_{^{12}\text{C}-^{12}\text{C}}}}} = \omega_{^{12}\text{C}-^{12}\text{C}} \times 0.9608 \quad (8.1)$$

Whereas the same effect, much less prominent in the case of $^{13}\text{C-H}$ and $^{12}\text{C-H}$ vibration mode is given as

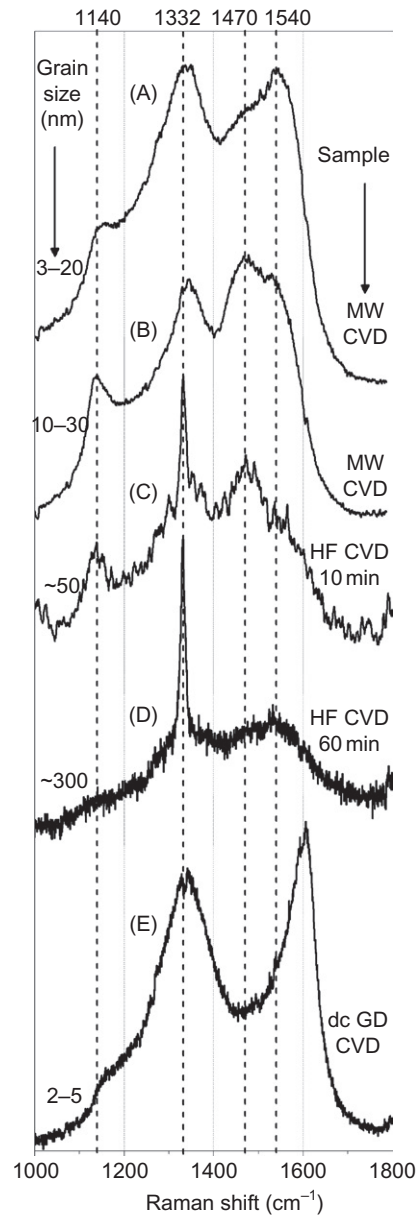
$$\omega_{^{13}\text{C-H}} = \frac{\omega_{^{13}\text{C-H}}}{\sqrt{\frac{\mu_{^{13}\text{C-H}}}{\mu_{^{13}\text{C-H}}}}} = \omega_{^{12}\text{C-H}} \times 0.997 \quad (8.2)$$

We determined that the 1140cm^{-1} Raman peak is associated most likely with the bending mode of hydrogenated sp^2 carbon bonded to diamond grain *surface*. This mode is present on the spectrum of hydrogenated carbon solely if the film is constituted of diamond grains. Our studies of dc GD CVD nanodiamond film evolution on hydrogenated graphitic/amorphous carbon precursor clearly show [46] that this mode is absent from the spectrum of hydrogenated carbon (~ 20 min deposition) and appears only when nanodiamond crystallites precipitate in dense hydrogenated amorphous carbon matrix (~ 30 min deposition). Since hydrogen atom concentration nearly scales with diamond grain surface ratio, it may be guessed that this mode is related to diamond phase itself, e.g., belongs to sp^2 carbon bonded to diamond grain *surface*. Our work on thermal stability of carbon–hydrogen bonding [46] provides direct evidence that this mode is stable up to temperatures typically associated to hydrogen desorption from diamond surfaces (up to 1000°C). On the other hand, nearly all kinds of hydrogenated carbon with different sp^2/sp^3 ratios decompose at temperatures up to $\sim 600^\circ\text{C}$. In Section 8.5.2, we correlate the 1140cm^{-1} Raman mode with $(\text{sp}^2)\text{-C-H}$ stretching vibration detected by HR-EELS.

8.4.2 The impact of diamond grain size and hydrogen concentration on the shape of the Raman spectra

In Section 8.3, we showed that a substantial amount of hydrogen is trapped within diamond films grown by three different kinds of CVD. Independent of the gas mixture composition, the hydrogen retention within the films scales with the diamond grain size: the smaller grains give rise to higher hydrogen retention. In this section, we correlate the hydrogen retention with the shape of the Raman peak.

The hydrogen bonding and the crystalline nature of the different films were characterized by Raman (Figure 8.5). Spectra A and B in Figure 8.5 correspond to the MW CVD films grown for 1 h, samples MW-CVD-3-20 nm and MW-CVD-10-30 nm, respectively. Spectra C and D in Figure 8.5 were measured on the HF CVD diamond films grown for 10 min (~ 100 nm film thickness, spectrum C) and 60 min (~ 700 nm thickness, spectrum D), respectively (their SEM micrographs were shown in Figure 8.1). Spectrum E in Figure 8.5 was measured on dc GD CVD film grown for 60 min. Besides spectrum D, all spectra display most of the characteristic Raman modes of nanodiamond films discussed in Section 8.4.1: two broad peaks at $\sim 1350\text{cm}^{-1}$ (D peak) and 1530cm^{-1} (G peak), associated with sp^2 -bonded carbon, and ν_1 and ν_3 modes of *t*-PA positioned at 1140 and 1480cm^{-1} , respectively [37,43]. Spectra C and D in Figure 8.5 display an additional peak positioned at

**FIGURE 8.5**

Raman spectra of the different diamond samples. (A) MW CVD sample with grain size of 3–20 nm. (B) MW CVD sample with grain size of 10–30 nm. (C) HF CVD diamond film deposited for 10 min (~50 nm grain size). (D) HF CVD diamond film deposited for 1 h (~300 nm grain size). (E) dc GD CVD diamond film deposited for 1 h (~5 nm grain size).

1332 cm^{-1} attributed to the diamond optical phonon. Spectrum D was measured on a thick HF CVD diamond film and is attributed to high-quality diamond film. Here, the diamond peak at $\sim 1332\text{ cm}^{-1}$ is sharp, well pronounced, and large compared to the background contributions of the sp^2 -related D and G peaks, reflecting the much larger diamond crystalline size, reduced grain boundary, and defect densities. The t -PA vibrational modes at 1140 and 1480 cm^{-1} are practically absent, indicating a much smaller amount of C–H bonding at grain boundaries in comparison to the 100 nm thick HF CVD film.

It was shown that the three different classes of diamond films follow the same tendency: smaller grain size results in higher hydrogen retention. It is possible, therefore, to associate the shape of the Raman spectrum with diamond grain size and hydrogen content therein. The high hydrogen concentration results in appearance of pronounced t -PA-associated Raman modes at 1140 and 1480 cm^{-1} . In addition, the sharp diamond optical phonon mode at 1332 cm^{-1} is broader for grain size smaller than 50 nm , and for 10 – 30 nm crystallites the graphitic D peak at 1350 cm^{-1} appears. For the smallest grain size (e.g., $\sim 5\text{ nm}$ in the case of dc GD nanodiamond films, spectrum E in Figure 8.5), however, the intensity of 1140 cm^{-1} is diminished relative to carbon-associated D and G peaks in comparison to spectra B and C in Figure 8.5. From the SIMS measurements it is known that the dc GD sample contains the highest (among the investigated films) concentration of the trapped hydrogen atoms. Why is the intensity of carbon–hydrogen bonding less pronounced in more “hydrogen-rich” samples of smaller grain size?

Our results suggest that for diamond films composed of crystallites of $\sim 5\text{ nm}$, so-called ultrananocrystalline (UNC) diamond films, the intensity of hydrogen-associated peaks is diminished relative to the carbon-associated modes. In Section 8.5.2, additional evidence of this phenomenon comes from HR-EELS measurements of C–H stretching vibrations on UNC diamond surface. A similar tendency was found in IR measurements of diamond C–H stretching mode as a function of diamond grain size [47–49]. The intensity of C–H stretching mode at 2834 cm^{-1} decreases with decreasing diamond grain size ($350 \rightarrow 5\text{ nm}$). In that case, the proposed explanation of this phenomenon (based on density functional calculations) is an absence of well-defined facets on the surface of 5 nm size diamond crystallites [47,48].

We conclude that the shape of the Raman spectrum is strongly affected by diamond grain size (and, therefore, by hydrogen atoms concentration within the film). While the spectrum of the film that consists of diamond grains the size of a few hundred nanometers is dominated by diamond optical phonon loss at 1332 cm^{-1} with minor contribution from mixed sp^2/sp^3 carbon (the band near 1500 cm^{-1}), the smaller diamond crystallites result in enhanced sp^2 -carbon–hydrogen peaks near 1140 and 1480 cm^{-1} . However, for UNC diamond films (grain size $\sim 5\text{ nm}$), the intensity of these peaks decreases and the spectrum is dominated by graphitic D and G peaks at 1350 and 1580 cm^{-1} . Obviously, reducing grain size may affect the complex bonding configuration of carbon atoms within the film, namely, sp^2/sp^3 ratio, the ordering of sp^2 component, etc., not just the amount of hydrogen atoms bonded to sp^2 -hybridized carbon.

8.5 Hydrogen bonding configuration on diamond film surface studied by HR-EELS

HR-EELS is a very powerful surface characterization probe that may provide direct information about hydrogen bonding on surfaces [50]. The electron spectroscopy measurements reported in our studies were carried out using an ultra-high vacuum (UHV) system consisting of two chambers connected in tandem. In the first chamber annealing, XPS and ion irradiation experiments were carried out, whereas the second chamber is dedicated to HR-EELS. The samples can be heated *in situ* up to $\sim 1000^\circ\text{C}$ and exposed to thermally activated hydrogen. The HR-EELS chamber is equipped with a Delta 0.5 spectrometer (VSI-SPECS) consisting of a double monochromator and a single analyzer housed in an UHV system with a base pressure of $\sim 8 \times 10^{-10}$ Torr. All spectra were recorded up to loss energies of 700 meV at room temperature in the specular geometry with an incident angle of 55° from the surface normal, incident energy of 5 eV, and energy resolution of 5–8 meV (according to full width half maximum (FWHM) of the elastic peak). The XPS measurements were carried out using Al K α (1486.6 eV) photon irradiation. The surface quality and phase composition of the films were investigated by C(1s) photoelectron energy-loss spectra. A fine-focused Ar $^+$ ion source IQE 12/38 of SPECS was used for ion irradiation experiments. The beam energy could be varied in the 200 eV to 5 keV range, and typical beam currents were up to 10 μA .

In Section 8.5.1, we assign the different HR-EELS peaks to specific vibrational modes of well-defined diamond surface by means of isotopic exchange. In Table 8.3 we compare our assignments with assignment found in the literature [51–71]. In Section 8.5.2, the impact of diamond grain size on the shape of HR-EEL spectra is discussed. The influence of hydrogenated sp^2 -hybridized carbon most likely originated from diamond grain boundaries is shown.

8.5.1 The hydrogen and carbon bonding configuration of nanoscale-defined hydrogenated polycrystalline diamond surface: the assignment of HR-EELS peaks

In the following discussion, we compare the samples grown from isotopic mixtures with the sample grown from the “common” gas mixture ($^{12}\text{CH}_4 + \text{H}_2$) by HF CVD. For simplicity we shall refer to the last gas mixture as the “common” gas mixture and to the sample as the “common” sample.

HR-EEL spectra of the films deposited from isotopic mixtures are shown in Figure 8.6. The sample deposited from $^{12}\text{CH}_4 + \text{H}_2$ and $^{13}\text{CH}_4 + \text{H}_2$ was treated *ex situ* in MW-H plasma for 20 min, while the sample $^{12}\text{CD}_4 + \text{D}_2$ was treated in MW-D plasma for the same time. Each sample was annealed to $450\text{--}500^\circ\text{C}$ in UHV conditions before measurements. Different vibrational modes are enumerated on top of Figure 8.6. Each peak was fitted for contributions from two possible modes: C–H (or C–D) and C–C. Notice that in spectrum B in Figure 8.6

Table 8.3 Assignment of HR-EELS Modes Relevant to the Present Discussion

HR-EELS Mode Position	Assignment Based on Literature Survey	Our Present Assignment
Hydrogenated Diamond (C-12) Surface		
~155 meV	C-H bending modes [50–56]; mixed C-H bend and C-C stretch modes [57–69]	Mixed ^{12}C -H bend and ^{12}C - ^{12}C stretch modes
300 meV	First overtone of C-H modes [51,53–55]; first overtone of C-C modes [52,57,58,62–67]	First overtone of ^{12}C diamond optical phonon
358–362 meV	C-H stretching mode [49–70]	^{12}C -H stretching mode
450 meV	Second overtone of C-H modes [51,53,54]; second overtone of C-C modes [62–67]	Second overtone of ^{12}C diamond optical phonon
510 meV	Coupled C-H deformation and C-H stretching modes [50]; coupled C-C stretch and C-H bend modes [67,70]	Overlapping of both ^{12}C -H bend and ^{12}C -H stretching modes and ^{12}C - ^{12}C stretch and ^{12}C -H bend modes
600 meV	Third overtone of C-C modes [67]	Third overtone of diamond optical phonon
Deuterated Diamond (C-12) Surface		
~110 meV	C-D bending modes [52–54,57,58]	^{12}C -D bending modes
150 meV	C-C stretching modes [52,57,58,61]	^{12}C - ^{12}C stretching modes
~270 meV	C-D stretching modes [52–54, 57–59,61,71,72]	^{12}C -D stretching modes
300 meV	First overtone of C-C mode [52,57]	First overtone of ^{12}C diamond optical phonon
~380 meV	–	Coupling of ^{12}C -D bend and ^{12}C -D stretch modes
420 meV	–	Coupling of ^{12}C - ^{12}C stretch and ^{12}C -D stretch modes
450 meV	–	Second overtone of ^{12}C diamond optical phonon
Hydrogenated Diamond (C-13) Surface		
148 meV	–	Mixed ^{13}C -H bend and ^{13}C - ^{13}C stretch modes
290 meV	–	First overtone of ^{13}C diamond optical phonon
358 meV	–	^{13}C -H stretching mode

(Continued)

Table 8.3 Assignment of HR-EELS Modes Relevant to the Present Discussion (Continued)		
HR-EELS Mode Position	Assignment Based on Literature Survey	Our Present Assignment
435 meV	–	Second overtone of ^{13}C diamond optical phonon
508 meV	–	Overlapping of both ^{13}C –H bend and stretching modes and ^{13}C – ^{13}C stretch and ^{13}C –H bend modes
580 meV	–	Third overtone of ^{13}C diamond optical phonon

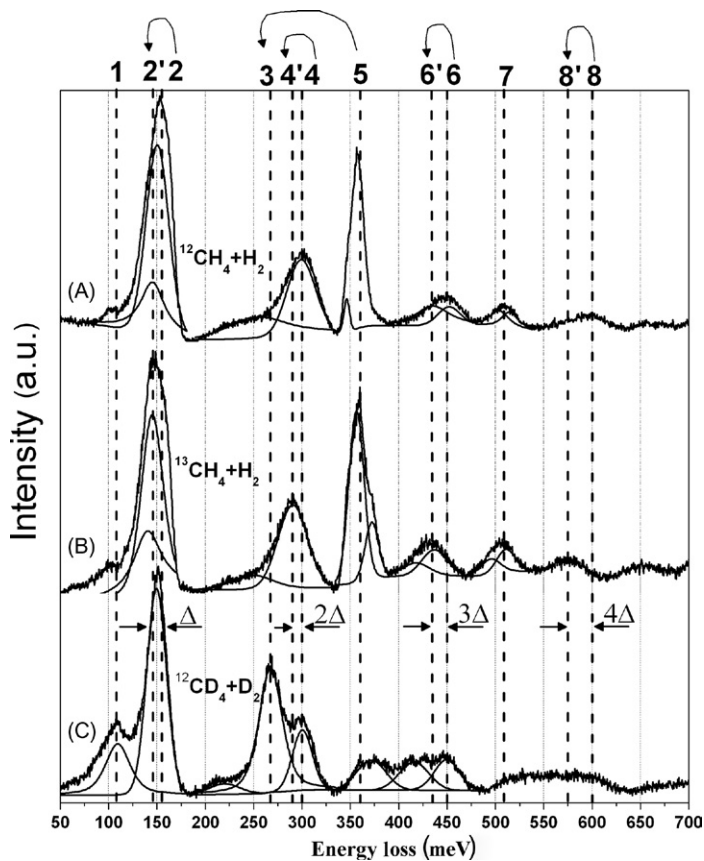


FIGURE 8.6 Three HR-EEL spectra of diamond films deposited from isotopic gas mixtures with peak fitting. Each peak was fitted for two possible contributions of C–C and C–H vibrational modes.

($^{13}\text{CH}_4 + \text{H}_2$) modes #2, #4, #6, and #8 (positioned at 155, 300, 450, and 600 meV, respectively) are shifted toward lower loss energies by Δ , 2Δ , 3Δ , and 4Δ ($\Delta = 5$ meV), correspondingly, compared to modes of spectrum A in Figure 8.6 ($^{12}\text{CH}_4 + \text{H}_2$). Mode #7 is nearly unaffected by isotopic carbon substitution (spectra A and B; $^{12}\text{CH}_4 + \text{H}_2$ and $^{13}\text{CH}_4 + \text{H}_2$) whereas it completely disappears where hydrogen atom was replaced by deuterium (spectrum C; $^{12}\text{CD}_4 + \text{D}_2$). The most probable isotopic shift of this mode is within the complex band around 350–450 meV in $\text{CD}_4 + \text{D}_2$ (spectrum C). We can thus discuss three families of peaks: (1) pure C–C peaks, (2) pure C–H peaks, and (3) coupling of C–C and C–H peaks. In Table 8.3, the peak assignment of the HR-EELS of the hydrogenated diamond based on our studies are summarized.

Our findings provide direct evidence and are in accordance with the recent work of Lafosse et al. [68] who report on vibrational excitation function of diamond surface. The shape of excitation function is governed (among other things) by the electronic density of states, which gives rise to a peak around 13 eV (incident electron energies) due to the second absolute diamond band gap. In this case the reflectivity of the electron beam increases and losses are dominated by surface vibrations (e.g., C–H) and not by deeper atoms (C–C modes). Indeed, the intensity of the peaks at 150, 300, 450, and 600 meV substantially decreases for electron energy of 13 eV (the case of high reflectivity) as expected for C–C rather than C–H modes. These facts suggest the assignment of these overtones to the lattice C–C vibrations.

At this point we should stress the absence of the overtones #4, #6, and #8 from the HR-EEL spectrum of amorphous carbon films reported in the literature [72–74] and in our previous works [46,69]. Mode #2 is nevertheless present and prominent. On the other hand, these overtones are observed on the well-defined (100), (111), and polycrystalline diamond surfaces [52–55,58,59,63–68].

In order to clarify the origin of the peaks at 300, 450, and 600 meV, an ion irradiation experiment was done on well-defined diamond surface [75,76]. Ion irradiation results in partial amorphization of the film surface, therefore, the change in the shape of the spectrum following the ion irradiation may be associated with the change of the surface crystalline structure. Our results show that the intensity of these three overtone HR-EEL peaks (300, 450, and 600 meV) decreases most significantly after the diamond surface has been irradiated with low energy Ar ions. In this case, the characteristic diamond loss features (the surface and bulk diamond plasmon) are replaced by amorphous carbon losses [76]. These modes should be, therefore, associated with well-defined diamond surfaces rather than with amorphous carbon surfaces. We thus conclude that appearance of the three modes #4, #6, and #8 at 300, 450, and 600 meV in the HR-EEL spectrum of diamond should be attributed to higher losses of the slow electron onto diamond optical phonon and may serve as a fingerprint of nanoscale-defined diamond surfaces. We use this finding in the next section to study the impact of diamond grain size on the shape of HR-EEL spectra.

8.5.2 The impact of diamond grain size on the shape of HR-EEL spectra

In Section 8.5.1, the assignment of HR-EELS peaks characteristic to hydrogenated nanoscale-defined diamond surface was summarized. In the present section we use this assignment to study the impact of diamond grain size on the shape of the HR-EEL spectrum of diamond surfaces deposited by three different CVD techniques described above (Section 8.2).

We start with the analysis of the C–H stretching mode of *as-deposited* HF CVD diamond film (grain size ~ 300 nm) as a function of thermal annealing. In Figure 8.7,

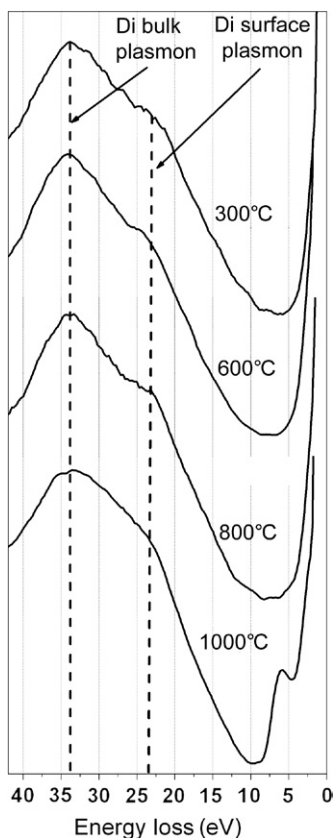


FIGURE 8.7

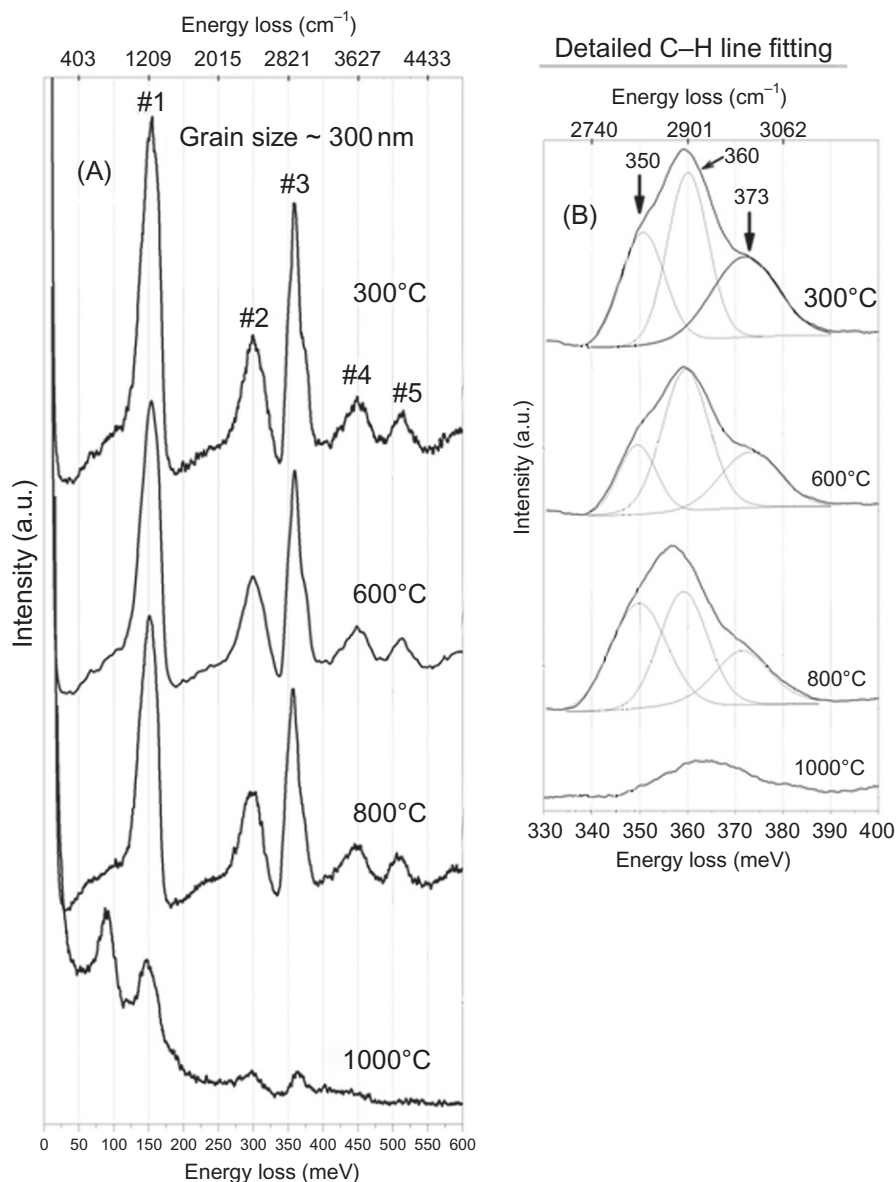
Electronic EEL spectra of HF CVD diamond films as a function of annealing temperature. Primary electron energy $E_p = 500$ eV. The shape of the spectrum is nearly unchanged up to annealing temperature $T_A = 800^\circ\text{C}$, while $T_A = 1000^\circ\text{C}$ results in appearance of the graphitic $\pi \rightarrow \pi^*$ associated plasmon at ~ 6 eV. Notice the correlation of this graphitic feature with hydrogen desorption detected by HR-EEL spectroscopy.

the electronic EEL spectra (electron primary energy, $E_p = 500\text{eV}$) of the as-deposited HF CVD film as a function of annealing temperature is shown. Diamond plasmon losses are nearly unaffected by heating at $T < 800^\circ\text{C}$, while heating at $T = 1000^\circ\text{C}$ results in appearance of graphitic π electrons ($\sim 6\text{eV}$ energy loss). In Figure 8.8A, the HR-EEL spectra of the same *as-deposited* HF CVD diamond samples are shown as a function of annealing temperature. The shape of the spectra is nearly unaffected by $T < 800^\circ\text{C}$ while $T = 1000^\circ\text{C}$ results in elimination of hydrogen-associated features (360 and 510 meV peaks) and addition of the $\sim 90\text{meV}$ peak associated with C=C dimer. Notice the correlation between hydrogen desorption detected by HR-EELS (Figure 8.8A) and the appearance of graphitic features detected by electronic EELS (Figure 8.7). While the hydrogen stretching mode is clearly present in the HR-EEL spectra of diamond up to annealing to 800°C , annealing to 1000°C results in its disappearance alongside with the emergence of the $\sim 90\text{meV}$ positioned peak associated with the C=C dimer and surface reconstruction. These dimers (which are detected as $\sim 90\text{meV}$ HR-EELS peak) contribute to graphitic π plasmon detected by electronic EELS measurements.

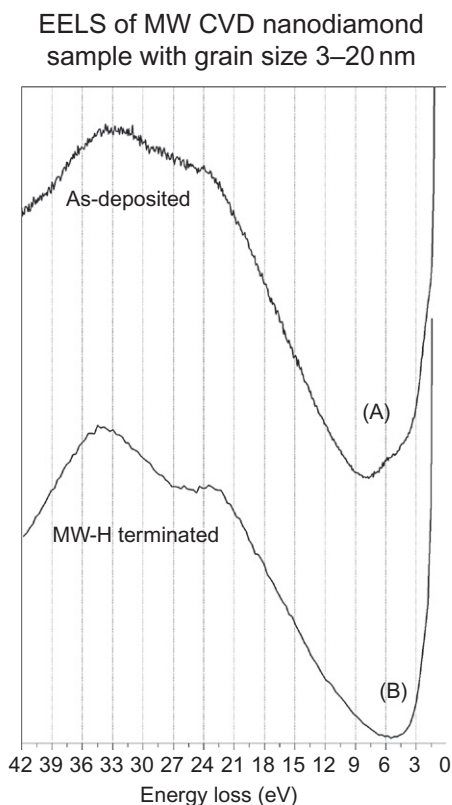
The detailed peak fitting procedure of C–H stretching HR-EELS mode (Figure 8.8B) reveals at least three different contributions at ~ 350 , ~ 360 , and $\sim 373\text{meV}$. The first two are most likely associated with diamond (111) and (100) surfaces, [62] while the last one may be attributed to sp^2 -hybridized carbon [77,78]. Upon annealing to 800°C , the maximum peak position is slightly shifted to smaller loss energies (from 359 to 357 meV) while the sp^2 -associated mode at $\sim 373\text{meV}$ is still prominent. According to thermal stability studies of different kinds of hydrogenated amorphous carbon matrixes [22,79–84], annealing to a temperature of $>700^\circ\text{C}$ results in desorption of hydrogen atoms alongside with hydrocarbon species, independent of the method used for amorphous carbon film preparation. This allows us to attribute the $\sim 375\text{meV}$ HR-EELS mode to hydrogen bonding to *diamond grain boundary*, which may be stable up to these high temperatures. This suggestion may be confirmed by HR-EELS studies of *nanodiamond* material discussed below.

Now we turn to analyze the vibrational modes on the surface of nanodiamond films deposited by MW CVD. Figure 8.9 shows the electronic EEL spectra of a MW-CVD-3-20nm sample recorded at primary electron energies of $E_p = 500\text{eV}$ before and after *ex situ* MW hydrogenation. Both spectra are dominated by characteristic diamond losses, namely, bulk and surface diamond plasmons at 33 and 23 eV, respectively. It can be concluded from the comparison of the spectra of *as-deposited* films and the *ex situ* MW hydrogenated films that *ex situ* MW hydrogenation results in increasing intensity of the diamond surface plasmon at 23 eV, which may be associated with etching of the amorphous carbon component present on the surface of as-deposited film. The direct evidence of this fact comes from HR-EELS analysis of these samples discussed below.

HR-EEL spectra of MW-CVD-3-20nm nanodiamond film deposited by MW CVD are shown in Figure 8.10. The upper line (A) corresponds to the *as-deposited* sample followed UHV annealing to 700°C . Detailed analysis of C–H stretching mode is shown in Figure 8.10D. Spectrum A in Figure 8.10 is dominated by a mixed C–C stretching and C–H bending mode at 155 meV, the overtones of the diamond

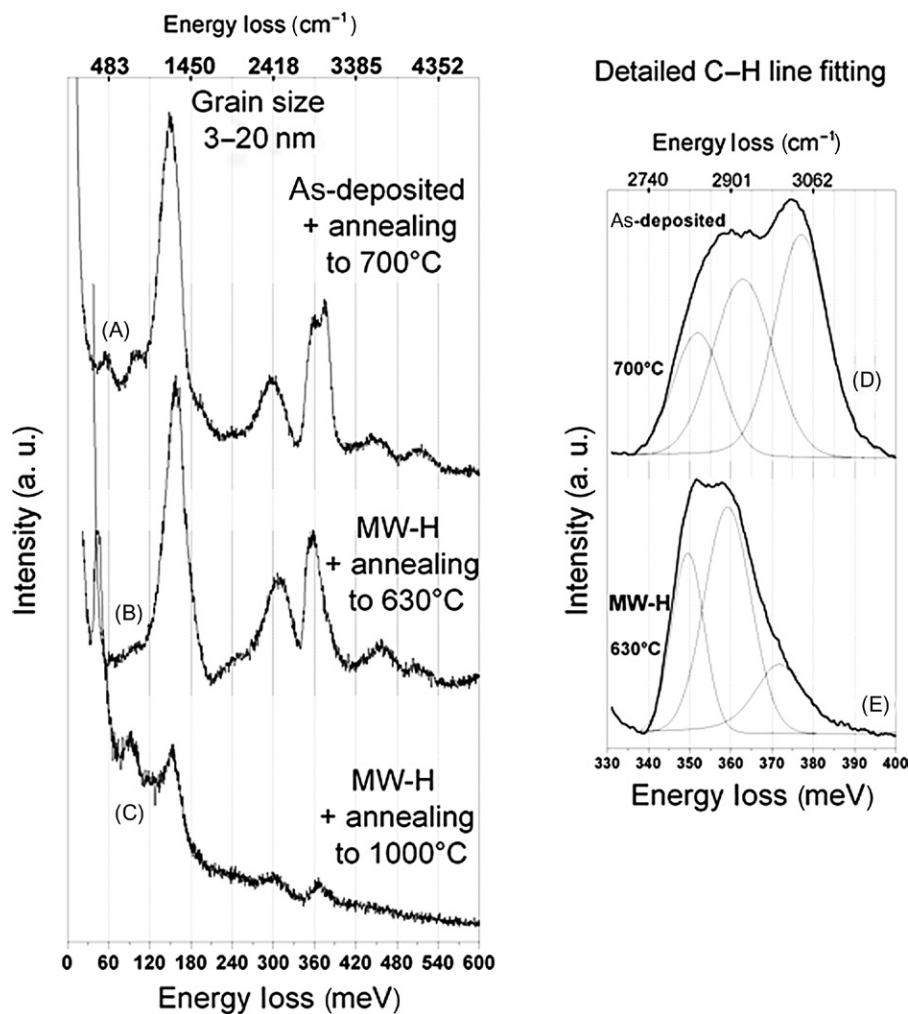
**FIGURE 8.8**

(A) HR-EEL spectra of as-deposited HF CVD films as function of annealing temperature. The primary electron energy was 5 eV and FWHM of elastic peak 7–8 meV. The shape of the spectrum is nearly unchanged up to $T_A = 800^\circ\text{C}$. $T_A = 1000^\circ\text{C}$ results in complete hydrogen desorption (the absence of ~360 meV peak) alongside appearance of C=C dimer mode at ~90 meV. (B) Detailed analysis of HR-EELS C–H stretching mode of as-deposited HF CVD diamond film (data were taken from spectrum A). Peak fitting procedure reveals three different contributions at ~350, ~360, and ~375 meV energy loss.

**FIGURE 8.9**

EEL spectra of MW CVD nanodiamond film with grain size 3–20 nm. The primary electron energy $E_p = 500$ eV. (A) As-deposited sample annealed to 700°C. (B) *Ex situ* MW-H terminated sample annealed to 630°C. Notice the enhancement of diamond surface plasmon at energy loss 23 eV followed by *ex situ* MW hydrogenation.

optical phonon at 300 and 450 meV, and C–H stretching vibration at 360–375 meV. Notice the strong splitting of CH stretching mode in this spectrum: the two maxima are positioned at ~ 360 and ~ 375 meV, reflecting hydrogen bonding to sp^3 and sp^2 carbon, correspondingly (spectrum D in Figure 8.10). Following MW hydrogenation and subsequent UHV annealing to 630°C (spectrum B in Figure 8.10), the diamond overtones underwent enhancement relative to C–H-associated modes. The splitting of C–H stretching vibrations disappears and now this mode is centered at 360 meV indicating preferential etching of sp^2 carbon by atomic hydrogen (only sp^3 C–H modes are present; spectrum E in Figure 8.10). We conclude, therefore, that *ex situ* exposure to atomic hydrogen results in preferential etching of sp^2 carbon leaving well-defined diamond surface with complete hydrogenation. Annealing to 1000°C results in hydrogen desorption and appearance of ~ 90 meV peak (C=C dimer) in similar way as for HF CVD diamond films with ~ 300 nm grain size (Figure 8.8).

**FIGURE 8.10**

HR-EEL spectra of MW CVD deposited nanodiamond films: (A) as-received sample annealed to 700°C; (B) as-deposited sample followed by MW-H treatment for 15 min and subsequent annealing to 630°C; (C) followed by further annealing to 1000°C. (D and E) Detailed analysis of HR-EELS C-H stretching mode (data originated from spectra A and B).

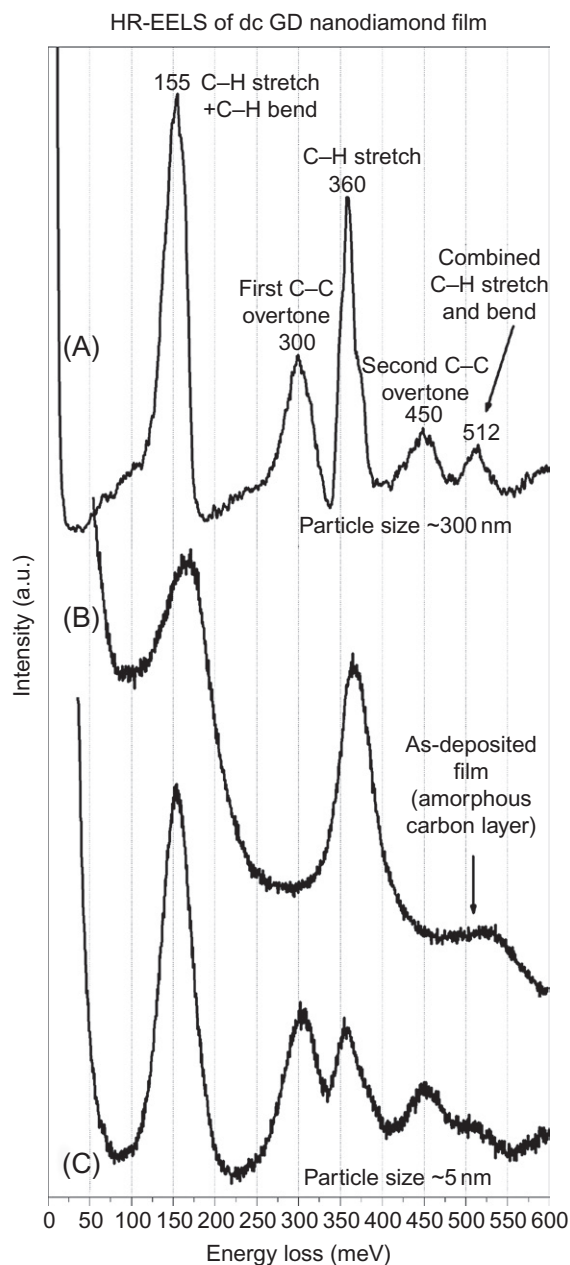
Now we compare the HR-EELS analysis of as-deposited MW CVD nanodiamond (spectra A and D in Figure 8.10) with the as-deposited HF CVD submicron crystalline samples (Figure 8.8). As can be seen in Figure 8.8B, the HR-EEL spectrum of as-deposited HF CVD films with ~ 300 nm grains also display contributions at ~ 350 , ~ 360 , and ~ 375 meV within the C-H stretching modes, which are stable up to 800°C. Similar annealing experiments performed on MW-CVD-10-30 nm

sample [85] show that the ~ 375 meV mode is stable up to at least 800°C . Obviously, the density of grain boundaries in the case of nanodiamond films exceeds that of submicron crystallites. Since the contribution of the ~ 375 meV mode is much more prominent in the case of nanometric grains, this mode may be associated with hydrogen bonded to the *surface* and *grain boundary* of the nanodiamond film. This is a very exciting feature. In our studies of hydrogen adsorption on ion-irradiated diamond surface [86], we concluded that nearly all kinds of hydrogenated carbon decompose near $\sim 600^\circ\text{C}$. This is in agreement with other studies of thermal stability of diamond-like carbon, which undergoes erosion/destabilization at a temperature of about 600°C independently during the deposition process [22,79–84]. The present results show that $\text{C}(\text{sp}^2)\text{-H}$ bonds are stable up to temperatures above 800°C . This finding allows one to distinguish the $\text{C}(\text{sp}^2)\text{-H}$ species bonded to diamond grains from hydrogenated species on polycrystalline diamond bonded in a $\text{C}(\text{sp}^3)\text{-H}$ configuration surface by simple annealing procedure.

It is very interesting to note at this stage the possible correlation between the ~ 375 meV HR-EELS mode and the Raman 1140cm^{-1} peak of nanodiamond. It was shown in Section 8.4.1 that the 1140cm^{-1} Raman peak is attributed to C–H bending mode of sp^2 carbon and positioned most likely in the diamond grain boundary. Both peaks (Raman 1140cm^{-1} and HR-EELS ~ 375 meV mode) are attributed to $(\text{sp}^2)\text{-carbon-hydrogen}$ vibration. Both peaks are stable up to elevated temperatures, where hydrogen bonded to amorphous carbon undergoes desorption. Both peaks are strongly enhanced in the case of nanodiamond grains. Therefore, our results strongly suggest that the ~ 375 meV mode can be attributed to the stretching of the same C–H vibration, which contributes to the 1140cm^{-1} Raman peak (currently attributed to ν_1 mode of *t*-PA; the bending of sp^2 C–H). Both peaks may serve as indication of the nanocrystalline character of diamond films. However, due to the different probing depths of Raman and HR-EEL spectroscopies (tens or hundreds of nanometers in the case of Raman and 1–2 nm in the case of HR-EELS), quantitative comparison of these two peaks is impossible. It should be stressed that this assignment of the 375 meV peak is circumstantial; a computational study of this mode is in progress in our laboratory.

Now we turn to analyze HR-EEL spectra of nanodiamond films deposited by dc GD CVD (Spectra B and C in Figure 8.11). Typical HR-EEL spectrum of well-defined diamond surface with grains of ~ 300 nm (Spectra A in Figure 8.11) is shown for comparison. First, we compare this spectrum of the well-defined diamond surface with Spectrum B of Figure 8.10, a predominantly amorphous carbon layer.

The Figure *as-deposited* dc GD nanodiamond film represented by spectrum B of Figure 8.11 is dominated by mixed C–C and C–H vibration (a broad band with maximum near 160 meV), a mixed sp^2/sp^3 carbon–hydrogen stretching mode near 370 meV, and a broad peak near ~ 510 meV. It was briefly discussed in Section 8.2 that the subplantation mechanism that led to nanodiamond formation leaves the upper surface region consisting of hydrogenated amorphous carbon [11,32]. Notice the absence of the overtones at 300, 450, and 600 meV in this spectrum compared to the well-defined diamond surface of spectrum A of Figure 8.11. This

**FIGURE 8.11**

HR-EEL spectra of carbon films: (A) as-deposited HF CVD high-quality diamond film (grain size 300 nm); (B) as-deposited dc GD nanodiamond films; and (C) as-deposited dc GD film followed by 2 min MW-H treatment (grain size ~5 nm).

result further corroborates our previous assumption (Section 8.5.1) that these overtones originated from diamond optical phonon and are characteristic solely to well-defined diamond surfaces.

Spectrum C in Figure 8.11 presents the HR-EEL spectrum of nanodiamond film, which underwent a short time *ex situ* exposure to MW-H plasma. This treatment leads to preferential etching of sp^2 carbon leaving hydrogenated nanodiamond grains (~ 5 nm) exposed to the vacuum. It also results in compelled hydrogenation of nanodiamond crystallites. C displays overtones of diamond optical phonon and, therefore, is characteristic to well-defined diamond hydrogenated surface. Comparing spectra A and C in Figure 8.11 (submicron grains versus nanocrystallites), one sees the change in relative intensity of pure C–C originated vibrations (300 and 450 meV) to those originated from pure C–H modes (360 and 510 meV). Thus, in the case of nanodiamond surface (Spectrum C) the first overtone of diamond optical phonon seems to be enhanced relative to C–H stretching mode vibration (360 meV). The same is true for the second overtone at 450 meV relative to the coupled mode of C–H stretch and C–H bending (or C–C stretching) vibrations at ~ 510 meV.

The HR-EEL spectra of nanodiamond films are different from those of submicron grain size in the relative intensities of C–C related modes relative to C–H vibrations. Figure 8.12 shows a comparison between the HR-EEL spectra measured for the three kinds of diamond films grown for 1 h by different methods: HF CVD, dc GD CVD, and MW CVD. In order to compare these spectra all films were exposed to the same surface treatment in MW-H plasma for ~ 10 min. Since the first strong peak at ~ 155 meV is composed of mixed C–C and C–H modes, we should compare only *pure* C–C vibration modes with *pure* C–H modes, namely, overtones of diamond optical phonon at 300 meV with C–H stretching mode at 360 meV. In the case of HF CVD (grain size ~ 300 nm), the relative ratio of intensity of 360 meV mode with respect to the intensity of 300 meV phonon overtone is 1.88. In the case of nanodiamond films deposited by MW CVD (grain size lays in 3–20 nm range) the same ratio is 1.2, while for dc GD CVD nanodiamond films (grains ~ 5 nm) this ratio is 0.9. This ratio is correlated with diamond grain size, namely, the smaller the diamond grain, the smaller ratio of the intensity of the pure C–H/C–C-associated modes.

We reported [87] that HR-EELS modes associated with C–C lattice phonons are comparably more intense than modes associated with the C–H surface vibrational modes in the case of nanocrystalline compared to microcrystalline diamond films. Excitation function measurements of the different modes [87] show a pronounced maximum at ~ 8 eV for the nanodiamond films, whereas for microcrystalline films similar modes showed maximum intensities at 13 eV with a smaller contribution at 8 eV. It is reported that the elastic electron reflectivity is substantially larger for the nanodiamond films, showing broad maxima at ~ 8 and ~ 13 eV in both cases. It is suggested [87] that these effects are associated with the larger probability for inelastic scattering of electrons by lattice phonons mediated by scattering with internal grain boundaries and defects in the case of nanocrystalline diamond films.

We conclude, therefore, that diamond grain size impacts the shape of HR-EEL spectra. Hydrogen bonding to surfaces and grain boundaries of *nanodiamond* films

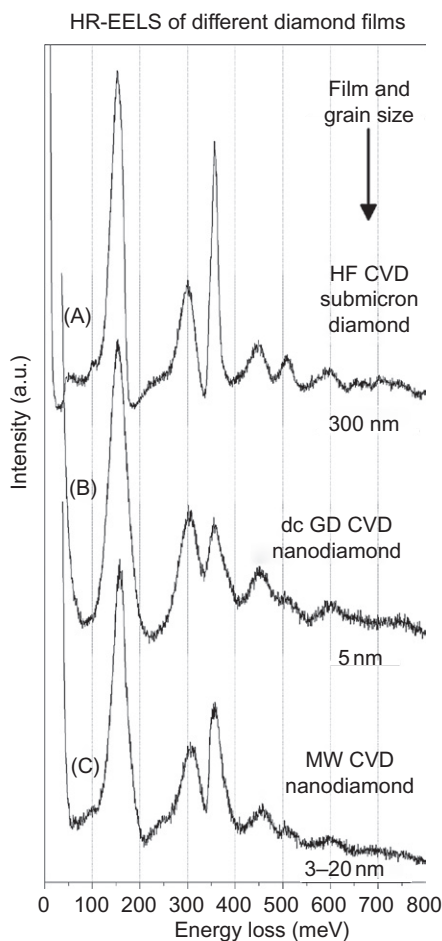


FIGURE 8.12

Comparison of HR-EEL spectra of three different diamond films that underwent MW-H treatment: (A) HF CVD film grown for 1 h (grain size ~ 300 nm); (B) nanodiamond film grown by dc GD method (grain size ~ 5 nm); and (C) MW CVD sample (grain size 3–20 nm). Notice the different ratio of C–C-associated modes relative to C–H vibrations.

display a clear contribution to the HR-EELS at ~ 375 meV, which differs from bonding to the *microcrystalline* diamond surfaces whose main contribution is centered around 360 meV. The ~ 375 meV mode is stable up to elevated temperatures of $\sim 800^\circ\text{C}$ where all kinds of hydrogenated amorphous carbon are decomposed. The intensity of this mode is drastically decreased following *ex situ* treatment in MW-activated hydrogen plasma, most likely due to preferential etching of sp^2 carbon bonded to diamond grain *surfaces* and *boundaries*. In addition, the spectrum of the fully hydrogenated UNC diamond surface (5 nm grain size, *ex situ* exposed

to atomic hydrogen plasma) shows decrease of C–H-associated mode intensity relative to pure C–C modes, comparatively to microcrystalline grains. The last phenomena are correlated with our Raman data (Section 8.4.1) as well as with IR measurements reported by others [47–49].

8.6 Bulk and surface thermal stability of UNC diamond films with 10–30 nm grain size

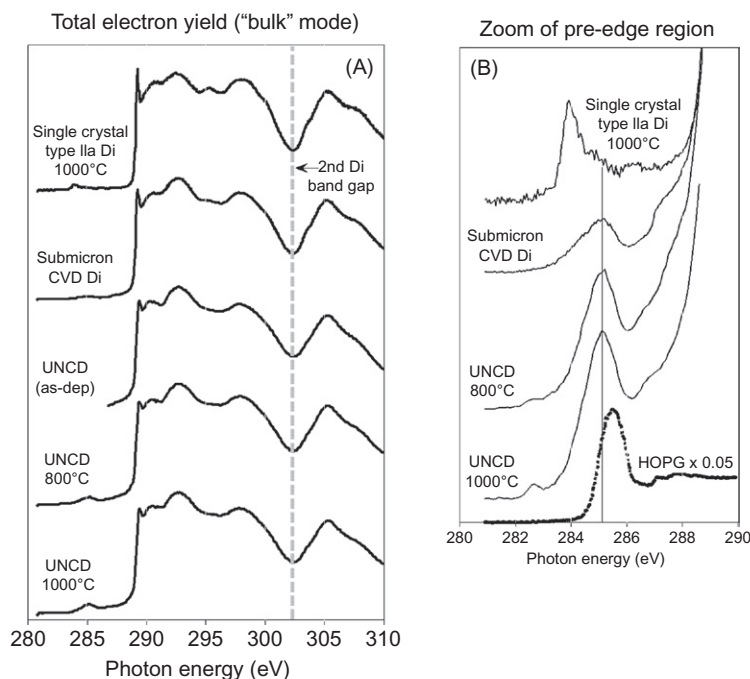
In this section, we contrast the surface and bulk stability of nanocrystalline diamond films and compare them with submicron and single crystal diamond. Analysis techniques include Raman spectroscopy for bulk analysis, while near-edge X-ray absorption fine structure (NEXAFS) can be utilized to independently analyze both bulk and surface regions. NEXAFS spectroscopy can be recorded by measuring both the bulk sensitive total electron yield (TEY) and the surface sensitive partial electron yield (PEY) from the sample. When recorded as a function of the photon excitation energy, exciting from the C(1s) core level, it has been shown to be a powerful probe of the diamond electronic structure [88–91]. Unlike Raman spectroscopy, NEXAFS has a similar cross section for different carbon allotropes and it is sensitive to local chemical bonding, which enables analysis of nanosized carbon materials [92,93].

In Section 8.6.1, the bulk thermal stability is studied with Raman and NEXAFS spectroscopies (the latter recorded in bulk sensitive mode), while the SIMS technique is applied to study the relative decrease in hydrogen atom concentration following 1000°C annealing. In Section 8.6.2, the nanodiamond surface stability is studied with NEXAFS spectroscopy using PEY (surface sensitive mode). In Section 8.6.3, we suggest a possible explanation for the enhanced stability of CVD nanodiamond bulk versus its surface region.

8.6.1 Nanodiamond *bulk* thermal stability study

First, we refer to the NEXAFS TEY results recorded in bulk sensitive mode, shown in Figure 8.13. We estimate that NEXAFS measured in the TEY mode is sensitive down to the 50–100 Å near-surface region. Figure 8.13A shows the spectra of the nanodiamond film as-deposited and after annealing at 800°C and 1000°C. A single crystal (type IIA) sample that underwent 1000°C treatment and an as-deposited polycrystalline diamond film with submicron grain size are included for comparison.

The well-defined single crystalline diamond spectrum (upper line) is dominated by a sharp exciton peak at 289.3 eV and a broad dip fixed at 302.4 eV, which is associated with the second absolute band gap of diamond. A zoom of the pre-edge region is shown in Figure 8.13B. The peak at ~285 eV, which is due to the C(1s) → π^* resonance, can be used as a fingerprint of sp²-coordinated carbon atoms. Analysis and comparison of the graphitic and diamond associated peaks may

**FIGURE 8.13**

(A) NEXAFS spectra recorded in the 280–310 eV photon energy range in the TEY mode of single crystal type IIA, microcrystalline CVD diamond film, and nanodiamond film following thermal annealing. (B) Zoom of C(1s) core level pre-edge excitation region in 280–290 eV range. The spectrum of the Highly Ordered Pyrolytic Graphite (HOPG) sample is shown for comparison.

provide information on the extent of graphitization in each material. Since NEXAFS spectroscopy is equally sensitive to both sp^3 and sp^2 phases of carbon [92,93], a semiquantitative estimation of the carbon phase composition can be usefully derived from these spectra.

In order to compare the extent of graphitization, peak fitting was performed on the samples that underwent 1000°C annealing. According to peak fitting analysis, the area ratio of the graphitic peak positioned near 284 eV to the area of the diamond second absolute band gap dip¹ positioned near 302 eV is $I_{284}/I_{302} = 3.5\%$ for a single crystal type IIA diamond sample, while for nanodiamond the same ratio is $I_{284}/I_{302} = 5.3\%$ (Figure 8.13). These relative graphitization values are much smaller than that derived from NEXAFS analysis of the spectra recorded in surface

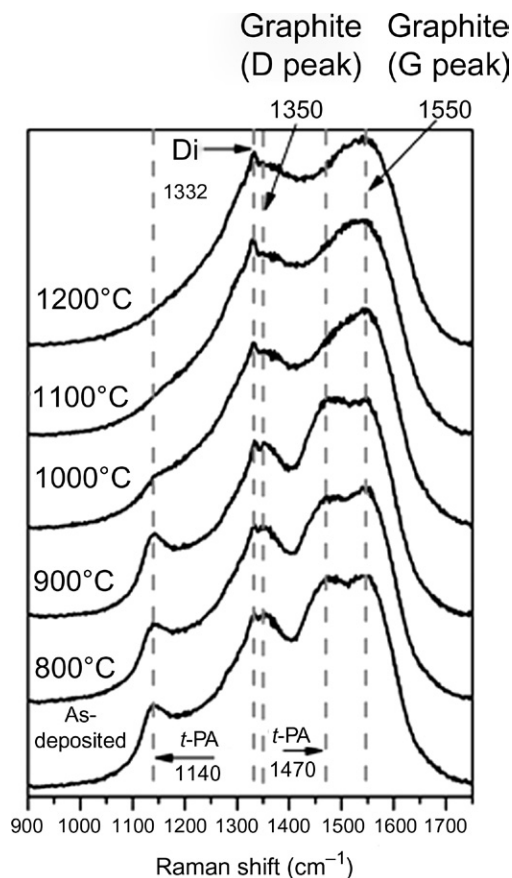
¹The area of the second absolute diamond band gap dip was calculated in the following way: a background line was defined between two local maxima at 297 and 305 eV and a module of the obtained dip area was calculated by means of usual software.

sensitive mode (see below). In addition, comparing the spectra of as-deposited 800°C and 1000°C annealed nanodiamond, no drastic change in the line shape or area is observed. It is assumed that in the case of a single crystal diamond sample the only possible graphitization channel is the reconstruction of the film surface (i.e., film/vacuum region). Therefore, the observed 3.5% graphitization of this sample is due to the contribution of the sp^2 -hybridized surface atoms to the TEY NEXAFS spectrum. Consequently, we can conclude that the observed graphitization signal of these nanodiamond films comes from the surface area, while the film's bulk remains nearly unaffected by high-temperature annealing. Additional confirmation of this hypothesis may come from the Raman analysis discussed below.

In Figure 8.14, the Raman spectra of these nanodiamond films are displayed as a function of annealing temperature up to 1200°C. The spectrum from the as-deposited film is dominated by well-known “nanodiamond” features [37,43], such as the well-known D and G peaks at ~ 1350 and $\sim 1560\text{ cm}^{-1}$, respectively, and the *t*-PA-associated vibrations at 1140 and 1480 cm^{-1} , while diamond's optical phonon line at 1332 cm^{-1} is strongly overlapped by the graphitic D peak [37,43]. The predominant sp^2 carbon character of the spectrum is due to the higher cross section of the scattered light (at the current wavelength) to sp^2 -hybridized carbon, which decreases the sensitivity of the Raman technique to diamond sp^3 carbon [37]. Therefore, the Raman spectrum reflects mainly the grain surface and boundary composition, while the presence of diamond phase is associated with the small peak at 1332 cm^{-1} .

It can be seen from Figure 8.14 that the Raman spectra of the nanodiamond film annealed at 800°C and 900°C are similar to that measured for the as-deposited film. However, following annealing at 1000°C the intensity of *t*-PA-associated features decreases, suggesting thermally enhanced hydrogen (or hydrocarbon) desorption and consequent breaking of *t*-PA-like bonds. Further, annealing at 1100°C and 1200°C results in complete disappearance of *t*-PA-associated peaks, probably indicating bond reconstruction in the film bulk.

A few things may be mentioned regarding this Raman analysis. First, the stability of the diamond phase up to 1200°C annealing is indicated by the presence of the diamond optical phonon peak at 1332 cm^{-1} . Second, breaking of C–H bonds positioned in grain boundary regions start only at 1000°C, indicating high thermal stability of hydrogen atoms in the nearest proximity to diamond grains. For comparison, the thermal stability of C–H bonds detected in amorphous carbon does not exceed 600–700°C [22,81–84]. Finally and most interesting, it may be observed that breaking CH bonds of *t*-PA-like fragments does not drastically change the shape of the Raman spectrum. The unchanging graphitic G peak suggests either a gentle rearrangement of carbon sp^2 bonds in the grain boundary or desorption of entire hydrocarbon species, rather than an increase in graphitic bond production following C–H bond breaking. An estimation of the hydrogen concentration decrease in the films upon annealing to 1000°C can be derived from SIMS measurements, shown in Figure 8.15. It may be concluded that, following annealing at 1000°C, the concentration of hydrogen atoms decreases by $\sim 30\%$ as compared to

**FIGURE 8.14**

Raman spectra of nanodiamond diamond films. As-deposited on silicon and following 5×10^{-6} Torr vacuum annealing for 30 min at 800°C, 900°C, 1000°C, 1100°C, and 1200°C, as indicated on the plot. Notice that *t*-PA-associated peaks at 1140 and 1480 cm^{-1} are stable up to 800°C anneal, decrease in intensity upon 1000°C anneal, and completely disappear from the spectrum under anneal at 1100°C.

the as-deposited film. When compared to the complete removal of the *t*-PA-Raman peak, it must be concluded that either the *t*-PA-bonded hydrogen does not account for the entire hydrogen population within the film, or the *t*-PA-like bonds partially restructure upon annealing, hence maintaining some hydrogen content in the films above 1000°C. Obviously, higher temperature annealing increases hydrogen loss from the film's bulk. However, neither NEXAFS nor Raman analysis provide clear evidence of graphitization of the bulk region of the film. We leave these puzzling results for discussion in Section 8.6.3.

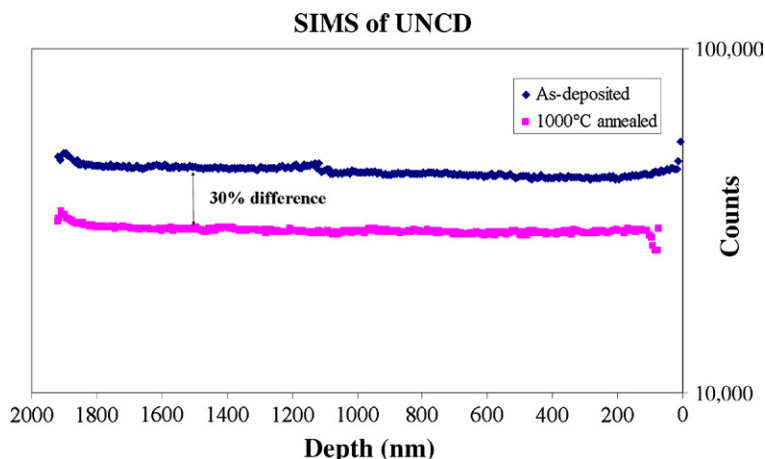


FIGURE 8.15

SIMS profile of hydrogen within nanodiamond film. Notice the decrease of H concentration by 30% following 1000°C annealing.

8.6.2 Nanodiamond *surface* thermal stability study

Surface stability of the nanodiamond films was studied by NEXAFS spectroscopy, recorded in PEY. In addition, we refer to our recent studies of nano- and submicron diamond surface stability investigated by HR-EELS [94], which is ultimately sensitive to the few upper atomic layers [50].

In Figure 8.16, NEXAFS spectra of the same films as in Figure 8.13 are shown now recorded in the surface sensitive mode. These spectra are dominated by the same diamond features as before, while the bulk diamond signatures are less pronounced: for example, the contrast of the second absolute diamond band gap at ~ 302 eV is smaller compared to the surface originated mode at ~ 284 eV. Comparison of the ratio of these two peak areas reveals $I_{284}/I_{302} = 31.6\%$ and $I_{284}/I_{302} = 46.6\%$ for single crystal and nanodiamond samples, respectively (Figure 8.16). These values are nearly one order of magnitude greater than those derived from bulk sensitive NEXAFS spectra (Figure 8.13). It may be concluded that, similar to single crystal samples, surface graphitization of nanodiamond films occurs to a much greater extent than within the film bulk.

We can corroborate these results by looking at recent studies of the thermal stability of fully hydrogenated submicron and nanodiamond film surface by means of HR-EELS [94]. Complete hydrogen loss was detected on both kinds of surfaces under flash annealing at 1000°C, which results in reconstruction of surface and appearance of C=C dimer features (emerging as HR-EELS peak at ~ 90 meV energy loss for submicron films). In addition, the extent of graphitization was stronger on the surface of nanodiamond films,

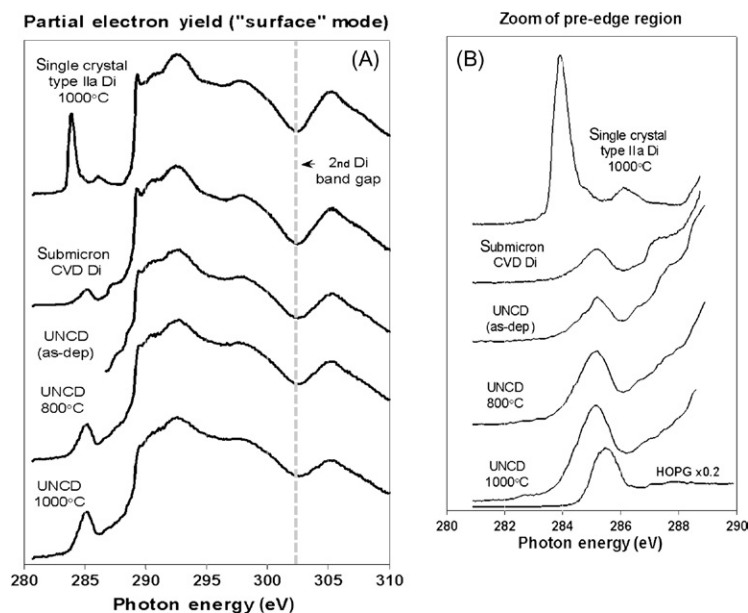


FIGURE 8.16

(A) NEXAFS spectra recorded in the 280–310 eV photon energy range in PEY mode collecting 8 eV electrons of single crystal type IIA, microcrystalline CVD diamond film, and nanodiamond film following thermal annealing. (B) Zoom of C(1s) core level pre-edge excitation region in 280–290 eV range. The spectrum of the Highly Ordered Pyrolytic Graphite (HOPG) sample is shown for comparison.

in agreement with theoretical predictions of lower thermal stability of nanosized diamond crystallites, compared to submicron ones [95]. However, in that work no comparison with the film's bulk is shown in terms of the extent of graphitization.

8.6.3 Discussion of nanodiamond bulk versus surface thermal stability

Based on the aforementioned analysis of the bulk and surface thermal stability of nanodiamond films, the following main experimental conclusions may be listed:

1. NEXAFS analysis reveals that the diamond *bulk* region is stable up to at least 1000°C annealing, while according to Raman spectroscopy no visible graphitization is observed up to 1200°C.
2. SIMS spectroscopy detects loss of ~30% of hydrogen atoms following annealing at 1000°C, despite a complete loss of the *t*-PA-Raman signature. Importantly, this loss of hydrogen atoms is not followed by film bulk graphitization.

3. Surface analysis by means of NEXAFS reveals nearly full graphitization of the surface area, which is confirmed by a previous HR-EELS study [94]. Our conductive probe atomic force microscopy measurements (data not shown) confirm this finding detecting ~40% increase in average conductivity and conductivity spikes possibly associated with graphitization of the small grains in the closest vicinity on the film's surface.

The aforementioned experimental findings may be discussed from the standpoint of the presently accepted nanodiamond stability model [95] together with a few new suggestions.

We start the analysis by considering the lower stability of the film's surface region as compared to the film bulk. This issue may be explained in terms of high energy surface atom rearrangement and the lack of volume constraint effects on the film's surface. It was previously found that at 927°C (1200 K) nanocrystalline diamond prepared by a detonation method transforms into bucky diamond [96], and raising the annealing temperature to 1227°C (1500 K) led to a cluster with graphitic shells and a diamond core. An HR-TEM study has shown that graphitization starts from the surface of individual nanodiamond crystallites [97]. The widely accepted scenario [95] of nanodiamond thermal reconstruction is that nanodiamond graphitization under annealing proceeds from the surface to the bulk and also that edges of exfoliated graphite-like sheets merge with the upper untransformed diamond phase. The presence of surface terminating groups affects the onset temperature of this process: graphitization cannot begin until the surface groups start to decompose [95]. Recently, we have shown that graphitization of fully hydrogenated diamond films composed of submicron and nanocrystalline grains starts only following H atom desorption, and similarly proceeds from the surface toward the crystalline bulk [94]. The extent of graphitization is larger in the case of nanodiamond films, which cannot be restored by subsequent *in situ* atomic hydrogen adsorption. In addition, according to the density difference, diamond→graphite transition requires ~30% volume expansion, which may be hampered in the film's bulk by tight binding of the crystallite agglomerates.

Now we turn to the analysis of the bulk graphitization of CVD nanodiamond films. Two mutually contradictory experimental results may be seen: there was a lack of noticeable bulk graphitization up to 1200°C anneal (Raman, NEXAFS), while visible degradation of *t*-PA-Raman peaks were observed alongside with ~30% decrease of bulk hydrogen atom concentration (SIMS).

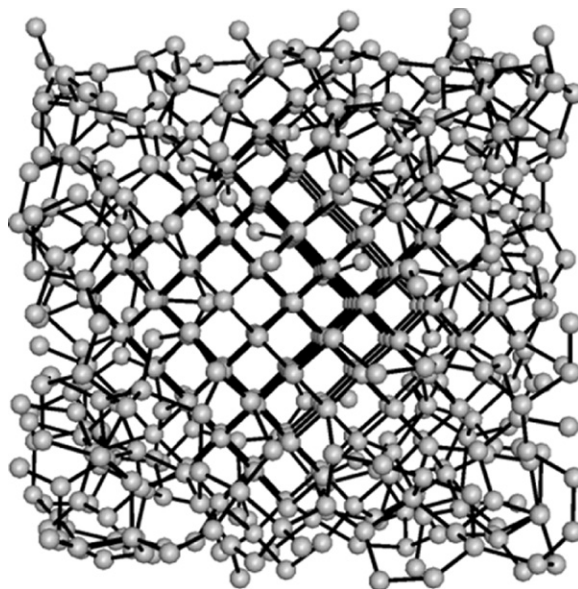
It has been commonly accepted since 2001 that diamond films prepared by CVD methods contain sp^2 -hybridized hydrogenated carbon, which is bonded in a similar way as *t*-PA molecule within the grain boundary region [36]. Many studies were done to clarify the origin of this bonding by means of isotopic substitution (H/D and $^{12}\text{C}/^{13}\text{C}$) and thermal annealing [37,43]. It was previously observed and reported that upon annealing to elevated temperatures (~1200°C) the ν_1 and ν_3 peaks associated with C–H bending and C=C stretching vibrations detected at 1140 and 1480 cm^{-1} by Raman spectroscopy are completely removed from the spectrum [37,43]. This is explained by thermal decomposition of *t*-PA-like bonds

at the nanodiamond crystallites grain boundaries. Similar to the present case, no additional change in the spectra shape was detected [37,43]. Since Raman spectroscopy is usually more sensitive to sp^2 carbon phases, some enhancement in G peak intensity may be expected following *t*-PA bonding decomposition. However, Ferrari and Robertson [37] noted that the rest of the spectrum is substantially unchanged following 1200°C annealing, while in the work of Pfeiffer et al. [98] following 1200°C annealing the diamond 1332 cm^{-1} line is even more pronounced than for as-deposited films. Present NEXAFS measurements confirm Raman results revealing at most only minor bulk graphitization of the film.

These findings suggest that during thermal decomposition of the *t*-PA-like bonds no graphitization occurs within the film bulk, while 30% of hydrogen atoms were lost after the annealing procedure. Therefore, the hydrogen/hydrocarbon atoms produced by thermal decomposition of *t*-PA seem to play an important role in dynamic stability of nanodiamond grains during annealing. Indeed, studying detonation nanodiamond films by X-ray scattering and diffraction techniques, Alexenskii et al. [99] found that annealing the film in a molecular hydrogen atmosphere for different temperatures increases the relative amount of diamond component within the bulk with a maximum at 800°C, while the same annealing in Ar atmosphere does not result in this maximum. This effect was attributed to preferential etching of sp^2 carbon atoms by hydrogen as during the CVD process itself [99]. This may be also true in these present results, with the hydrogen atoms being produced by decomposition of hydrocarbons in the grain boundaries, subsequently etching out the loosely bonded sp^2 carbon matrix.

In addition, partial transfer of carbon from the shell to the core with the intermediate formation of hydrocarbon cannot be ruled out. The coalescence of a few grains into single crystal was observed by Alexenskii et al. [99] during annealing in hydrogen, while Lytovich and Banhart [100] directly observed growth of diamond crystallites from graphite phase by electron irradiation. It is well known that up to ~5 nm size nanodiamond particles are energetically preferred over nanographite [101,102]. Moreover, the presence of hydrogen atoms and C—H surface bonding increases the thermodynamic stability range up to ~10 nm (i.e., up to relevant size of the present study) [103]. Therefore, it is a reasonable suggestion that following C—H bond breaking (bond energy of ~3.5 eV [104]) excited carbon atoms may be incorporated into more stable diamond cores, especially in the case of nanodiamond crystallites.

It should be noted finally that the onset for bulk graphitization commonly detected for detonation of nanodiamond is ~800°C [95], while present results suggest that bulk of the CVD nanodiamond films resists graphitization up to 1200°C. The difference between these two kinds of materials, among other things, is the composition of intergrain regions; for example, in Raman spectra of detonation films, *t*-PA features are absent. It may be concluded that hydrogen termination of grain surfaces and the presence of hydrocarbon molecules within the film's grain boundary region intrinsically increases the films' stability against elevated temperatures.

**FIGURE 8.17**

Simulated sample of a nanodiamond of ordered atoms surrounded by an amorphous shell.

8.7 Computational study

In this section, we briefly summarize some of our computer simulation studies of hydrogen atoms at interstitial sites at interfaces between diamond and amorphous carbon in order to have a deeper understanding of our experimental results. We compared the interstitial energy of hydrogen atoms between simulated samples of pure diamond and amorphous carbon, and within the interface between nanodiamond and amorphous carbon films. Samples of diamond and amorphous carbon were obtained using the molecular dynamics algorithm. We also built samples with a core of nanodiamond surrounded by amorphous carbon atoms (mixed sample). Each sample had 512 carbon atoms in a (100) cubic cell with full periodic boundary conditions. The mixed sample (nanodiamond surrounded by an amorphous shell) consisted of a core of 150 atoms in a diamond structure surrounded by 362 amorphous carbon atoms. Hydrogen atoms were inserted into the mixed sample and static optimization techniques were applied to calculate the atomic configuration at the local minimum of energy. The details of our calculations are presented in Ref. [105]. In Figure 8.17, an image of the simulated structure of the nanodiamond core with the amorphous shell is shown.

Figure 8.18 shows the sample at the end of the simulation where the gray circles depict the carbon atoms, and the black small circles depict hydrogen atoms. From this picture one may observe that most of the hydrogen atoms diffused from the

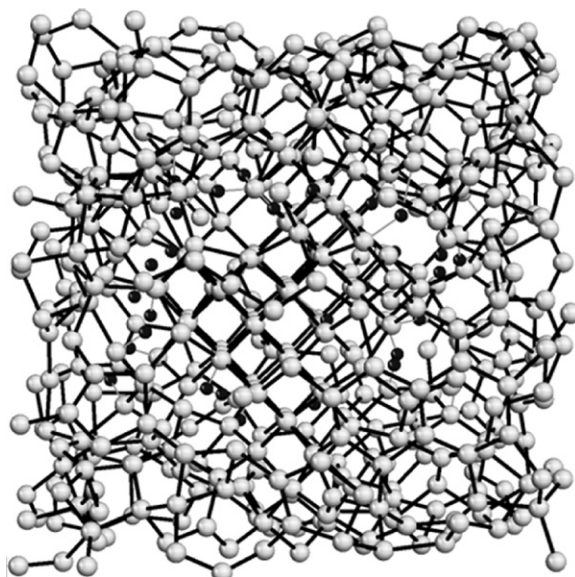


FIGURE 8.18

A mixed sample with 36 hydrogen atoms at the end of the molecular dynamics simulation. The gray circles depict carbon atoms, and the black small circles depict hydrogen atoms.

crystalline region to the amorphous region. The hydrogen atoms escaped from the interface region but remained close to the interface on the amorphous side.

8.8 Summary

In this chapter, we summarized our studies related to the impact of diamond grain size on the composition and properties of polycrystalline diamond films deposited by three different CVD methods. The films were grown from hydrogen-rich gas mixtures (HF and dc GD CVD) and an Ar-rich/hydrogen-poor gas mixture (MW CVD). SIMS studies provide direct evidence of the correlation between the concentration of hydrogen atom trapped within the films and diamond grain size, independently of deposition conditions: the *smaller* diamond grains result in *higher* hydrogen atom retention within the films. The hydrogen atoms are most likely bonded to the internal grain surfaces and within the grain boundary region. High hydrogen concentration in nanodiamond films has an impact on the shape of the Raman and HR-EEL spectra of nanodiamond films. Thus, the carbon–hydrogen-associated 1140 cm^{-1} Raman peak (C–H bending mode) undergoes enhancement in the case of nanocrystalline films alongside the HR-EELS 375 meV C–H stretching mode. Based on thermal stability studies, we associate these vibrational modes with $(\text{sp}^2)\text{-C-H}$ vibration originated from diamond surface. Both Raman and HR-EELS C–H-associated peaks undergo

intensity decrease relative to pure carbon vibrational modes in the case of UNC diamond (grain size ~ 5 nm). These findings are corroborated by IR measurements of other groups [46–48] and current investigations in our laboratory.

The relative thermal stability of CVD nanodiamond surface and bulk regions was studied by NEXAFS and Raman spectroscopies. It was found that the surface of the film undergoes nearly complete graphitization at 1000°C, while the bulk region is stable beyond 1200°C. This is in contrast to the graphitization onset of $\sim 800^\circ\text{C}$ reported by other authors for detonation nanodiamond. SIMS analysis showed that annealing at 1000°C results in a $\sim 30\%$ decrease in the hydrogen concentration, which correlates well with the disappearance of *t*-PA-associated Raman peaks. Notably, breaking of C–H bonds and desorption of H atoms does not result in substantial graphitization of the film's bulk region. The proposed function of hydrogen atoms is a stabilization of diamond grains together with possible preferential etching of nondiamond phase during thermal decomposition of *t*-PA-like hydrocarbons. The hydrogen atoms are most likely bonded to the internal grain surfaces and within the grain boundary region to carbon atoms bonded in a predominant sp^2 configuration. Our simulations suggest that hydrogen is expected to decorate the boundaries between a nanodiamond core and an amorphous shell. Assuming that the amorphous shell may be considered similar to nanodiamond grain boundaries, our model's computational studies support our experimental results and conclusions.

References

- [1] S.Y. Luo, J.K. Kuo, B. Yeh, J.C. Sung, C.W. Dai, T.J. Tsai, The tribology of nano-crystalline diamond, *Mat. Chem. Phys.* 72 (2001) 133.
- [2] L.Y. Huang, K.W. Xu, J. Lu, B. Guelorget, Analysis of nano-scratch behavior of diamond-like carbon films, *Surf. Coat. Technol.* 154 (2002) 232.
- [3] N. Jiang, K. Sugimoto, K. Nishimura, Y. Shintani, A. Hiraki, Synthesis and structural study of nano/micro diamond overlayer films, *J. Cryst. Growth* 242 (2002) 362.
- [4] K.H. Wu, X.R. Wang, S. Liu, E.G. Wang, Bistable characteristic and current jumps in field electron emission of nanocrystalline diamond films, *J. Appl. Phys.* 90 (2001) 4810.
- [5] N.G. Ferreira, L.L.G. Silva, E.J. Corat, Electrochemical activity of boron-doped diamond electrodes grown on carbon fiber cloths, *Diamond Relat. Mater.* 11 (2002) 657.
- [6] Q.Y. Chen, D.M. Gruen, A.R. Krauss, T.D. Corrigan, M. Witek, G.M. Swain, The structure and electrochemical behavior of nitrogen-containing nanocrystalline diamond films deposited from $\text{CH}_4/\text{N}_2/\text{Ar}$ mixtures, *J. Electrochem. Soc.* 148 (2001) E44.
- [7] J.Q. Li, D.Y. He, W.T. Guo, J.H. Zhang, Y.N. Sun, Q.S. Lei, X. Gao, Nanocrystalline diamond thin films as infrared optical protective coatings, *Int. J. Mod. Phys. B* 16 (2002) 1013.
- [8] W.B. Yang, F.X. Lu, Z.X. Cao, Growth of nanocrystalline diamond protective coatings on quartz glass, *J. Appl. Phys.* 91 (2002) 10068.
- [9] S. Bhattacharyya, O. Auciello, J. Birrell, J.A. Carlisle, L.A. Curtiss, A.N. Goyette, et al., Synthesis and characterization of highly-conducting nitrogen-doped ultrananocrystalline diamond films, *Appl. Phys. Lett.* 79 (2001) 1441.
- [10] D.M. Gruen, Nanocrystalline diamond films, *Ann. Rev. Mater. Sci.* 29 (1999) 211.

- [11] Y. Lifshitz, Th. Kohler, Th. Frauenheim, I. Guzman, A. Hoffman, R.Q. Zhang, et al., The mechanism of diamond nucleation from energetic species, *Science* 297 (2002) 1531.
- [12] J.B. Cui, J. Ristein, L. Ley, Electron affinity of the bare and hydrogen covered single crystal diamond (111) surface, *Phys. Rev. Lett.* 81 (1998) 429.
- [13] I.L. Krainsky, V.M. Asnin, G.T. Mearini, J.A. Dayton, Negative-electron-affinity effect on the surface of chemical-vapor-deposited diamond polycrystalline films, *Phys. Rev. B* 53 (1996) R7650.
- [14] J. Ristein, F. Maier, M. Riedel, M. Stammer, L. Ley, Diamond surface conductivity experiments and photoelectron spectroscopy, *Diamond Relat. Mater.* 10 (2001) 416.
- [15] O. Ternyak, A. Cimmino, S. Praver, A. Hoffman, Ultrathin continuous undoped diamond films: investigation of nanoscale conduction properties, *Diamond Relat. Mater.* 14 (2005) 272.
- [16] O. Ternyak, Sh. Michaelson, R. Akhvediani, A. Hoffman, Enhancement of electron emission from near-coalescent nanometer thick continuous diamond films, *Diamond Relat. Mater.* 15 (2006) 850.
- [17] W. Zhu, G.P. Kochanski, S. Jin, Low-field electron emission from undoped nanostructured diamond, *Science* 282 (1998) 1471.
- [18] P. Ascarelli, E. Cappelli, F. Pinzari, M.C. Rossi, S. Salvatori, P.G. Merli, et al., Secondary electron emission from diamond: physical modeling and application to scanning electron microscopy, *J. Appl. Phys.* 89 (2001) 689.
- [19] M. Bertin, A. Lafosse, R. Azria, Sh. Michaelson, O. Ternyak, A. Hoffman, Vibrational study of hydrogen bonding to ion irradiated diamond surfaces, *Appl. Phys. Lett.* 90 (2007) 061918.
- [20] Sh. Michaelson, O. Ternyak, A. Hoffman, Y. Lifshitz, Hydrogen incorporation processes in nanodiamond films studied by isotopic induced modifications of Raman spectra, *Appl. Phys. Lett.* 89 (2006) 131918.
- [21] P. Reichart, G. Datzmann, A. Hauptner, R. Hertenberger, C. Wild, G. Dollinger, Three-dimensional hydrogen microscopy in diamond, *Science* 306 (2004) 1537.
- [22] M. Benlahsen, B. Racine, K. Zellama, G. Turban, On the hydrogen incorporation, intrinsic stress and thermal stability of hydrogenated amorphous carbon films deposited from an electron cyclotron resonance plasma, *J. Non-Cryst. Sol.* 283 (2001) 47.
- [23] B. Racine, M. Benlahsen, K. Zellama, P. Goudeau, M. Zarrabian, G. Turban, Effect of the hydrogen on the intrinsic stress in hydrogenated amorphous carbon films deposited from an electron cyclotron resonance plasma, *Appl. Phys. Lett.* 73 (1998) 3226.
- [24] J. Robertson, Clustering and gap states in amorphous carbon, *Philos. Mag. Lett.* 57 (1988) 143.
- [25] J. Robertson, Mechanical properties and coordinations of amorphous carbons, *Phys. Rev. Lett.* 68 (1992) 220.
- [26] W. Jacob, Surface reactions during growth and erosion of hydrocarbon films, *Thin. Solid Films.* 326 (1998) 1.
- [27] P. Reinke, W. Jacob, W. Moller, Influence of the ion energy on the growth and structure of thin hydrocarbon films, *J. Appl. Phys.* 74 (1993) 1354.
- [28] A. Hoffman, A. Heiman, R. Akhvediani, E. Lakin, E. Zolotoyabko, C. Cyterman, Hydrogen content and density in nanocrystalline carbon films of a predominant diamond character, *J. Appl. Phys.* 94 (2003) 4589.
- [29] E. Titus, D.S. Misra, A.K. Sikder, P.K. Tyagi, M.K. Singh, A. Misra, et al., Quantitative analysis of hydrogen in chemical vapor deposited diamond films, *Diamond Relat. Mater.* 14 (2005) 476.

- [30] D.F. Talbot-Ponsonby, M.E. Newton, J.M. Baker, G.A. Scarsbrook, R.S. Sussmann, A.J. Whitehead, et al., Multifrequency EPR, ^1H ENDOR, and saturation recovery of paramagnetic defects in diamond films grown by chemical vapor deposition, *Phys. Rev. B* 57 (1998) 2264.
- [31] R.D. Maclear, J.E. Butler, S.H. Connell, B.P. Doyle, I.Z. Machi, D.B. Rebuli, et al., The distribution of hydrogen in polycrystalline CVD diamond, *Diamond Relat. Mater.* 8 (1999) 1615.
- [32] Y. Lifshitz, X.M. Meng, S.T. Lee, R. Akhvlediani, A. Hoffman, Visualization of diamond nucleation and growth from energetic species, *Phys. Rev. Lett.* 93 (2004) 056101.
- [33] R. Akhvlediani, I. Lior, Sh. Michaelson, A. Hoffman, Nanometer rough, sub-micrometer-thick and continuous diamond chemical vapor deposition film promoted by a synergetic ultrasonic effect, *Diamond Relat. Mater.* 11 (2002) 545.
- [34] D. Zhou, D.M. Gruen, L.C. Qin, T.G. McCauley, A.R. Krauss, Control of diamond film microstructure by Ar additions to CH_4/H_2 microwave plasmas, *J. Appl. Phys.* 84 (1998) 1981.
- [35] Sh. Michaelson, Y. Lifshitz, O. Ternyak, R. Akhvlediani, A. Hoffman, Hydrogen incorporation in diamond films, *Diamond Relat. Mater.* 16 (2007) 845.
- [36] A.C. Ferrari, J. Robertson, Origin of the 1150-cm^{-1} Raman mode in nanocrystalline diamond, *Phys. Rev. B* 63 (2001) 121405.
- [37] A.C. Ferrari, J. Robertson, Raman spectroscopy of amorphous, nanostructured, diamond-like carbon, and nanodiamond, *Phil. Trans. Royal Soc. A* 362 (2004) 2477.
- [38] A.C. Ferrari, S.E. Rodil, J. Robertson, Resonant Raman spectra of amorphous carbon nitrides: the G peak dispersion, *Diamond Relat. Mater.* 12 (2003) 905.
- [39] N. Wada, P.J. Gaczi, S.A. Solin, "Diamond-like" 3-fold coordinated amorphous carbon, *J. Non-Cryst. Sol.* 35 (1980) 543.
- [40] R.J. Nemanich, J.T. Glass, G. Lukovsky, R.E. Shroder, Raman scattering characterization of carbon bonding in diamond and diamondlike thin films, *J. Vac. Sci. Technol. A* 6 (1988) 1783.
- [41] R.E. Shroder, R.J. Nemanich, J.T. Glass, Analysis of the composite structures in diamond thin films by Raman spectroscopy, *Phys. Rev. B* 41 (1990) 3738.
- [42] W.A. Yarbrough, R. Messier, Current issues and problems in the chemical vapor deposition of diamond, *Science* 247 (1990) 688.
- [43] H. Kuzmany, R. Pfeiffer, N. Salk, B. Günther, The mystery of the 1140cm^{-1} Raman line in nanocrystalline diamond films, *Carbon* 42 (2004) 911.
- [44] T. Lopez-Rios, D. Mendoza, F.J. Garcia-Vidal, J. Sanchez-Dehesa, B. Pannetier, Surface shape resonances in lamellar metallic gratings, *Phys. Rev. Lett.* 81 (1998) 665.
- [45] I.Y. Koenka, A. Stacey, R. Akhvlediani, S. Praver, A. Hoffman, The impact of H/D substitution on the structure, composition and thermal stability of grain boundaries in sub-micron diamond films deposited on silicon, *Diamond Relat. Mater.* 22 (2012) 59.
- [46] Sh. Michaelson, A. Hoffman, Hydrogen bonding, content and thermal stability in nanodiamond films, *Diamond Relat. Mater.* 15 (2006) 486.
- [47] C.-F. Chen, C.-C. Wu, C.-L. Cheng, S.-Y. Sheu, H.-C. Chang, The size of interstellar nanodiamonds revealed by infrared spectra of CH on synthetic diamond nanocrystal surfaces, *J. Chem. Phys.* 116 (2002) 1211.
- [48] Y.-R. Chen, H.-C. Chang, C.-L. Cheng, C.-C. Wang, J.C. Jiang, Size dependence of CH stretching features on diamond nanocrystal surfaces: infrared spectroscopy and density functional theory calculations, *J. Chem. Phys.* 119 (2003) 10626.

- [49] C.-L. Cheng, C.-F. Chen, W.-C. Shaio, D.-S. Tsai, K.-H. Chen, The CH stretching features on diamonds of different origins, *Diamond Relat. Mater.* 14 (2005) 1455.
- [50] H. Ibach, D.L. Mills, *Electron Energy Loss Spectroscopy And Surface Vibrations*, Academic Press, New York, NY, 1982, p. 199.
- [51] B.J. Wacławski, D.T. Pierce, N. Swanson, R.J. Celotta, Direct verification of hydrogen termination of the semiconducting diamond(111) surface, *J. Vac. Sci. Technol.* 21 (1982) 368.
- [52] B.D. Thoms, J.E. Butler, HREELS scattering mechanism from diamond surfaces, *Phys. Rev. B* 50 (1994) 17450.
- [53] B.D. Thoms, J.E. Butler, HREELS and LEED of H/C(100): the 2×1 monohydride dimer row reconstruction, *Surf. Sci.* 328 (1995) 291.
- [54] B. Sun, X. Zhang, Q. Zhang, Z. Lin, Investigation of the growth mechanism of diamond (111) facets using high resolution electron energy loss spectroscopy, *Appl. Phys. Lett.* 62 (1993) 31.
- [55] B. Sun, X. Zhang, Z. Lin, Growth mechanism and the order of appearance of diamond (111) and (100) facets, *Phys. Rev. B* 47 (1993) 9816.
- [56] S.T. Lee, G. Apai, Surface phonons and CH vibrational modes of diamond (100) and (111) surfaces, *Phys. Rev. B* 48 (1993) 2684.
- [57] T. Aizawa, T. Ando, M. Kamo, Y. Sato, High-resolution electron-energy-loss spectroscopic study of epitaxially grown diamond (111) and (100) surfaces, *Phys. Rev. B* 48 (1993) 18348.
- [58] P.E. Pehrsson, T.W. Mercer, Oxidation of the hydrogenated diamond (100) surface, *Surf. Sci.* 460 (2000) 49.
- [59] P.E. Pehrsson, T.W. Mercer, Oxidation of heated diamond C(100): H surfaces, *Surf. Sci.* 460 (2000) 74.
- [60] J. Kinsky, R. Graupner, M. Stämmler, L. Ley, Surface vibrations on clean, deuterated, and hydrogenated single crystal diamond (100) surfaces studied by high-resolution electron energy loss spectroscopy, *Diamond Relat. Mater.* 11 (2002) 365.
- [61] K. Okada, T. Aizawa, R. Souda, S. Komatsu, S. Matsumoto, Vibrational studies of microcrystalline diamond and diamond-like carbon by high resolution electron energy loss spectroscopy, *Diamond Relat. Mater.* 10 (2001) 1991.
- [62] T. Aizawa, T. Ando, K. Yamamoto, M. Kamo, Y. Sato, Surface vibrational studies of CVD diamond, *Diamond Relat. Mater.* 4 (1995) 600.
- [63] A. Lafosse, D.T. Billy, J.P. Guilloin, Y. Le Coat, R. Azria, A. Laikhtman, et al., Role of electronic band structure and resonances on electron reflectivity and vibrational excitation functions: the case of hydrogenated diamond, *Phys. Rev. B* 68 (2003) 235421.
- [64] A. Laikhtman, A. Lafosse, Y. Le Coat, R. Azria, A. Hoffman, Clarification of oxygen bonding on diamond surfaces by low energy electron stimulated desorption and high resolution electron energy loss spectroscopy, *J. Chem. Phys.* 119 (2003) 1794.
- [65] A. Laikhtman, A. Lafosse, Y. Le Coat, R. Azria, A. Hoffman, Interaction of water vapor with bare and hydrogenated diamond film surfaces, *Surf. Sci.* 551 (2004) 99.
- [66] A. Lafosse, D. Caceres, M. Bertin, A. Hoffman, R. Azria, Role of electronic band structure and resonances on electron-scattering. The case of the hydrogenated polycrystalline diamond, *Surf. Sci.* 587 (2005) 134.
- [67] M. Bertin, A. Domaracka, D. Pliszka, A. Laffosse, R. Azria, Diamond surface modification following thermal etching of Si supported hydrogenated diamond films by DBr, *Surf. Sci.* 600 (2006) 847.
- [68] A. Lafosse, A. Hoffman, M. Bertin, D. Teillet-Billy, R. Azria, Density-of-states effect on surface and lattice vibrational modes in hydrogenated polycrystalline diamond, *Phys. Rev. B* 73 (2006) 195308.

- [69] Sh. Michaelson, A. Hoffman, Hydrogen in nano-diamond films, *Diamond Relat. Mater.* 14 (2005) 470.
- [70] Sh. Michaelson, O. Ternyak, R. Akhvediani, A. Hoffman, A. Lafosse, R. Azria, et al., Hydrogen concentration and bonding configuration in polycrystalline diamond films: from micro- to nanometric grain size, *J. Appl. Phys.* 102 (2007) 113516.
- [71] H. Okuyama, S. Thachepan, T. Argua, T. Ando, M. Nishijima, Overtones of the C—H stretch vibrations on C(001)(2×1)—H, *Chem. Phys. Lett.* 381 (2003) 535.
- [72] J. Biener, A. Schenk, B. Winter, C. Lutterloh, U.A. Schubert, J. Küppers, Spectroscopic identification of C—H species in C:H films using HREELS, *Surf. Sci. Lett.* 291 (1993) L725.
- [73] J. Biener, A. Schenk, B. Winter, C. Lutterloh, U.A. Schubert, J. Küppers, Hydrogenation of amorphous C:H surfaces by thermal H (D) atoms, *Surf. Sci.* 307 (1994) 228.
- [74] A. Horn, J. Biener, A. Schenk, C. Lutterloh, J. Küppers, H/D exchange reaction at graphitic CH groups by thermal H(D) atoms, *Surf. Sci.* 331 (1995) 178.
- [75] Sh. Michaelson, Y. Lifshitz, A. Hoffman, Determination of vibrational modes in electron energy loss spectroscopy of polycrystalline diamond surfaces by isotopic exchange, *Appl. Phys. Lett.* 89 (2006) 223112.
- [76] Sh. Michaelson, Y. Lifshitz, A. Hoffman, High resolution electron energy loss spectroscopy of hydrogenated polycrystalline diamond: assignment of peaks through modifications induced by isotopic exchange, *Diamond Relat. Mater.* 16 (2007) 855.
- [77] J. Ristein, R.T. Stief, L. Ley, W. Beyer, A comparative analysis of a-C:H by infrared spectroscopy and mass selected thermal effusion, *J. Appl. Phys.* 84 (1998) 3836.
- [78] Th. Frauenheim, Th. Kohler, M. Sternberg, D. Porezag, M.R. Pederson, Vibrational and electronic signatures of diamond surfaces, *Thin. Solid Films* 272 (1996) 314.
- [79] R. Kalish, Y. Lifshitz, K. Nugent, S. Praver, Thermal stability and relaxation in diamond-like-carbon. A Raman study of films with different sp^3 fractions (ta-C to a-C), *Appl. Phys. Lett.* 74 (1999) 2936.
- [80] R. Kalish, , in: A. Paoletti A. Tucciarone (Eds.), *The Physics of Diamond International School of Physics Enrico Fermi*, vol. 135, IOS, Amsterdam, 1997, pp. 373.
- [81] Ch. Wild, P. Koidl, Thermal gas effusion from hydrogenated amorphous carbon films, *Appl. Phys. Lett.* 51 (1987) 1506.
- [82] J.K. Walters, D.M. Fox, T.M. Burke, O.D. Weedon, R.J. Newport, W.S. Howells, The effect of temperature on the structure of amorphous hydrogenated carbon, *J. Chem. Phys.* 101 (1994) 4288.
- [83] J.K. Walters, J.S. Rigden, R.J. Newport, S.F. Parker, W.S. Howells, The effect of temperature on the structure of amorphous hydrogenated carbon, *Phys. Scr. T* 57 (1995) 142.
- [84] M. Lejeune, M. Benlahsen, R. Bouzerar, Stress and structural relaxation in amorphous hydrogenated carbon films, *Appl. Phys. Lett.* 84 (2004) 344.
- [85] Sh. Michaelson, O. Ternyak, A. Hoffman, O. Williams, D. Gruen, Hydrogen bonding at grain surfaces and boundaries of nanodiamond films detected by high resolution electron energy loss spectroscopy, *Appl. Phys. Lett.* 91 (2007) 103104.
- [86] Sh. Michaelson, O. Ternyak, A. Hoffman, Y. Lifshitz, Correlation between diamond grain size and hydrogen retention in diamond films studied by scanning electron microscopy and secondary ion mass spectroscopy, *Appl. Phys. Lett.* 90 (2007) 031914.
- [87] A. Hoffman, A. Lafosse, Sh. Michaelson, M. Bertin, R. Azria, Nano size effects in the high resolution electron energy loss spectra and excitation function of hydrogenated diamond films, *Surf. Sci.* 602 (2008) 3026.

- [88] J.F. Morar, F.J. Himpsel, G. Hollinger, G. Hughes, J.L. Jordan, Observation of a C-1s core exciton in diamond, *Phys. Rev. Lett.* 54 (1985) 1960.
- [89] G. Comelli, J. Storh, C.J. Robinson, W. Jark, Structural studies of argon-sputtered amorphous carbon films by means of extended x-ray-absorption fine structure, *Phys. Rev. B* 38 (1988) 7511.
- [90] J.F. Morar, F.J. Himpsel, G. Hollinger, J.L. Jordon, G. Hughes, F.R. McFelly, C 1s excitation studies of diamond (111). II. Unoccupied surface states, *Phys. Rev. B* 33 (1986) 1346.
- [91] J.F. Morar, F.J. Himpsel, G. Hollinger, G. Hughes, F.R. McFeely, C 1s excitation studies of diamond (111). I. Surface core levels, *Phys. Rev. B* 33 (1986) 1340.
- [92] F.L. Coffman, R. Cao, P.A. Pianetta, S. Kapoor, M. Kelly, L.J. Terminello, Near-edge x-ray absorption of carbon materials for determining bond hybridization in mixed sp^2/sp^3 bonded materials, *Appl. Phys. Lett.* 69 (1996) 568.
- [93] A. Heiman, I. Gouzman, G. Comtet, L. Hellner, G. Dujardin, S. Christiansen, et al., Evolution and properties of nanodiamond films deposited by direct current glow discharge, *J. Appl. Phys.* 89 (2001) 2622.
- [94] Sh. Michaelson, R. Akhvlediani, A. Hoffman, Hydrogenation and thermal stability of nano- and microcrystalline diamond films studied by vibrational electron spectroscopy, *J. Appl. Phys.* 104 (2008) 083527.
- [95] V.L. Kuznetsov, Y.V. Butenko, in: O.A. Shenderova, D.M. Gruen (Eds.), *Ultra Nanocrystalline Diamond Films: Synthesis, Properties and Applications*, William Andrew, New York, NY, 2006, pp. 405 and references therein.
- [96] J.-Y. Raty, G. Galli, C. Bostedt, T.W. Buuren, L.J. Terminello, Quantum confinement and fullerene-like surface reconstructions in nanodiamonds, *Phys. Rev. Lett.* 90 (2003) 037401.
- [97] V.L. Kuznetsov, A.L. Chuvilin, Y.V. Butenko, I.L. Malkov, V.M. Titov, Onion-like carbon from ultra-disperse diamond, *Chem. Phys. Lett.* 222 (1994) 343.
- [98] R. Pfeiffer, H. Kuzmany, P. Knoll, S. Bokova, N. Salk, B. Gunther, Evidence for trans-polyacetylene in nano-crystalline diamond films, *Diamond Relat. Mater.* 12 (2003) 268.
- [99] A.E. Aleksenskii, M.V. Baidakova, A.Y. Vul', A.T. Dideikin, V.I. Siklitskii, S.P. Vul', Effect of hydrogen on the structure of ultradisperse diamond, *Phys. Solid State* 42 (2000) 1575.
- [100] Y. Lytovich, F. Banhart, Low-pressure transformation of graphite to diamond under irradiation, *Appl. Phys. Lett.* 74 (1999) 659.
- [101] M.Y. Gamarnik, Energetical preference of diamond nanoparticles, *Phys. Rev. B* 54 (1996) 2150.
- [102] M.Y. Gamarnik, Size-related stabilization of diamond nanoparticles, *Nanostruct. Mater.* 7 (1996) 651.
- [103] A.S. Barnard, Theory and modeling of nanocarbon phase stability, *Diamond Relat. Mater.* 15 (2006) 285.
- [104] B. deB., Darwent, *Bond Dissociation Energies in Simple Molecules*, National Bureau of Standards, Washington, DC, 1970.
- [105] Sh. Michaelson, R. Akhvlediani, A. Hoffman, A. Silverman, J. Adler, Hydrogen in nano-diamond films: experimental and computational studies, *Phys. Status Solidi A* 205 (2008) 2099.

Recent Results on Characterization of Detonation Nanodiamonds

9

Igor I. Vlasov^a, Stuart Turner^b, Gustaaf Van Tendeloo^b, and Andrey A. Shiryaev^c

^a*General Physics Institute, Russian Academy of Sciences, Moscow, Russia,*

^b*EMAT, University of Antwerp Groenenborgerlaan, Antwerp, Belgium,*

^c*Institute of Physical Chemistry and Electrochemistry, Russian Academy of Sciences,
Moscow, Russia*

CHAPTER OUTLINE

9.1 Introduction	292
9.2 TEM and electron energy-loss spectroscopy	292
9.2.1 Bright-field TEM imaging and electron diffraction of ND material	293
9.2.2 Aberration-corrected high-resolution imaging at low acceleration voltage.....	294
9.2.3 Scanning TEM	296
9.2.4 Electron energy-loss spectroscopy.....	297
<i>Low-loss EELS</i>	<i>298</i>
<i>Core-loss EELS: ND carbon K-edge ELNES.....</i>	<i>299</i>
<i>Core-loss EELS: local dopant detection and coordination determination ...</i>	<i>300</i>
9.3 Near-edge X-ray absorption fine structure spectroscopy	305
9.4 XRD and small-angle X-ray scattering	308
9.4.1 X-ray diffraction	308
9.4.2 SAXS	309
9.4.3 Microstructure of NDs from X-ray data	311
9.5 ESR spectroscopy	313
9.6 Photoluminescence spectroscopy	315
9.6.1 Time-resolved PL of DND	316
9.6.2 Confocal PL spectroscopy of single DND particles	316
9.6.3 PL spectroscopy of HPHT-sintered DND	320
9.7 Conclusion	321
References	322

9.1 Introduction

Main results on the characterization of detonation nanodiamond (DND), accumulated over many years of material production and investigation, were presented in the first edition of this book, *Ultrananocrystalline Diamond* (2006). This (second) edition is mainly focused on new results on DND characterization resulting from recent progress in instrumentation and methodological development of the techniques traditionally used for DND characterization, such as transmission electron microscopy (TEM), X-ray diffraction (XRD), electron spin resonance (ESR) and photoluminescence spectroscopy.

9.2 TEM and electron energy-loss spectroscopy

The focus of this section will be on concrete characterization results on nanodiamond (ND) material by TEM and electron energy-loss spectroscopy (EELS) in an electron microscope. It is by no means a complete reference on TEM or EELS; only a short introduction will be given into each technique. The reader is referred to the many excellent books on scanning TEM (STEM) and EELS in the literature (Refs. [1–4] amongst many others) for a more in-depth discussion of the techniques presented here.

TEM uses high-energy electrons in combination with electromagnetic lenses to focus the electron beam on a given sample and image the sample on a suitable recording device like a CCD camera. Owing to the high acceleration voltages used in TEM (typically several hundred kilovolts), the wavelength of the accelerated electrons is far shorter than the typical wavelength of light, making the resolving power of an electron microscope far greater than that of its optical counterpart. There are two main modes of operation in an electron microscope; in TEM the whole sample is simultaneously illuminated by a wide electron beam, while in STEM, a fine probe is scanned over the sample, and the scattered electrons are collected in each scan point to create an image.

The limiting factor for (S)TEM image resolution was long not the electron wavelength (~ 2 pm for a 300 kV acceleration voltage), but rather lens aberrations like spherical and chromatic aberration caused by the use of round electromagnetic lenses in a conventional transmission electron microscope [5]. These aberrations limited resolutions in a typical high-resolution TEM (HRTEM) to a point resolution at optimal defocus of ~ 1.7 Å (170 pm), far from theoretical resolutions of only a few picometers. Thanks to the recent successful implementation of spherical aberration-correction in electron microscopy, modern instruments are able to reach image resolutions of 50 pm (0.5 Å) in both TEM and STEM mode at conventional acceleration voltages of 300 kV, but can also be operated at lower voltages of 80, 60, or even 40 keV while keeping the atomic resolution [6–10]. Low voltage microscopy has previously been highly used to great success in imaging beam sensitive materials like nanotubes, graphene, and hexagonal BN [11,12], and can allow for prolonged and detailed experiments to be performed while minimizing the risk of knock-on damage or surface graphitization in the case of ND [13].

9.2.1 Bright-field TEM imaging and electron diffraction of ND material

In bright-field TEM, the sample is imaged using a parallel incoming electron beam. In general, only a (small) amount of the electrons that have passed through the specimen are used for imaging in the bright-field imaging mode; an objective aperture can be placed in the back-focal plane of the objective lens to cut out all electrons except the transmitted beam or a selected amount of reflections, providing a bright-field image with enhanced contrast. There are two main contrast regimes in bright-field imaging. For noncrystalline materials, *mass-thickness contrast* (also known as absorption contrast) is dominant. In crystalline materials like ND, this amplitude-type contrast is in direct competition with *diffraction contrast*, which originates from elastic Bragg scattering in the crystal and is dependent upon the orientation of the crystalline specimen with respect to the incoming electron beam. In an electron microscope, diffraction and imaging go hand-in-hand. The back-focal plane of the objective lens in a TEM is also the diffraction plane, as the back-focal plane is the Fourier conjugate of the object plane. This means that the microscope operator can switch between the diffraction pattern and the real space image by a simple push of a button.

A typical bright-field TEM image and electron diffraction pattern from an ozone-treated, clean DND sample are displayed in Figure 9.1 [14,15]. The DND particles have primary particle sizes ranging between ~2 and 20 nm, and are in general agglomerated

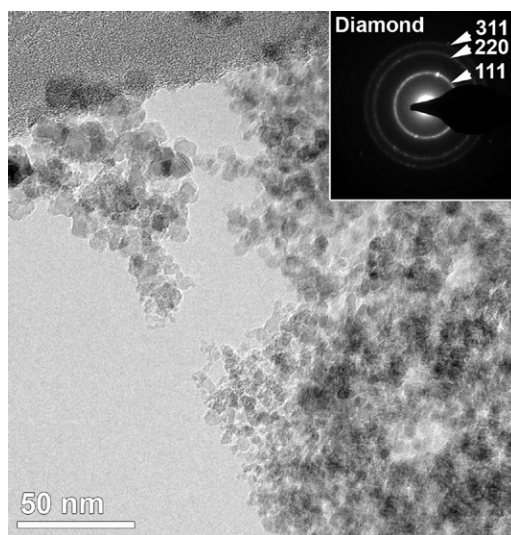


FIGURE 9.1

Low-magnification image of DND particles [14]. The particles have sizes ranging from ~2 to 20 nm. The inset electron diffraction ring pattern evidences the diamond crystal structure.

into larger structures [16]. The agglomeration of the DND particles is typical for nano-sized material, and is mainly due to Van der Waals attractive forces [17,18].

The crystal structure of the particles can be determined from the inset electron diffraction ring pattern. As the diffraction pattern is taken from many ND particles with varying orientations simultaneously, the angular information is lost leaving only the ring interspacings to determine the crystal phase through Bragg's law (like an XRD pattern) [19]. In this case, only rings corresponding to the diamond crystal structure (Fd-3m, Space Group number 227) are present. No graphite or n-diamond [20] reflections are visible, an important indication for a high purity of the DND material.

9.2.2 Aberration-corrected high-resolution imaging at low acceleration voltage

Unlike X-ray or neutron diffraction, electron diffraction is highly dynamical, meaning that multiple electron scattering with large phase changes occurs frequently in an electron microscope. In HRTEM a large objective aperture (or no aperture at all) is inserted in the back-focal plane of the objective lens, allowing diffracted beams to interfere both with each other and the transmitted beam, forming an interference (fringe) pattern. As a result the contrast in such an image is dependent on the phase of the various beams, giving rise to the name phase-contrast imaging for HRTEM imaging. In some cases these interference patterns or high-resolution images can be directly interpreted, usually however image simulations need to be carried out to interpret the images.

A high-resolution, aberration-corrected TEM image of a typical nanoparticle in the sample is presented in Figure 9.2. To obtain this image, the electron microscope was operated at 80kV (below the knock-on damage threshold for diamond) with the spherical aberration coefficient (C_s) corrected and tuned to $+15\mu\text{m}$. To extend the information limit of the microscope (which is normally limited by chromatic aberration), the monochromator of the microscope was excited to achieve an energy spread of the order of 0.3 eV for the illuminating electron beam. By further extending the information transfer of the microscope, intricate details of the ND surface become visible (see Figure 9.2A). The DND particle is imaged along the [011] zone axis orientation (as evidenced by the inset Fourier transform (FT)), allowing $\{111\}$ -type surface facets and $\Sigma = 3 \{111\}$ twin boundaries to be imaged edge-on. Two coherent $\Sigma = 3 \{111\}$ twin boundaries run through the particle. This type of twin is typical for DND as it has the lowest defect energy of all diamond defects. This results from the fact that this twin type only demands a small deviation from the ideal lattice, namely only in the fourth neighbor lattice positions. The abundance of these defects has been attributed to the increased growth rate of twinned NDs in comparison to untwinned ND under detonation synthesis conditions [22].

The nanoparticle shows mainly $\{111\}$ -type surface facets with some $\{100\}$ truncation, a result of the low surface energy of these low-index facets [19]. The $\{100\}$ truncation is imaged in more detail in Figure 9.2B. Under the imaging conditions used ($C_s = +15\mu\text{m}$, 4nm underfocus) the atomic columns are imaged in

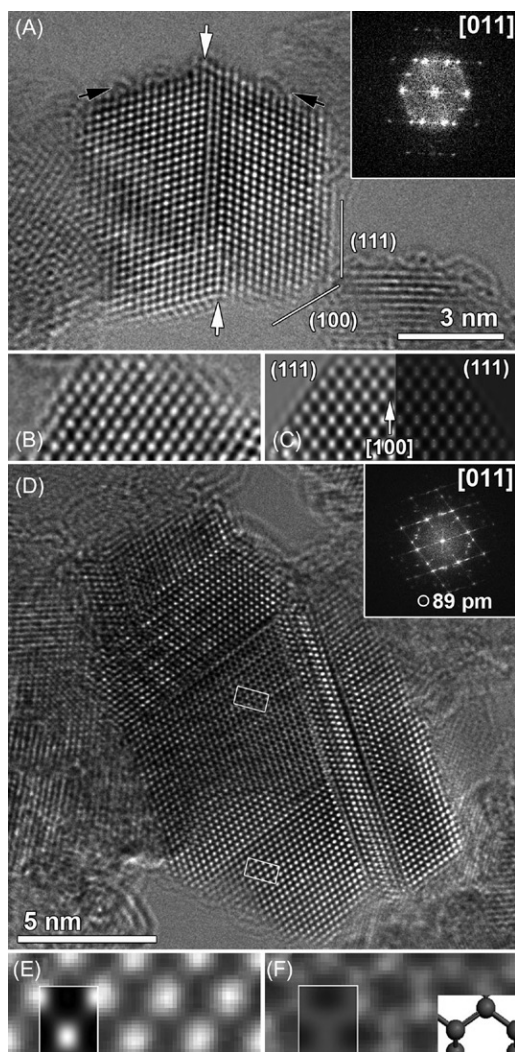


FIGURE 9.2

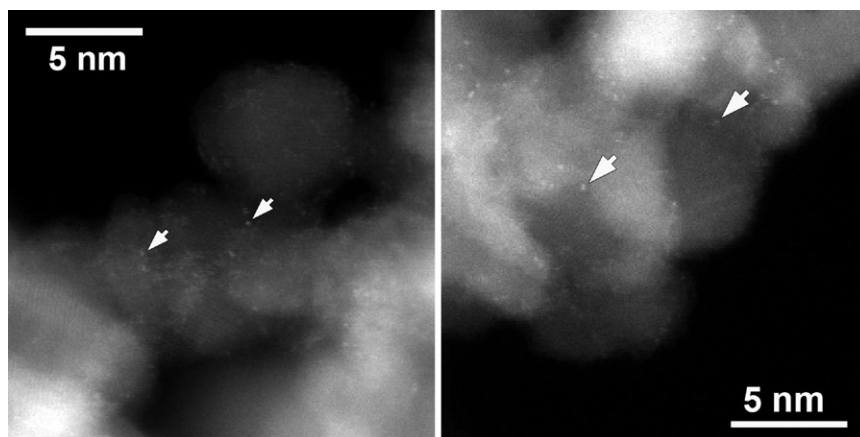
Low voltage, aberration-corrected images of DND particles [14,21]. (A) HRTEM image of a typical DND particle exhibiting two coherent $\Sigma = 3$ {111} twin defects. The diamond surfaces show minimal presence of graphitic material. (B) Enlarged image of the {100} truncation in the bottom right of (A). Both {100}- and {111}-type surface facets are clean. (C) Image simulation performed for $C_s = 15 \mu\text{m}$, $\Delta f = -4 \text{ nm}$. The right-hand side has the projected potential overlaid, demonstrating the white image contrast peaks at the atomic positions. (D) HRTEM image of a multiple-twinned DND particle. Inset simulations performed for $C_s = 15 \mu\text{m}$, $\Delta f = -4 \text{ nm}$, and thickness = 4 and 14 nm.

white, as evidenced by the simulation of a truncated diamond particle in Figure 9.2C. The atomic potential overlay in Figure 9.2C also demonstrates that even though the information transfer of the microscope is extended by use of the monochromator, the 89pm carbon dumbbells are not directly resolved in the image. An elongation of the column contrast in the dumbbell direction is visible. The combination of the HRTEM image and image simulation allows us to conclude that the surfaces (both the {111}- and {100}-type surfaces are extremely clean. On the region cut out in Figure 9.2B, no graphitic surface material can be made out (although a minimal surface layer is visible on the top two {111} facets in Figure 9.2A as indicated by black arrows).

A second, multiple-twinned nanoparticle is imaged in Figure 9.2D. This type of multiple-twinned nanoparticle was previously reported by our group [23]. As was the case for the particle in Figure 9.2A, this multiple-twinned ND is imaged along the [011] zone axis orientation, with mainly {111}-type and some {100}-type surface facets visible. The [011] zone axis orientation is evidenced by the inset FT. Interestingly, this FT (unlike the FT for the smaller ND) shows the presence of a (400) reflection corresponding to the 89pm dumbbell spacing. In Figure 9.2E and F two enlarged regions of the particle are imaged, together with their corresponding image simulations. In Figure 9.2E, arising from a thin region of the particle (indicated by a rectangle in Figure 9.2A), the 89pm dumbbells are imaged as elongated white contrast (as was the case in Figure 9.2A). However, in the thicker region of the particle the dumbbell is clearly resolved, most likely due to dynamical scattering effects. Although the presence of multiple coherent {111} twins was apparent from earlier conventional HRTEM work, several features remained unclear until now. The first is the surface structure, which in this sample exhibits a minimal graphitic presence. Secondly, the details of the multiple twin boundaries are imaged; no indication for an enrichment of amorphous carbon or nitrogen clusters at the twin boundaries can be derived from the HRTEM image. To determine whether amorphous carbon or nitrogen atoms are enriched at the defects and twin boundaries, spatially resolved EELS can be carried out.

9.2.3 Scanning TEM

In STEM the electron beam is focused to an angström-sized probe and is scanned over the sample by deflection coils. Depending upon the transmitted electrons that are used to form the image, a bright-field STEM image or dark-field STEM image can be formed [4]. The most-used detector in STEM is by far an annular detector, used to form annular dark-field images. By using the intermediate lenses to change the camera length used in STEM mode, the angular range of electrons falling onto the annular detector can be controlled. In high-angle annular dark-field STEM only the electrons that have been scattered under large angles by the specimen (Rutherford-like scattering) are collected on the annular detector. This type of imaging is also known as Z-contrast imaging, as the Rutherford-like scattering of the electrons scattered to high angles leads to an image intensity that is approximately

**FIGURE 9.3**

Aberration-corrected HAADF-STEM images of ozone-treated DND particles [14,21]. Individual heavy Fe atoms from the detonation process decorate the low-contrast diamond nanoparticles.

proportional to the square of the atomic number (Z^2) and to the thickness of the specimen. High-angle annular dark field STEM (HAADF-STEM) imaging is therefore both chemically sensitive and thickness sensitive. This imaging mode is also known as incoherent imaging, as the image that is formed, e.g., in high-resolution HAADF-STEM, is no longer a phase-contrast image like in HRTEM, but is rather a directly interpretable mass-thickness projection of the imaged crystal. An example of the sensitivity of HAADF-STEM imaging is displayed in Figure 9.3; the images show that typical DND material is covered with individual, heavy Fe atoms from the detonation process, which cannot be seen in conventional HRTEM images.

By using an annular detector to collect the electrons scattered by the sample over larger angles, image acquisition and the collection of forward scattered electrons using an energy filter for EELS can happen simultaneously. This makes HAADF-STEM-EELS ideally suited for the study of 0D nanomaterials as imaging can be directly combined with local chemical information down to the angström level.

9.2.4 Electron energy-loss spectroscopy

When incoming fast electrons are scattered inelastically in a solid, conservation of total energy dictates that the energy transferred in a single-electron excitation or in the excitation of a phonon or plasmon is equal to that lost by the scattered fast electron. In EELS the processes of electron excitation are studied by measuring the energy-loss of the primary fast electrons. EEL spectroscopy is particularly well suited to study light elements like nitrogen, oxygen, boron, and carbon. Heavy elements like gold and platinum are generally not well suited to EELS.

A typical EELS spectrum consists of three major regions:

- The zero-loss peak at 0 eV from the electrons that are elastically scattered (the majority of the fast electrons) and from electrons that have transferred less energy than the energy resolution of the energy filter and the incoming electron beam.
- The low-loss region from 1–100 eV showing characteristic peaks from the band gap, interband transitions, and from the excitation of bulk and surface plasmons.
- The core-loss region from 100 eV onward showing the element-specific ionization edges on top of a decaying background, which can usually be approximated by a power-law function ($A \cdot E^{-r}$). The excitation edges correspond to the energy-loss of inner-shell electrons that are excited to a higher, unoccupied state above the Fermi level.

Low-loss EELS

Reference low-loss spectra for diamond, graphite, and amorphous carbon are shown in Figure 9.4, together with low-loss EELS data from three individual clean NDs with different sizes. The low-loss EELS spectra in Figure 9.4B all show a prominent plasmon peak around 34 eV; this is close to the plasmon energy of bulk diamond (33 eV) confirming that the bulk of DND material is diamond [21–27]. A small shoulder is measured around 22 eV, which is attributed to the diamond surface plasmon. The peak does not arise from graphitic or amorphous material, as no π -plasmon is visible. The smaller the particle, the more prominent the surface

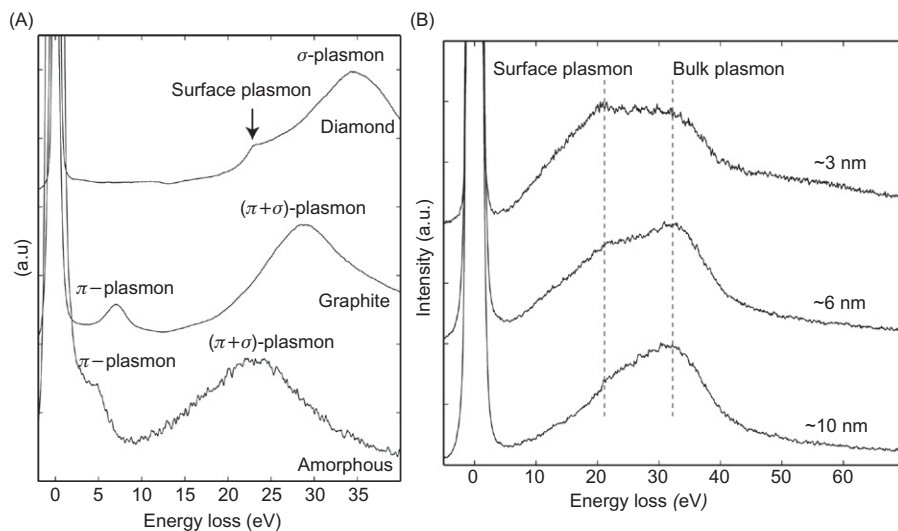


FIGURE 9.4

(A) Diamond, graphite, and amorphous carbon low-loss spectra together with (B) low-loss spectra taken from individual DND particles from a clean DND sample [24,25].

plasmon peak becomes, as the surface to volume ratio increases [24]. The band gap around 5–6 eV can also be measured under specific experimental conditions [16].

Core-loss EELS: ND carbon K-edge ELNES

In the core-loss EELS region, the shape of the excitation edges is linked to this unoccupied density of states and is called the energy-loss near-edge structure (ELNES). The ELNES therefore contains information about the bonding and electronic state of the probed material and as a result can be used to distinguish between allotropes of the same material and to determine local bonding. A typical example is the difference between the fine structure of the carbon K-edge in the case of diamond (sp^3 -bonded carbon) and graphite or amorphous carbon (sp , sp^2 -bonded carbon). Typical EELS spectra taken from cleaned DND samples are displayed in Figure 9.5B [23].

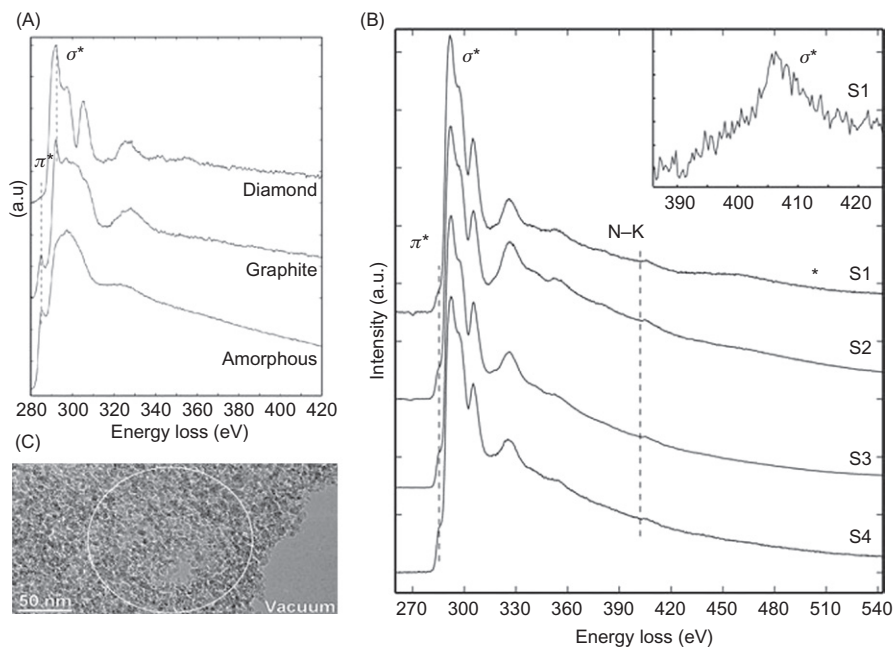


FIGURE 9.5

Diamond, graphite, and amorphous carbon K-edge ELNES signatures taken as a reference from a thin diamond film, a thin graphite film, and an amorphous carbon support (top panel) together with background subtracted, normalized core-loss EELS spectra from several cleaned DND samples [23]. Nitrogen is detected in all samples through the K-edge with half maximum at 403 eV. No oxygen is detected at 532 eV (indicated by asterisk). Inset: background subtracted nitrogen K-edge signal from sample S1 showing the nitrogen σ^* peaking at 406 eV. The image in (C) indicates a typical investigated area for TEM-EELS.

All ND EELS spectra are aligned to the carbon K-edge onset at 284 eV. The spectra show typical diamond-like (σ^*) ELNES starting at 292 eV (see diamond reference). The spectra also show a small carbon pre-peak, typical for graphitic material at 285 eV (σ^* contribution—see also graphite reference) [28], arising from surface carbon [27]. In many ND samples, a clear signal for nitrogen (nitrogen K-edge) can be measured, with half maximum at 403 eV and peaking at 406 eV. A typical background subtracted nitrogen K-edge is shown in the inset as an example. No oxygen signal (oxygen K-edge at 532 eV) can be detected in the investigated samples.

The area under the ionization edges can be used for elemental quantification. In conventional quantification, the decaying background is removed and the integrated intensity under the edges is measured and quantified using a suitable atomic cross section (effectively a probability for inelastic scattering). Model-based quantification can be used to obtain the most precise and accurate results possible [29]. Typical DND particles can contain up to several at.% of embedded nitrogen [23,30].

Core-loss EELS: local dopant detection and coordination determination

Besides confirming the presence of impurities like nitrogen ND particles through core-loss EELS of many particles simultaneously, spatially resolved EELS in a STEM can be used to locally determine the position of, e.g., nitrogen, in the diamond lattice [31,32]. Using STEM-EELS, points analysis, 2D line scans, and 3D “spectrum images” can be carried out by acquiring an EELS spectrum at each probe position. In modern aberration-corrected instruments, probe sizes well below 1 Å are feasible, allowing atomic resolution analysis [8].

An example of a line-scan experiment is displayed in Figure 9.6. The particle is a single diamond crystal, ~13 nm in diameter; the performed line scan is displayed by an arrow in Figure 9.6A. In total 20 EELS spectra were recorded in the line scan of the 13 nm grain. Two typical spectra—one at position A and one at position B on the particle—are displayed in Figure 9.6B. Both spectra show a carbon K-edge with σ^* contributions typical for diamond at 292 eV and small π^* contributions at 285 eV arising from sp^2 -hybridized surface carbon. Spectrum B shows a larger graphitic π^* contribution than spectrum A, which is to be expected as a larger surface contribution is measured at the thinner position B. The spectrum at position A clearly shows a nitrogen signal at 403 eV (indicated by an asterisk), while the spectrum from position B does not. Using model-based quantification methods, the nitrogen content was determined over the whole line scan. It is plotted in Figure 9.6C as the nitrogen signal strength, together with the carbon signal strength and the HAADF-STEM signal intensity, which may be regarded as a thickness profile. In Figure 9.6D, the normalized sp^2 and sp^3 content is plotted. These values were obtained by modeling the π^* and σ^* contribution using a Lorentzian at 285 and 292 eV, respectively. To obtain the plot, the area under the modeled Lorentzian peaks was divided by the total intensity of the π^* and σ^* contribution. In this way the sp^2 content was determined to be only 5% at the core positions, rising at the edge of the particle to a maximum of 14% sp^2 . It can be seen from the plots in Figure 9.6C and D that there is only a detectable nitrogen signal within the inner

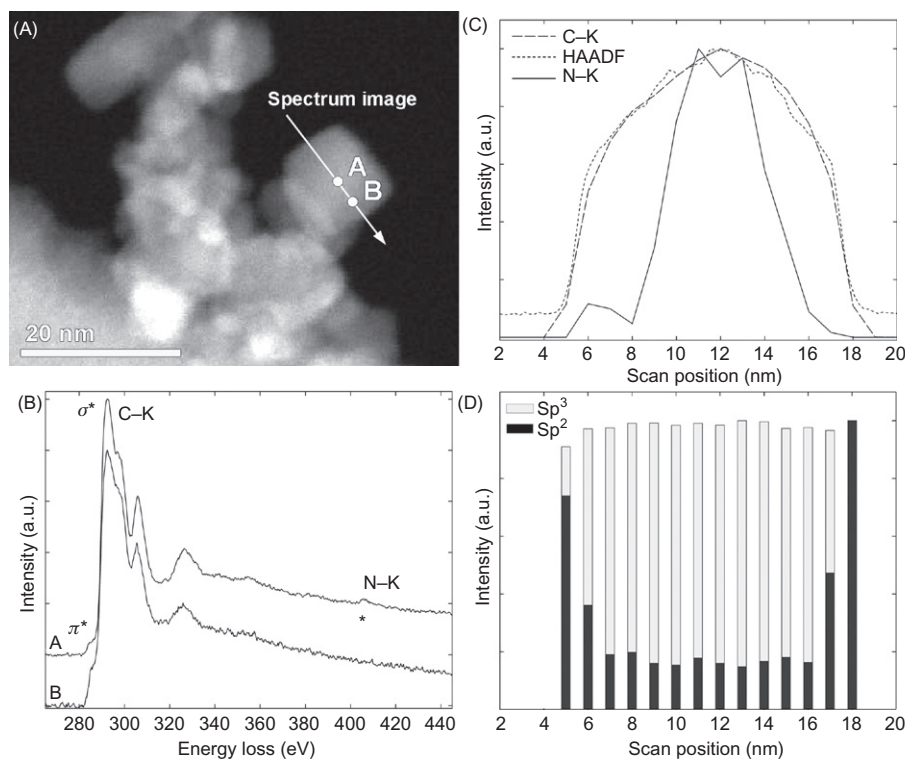
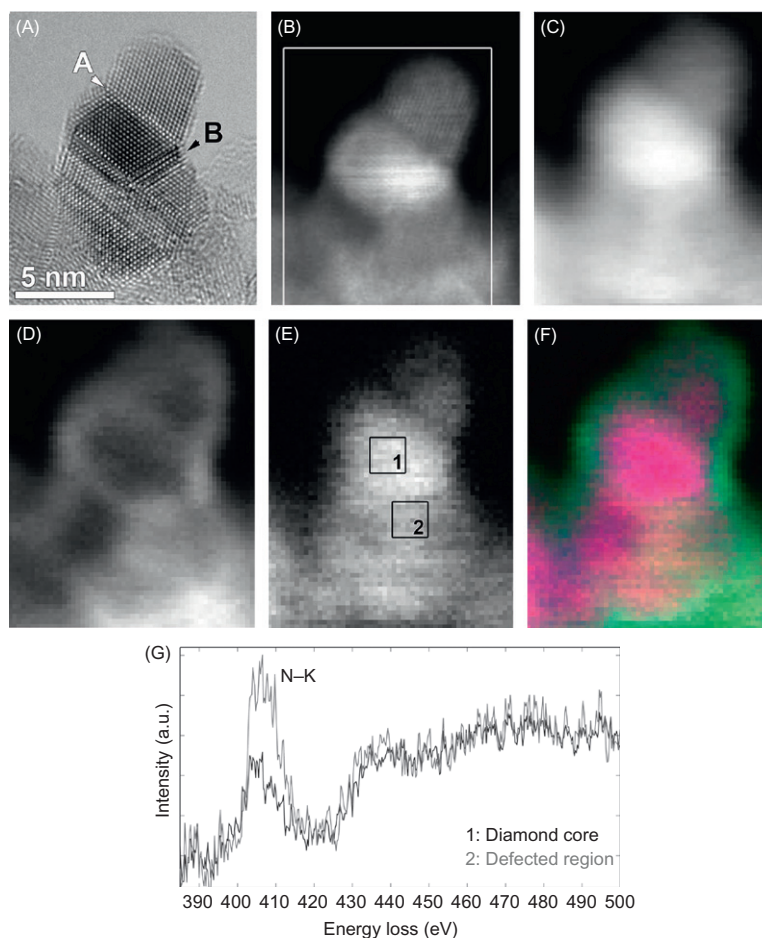


FIGURE 9.6

Central nitrogen embedding in a DND nanoparticle [25,33]. (A) HAADF-STEM image of a large DND nanoparticle. The 20 point line scan is indicated by an arrow. (B) Background subtracted, normalized EELS spectra from positions A and B from the large DND particle. Position A on the particle shows a clear nitrogen peak at 403 eV; position B closer to the surface does not. (C) Normalized nitrogen peak strength, carbon peak strength, and HAADF-STEM image intensity for the line scan from (A). (D) Normalized sp^2 and sp^3 content at each scan position modeled by a Lorentzian at 285 and 292 eV for the π^* and σ^* contribution, respectively. The sp^3 content at the center is ~95% and at the edge ~86%.

6 nm core of the DND particle. Toward the surface of the particle where the sp^2 ratio is higher, no nitrogen is detected. The maximum nitrogen content in the core of the particle was measured to be 3.5 at.%. The lack of an N signal toward the surface is not due to noise, as can be seen when comparing spectra A and B in Figure 9.6B.

Similar line-scan experiments were carried out by other groups on high nitrogen-doped DND material. These results also indicated the nitrogen was preferentially embedded in the diamond cores [30].

**FIGURE 9.7**

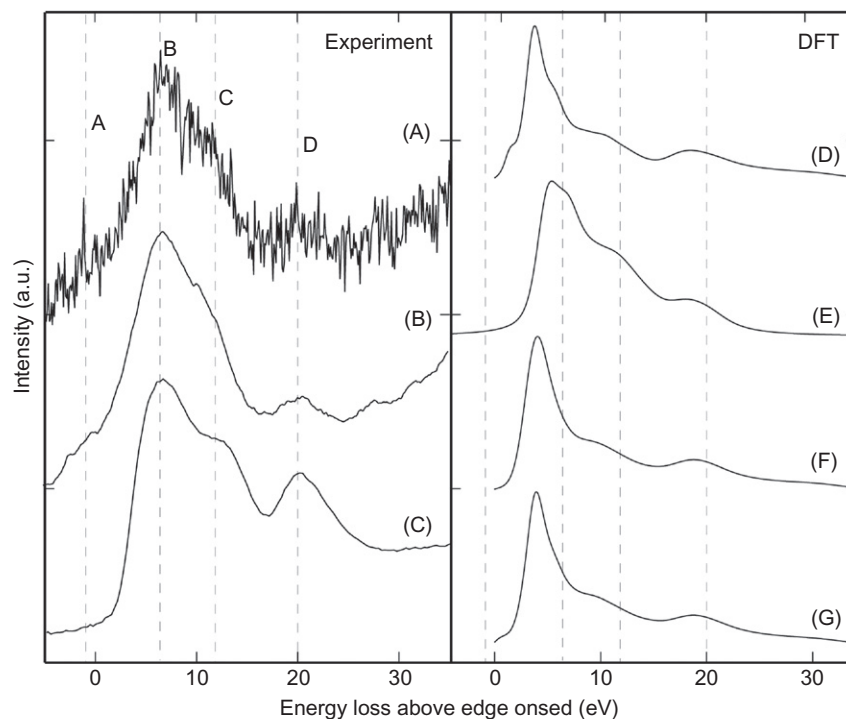
Core-loss STEM-EELS analysis of a multiple-twinned ND [14]. (A) HRTEM image of a multiple-twinned ND with single coherent twins as indicated by A and multiple lamellar twin regions as indicated by B. (B) Corresponding ADF-STEM image, indicating the area of the 53×67 pixel spectrum image (C) sp^3 map, (D) $sp-sp^2$ map, and (E) N map—the maximum N to C ratio is 4.0 at.%; (F) color map (green= $sp-sp^2$; blue= sp^3 ; red=N); (G) nitrogen K-edge spectra from region 1 to region 2 indicated in (E). Defected region 2 shows a clear enrichment of nitrogen.

In a second example, the multiple-twinned ND displayed in Figure 9.7A was investigated using the spectrum imaging method, to determine whether any enrichment of nitrogen at grain or twin boundaries occurs in DND. The HRTEM image of the multitwin again shows the presence of simple $\Sigma = 3$ coherent twin boundaries

and lamellar multiple-twinned regions, probably containing a large degree of point and planar defects [34]. The particle surface appears to be nearly non-sp³ carbon free. For this particle, a 53 × 67 pixel spectrum image (SI) was acquired at 2 Å interspacing. The sp-sp², sp³, and N maps are displayed in Figure 9.7C–E. As was the case for the line scan in Figure 9.6, the sp³ map follows the annular dark field (ADF) signal nicely, and the intensity in the map can be seen as a thickness fingerprint. Although only minimal graphitic material was visible in the HRTEM image, the sp-sp² map clearly follows the surface contours of the ND particle. The origin of this signal is therefore attributed mainly to dangling bonds and to some rest non-sp³ material at the surface of the ND particle. A significant sp-sp² signal is also measured from both the coherent $\Sigma = 3$ twin boundary (example indicated by A) as well as the lamellar twinned regions (example indicated by B). This nondiamond signal must once again arise from dangling bonds, indicating that even the coherent twin boundaries are not sp² carbon free. The nitrogen K-edge signal is mapped in Figure 9.7E. The nitrogen is embedded in the ND matrix, in good agreement with earlier measurements. Interestingly, an enrichment of nitrogen at the multiple-twinned region is clear from the map. As thickness effects can play a role in the visual interpretation of the nitrogen map, and the map displays a relatively high noise level due to the low nitrogen signal, the nitrogen K-edge from two regions, region 1 being a nondefected diamond region and region 2 being the multiple-twinned region, are plotted in Figure 9.7G. The spectra have been aligned to their continuum level, and it is clear that even though the nondefected region clearly contains nitrogen, the multiple-twinned area is enriched in nitrogen. No such clear nitrogen enrichment was measurable for the coherent twin boundary A.

As mentioned above, the fine structure of EELS edges is known to be related to the local symmetry and environment of the excited atomic species [21,35]. Therefore, the shape of the nitrogen K-edge fine structure should provide clues about the form in which nitrogen is embedded into the ND particles. In previous experiments, the shape and position of the nitrogen K-edge fine structure led our and other groups to the conclusion that nitrogen was tetrahedrally embedded in the diamond particles [23,30].

The averaged experimental nitrogen K-edge fine structure from a diamond core region (both raw data and smoothed) and the experimental carbon K-edge of ND are plotted in Figure 9.8 (left panel). The experimental nitrogen K-edge shows a distinct triangular shape with three pronounced peaks B, C, and D and a less-pronounced pre-peak A (the size of which can vary). This nitrogen ELNES shape was found to be similar in other DND samples, even in samples with very high-nitrogen doping [30]. A striking similarity exists between the nitrogen and the carbon (diamond) K-edge fine structures. Peaks B, C, and D are all present in both ELNES spectra, and in the case of the carbon K-edge the pre-peak A at 285 eV is known to be related to sp- and sp²-hybridized carbon. The striking similarity between the N and C ELNES points to the fact that nitrogen is embedded into an environment that is highly similar to carbon embedded in diamond, namely a dominant sp³ symmetry.

**FIGURE 9.8**

Analysis of the nitrogen K-edge fine structure (ELNES) [14]. Left column—experimental data: (A) experimental N-K ELNES, (B) 1.5 eV smoothed N-K ELNES, and (C) experimental ND C-K ELNES. For nitrogen, peak B corresponds to 406 eV in absolute energy scale and for carbon, peak B corresponds to 292 eV. Right column—DFT-calculated data: (D) single substitutional nitrogen N_s , (E) A-center (2N), (F) NV^0 , and (G) NV.

In an attempt to provide more accurate information on type of nitrogen embedding, we performed detailed Density functional theory (DFT) calculations to calculate the nitrogen K-edge ELNES for four possible embedded states of nitrogen, namely:

- Single substitutional nitrogen, N_s or P1 center
- Two neighboring embedded nitrogen atoms, A-center
- The charge neutral nitrogen-vacancy (NV) center— NV^0
- The negatively charged NV center— NV^-

The DFT-calculated spectra, performed in the GGA approximation on $2 \times 2 \times 2$ supercells in the full core hole approximation using the code WIEN2k, are plotted in Figure 9.8 (right panel). At first glance, all four calculated N-K-edge spectra look similar, a result of the similarity of the nitrogen coordination in all four cases. However, small differences can be made out. The spectra for NV^- and NV^0 centers are near identical, and clearly differ from the experimental nitrogen K-edge. Although

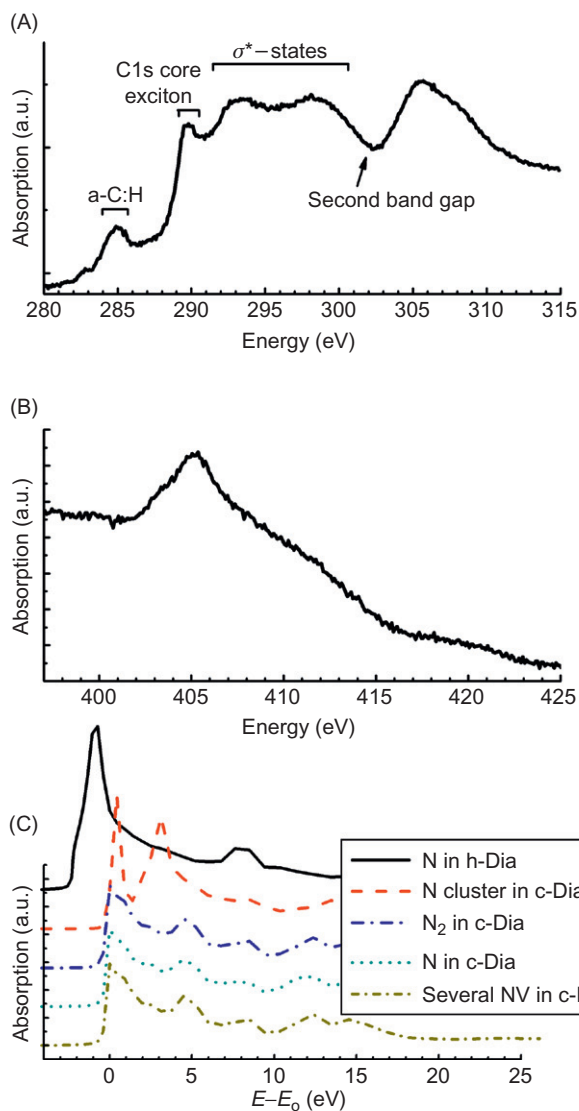
all calculated spectra have been broadened by 1 eV (to correspond to the experimental broadening), the spectra for NV^- and NV^0 are narrower and display fewer features than the experimental spectra. This appears to indicate that the nitrogen present in as-synthesized ND is not present in large amounts of NV^- or NV^0 centers, which is in good agreement with literature [34]. These optically active structures are only obtained in large amounts after vacancy creation and sintering treatments [36–38].

The triangular spectrum for single substitutional nitrogen N_s shows more similarities to the experimental nitrogen K-edge ELNES, reproducing features B, C, and D as well as a pre-peak to the main feature B. This so-called π^* contribution arises from bond length elongation of one of the CN bonds by $\sim 30\%$, a result of the energy relaxation step in the calculation, and which is in good agreement with the literature [39]. Due to this elongation, the nitrogen atom is present in a more planar coordination with respect to the other three bonding carbon atoms, giving rise to the π^* contribution. As was the case for the NV^- and NV^0 spectra, the spectrum is clearly less broadened than the experimental spectrum. The best correspondence is clearly given by the calculated spectrum for two neighboring, substitutional nitrogen atoms (the A-center model). All three peaks at B, C, and D are reproduced in this model, and the peak positions fit well with the experimental positions. The small pre-peak A that is present in the experimental ELNES is however not reproduced by the A-center model, even though it was reproduced in earlier ELNES simulations using multiple-scattering theory [40].

9.3 Near-edge X-ray absorption fine structure spectroscopy

Near-edge X-ray absorption fine structure (NEXAFS) is a type of absorption spectroscopy. The fundamental phenomenon underlying NEXAFS is the absorption of an X-ray photon by a core level of an atom in a solid and the consequent emission of a photoelectron. The resulting core hole is filled either via an Auger process or by capture of an electron from another shell followed by emission of a fluorescent photon. NEXAFS is very sensitive to the bonding environment of the absorbing atom. Often one can use a spectral “fingerprint” technique to identify the local bonding environment.

The nitrogen speciation in DND sample produced from TNT/RDX was assessed by imaging NEXAFS performed at WERA beamline at ANKA synchrotron source, Karlsruhe [41] according to approach described in [42]. Figure 9.9A shows the carbon edge for the DND. The spectra are typical for macro- [43] and ND [41,44,45]. They show the typical features of diamond: an absorption edge representing the conduction band edge, a C 1s core exciton, and a series of structures resulting from a band of σ^* states and the second absolute band gap. The relative intensities of the features around the absorption edge could be slightly different from an ideal diamond due to difficulties in subtraction of the background in this region. Note the presence of a small peak at 285 eV indicating a small amount of sp^2 carbon (graphitic), also typical for NDs.

**FIGURE 9.9**

NEXAFS spectra at carbon (A) and nitrogen (B) absorption K-edges of DND, and (C) NEXAFS spectra of various configurations of nitrogen in cubic (c-dia) and hexagonal (h-dia) diamond lattices calculated using FEFF 8.2. The curves are displaced vertically for clarity; the horizontal axis shows energy relative to the absorption edge. Marked differences between the shapes of the experimental and modeled absorption spectra are obvious.

The nitrogen absorption spectra (Figure 9.9B) are noisier; this clearly results from relatively low concentration of this element. The main absorption edge is observed at 405 eV. This position is indicative of N in sp^3 -bonding configurations (see below). It should be noted that the N NEXAFS spectra of ultrananocrystalline diamond (UNCD) [44] and EELS spectra (DNDs [30]) are similar to those observed by us.

Using the FEFF 8.2 code [46] we have performed theoretical modeling of N NEXAFS spectra in cubic and hexagonal diamond polytypes. Figure 9.9C shows modeled spectra for nitrogen configurations usually encountered in macrodiamonds (substitutional single and paired nitrogen atoms with several values of lattice relaxation), as well as for some other configurations of several N's and vacancies. They are obviously different from the experimental spectra. Spectra of nitrogen atoms surrounded by various arrangements of vacancies and carbons are characterized by fewer broad spectral features, making them qualitatively more similar to the observations. Results of our modeling are qualitatively similar to earlier calculations of EELS spectra of N in diamonds [40].

The XPS spectra for N in UNCD and DND suggest the presence of two or perhaps three types of N environment [47,48]. Unique interpretation of the N XPS and NEXAFS spectra in the C–N systems is not yet possible, but according to Ref. [48] the observed features originate from nitrogen occupying two- and three-coordinated structures with at least one of the nearest neighbors being also a two- or three-coordinated carbon. This assignment corresponds well to a suggestion that N in UNCD [49,44], in DND [34], and in NDs from meteorites [41] is largely confined to grain and intercrystallite boundaries and other extended defects. This might indicate that the local environment of nitrogen in NDs is closer to that in hexagonal polytypes. Following the XPS results [47,48,50], we suggest that N in NDs is most likely distributed among several main atomic configurations, thus blurring the absorption spectra. However, the set of these configurations is not completely random and/or sample dependent, which is indicated by the consistent shape of the absorption spectra. Anyway, the atomic-level N environment in ND is markedly different from the bulk diamond lattice and, therefore, its manifestations in infrared absorption and luminescence must be different.

Interestingly, controlled oxidation of DNDs and of NDs separated from meteorites shows that peak of nitrogen release coincides with the main peak of carbon, even when small temperature steps (30–50°C) are used. In the same time, during pyrolysis (heating in high vacuum without oxygen) nitrogen release is observed only at temperature of ~1100°C, corresponding to thermal-driven graphitization of diamond structure [51]. These facts indicate that nitrogen impurity is indeed chemically bound to the diamond lattice.

Most likely, the atomic environment of N in NDs can be understood using experimental NEXAFS data and theoretical modeling. However, this approach requires molecular dynamics or Monte Carlo simulation of several plausible configurations as a starting model.

9.4 XRD and small-angle X-ray scattering

XRD and scattering are widely used for investigation of structure of various materials. The most widely used methods are XRD and small-angle X-ray scattering (SAXS). In the last decade, with the advent of modern synchrotron sources with high intensity of hard (i.e. short wavelength) X-rays, high-energy XRD (HEXRD) is becoming an important additional approach to decipher fine details of the structure of nanoparticles and disordered materials.

Very often the X-ray methods are used to infer dimensions of nanoparticles. However, the sizes obtained by diffraction and scattering usually differ. The reason for these differences is due to various aspects of interaction of X-rays with matter revealed by XRD and by SAXS. The XRD pattern results from constructive interference of diffracted X-rays and physical broadening of the diffraction peaks provides information about sizes of so-called coherently scattering domains. In many fields these domains are called crystallites. The SAXS signal comes from heterogeneities of the electron density which, in the case of nanoparticles, usually corresponds to the overall dimensions of the particle. Therefore, in most cases the sizes extracted from the width of X-ray reflections is smaller than those from SAXS. The sizes obtained from electron microscopy are usually similar to the SAXS values. Notice that the sizes obtained from dynamic light scattering are often much larger since this method gives the so-called hydrodynamic radius, which reflects peculiarities of interaction of the particle with the solvent and, in the case of NDs, usually corresponds to aggregates of primary particles.

9.4.1 X-ray diffraction

Intense studies of NDs using X-ray methods give rather consistent results. Already the first diffraction studies of NDs lead to a conclusion that the size of the diamond core is 4–5 nm. Subsequent studies combining XRD, SAXS, and other techniques helped to develop a more elaborate model of a ND grain. The main feature of these models is the hypothesis that the grains are nonuniform and could be described by a core-shell model. The first such model was proposed in 1999 [52]; the subsequent advances aim to explain various fine details of diffraction patterns acquired in very wide angular ranges. One of the two advanced models suggests that the ND grain consists of three shells: a diamond core with a diameter of ~3 nm, surrounded by a sp²/sp³ layer of nongraphitic carbon (probably similar to diamond-like carbon), and 1–2 outermost layers that are onion-like [53]. Partial graphitization of the outermost layers on some faces of the nanograins was suggested in a HEXRD study [54]. Another approach suggests that the “perfect” diamond core is surrounded by a shell of strained diamond material with the lattice parameter different from that of the ideal diamond lattice [55,56]. An interesting observation made in several independent X-ray studies is the hkl-dependence of the physical broadening of diffraction peaks. Such broadening is logically explained by a slight distortion of the cubic diamond structure toward hexagonal. Several other models were suggested, and include,

for example, a model suggesting that the ND grains are hollow [57]. However, these models are not widely accepted.

The nitrogen concentration in NDs is usually below 2–3 at.% [58]. These values are very high in comparison with macroscopic diamonds. Such concentrations of impurities may influence the lattice strongly enough to be observed in diffraction. A good example is considerable increase of the lattice parameters by single substitutional nitrogen atoms in high-pressure high-temperature (HPHT) diamonds (e.g., Ref. [59]). Up to the present, all X-ray-based models of NDs consider only pure carbon grains; impurities such as nitrogen are not accounted for. The correct model of NDs should include impurities-related lattice distortions; this work is currently underway.

An important problem in interpretation of XRD from NDs lies in possible contribution of hexagonal diamond polytypes. The main difficulty results from heavy overlap of principal 111 peak of cubic diamond with the most prominent 002 peak of hexagonal and rhombohedral polytypes; this situation is common to many polytypic substances (e.g., SiC). Although formally the separation of the peaks is sufficient to be reliably measured by modern X-ray diffractometers, the size-strain-related peak broadening and shift makes the task demanding and ambiguous. Moreover, if graphitic carbon is also present in the sample, it will also contribute to the broadening of the main diamond peak.

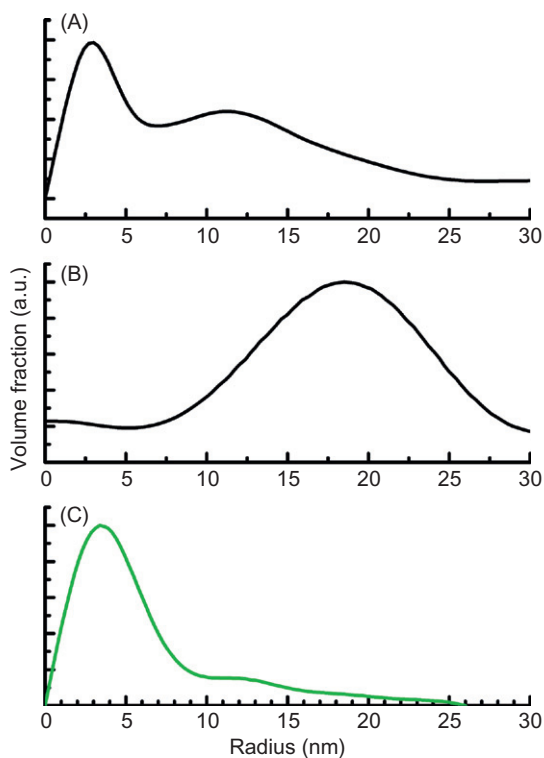
From a crystallography point of view, certain types of stacking faults in a cubic lattice can be considered as lamellae of a hexagonal polytype. Investigation of pure lonsdaleite would help to decipher the XRD patterns. However, this polytype is not available as a pure phase. Detailed studies of lonsdaleite-rich diamond samples show [60,61] that cubic and hexagonal polytypes are intermixed on nanometer scale. This structure is perfectly compatible with the stacking-fault concept described above.

Reliable observation of diamond polytypes in NDs using XRD requires data acquisition with very high statistics in a broad angular range in order to monitor presence of weak peaks. It would be beneficial to additionally use radiation with wavelengths longer than conventional copper. This would give larger separation of overlapping peaks.

9.4.2 SAXS

The first SAXS studies of NDs were performed a long time ago [62]. In general, results of the early studies are consistent with the more recent works. Interpretation of many SAXS studies of UDD is performed in the framework of the fractal model ([63]). However, physics of such approximation remains unclear and, in general, the application of the fractal concept to SAXS from carbons must be performed only after critical assessment of the correctness of background subtraction [64].

One of the most important parameters extracted from a SAXS curve is the size distribution of the scatterers. Mathematically, the extraction of the shape and size of the scatterers from the 1D SAXS curve is an ill-posed problem. Therefore, while working with a polydisperse system (i.e., the particles are not strictly identical) one needs certain assumptions about the shape of the scatterers. In the case of a

**FIGURE 9.10**

Size distribution of the scatterers obtained from the SAXS curves assuming a spherical shape. (A) Nanodiamond produced from graphite precursor; (B) ND from a graphite-hexogen mixture; and (C) conventional DND.

polydisperse system the scattering patterns of spheres and of other roughly isometric particles (e.g., cubes) are fairly close to each other. Therefore, unless reliable information from an independent technique is available, spherical shape of nanoparticles is assumed. This hypothesis also applies to disperse NDs.

A typical SAXS curve and size distribution of the scatterers for a conventional DND sample is shown in Figure 9.10C. A common feature of the size distribution for the absolute majority of UDD studied is the presence of the main peak around 4–5 nm, which is in good agreement with XRD data. However, one can clearly see a long “tail” toward large sizes. The origin of this tail is the subject of debates, since several explanations could be proposed. It can be due to presence of (a) large diamond particles [34,64], (b) nondiamond carbon envelope of the grains and other residues of the chemical purification and, finally, (c) the ND particles could be nonisometric and fairly close to a monodisperse system of nonisometric particles with elongation along some directions. The latest suggestion was explored by Ref. [65].

The size distribution curve for purified NDs with XRD peaks corresponding only to the diamond phase is rather narrow. Moreover, incorporation of the NDs into polymer matrix gave very similar results. Application of advanced algorithms for shape reconstruction of monodisperse nanoparticles (DAMMIN, [66]) led to the conclusion that the NDs are not strictly spherical, but rather have a V-like shape. SAXS provides information averaged over the whole sample and the V-like shape may indicate high concentration of twinned ND particles. Many TEM studies of UDD are known and twinned grains are not rare. However, the V-like twins apparently are not dominating. This issue clearly requires a more detailed consideration. Imposing symmetry one obtains a more isometric shape, for example, resembling interpenetrant cubes or octahedra, i.e., special types of twins [65]. Our own measurements and calculations gave similar results.

Mikhaylyuk [53] suggested that the SAXS curves of NDs should be treated in the framework of a spherical core with radii of $\sim 30\text{\AA}$ and covered by a graphitic sheath with gradually changing electron density. Although such a model seems reasonable from general point of view, its applicability to real ND powders is uncertain, since even a moderate degree of polydispersity of grain sizes may explain the observations. In general, when the system under investigation may be represented as a two-phase system with exponentially changing electron density, one should observe a linear Debye–Bueche plot $(I(s))^{-1/2}$ versus s^2 , where s is the scattering vector, determined as $s \equiv 4\pi \sin(\theta)/\lambda$, which is indeed the case for some carbons [67]. The linearity of this plot is indeed observed for UNCD films grown with high amounts of N_2 in the growth medium and is explained by contributions from ND rods encased into graphitic carbon sheath [68]. Therefore, the applicability of Mikhaylyuk's model to disperse NDs should be considered only after thorough investigation of the system.

9.4.3 Microstructure of NDs from X-ray data

The first systematical study of the phase composition and size distribution for the main representative classes of NDs using XRD and SAXS has been carried out by Shenderova et al. [32].

The XRD patterns are shown in Figure 9.11. For all samples the diamond phase dominates, which is evidenced by a strong peak at $2\Theta \sim 44^\circ$ (the 111 reflection), but minor amounts of graphitic carbon are also observed (002 peak at $2\Theta \sim 26.9^\circ$). The diamond 111 peak is nonsymmetric. The observed shoulder is due to an overlap of the diamond 111 and graphite 101 peaks. In addition, several diffraction peaks (100, 002) of hexagonal diamond (h-dia)—lonsdaleite—likely also contribute to the main peak. However, the lonsdaleite peak is clearly of minor importance.

The overlap of the peaks from diamond and graphite (hexagonal and rhombohedral) polytypes makes a reliable determination of the crystal size of the corresponding phases difficult. Panels A and B of Figure 9.11 show examples of decomposition of the main peak into several components (Pearson VII shape of the peaks is assumed). The dimensions of the diamond crystallites are estimated from the Debye–Scherrer formula and are $\sim 13.6\text{nm}$ for the 111 direction and 9.6nm for

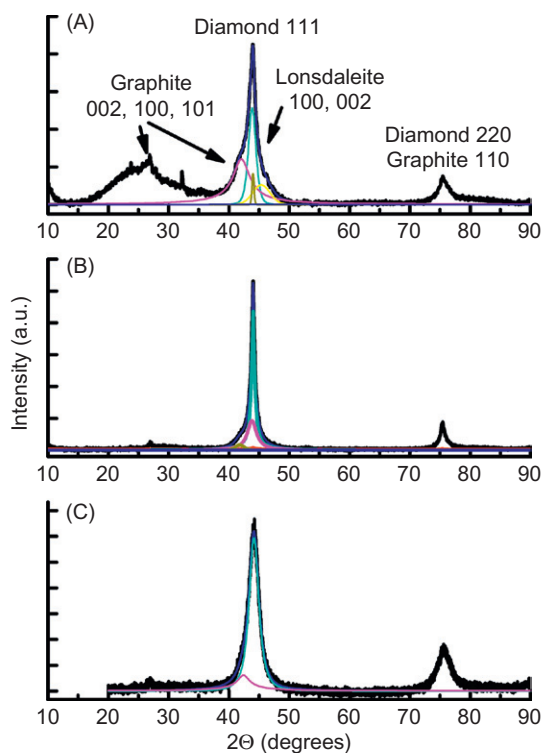


FIGURE 9.11

XRD patterns of the NDs. (A) NDs from graphite precursor; (B) from graphite-hexogen mixture; and (C) DND of wet synthesis. Decomposition of the main peak at $2\theta = 44^\circ$ is shown; Pearson VII shape is assumed for all components.

the 110 peak for the ND-G/RDX150 sample; 8 nm for the ND-G sample; and 4 nm for DNDs produced from explosives. A very rough estimation of the possible lonsdaleite grain size gives 2.4 nm for the ND-G sample. This value is similar to the one reported by Refs. [69] and [60] for h-dia produced by shock-conversion of graphite and is considerably smaller than the sizes of the cubic diamond crystallites.

In the sample made from graphite precursor a rather strong peak from graphite and of other similar phases is present. This is evidenced by a broad halo centered roughly at $2\theta \sim 26.9^\circ$, and a number of superimposed sharp peaks. Interestingly, the lonsdaleite peak is also weak, in contrast to some static experiments on HOPG at very high P–T conditions [70].

We have already discussed various approaches to describe the SAXS curves from NDs. In our work, we stick to the model describing the ND sample as a system of quasi-spherical grains and calculate their size distribution using the standard mathematical model for polydisperse spheres [71]. For all samples, the crystal size

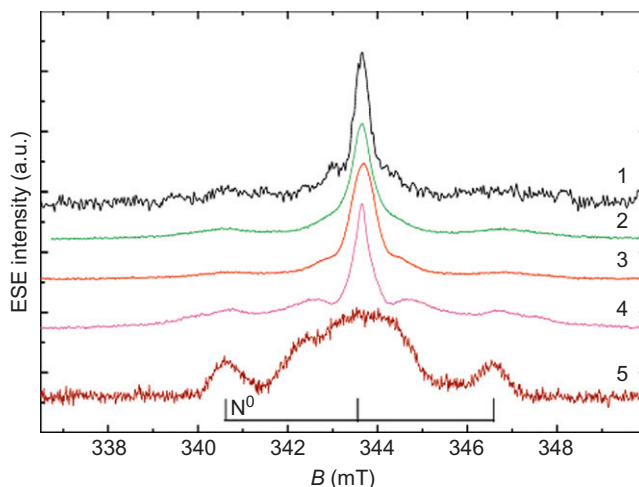
of the dominant fraction determined by SAXS is larger than the size determined from the broadening of the Bragg peaks. The discrepancy in the crystal size determined by both techniques reflects the fact that many ND particles consist of several crystallites within a single grain.

The SAXS data for the ND-G sample (Figure 9.10A) show a bimodal size distribution of the particles with peaks (diameters) at ~6 nm and at ~23 nm. Unfortunately, the SAXS curves do not allow one to unambiguously determine whether the “small” and “large” particles represent different phases or not. The size distribution of the NDs produced from explosives (Figure 9.10C) is typical for DNDs: the main peak shows diameters around 6 nm and a broad tail stretching out to larger sizes. It should be noted that the fraction of particle crystal sizes exceeding 6 nm is larger for ND of dry synthesis as compared to ND of wet synthesis (Figure 9.10C). The secondary peaks at larger sizes in DND of dry synthesis most probably belong to a graphite phase, since ND particles with grain sizes larger than 10 nm were not observed by HRTEM for this sample.

Finally, the size distribution for the ND-G/RDX sample (Figure 9.10B) differs considerably from the majority of the NDs studied within this work, since this sample possesses a relatively broad size distribution centered at ~34 nm. Moreover, this is the only ND sample for which linearity of the Debye–Bueche plot may be present. Notice that for this work polycrystalline, i.e., not deagglomerated, powder was used. The comparison of the SAXS and TEM data for this sample shows that the sample consists of particles with fairly broad size distribution and with various shapes (isometric and elongated). Therefore, it is uncertain whether the suspected plot linearity reflects the existence of the electron density fluctuations or results from polydispersity of the particles.

9.5 ESR spectroscopy

ESR spectroscopy is commonly used for a detection of nitrogen-related impurities in synthetic diamonds with a very low detection limit ($\sim 10^{12}$ spins). Nitrogen mostly incorporates in the synthetic diamonds in the form of single substitutional atoms that are paramagnetic. For a long time the ESR analysis in its traditional continuous-wave (CW) version was not informative in DND characterization. Strong background signal from presumably surface structure defects [72,73] of DND particles dominated the ESR spectra, preventing detection of paramagnetic nitrogen (P1 center) in a diamond core. An advanced pulse ESR approach, in particular the electron spin echo (ESE) technique, allows efficient time selection for spins having different relaxation times. Using the ESE at liquid helium temperatures, P1 centers were discerned for the first time from the strong background signal in DND produced from TNT/RDX mixture [74]. Later, Fionov et al. [75] estimated the concentration of paramagnetic nitrogen in DND to be 2 ± 1 ppm, by modeling and subtracting the broad background in CW ESR spectra. A strong increase of ESR signal from paramagnetic N has been

**FIGURE 9.12**

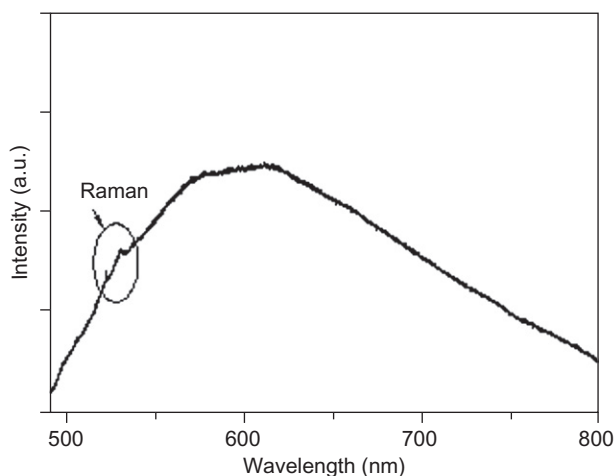
ESE spectra of the different ND samples: ND-TNT/HNSw (spectrum 1), ND-TNT/RDXw (spectrum 2), ND-TNT/RDXd (spectrum 3), ND-G/RDX150 (spectrum 4), and ND-G (spectrum 5). Measurements are carried out in X-band mode at room temperature.

observed using pulsed EPR in DND sintered under HPHT treatment (800°C and a pressure of 6 GPa) [38]. A new approach for efficient depletion of the strong background ESR signal in DNDs was suggested by Orlinskii et al. [76]. ND of dynamic synthesis with an average grain size of ~30 nm (based on SAXS measurements) was studied in that work. The ND was produced from a mixture of graphite and RDX. The ND powder was dispersed in ice and subsequently analyzed by the ESE technique. That allowed an essential decrease of the spin relaxation time of dominant nonnitrogen defects, while keeping the P1 spin relaxation time unchanged. Observed effect was able to assign the dominant signal in the ESR spectra of the NDs to surface defects.

The systematical pulse ESR study of the main representative classes of NDs produced by detonation shock-wave conversion of different carbon precursor materials, namely, graphite and a graphite/RDX mixture into ND, as well as ND produced from different combinations of explosives using different cooling methods (wet or dry cooling) has been carried out by Shenderova et al. [32]. ESE technique in the X-band of microwave frequencies has been used to detect single substitutional P1 centers and to estimate their concentration in the studied ND samples. The measured ESE spectra are shown in Figure 9.12. The ESR signal from substitutional N was easily separated from the background in the TNT/RDXw (spectrum 2) and graphite/RDX (spectrum 4) samples. The estimated concentrations of P1 centers in the samples are given in Table 9.1.

Table 9.1 Nitrogen Concentration Estimated by ESE Analysis for Different Classes of NDs

Sample	ND-G	ND-G/RDX	ND-TNT/RDXw	ND-TNT/HNSw	ND-TNT/RDXd
P1 (ppm)	–	0.6	0.02	<0.006	–

**FIGURE 9.13**

Typical RT PL spectrum of DND recorded at 488nm excitation. Two narrow lines in the range 520–530nm are characteristic of Raman scattering in the DND [79].

9.6 Photoluminescence spectroscopy

Photoluminescent (PL) spectroscopy is used to inspect structural perfection of a diamond lattice, revealing impurities and structural defects emitting in a wide range of diamond transparency under their photo-excitation. For the last decade, an interest in the PL characterization of ND has increased. This is explained by promising results on the use of luminescent NDs as a source of a single-photon emission for quantum information technologies [77] or, alternatively, as a bright light source applicable for biolabeling [78].

For a long time, PL characterization of DNDs was confined to broad-band PL registration in the range 400–700 nm. The typical PL spectrum recorded for DND at 488nm excitation is shown in Figure 9.13 [79].

As this broad PL starts to dominate with decreasing of ND grain sizes [80] when the fraction of surface carbon became essential (about 0.1 for 5 nm diamond grain), it makes sense to relate this PL band with surface defects enabling them to create continuously distributed energy states in the band gap of diamond [81]. One more piece of evidence in favor of PL band identification with surface defects is strong

variations of the PL intensity with ND surface functionalization [78,82–84]. The strong “surface” PL of DND powder interferes with detection of luminescent defects formed in an ND core. In the first place it concerns the detection of nitrogen-related centers as it was found that nitrogen impurities are present in a large amount in a DND core [79,85]. NV centers are one of the structural forms of optically active N-related defects, formation and control of which in the ND is one of the most actual task for modern nanotechnologies. It was demonstrated that NDs containing NV centers represent an advanced material platform for production of quantum information bits and/or fluorescent biolabels [77,78]. Two types of luminescent NV centers are distinguished: the negatively charged (NV^-) and the neutral (NV^0) ones, characterized by zero-phonon lines (ZPLs) at 638 and 575 nm, respectively.

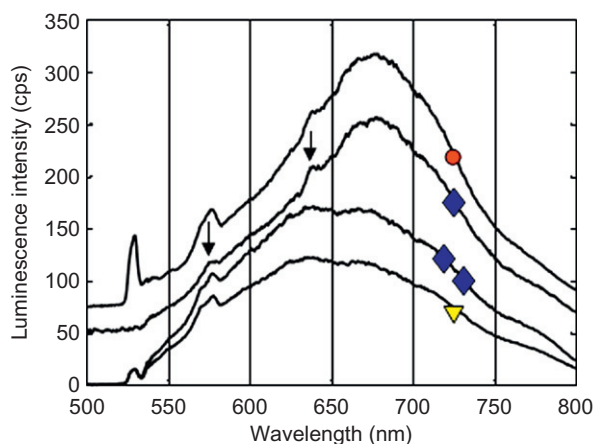
Recently, two main approaches were applied to detect the NV PL in DND with high sensitivity efficiently depleting the “surface” PL. In the first approach, a time-resolved PL spectroscopy was used [86]. The approach is based on the fact that radiative relaxation times from excited electronic states are much shorter for the surface defects (<0.5 ns) [86,87] than for the NV centers (~ 10 ns) in NDs. In the second approach, a confocal PL spectroscopy of a single nanoparticle was used [32,88]. Much higher quantum yield of NV PL as compared to that of “surface” PL allows the detection of even single NV centers in individual 5–10 nm diamond particles [89,90]. Recently, an innovative approach for strong enhancement of NV PL in DND using sintering treatment was suggested in Ref. [38].

9.6.1 Time-resolved PL of DND

PL from NV centers was found in DND for the first time under use of time-resolved PL spectroscopy [86]. Experiments on time-resolved PL detection were held for typical DND produced from a mixture of TNT and RDX explosives. A pulsed excitation was realized by laser with 531 nm light emission and a pulse width of 0.6 ns. A standard technique on increasing the NV concentration in the diamond doped with nitrogen was applied: the DND powder was irradiated with high-energy particles (protons) followed by sample annealing. Featureless “surface” PL was observed for the DND sample before and after the sample treatment (Figure 9.14, two bottom lines marked with triangle and two diamonds) when no time delay was applied under PL registration. When the proton-irradiated sample was measured using time-gating with a delay time of 3.5 ns after the excitation pulse (third line, single diamond) ZPLs of NV^- and NV^0 color centers become visible at 637 and 575 nm, respectively (marked with arrows).

9.6.2 Confocal PL spectroscopy of single DND particles

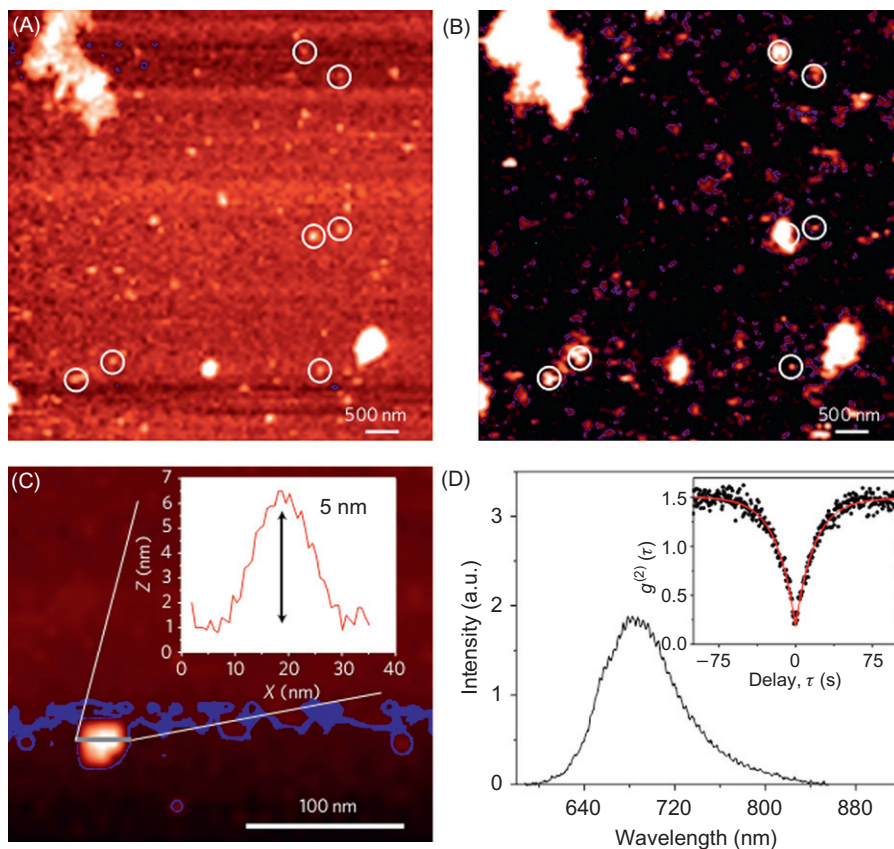
Contrary to time-resolved PL experiments that do not require a special preparation of the DND powder for testing, a thorough dispersion of the aggregated DND particles in a solution is required at sample preparation for the confocal PL analysis of single DND particles. Well-dispersed low-concentrated DND solution then is either dropped or spin-coated onto a glass coverslip (or other convenient substrate).

**FIGURE 9.14**

Time-resolved PL of NDs under 531 nm excitation. PL spectra of 5 nm diamond before (bottom line, triangle) and after (second bottom, two diamonds) proton-irradiation and annealing. The two spectra are featureless aside from the diamond (1330 cm^{-1}) and graphite (1600 cm^{-1}); Raman lines visible at 572–578 nm. When the proton-irradiated sample is measured using time-gating with a delay time of 3.5 ns after the excitation pulse, (third line, single diamond) ZPLs of NV^- and NV^0 color centers become visible at 637 and 575 nm, respectively (marked with arrows). NV luminescence of 55 nm HPHT diamond proton-irradiated and annealed, measured without time-gating is shown for comparison (the top line, circle). Stray light from the excitation pulse is responsible for the feature at 531 nm in all spectra except the time-delayed one [86].

To distinguish between neighbor ND particles during laser beam scanning of glass substrate, the density of the ND particles should be less than $5\text{ }\mu\text{m}^2$. As long as all analyzed ND particles can be placed in a focal plane of an objective used for laser beam focusing, then a collection of the PL from only a thin volume layer adjacent to the focal plane (a confocal collection) supplies the highest signal/noise ratio for single ND PL detection.

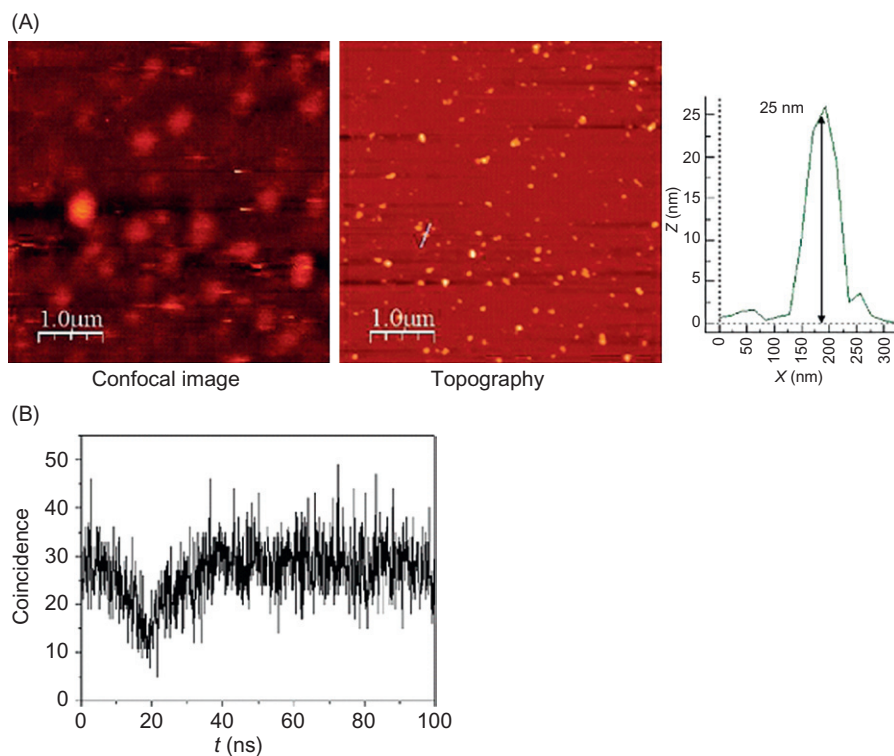
The first direct observation of NV centers in discrete 5 nm NDs at room temperature using confocal PL spectroscopy was reported in Ref. [88]. The NDs were produced from TNT/RDX mixture. Figure 9.15 presents data from the analyzed sample, collected with the combined confocal scanning luminescence and atomic force microscope (AFM). The AFM-based measurements clearly show areas of the sample with a sparse spatial distribution of nanoparticle (Figure 9.15A) with a typical size in the 5 nm range (Figure 9.15C). As shown, some isolated nanoparticles (1%) were luminescent (Figure 9.15B), and their spectra (Figure 9.15D) were consistent with those reported for NVs in ND [89,90]. Furthermore, the second-order correlation function $g^{(2)}(t)$ confirmed that the emission originated from a single center (Figure 9.15D, inset).

**FIGURE 9.15**

Characterization of discrete 5 nm diamonds on a glass coverslip. (A) AFM image of NDs. The brightness of the spots is proportional to the height of the crystals (circles highlight the correspondence between the AFM image and the confocal image of (B)). (B) Corresponding confocal scanning fluorescence microscopy image. Bright spots indicate NV emitters. (C) Magnified AFM image and corresponding surface profile (inset) of a representative nanocrystal 5 nm in height. (D) Emission spectrum of an NV center in a 5 nm crystal host and corresponding second-order correlation function $g^{(2)}$ (inset) [88].

During confocal PL study of the isolated DND [88], a new property of NV centers, luminescence intermittency or “blinking,” was found for some luminescent ND particles (for about 25%). Possible reasons for the appearance of this property are discussed in detail in Chapter 10 of this book.

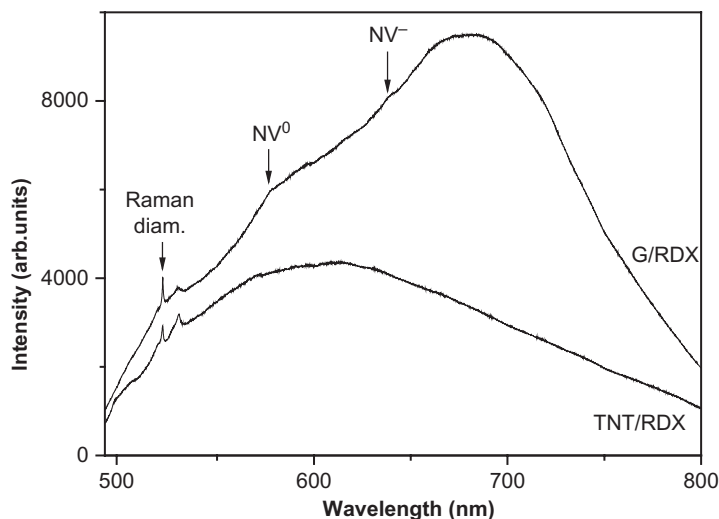
To this date, most PL research of DND material has been limited to a study of NDs produced from TNT/RDX detonation mixture. The first and still only systematic PL study of the main representative classes of NDs produced by detonation

**FIGURE 9.16**

(A) Confocal fluorescent and topographical images of sample G/RDX. (B) Photon antibunching curve, measured for the emitting point marked with white line on the topographical image [32].

shock-wave conversion of different carbon precursor materials, namely, graphite and a graphite/RDX mixture into ND, as well as ND produced from different combinations of explosives using different cooling methods (wet or dry cooling) has been carried out by Shenderova et al. [32]. It was demonstrated that (i) ND particles larger than ~20 nm may contain *in situ* produced optically active NV centers, (ii) in ND produced from explosives, NV centers are detected only in ND produced by wet synthesis, and (iii) ND synthesized from a mixture of graphite/RDX (G/RDX) contains the largest amount of NV centers formed during synthesis among all studied NDs. Confocal luminescent and topographical images of the G/RDX sample are shown in Figure 9.16A. From the measurements of photon statistics (second-order intensity correlation function), the maximum concentration of ~3 NV centers per particle (Figure 9.16B) was estimated. NV PL was observed in more than 20% ND particles.

The concentration of the NV centers in G/RDX ND is so high that it is detected even by conventional PL spectroscopy used for the ND powder, as shown in

**FIGURE 9.17**

PL spectra of G/RDX ND and TNT/RDX ND recorded at 488nm excitation under RT. The Raman diamond line and, ZPLs of NV^0 and NV^- are indicated by arrows at 522, 576, and 639nm, respectively.

Figure 9.17. ZPLs of NV^0 and NV^- centers are resolvable at, respectively, 576 and 639nm. NV PL is so strong for the G/RDX ND that no “surface” PL is enough to overshadow it, contrary to the typical DND produced from TNT/RDX mixture for which the “surface” PL dominates the spectrum (**Figure 9.17**).

G/RDX ND has larger typical primary grains (34nm) and lower N concentration (<0.5%) as compared to TNT/RDX ND (grain size is 6 nm, N concentration is 2–3%). Still it is not clear which of these two characteristics play a crucial role in the increased NV concentration for G/RDX ND as compared to that for TNT/RDX ND. The N atoms at high concentrations are possibly prone to the formation of complexes that are not optically active. In addition, at high concentrations, N atoms can suppress an optical activity of neighboring NV defects. Alternatively, a decrease of ND particle size results in an efficient interaction of the NV centers with surface defects including a charge interaction between them. As a result, the NV^0 and NV^- could be transferred into optically inactive NV^+ centers in small NDs. The NV interaction with ND surface defects will be discussed in more detail in Chapter 10.

9.6.3 PL spectroscopy of HPHT-sintered DND

Baranov et al. [38] have presented the first results on an observation of a strong increase of NV PL by an HPHT sintering (800°C and 6 GPa for 11 s) of DND particles, which were produced from TNT/RDX mixture. **Figure 9.18A** shows the

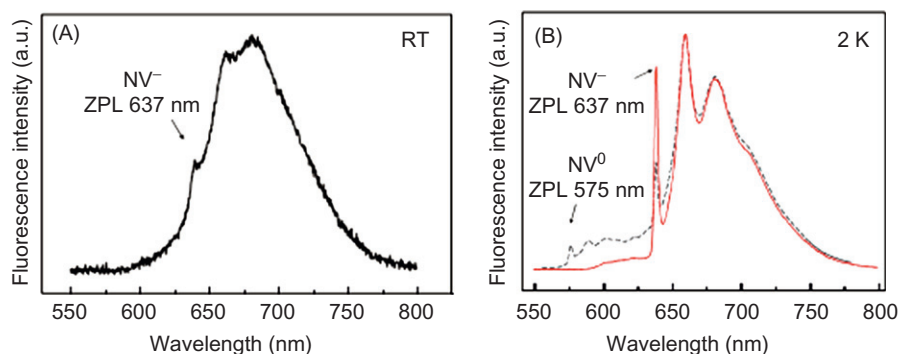


FIGURE 9.18

(A) RT PL spectrum of a single NV-containing cluster. (B) Low-temperature PL spectra of a single NV-containing sintered DND cluster (solid line) and commercial electron-irradiated HPHT diamond containing 10 ppm NV centers (dashed line).

room temperature 532 nm laser-induced luminescence spectrum measured on a single 12 μm ND cluster. A quite well-distinguished NV^- ZPL at 637 nm followed by prominent vibronic sidebands is observed in the spectrum. The low-temperature PL spectrum (Figure 9.18B, solid line) demonstrates narrowing of 637 nm ZPL as well as reveals the presence of neutral NV (ZPL at 575 nm) inside the sintered DND cluster. For comparison the low-temperature PL spectrum of irradiated and annealed 50 μm HPHT diamond crystal with estimated concentration of NV^- centers of order of 10 ppm is shown in Figure 9.18B (dashed line). No reasonable explanation of the strong increase of NV PL in sintered DND was suggested. In our opinion, removing of NV centers–ND surface interaction accompanied by recovering of NV^- from NV^+ could be one of the possible explanations of the observed phenomenon.

9.7 Conclusion

Essential progress in the characterization of DND has been made over the past few years. The main achievements are related to the study of nitrogen impurities in DND. The presence of nitrogen within the “core” of DND grains has been unambiguously proven. Two configurations of nitrogen defects have been detected in the DND particles: single paramagnetic nitrogen centers and NV complexes. Difficulties in the study of the nitrogen in DND arise from the small sizes of the diamond crystallites and from the presence of a non-negligible fraction of surface atoms. Progress in spatial resolution of nanoscale analysis techniques and the development of new methodologies is helping investigators to gain a step-by-step understanding of the peculiarities of nitrogen incorporation in NDs.

References

- [1] R.F. Egerton, *Electron Energy-Loss Spectroscopy in the Electron Microscope*, Springer, (2011).
- [2] D.B. Williams, C.B. Carter, *Transmission Electron Microscopy: A Textbook for Materials Science*, Springer, (2009).
- [3] R. Erni, *Aberration-Corrected Imaging in Transmission Electron Microscopy*, Imperial College Press, 2010.
- [4] A.I. Kirkland, J.L. Hutchison, (Eds.), *Nanocharacterisation*, RSC Publishing, Cambridge, (2007).
- [5] O. Scherzer, Über einige Fehler von Elektronenlinsen, *Z. Phys. A Hadrons Nucl.* 101 (1936) 593–603.
- [6] M. Haider, A spherical-aberration-corrected 200 kV transmission electron microscope, *Ultramicroscopy* 75 (1998) 53–60.
- [7] O.L. Krivanek, N. Dellby, A.R. Lupini, Towards sub-angstrom electron beams, *Ultramicroscopy* 78 (1999) 1–11.
- [8] R. Erni, M.D. Rossell, C. Kisielowski, U. Dahmen, Atomic-resolution imaging with a sub-50-pm electron probe, *Phys. Rev. Lett.* (2009) 102, 096101.
- [9] C. Kisielowski, R. Erni, B. Freitag, Object-defined resolution below 0.5 Å in transmission electron microscopy—recent advances on the TEAM 0.5 instrument, *Microsc. Microanal.* 14 (Suppl. 2) (2008).
- [10] D.C. Bell, C.J. Russo, D.V. Kolmykov, 40 keV atomic resolution TEM, *Ultramicroscopy* 114 (2012) 38–45.
- [11] N. Alem, Atomically thin hexagonal boron nitride probed by ultrahigh-resolution transmission electron microscopy, *Phys. Rev. B* (2009) 80, 155425.
- [12] C.O. Girit, Graphene at the edge: stability and dynamics, *Science* 323 (2009) 1705–1708.
- [13] A.V. Krashennnikov, K. Nordlund, Ion and electron irradiation-induced effects in nanostructured materials, *J. Appl. Phys.* (2010) 107, 071301.
- [14] S. Turner et al., Aberration-corrected microscopy and spectroscopy analysis of pristine, nitrogen containing detonation nanodiamond, submitted for publication, 2012.
- [15] O. Shenderova, Surface chemistry and properties of ozone-purified detonation nanodiamonds, *J. Phys. Chem. C* 115 (2011) 9827–9837.
- [16] K. Iakoubovskii, K. Mitsuishi, K. Furuya, High-resolution electron microscopy of detonation nanodiamond, *Nanotechnology* (2008) 19, 155705.
- [17] Y.J. Min, M. Akbulut, K. Kristiansen, Y. Golan, J. Israelachvili, The role of interparticle and external forces in nanoparticle assembly, *Nature Mater.* 7 (2008) 527–538.
- [18] O. Shenderova, D.M. Gruen, (Eds.), *Ultrananocrystalline Diamond: Synthesis, Properties and Applications*, William Andrew, New York, NY, 2006.
- [19] Z.-L. Wang (Ed.), *Characterization of Nanophase Materials*, Wiley-VCH, Weinheim, 2000.
- [20] B. Wen, J. Zhao, T. Li, Synthesis and crystal structure of n-diamond, *Int. Mater. Rev.* 52 (2007) 131–151.
- [21] R.F. Egerton, *Electron Energy-Loss Spectroscopy in the TEM*, Plenum Press, New York, NY, 1996.
- [22] T.L. Daulton, D.D. Eisenhour, T.J. Bernatowicz, R.S. Lewis, P.R. Buseck, Genesis of presolar diamonds: comparative high-resolution transmission electron microscopy study of meteoritic and terrestrial nano-diamonds, *Geochim. Cosmochim. Acta* 60 (1996) 4853–4872.

- [23] S. Turner, Determination of size, morphology, and nitrogen impurity location in treated detonation nanodiamond by transmission electron microscopy, *Adv. Funct. Mater.* 19 (2009) 2116–2124.
- [24] L. Zhang, S. Turner, F. Brosens, J. Verbeeck, Model-based determination of dielectric function by STEM low-loss EELS, *Phys. Rev. B* (2010) 81, 035102.
- [25] S. Turner, Transmission Electron Microscopy Characterisation of 0-D Nanomaterials, Thesis, University of Antwerp, Antwerp, 2010.
- [26] J.L. Peng, S. Bulcock, P.I. Belobrov, L.A. Bursill, Surface bonding states of nano-crystalline diamond balls, *Int. J. Mod. Phys. B* 15 (2001) 4071–4085.
- [27] P.I. Belobrov, L.A. Bursill, K.I. Maslakov, A.P. Dementjev, Electron spectroscopy of nanodiamond surface states, *Appl. Surf. Sci.* 215 (2003) 169–177.
- [28] R.F. Egerton, Electron energy-loss spectroscopy in the TEM, *Rep. Prog. Phys.* (2009) 016502.
- [29] J. Verbeeck, S. Van Aert, Model based quantification of EELS spectra, *Ultramicroscopy* 101 (2004) 207–224.
- [30] V. Pichot, High nitrogen doping of detonation nanodiamonds, *J. Phys. Chem. C* (2010) 114.
- [31] A.V. Kvit, V.V. Zhirnov, T. Tyler, J.J. Hren, Aging effect and nitrogen distribution in diamond nanoparticles, *Comp. Part B Eng.* 35 (2004) 163–166.
- [32] O.A. Shenderova, Nitrogen control in nanodiamond produced by detonation shock-wave-assisted synthesis, *J. Phys. Chem. C* 115 (2011) 14014–14024.
- [33] I.I. Vlasov, Hybrid diamond-graphite nanowires produced by microwave plasma chemical vapor deposition, *Adv. Mater.* 19 (2007) 4058–4062.
- [34] I.I. Vlasov, Nitrogen and luminescent nitrogen-vacancy defects in detonation nanodiamond, *Small* 6 (5) (2009) 687–694.
- [35] R. Brydson, in: A.I. Kirkland, J.L. Hutchison, (Eds.), *Nanocharacterisation*, RSC Publishing, Cambridge, 2007.
- [36] M. Baidakova, A. Vul', New prospects and frontiers of nanodiamond clusters, *J. Phys. D Appl. Phys.* 40 (2007) 6300–6311.
- [37] A. Soltamova, Electron paramagnetic resonance detection of the giant concentration of nitrogen vacancy defects in sintered detonation nanodiamonds, *JETP Lett.* 92 (2010) 102–106.
- [38] P.G. Baranov, Enormously high concentrations of fluorescent nitrogen-vacancy centers fabricated by sintering of detonation nanodiamonds, *Small* 7 (2011) 1533–1537.
- [39] S.A. Kajihara, A. Antonelli, J. Bernholc, R. Car, Nitrogen and potential n-type dopants in diamond, *Phys. Rev. Lett.* 66 (1991) 2010–2013.
- [40] R. Brydson, L.M. Brown, J. Bruley, Characterizing the local nitrogen environment at platelets in type Ia A/B diamond, *J. Microsc.* 189 (1998) 137–144.
- [41] A.A. Shiryaev, A.V. Fisenko, I.I. Vlasov, L.F. Semjonova, P. Nagel, S. Schuppler, Spectroscopic study of impurities and associated defects in nanodiamonds from Efremovka (CV3) and Orgueil (CI) meteorites, *Geochim. Cosmochim. Acta* 75 (2011) 3155–3166.
- [42] T. Berg, J. Maul, N. Erdmann, P. Bernhard, S. Schuppler, P. Nagel, et al., Coupling of imaging NEXAFS with secondary ion mass spectrometry for the chemical and isotopic analysis of presolar cosmic grains, *Anal. Bioanal. Chem.* 386 (2006) 119–124.
- [43] J.F. Morar, F.J. Himpsel, G. Hollinger, G. Hughes, J.L. Jordan, Observation of C 1s core exciton in diamond, *Phys. Rev. Lett.* 54 (1985) 1960–1963.
- [44] J. Birrell, J.E. Gerbi, O. Auciello, J.M. Gibson, D.M. Gruen, J.A. Carlisle, Bonding structure in nitrogen doped ultrananocrystalline diamond, *J. Appl. Phys.* 93 (2003) 5606–5612.

- [45] T. Berg, E. Marosits, J. Maul, P. Nagel, U. Ott, F. Schertz, et al., Quantum confinement observed in the X-ray absorption spectrum of size distributed meteoritic nanodiamonds, *J. Appl. Phys.* 104 (2008) 064303.
- [46] A.L. Ankudinov, B. Ravel, J.J. Rehr, S.D. Conradson, Real space multiple scattering calculation of XANES, *Phys. Rev. B* 58 (1998) 7565.
- [47] G.F. Zhang, D.S. Geng, Z.J. Yang, High nitrogen amounts incorporated diamond films deposited by the addition of nitrogen in a hot-filament CVD system, *Surf. Coat. Technol.* 122 (1999) 268–272.
- [48] J.T. Titantah, D. Lamoén, Carbon and nitrogen 1s energy levels in amorphous carbon nitride systems: XPS interpretation using first-principles, *Diam. Relat. Mater.* 16 (2007) 581–588.
- [49] P. Zapol, M. Sternberg, L.A. Curtiss, T. Frauenheim, D.M. Gruen, Tight-binding molecular-dynamics simulation of impurities in ultrananocrystalline diamond grain boundaries, *Phys. Rev. B* 65 (2001) 045403.
- [50] A. Dementjev, K. Maslakov, I. Kulakova, V. Korolkov, V. Dolmatov, State of C-atoms on the modified nanodiamond surface, *Diam. Relat. Mater.* 16 (2007) 2083–2086.
- [51] A.B. Verchovsky, A.V. Fisenko, L.F. Semjonova, I.P. Wright, M.R. Lee, C.T. Pillinger, Noble gas isotopes in grain size separates of presolar diamonds from Efremovka, *Science* 281 (1998) 1165–1168.
- [52] A.E. Aleksenskii, M.V. Baidakova, A.Y. Vul', V.I. Siklitskii, The structure of diamond nanoclusters, *Phys. Solid State* 41 (1999) 668–671.
- [53] O.O. Mykhaylyk, Y.M. Solonin, D.N. Batchelder, R. Brydson, Transformation of nanodiamond into carbon onions: a comparative study by high-resolution transmission electron microscopy, electron energy-loss spectroscopy, x-ray diffraction, small-angle x-ray scattering, and ultraviolet Raman spectroscopy, *J. Appl. Phys.* 97 (2005) 074302.
- [54] L. Hawelek, A. Brodka, J.C. Dore, V. Honkimaki, S. Tomita, A. Burian, Structural studies of nanodiamond by high-energy X-ray diffraction, *Diamond Relat. Mater.* 17 (2008) 1186–1193.
- [55] B. Palosz, C. Pantea, E. Grzanka, S. Stelmakh, Th. Proffen, T.W. Zerda, et al., Investigation of relaxation of nanodiamond surface in real and reciprocal spaces, *Diamond Relat. Mater.* 15 (2006) 1813–1817.
- [56] B. Palosz, S. Stelmakh, E. Grzanka, S. Gierlotka, W. Palosz, Application of apparent lattice parameter to determination of core-shell structure of nanocrystals, *Z. Kristallogr.* 222 (2007) 580–594.
- [57] A.L. Vereschagin, G.V. Sakovich, Structure of detonation nanodiamonds, *Mendelev Commun.* 1 (2001) 39–41.
- [58] V.Y. Dolmatov, Detonation-synthesis nanodiamonds: synthesis, structure, properties and applications, *Russ. Chem. Rev.* 76 (2007) 339–360.
- [59] A.R. Lang, M. Moore, A.P.W. Makepeace, W. Wierzchowski, C.M. Welbourn, On the dilatation of synthetic type Ib diamond by substitutional nitrogen impurity, *Phil. Trans. R. Soc. Lond. A337* (1991) 497–520.
- [60] A.V. Kurdyumov, N.F. Ostrovskaya, A.N. Pilyankevich, Real structure of dynamic synthesis diamonds, *Sov. Powder Metall. Met. Ceram.* 27 (1988) 32–37.
- [61] A. Yoshiasa, Yu. Murai, O. Ohtaka, T. Katsura, Detailed structures of hexagonal diamond (lonsdaleite) and wurtzite-type BN, *J. Appl. Phys.* 42 (2003) 1694–1704.
- [62] V.L. Kuznetsov, M.N. Aleksandrov, I.V. Zagoruiko, A.L. Chuvilin, E.M. Moroz, V.N. Kolomiichuk, et al., Study of ultradispersed diamond powders obtained using explosion energy, *Carbon* 29 (1991) 665–668.

- [63] M.V. Baidakova, A.Y. Vul', V.I. Siklitski, N.N. Faleev, Fractal structure of ultradisperse-diamond clusters, *Phys. Solid State* 40 (1998) 715–718.
- [64] W. Ruland, Apparent fractal dimensions obtained from small-angle scattering of carbon materials, *Carbon* 39 (2001) 287–324.
- [65] A.N. Ozerin, T.S. Kurkin, L.A. Ozerina, V.Y. Dolmatov, X-ray diffraction study of the structure of detonation nanodiamonds, *Crystallogr. Rep.* 53 (1) (2008) 60–67.
- [66] D.I. Svergun, Restoring low resolution structure of biological macromolecules from solution scattering using simulated annealing, *Biophys. J.* 76 (6) (1999) 2879–2886.
- [67] E. Hoinkis, Small angle scattering of neutrons and x-rays from carbons and graphites, in: P.A. Thrower (Ed.), *Chemistry and Physics of Carbon*, vol. 25, Dekker, New York, NY, 1997, pp. 71–241.
- [68] I.I. Vlasov, M.V. Kanzyuba, A.A. Shiryayev, V.V. Volkov, V.G. Ralchenko, V.I. Konov, Percolation model of dielectric-conductor transition in ultrananocrystalline diamond films, *JETP Lett.* (2012).
- [69] L.F. Trueb, An electron microscopy study of shock-synthesised diamond, *Appl. Phys.* 39 (1968) 4707–4716.
- [70] C. Le Guillou, F. Brunet, T. Irifune, H. Ohfuji, J.-N. Rouzaud, Nanodiamond nucleation below 2273 K at 15 GPa from carbons with different structural organizations, *Carbon* 45 (2007) 636–648.
- [71] D.I. Svergun, Determination of the regularization parameter in indirect-transform methods using perceptual criteria, *J. Appl. Cryst.* 25 (1992) 495–503.
- [72] N.D. Samsonenko, E.V. Sobolev, *JETP Lett.* 5 (1967) 250.
- [73] A.I. Shames, A.M. Panich, W. Kempinski, et al., Defects and impurities in nanodiamonds: EPR, NMR and TEM study, *J. Phys. Chem. Solids* 63 (2002) 1993–2001.
- [74] B.R. Smith, D. Inglis, B. Sandnes, J. Rabeau, A.V. Zvyagin, D. Gruber, et al., Lighting up 5-nm monocrystalline nanodiamond with luminescent nitrogen-vacancy defect centers, *Small* 5 (2009) 1649–1653.
- [75] A.V. Fionov, A. Lund, W.M. Chen, et al., Paramagnetic centers in detonation nanodiamonds studied by CW and pulse EPR, *Chem. Phys. Lett.* 493 (2010) 319–322.
- [76] S.B. Orlinskii, R.S. Bogomolov, A.M. Kiyamova, et al., Identification of Substitutional Nitrogen and Surface Paramagnetic Centers in Nanodiamond of Dynamic Synthesis by Electron Paramagnetic Resonance, *Nanosci. Nanotechnol. Lett.* 3 (2011) 63–67.
- [77] P. Neumann, N. Mizuochi, F. Rempp, P. Hemmer, H. Watanabe, S. Yamasaki, et al., Multipartite entanglement among single spins in diamond, *Science* 320 (2008) 1326–1329.
- [78] A.M. Schrand, S.C. Hens, O.A. Shenderova, Nanodiamond Particles: Properties and Perspectives for Bioapplications, *Crit. Rev. Solid State Mater. Sci.* 34 (2009) 18–74.
- [79] I.I. Vlasov, O. Shenderova, S. Turner, O.I. Lebedev, A.A. Basov, I. Sildos, et al., Nitrogen and Luminescent Nitrogen-Vacancy Defects in Detonation Nanodiamond, *Small* 6 (2010) 687–694.
- [80] P.H. Chung, E. Perevedentseva, C.L. Cheng, The particle size dependent photoluminescence of nanodiamonds, *Surface Sci.* 601 (2007) 3866–3870.
- [81] F. Cleri, P. Keblinski, L. Colombo, D. Wolf, S.R. Phillpot, On the electrical activity of sp²-bonded grain boundaries in nanocrystalline diamond, *Europhys. Lett.* 46 (1999) 671.
- [82] V. Mochalin, Y. Gogotsi, Wet chemistry route to hydrophobic blue fluorescent nanodiamond, *J. Am. Chem. Soc.* 131 (13) (2009) 4594–4595.
- [83] S. Hu, F. Tian, P. Bai, S. Cao, J. Sun, J. Yang, Synthesis and luminescence of nanodiamonds from carbon black, *Mater. Sci. Eng. B* 157 (2009) 11–14.

- [84] O. Shenderova, S.C. Hens, I. Vlasov, V. Borjanovic, G. McGuire, Nanodiamond particles in electronic and optical applications, *Mater. Res. Soc. Symp. Proc.* 1203 (2010) 69–81.
- [85] S. Turner, O.I. Lebedev, O. Shenderova, I.I. Vlasov, J. Verbeeck, G. VanTendeloo, Determination of size, morphology, and nitrogen impurity location in treated detonation nanodiamond by transmission electron microscopy, *Adv. Funct. Mater.* 19 (2009) 2116.
- [86] B.R. Smith, D.W. Inglis, B. Sandnes, J.R. Rabeau, A.V. Zvyagin, D. Gruber, et al., Five-nanometer diamond with luminescent nitrogen-vacancy defect centers, *Small* 5 (2008) 1649.
- [87] F.L. Zhao, Z. Gong, S.D. Liang, N.S. Xu, S.Z. Deng, J. Chen, et al., Ultrafast optical emission of nanodiamond induced by laser excitation, *Appl. Phys. Lett.* 85 (2004) 914–916.
- [88] C. Bradac, T. Gaebel, N. Naidoo, M.J. Sellars, J. Twamley, L.J. Brown, et al., Observation and control of blinking nitrogen-vacancy centres in discrete nanodiamonds, *Nat. Nanotech.* 5 (2010) 345–349.
- [89] J. Tisler, G. Balasubramanian, B. Naydenov, R. Kolesov, B. Grotz, R. Reuter, et al., Fluorescence and spin properties of defects in single digit nanodiamonds, *ACS Nano* 3 (2009) 1959–1965.
- [90] J.-P. Boudou, P.A. Curmi, F. Jelezko, J. Wrachtrup, P. Auber, M. Sennour, et al., High yield fabrication of fluorescent nanodiamonds, *Nanotechnology* 20 (2009) 235602.

Optical and Spin Properties of Nitrogen-Vacancy Color Centers in Diamond Crystals, Nanodiamonds, and Proximity to Surfaces

10

Andrei V. Zvyagin^a and Neil B. Manson^b

^a*MQ Photonics Research Centre, Macquarie University, Sydney, NSW, Australia,*

^b*Laser Physics Centre, RSPE, Australian National University, Canberra, ACT, Australia*

CHAPTER OUTLINE

10.1 Introduction	327
10.2 Electronic structure and emission properties of the NV center	330
10.2.1 Introduction	330
10.2.2 Electronic model.....	334
10.2.3 Parameter justification	335
10.3 NV center interconversion	336
10.4 Recent progress toward production and understanding of ultra-small NV-NDs	341
10.4.1 Theoretical modeling.....	342
10.5 Diamond matrix size and surface effects on NV color center emission properties	344
10.5.1 NV emission quenching by the lax graphite sp^2 layer	344
10.5.2 Surface functional groups affect the emission.....	345
10.5.3 NV center blinking	346
10.6 Conclusion.....	349
References	350

10.1 Introduction

The nitrogen-vacancy (NV) center was first identified by du Preez in 1965 [1] and the significant optical characteristics of the observed center were given by Davies and Hamer in 1976 [2]. However, there has been phenomenal interest in the centers

since its observation at the single-center level and a multitude of applications have resulted. The observation of the single site was reported in 1997 [3].

The acclaimed merits of the NV center are commonly associated with the negative charge state of the NV center (NV^-), and can be interpreted in terms of its physical, optical, and magneto-optical properties. Firstly, the NV center is hosted in a diamond crystalline matrix (the most rigid material on Earth made of carbon atoms bonded together with energy of ~ 7.4 eV per atom). The diamond core is also chemically inert, so that the NV center is well secluded from environmental perturbations in such a crystal host. Even harsh environments, such as high-energy cosmic radiation, inflict little damage to this crystalline material. At the same time, diamond surface is chemically reactive, especially when the surface is well developed, as in case of nanodiamonds (NDs), and/or surface functionalization. For example, the most popular acid treatment [4–6] or high-temperature annealing in air [7–10] results in formation of oxygen-containing surface moieties on the diamond surface that facilitate interfacing with photonic devices and macromolecules.

The wide bandgap of diamond (5.5 eV) provides ample energy space to as many as ~ 500 reported color centers, where the NV center is among the brightest. The center action cross section is large, $\eta\sigma_a \cong 3 \times 10^{-17} \text{ cm}^2$ (σ_a —absorption cross section; η —quantum yield) [11], with quantum yield reaching $\sim 80\%$ under favorable excitation conditions. The remarkable photostability of the NV center is another important property that manifests itself by uninterrupted continuous emission under continuous excitation. This is in contrast with the poor photostability of the widespread emitters, organic fluorescent dyes that undergo irreversible conversion to a low- η or nonemission state after, approximately, one million excitation cycles. The process is referred to as photobleaching. Luminescence intermittency, or blinking, represents another photostability impairment mechanism, and is reported in virtually all single emitters [12,13] being especially profound in semiconductor quantum dots [14–16]. Although the NV^- centers have been also reported to exhibit blinking behavior, this can be readily avoided under controllable conditions [17].

Depopulation of the spin-specific ($m_S = \pm 1$) ground state at room temperature in favor of the $m_S = 0$ ground state in the course of optical excitation represents a unique and valuable property of the NV^- center, which is leveraged by a possibility to read out thus prepared spin state by optical means. The coherence time of this spin state at room temperature is usually limited to the microsecond time scale, but its extension to 1 ms has been demonstrated by the appropriate choice of an ultrapure diamond host type IIa [18]. This provides crucial flexibility in preparing and interrogating the entangled spin states.

It is the combination of the outlined physical and optical properties of the NV center that affords a broad range of applications spanning from quantum information and encryption technology [19–21] to ultrasensitive magnetometry [22,23] through to biomedical imaging/sensing [24]. The quantum science applications rely on preparation of an NV^- center spin state, called qubit, followed by its coupling to the other spins associated with impurity defects, such as NV center spins, substitutional nitrogen (N_s), or isotopic C^{13} nuclear spins, creating quantum entanglement of the qubits.

The NV^- entangled spin state can be subsequently read out optically and, hence, measurements can be made of the entangled state of the ensemble. The magnetometry applications rely on the high sensitivity of the NV center polarized spin state to (local) magnetic fields. The spin state perturbed by external magnetic fields to be probed is read out optically and reports on the local value of the magnetic field vector. The ultimate sensitivity can be at the level of the single spin and at the nanoscale [23].

It has been realized, however, that the NV center nanometer-scale proximity to the diamond host surface is vital for practical applications. For example, high-efficiency radiation coupling of the NV center to photonic devices is important to support quantum communication between distant qubits, and can be achieved by bringing the centers to within 100 nm distance of the photonic device interface [25,26], or even directly embedding diamond nanocrystals into the devices [27]. This nanoscale proximity can be realized either by forming the NV center(s) in the nanosized subsurface layers or in diamond nanocrystals, i.e., NDs. In particular, sensing applications, including Förster resonance energy transfer [28] and single-spin-sensitive magnetometry [23], require the ND layer to be pared back to exploit the strong dependence of the signal on the interaction radius r ($1/r^3$ and $1/r^6$, respectively). For example, the recently reported optical imaging magnetometry demonstrated the potential of local magnetic field imaging with nanometer resolution, where a sharp magnetic nanotip was imaged by using the single NV center encapsulated in a 40 nm ND [22]. The small ND host was essential to sensitively probe both the rapidly decaying magnetic field amplitude and its spatial gradient to accurately locate the magnetic nanotip. Maze et al. [23] have reported single-spin-sensitive imaging at the nanoscale, which led to an estimation that the NV^- center had to be as close as 10 nm to a single spin under investigation for reliable detection. In biological imaging applications, small diamonds are crucial to minimize disruption to the molecular trafficking under observation [29]. It is desirable to reduce the size of NDs to be, at least, comparable with the size of an average protein, i.e., 5 nm, which is achievable due to the progress in production of ultra-small NDs, also referred to as single-digit NDs, or ultradispersed NDs [30]. It has been also reported that NV–NDs in the size range less than 10 nm retain their luminescent properties characteristic of the NV centers.

At the same time, the NV center configurational stability sets an ultimate size limit on the NV–ND matrix—a 2.5 nm diamond nanocrystallite may be incapable of hosting an NV center in the core, as predicted theoretically [31]. The environmental susceptibility of the NV–ND emission in small crystals, or NV centers in the subsurface nanolayer, is also anticipated and has been reported on several occasions [17,32,33].

With this backdrop, the main purpose of this chapter is twofold: firstly, consolidation of the existing knowledge base on the NV center, including its unique emission properties, with a particular focus on the mechanisms underlying spin-sensitive optical transitions of NV^- centers. These key properties, are, however, compromised by effects, such as the interconversion of the NV center charge states and surface-related emission quenching and blinking. These effects will be reviewed and an

account of the most recent developments toward their interpretation and control will be given. This chapter is organized as follows. We will review fundamentals of the electronic structure and mechanisms behind the unique emission properties of the NV center in Section 10.2. In Section 10.3, the mechanisms of the interconversion between the negative and neutral charge states of the NV centers will be addressed. The simpler case of the interconversion in bulk diamond is attempted first, followed by the next sections addressing new complexity in the photophysics of NV centers related to the ND and surfaces that are more relevant to this book's topics. Section 10.4 summarizes recent progress in production and theoretical modeling of ultra-small NV-NDs (defined as maximum linear size less than 10nm), and formation of NV centers within nanometers of the diamond surface. In Section 10.5, we will discuss the effects of surface on the emission properties of the NV centers, with an emphasis on the emission surface quenching and blinking.

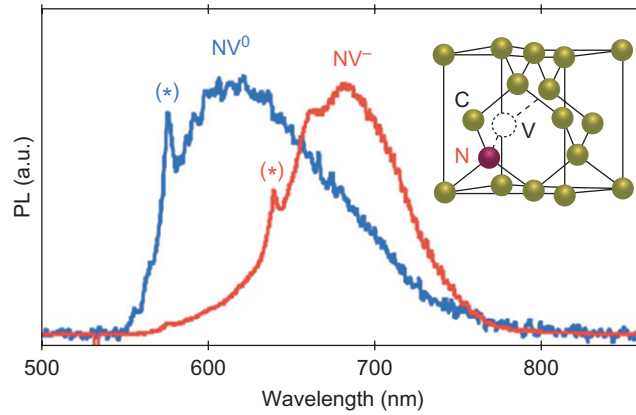
10.2 Electronic structure and emission properties of the NV center

10.2.1 Introduction

The observation of the single site was reported in 1997 but despite the activity since that date the center is still not fully understood. The properties of particular interest are those of the negative charge state of the NV center, but this center can convert to a charge neutral state. The reason for the occurrence of one or other of the charge states, NV^- and NV^0 , has not been fully established and this will be discussed in the following sections. The purpose of this section is to provide a summary of the current theoretical understanding of the electronic structure and optical selection rules associated with the emission (Figure 10.1).

Spin and orbit in color centers in diamond are good quantum numbers and spin and orbit are usually studied by different experimental techniques as they are susceptible to different perturbations. For example, orbits are sensitive to the local crystal environment, and by lowering the symmetry using uniaxial stress it is possible to determine the degeneracy of the orbital states and orientation of center. Using this approach, Davies has shown that the characteristic optical transition in both the NV^- and NV^0 centers are associated with transitions at sites of trigonal symmetry between states of A and E orbital symmetry. The NV^0 center has a zero-phonon line at 2.16eV (575nm) and the uniaxial stress measurements show that the transition is from an orbitally degenerate ground state to an orbital singlet excited state (E–A transition in C_{3v} symmetry) [34], whereas the NV^- center has a zero-phonon line at 1.945eV (637nm) and the transition is from an orbital singlet ground state to an orbitally degenerate excited state (A–E transition in C_{3v} symmetry) [2].

The 2.16eV center occurs in samples where the vacancy concentration is as high as the nitrogen concentration, and Mita [35] considered it was most likely the transition was associated with an NV center in the neutral charge state NV^0 . This is considered to be an even electron system and the zero-phonon line attribute to

**FIGURE 10.1**

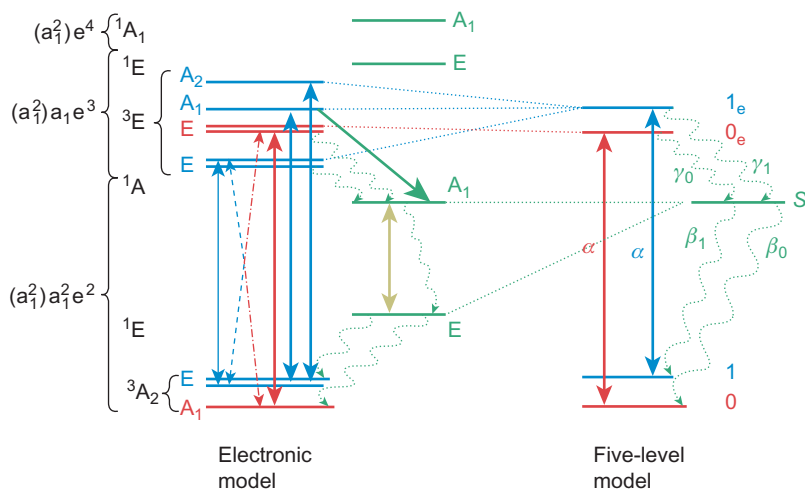
Luminescence spectra normalized to their respective maximum value of single NV^- (red (gray) curve) and NV^0 (blue curve) color centers in diamonds. The zero-phonon lines (demarcated *) of NV^- and NV^0 emissions are located at wavelengths 637 and 575 nm, respectively. The inset shows the atomic structure of the NV defect, consisting of a substitutional nitrogen atom (N_s , demarcated N) associated to a vacancy (V) in an adjacent lattice site of the diamond crystalline matrix.

Source: Reproduced with permission from Ref. [33].

an ${}^2\text{E} \rightarrow {}^2\text{A}$ transition. Experiments have not been able to prove this, as no Zeeman splitting or electron paramagnetic resonance (EPR) of the ${}^2\text{E}$ lower state has been detected. The absence of an EPR signal was attributed to a dynamic Jahn–Teller effect in the ground state. However, an EPR signal has been obtained upon optical illumination and is considered to be associated with a metastable ${}^4\text{A}$ state of the NV^0 center [36]. Further discussion of the energy levels and optical cycle of the NV^0 center is presented later.

In the case of the 1.945 eV center an $S = 1$ EPR signal associated with a trigonal center was reported by Wyk and Loubser [37]. The signal was obtained using optical illumination and the strength of the signal correlated with the 1.945 eV optical transition. The spectrum indicated preferential population of the $m_S = 0$ level. It is now well established that this EPR signal is associated with the ground state of the NV^- center, and the spin polarization and enhanced signal arise as a consequence of the optical cycle. Optical transitions conserve spin and, therefore, the transition at 1.945 eV can be assigned to a ${}^3\text{A} \rightarrow {}^3\text{E}$ transition at the NV^- center.

The ground state of NV^- is an orbital singlet and spin triplet. In trigonal symmetry the spin $m_S = +1$ and -1 states are exactly degenerate and when modeling the optical cycle of the NV^- center the $m_S = \pm 1$ can be described by one level (assuming no magnetic fields). The excited state is also a spin triplet, but stress has indicated that the orbital state is degenerate. However, in the phenomenological

**FIGURE 10.2**

Schematic diagram of the electronic levels of the NV color center (left) and the simplified five-level model appropriate for room temperature (right). The $m_s = 0$ levels are indicated in red, the $m_s = \pm 1$ in blue, and the singlets in green. The arrows with double arrow heads indicate the radiative transitions. The solid blue and red arrows give the spin conserving transitions in the visible and the blue and red dashed arrows give the weak nonspin conserving transitions. The pale green gives the infrared transition. The dark green arrows (single arrow heads) indicate nonradiative decay. The solid green involves A_1 vibrations and the wavy lines E -vibrations. The dashed lines between the left-hand side and right-hand side indicates what states collapse to give the simpler energy diagram. (For interpretation of the references to color in this figure legend, the reader is referred to the web version of this book.)

model, the excited state is treated as an orbital singlet and this will be justified below. The proposed model, therefore, includes two spin levels, 0 and 1, in the ground electronic state and two electronic states in the excited state, 0_e and 1_e (Figure 10.2). The optical transition (at rate α) between the ground and excited state is independent of the spin projection and, therefore, there are two transitions of identical strength between levels 0 and 0_e and between 1 and 1_e , where the spin projection does not change. Vibrations couple to these transitions, but no spin change is involved. Should these be the only energy levels and only transitions, the center would cycle between the ground and excited states with constant spin projection. However, the situation is entirely changed by the presence of an intermediate state. The intermediate state is attributed to a spin singlet (or state) $S = 0$, and so there is no spin projection. There is intersystem crossing from the excited state to the singlet and from the singlet to the ground state. These crossings indicated in Figure 10.2 are spin dependent and give rise to the spin polarization and spin readout.

The approximate rates of the crossing from the excited state spin levels to the singlet are $\gamma_1 = 0.55\alpha$ and $\gamma_0 = 0.15\alpha$ and from the singlet to the ground state spin levels are $\beta_0 = 0.035\alpha$ and $\beta_1 = 0.022\alpha$ (Figure 10.2). It can be seen from the β values that the decay rate from the singlet to the ground state is low with a combined rate of 0.056α (corresponding to effective life time of 178 ns). Also the transitions are not particularly spin selective, and so only have a secondary role in creating the spin polarization. The decay out of the triplet to the singlet is comparable to the optical transition and the rate associated with $m_S = \pm$ states (from 1_e) is more rapid than for $m_S = 0$ states (from 0_e). These intersystem crossings are central to giving the NV⁻ center its unique properties. They result in (i) population being transferred out of $m_S = \pm$ states, (ii) the emission rates from $m_S = \pm$ states being weaker than from $m_S = 0$ states, and (iii) the associate lifetime (in diamond crystals) from $m_S = \pm$ states being shorter at 7.8 ns than that from $m_S = \pm$ states at 12 ns [38].

With continuous excitation, the relative population in the excited state is given by P_{\pm}/P_0 (calculated as $\gamma_0/\gamma_1 \times \beta_1/\beta_0 = 0.15/0.55 \times 0.022/0.035 = 0.17$). This implies 14.5% of the population is in the excited $m_S = \pm$ spins and 85.5% is in $m_S = 0$. The ground state polarization is less by the ratio of the lifetimes 7.8/12 and, hence, somewhat lower at 74% in $m_S = 0$.

The simple five-level model is only appropriate for nonselective excitation and detection. However, this is the more common situation and always the case at room temperature. The detection is nonselective given that emission is collected over the emission band from 650 to 800 nm. Also excitation is nonselective when exciting within the vibration sideband such as at 532 nm. The only situation where the model is not appropriate is for resonant excitation with the sample at low temperature. In this case, the laser will be resonant with a transition for one spin projection and the population will be pumped to the other spin projection. The spin polarization can be complete with the only limitation being due to weak spin nonconserving transitions (dashed lines in Figure 10.2). These are of the order of 2% of the spin-allowed transition and, hence, spin polarizations of the order of 98% can be attained. This is not a situation likely to be encountered with NDs, and polarizations closer to the above 80% are more plausible. Variable polarizations, including higher values, have been reported and this implies that the above parameters are not constant. The reason for the variation remains to be explained.

The parameters given above have been obtained from measurements of ensembles [39], and from excellent systematic studies of single centers [40]. Information can be obtained by gating on excitation at 532 nm and monitoring the red emission, >640 nm. The emission starts at a low level and increases a further 20% as the system becomes spin polarized. To obtain such an increase, the optical cycle pumping population from state 1 to 0 has to be faster than the spin-lattice relaxation time maintaining the population between the 0 and 1 states. It is possible to establish the period the system remains polarized by gating off the excitation for progressively longer periods and investigate how long it requires for the emission to be at the low level when gating back on. With this simple measurement the spin-lattice relaxation time can be determined. This spin-lattice relaxation time is very susceptible to temperature and varies from milliseconds at room temperature to hundreds of seconds at

helium temperatures [41]. Consequently, the minimum excitation intensity required to obtain and maintain spin polarization becomes less with lowering temperature.

At low excitation levels, no population is stored in the intermediate state, and feeding and decay rates cannot be determined. Such information requires high excitation intensity. Turning on high intensity excitation gives intense emission but the level rather than rising rapidly drops as a fraction of the center is transferred to the intermediate state. The rate at which this occurs is different for the $m_S = \pm$ and $m_S = 0$ spins. If the system is spin polarized, the decay of the emission is at one rate given by γ_0 , whereas if the spin polarization is reversed by applying a π microwave pulse resonance with ground state spin separation, the decay is at a faster rate given by γ_1 (see Figure 10.5 in Ref. [40]). The transients enable the feeding rates to be determined and for a single center values of the order of $\gamma_1 = 0.55\gamma$ and $\gamma_0 = 0.15\gamma$ have been obtained. The lifetime of the intermediate singlet state can be obtained by determining how long it takes in the dark for the initial transient to be repeated. However, this gives the combined decay to the ground state irrespective of final spin. Determining the individual rates requires more detailed measurements. Robledo et al. [40] has obtained these from a series of measurements of a single center. The degree of spin polarization of the center is determined by the component's bi-exponential decay following a single laser pulse and this polarization is monitored following successive pulses. The values obtained for one center were $\beta_0 = 0.035\gamma$ and $\beta_1 = 0.022\gamma$, although there was 40% variation between the rates for different centers.

10.2.2 Electronic model

To understand the validity of the optical cycling proposed by the above model, it is necessary to consider the electronic states at the NV complex. The states are localized and it is normally sufficient to consider the electron orbits adjacent to the vacancy in a “pseudo-molecule” approach as first introduced for semiconductors by Coulson and Kearsley [42]. There are three molecular orbits for a vacancy at the C_{3v} site. One is twofold degenerate of E symmetry and labeled as e and the second is nondegenerate with A_1 symmetry, labeled a_1 .

The a_1 orbits have the lowest energy and the second (a_1) orbit being within the valence band is always occupied and will be included in parentheses. There are five electrons for NV_0 and the lowest energy states are then $(a_1^2)a_1^2e(E)$, $(a_1^2)a_1e^2(^4A_2, 2A_2, ^2E, 2A_1)$, and $(a_1^2)e^3(^2E)$. There are six electrons for NV^- , and the states are $(a_1^2)a_1^2e^2(^3A_2, ^1E, ^1A_1)$ and $(a_1^2)a_1e^3(^3E, ^1E)$, $(a_1^2)e^4(^1A_1)$. The states formed allowing for Coulomb interaction from each configuration is given in parentheses. For a more up-to-date treatment of the electronic states, see Doherty et al. [43] and Maze et al. [44]. For NV^- , the ground and excited states have been associated with spin triplets, $S = 1$, and so the optical zero-phonon line is attributed to the transition between the 3A_2 ground and the 3E excited states. It can be seen that there are two aspects of this electronic model that differ from that indicated by the phenomenological five-level model. The excited state is an orbital doublet but is treated as an orbital singlet. Also there are two intermediate states whereas these are modeled as one level.

Spin-orbit interaction (of the order of 5 GHz) splits the 3E state into four spin-orbit levels (and six when combined with stress), and these have been observed for single centers at low temperature by direct absorption from the ground state [45]. Experimentally, it is found that this fine structure is different for every center and can be attributed to the orbital state being very susceptible to the random strain that varies from site to site. These observations are for helium temperatures. As temperature is raised, the situation is changed. For example, it is found that the optical transition exhibits an unusual T^5 broadening rather than the more common T^7 dependence [46]. This is due to the excited state being susceptible not only to static distortions, but also to dynamic distortions. The dynamic distortions induce transitions between the two orbital levels averaging the orbital angular momentum to zero [47]. The result is that at high temperature all effects relying on nonzero angular momentum, such as spin-orbit splitting, are totally quenched. There is no longer fine structure and clearly no longer variation from site to site. This is very important for room temperature behavior, as it means that it becomes valid to treat the excited state as an effective orbital singlet, as is the case in the phenomenological model.

There are two intermediate singlet states and uniaxial stress measurements of the zero-phonon emission line at 1042.6 nm confirm that the states have A and E symmetries consistent with the electronic model [48]. The infrared emission is very weak, as it is dominated by nonradiative decay. This results in a very fast decay (\ll ns) from the upper level to the lower state that has a longer lifetime (>100 ns). As there is only one decay path to this lower level, the presence of the upper level can be ignored and this justifies the use of just one singlet level in modeling the optical cycle.

10.2.3 Parameter justification

Intersystem crossing between triplets and singlets arise from spin-orbit interaction. The highest rates are between adjacent states mixed by spin-orbit interaction, and symmetric vibrations absorb the mismatch in energy. The symmetry of the spin-orbit states are given in Figure 10.2, and the only intersystem crossing allowed by the above rule is that between the A_1 components of 3E and 1A_1 . This intersystem crossing is, therefore, allowed, and it is the main contributor to the creation of spin polarization. The large intersystem crossing rate of $\gamma_1 = 0.55\gamma$ indicates that the 1A_1 must lie close in energy to 3E , probably, within one phonon energy, but its exact location has not yet been established. In the ground state, there is an E spin-orbit component within 3A_2 and intersystem crossing from 1E must be considered. However, it is found that there is no spin-orbit mixing with the 1E , and so there is no decay to the ground state via symmetric vibrations. The result is that population can decay to the 1E level, but no further with conventional relaxation mechanisms. The great difficulty with the spin polarizing optical cycle of the NV^- center has been in understanding how the system does decay from the 1E level to the ground state. The answer is that the decay involves degenerate E-vibrations, and it is found that the relaxation can be to either of the ground state spin levels [49]. This is consistent with observation as the earlier parameters indicate there is not a strong preference for either spin projection. The

spin polarization is more reliant on the above relaxation out of 3E favoring transfer out of $m_S = 1$. Other decay can be enabled by the coupling of E-vibrations, and these account for the weaker decay channels. In Figure 10.2, all of the nonradiative decay channels involving E-vibrations are indicated in green.

It can be seen from the above summary that many of the unusual properties of the NV center arise from its susceptibility to distortion and consequential interaction with E-vibrations. The electron–E-vibration interaction affects the degenerate states, but their more profound effect is on the intersystem crossing. Should there be no such interaction, the center would be more conventional in transfer to the singlet levels but no transfer out of the singlets and all emission would be lost. The processes are now understood in principle, but there has been no calculation of the intersystem crossing rates or any knowledge as to how they may be varied. Varying the intersystem crossing would be important as the spin polarization could be controlled and even enhanced and have important implications for applications. There is therefore need for theoretical work in this area.

10.3 NV center interconversion

It is normally preferred to have material with only the NV^- charge state, and there has been reasonable success at achieving this, including in NDs and at surfaces, as can be seen from discussion elsewhere. However, even when it is in the correct NV^- charge state, the necessary optical manipulation required for applications can result in converting the center to the neutral NV^0 charge state, and this can be a great inconvenience. There have been several studies of the NV^- and NV^0 photoconversion, but the different mechanisms are not fully appreciated or yet fully established. The interconversion between NV^- and NV^0 is more straightforward within diamond crystals than for NDs or close to surfaces, and the discussion here will be restricted to this simpler situation.

Within diamond crystals there are two different mechanisms whereby the conversion can occur and they have different characteristics. In one case, the conversion is linearly dependent on intensity and occurs when the nitrogen concentration is high [50]. In the second case, the conversion has a quadratic dependence on excitation intensity [51], and is the one relevant to low-nitrogen concentration samples, as used in many applications involving spin.

There are several color centers in diamond that can exist in more than one charge state, and it is generally recognized that the preferred charge state depends largely on the local environment and, in particular, whether there are donors close to the center [52]. The situation can be complicated if there are several impurities and possible donors in the neighborhood and substitutional nitrogen, N_s , is by far the most prevalent donor. When there is an N_s adjacent to the NV complex, the center obtains an electron from N_s to form the negative charge center NV^- . This situation implies that $NV^- - N_s^+$ has lower energy than $NV^0 - N_s^0$, and that an electron moves from the N_s to the NV. This has to be achieved by a tunneling process and tunneling depends on

distance, usually exponentially on the distance between the donor and acceptor. Thus, when the N_s^0 is close to the NV^0 , the tunneling will be rapid and highly probable. This is the situation in high-nitrogen concentration diamonds, as all the centers are likely to have an adjacent donor and accordingly will be in the NV^- charge state. In the other extreme, should the N_s^0 impurities all be multiple atomic distances away from the NV^0 center, as with the lower concentration diamonds, then the tunneling will be slow. In some cases, the tunneling can be ignored and the center will remain in the neutral N_s^0 charge state. Thus the tunneling rate has an enormous influence on the charge state in the absence of light. It is important to note that tunneling also occurs in the excited state, and it will be shown that the tunneling rate also has a larger effect on the behavior under optical illumination and in determining what process dominates the NV^- and NV^0 photoconversion.

Tunneling must involve a change of only one electron orbit. As given in the previous section, the NV centers are normally modeled in terms of the two a_1 and the one e molecular orbitals at the C_{3v} site. The a_1 s have the lowest energy and one of these is filled throughout, and included in parentheses. The ground configuration of NV^- and NV^0 are $(a_1^2)a_1^2e^2$ and $(a_1^2)a_1^2e$, respectively. Thus, the tunneling requires the electron to move from the N_s to an e-orbit of the NV center. Where this occurs, it converts $NV^0-N_s^0$ to $NV^-N_s^+$, as indicated in Figure 10.3. When excited to the state at 1.945 eV, the $NV^-N_s^+$ pair will have greater energy than the ground state of the $NV^0-N_s^0$ pair. However, the excited NV^- state has an $(a_1^2)a_1e^3$ configuration, and the possibility of tunneling to the $(a_1^2)a_1^2e$ ground configuration of NV^0 will be prohibited, as it would require a change of three orbits. Hence, photoconversion of an excited NV^- will not occur directly to the NV^0 ground state. (Obviously, it cannot relax to the excited state of the NV^0 center at 2.17 eV, as it has higher energy.) However, there are other states of the NV^0 center that have intermediate energy, and these states are associated with an $(a_1^2)a_1e^2$ configuration. Accepting some of these states have lower energy than that of the excited $NV^-N_s^+$, tunneling will occur, as it involves the reverse one-electron transfer that already occurs in the ground states, from e-orbit of NV to N_s (Figure 10.3). There is the obvious difference that the tunneling has to occur within the excited state lifetime, but the tunneling probability is the same as in the ground state, and will take place with regular cycling.

The observations of reference [50] are consistent with the above processes. The fraction of NV^- centers photoconverted to the NV^0 charge state is linearly dependent on the excitation intensity. The observations were for an ensemble, where there was a wide range of $NV-N_s$ distances and correspondingly a range of conversion rates from less than microseconds to seconds. When the excitation is reduced the recovery can be monitored, and it was observed that there were similar rates. The recovery will arise with the NV^0 in the ground state, and so is simply the process by which the center was originally preferred to be in the $NV^-N_s^+$ charge situation. From consideration of the molecular orbitals it is conceivable that some of the recovery can occur from the excited state of NV^0 , $(a_1^2)a_1e^2$ directly the excited state of NV^- , $(a_1^2)a_1e^3$, but it is less likely, as it has to occur within the 20 ns lifetime.

In low-nitrogen concentration diamonds such as type IIa, the $NV-N_s$ separation can be several hundreds of atomic spacing and tunneling between the N_s and the

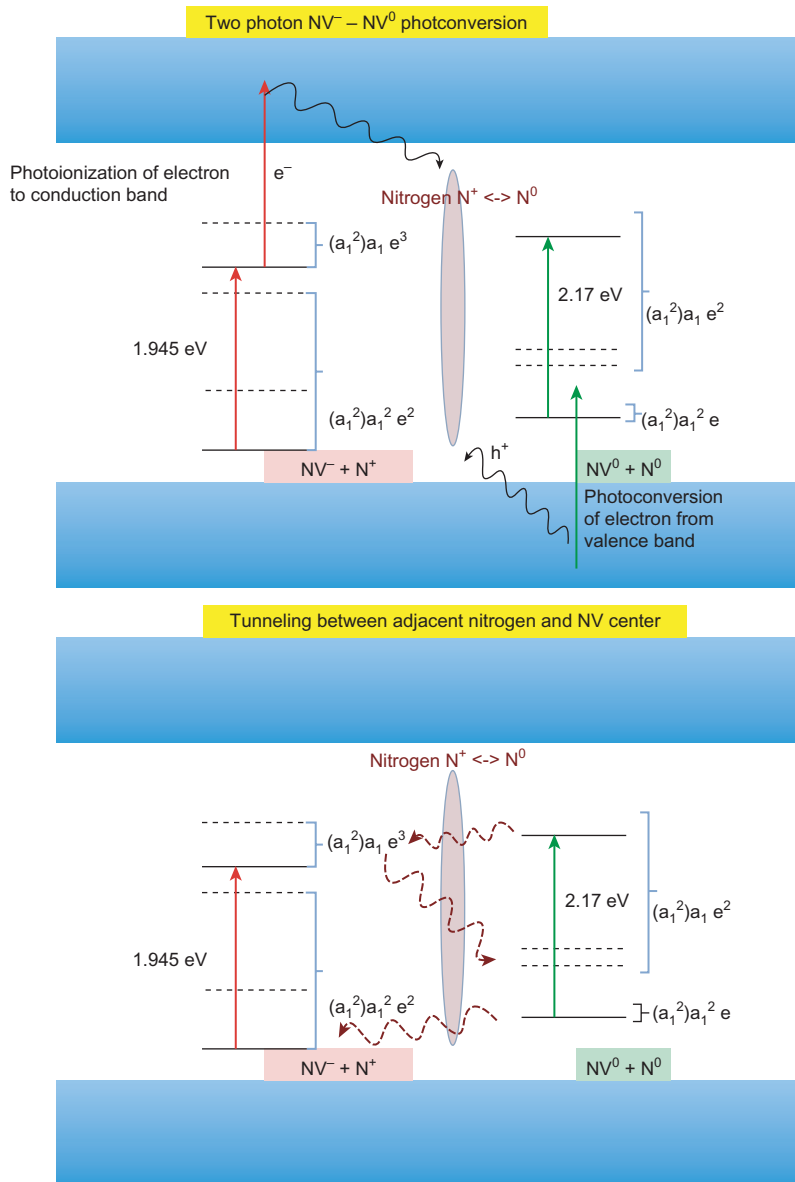


FIGURE 10.3

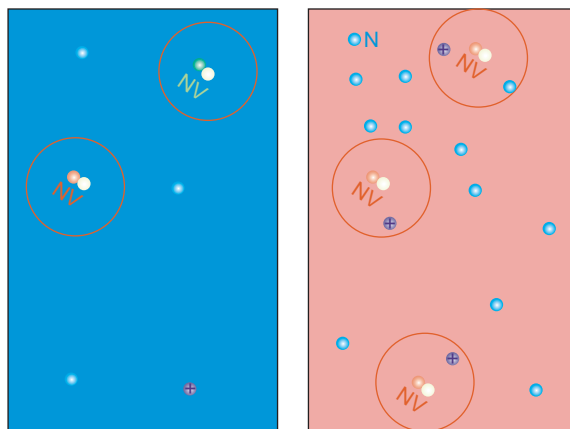
Representation of the photoconversion processes between NV^- and NV^0 (two-photon process in upper panel and tunneling in lower panel). The blue bands indicate the conduction and valence bands, and the solid lines give the energy levels of the NV^- and NV^0 within the band gap. The levels are associated with different configurations and the one-electron states associated with these configurations are given toward the right. The red arrows indicate the one-electron radiative transitions, and the wavy arrows indicate the one-electron nonradiative transitions. The latter must involve an electron on the substitutional nitrogen and a reservoir of nitrogen atoms is indicated between the NV^- and NV^0 energy levels. (For interpretation of the references to color in this figure legend, the reader is referred to the web version of this book.)

NV will be very slow or negligible. Thus, there is no photoconversion via the above tunneling mechanism but a quadratic photoionization process has been reported for such samples. In single-center studies, Waldherr et al. [51] reported a quadratic power dependence and a simple exponential response indicating a single two-photon process. The first photon takes the NV^- center to the $(a_1^2)a_1e^3$ excited state at 1.945 eV, and the second photon excites an e-electron to the conduction band. The conduction band electron will eventually combine with an acceptor in the lattice leaving the system in $(a_1^2)a_1e^2$ (Figure 10.3). In a further study of ultrapure diamond, Beha et al. (unpublished, 2012) have observed this process, and also showed that the reverse photoconversion of $\text{NV}^0\text{--NV}^-$ occurs likewise quadratic in the laser intensity. In this situation, an electron most likely is involved in exciting an (a_1) electron that is situated within the valence band, and then the hole in the valence band gets rapidly filled from an acceptor (Figure 10.3).

As both $\text{NV}^0\text{--NV}^-$ and $\text{NV}^-\text{--NV}^0$ quadratic conversion processes require light, no emission is found when the laser only excites one of the centers NV^0 or NV^- . The center is immediately converted to the alternative charge state and is out of resonance. Should the laser be at an energy exciting both centers, then there is rapid transfer between the two charge states, and the emission of both charge states is detected. The relative intensity of the two centers depends on the wavelength but not on the laser intensity. For these samples, the relative strengths of the $\text{NV}^0\text{--NV}^-$ emission only depends on the excitation wavelength, and is a signature of the two-photon mechanism being the dominant process. The laser power dependency is very different to that observed for a high N_s concentration sample and highlights the different photoconversion mechanisms.

When an NV center is continually excited, it is unlikely that the same N_s center is responsible for donating the electron every time the center is in the NV^- charge state, and this is true regardless of the photoconversion processes. The NV^- center does not move, but the location of the N^+ will vary (Figure 10.4). This variation in the position of the charged ion gives a variable electric field and will Stark shift the optical frequencies of the NV^- center. Should all of the possible donors be remote, it is possible that this shift is small but even at the lowest concentrations, jitter on the order of 100 MHz is observed. This cannot be avoided and only minimized by using the lowest possible intensities. If such an event occurs, the practice has been to refresh the NV^- center using an intense pulse involving a reverse two-photon process.

When the N^+ are close to the NV center, the Stark shifts become readily observable and single site optical frequencies are found to jump between various fixed values. In the low-nitrogen concentration samples, it is common for this jitter to be within the several GHz scan of tuneable lasers (see Figure 10.3; Ref. [46]). With the higher concentrations of nitrogen, the Stark shifts can be 100–300 GHz ($3\text{--}10\text{ cm}^{-1}$), and it contributes to the large inhomogeneous broadening observed for the $^3A_2\text{--}^3E$ optical transition. When an inhomogeneous broadened line is excited with a fixed frequency laser the resonant centres are Stark shifted out of resonance leading to a loss of absorption at the laser frequency. Clearly this is the process involved in spectral hole-burning.

**FIGURE 10.4**

The left and right panels illustrate low- and high-nitrogen concentration diamond, respectively. In the low concentration, there is little correlation in the position of the nitrogen donating the electron with the position of the NV. In high concentration, the electron is likely donated from an adjacent nitrogen. With optical excitation, the location of the donor can change and the movement of the positive charge will alter the electric field at the NV center. Notice that both NV^0 and NV^- can coexist in the low-concentration sample. In the high-concentration sample, the extra electron that changes NV to the negative charge state comes from adjacent nitrogen donors.

These large Stark effects are due to the associated nitrogen atoms or donors being very close to the NV center and this clearly has to be the case for NDs and near surfaces. They consequently also exhibit very large inhomogeneous broadening or shifts in the position of zero-phonon line. If the extra electron can come from a variation of donors, then there will be jitter in the position of the optical line, but this will only be seen, as blinking, when the resonant excitation is used. Blinking at room temperature or with nonresonant excitation must arise in other ways, as will be discussed later.

As mentioned earlier, the situation regarding the NV^-/NV^0 photoconversion is very much simpler in the bulk than near surfaces or in NDs. When diamond surface traps are brought within the interaction range to the N_s and NV centers, the NV^- emission behavior becomes more complicated and the luminescence can be intermittent or blink. There are other even more fundamental issues, such as to whether the NV complex itself can be formed and is stable. Also there are other conceptually simple issues, such as the other absorption obscuring the excitation or emission, so that the centers may be present but undetectable. In the following sections, we will review these issues, as well as NV^-/NV^0 conversion. We will provide some estimation of this interaction range, and review experimental methods of creating NV centers within the nanometer range to the diamond surface. This brings about the more fundamental question on what is the most proximal location of the NV center to the diamond's host surface.

10.4 Recent progress toward production and understanding of ultra-small NV-NDs

The question of the configurational stability of the NV center versus its distance to the diamond surface became essential two decades ago due to the availability of the ultra-small NDs produced by detonation [4]. When the disintegration of as-produced tight detonation ND aggregates into monodisperse 5 nm NDs was demonstrated [5], the problem of the existence of NV centers in such small nanocrystals became a hot research topic in view of the significant appeal of their applications. The experimental observations, however, provided little support in favor of the existence of the NV-ND of the detonation origin. For example, theoretical calculations of the crystal energy budget favors the location of nitrogen on the surface rather than the core, which seems to explain the limited observation of NV centers in chemical vapor deposition (CVD) and high-pressure high-temperature (HPHT) grains less than 40 nm in size [53,54], and favors the prediction that NDs smaller than 10 nm in size do not contain NV centers [31,55]. In particular, the spectroscopic studies revealed broadband luminescence [56] that was wavelength blue-shifted from the characteristic NV spectra, as shown in Figure 10.1. The origin of this luminescence was attributed to a graphitic layer that abundantly formed in the detonation process, which was also corroborated by the photoluminescence excitation spectra analysis of HPHT and CVD diamonds showing a broadband component attributed to amorphous carbon phase [57]. Based on the increased conductivity, it was suggested that N_s was concentrated at the grain boundaries of CVD-grown ultrananocrystalline diamond [58], which was predicted by the theoretical simulations that favored N_s positions on the grain surfaces by 3–5 eV to that in the grain [59]. The traces of N_s spins were also sought by means of nuclear magnetic resonance [60], and high-sensitivity EPR spectroscopy [61], with the negative results due to the obscuring effects of a multitude of paramagnetic centers created by structural defects (dangling C–C bonds) on the ND surface, or at the interface of the sp^2 – sp^3 ND layers.

It was not until recently that it was reported that the N_s centers did exist in the detonation ND hosts by performing ultrahigh-sensitivity pulsed EPR measurements at liquid helium temperature [32]. In the same work, the overshadowing contribution of the graphite layer to the overall luminescence signal from NV-NDs was suppressed by employing a time-gated detection scheme making use the difference in the luminescence lifetimes of graphite and NV^- (subnanosecond versus ~10–20 ns, respectively). As a result, the characteristic NV^- center spectral signature was observed, thus providing unambiguous evidence of the existence of the NV centers in detonation NDs [32]. A powerful method to obviate the obscuring luminescence signal overhead from the graphite layer was demonstrated by Bradac et al. [17]. Thoroughly acid-cleaned discrete detonation NDs were deposited on a glass slide and interrogated individually, thus minimizing the graphite luminescent signal overhead, so that a signal originated from one ND only became observable. As a result, characteristic NV^- spectral signatures from single centers were acquired.

An alternative top-down approach of production of the ultra-small NDs has been reported by Tisler et al. [62]. This approach was based on milling a millimeter-sized

diamond crystal, following NV center implantation using the conventional high-energy electron radiation, high-temperature annealing procedure. The authors reported stable luminescence and high-contrast optically detected electron spin resonance from single NV centers in NDs sized less than 8 nm. The key optical and magneto-optical parameters, including luminescence lifetime (~ 17 ns) and decoherence time (approximately milliseconds in microdiamonds and microseconds in NDs) were found to be comparable with those of the type Ib bulk diamond crystals.

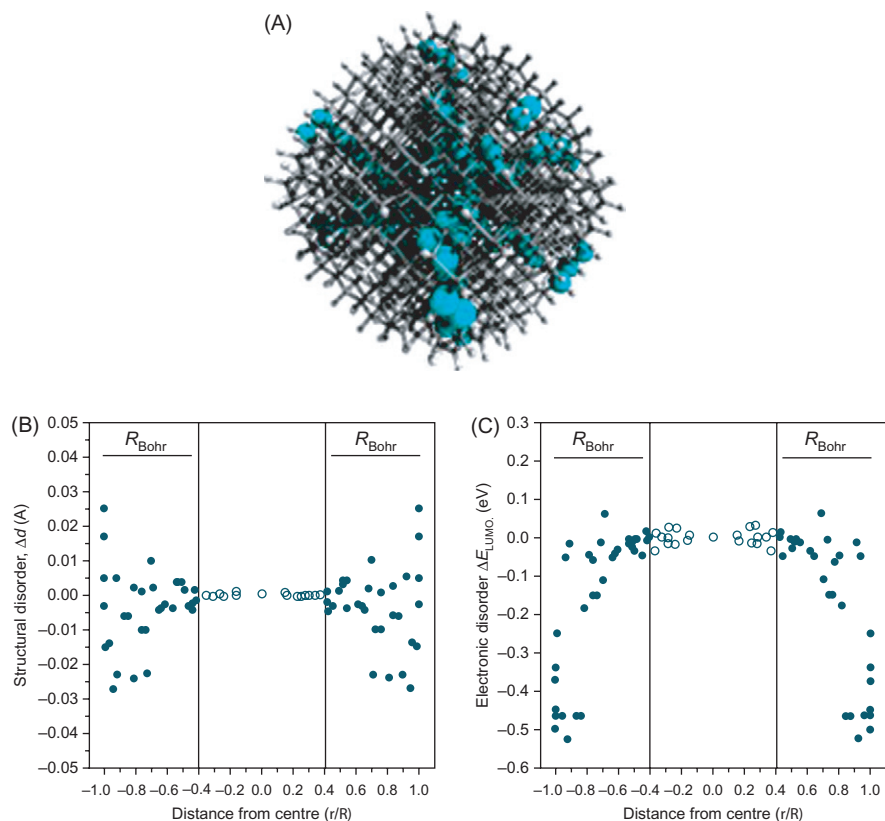
Oxidative etching in air/oxygen at high temperature is another top-down approach of production of ultra-small NDs. This method relies on removal of carbon atoms from the ND surface at a controllable rate via the oxidation reactions. Since an outer ND layer in the graphitized (sp^2) form is removed at a higher rate [9,63,64] than that of the diamond sp^3 phase, this method was originally employed to remove sp^2 carbon from ND, as a surface-cleaning procedure [10]. This method, however, appears also useful for *in situ* studies of ND size evolution, as the oxidative etching in air provides the least-disruptive method to date of graphite cleaning and following size reduction of the ND core [65]. NV^- emission in the ND crystals sized less than 10 nm has been reported [66].

Santori et al. [67] have observed optically active NV centers in diamond created in close proximity to the surface through the ion implantation and annealing of HPHT diamond crystals and CVD films. This method exemplifies an approach of forming NV centers in the nanometer-scale subsurface layer, while retaining relatively large micron-sized crystalline matrix. A similar approach has been demonstrated by Hauf et al. [68]. It is worthwhile to note that diamond surface etching based on the O_2/Ar procedure permitted very fine sampling (~ 1 nm) of the diamond layer content in terms of the presence of NV centers, and sampling their vertical distribution in depth [67]. Despite that this measurement revealed strong NV distribution dependence on the native nitrogen concentration; in general, the presence of the NV centers were detected in very close proximity (~ 1 nm) to the diamond surface.

These experimental results need to be interpreted in the framework of the theoretical modeling that is outlined in the following subsection.

10.4.1 Theoretical modeling

The earlier theoretical studies of stability of the NV center comprising defects indicated intrinsic instability of both vacancy (V) and substitutional nitrogen (N_s) that were able to migrate in diamond crystal [31]. At the same time, the NV center represents a more stable defect whose stability depends on the degree of disorder in an ND. In detonation ND, an NV center is situated in a ~ 5 nm crystal comprising a crystalline diamond core sized 2–3 nm and a mixed sp^2 – sp^3 hybridization shell of quasi-spherical shape [69] distorted by the large proportion of surface dangling bonds ($\sim 20\%$ of total carbon atoms) [10], dislocations [70], and impurities. The outer shell has been found to regain some sp^3 hybridization by surface passivation, e.g., with oxygen-containing moieties [10,71]. A series of density functional tight-binding simulations on an ultra-small ND model, with all surfaces fully passivated

**FIGURE 10.5**

Theoretical characterization of the structural and electronic disorder. (A) The ND model, with all NV sites shown simultaneously (blue), (B) site-dependent change in the average CN bond length (Δd), and (C) the site-dependent change in ΔE_{LUMO} . Closed symbols denote NVs located within R_{Bohr} from surfaces/edges/corners, where atoms with mixed hybridization reside. Open symbols denote NVs located beyond the R_{Bohr} from surfaces/edges/corners (i.e., within the core, where atoms are entirely sp^3 hybridized). (For interpretation of the references to color in this figure legend, the reader is referred to the web version of this book.)

Source: Reproduced with permission from Ref. [17].

with hydrogen atoms ($\text{C}_{837}\text{H}_{252}$) was performed, with NV defects individually inserted into over 50 unique lattice sites within the particle, as shown in Figure 10.5A [17]. A number of parameters were used to assess the local crystal disorder at these sites, including the change in the average C-N bond length (Δd), as shown in Figure 10.5B. When sufficient disorder is present, there will be a shift in the electronic states, so the change in the energy of the lowest unoccupied molecular orbital

(ΔE_{LUMO}) was also considered, as shown in Figure 10.5C. The disorder is extreme when the site is within the excitonic radius (R_{Bohr}) from the surfaces, edges, and corners (closed symbols), and NVs within the core of the particle (where disorder is absent or insignificant) are the only centers that are likely to be optically active (open symbols).

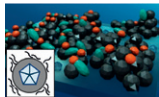

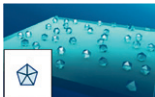
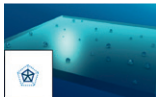
It should be noted that this theoretical model does not fully capture the diversity of the experimental results, including the existence of subsurface implanted NV centers in a 1 nm surface-proximal layer [67]. We speculate that this model considers idealized ND crystal structure that may contain local energy traps that preclude translocation of the NV center to the edge even when it is situated in the unstable subsurface layer (<2.5 nm). Also, the activation energy is an important parameter [72,73] that determines the center mobility under various activation conditions, including temperature. Besides, crystal defects, including dislocations, can have sufficient energy to trap the migrating defects.

10.5 Diamond matrix size and surface effects on NV color center emission properties

Diamond surface effects appear to play a considerable role in the emission behavior of the NV centers, when these are situated in nanometer proximity. We need to consider three principal cases of the surfaces state: (1) emission quenching by the graphite sp^2 layer; its removal “liberates” NV emission; (2) surface functional groups affect NV emission: O- or H-based groups promote or inhibit NV emission; and (3) NV centers’ luminescence intermittency (blinking), important for elucidation of the NV center photophysics, is observed depending on the proximity to and type of interface.

10.5.1 NV emission quenching by the lax graphite sp^2 layer

It has been demonstrated that a graphite (sp^2) shell surrounding the detonation NDs caused suppression of the overall NV luminescence [32], whereas oxygen-containing surface groups appeared to activate the NV emission [68]. This shell represents a low-density layer of graphite, which is impregnated with noncarbon impurities, and loosely attached to the ND surface, as schematically shown in Table 10.1 (Phase 0). This lax graphite layer can be easily removed by acid cleaning and/or oxidative etching. As a result, the NV emission is “liberated” in the ND crystal host, i.e., the NV centers conversion from the latent nonemission state to active emission state takes place. In addition, the black carbon attenuation effect is dramatically reduced improving the NV excitation/emission optical properties. This was confirmed in HPHT NDs, whereby the latent NV centers were activated from 2% to ~8% of the total NDs that exhibited NV luminescence (compare Phase 0 and Phase 1, Table 10.1). The sp^2 layer consents to function as an electron acceptor causing discharge of the NV center to NV^0 or nonemission state [33,67].

Table 10.1 NV–ND Luminescence Analysis through the Treatment Phases				
Progressive Treatment	Phase 0: As Received	Phase 1: Acid Cleaning	Phase 2: Oxidize	Phase 3: Oxidize
Sample composition	Water, physisorbed impurities, graphitic carbon (sp ²), ND core (sp ³)	Traces of graphitic and amorphous carbon (sp ²) shell, ND core (sp ³)	ND core (sp ³)	Reduced ND core (sp ³)
Sample schematic view				
η_{em}	~2%	~8%	~8%	~8%
η_{blink}	<1%	~1%	~10%	~10%

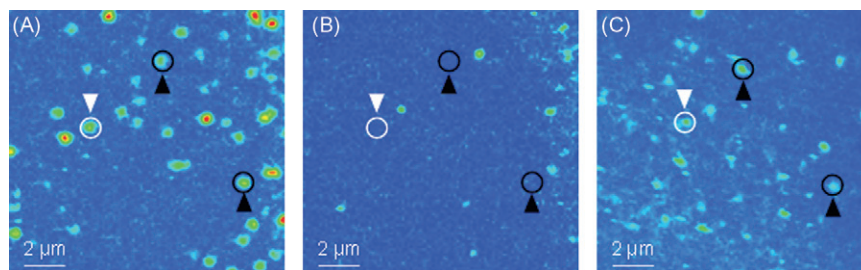
Source: Reproduced with permission from Ref. [66].
 Analysis of the NV centers' luminescence after progressive treatment of the hosting NDs. The sample composition and the luminescence of the NV centers are different at each progressive phase of the treatment. The quantity $\eta_{em} = N_{NV^-}/N_{ND}$ is the ratio between the number of luminescent NDs due to NV emitters (N_{NV^-}) and the total number of nanocrystals (N_{ND}). The quantity $\eta_{blink} = N_{blink}/N_{NV^-}$ is the ratio between the number of blinking centers (N_{blink}) and the number of luminescent NDs (N_{NV^-}).

10.5.2 Surface functional groups affect the emission

The surface functional groups appear to play a significant role in NV emission behavior. First of all, the surface oxidation is consented to activate the NV centers, and is commonly implemented by performing acid washing or thermal oxidative etching, or both. This is shown in Table 10.1, where the primary surface oxidation step resulted in profound recovery of the NV[−] centers.

It is the removal of the lax graphite layer that suppresses emission of the NV centers that is partly responsible for the emission recovery compounded by a healing effect of the surface carbon dangling bonds that results in restoring the ND crystal order [10]. It is important to note that the tight amorphous sp² carbon layer that is left after the acid washing of the HPHT ND sample has a low impact on the NV center emission states.

The hydrogen termination (C–H) of the ND surface resulted in a number of active NV emitters diminished almost 10-fold in comparison with that of the original oxygenated (C–O) NV–ND sample (Figure 10.6; not shown in Table 10.1). A subsequent oxidative treatment, such as the treatment used to remove a tight graphite layer (Phase 2) resulted in an almost complete recovery of the NV emission, as shown in Figure 10.6C, where a number of the NV luminescent centers reappeared at their original sites. Also, note that a number of blinking centers recovered their original blinking behavior after surviving in a latent dark state and when H terminated (marked by a white downward arrowhead; Figure 10.6).

**FIGURE 10.6**

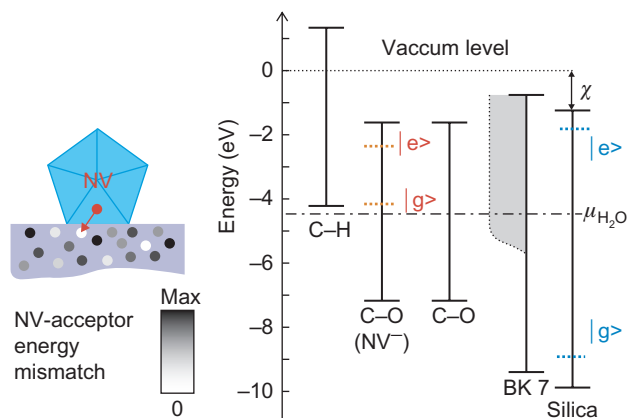
The effect of surface hydrogenation on the luminescent NDs. (A) NV luminescence after thermal oxidation. The black and white arrowheads point to stable and blinking NV emitters. (B) Hydrogenated NV centers exhibit diminished emission. (C) Reoxidation of the sample led to recovery of the NV emission and blinking. Additional emission sites are not NV centers being background fluorescence activated by the H- and O-treatment.

Source: Reproduced with permission from Ref. [66].

The effect of the ND surface hydrogenation (mediated by a layer of adsorbed water) on the charge state of the NV electron configuration has received much attention lately [68,74]. In brief, the H-moieties cause an upshift of the NV energy structure in the diamond subsurface layer due to the electron affinity modification, as shown in Figure 10.7, right panel (C–H). As a result, the valence band energy edge becomes leveled slightly above the electrochemical potential of water ($\mu_{\text{H}_2\text{O}}$), thereby driving electrons from the ND subsurface (several nanometers) layer to water until the ND subsurface layer of holes compensates the gradient forces. It causes charge depletion of the NV^- center that enters either NV^0 charge state [68] or an “unknown” dark (latent) state [68]. The overall effect of the surface functional groups on the NV emission state can be summarized as follows: the emission is immune to the surface effects, as long as the surface hosts no e^- acceptors, and the structural integrity of the diamond crystal host is not considerably compromised. This condition is realized in the case of the surface oxygenated ND, even though the surface is as proximal as 1 nm [33,75]. Otherwise, the surface e^- acceptors tend to scavenge the electrons from the NV center depleting the subsurface NVs, where the acceptor nature can represent either defects in the graphite layer produced by irradiation/annealing [33,67], or charge depletion by water in the case of ND surface hydrogenation [68]. A reservoir of e^- acceptors in the form of a nanometer-proximal substrate can, probably, trap the NV electrons in a reversible manner that is manifested via the blinking phenomenon that is considered in more detail in the following subsection.

10.5.3 NV center blinking

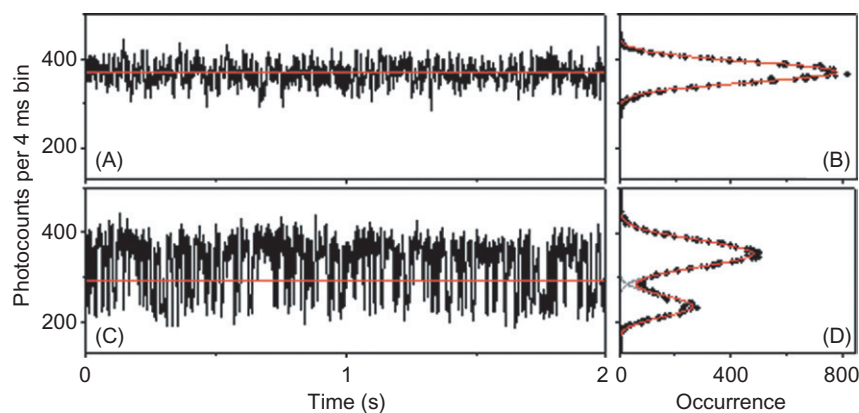
It has been reported that the NV center exhibits luminescence intermittency or blinking under certain experimental conditions, with emission randomly switching

**FIGURE 10.7**

(Left panel) A pictorial representation of the tunneling probability of the photoexcited electron from an NV site (red dot) to one of the acceptor site (gray dots), which must satisfy two conditions of proximity and small energy mismatch (shown by a red arrow). The energy mismatch between the NV center and the acceptor energy levels are gray color-coded, where the white color represents the equal match. (Right panel) Energy levels of some quantum systems with respect to the vacuum energy level, as inferred from the electron affinity (χ) data for silica, borosilicate glass, BK7. The gray-shaded area plot at BK7 represents a defect-populated absorption band. $\mu_{\text{H}_2\text{O}}$ denotes an electrochemical potential of pure water. C—O and C—H denote oxygen- and hydrogen-ND surface moieties. (For interpretation of the references to color in this figure legend, the reader is referred to the web version of this book.)

Source: Reproduced with permission from Ref. [66].

between “on” and “off” states, as shown in Figure 10.8 [17]. The vast theoretical and experimental knowledge base on the blinking phenomenon spans several types of individual quantum emitters, including single fluorescent molecules, atoms, and quantum dots [76,77]. Taken together, the fundamental complexity of this process is recognized as one of the challenges of modern physics [78]. The semiconductor quantum dot system is particularly important, as it is not susceptible to photobleaching, so that its emission statistics can be analyzed over tens of minutes. Quantum dot blinking is regarded as overly complex. The existing theoretical models, dominated by the Auger-assisted nonradiative relaxation concept, fail to capture the complex blinking statistics of single emitters [79]. The excitation/emission process in semiconductor quantum dots occurs via formation of an electron-hole charge pair (exciton), which is unbound, i.e., its probability distribution extends over the entire crystal. The blinking is thought to occur via reversible sequestration of one of the excitonic charges, such as the electron, to one of the surface or surrounding medium traps. Therefore, the quantum dot nanocrystal surface state and

**FIGURE 10.8**

Analysis of blinking statistics from the NV center in a detonation ND. (A) NV luminescence from NDs embedded in a PVA (Polyvinyl alcohol) polymer film, with (B) corresponding histogram fitted with a single Gaussian. (C) A single blinking NV-ND with (D) the corresponding histogram of the trajectory. Red lines in (A) and (C) show the mean count rate. (For interpretation of the references to color in this figure legend, the reader is referred to the web version of this book.)

Source: Reproduced with permission from Ref. [17].

adjacent surrounding profoundly affect the exciton and hence blinking behavior. The NV center has a comparable nonphotobleaching property. In contrast to semiconductor quantum dots, an exciton associated with the NV center is localized, and hence less susceptible to the surface state, offering a unique test base for the theoretical models developed for semiconductor quantum dot blinking emitters.

Referring to the NV-ND quantum system considered in Section 10.2, the blinking behavior of the nitrogen-color system was observed [66]. In particular, removal of the sp^2 tight amorphous carbon layer (Phase 2, Table 10.1) led to a dramatic increase in the percentage ratio of the blinking centers to the NV total number from ~1% (Phases 0 and 1, Table 10.1) to 10% (Phase 2, Table 10.1).

The dependence of blinking on the surface proximity invites an interpretation of the NV center blinking mechanism in terms of the charge separation and recombination, which is broadly in line with the existing theoretical framework developed for the semiconductor quantum dots [12]. The observed NV blinking can be explained as follows. An electron-hole pair generated by the NV center photoexcitation can lead to the electron (or hole) capture by an external trap located on the ND surface or adjacent medium, which results in the emission interruption, until the electron is not released from the trap to the NV center, or replaced with a donor electron, as e.g., from a N_s . The statistical analysis of the onset of blinking and subsequent annihilation revealed that a blinking center's most probable location was at 8 ± 4 nm from the interface [66]. It is consistent with the estimates of the tunneling barrier width in the blinking model for quantum dots [79]. This observation can be interpreted in terms

of the charge separation by assuming a photoexcited electron tunneling from the surface-proximal NV site to an electron-acceptor trap located in the adjacent medium. Two main conditions must be satisfied to make this process probable. Firstly, the NV site and acceptor must be close together (separated by ~ 5 nm) [77]. Secondly, the energy levels of the participating quantum systems must be close [79]. So, the blinking is probable only if an NV center has proximal access to a reservoir of quantum systems whose energy levels are distributed around the photoexcited NV energy level. The first condition was most likely satisfied as the surface proximity for blinking centers occurred at $d \cong 7$ nm. The second condition was tested by examining the energy level structures of the surface-oxidized (C—O) NV—ND and BK7, silica, and CO diamond for an acceptor level suitable for the tunneling process. The borosilicate glass and silica are particularly useful materials, as the former is a heavily doped derivative of the latter (compare Figure 10.7). The pure silica wide bandgap of ~ 9 eV is scarcely populated by defects, whereas the BK7 bandgap is heavily populated with defects leaving an ~ 4 eV unoccupied band, as shown in Figure 10.7. Hence, the BK7 substrate offers considerably more electron-acceptor energy levels for the tunneling electron, in comparison with the silica substrate.

One might think that losing one electron to the acceptor reservoir in the process of blinking converts the NV^- to an NV^0 center. However, no NV^0 centers were observed by Bradac et al. in both HPHT [65] and detonation NDs [17] that exhibited blinking. This is at odds with the existing body of results on the NV centers that exhibited interconversion between the neutral and negative charge states, as discussed in Section 10.3. Instrumental artifacts of these observations were ruled out by occasionally observing NV^0 centers in the NV—ND samples using the same experimental set up [17,65,66]. This observation can be explained by assuming the NV^- center conversion to an unknown “dark state,” as described by several authors [33,67,68]. Alternatively, NV^- can be converted to a neutral charge state, which is essentially nonradiative, that might relate to the “dark state.” In either case, this phenomenon warrants further study.

10.6 Conclusion

In this chapter, we reviewed the recent progress in understanding and harnessing the unique luminescent properties of an NV color center in diamond. Attention is focused on the understanding of spin polarization, the photoconversion between the charge states, and the influence the surface effects have on NDs and centers within nanometers of the surface.

The ground state has a spin $S = 1$, and optical excitation at room temperature transfers population from a spin projection of $m_S = \pm 1$ to the $m_S = 0$ spin projection. This can be explained through optical excitation of the spin triplet system with spin selective decay via singlet. The optical cycle at room temperature can be modeled in terms of a five-level model and it is shown how this is justifiable even with many other levels in the actual defect center. It is also explained how the interaction

of degenerate E-vibrations play a vital role in the intersystem crossing and contribute to making the NV center unique.

The photoconversion mechanism in diamond crystals that manifests itself via switching between the neutral and negative NV charge states is underpinned by the two different mechanisms and power dependence. There is an intrinsic two-photon process where electrons (holes) are excited to the conduction band that results in a reversible conversion between NV^- and NV^0 . This is the important process for low-concentration diamonds, which are involved in most spin applications. In high-nitrogen concentration diamonds, the NV center scavenges an electron from the close-by N_s via tunneling, and turns into NV^- . However, it is pointed out that if this occurs in the ground state the reverse process will occur in the excited state and so with excitation there will be conversion between NV^- and NV^0 .

The diamond surface proximity at the nanometer scale brings new effects into NV center emission behavior. Although it potentially can compromise the stability of the NV center resulting in its annihilation, the existing body of experimental evidence points to extraordinary stability of the center in as small as 4 nm ND host, and as small as 1 nm proximity to the diamond surface in macrocrystals. At the same time, the surface proximity can result in NV emission quenching by graphite sp^2 layer, where the removal of the sp^2 layer “liberates” emission. The surface functional groups affect the emission: the surface oxidation was found to promote the emission, whereas the surface hydrogenation turned out to inhibit it. Blinking, observed as a reversible random process of the luminescence interruption, is another surface-related effect that can be interpreted as the photoinduced excitonic charge tunneling (through the barrier width of ~ 7 nm) from the NV site to a close-by reservoir of the charge acceptors. Blinking is observed in many quantum systems in nature and explaining it in the case of this NV will be invaluable for understanding the process in the wider context.

The reviewed properties are believed to aid progress in biomedicine, quantum information science, and ultrasensitive magnetometry, which demand both the fundamental understanding of the NV optical and magneto-optical properties, and summary of the diamond surface effects that need to be precisely controlled to foster these applications.

References

- [1] L. du. Preez, Phd Thesis, University Witwatersrand, 1965.
- [2] G. Davies, M.F. Hamer, Optical studies of the 1.945 eV vibronic band in diamond, *Proc. Royal Soc. London Ser. A* 348 (1653) (1976) 285–298.
- [3] A. Gruber, A. Drabentstet, C. Tietz, L. Fleury, J. Wrachtrup, C. von Borczyskowski, Scanning confocal optical microscopy and magnetic resonance on single defect centers, *Science* 276 (5321) (1997) 2012–2014.
- [4] V. Dolmatov, M. Veretennikova, V. Marchukov, V. Sushchev, Currently available methods of industrial nanodiamond synthesis, *Phys. Solid State* 46 (4) (2004) 611–615.
- [5] E. Osawa, Monodisperse single nanodiamond particulates, *Pure. Appl. Chem.* 80 (7) (2008) 1365–1379.

- [6] S. Turner, O.I. Lebedev, O. Shenderova, I.I. Vlasov, J. Verbeeck, G. Van Tendeloo, Determination of size, morphology, and nitrogen impurity location in treated detonation nano-diamond by transmission electron microscopy, *Adv. Funct. Mater.* 19 (13) (2009) 2116–2124.
- [7] F.K. de Theije, O. Roy, N.J. van der Laag, W.J.P. van Enckevort, Oxidative etching of diamond, *Diamond Relat. Mater.* 9 (3–6) (2000) 929–934.
- [8] F.K. de Theije, N.J. van der Laag, M. Plomp, W.J.P. van Enckevort, A surface topographic investigation of {001} diamond surfaces etched in oxygen, *Philos. Mag. A* 80 (3) (2000) 725–745.
- [9] R.R. Nimmagadda, A. Joshi, W.L. Hsu, Role of microstructure on the oxidation behavior of microwave plasma synthesized diamond and diamond-like carbon films, *J. Mater. Res.* 5 (11) (1990) 2445–2450.
- [10] S. Osswald, G. Yushin, V. Mochalin, S.O. Kucheyev, Y. Gogotsi, Control of sp²/sp³ carbon ratio and surface chemistry of nanodiamond powders by selective oxidation in air, *J. Am. Chem. Soc.* 128 (35) (2006) 11635–11642.
- [11] T.L. Wee, Y.K. Tzeng, C.C. Han, H.C. Chang, W. Fann, J.H. Hsu, et al., Two-photon excited fluorescence of nitrogen-vacancy centers in proton-irradiated type Ib diamond, *J. Phys. Chem. A* 111 (38) (2007) 9379–9386.
- [12] F. Cichos, C. von Borczyskowski, M. Orrit, Power-law intermittency of single emitters, *Curr. Opin. Colloid. Interface Sci.* 12 (6) (2007) 272–284.
- [13] R.M. Dickson, A.B. Cubitt, R.Y. Tsien, W.E. Moerner, On/off blinking and switching behaviour of single molecules of green fluorescent protein, *Nature* 388 (6640) (1997) 355–358.
- [14] M. Kuno, D.P. Fromm, H.F. Hamann, A. Gallagher, D.J. Nesbitt, Nonexponential “blinking” kinetics of single CdSe quantum dots: a universal power law behavior, *J. Chem. Phys.* 112 (7) (2000) 3117–3120.
- [15] P.A. Frantsuzov, R.A. Marcus, Explanation of quantum dot blinking without the long-lived trap hypothesis, *Phys. Rev. B* 72 (15) (2005) 155321.
- [16] T. Jau, R.A. Marcus, Mechanisms of fluorescence blinking in semiconductor nanocrystal quantum dots, *J. Chem. Phys.* 123 (5) (2005) 054704.
- [17] C. Bradac, T. Gaebel, N. Naidoo, M.J. Sellars, J. Twamley, L.J. Brown, et al., Observation and control of blinking nitrogen-vacancy centres in discrete nanodiamonds, *Nat. Nano.* 5 (5) (2010) 345–349.
- [18] G. Balasubramanian, P. Neumann, D. Twitchen, M. Markham, R. Kolesov, N. Mizuochi, et al., Ultralong spin coherence time in isotopically engineered diamond, *Nat. Mater.* 8 (5) (2009) 383–387.
- [19] G.J. Milburn, Quantum measurement and control of single spins in diamond, *Science* 330 (6008) (2010) 1188–1189.
- [20] L. Childress, M.V. Gurudev Dutt, J.M. Taylor, A.S. Zibrov, F. Jelezko, J. Wrachtrup, et al., Coherent dynamics of coupled electron and nuclear spin qubits in diamond, *Science* 314 (5797) (2006) 281–285.
- [21] N. Gisin, G. Ribordy, W. Tittel, H. Zbinden, Quantum cryptography, *Rev. Mod. Phys.* 74 (1) (2002) 145.
- [22] G. Balasubramanian, I.Y. Chan, R. Kolesov, M. Al-Hmoud, J. Tisler, C. Shin, et al., Nanoscale imaging magnetometry with diamond spins under ambient conditions, *Nature* 455 (7213) (2008) 648–651.
- [23] J.R. Maze, P.L. Stanwix, J.S. Hodges, S. Hong, J.M. Taylor, P. Cappellaro, et al., Nanoscale magnetic sensing with an individual electronic spin in diamond, *Nature* 455 (7213) (2008) 644–647.

- [24] A.M. Schrand, S.A.C. Hens, O.A. Shenderova, Nanodiamond particles: properties and perspectives for bioapplications, *Crit. Rev. Solid State Mater. Sci.* 34 (1–2) (2009) 18–74.
- [25] M. Barth, N. Nüsse, B. Lochel, O. Benson, Controlled coupling of a single-diamond nanocrystal to a photonic crystal cavity, *Opt. Lett.* 34 (7) (2009) 1108–1110.
- [26] K.M.C. Fu, C. Santori, P.E. Barclay, I. Aharonovich, S. Prawer, N. Meyer, et al., Coupling of nitrogen-vacancy centers in diamond to a gap waveguide, *Appl. Phys. Lett.* 93 (2008) 23.
- [27] M.R. Henderson, B.C. Gibson, H. Ebendorff-Heidepriem, K. Kuan, S. Afshar, J.O. Orwa, et al., Diamond in tellurite glass: a new medium for quantum information, *Adv. Mater.* 23 (25) (2011) 2806.
- [28] Y.-Y. Chen, H. Shu, Y. Kuo, Y.-K. Tzeng, H.-C. Chang, Measuring Forster resonance energy transfer between fluorescent nanodiamonds and near-infrared dyes by acceptor photobleaching, *Diamond Relat. Mater.* 20 (5–6) (2011) 803–807.
- [29] Y.-R. Chang, H.-Y. Lee, K. Chen, C.-C. Chang, D.-S. Tsai, C.-C. Fu, et al., Mass production and dynamic imaging of fluorescent nanodiamonds, *Nat. Nano.* 3 (5) (2008) 284–288.
- [30] A. Krüger, F. Kataoka, M. Ozawa, T. Fujino, Y. Suzuki, A.E. Aleksenskii, et al., Unusually tight aggregation in detonation nanodiamond: identification and disintegration, *Carbon* 43 (8) (2005) 1722–1730.
- [31] A.S. Barnard, M. Sternberg, Substitutional nitrogen in nanodiamond and bucky-diamond particles, *J. Phys. Chem. B* 109 (36) (2005) 17107–17112.
- [32] B.R. Smith, D.W. Inglis, B. Sandnes, J.R. Rabeau, A.V. Zvyagin, D. Gruber, et al., Five-nanometer diamond with luminescent nitrogen-vacancy defect centers, *Small* 5 (14) (2009) 1649–1653.
- [33] L. Rondin, G. Dantelle, A. Slablab, F. Grosshans, F. Treussart, P. Bergonzo, et al., Surface-induced charge state conversion of nitrogen-vacancy defects in nanodiamonds, *Phys. Rev. B* 82 (11) (2010) 115449.
- [34] G. Davies, Dynamic Jahn–Teller distortions at trigonal optical centres in diamond, *J. Phys. C Solid State Phys.* 12 (13) (1979) 2551.
- [35] Y. Mita, Change of absorption spectra in type-Ib diamond with heavy neutron irradiation, *Phys. Rev. B Condens. Matter* 53 (17) (1996) 11360–11364.
- [36] S. Felton, A.M. Edmonds, M.E. Newton, P.M. Martineau, D. Fisher, D.J. Twitchen, Electron paramagnetic resonance studies of the neutral nitrogen vacancy in diamond, *Phys. Rev. B* 77 (8) (2008) 081201.
- [37] J.H.N. Loubser, J.A. van Wyk, Electron spin resonance in the study of diamond, *Rep. Prog. Phys.* 41 (8) (1978) 1201–1248.
- [38] A. Batalov, C. Zierl, T. Gaebel, P. Neumann, I.Y. Chan, G. Balasubramanian, et al., Temporal coherence of photons emitted by single nitrogen-vacancy defect centers in diamond using optical rabi-oscillations, *Phys. Rev. Lett.* 100 (7) (2008) 077401.
- [39] N.B. Manson, J.P. Harrison, M.J. Sellars, Nitrogen-vacancy center in diamond: model of the electronic structure and associated dynamics, *Phys. Rev. B Condens. Matter* 74 (10) (2006) 104303–104311.
- [40] L. Robledo, H. Bernien, T. van der Sar, R. Hanson, Spin dynamics in the optical cycle of single nitrogen-vacancy centres in diamond, *New J. Phys.* (2011) 13.
- [41] A. Jarmola, V.M. Acosta, K. Jensen, S. Chemerisov, D. Budker, Temperature and magnetic field dependent longitudinal spin relaxation in nitrogen-vacancy ensembles in diamond 112 (2012) 5936.
- [42] C.A. Coulson, M.J. Kearsley, Colour centres in irradiated diamonds, *Proc. R. Soc. London Ser. A Math. Phys. Sci.* 241 (1227) (1957) 433–454.

- [43] M.W. Doherty, N.B. Manson, P. Delaney, L.C.L. Hollenberg, The negatively charged nitrogen-vacancy centre in diamond: the electronic solution, *New J. Phys.* (2011) 13.
- [44] J.R. Maze, A. Gali, E. Togan, Y. Chu, A. Trifonov, E. Kaxiras, et al., Properties of nitrogen-vacancy centers in diamond: the group theoretic approach, *New J. Phys.* (2011) 13.
- [45] A. Batalov, V. Jacques, F. Kaiser, P. Siyushev, P. Neumann, L.J. Rogers, et al., Low temperature studies of the excited-state structure of negatively charged nitrogen-vacancy color centers in diamond, *Phys. Rev. Lett.* 102 (2009) 19.
- [46] K.-M.C. Fu, C. Santori, P.E. Barclay, L.J. Rogers, N.B. Manson, R.G. Beausoleil, Observation of the dynamic Jahn–Teller effect in the excited states of nitrogen-vacancy centers in diamond, *Phys. Rev. Lett.* 103 (25) (2009) 256404.
- [47] L.J. Rogers, R.L. McMurtrie, M.J. Sellars, N.B. Manson, Time-averaging within the excited state of the nitrogen-vacancy centre in diamond, *New J. Phys.* (2009) 11.
- [48] L.J. Rogers, S. Armstrong, M.J. Sellars, N.B. Manson, Infrared emission of the NV centre in diamond: Zeeman and uniaxial stress studies, *New J. Phys.* (2008) 10.
- [49] N. Manson, L. Rogers, M. Doherty, L. Hollenberg, Optically induced spin polarisation of the NV-centre in diamond: role of electron-vibration interaction, arXiv:1011.2840v1, 2010.
- [50] N.B. Manson, J.P. Harrison, Photo-ionization of the nitrogen-vacancy center in diamond, *Diamond Relat. Mater.* 14 (10) (2005) 1705–1710.
- [51] G. Waldherr, J. Beck, M. Steiner, P. Neumann, A. Gali, T. Frauenheim, et al., Dark states of single nitrogen-vacancy centers in diamond unraveled by single shot NMR, *Phys. Rev. Lett.* 106 (15) (2011) 157601.
- [52] A.T. Collins, The Fermi level in diamond, *New J. Phys. Condens. Matter* 14 (14) (2002) 3743.
- [53] C. Bradac, T. Gaebel, N. Naidoo, J.R. Rabeau, A.S. Barnard, Prediction and measurement of the size-dependent stability of fluorescence in diamond over the entire nanoscale, *Nano. Lett.* 9 (2009) 3555–3564.
- [54] J.R. Rabeau, A. Stacey, A. Rabeau, S. Prawer, F. Jelezko, I. Mirza, et al., Single nitrogen vacancy centers in chemical vapor deposited diamond nanocrystals, *Nano. Lett.* 7 (11) (2007) 3433–3437.
- [55] I. Vlasov, O. Shenderova, S. Turner, O.I. Lebedev, A.A. Basov, I. Sildos, et al., Nitrogen and luminescent nitrogen-vacancy defects in detonation nanodiamond, *Small* 6 (2009) 687–694.
- [56] P.H. Chung, E. Perevedentseva, C.L. Cheng, The particle size-dependent photoluminescence of nanodiamonds, *Surf. Sci.* 601 (18) (2007) 3866–3870.
- [57] K. Yakubovskii, G.J. Adriaenssens, Luminescence excitation spectra in diamond, *Phys. Rev. B* 61 (15) (2000) 10174–10182.
- [58] S. Bhattacharyya, O. Auciello, J. Birrell, J.A. Carlisle, L.A. Curtiss, A.N. Goyette, et al., Synthesis and characterization of highly-conducting nitrogen-doped ultrananocrystalline diamond films, *Appl. Phys. Lett.* 79 (10) (2001) 1441–1443.
- [59] M. Sternberg, P. Zapol, T. Frauenheim, D.M. Gruen, L.A. Curtiss, Molecular dynamics simulation of impurities in nanocrystalline diamond grain boundaries, in: J.P. Sullivan, J. Robertson, O. Zhou, T.B. Allen, B.F. Coll (Eds.), *Amorphous and Nanostructured Carbon*, vol. 593, Materials Research Society Symposium Proceedings. Materials Research Society, Warrendale, PA, 2000, pp. 483–487.
- [60] A.M. Panich, A.I. Shames, H.M. Vieth, E. Osawa, M. Takahashi, A.Y. Vul, Nuclear magnetic resonance study of ultrananocrystalline diamonds, *Eur. Phys. J. B* 52 (3) (2006) 397–402.
- [61] A.I. Shames, A.M. Panich, W. Kempinski, A.E. Alexenskii, M.V. Baidakova, A.T. Dideikin, et al., Defects and impurities in nanodiamonds: EPR, NMR and TEM study, *J. Phys. Chem. Solids* 63 (11) (2002) 1993–2001.

- [62] J. Tisler, G. Balasubramanian, B. Naydenov, R. Kolesov, B. Grotz, R. Reuter, et al., Fluorescence and spin properties of defects in single digit nanodiamonds, *ACS Nano*. 3 (7) (2009) 1959–1965.
- [63] Z. Du, A.F. Sarofim, J.P. Longwell, C.A. Mims, Kinetic measurement and modeling of carbon oxidation, *Energy Fuels* 5 (1) (1991) 214–221.
- [64] T. Ando, K. Yamamoto, M. Ishii, M. Kamo, Y. Sato, Vapour-phase oxidation of diamond surfaces in O₂ studied by diffuse reflectance Fourier-transform infrared and temperature-programmed desorption spectroscopy, *J. Chem. Soc. Faraday Trans.* 89 (19) (1993) 3635–3640.
- [65] T. Gaebel, C. Bradac, J. Chen, J.M. Say, L. Brown, P. Hemmer, et al., Size-reduction of nanodiamonds via air oxidation, *Diamond Relat. Mater.* 21 (0) (2011) 28–32.
- [66] C. Bradac, T. Gaebel, C.I. Pakes, A.V. Zvyagin, J.R. Rabeau, Effect of the nanodiamond host on a nitrogen-vacancy colour-centre emission state, in review, 2012.
- [67] C. Santori, P.E. Barclay, K.M.C. Fu, R.G. Beausoleil, Vertical distribution of nitrogen-vacancy centers in diamond formed by ion implantation and annealing, *Phys. Rev. B* 79 (12) (2009) 8.
- [68] M.V. Hauf, B. Grotz, B. Naydenov, M. Dankerl, S. Pezzagna, J. Meijer, et al., Chemical control of the charge state of nitrogen-vacancy centers in diamond, *Phys. Rev. B* 83 (8) (2011) 081304.
- [69] B. Palosz, C. Pantea, E. Grzanka, S. Stelmakh, T. Proffen, T.W. Zerda, et al., Investigation of relaxation of nanodiamond surface in real and reciprocal spaces, *Diamond Relat. Mater.* 15 (11–12) (2006) 1813–1817.
- [70] K. Iakoubovskii, M.V. Baidakova, B.H. Wouters, A. Stesmans, G.J. Adriaenssens, A.Y. Vul, et al., Structure and defects of detonation synthesis nanodiamond, *Diamond Relat. Mater.* 9 (2000) 861–865.
- [71] S.P. Russo, A.S. Barnard, I.K. Snook, Hydrogenation of nanodiamond surfaces: structure and effects on crystalline stability, *Surf. Rev. Lett.* 10 (2–3) (2003) 233–239.
- [72] A. Mainwood, Nitrogen and nitrogen-vacancy complexes and their formation in diamond, *Phys. Rev. B Condens. Matter* 49 (12) (1994) 7934–7940.
- [73] J. Martin, R. Wannemacher, J. Teichert, M. Bischoff, B. Kohler, Generation and detection of fluorescent color centers in diamond with submicron resolution, *Appl. Phys. Lett.* 75 (20) (1999) 3096–3098.
- [74] M.T. Edmonds, C.I. Pakes, S. Mammadov, W. Zhang, A. Tadich, J. Ristein, et al., Surface band bending and electron affinity as a function of hole accumulation density in surface conducting diamond, *Appl. Phys. Lett.* 98 (10) (2011) 102101.
- [75] K.M.C. Fu, C. Santori, P.E. Barclay, R.G. Beausoleil, Conversion of neutral nitrogen-vacancy centers to negatively charged nitrogen-vacancy centers through selective oxidation, *Appl. Phys. Lett.* 96 (12) (2010) 121907.
- [76] F.D. Stefani, J.P. Hoogenboom, E. Barkai, Beyond quantum jumps: blinking nanoscale light emitters, *Phys. Today* 62 (2) (2009) 34–39.
- [77] F. Cichos, C. von Borczyskowski, M. Orrit, Power-law intermittency of single emitters, *Curr. Opin. Colloid. Interface Sci.* 12 (6) (2007) 272–284.
- [78] P. Frantsuzov, M. Kuno, B. Janko, R.A. Marcus, Universal emission intermittency in quantum dots, nanorods and nanowires, *Nat. Phys.* 4 (5) (2008) 519–522.
- [79] M. Kuno, D.P. Fromm, S.T. Johnson, A. Gallagher, D.J. Nesbitt, Modeling distributed kinetics in isolated semiconductor quantum dots, *Phys. Rev. B* 67 (12) (2003) 125304.

Nanocarbons in Energy Conversion

11

Dieter M. Gruen

Materials Science Division, Argonne National Laboratory, Argonne, IL

CHAPTER OUTLINE

11.1 Introduction	357
11.2 Entropy-of-mixing of charge carriers with quantum states.....	359
11.3 Thermoelectric properties of core/shell UNCD/graphene.....	362
11.3.1 Ensembles.....	362
11.4 Synthesis and properties of nanosilicon carbide core/graphene shell nanoensembles.....	370
11.5 Concluding remarks	376
Acknowledgments.....	378
References	378

11.1 Introduction

All human activity requires energy. The assured availability of large amounts of energy at affordable cost therefore constitutes the basis for the continued existence and progress of civilization. The realization of that goal will ultimately require the development of alternative energy sources.

The quest for alternative energy has spurred intense efforts by scientists, technologists, industrialists, politicians, and others because of the worldwide recognition of the magnitude of the problem. Vast structural changes and capital investments are required to implement new energy systems. In particular, the nature of the scientific and technical problems are coming into sharper focus and are becoming ever more apparent as concrete steps are taken to replace fossil fuels on a meaningful scale with fission, fusion, or solar energy sources.

All energy systems have three major components: production, storage, and distribution. A widely accepted recognition is emerging that identifies many of the

crucial problems associated with implementation of each of these three components as due to a lack of suitable materials. New, still to be discovered materials are needed that can perform their tasks under the extremely stringent conditions typically associated with sustainable energy systems. Only major breakthroughs can lead to the creation of such materials.

The discovery and development of nanocarbons may constitute one of the needed breakthroughs that has come along in time to have an impact on energy technologies by providing new materials with potentially improved performance characteristics. Nanocarbons were virtually unknown just 20 years ago. This situation changed dramatically with the discovery of the fullerenes, which led to still further nanocarbon discoveries such as nanotubes, ultrananocrystalline diamond (UNCD) films, and graphene. This chapter will describe recent research results obtained with a view to eventual application of nanocarbon materials to problems in energy conversion. As will become apparent, UNCD, graphene, and nanosilicon carbide, and another sp^3 -bonded nanocarbon have played a central role in this effort.

State-of-the-art thermoelectric materials have heat to electricity conversion efficiencies of about 10%. One has to be able to reach efficiencies of 30–40% in order to compete with engines using electromagnetic induction technology. Clearly, to meet this enormous challenge, new breakthrough materials are required that can reach figure of merit values for ZT of four or above compared to present-day values near unity [1]. Although thermodynamics does not place an upper limit on ZT , other considerations, such as the Wiedemann–Franz law, show that achieving $ZT=4$ presents major materials hurdles.

This chapter presents and elucidates one such approach from both experimental and theoretical points of view. We examine the role entropy plays as a factor determining thermoelectric conversion efficiency. Synthetic procedures to enhance entropic flows will be explored and theoretical considerations discussed that inform the experiments. The starting point is the very definition of thermopower in terms of the entropy transported along a temperature gradient per added charge carrier. Since thermopower enters the figure of merit as the square of that quantity, its optimization should obviously be of the highest priority in the quest for high ZT . Of course, a low value of the thermal conductivity is also extremely important as well as a high value of the electrical conductivity.

Many years ago, Jonker [2,3] showed the existence of a strong coupling between thermopower and carrier density. At constant density of states, the former decreases linearly as a logarithmically increasing function of the latter. The existence of this coupling is one of the major factors that has frustrated the achievement of a high power factor (PF), the product of the square of the thermopower and the electrical conductivity. The supposition underlying the approach to thermoelectricity presented in this chapter is that the achievement of high ZT requires at least the efficient conversion of configurational entropy to electronic entropy. It follows from that supposition that one must be able to optimize those two quantities

simultaneously. The theoretical foundation for these statements will be presented in the body of this chapter. For now, it will suffice to say that the nanoensemble approach with which this chapter is concerned was adopted by us in order to create possibilities from a materials point of view for the simultaneous optimization of these two very important quantities. If successful, this approach should enable one to treat thermopower and electrical conductivity as independent experimental variables. In principle, such an approach has the potential to achieve higher PFs than possible up to now. This chapter focuses on the problems that must be overcome to make entropy transport across interfaces a viable alternative way to achieve high efficiency thermoelectrics.

11.2 Entropy-of-mixing of charge carriers with quantum states

A crucial unsolved problem in thermoelectricity is the enhancement of the conversion efficiency of heat to electricity. This can only be done by discovering and developing ever more efficient thermoelectric materials. Since thermoelectric devices are heat engines, the Carnot efficiency is the highest achievable efficiency. For power generation, thermoelectrics operating in the temperature range of about 300–1200 K, the Carnot efficiency is 75%. Unfortunately, the performance of state-of-the-art materials is only about 10% leaving much room for improvement. Although reaching 30–40% efficiencies would constitute a very important breakthrough in energy conversion technology and is not theoretically excluded, the achievement of this goal is daunting indeed.

It would clearly be advantageous to base an effort in thermoelectric materials development on a complete theoretical treatment of the thermoelectric effect. However, such a treatment grounded on a detailed transport theory involving aspects of Onsager's irreversible thermodynamics [4] as well as Feynman's variational approach to electron–phonon interactions [5] is not available at present. It appears to us that any such theory, should it be developed, will have to involve entropy as a central concept underlying thermoelectric performance. Thus, we have chosen to concentrate our attention on a search for a new class of thermoelectric materials with properties designed simultaneously to optimize both the transformation of lattice to carrier entropy and the transport of carrier entropy in a thermal gradient.

The thermoelectric power, α , according to a thoroughgoing analysis by Callen [6] based on irreversible thermodynamics, can be considered as the entropy transported per coulomb of electron flow. According to this view, the fundamental quantities associated with variations in the magnitude of the thermopower then are due to changes in the amounts of carrier entropy. It follows that thermoelectricity is due to the transformation of heat, lattice vibrational entropy, into electronic entropy. Clausius coined the term “entropy,” which means transformation, in the 1850s when he and Lord Kelvin found entropy to be a necessary concept in the formulation of the

second law of thermodynamics. Only later was entropy associated with probability as expressed in the famous equation

$$S = k \ln W \quad (11.1)$$

where S equals entropy and W the number of states of a system. Although the Boltzmann formalism codified in 1882 in Eq. (11.1) has many interpretations, it was Planck who recognized its importance as the link between classical thermodynamics and quantum theory. In the intervening years, much has been done to develop an understanding of the relationship between entropy and thermoelectricity based on quantum mechanical considerations [7]. Here, use is made of some of the salient results of this extensive body of work. In the following paragraphs, a heuristic attitude is taken both as regards these theoretical developments and particularly their potential applications to the development of new materials. The approach taken here is clearly only one of a number of different ways that insights into carrier entropy transport and might be translated into the development of new thermoelectric materials.

If one restricts oneself to noninteracting charge carriers, then the contribution to the Seebeck coefficient is the entropy-of-mixing associated with adding a single charge carrier. Considering an idealized situation in which n fermion charge carriers are distributed among N states, one can derive the following expression, after applying the Stirling approximation [8]:

$$dS/dn = k \ln[(1 - c)/c] \quad (11.2)$$

where $c = n/N$. The validity of the underlying assumption of noninteracting carriers depends very much on the details of the structure and composition of the particular material under investigation. In any event, one of the aims of the current development effort is to synthesize materials where the degree of carrier interaction with phonons is one of the variables over which one can exercise a certain amount of control.

It is instructive to examine Eq. (11.2) in more detail in order to better understand some of the basic factors influencing the magnitude of S . One would like to be able to achieve as large a value of S as possible since it enters the expression for the figure of merit as the square. Clearly, increasing S can be achieved by decreasing c . At constant N , a decrease in c means a corresponding decrease in n . Since the product of n and the carrier mobility equals the conductivity, σ , the reduction in n has a negative effect on the magnitude both of the PF and the figure of merit, Z . Alternatively, one can decrease c by increasing N while keeping n fixed. As can be seen, Eq. (11.2) makes clear the underlying reason for the universally observed close coupling of thermopower and electrical conductivity. Experience shows that optimizing the PF always involves a compromise between the magnitudes of these two quantities if one restricts oneself, as customary, to monophasic systems. A reasonable conclusion considering this state of affairs might be that uncoupling thermopower from electrical transport can have only limited success if one restricts oneself to monophasic systems.

In principle, the limitation described above could perhaps be ameliorated if it were possible simultaneously to increase both n and N enabling their ratio to be kept at a low value. This approach would have the effect of increasing the conductivity without decreasing S . One way of accomplishing such a desirable outcome would be the introduction of a biphasic system, one of whose components primarily controls the carrier density and mobility while the other primarily provides a high density of states within thermal energies of the Fermi level. Implementation of such an approach will require appropriate “carrier” and “state” materials that are strongly interactive in the sense of promoting the creation of interfacial regions conducive to enhancing the thermoelectric phenomena resulting from the entropy-of-mixing process.

Considering the thermoelectric effect to be composed of two linked processes, entropy transfer and entropy transport, suggests the use of a biphasic material composed of a semiconductor in contact with a metal. The nature of the junction between these two phases then comes to play a crucial role in that carriers must be able to move relatively freely from one phase to the other. To accomplish the transformation of the semiconductor’s configurational entropy into carrier entropy appears to require slow carriers self-trapped in the “polaron” field of the semiconductor. On the other hand, efficient transport of that entropy requires high carrier mobility. When carriers cross the interface and reenter the metallic phase, the resultant increase in electrical conductivity can be expected to be that characteristic of electrons in metals. Clearly, establishing an appropriate balance between carrier–lattice interactions in the two components constituting the biphasic nanoensembles will determine to a considerable extent the difference in electron mobility in the two phases. This requirement, although challenging, may be met through advances in areas such as the design of compatible semiconductor/metal orbital energy level structures leading to ohmic junctions with barriers whose heights can be adjusted to a certain degree by a variety of different methodologies [9].

The interfacial regions in which the thermoelectric phenomena described above are active will almost surely be limited by “proximity” effects because the excess energy in the form of entropy that enables carriers to cross the interfacial barrier will be attenuated at a certain rate in the metallic phase. A relatively thin coating of the metallic phase surrounding nanostructured semiconductors is therefore a preferred embodiment. The synthesis of materials with substantial volumetric ratios of interface to bulk is desirable also from the point of view of maximizing the impact on the intrinsic thermoelectric properties of a material. These requirements could be fulfilled by bulk structures composed of nanoparticles each in turn constituted of semiconducting cores surrounded by metallic shells. Reflecting the interactive nature of the nanoparticles, we call the resulting substances bulk nanoensembles. In order to gain an understanding of the problems that have been encountered in our systematic attempt to create materials that would ultimately allow optimization of entropy transformation and entropy transport processes, we describe the sequential steps that have been taken in this quest up to now.

11.3 Thermoelectric properties of core/shell UNCD/graphene

11.3.1 Ensembles

To achieve high Carnot efficiency one requires refractory nanomaterials that resist recrystallization at high temperatures. To have an impact on global electricity generation, these materials must not be resource limited, be relatively inexpensive, and be environmentally benign. The list of candidate materials fulfilling these demanding requirements is very short. The choice of materials is even further restricted by the need to use two materials, one to function in the role of an entropy transfer agent and the other to enhance entropy transport.

The first stage in a still continuing materials development program was focused on the synthesis and characterization of nanocarbon ensembles composed of nano-diamond cores and nanographite (NG) shells. The experimental results as well as their theoretical treatment will now be briefly described.

Doped diamond is known to have excellent semiconducting properties and doped graphite is a well studied semimetal. The thermoelectric properties resulting from a combination of these two materials provide considerable insight into the validity of the current approach in part because density functional theory can be applied in a relatively straightforward and rigorous way to this low atomic number monoelemental but nonetheless biphasic nanoensemble.

It was shown that reaction of mixtures of disperse UNCD having particle sizes of about 5 nm and 5 wt% boron carbide (B₄C) with methane gas at temperatures near 1200 K results in mechanically rigid compacts resulting in boron-doped nanocarbon ensembles [10,11]. The amount of boron that enters into substitutional solid solution in the nanocarbon ensembles as a dopant is only a small fraction of the quantity added initially [12]. Strongly temperature-dependent PFs ($PF = \alpha^2 \sigma$, where α is the Seebeck coefficient and σ the electrical conductivity) that increase 30- to 40-fold between ambient and 1000 K were found for boron-doped versus undoped material. Measurements of PFs were made up to 1200 K on samples annealed at temperatures up to 2500 K. The nanoensembles that gained between 70% and 100% in weight, with the greatest change occurring between 950 and 1050 K during reaction with methane, had densities of 1.5–1.7 g/cm³. Ensembles heated to 1200 K are called “as-fabricated” samples to distinguish from samples that have been annealed in a mixture of Ar-4% H₂ in a furnace with SiC heating elements to 1700 K and in a carbon furnace in argon to 2500 K for varying lengths of times.

Scanning electron microscopy (SEM) micrographs were obtained using a HITACHI S-4700 field emission gun scanning electron microscope. Raman spectra at an excitation wavelength of 632.8 nm were collected at room temperature, using a Renishaw micro-Raman RM2000 on a 50X objective over the range of 50–4000 cm⁻¹ using an ~1 μ m spot size. X-ray diffraction (XRD) data (Rigaku miniflex + diffractometer with Cu–K-alpha radiation ($\lambda = 0.154$ nm)) were collected from 3° to 90° 2 θ with a scan speed of 2s/step and a step size of 0.02°. Diffraction patterns were taken of as fabricated and as well as of annealed samples. Phase identification was based on the International Center for Diffraction Data Base.

High-resolution transmission electron microscopy (HRTEM) was performed using a field emission FEI Tecnai F20 operating at 200 keV. The TEM samples were prepared by scraping the compact bulk samples and dispersing the resulting powders in ethanol. The dispersions were ultrasonicated and subsequently deposited on a holey carbon 3 mm copper grid.

Seebeck coefficients and dc electrical conductivities were measured using an apparatus based on a well-established design [13]. It consists of a 1800 K, single-zone tube (mullite, 4.4 cm inside diameter) furnace and controller, a Keithly 2700 multimeter/data acquisition system, and a Keithly 6220 current source, all controlled by a computer using LABVIEW. The ends of the tube were water cooled and sealed with end caps that allowed fittings for thermocouples and gas inlet/outlet valves.

SEM measurements demonstrated that the original UNCD particles retained their shape and size though they agglomerate and are surrounded by carbon deposits that grew as a result of the reaction with methane.

The Raman scattering spectra, typical of high temperature carbon nanostructured materials under red laser excitation, reveal peaks at around 1330 and 1595 cm^{-1} , which are assigned to the disorder-induced and E_{2g} modes of graphite, respectively (Figure 11.1). The D/G intensity peak ratio, extrapolated from the spectra after fitting of the data with a Gaussian function and subtraction of the baseline for each spectrum, is related to the cluster size or in-plane correlation length

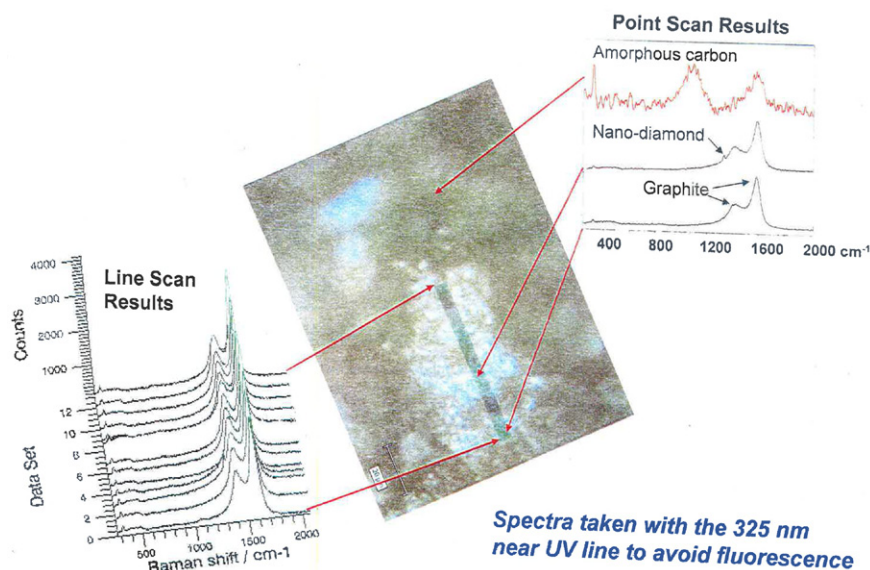
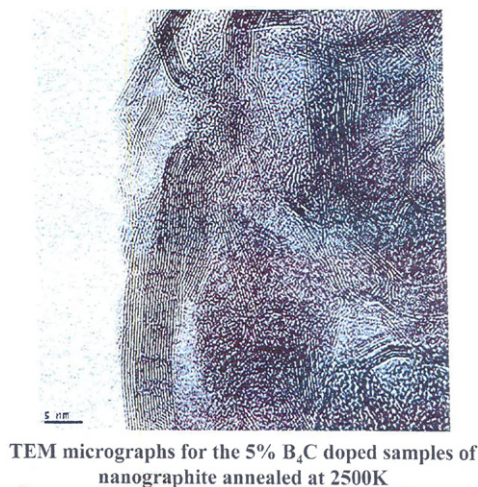


FIGURE 11.1

Raman spectra of nanocarbon ensembles containing UNCD cores surrounded by graphitic and amorphous carbon shells.

**FIGURE 11.2**

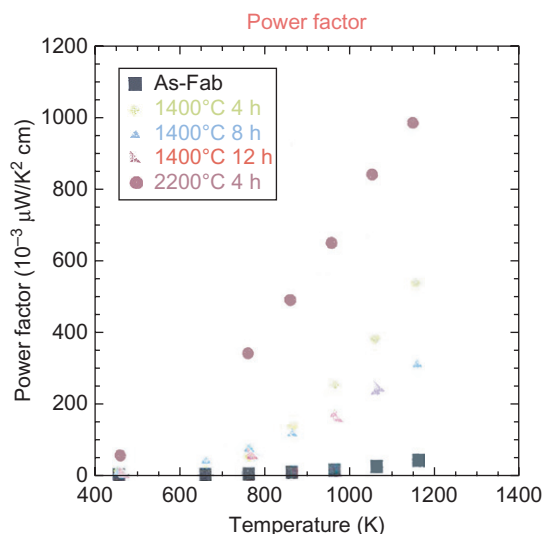
HRTEM of highly electrically conducting hollow polyhedral NG structures formed at annealing temperatures of 2500K.

($L\alpha$) [14,15] which turned out to be about 26nm, consistent with TEM measurements. Graphite peak intensity increased and peak width decreased with annealing temperatures above 1500 K as expected. Diamond content decreased as a function of temperature, and graphitization was complete above about 1700 K.

TEM shows that reaction with methane surrounds the original UNCD particles with several kinds of sp^2 -bonded carbons. Annealing of the as-fabricated ensembles at 1700 K for 12 h induces graphitization of the UNCD particles. This process becomes more pronounced as the annealing time is increased from 12 to 16 h. After the longer annealing time, the UNCD content is reduced and is replaced by a complex mixture of nanocarbon filaments, needles, and cones. Annealing at 2500 K for 4 h completely transforms the original ensembles. The amount of sp^3 -bonded carbon is significantly reduced and replaced by agglomerates of nonporous structures, showing graphitic curved surfaces (Figure 11.2).

Seebeck coefficient (α) and dc electrical conductivity (σ) measurements showed that increasing annealing temperature and times strongly enhanced the Seebeck coefficients and increases the PF by as much as an order of magnitude. The 2500 K anneals produced the highest PF in part because of the dramatic increase in electrical conductivity (Figure 11.3). Thermal conductivities of the nanoensembles are in the range of 0.03–0.07 W/cm K [16]. Figures of merit calculated for the nanocarbon ensembles are too low to be of practical interest.

It has been known for a long time, based on band structure calculations of graphite, that boron doping induces an acceptor-like feature near the top of the valence band. Subtle details of changes in the electronic structure of graphitic

**FIGURE 11.3**

PFs of nanocarbon ensembles as a function of temperature after various temperature anneals.

materials resulting from boron substitutions, however, cannot be deduced from such calculations. On close consideration of this and other thermoelectric systems it became apparent that the details of dopant substitution in the graphite as well as in other lattices likely play a crucial role in determining thermoelectric properties. A plausible postulate was therefore advanced [10] that a multitude of boron substitutional configurations each with a distinctive energy leading to a plethora of electronic states are intimately involved in determining the thermopower of a material. A corollary of that postulate is that various boron dopant configurations provide a mechanism by means of which large configurational entropies can be created [10].

These key insights stimulated a collaboration with L. Curtiss and P. Redfern that led to a reexamination of the nature of the acceptor-like feature using density functional calculations. In the calculational work, boron-substituted polyaromatics served as molecular models with results also on stacked graphene sheets [17]. Quantitative relative stabilities of Kekule versus non-Kekule structures and orbital energetics of various boron substitutional configurations were obtained which will be detailed below. Anticipating the more complete discussion to follow, one may conclude that the molecular analogue calculations confirm in exquisite detail the main features of the arguments set out in Ref. [10].

The magnitude of the electrical conductivity, σ , suggests that one is dealing with hopping conductivity [18] characteristic of disordered materials with a local disordering length of a few interatomic distances. A qualitative description of the conductivity changes observed in the nanocarbon ensembles can be given on the

basis of Mott's concept of hopping conductivity [19]. At annealing temperatures up to 1700 K, conductivity occurs primarily along carbon chains and defected planes. At higher temperatures, graphene sheets, fullerenic structures, and other curved surfaces provide better conduction paths. Finally, at the highest annealing temperatures, 2500 K, the formation of hollow polyhedral NG structures with reduced numbers of defects provides excellent conduction paths leading to σ values of 300 S/cm and above. Clearly, a more detailed understanding of conductivity in these materials will require both extensive experimental measurements, for example, of the temperature dependence of the conductivity and of the Hall coefficients. Thoroughgoing theoretical treatment of electronic transport in these nanoporous materials will also be necessary. In any event the dramatic effects of annealing on the magnitude of α and σ can be qualitatively understood on the basis of an increased solubility of boron in graphite with temperature on the one hand and more favorable conduction paths arising from highly ordered and less-defective graphite layers on the other.

The results on the nanocarbon ensembles are interesting particularly from the point of view of the light they shed on the transformation of UNCD to NG as a function of temperature. Of particular relevance is the work of Kuznetsov and Butenko [18] and Kuznetsov et al. [20] as well as that of Andersson et al. [21]. This by now a quite well-developed subject will be discussed here only to the extent that it relates to thermoelectric properties. Annealing affects on the magnitudes of α and σ occur not only because of changes in boron solubility and ordering of graphene structures but also because of the transformation of UNCD to NG. In the as-fabricated ensembles, UNCD is the primary constituent prior to reaction with methane. The UNCD to NG transformation has been followed using XRD, HRTEM, and Raman characterization techniques. The diamond (111) reflection is at a somewhat smaller 2θ angle than the graphite (100) and (101) reflections and overlaps the latter two reflections, thus making it difficult to use the Bragg region to follow the transformation quantitatively. Data analysis is therefore based on a determination of the ratios of intensities of the diamond (002) near 75° relative to the graphite reflections near 80° . In this Bragg region, the diamond and graphite reflections are reasonably well resolved. The detailed work of Andersson et al. [21] provides baseline information regarding the temperature-dependent transformation of disperse UNCD to graphite. Their data and those described here are in excellent agreement.

The HRTEM micrographs taken after various annealing temperature treatments substantiate the conclusions reached on the basis of the XRD measurements. As an example, nanodiamond ensembles (NDEs) annealed at 2100 K show a greatly diminished number of UNCD crystallites compared to the as-fabricated compacts with only a few 2–5 nm UNCD particles remaining after 2100 K treatment. Structures displaying graphitic and curved surfaces abound with equidistant sheets forming essentially defect-free layers.

Density functional theory was used to explore the concept of configurational entropy mentioned above, which is an important aspect of the approach to thermoelectricity that is examined here. The basic idea is that dopant configurations allow

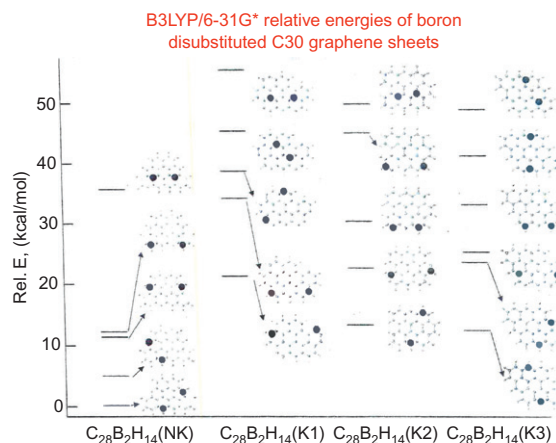
one, under certain circumstances, to introduce a plethora of electronic states that lie within thermal energies of the Fermi level allowing a semiconductor having these characteristics to efficiently transform configurational to electronic entropy. The molecular analogue calculations employed here examine in great detail the wave functions associated with each individual dopant configuration and the relevant energetics and orbital hybridizations. Acquiring a detailed understanding of the electronic structure of the solid involved in the transformation of heat to electricity represents an important step in gaining a fundamental understanding of this process.

The calculations were done with the B3LYP functional [22] along with the 6-31 G* basis set. The GAUSSIAN03 set of computer codes [23] was used for all calculations. Spin-unrestricted methods were used for open-shell species. All calculations were done as molecular systems, i.e., nonperiodic. Unless noted, the results are based on complete geometry optimizations, including the boron-substituted nanographene which were investigated as models both for Kekule and non-Kekule systems. In previous studies, the B3LYP density functional methods have been found to give reliable HOMO-LUMO gaps for related species [24] as well as singlet–triplet energy differences [25,26]. Stacks of nanographene sheets were also investigated and their energy levels were determined with density functional based tight binding (DFTB) [27–29], which has proven reliable for studies on a variety of carbon-based materials [30,31].

Non-Kekule structures have an even number of π electrons, but the topology of the sheet makes it impossible to write a resonance structure in which each π electron is paired with another on a neighboring carbon [32,33]. Importantly, these calculations determined the stabilities of non-Kekule graphene structures, which may very likely be present in the nanocarbon ensembles [10,11] relative to the stabilities of Kekule-type structures. For example, the B3LYP/6-31 G* relative energies of different spin multiplicities of the non-Kekule $C_{22}H_{12}$ show that the triplet is 23.4 kcal/mol more stable while in the case of the $C_{30}H_{14}$ structure the triplet is 19.4 kcal/mol more stable.

For the $C_{30}H_{14}$ graphene sheet, a more extensive investigation of various substitutional sites for borons was carried out with full geometry optimization so that they would be consistent with unsubstituted all-carbon sheets. Figure 11.4 illustrates the relative energies of different double boron substitutions in four different $C_{28}B_2H_{14}$ graphene structures. The results indicate that the most stable doubly substituted graphene sheet is the one with the non-Kekule form for the pristine sheet. In addition, the results in Figure 11.4 indicate that boron substitution in the non-Kekule structure generally results in a more stable structure than for substitution in a Kekule structure, if one considers similar boron siting. The boron substitutions in non-Kekule graphene structures tend to be more stable than in the Kekule graphene structures because the high spin non-Kekule graphene ground states have three coordinated carbons with an unpaired electron that are favorable for boron substitution.

The reaction energy for double boron substitution in $C_{30}H_{14}$ is endothermic by 55–110 kcal/mol relative to removal of two carbon atoms for different

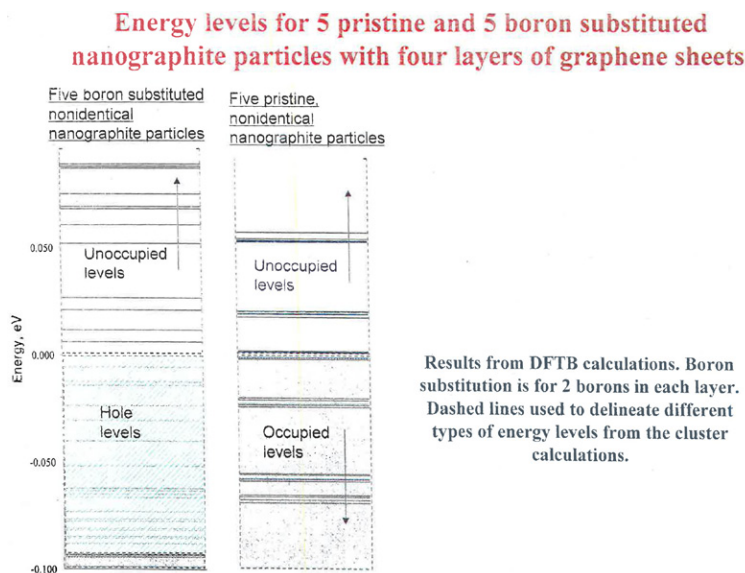
**FIGURE 11.4**

Relative energies between four different boron configurations comparing one non-Kekule (NK) with three different Kekule (K1, K2, and K3) graphene structures each composed of $C_{28}B_2H_{14}$.

boron-substituted structures considered for $C_{30}H_{14}$. The large endothermic reaction energies for boron substitution are consistent with the low solubility of boron in graphite of about 2% at high temperatures [12].

The results of the density functional calculations on the pristine and boron-doped graphene systems provide a framework for considering certain aspects of the behavior of the Seebeck (S) coefficient found for boron-doped NG [10,11]. First, the calculations indicate that in the pristine systems the electronic states are high spin when the system has a large enough number of carbon atoms. This occurs at around 72 carbon atoms for Kekule structures and at the smallest number of carbons necessary to form a non-Kekule structure. The high spin state of all carbon systems implies the existence of both p- and n-type carriers leading to small S values [34]. This conclusion is consistent with the small S values that were experimentally found for all the carbon NG ensembles without boron doping where the S values are found to be close to zero with little temperature dependence [10].

The calculations also show that boron substitution leads to low spin nanographene sheets, unlike the pristine unsubstituted all carbon sheets. This implies that boron lowers the energy of the highest occupied orbital resulting in holes in the valence orbital energy levels. These results are consistent with a number of experimental as well as theoretical studies of boron substitution in bulk graphite, nanotubes, and graphene nanoribbons that show boron creating holes at the top of the valence band and a lowering of the Fermi level [35,36]. These previous theoretical results described in the literature have been based on periodic density functional calculations. A similar situation occurs in the finite or molecular analogue

**FIGURE 11.5**

Calculated energy levels near the HOMO-LUMO gap for five pristine (unsubstituted) particles compared with five substituted particles each consisting of a stack such as shown in Figure 11.6.

nanographene systems as well but here it is possible to show in detail that each boron “configuration” gives rise to a unique electronic state signature reflecting subtle changes in orbital energies.

In addition to the calculations on small individual graphene sheets, DFTB calculations were also done on a model of four stacked graphene sheets each consisting of about 100 carbon atoms. Each of these sheets can have almost $5 \times 10 + 3$ different configurations of doubly substituted borons. The calculated energy levels near the HOMO-LUMO gap for the pristine and di-boron-substituted system of five NG particles, each consisting of a stack of four 100 carbon atom sheets, are illustrated in Figure 11.5. The figure shows the levels corresponding to the creation of holes due to boron substitution and a concomitant lowering of the highest occupied energy level by 0.1 eV.

In the carbon ensembles studied experimentally [10,11] where the number of carbon atoms is $10 + 5 - 10 + 7$ instead of $10 + 2$, the number of possible boron geometric configurations in each nanoparticle becomes quite large. Each configuration, as we have seen, is associated with a distinct NG structure, and because of the subtleties of orbital energy levels each structure gives rise to a distinct electronic state. In principle then, the creation of “holes” at the top of the valence band by the electron-deficient borons creates many empty, perhaps nearly degenerate electronic states. The model presented here suggests that boron substitution lowers the Fermi

level of graphene sheets by about 0.1 eV. The large number of empty states that owing to this circumstance can be populated thermally thus provides a mechanism for the efficient transformation of configurational to electronic entropy and thus for the conversion of heat to electricity.

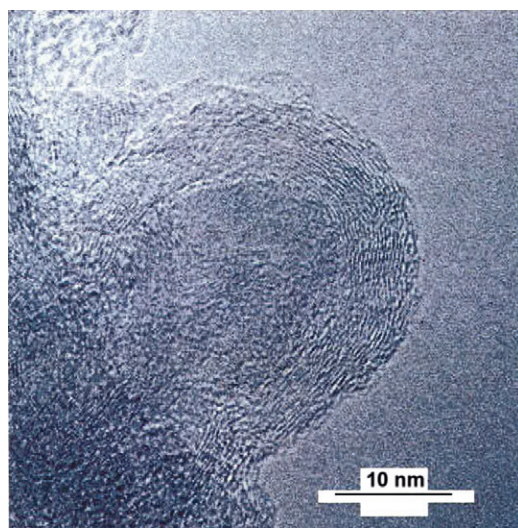
11.4 Synthesis and properties of nanosilicon carbide core/graphene shell nanoensembles

The work on UNCD/graphene nanoensembles has shown that the thermopower of boron-doped diamond, which exceeds $300\mu\text{V/K}$ according to published reports [37], is not maintained in the nanoensembles where it did not exceed about $50\mu\text{V/K}$ thus severely limiting the thermoelectric performance of the nanoensembles. The reduction in the thermopower of diamond in our nanoensembles is likely due to the fact that the thick graphene shell carries an overwhelming fraction of the total current and severely dilutes the expected entropy enhancement effect due to the presence of highly mobile carriers. A new ensemble that allows one to control the ratio of core to shell so as to be able to control the fraction of current carried by the shell is required. As will be seen, such an ensemble has in fact been realized through the creation of nanosilicon carbide core/graphene shell structures.

It has been shown by several different groups of investigators, for example, by Charrier et al. [38], that the thermal decomposition of single crystal electronic grade silicon carbide wafers between 1380 and 1620 K results in layer by layer growth of unconstrained, hetero-epitaxial single crystalline graphite. Synthetic graphite thin films have also been grown on metals [39] and carbides [40] by catalytic decomposition of C-containing gases. The nature of ultrathin graphite is a subject of continuing interest and the details of the interactions between graphene layers in multilayer stacks which determine electron transport continue to produce important research results [41].

In principle then it should be possible to create silicon carbide/graphene nanocomposites that have superior thermoelectric performance because boron-doped SiC has thermopowers whose magnitudes exceed those of boron-doped diamond. The thermopowers (Seebeck coefficients) and electrical conductivities of SiC as a function of temperature are displayed in Figure 11.9. The thermopower of SiC is seen to increase strongly in the range 400–800 K reaching a plateau at about $350\mu\text{V/K}$. The electrical conductivity increases over the entire temperature regime investigated and continues to increase even at the highest measuring temperature of 1100 K reaching a value near 2 S/cm [42]. These results are consistent with those reported by Koumoto [43] and by Pai [44,45] on boron-doped SiC.

Starting with cubic nano-SiC as a template, we have shown that the growth of graphene occurs by the catalytic decomposition of methane in the temperature interval 1000–1200 K. We have been able to demonstrate that the growth of graphene most likely occurs in a layer by layer fashion so that the thickness of the graphene shells can be precisely controlled and can be made to range between 1 and about 20 monolayers. The work on the silicon carbide/graphene nanostructures was done



Cropped and expanded view from previous side.

FIGURE 11.6

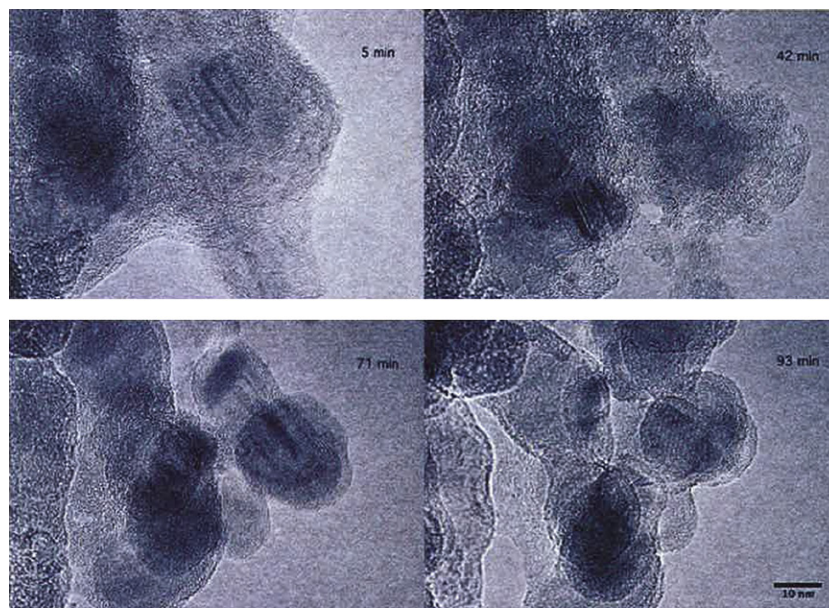
HRTEM photomicrograph of typical UNCG cylinder surrounding a SiC nanoparticle.

in collaboration with Marshall Mendelsohn and Marquis Kirk. In brief, the deposits consist at least in part of curved graphene sheets surrounding individual SiC particles to form 30–40 nm diameter cylindrical structures with aspect ratios near unity displayed in the HRTEM micrograph of [Figure 11.6](#). The cylinder walls are composed of 10–20 carbon layers having interlayer spacings of 0.36–0.34 nm. The graphene content of these core/shell structures is typically 90 mol% but can be controlled by varying synthesis conditions. The mechanically rigid compacts are less than half theoretical density but for the materials described here they are in the range 1.0–1.2 g/cm³. Nonetheless, the electrical conductivities are sizable, 300–400 S/cm, the range of values again reflecting changes in synthesis conditions. We have chosen to call this material ultrananocrystalline graphene (UNCG) in order to reflect its unusual molecular architecture. To the degree that structure determines function, one can expect that properties currently being studied such as those concerning energy storage capacity of this novel material will in part be owing to its architecture.

The HRTEM data were obtained by suspending powdered composite in a drop of methanol, which was deposited onto a holey carbon film on a Cu TEM grid. Microscopy and irradiations were performed at room temperature with 300 keV electrons in the IVEM-Tandem Facility at Argonne National Laboratory. The LaB₆ electron emitting filament produced a current of about 4 nA into a focused area of about 200 nm diameter, resulting in an electron flux of about 8×10^5 electrons/nm²/s on the sample. Image and diffraction data were recorded digitally as a

function of time in the same area of sample overhanging a hole in the supporting amorphous carbon film.

A number of micrographs similar to that shown in Figure 11.6 were obtained on different sampling areas. It was found that continued irradiation of a particular area resulted over time in the progressive sputtering away of the graphene structures as illustrated in Figure 11.7. After 5 min, before this sputtering process manifests itself in a significant way, it can be seen that graphene forms layers of “ribbons” presumably surrounding SiC particles. The edge on resolved interplanar layer spacing averages 0.35 nm, ranging from 0.36 to 0.34 nm as one moves from the inner graphene walls toward their peripheries. After 93 min of irradiation, graphene has been entirely removed leaving individually exposed core SiC particles. Such electronic sputtering of graphene and other carbon films is well known and has in fact been extensively studied [46–49]. In our work, this phenomenon gives information on core/shell structural details that would otherwise be very difficult to establish. Interestingly, the sputtering rate involving the sequential removal of 10–20 graphene layers in 93 min is in reasonable agreement with the rate calculated from Mott cross sections for 300 keV electrons [46].



HRTEM images of sequential electronic sputtering of UNCG layers surrounding SiC nanoparticles as a function of electron irradiation time at 300 keV and 8×10^5 electron/nm² sec

FIGURE 11.7

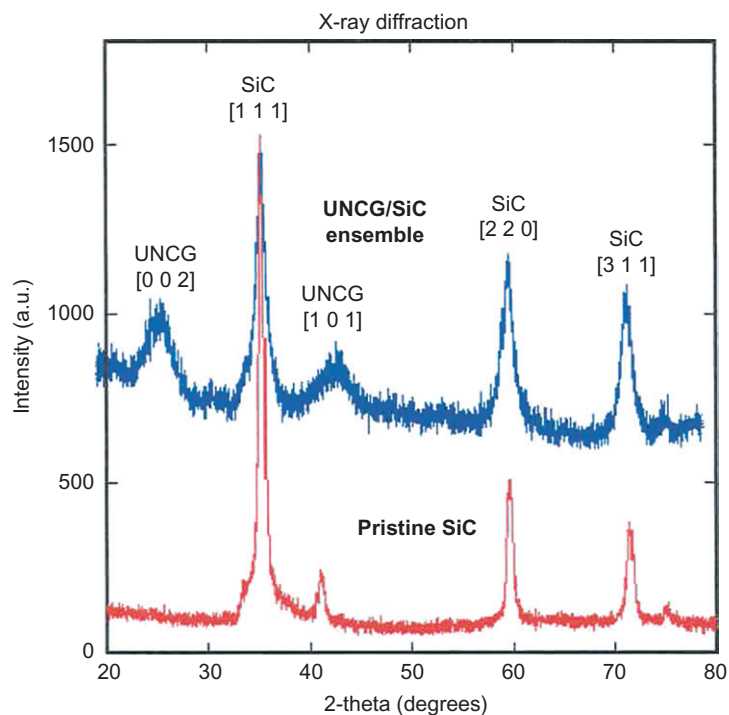
TEM images of graphene sputtered to expose SiC nanoparticle templates as a function of electron irradiation time.

The electron diffraction patterns of UNCG at the beginning and at the end of electron irradiation confirm the expected cubic structure of the SiC templates that form the cores of the surrounding graphene nanocylinders, and these persist unchanged in position with irradiation. We attribute diffuse rings that disappear as a result of electron irradiation to the graphene shells. Their width can be ascribed to a combination of lack of structural perfection and the spread in interplanar spacings between 0.36 and 0.34 nm characteristic of multilayer graphene. Amorphous carbon, if present, would have resulted in considerably broader rings than observed.

Lattice fringes of SiC (111 planes at 0.25 nm) are resolved in several of the nanoparticles throughout the entire irradiation sequence. The absence of damage to SiC particles by electron bombardment was confirmed in a separate irradiation experiment using pristine (agglomerated) nano-SiC powder prior to the reaction with methane, which results in the formation of graphene. The SiC particles after reaction with methane are deagglomerated and have a diameter of 25 ± 10 nm. They possess a degree of faceting of as yet undetermined character. Close examination of SiC nanoparticles either pristine or after sputtering away the surrounding graphene reveals that each particle comes equipped with its own 2–3 nm amorphous shell that is stable to electron irradiation. This shell is probably carbon-rich SiC [50]) since a chemical analysis of the as-received beta SiC indicates an excess of carbon over that expected assuming unit stoichiometry. The synthesis of beta SiC involves use of a mixture of silicon- and carbon-containing gases under plasma conditions which could lead to small changes in the composition of the product and the observed morphology.

Further characterization studies of UNCG include importantly XRD data obtained by using a Rigaku miniflex + diffractometer with Cu–K-alpha radiation from 3° to 80° (2θ) with a scan speed of 1s/step and a step width of 0.02° . The data are displayed in Figure 11.8, where the peaks belonging to UNCG and its associated SiC as well as those of pristine SiC obtained in a separate experiment are appropriately labeled. It can be seen that the peaks due to diffraction from SiC after reaction with methane and resultant UNCG deposition are wider than on pristine SiC before reaction. This effect is not fully understood but may possibly be associated with deagglomeration of SiC particles as the graphene shells are formed. The full width at half maximum (FWHM) of the 002 graphene peak studied in the present work is 4.0° . This value is essentially identical to that observed by Andersson et al. [21] in their detailed and careful work on graphite nanoparticles prepared by graphitization of UNCD powder at 1900 K. They, as we, also observe a diffraction peak where graphite 101 and 100 peaks merge into a single peak at around 45° .

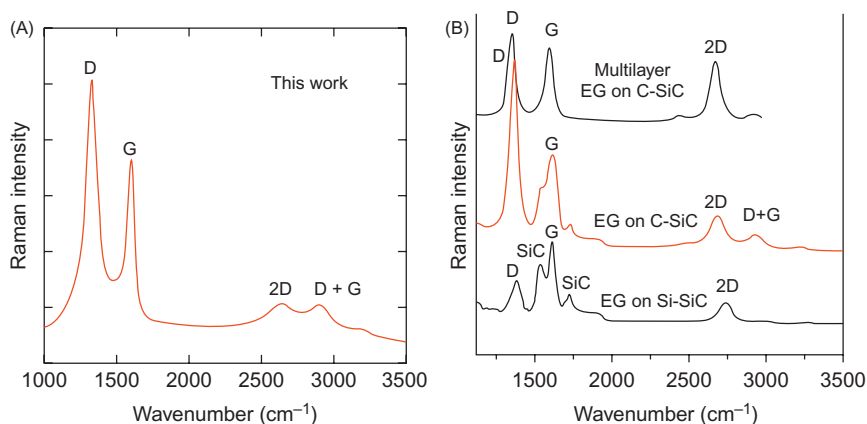
As described above, reactions of methane at 1200 K with UNCD powder rather than SiC powder as template were carried out [10]. These composites prepared with UNCD templates have a much broader diffraction peak between 23° and 26° with FWHM of 8° , characteristic of the deposition of amorphous carbon. This interpretation was confirmed in an extensive series of further experiments with UNCD using XRD, HRTEM, and Raman techniques [11]. The UNCD/amorphous carbon composites had to be annealed at a temperature of 2100 K to decrease the FWHM of the 002 peak from 8° to about 4° [11]. This narrowing is due to ordering

**FIGURE 11.8**

RD patterns of pristine SiC nanoparticles (red) and UNCG/SiC composite.

processes, which the work of Andersson et al. has shown to begin at about 1900 K [9]. HRTEM data on the UNCD/amorphous carbon samples annealed at 2100 K in fact show the onset of curved graphene structures [11] similar to those seen in the present work already at 1200 K.

The facile production of the graphene cylindrical structures deposited on nano-SiC is remarkable since it occurs at almost 1000 K, lower temperatures compared to depositions on UNCD powder. To fully elucidate the fundamental reasons for this difference in behavior will require considerably more experimental as well as theoretical work. Presumably, differences in the nanoscale surface topographies of the two substances are involved at least in a general way. To account for the much enhanced catalytic activity of beta SiC, the nature of surface sites such as terraces, steps, kinks, adatoms, and vacancies need to be taken into account. The special, still to be explored surface electronic structure of nano-SiC presumably directs the energetics of the chemical vapor deposition reactions. The outcomes of the complex series of reactions that methane undergoes on the surface of beta SiC clearly favor the formation under relatively mild conditions of the unusual graphene structures that are observed, but the detailed mechanism is still unclear.

**FIGURE 11.9**

(A) Micro-Raman spectrum of UNCG (this work) and (B) micro-Raman spectra of graphene bilayers and multilayers on carbon- and silicon-terminated SiC as described in text.

In addition to HRTEM and XRD measurements, Raman spectra were also obtained on the UNCG samples. These were collected at an excitation wavelength of 632.8 nm using a Renishaw micro-Raman RM2000 with a 50X objective over the wavelength range 1000–3500 cm⁻¹ and one micrometer spot size. Several measurements were carried out for each sample and found to be highly reproducible and independent of location over an area of about 1 cm². A typical Raman spectrum obtained on a UNCG sample is shown in Figure 11.9A. The wavelengths of the D, G, 2D, and D+G peaks of UNCG are almost identical with those of graphene grown by Ni et al. [12] on C-terminated single crystal 6HSiC [12]. Their data using an excitation frequency of 532 nm are shown in Figure 11.9B (curve II, bilayer; curve III, multilayer). Data comparisons were made using a D-band wavelength corrected for the difference in laser excitation frequencies in the two experiments [51]. We conclude that graphene growth resulting in the synthesis of UNCG most likely occurs on C-terminated 3CSiC, a conclusion that is in consonance with the likely presence of a carbon shell surrounding each nano-SiC particle as suggested by the HRTEM results.

Ni et al. [52] also obtained Raman spectra of graphene grown on Si-terminated SiC, which are shown in Figure 11.9B as well (curve I, bilayer). There are distinct differences between growth on C and Si-terminated SiC surfaces. In addition to wavelength shifts, peak relative intensities also change. The defect-induced D band is much stronger for C-terminated growth giving rise to a D+G band in the overtone region, which is absent in the Si-terminated growth mode. These differences in Raman spectra reflect the fact that growth on C rather than Si-terminated surfaces has far reaching consequences for the electronic structure of graphene. For example, the interface of graphene with SiC is predicted to be semiconducting or

semimetallic for C-termination but metallic for Si-termination [53]. Furthermore, it has been shown experimentally that multilayer graphene sheets grown on C-terminated SiC surfaces contain rotational stacking faults. Density functional calculations demonstrate that such faults induce an electronic structure indistinguishable from an isolated single graphene layer in the vicinity of the Dirac point [54]. The stacking faults decouple adjacent graphene sheets so that their band structure is nearly identical to that of isolated graphene thus rationalizing experimental results that show single layer electronic properties even for epitaxial graphene films tens of layers thick [55,56]. Further work is required to determine whether the large electrical conductivity as well as other properties of UNCG bear evidence of the influence of rotational faults.

The graphene synthesized in the manner described above is called ultranano-crystalline graphene (UNCG). The properties of the SiC/UNCG materials so far described were obtained by heating the SiC nanopowders in methane for 10h at 1200 K. That treatment results in materials that are constituted of 90mol% graphene shown by TEM studies to be composed of about 20 multilayer cylinders surrounding SiC nanoparticle templates.

In an important series of experiments we have heated the nano-SiC powders in methane gas in carefully controlled, incremental periods of time from minutes up to 10h. After each heating period, the sample is allowed to cool so that the weight gain after each heating period can be determined from which the carbon mol fraction added per unit reaction time is calculated. Plotting the logarithm of 1-carbon mol fraction versus heating time reveals a straight line relationship. Assuming a constant cylinder aspect ratio during the growth process, one can readily deduce the C mol fraction change per unit graphene layer added.

Control of added carbon to within one or two graphene monolayers is readily achievable. This remarkable result establishes the nano-SiC/UNCG nanoensembles as a new and potentially important model system. Using the nanoensembles with varying shell thicknesses will enable one quantitatively to test the hypothesis underlying the approach advanced in this chapter. The basic idea is that conversion of configurational to electronic entropy can be enhanced in a biphasic system by taking advantage of carrier transport across interfaces in appropriately designed semiconductor/metal nanocomposites. In particular, one will be able to examine the functional relationship between thermopower and the number of graphene monolayers. This parameter presumably determines to a considerable extent the electrical conductivities of the ensembles with their attendant effect on thermopower.

Measurements to evaluate the thermoelectric performance of nano-SiC/UNCG ensembles are currently under way.

11.5 Concluding remarks

A novel approach to the development of high-performance thermoelectric materials has been presented. It is focused on the transformation of configurational to carrier

entropy in a doped semiconductor core with subsequent transport of carrier entropy in a metallic shell. The concept involves the creation of bulk nanoensembles to minimize thermal and maximize electrical conductivity.

Two systems meeting the requirements of non-resource-limited environmentally benign, economically viable, and thermally stable materials have been investigated: UNCD cores surrounded by graphene shells and nanocrystalline silicon carbide cores surrounded by cylindrical multilayer graphene shells. The latter system is of particular interest because it allows one to control the number of multilayers in the graphene shells in a facile way and thus precisely to control the fraction of the total current carried by the shells. The effectiveness of the conversion of configurational to carrier electronic entropy depends on the magnitude of “proximity” effects that arise as a result of the complex interactions of the shell with the core. The magnitude of these effects is crucially dependent on shell thickness. Therefore, the ability to exercise control over graphene growth in this system will allow one to optimize “proximity” effects and to develop materials displaying strongly enhanced thermoelectric properties.

Fundamental and detailed insights into the electronic structure of doped semiconductors are required to implement the program outline above. These have been provided by density functional cluster calculations. They have confirmed, in the two model systems described above, the supposition that multitudes of doping configurations lead to a plethora of unique electronic states frequently situated within thermal energies of the Fermi level. The extremely sensitive dependence of the shapes of orbital wavefunctions on very small differences in orbital composition in turn reflects small differences in orbital energies. This of course is the underlying reason for the large number of distinct quantum states leading to sizeable configurational entropies in doped semiconductors. As already stated, many of these states, created by substitutional doping, lie within thermal energies of the Fermi level. Thermally excited carriers can therefore occupy these states and transport their excitation energy encoded as carrier entropy in the presence of a thermal gradient. We suppose that this sequence of events is closely associated with the basic mechanism giving rise to the thermoelectric effect, the solid state process by means of which heat is directly converted to electricity. The efficiency of that process is, by definition, determined by the change in entropy per added carrier which, according to our view is enhanced by the “proximity” of appropriately tailored interfaces.

We have shown that configurational entropies generated by the doping of semiconductors can usefully be explored by molecular analogue calculations. These are currently being extended to include coupling of plasmons by longitudinal optical phonons [57].

Finally, it has been a chief purpose of the work reported here to emphasize the important role played by entropy flows in determining the magnitude of the subtle thermoelectric phenomenon. Interestingly, entropy flows have recently been invoked to explain an equally subtle phenomenon, the accelerating expansion of the universe [58].

Acknowledgments

It is a pleasure to acknowledge the work of my collaborators Drs. Paola Bruno, Ming Xie, Raul Arenal, Dileep Singh, and Jules Routbort on UNCD/graphene nanoensembles and that of Marshall Mendelsohn and Marquis Kirk on SiC/graphene nanoensembles. The work was performed under the auspices of the US Department of Energy, Office of Basic Energy Sciences, Contract No. DE-AC02-06CH11357.

References

- [1] M. Xie, D.M. Gruen, Potential impact of $ZT=4$ thermoelectric materials on solar thermal energy conversion technologies, *J. Phys. Chem. B* 114 (2010) 14439.
- [2] G.H. Jonker, The application of combined conductivity and Seebeck-effect plots for the analysis of semiconductor properties, *Philips Res. Rep.* 23 (1968) 131.
- [3] N. Mansourian-Hadavi, D. Ko, T.O. Manson, K.R. Poeppelmeier, Quadruple and quintuple perovskite-layered cuprates ($\text{NdDyBa}_{2-x}\text{SrxCu}_2+\text{yTi}_2-\text{yO}_{11-\text{delta}}$ and $\text{NdDyCaBa}_{2-x}\text{SrxCu}_2+\text{yTi}_3-\text{yO}_{14-\text{delta}}$): their defect chemistry and electrical properties, *J. Solid State Chem.* 155 (2000) 21.
- [4] L. Onsager, Reciprocal relations in irreversible processes. I. Reciprocal relations in irreversible processes. II, *Phys. Rev.* 37 (1931) 405; 38 (1931) 2265.
- [5] R. Feynman, Slow electrons in a polar crystal, *Phys. Rev.* 97 (1955) 660.
- [6] H. Callen, *Thermodynamics and an Introduction to Thermostatistics*, second ed., John Wiley & Sons, New York, NY, 1985, p. 316.
- [7] P.M. Chaikin, G. Beni, Thermopower in the correlated hopping regime, *Phys. Rev. B* 13 (1976) 647.
- [8] D. Emin, Thermoelectric power due to electronic hopping motion, *Phys. Rev. Lett.* 35 (1975) 882. Effects of charge carriers' interactions on Seebeck coefficients, in: D.M. Rowe (Ed.), *Thermoelectrics Handbook*, Taylor and Francis, 2006 (Chapter 5).
- [9] E. Alptekin, M.C. Ozturk, Tuning of nickel silicide Schottky barrier height on p-type silicon by indium implantation, *IEEE. Electron. Device Lett.* 30 (2009) 1272.
- [10] D.M. Gruen, P. Bruno, M. Xie, Configurational, electronic entropies and the thermoelectric properties of nanocarbon ensembles, *Appl. Phys. Lett.* 92 (2008) 143118.
- [11] D.M. Gruen, P. Bruno, R. Arenal, J. Routbort, D. Singh, M. Xie, Thermoelectric power factors of nanocarbon ensembles as a function of temperature, *J. Appl. Phys.* 105 (2009) 073710.
- [12] C.E. Lowell, Solid solution of boron in graphite, *J. Am. Ceram. Soc.* 50 (1967) 142.
- [13] B.-S. Hong, S.J. Ford, T.O. Mason, Equilibrium electrical property measurements in electroceramics, *Key. Eng. Mater.* 163 (1997) 125–126.
- [14] A.C. Ferrari, J. Robertson, Resonant Raman spectroscopy of disordered, amorphous, and diamondlike carbon, *Phys. Rev. B* 64 (2001) 075414.
- [15] R. Arenal, G. Montagnacm, P. Bruno, D.M. Gruen, Multiwavelength Raman spectroscopy of diamond nanowires present in n-type ultrananocrystalline films, *Phys. Rev. B* 76 (2007) 245316.
- [16] Measurements of thermal conductivity and confirmation of previously measured thermopower were made at the High Temperature Laboratory, Oak Ridge, TN. See Ref. [11] for details.

- [17] P.C. Redfern, D.M. Gruen, L.A. Curtiss, Effect of boron substitution on the electronic structure of nanographene and its relevance to the thermoelectric transport properties of nanocarbon ensembles, *Chem. Phys. Lett.* 471 (2009) 264.
- [18] V.L. Kuznetsov, Y.V. Butenko, in: O.A. Shenderova, D.M. Gruen, (Eds.), *Ultrananocrystalline Diamond*, William Andrew, Norwich, NY, 2006, p. 405.
- [19] N. Mott, *Conduction in Non-Crystalline Materials*, second ed., Oxford Science, New York, NY, 1993.
- [20] V.L. Kuznetsov, Y.V. Butenko, A.L. Chuvilin, A.I. Romanenko, A.V. Okotrub, Electrical resistivity of graphitized ultra-disperse diamond and onion-like carbon, *Chem. Phys. Lett.* 336 (2001) 397.
- [21] O.E. Andersson, B.L.V. Prasad, H. Sato, E. Enoki, Y. Hishiyama, Y. Kaburagi, et al., Structure and electronic properties of graphite nanoparticles, *Phys. Rev. B* 58 (1998) 16387.
- [22] A.D. Becke, Density-functional thermochemistry. 3. The role of exact exchange, *J. Chem. Phys.* 98 (1993) 5648.
- [23] M.J. Frisch, et al., GAUSSIAN03, 2003.
- [24] D. Moran, F. Stahl, H.F. Bettinger, H.F. Schaefer, P.V. Schleyer, Towards graphite: magnetic properties of large polybenzenoid hydrocarbons, *J. Am. Chem. Soc.* 125 (2003) 6746.
- [25] L.A. Curtiss, K. Ragavachari, P.C. Redfern, J.A. Pople, Assessment of Gaussian-2 and density functional theories for the computation of enthalpies of formation, *J. Chem. Phys.* 106 (1997) 1063.
- [26] P.C. Redfern, P. Zapol, M. Sternberg, S.P. Adiga, S.A. Zygmunt, L.A. Curtiss, Quantum chemical study of mechanisms for oxidative dehydrogenation of propane on vanadium oxide, *J. Phys. Chem. B* 110 (2006) 8363–8371.
- [27] T. Frauenheim, Atomistic simulations of complex materials: ground-state and excited-state properties, *J. Phys. Condens. Matter.* 14 (2002) 3015.
- [28] T. Frauenheim, A self-consistent charge density-functional based tight-binding method for predictive materials simulations in physics, chemistry and biology, *Phys. Status Solidi B* 217 (2000) 41.
- [29] D. Porezag, T. Frauenheim, T. Kohler, G. Seifert, R. Kaschner, A self-consistent charge density-functional based tight-binding method for predictive materials simulations in physics, chemistry and biology, *Phys. Rev. B* 51 (1995) 12947.
- [30] M. Sternberg, P. Zapol, L.A. Curtiss, Carbon dimers on the diamond (100) surface: growth and nucleation, *Phys. Rev. B* 68 (2003) 9.
- [31] M. Sternberg, L.A. Curtiss, D.M. Gruen, K. Kedziora, D.A. Horner, P.C. Redfern, et al., Carbon ad-dimer defects in carbon nanotubes, *Phys. Rev. Lett.* 96 (2006) 4.
- [32] G. Allinson, R.J. Bushby, J.L. Paillaud, M. Thorntonpett, Synthesis of a derivative of triangulene—the first non-Kekule polynuclear aromatic, *J. Chem. Soc. Perkin. Trans.* 1 (1995) 385.
- [33] S.J. Cyvin, J. Brunvoll, B.N. Cyvin, A periodic-table for all-benzenoid hydrocarbons and enumerations of some polyhex isomers, *J. Math. Chem.* 8 (1991) 63.
- [34] H.I. Zhang, J.F. Li, B.P. Zhang, K.F. Yao, W.S. Liu, H. Wang, Electrical and thermal properties of carbon nanotube bulk materials: experimental studies for the 328–958 K temperature range, *Phys. Rev. B* 75 (2007) 205407.
- [35] K. McGuire, N. Gothard, P.L. Gai, M.S. Dresselhaus, G. Sumanasekera, A.M. Rao, Synthesis and Raman characterization of boron-doped single-walled carbon nanotubes, *Carbon* 43 (2005) 219.

- [36] D.L. Carroll, Ph. Redlich, X. Blase, J.-C. Charlier, S. Curran, P.M. Ajayan, et al., Effects of nanodomain formation on the electronic structure of doped carbon nanotubes, *Phys. Rev. Lett.* 81 (1998) 2332.
- [37] A. Balducci, M. Marinelli, M.E. Morgada, G. Pucella, G. Rodriguez, M. Soccia, et al., CVD-Diamond-based thermocouple for high sensitive temperature measurements, *Microsys. Technol.* 12 (2006) 365.
- [38] A. Charrier, A. Coati, T. Argunova, F. Thibaudau, Y. Garreau, R. Pinchaux, et al., Solid-state decomposition of silicon carbide for growing ultra-thin heteroepitaxial graphite films, *J. Appl. Phys.* 92 (2002) 2479.
- [39] A. Nagashima, N. Tejima, Y. Gamou, T. Kawai, C. Oshima, Electronic dispersion-relations of monolayer hexagonal boron-nitride formed on the Ni (111) surface, *Phys. Rev. B* 51 (1995) 4606.
- [40] H. Itoh, T. Ichinose, C. Oshima, T. Ichinokawa, T. Aizawa, Scanning tunneling microscopy of monolayer graphite epitaxially grown on a TiC (111) surface, *Surf. Sci.* 254 (1991) L437.
- [41] X. Wu, X. Li, Z. Song, C. Berger, W.A. De Heer, Weak antilocalization in epitaxial graphene: evidence for chiral electrons, *Phys. Rev. Lett.* 98 (2007) 136801.
- [42] D.M. Gruen, P. Bruno, M. Mendelsohn, J. Routbort, D. Singh, P. Redfern, et al., Core-shell silicon carbide-transition metal silicide thermoelectric ensembles, in: Symposium on Thermoelectric Materials for Solid-State Power Generation and Refrigeration, Material Research Society, Fall 2010 Meeting.
- [43] K. Koumoto, S. Takeda, C.H. Pai, H. Yanagida, High-resolution electron-microscopy observations of stacking-faults in beta-SiC, *J. Am. Ceram. Soc.* 72 (10) (1989) 1985–1987.
- [44] H. Pai, K. Koumoto, S. Takeda, H. Yanagida, Preparation of SiC hollow particles by gas-phase reaction and thermoelectric properties of sintered bodies, *Solid State Ionics.* 32/33 (1989) 669.
- [45] C.H. Pai, Thermoelectric properties of boron compound-doped alpha-SiC ceramics, *J. Ceram. Soc. Jpn.* 112 (2004) 88.
- [46] N.W. Ashcroft, N.D. Mermin, *Solid State Physics*, Thomson Learning Inc., London, 1976.
- [47] C. Jin, H. Lan, L. Peng, K. Suenaga, S. Iijima, Deriving carbon atomic chains from graphene, *Phys. Rev. Lett.* 102 (2009) 205501.
- [48] J.H. Warner, M.H. Rummeli, A. Bachmatiuk, B. Buchner, Examining the stability of folded graphene edges against electron beam induced sputtering with atomic resolution, *Nanotechnology* 21 (2010) 325702.
- [49] R.F. Egerton, P.A. Crozier, Erosion of TEM specimens in an intense electron beam, *Microsc. Microanal.* 10 (2004) 54.
- [50] R. Colby, M.L. Bolen, M.A. Capano, E.A. Stach, Amorphous interface layer in thin graphite films grown on the carbon face of SiC, *Appl. Phys. Lett.* 99 (2011) 101904.
- [51] C. Thomsen, S. Reich, Double resonant Raman scattering in graphite, *Phys. Rev. Lett.* 85 (2000) 5214.
- [52] Z.H. Ni, W. Chen, X.F. Fan, J.L. Kuo, T. Yu, A.T.S. Wee, et al., Raman spectroscopy of epitaxial graphene on a SiC substrate, *Phys. Rev. B* 77 (2008) 115416.
- [53] A. Mattausch, O. Pankratov, *Ab initio* study of graphene on SiC, *Phys. Rev. Lett.* 99 (2007) 076802.

- [54] J. Hass, F. Varchon, J.E. Millan-Otoya, M. Sprinkle, N. Sharma, W.A. de Heer, et al., Why multilayer graphene on 4h-SiC(000 $\bar{1}$) behaves like a single sheet of graphene, *Phys. Rev. Lett.* 100 (2008) 125504.
- [55] C. Berger, Z.M. Song, X.B. Li, X.S. Wu, N. Brown, C. Naud, et al., Electronic confinement and coherence in patterned epitaxial graphene, *Science* 312 (2006) 1191.
- [56] F. Varchon, R. Feng, J. Hass, X. Li, B.N. Nguyen, C. Naud, et al., Electronic structure of epitaxial graphene layers on SiC: effect of the substrate, *Phys. Rev. Lett.* 99 (2007) 126805.
- [57] B.B. Varga, Coupling of plasmons to polar phonons in degenerate semiconductors, *Phys. Rev.* 137 (1965) A1896.
- [58] D.A. Easson, P.H. Frampton, G.F. Smoot, Entropic accelerating universe, *Phys. Lett.* 696 (2011) 273.

Science and Technology of Ultrananocrystalline Diamond (UNCD™) Film-Based MEMS and NEMS Devices and Systems

Orlando Auciello

Materials Science Division, Argonne National Laboratory, Argonne, IL

CHAPTER OUTLINE

12.1 Introduction	384
12.2 Fundamentals of UNCD film synthesis and properties	385
12.2.1 Comparison of the synthesis of microcrystalline diamond, nanocrystalline diamond, and ultrananocrystalline diamond thin films	385
12.2.2 New advances on the synthesis of UNCD thin films: bias-enhanced nucleation/bias-enhanced growth	388
12.2.3 Review of properties of UNCD films critical to MEMS and NEMS devices	389
<i>Bulk and surface properties</i>	389
<i>Electrical properties of UNCD films</i>	393
<i>Dielectric properties of UNCD films</i>	393
<i>Thermal properties of UNCD films</i>	396
<i>Properties of UNCD films as a biomaterial for MEMS/NEMS devices implantable in the human body</i>	398
12.3 MEMS and NEMS devices based on UNCD films	399
12.3.1 Materials integration and process strategies for fabrication of MEMS/NEMS devices based on UNCD films	399
<i>Selective seeding and growth process for fabrications of UNCD–MEMS/NEMS devices</i>	400
<i>Photolithography plus RIE processes for surface micromachining fabrication of UNCD–MEMS/NEMS devices</i>	401
<i>UNCD film stress and ohmic contact of electrode layers on UNCD films</i>	401

	<i>Materials integration for hybrid piezoelectric/UNCD-based MEMS/NEMS devices</i>	402
12.3.2	Examples of MEMS/NEMS devices based on UNCD film technology	403
	<i>Electrostatically actuated UNCD-based MEMS resonators</i>	403
	<i>Piezoelectrically actuated UNCD-based MEMS resonators and NEMS switches</i>	404
	<i>Fabrication of monolithic UNCD cantilever/AFM tips and applications</i>	407
12.3.3	UNCD integration with CMOS devices	408
12.3.4	RF-MEMS switches with UNCD dielectric layer monolithically integrated with CMOS driving devices	408
12.3.5	MEMS/NEMS biosensors	413
12.4	Future scientific and technological developments based on UNCD films and integration into MEMS/NEMS structures	415
12.5	Conclusions	415
	Acknowledgments	416
	References	417

12.1 Introduction

A new paradigm in materials science, materials integration, micro- and nanofabrication, and new device architectures is underway to develop a new generation of microelectromechanical/nanoelectromechanical systems (MEMS/NEMS). It is evident that there is a need for new materials for MEMS/NEMS devices, since many Si-based MEMS/NEMS devices exhibit performance limitations due to the relatively poor mechanical and tribological properties of Si, as discussed in the section describing the mechanical and tribological properties of UNCD films in comparison with the equivalent properties of Si. This chapter focuses on presenting a review of the UNCD film technology developed and patented at Argonne National Laboratory, and its application to the development of a new generation of MEMS/NEMS devices impacting several technologies.

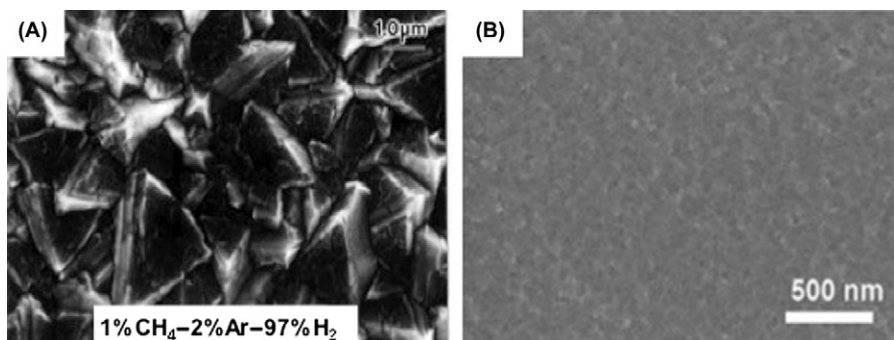
The fundamental and applied science performed to understand the synthesis [1–5] of UNCD films and develop applications [6–12] of the UNCD film technology demonstrated that UNCD films exhibit a synergistic combination of exceptional mechanical, tribological, chemical, electrical, thermal, electron emission, and biocompatible properties, which may enable a new generation of multifunctional devices from the macro- to the nanoscale. They are (1) coatings for mechanical pumps [13] seals with order of magnitude longer lifetime and lower friction coefficient than other materials for seals in the market today (UNCD-coated SiC mechanical pump seals have been introduced into the market in 2008 by Advanced Diamond Technology—see ADT website); (2) field emission cathodes, involving MEMS/NEMS structures [14,15] for field emission displays, high-frequency tubes, X-ray

sources and more; (3) Radio Frequency (RF) RF-MEMS/NEMS resonators and switches for wireless communications and radar systems [8]; (4) NEMS devices [11,12]; (5) Biomedical devices (e.g., bioinert coating [16] for encapsulation of a microchip implantable in the retina to restore sight to people blinded by retina degeneration, and UNCD tribological coating with low friction and negligible wear for prosthesis—knees, hips, heart valves); (6) biosensors, including MEMS/NEMS-based biosensors [17]; (7) UNCD as a platform for developmental biology [18], involving the growth of cells on the surface and potential differentiation; (8) UNCD as a platform for growth of multielement/multifunctional nanowires [19]; and (9) science and technology of UNCD nanowires (A.V. Sumant et al., work in progress).

12.2 Fundamentals of UNCD film synthesis and properties

12.2.1 Comparison of the synthesis of microcrystalline diamond, nanocrystalline diamond, and ultrananocrystalline diamond thin films

Several types of diamond thin films have been synthesized and systematically studied, and they exhibit different microstructure, surface morphology, and properties, as discussed below. For standard growth of diamond on nondiamond substrates using microwave plasma enhanced chemical vapor deposition (MPCVD) or hot filament CVD (HFCVD), or any other CVD method, it is necessary to do a surface pretreatment or “seeding,” (embedding micro- or nanodiamond particles on the surface) to enhance the nucleation for diamond film growth [1–23]. Following seeding, standard thin-film deposition methods, based on MPCVD and HFCVD, involve hydrogen-rich chemistry (H_2 (balance)/ CH_4 (0.1–4%)) [20–23], which results in microcrystalline diamond (MCD—1–5 μm grains and columnar microstructure) (for ~1% CH_4) and nanocrystalline diamond (NCD) (10–100 nm grains) (for ~4% CH_4) films, although high-quality NCD films can be deposited at relatively low methane percentage (0.3%) [23]. The MCD and NCD films grown on surfaces seeded with conventional solutions of diamond micro- or nanoparticles, without proper functionalization to reduce agglomeration, experience the drawback of relatively low initial nucleation density ($<10^{10}/\text{cm}^2$). The MCD film surface coarsens with thickness. Correspondingly, they exhibit a rough, highly faceted morphology with root mean square (RMS) roughness typically ~10% of the film thickness. On the other hand, when very high nucleation densities are achieved ($>10^{12}/\text{cm}^2$) using new optimized seeding processes [24] and an appropriate amount of CH_4 (~0.3%) relatively smooth, high-quality NCD films of various thicknesses can be grown [23] at temperatures ranging from 900°C down to as low as 450°C (not confirmed in the open literature). In any case, there is no report in the literature of successful integration of NCD films with Complementary Metal Oxide Semiconductor (CMOS) devices, which is a critical proof of low temperature growth of diamond films. The growth process related to the H_2/CH_4 chemistry is driven by CH_3 -radicals interaction with

**FIGURE 12.1**

SEM micrographs showing (A) the rough morphology of MCD versus (B) the morphology of the UNCD film.

Source: Reprinted from Ref. [11]. Copyright (2001), with permission from Elsevier.

the substrate surface, involving a hydrogen abstraction process, which ultimately results in carbon atoms inserting into the position corresponding to the diamond lattice. The atomic hydrogen in the plasma preferentially etches a graphitic phase that co-deposits with the diamond phase. However, atomic hydrogen also etches the diamond phase, although at a much lower rate (~50 times) than for graphite, resulting in the formation of intergranular voids and columnar morphology with large grains ($\geq 1 \mu\text{m}$). These grains are much larger than for the UNCD films described in this review (compare Figure 12.1A and B).

The MCD films exhibit high residual compressive stress, poor intergranular adhesion, and very rough surfaces, resulting in relatively high coefficients of friction [20,23]. Consequently, MCD films are not suitable for producing MEMS/NEMS structures, which require smooth surfaces, sharply defined geometries, and low coefficient of friction (COF). The grain size can be reduced to 30–100 nm, characteristic of films typically known as NCD, by increasing the CH₄/H₂ ratio in the plasma. This results in a smoother profile than MCD films, although at the cost of increased nondiamond components at the grain boundaries [25]. There is also another class of NCD with high sp³ content, [23,26] which is grown with the CH₄/H₂ gas chemistry with relatively low methane content (0.3%), but using a special diamond seeding/nucleation treatment [24]. In this case, the film exhibits the NCD structure as long as the film thickness is limited to few hundred nanometers; above that, grain coarsening starts to dominate due to lack of re-nucleation rate and the film grows in a columnar fashion, leading to increase in grain size and roughness with increased film thickness.

In contrast to the growth process for MCD and NCD films described above, the UNCD films discussed in this review are produced by MPCVD and more recently by a HFCVD process developed by Advanced Diamond Technologies (ADT), the company currently commercializing the UNCD films technology. This process involves a novel argon-rich chemistry (Ar (99%)/CH₄(1%)) with no hydrogen

added [1–19], which in turn produces carbon dimers (C_2) in the plasma, from methane decomposition via reactions (12.1) and (12.2) below:



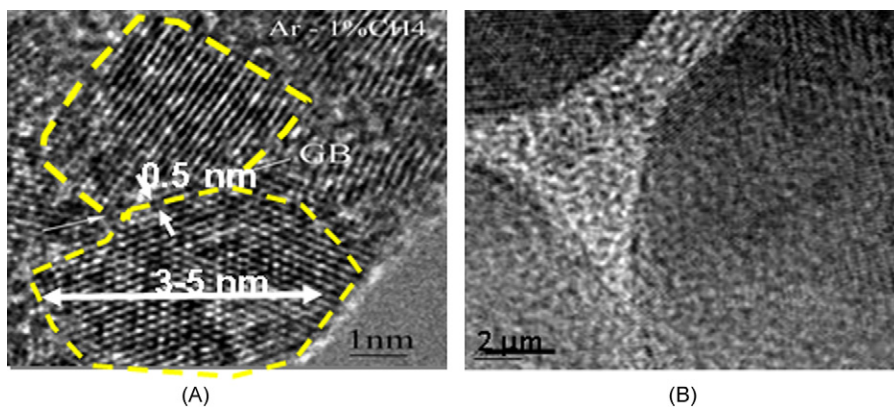
While the Ar-rich/ CH_4 plasma produces a complex mixture of carbon (C_2 dimers) and hydrocarbon species, including CH_3 and other hydrocarbons, the C_2 dimers have been proposed to play a critical role in the UNCD nucleation and growth process [27,28].

Calculations predict that the C_2 dimers have low activation energy (~6kcal/mol) for insertion into the surface of the growing film, thus establishing the growth characteristic of UNCD. Recent modeling efforts indicate that while the C_2 population in the plasma is high, the population near the surface may be low, and other hydrocarbon radicals (e.g., CH_3 , C_2H) are also substantial or main contributors to the UNCD growth [29,30]. This model, however, could not fully explain the low temperature growth of UNCD with a modest growth rate. Clearly, more experimental and modeling studies are needed. Regardless of the mechanism, the distinctive characteristic of the UNCD film growth process is that the plasma contains very small quantities of hydrogen, which arise mainly from the thermal decomposition of methane to acetylene in the plasma (about 1.5%).

A critical outcome of the UNCD nucleation and growth processes is that these films have been demonstrated to grow at temperatures as low as 350–400°C, as determined not only by thermocouple measurements during growth [4,5,11,31] but most importantly by the demonstration that CMOS devices exhibit practically the same performance before and after growing UNCD film on them [10,11]. Similar demonstration of the integration of low temperature NCD films with CMOS devices has not been published in the open literature yet. The demonstrated integration of UNCD films with CMOS devices is paving the way for the integration with CMOS for the development of monolithically integrated UNCD–MEMS/NEMS/CMOS devices, as recently demonstrated by Argonne researchers [8,10,11,12].

The UNCD nucleation and growth process results in a unique film nanostructure consisting of equiaxed 3–5 nm grains and 0.4 nm wide grain boundaries for plain UNCD [3] (Figure 12.2A) films, and extremely smooth as grown surface (~4–6 nm), when using optimized seeding techniques (see discussion in Section 12.2.3) and about 7–10 nm grains and 1–2 nm grain boundaries for UNCD films grown with nitrogen in the gas mixture (Figure 12.2B).

Early work indicated that nitrogen may be incorporated in the grain boundaries, promoting sp^2 bonds formation as shown in transmission electron microscopy (TEM) studies [33] and optical measurements and spectral photoconductivity [34]. The early work suggested that increase in the density of states due to sp^2 bonds created in the grain boundaries results in a grain boundary-mediated carrier hopping conductivity mechanism, as shown by Hall measurements performed by the Argonne group [32]. The early work suggested that nitrogen atoms are inserted into the UNCD grain

**FIGURE 12.2**

High Resolution Transmission Electron Microscopy (HRTEM) micrographs of plain UNCD (A) and nitrogen-grain boundary incorporated UNCD (B) films produced by MPCVD growth.

Source: Reprinted from Ref. [32]. Copyright (2001), with permission from the American Institute of Physics.

boundaries resulting into a semimetallic conductivity ($\sim 260 \text{ } (\Omega\text{cm})^{-1}$) [32]. More recent work, including detailed TEM, Energy Electron Loss Spectroscopy (EELS), and small angle neutron scattering (SANS), indicates that the drastic changes of the electrical conductivity behavior of nitrogen-incorporated UNCD (NUNCD) films when the nitrogen–argon ratios during film growth are increased are strongly correlated to significant changes in the microstructure of the NUNCD films. In particular, the new research [32] showed the transformation from randomly oriented 3–5 nm diamond crystallites to diamond nanowires surrounded by a largely sp^2 -bonded carbon sheath when N_2 contents of 10% and above in the plasma, during film growth, are combined with deposition temperatures of about 800°C and above. The authors of Ref. [32] suggested that the sheath ($\sim 1 \text{ nm}$ thick) of sp^2 -bonded carbon atoms make a major contribution to the high conductivity of the NUNCD films. Partial alignment of the diamond nanowires was evidenced by SANS analysis. The UNCD films exhibit pure sp^3 (diamond) carbon bonds in the grains and sp^3/sp^2 mixture in the grain boundaries as revealed by high-resolution TEM/EELS studies and synchrotron-based near-edge X-ray absorption fine structure (NEXAFS) analysis [2].

In concluding this section, UNCD and NCD are much smoother as grown films (see discussion on surface properties below) than the MCD films discussed above, and exhibit bulk and surface properties close to those of single crystal diamond [7].

12.2.2 New advances on the synthesis of UNCD thin films: bias-enhanced nucleation/bias-enhanced growth

Recently, Chen et al. [35] investigated the synthesis of UNCD, using a new low-pressure bias-enhanced nucleation and growth process (BEN-BEG). The BEN process investigated by several groups has several potential advantages over mechanical

polishing or ultrasonic seeding processes, particularly for application to the growing of UNCD films for MEMS/NEMS devices, namely (a) comparable or potentially better seeding efficiency [35], (B) stronger adhesion to substrates [35–39], and (c) an integrated fully dry nucleation/growth process using plasma processing only. Prior work [40] demonstrated that the BEN process can produce UNCD films, as indicated by Raman analysis [40]. However, in the work cited in Ref. [40], the UNCD films were grown using an Ar/CH₄ chemistry without bias, on BEN layers produced by 70mbar H₂/CH₄ plasma chemistry. Other prior work involving BEN plus BEG processes using H₂/CH₄ chemistries produced NCD (30–100nm grains) films. These NCD films exhibited formation of diamond clusters, relatively high surface roughness, high compressive stress, delamination of the film, and high content of nondiamond phase [37,38]. By contrast, the BEN-BEG process developed by Chen et al. [35] resulted in UNCD films identical to those produced by the Ar/CH₄ chemistry without bias, as shown by high-resolution TEM (Figures 12.3 and 12.4) [35,41].

The BEN-BEG process described in Ref. [35] involved relatively low-pressure (25mbar) H₂/CH₄ gas chemistry and an integrated BEN-BEG process that yields films with low stress, smooth surfaces (~4–6nm), high growth rates (~1μm/h) and uniform grain size (3–5nm) throughout the whole film area, making them potential candidate materials for the fabrication of UNCD-based MEMS/NEMS devices. However, extensive characterization of the mechanical, tribological, and other properties of the BEN-BEG UNCD films need to be performed to assure that these UNCD films are identical to those grown by the process without bias, extensively reported in the literature [1–19]. Further details of the BEN-BEG process for UNCD films can be found in Refs. [35,41].

A question to be asked is why it is relevant to develop an optimized BEN-BEG process to grow not only UNCD, but also NCD films on large area substrates (≥150mm in diameter). The answer relates to important issues, namely the following: (1) given the present state of safety considerations related to research in academic, national laboratories, and industrial environments, eliminating the need for seeding with nanoparticles would greatly reduce research laboratory and industrial safety issues; (2) having a whole plasma-based seeding process, without having to go through mechanical or ultrasonication seeding processes, can reduce cost for industrial processes, including elimination of the laboratory space and systems required for the mechanical or wet type of seeding; (3) for future fabrication of UNCD or NCD-based MEMS/NEMS devices in the necessary clean room environment, eliminating the need for nanoparticle-based seeding may be a necessity, since nanoparticle solution-based seeding will complicate the implementation of this process in industrial clean rooms.

12.2.3 Review of properties of UNCD films critical to MEMS and NEMS devices

Bulk and surface properties

UNCD films, as is the case for NCD films discussed above, exhibit a unique set of complementary mechanical and tribological properties extremely well suited

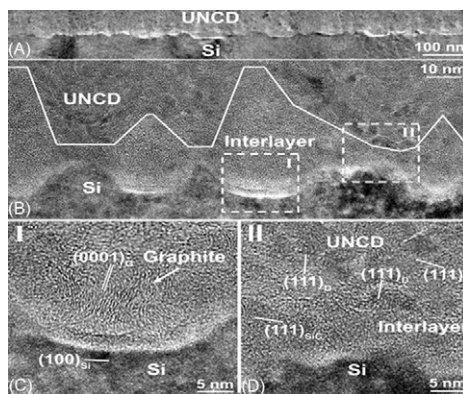


FIGURE 12.3

Cross-sectional low-magnification TEM (A) and HRTEM (B) images of a BEN-BEG UNCD film grown on a Si substrate. The white solid line in (B) shows the boundary between the UNCD and the interface layer, clearly demonstrating preferential nucleation of UNCD grains at the peaks of the Si triangular surface profile. The enlarged HRTEM images of (C) the valley area and (D) the peak area correspond to the dashed squares marked I and II, respectively, in (B). The interface layer in the valleys of the triangular Si surface profile is rich in the a-C and graphite phases. By contrast, some SiC grains are found in the 5 nm thick interlayer between the UNCD grains and the peaks of the Si substrate.

Source: Reprinted from Ref. [41]. Copyright (2009), with permission from the American Institute of Physics.

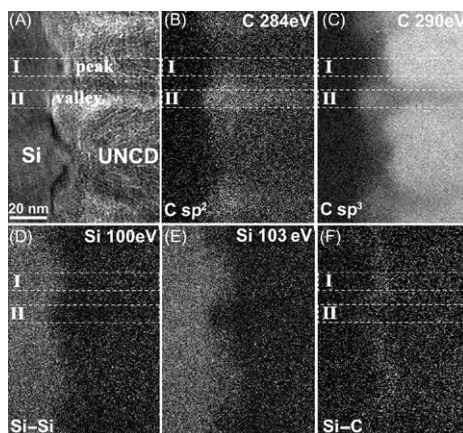


FIGURE 12.4

(A) TEM image of the UNCD films on the bias-pretreated Si substrate and the corresponding series of chemical bonding maps obtained from (B) the carbon π^* peak for carbon sp^2 bond, (C) the carbon σ^* peak for carbon sp^3 bond, (D) the Si K edge at 100 eV energy loss for Si-Si bond, and (E) the Si K edge at 103 eV energy loss for Si-C and Si-Si bond. (F) Difference in the Energy Filtered Transmission Electron Microscopy (EFTEM) images taken at 100 and 103 eV energy loss clearly distinguishes the Si-C bond from the Si-Si bond. The profiles of the dashed rectangles in (G) the peak area and (H) the valley area in the chemical maps from the Si-Si bond, the Si-C bond, and the C sp^2 and sp^3 bonds were taken as a line scan along the axis perpendicular to the Si surface, clearly revealing an interface layer containing SiC grains at the peaks and an interface layer rich in the a-C and graphite phases in the valleys.

Source: Reprinted from Ref. [41]. Copyright (2009), with permission from the American Institute of Physics.

for MEMS/NEMS devices in general. UNCD films exhibit hardness (98 GPa) and Young's modulus (980 GPa) [7] close to corresponding values for single crystal diamond (100 and 1200 GPa, respectively). The Young's modulus is reduced to about 880 GPa when adding about 3% N₂ in the gas phase to the plasma chemistry in order to produce electrically conductive UNCD films [7]. However, this value of Young's modulus is still superior to silicon and other MEMS/NEMS materials (see Table 12.1). Further addition of nitrogen (5–20%) in the plasma leads to decrease in Young's modulus down to 550 GPa.

For RF-MEMS resonators, one important figure of merit is acoustic velocity (AV). Diamond has the highest AV of any material, 16,760 m/s, compared to 11,700 m/s for high-quality AlN and 8100 m/s for single crystal silicon. This property along with high Young's modulus directly translates to higher frequency of operation for a given geometry but in the same token, it allows for larger devices for a given frequency, thus relaxing geometric tolerances and enhancing yield via improved manufacturability. Fixed-free UNCD resonators were fabricated and used to measure UNCD film's AV and quality factor (*Q*), using an AFM in vacuum to avoid damping effects due to air [10,11]. The measurements revealed AVs of 15,400 m/s. The quality factor *Q* of these low frequency resonators was measured using a ring-down approach, and ranged from 10,000 to 13,000 [42]. Here, it is relevant to mention that disk-shaped resonators based on NCD films exhibited some of the highest *Q*'s [12,21]. Exposing the fixed-free beam surface to atomic hydrogen removes contaminants and nondiamond (amorphous) carbon phases, resulting in significant and stable increases in *Q*, even in air. This is in contrast to Si resonators, which exhibit increased *Q* upon oxide removal by vacuum annealing, but only temporarily, due to new oxide formation upon exposure to air or low partial pressures of oxygen.

Fracture strength is another important bulk parameter, particularly for MEMS/NEMS devices where moving components are subject to impact. Measurement of

Table 12.1 Comparison of Mechanical and Tribological Properties Between Si, SiC, and Diamond

Property	Silicon	Silicon Carbide	Diamond
Lattice constant (Å)	5.43	4.35	3.57
Cohesive energy (eV)	4.64	6.34	7.36
Young's modulus (GPa)	130	450	1200
Shear modulus (GPa)	80	149	577
Hardness (kg/mm ²)	1000	3500	10,000
Fracture strength (GPa)	1.0	5.2	5.3
Flexural strength (MPa)	127.6	670	2944
Friction coefficient	0.4–0.6	0.2–0.5	0.01–0.04
Relative wear life	1.0		10,000

fracture strength of UNCD and silicon revealed that the fracture strength of UNCD is about five times larger than for silicon (see Table 12.1) [7]. For RF-MEMS, contact switches wear can seriously degrade the lifetime of the devices. A thin coating of conductive UNCD could potentially be used to provide longer wear life for such contacting surfaces.

Regarding surface properties, diamond exhibits surface inertness, a very stable surface chemistry, and low stiction. UNCD has the lowest COF (~ 0.01 – 0.05) when compared to silicon (~ 0.4 – 0.6), conventional diamond-like carbon (DLC) films (~ 0.2), and MCD films (~ 0.4) [7,11,43]. Recent self-mated tribology studies on UNCD surfaces have demonstrated the lowest COF measured (0.007) ever on UNCD (O. Auciello, unpublished work). AFM studies provided quantitative information on interfacial adhesion and friction between AFM tips and UNCD film surfaces in ambient air as well as before and after H-plasma treatment. Silicon exhibits the highest work of adhesion while the UNCD underside exhibits substantially lower work of adhesion, before H-exposure, than the “passivated” form of silicon (55 mJ/m^2 versus 106 mJ/m^2 , respectively) [44]. This value for UNCD is comparable to that of the untreated $\langle 111 \rangle$ diamond surface. The measured friction force for the as-released UNCD underside is comparable to that of the untreated diamond $\langle 111 \rangle$ surface. The very low nanoscale adhesion and friction revealed by the plain UNCD surfaces indicate that the underside of UNCD can significantly outperform Si in MEMS/NEMS devices where surface properties are critical for performance.

Another important surface property is the RMS roughness of the films. It has been shown that the surface roughness of UNCD and NCD films depend on the nucleation density and initial growth of diamond films [11,23]. Different seeding techniques have been established to enhance nucleation and film continuity and achieve smooth films [11,23]. Mechanical polishing with diamond micron and nanoparticles result in relatively low nucleation density [11,23], while ultrasonically treatment of the substrate surface in an organic suspension of nanometer-sized diamond (ND) particles prior to diamond film growth results in high nucleation densities (10^{11} sites/ cm^2) [11,23] even for low growth temperatures, as demonstrated for the case of UNCD films [5]. A nucleation process named “Rotter nucleation technique,” yields extremely high nucleation densities [24]. However, it involves an extra plasma exposure step separate from film growth, which also involves high substrate temperatures (800°C), making it impossible to use this process when trying to grow diamond films at $\geq 400^\circ\text{C}$ for integration with CMOS devices. On the other hand, work recently performed in our group demonstrated the growth of very smooth UNCD films (4 – 6 nm RMS roughness as determined by AFM analysis), both for thin (100 nm) and thick ($\sim 1 \mu\text{m}$) films, using a 10 nm tungsten (W) layer grown on silicon substrates as a template layer [45]. The W interlayer significantly increased the initial diamond nucleation density, thereby lowering the surface roughness, eliminating interfacial voids, and allowing thinner UNCD films to be grown. This structural optimization enhances the films’ properties and enables its integration with a wide variety of substrate materials. In addition, the use of the W layer enables the low temperature growth of UNCD films without any high temperature step as in the Rotter seeding technique, which is critical for the development of

monolithically integrated UNCD-based MEMS/CMOS devices. The W layer seeding approach may also be applied to grow NCD films.

The information presented above indicates that UNCD films exhibit superior mechanical and tribological properties than those of Si and other materials for key MEMS/NEMS devices, except for NCD films, particularly for high-frequency systems where AV and stable surface chemistries are key parameters to enable very high-frequency devices to the GHz range.

Electrical properties of UNCD films

The tuning of the electrical conductivity of UNCD films, as discussed in the film synthesis section, may provide additional flexibility in the design and realization of RF-MEMS devices such as electrostatically driven resonators or other actuators or sensors. An alternative to nitrogen-incorporated electrically conductive UNCD films, as well as NCD films, would be boron-doped UNCD and NCD films. Work on B-doping of NCD films is progressing well in different groups (see for example Refs. [46,47]), but is not within the scope of this review. In addition, work on B-doping of UNCD has progressed substantially recently in academia [48] and industry (Advanced Diamond Technology, a company that is now commercializing B-doped UNCD wafers, although no publication has been submitted yet—J. Carlisle private communication and ADT website).

Dielectric properties of UNCD films

The dielectric properties of UNCD and MCD thin films were recently studied by Liu et al. [49] using impedance and DC measurements on metal–diamond–metal capacitor test structures. Close correlations were observed between the hydrogen content in two types of diamond (MCD and UNCD) films, measured by elastic recoil detection (ERD), and their electrical conductivity and capacitance–frequency (C – f) behaviors. Addition of hydrogen gas in the Ar/CH₄ gas mixture used to grow the diamond films appears to have two main effects depending on the film microstructure, namely (a) in the UNCD films, hydrogen incorporates into the atomically abrupt grain boundaries satisfying sp² carbon dangling bonds, resulting in increased resistivity and (b) in MCD, atomic hydrogen produced in the plasma etches preferentially the graphitic phase co-depositing with the diamond phase, resulting in the statistical survival and growth of large diamond grains and dominance of the diamond phase, and thus having significant impact on the dielectric properties of these films.

In general, dielectric properties (dielectric constant and loss tangent) of diamond, single crystal homoepitaxial [50] and MCD [51] thin films were found to be frequency dependent, and it is widely accepted that dielectric loss is closely related to the quality of the diamond film, specifically the defects in the diamond layer. Higher loss tangents were observed for lower-quality diamond films [52]. Also, it was observed that the dielectric constant depends on the resistivity of the diamond film as well, i.e., the higher the resistivity, the lower the dielectric constant, for microcrystalline CVD diamond films [53].

The specific studies of the dielectric properties of UNCD thin films [49] focused on establishing correlations between the dielectric properties and the hydrogen-incorporation level in the grain boundaries, with a view to application of UNCD thin films as a dielectric layer for RF-MEMS switches. A plot of resistivity versus hydrogen content in the plasma during UNCD film growth is shown in Figure 12.5, obtained from the low electric field region of the I - E curves in order to minimize effects of nonlinearity observed at high fields [50]. It is observed that, as hydrogen percentage in the gas feedstock increases, the resistivity of UNCD thin films firstly decreases slightly, and then increases more than two orders of magnitude from 3% to 6% hydrogen concentration in the plasma during the deposition process. Then, the resistivity decreases as hydrogen percentage further increases. It should be noticed that the dip in the resistivity versus H_2 concentration curve at low H_2 percentage (1–3%) is not as significant as it appears because the curve is plotted in logarithmic scale.

For better understanding of the effect of hydrogen concentration in the UNCD film on its electrical conductivity behavior, Figure 12.5 is re-plotted in Figure 12.6 as curve (B) and compared with curve (A) (bulk hydrogen concentration in a UNCD thin film as a function of hydrogen concentration in the plasma during film growth). By taking the reciprocal of the original resistivity values in Figure 12.5, the curve in Figure 12.6 illustrates the conductivity of the UNCD thin film as a function of hydrogen concentration in the plasma. It can be observed that

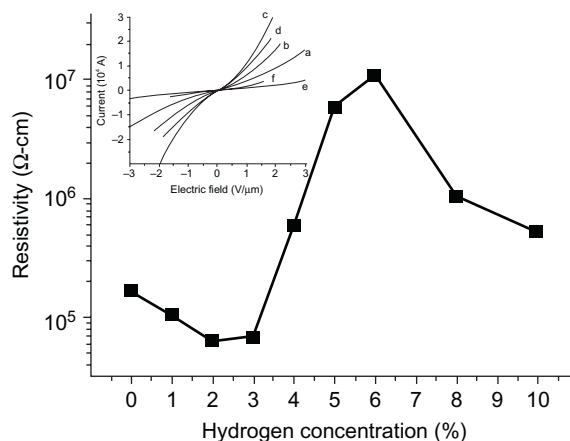


FIGURE 12.5

Plot of UNCD thin-film resistivity as a function of hydrogen percentage in the gas mixture during film growth. Inset: I - E curves measured from test structure with the UNCD thin films deposited in microwave plasmas with (a) 0%, (b) 1%, (c) 2%, (d) 3%, (e) 5%, and (f) 10% hydrogen in the Ar/CH_4 gas mixture (X axis: electric field ($V/\mu m$); Y axis: current ($10^{-4} A$)).

Source: Reprinted from Ref. [49]. Copyright (2007), with permission from the American Institute of Physics.

curves (A) and (B) follow each other in a very close manner, which indicates that the hydrogen concentration in the UNCD film has a fundamental impact on its electrical conductivity property. The inset in Figure 12.6 shows the electrical conductivity of a UNCD film (Y axis) as a function of bulk hydrogen concentration (X axis). The quasi-linear behavior of the data provides another indication of the close link between the hydrogen concentration in UNCD films and their electrical conductivity.

It has been reported that, besides defective regions in diamond grains, hydrogen is mainly incorporated in the grain boundaries, forming CH bonds such as hydrogen-terminated carbon dangling bonds [52]. When the hydrogen concentration in the gas mixture is below 2%, the microstructure of deposited diamond film is dominated by nanocrystalline grains. The hydrogen incorporations in these diamond films are enhanced as they have the relatively largest amount of grain boundaries ($\sim 10\%$ in volume), resulting in high bulk hydrogen concentrations in these films. On the other hand, the structure of the diamond films changes from ultra-nanocrystalline to mixture of NCD/MCD with increasing hydrogen concentrations in the plasma in the range of 4–10%. Smaller amount of grain boundaries exist in diamond films with nanocrystalline (up to a few hundred nanometers in diameter) and microcrystalline ($>1\mu\text{m}$ in diameter) structures as opposed to UNCD films that exhibit 2–5 nm diameter grains. This explains the smaller amount of hydrogen

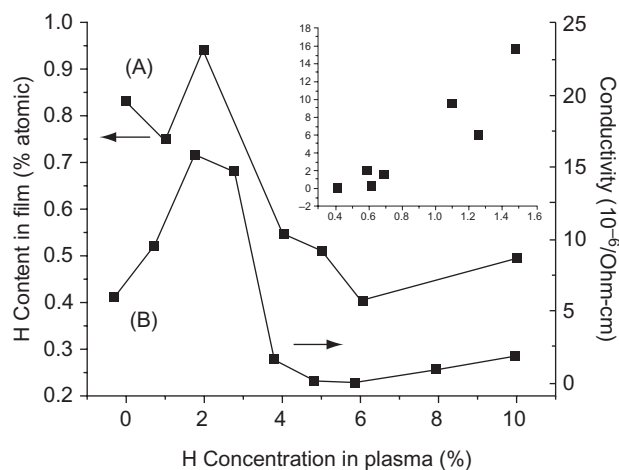


FIGURE 12.6

(A) Bulk hydrogen concentrations in a UNCD thin film as a function of hydrogen concentration in the plasma during film growth. (B) Re-plot of Figure 12.5 in linear scale by taking a reciprocal of resistivity data. Inset: A quasi-linear relationship between the electrical conductivity of UNCD films (Y axis) and their bulk hydrogen concentrations (X axis).

Source: Reprinted from Ref. [49]. Copyright (2007), with permission from the American Institute of Physics.

detected by ERD in NCD and MCD films, compared with the hydrogen content in the UNCD films. In the discussion presented above, an assumption has been made that hydrogen atoms incorporate into the diamond thin-film grain boundaries at a constant level regardless of the hydrogen concentration in the plasma during the deposition process, i.e., the absolute amount of hydrogen content in the CVD diamond thin film is proportional to the grain boundary volume in the film. It is known, from the literature, that hydrogen-incorporation into CVD diamond films depends strongly on the deposition conditions, among which substrate temperature is a key parameter. Given that the UNCD thin films discussed in this chapter were deposited at the same substrate temperature ($\sim 800^\circ\text{C}$), the above assumption is reasonable and valid.

The conclusion from the recent detailed studies of the dielectric properties of UNCD films is that the insertion of hydrogen into the grain boundaries controls extensively the charging and electrical conductivity behavior of the films and thus makes a major impact in the performance of UNCD as a dielectric layer with controlled charging–discharging behavior to enable reliable RF-MEMS switches, as recently demonstrated in a research and development program funded by DARPA to develop RF-MEMS switches based on UNCD as the dielectric layer [8].

Thermal properties of UNCD films

Thermal properties of diamond films may play a role in some MEMS/NEMS devices. Therefore, it is relevant to determine the thermal transport of UNCD films. Single crystal diamond has one of the highest known room temperature thermal conductivity ($k = 2200\text{ W/m}\cdot\text{K}$), while highly- sp^3 amorphous carbon films have $k < 15\text{ W/m}\cdot\text{K}$. Recently, researchers at Argonne conducted systematic integrated experimental and computer simulation studies to investigate the thermal transport properties of UNCD films [54]. The experiments showed that UNCD films with a grain size of 3–5 nm have thermal conductivities as high as $k = 12\text{ W/m}\cdot\text{K}$ at room temperature, comparable with that of the most conductive amorphous diamond films. This value corresponds to a grain boundary (Kapitza) conductance greater than $3000\text{ MW/m}^2\cdot\text{K}$, which is 10 times larger than that previously seen in any material. Computer simulations of both UNCD and individual diamond grain boundaries yield values for the grain boundary conductance consistent with the experimentally obtained value, leading to the conclusion that thermal transport in UNCD is controlled by the intrinsic properties of the grain boundaries. The thermal conductivity of UNCD films was measured using the 3Ω method [55] and analyzed using the offset model [56]. According to this model, the film is treated as a thermal resistor, which results in an experimental DT versus frequency curve that has the same shape as the curve calculated for uncoated silicon but is offset by an amount of DT_f given by

$$DT_f = [(P/l \cdot k)(t/2b)] \quad (12.3)$$

Equation (12.3) can be inverted to give the interfacial conductance:

$$G = \frac{k_o}{d} \left[\frac{1}{k_o/k - 1} \right] \quad (12.4)$$

Thermal conductivities obtained for a series of UNCD thin films grown on silicon substrates are shown as circles in Figure 12.7B. It can be noted that for all film thicknesses, the measured thermal conductivity ranged from as little as 1.2 W/m·K to as high as 12 W/m·K. Interestingly, as shown in Figure 12.7A, this lower value,

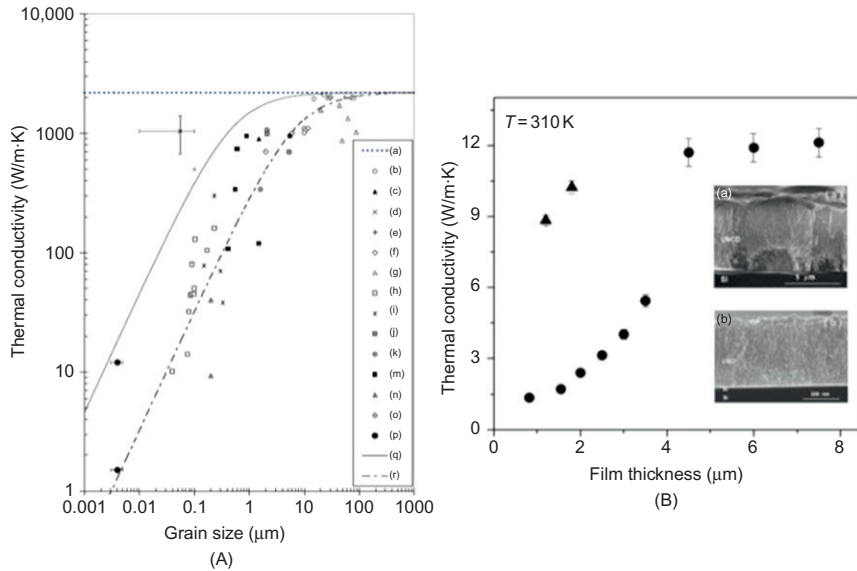


FIGURE 12.7

(A) Thermal conductivity versus grain size (μm). (a), (b), (c), (d), (e), (f), (g), (h), (i), (j), (k), (l), (m), (n), (o) represent data from many groups; (p) data from thermal transport measurements in UNCD films; (q) Eq. (12.4) for $G = 4600 \text{ MW/m}^2\cdot\text{K}$ obtained from simulation of UNCD; (r) fit of Eq. (12.3) to data (a)–(o) yields $G = 325 \text{ MW/m}^2\cdot\text{K}$. (B) thermal conductivity versus film thickness; \blacktriangle UNCD films grown on W/Si; \bullet UNCD films on Si. Insets show SEM cross sections of the film structure: (a) UNCD/Si with voids, and (b) UNCD/W/Si with dense interface. Each data point corresponds to a single sample of the indicated average grain size. Each error bar indicates the standard deviation from multiple measurements of that particular sample.

Source: Reprinted from Ref. [55]. Copyright (2001), with permission from the American Institute of Physics.

obtained for thinner films of UNCD grown directly on Si, is quite consistent with the extrapolation of the best fit to the previous experimental results.

A scanning electron microscopy (SEM) analysis of the thin-film microstructure of the UNCD films (inset (a) in Figure 12.7B) shows that there are voids at the interface, resulting from the relatively low seeding efficiency on Si surfaces. It thus seems that for these thin films, we are not measuring the intrinsic thermal properties of the diamond grain boundaries. By contrast, inset (b) shows that for UNCD grown on an intermediate W layer, there is no porosity at the interfaces, a consequence of the greatly enhanced initial nucleation density at the UNCD/W interface, thereby inhibiting the formation of voids seen at the UNCD/Si interface [57]. For the UNCD films grown on a W layer, the calculations give $k = 9\text{--}10\text{ W/m}\cdot\text{K}$; this higher value can be attributed to the absence of porosity and taken to be approaching the intrinsic thermal properties of NCD. Moreover, the considerable increase in the thermal conductivity of the UNCD/Si films over the thickness $3.5\text{--}5\mu\text{m}$ can then be due to a change in the interface structure from porous to nonporous one.

Further details on the measurements of thermal transport on UNCD films can be found in Ref. [54].

Properties of UNCD films as a biomaterial for MEMS/NEMS devices implantable in the human body

UNCD films are being developed as bioinert coating for encapsulation of a Si microchip implantable on the human retina as a key component of an artificial retina to restore sight to people blinded by retina degeneration [16]. UNCD films grown on high-conductivity Si substrates at $\sim 400^\circ\text{C}$, as required for this application of encapsulating a Si microchip without exceeding the thermal budget, exhibit similar surface morphology and microstructure characteristic of the best UNCD films grown at high temperature in early work at Argonne. Electrochemical tests of the plain UNCD coatings yielded relatively high leakage currents ($\sim 10^{-4}\text{ A/cm}^2$) that are not compatible with the needed functionality in the eye environment. Introducing hydrogen into Ar/ CH_4 mixture resulted in the incorporation of hydrogen into the grain boundaries and saturated the dangling bonds, thus leading to a greatly decreased leakage current. A competition between dynamic hydrogen incorporation and release exists when growing films in the range $600\text{--}800^\circ\text{C}$ with hydrogen content in the plasma in the range 1–20%. However, when the growth temperature is lowered to $\sim 400^\circ\text{C}$, then the UNCD films grown, using a $\text{CH}_4/\text{Ar}/\text{H}_2$ (1%) plasma, exhibit the lowest leakage current ($\sim 7 \times 10^{-8}\text{ A/cm}^2$) in a saline solution simulating the eye environment (Figure 12.8B), which correlates with the nanostructure characteristic of UNCD films with 2–5 nm grains (Figure 12.8A). This leakage is incompatible with the functionality of the first generation artificial retinal microchip. However, it is expected that when growing UNCD on top of the Si microchip passivated by a silicon nitride or an aluminum oxide layer, the electrochemically induced leakage will be reduced by at least one or two orders of magnitude. Long term (~ 6 months) *in vivo* tests, involving implantation of UNCD-coated Si chips in rabbit eyes (Figures 12.8D–F), demonstrated that UNCD is bioinert and biostable. These results provide preliminary validation of using

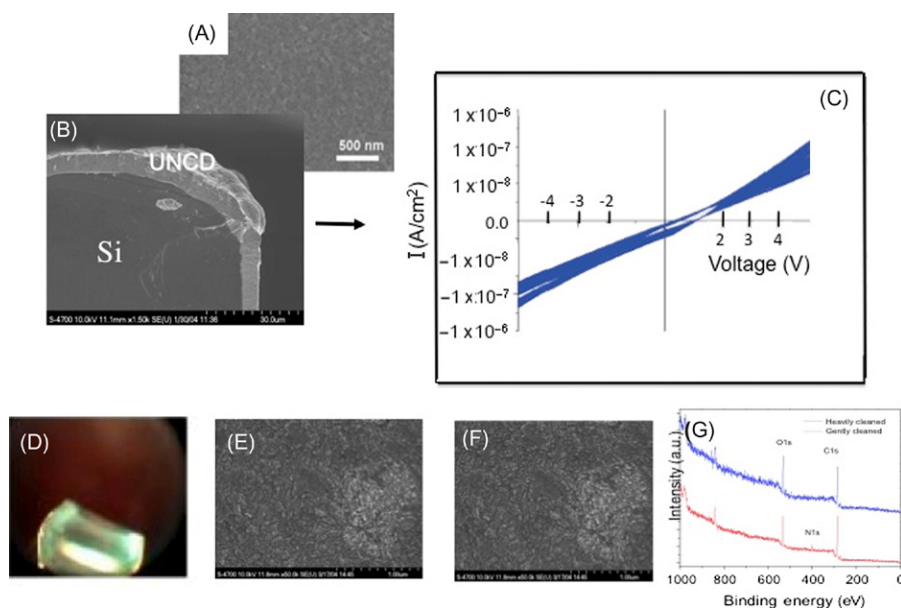


FIGURE 12.8

(A) Nanostructure of UNCD film grown with 1% H_2 in the Ar/CH_4 mixture (2–5 nm grain size); (B) cross-section SEM picture showing UNCD coating encapsulating a Si chip; (C) leakage current versus voltage in saline solution to test performance of UNCD encapsulating coating in the eye saline environment; (D) *in vivo* picture of UNCD-coated Si chip implanted in rabbit eye for 6 months; SEM pictures of UNCD coating before implantation (E) and after 6 month implantation in rabbit eye (F); and (G) XPS analysis of UNCD surface after 6 months implantation in rabbit's eye, showing no adsorption of biomolecules on the surface of UNCD.

Source: Reprinted from Ref. [11]. Copyright (2001), with permission from Elsevier.

low temperature UNCD as a hermetic coating for encapsulation of microchips for an artificial retina and other biomedical implants [16]. In addition, the *in vivo* tests of UNCD demonstrate that UNCD can be used for the development of a new generation of implantable MEMS/NEMS, such as for example drug-delivery systems.

12.3 MEMS and NEMS devices based on UNCD films

12.3.1 Materials integration and process strategies for fabrication of MEMS/NEMS devices based on UNCD films

Two main fabrication processes to produce UNCD-based MEMS/NEMS were developed by our group [6,11], based on prior fabrication processes developed previously for Si-based MEMS (lithography + reactive ion etching (RIE)) and for

selective growth of diamond films [6,11,58], although work reported in Ref. [58] was not applied to fabrication of diamond MEMS, namely (a) selective seeding and growth and (b) seeding plus photolithography followed by RIE. In both cases, the initial step is a seeding process whereby nanoparticles of diamond are embedded on the surface of the substrate via mechanical polishing or ultrasonic seeding via the exposure of the substrate to a solvent-based suspension of nanodiamond powder in an ultrasonic bath. The fabrication processes then proceed as described below.

Selective seeding and growth process for fabrications of UNCD–MEMS/ NEMS devices

In this process, the substrate is seeded by (a) using photoresist to prevent exposure of selected areas to the diamond powder, (b) using diamond-loaded photoresist to produce a patterned nucleation layer, or (c) seeding the substrate uniformly and then selectively etching portions of the surface to remove diamond-seeded areas. The feature resolution that can be achieved by this method is limited by the grain size. A schematic of the selective seeding plus UNCD growth process is shown in Figure 12.9A.

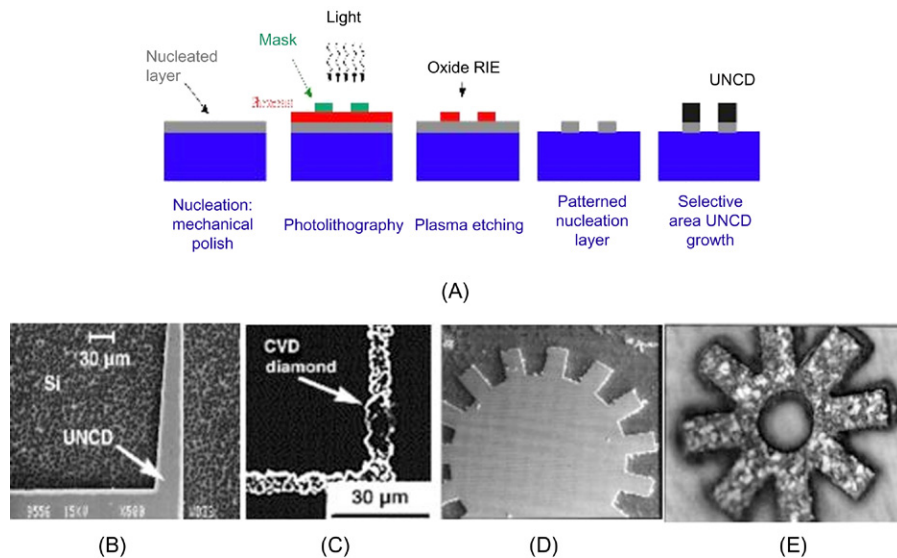


FIGURE 12.9

(A) Schematic showing selective seeding via uniform seeding of substrate, followed by photolithography and selectively etching of the substrate surface through vias open in the photoresist layer to remove diamond-seeded areas, and finally UNCD growth on selectively seeded areas; UNCD–MEMS structures are grown using selective seeding plus growth, using the UNCD growth process (B) and (D) and the MCD growth process (C) and (E); it is clear that the UNCD growth process produces MEMS structures with much higher resolution and smoother surface morphology than the MCD process.

Source: Reprinted from Ref. [11]. Copyright (2001), with permission from Elsevier.

Examples of MEMS structures produced by selective seeding and growth are shown in Figure 12.9B and D for UNCD-based structures and Figure 12.9C and E for MCD-based structures. It is clear that the resolution achieved by the UNCD-based process is far superior to that achieved with MCD films [6,11].

Photolithography plus RIE processes for surface micromachining fabrication of UNCD–MEMS/NEMS devices

In this fabrication process, blank UNCD layers are grown on a sacrificial release layer such as SiO₂ (e.g., thermal, LPCVD), using ultrasonic abrasion of the substrate surface exposed to a diamond powder suspension to produce a diamond seed layer. UNCD films grown using the Ar/CH₄ plasmas nucleate and grow directly on SiO₂ substrates with appropriate diamond seeding processes [4–13]. Thus, SiO₂ is used as a sacrificial layer for fabrication of UNCD-films-based MEMS/NEMS structures. As shown in Figure 12.10A, a UNCD layer is deposited on a thermal SiO₂ layer, followed by a second SiO₂ layer deposited by CVD. Photoresist is then used to pattern the hard SiO₂ mask using RIE with CF₄/CHF₃ gas mixture (2:1) plasma (Figure 12.10B and C). Oxygen plasma is then used to perform RIE etching of the UNCD pattern using the SiO₂ hard mask. UNCD films can be etched with rates of about 1 μm/h. Finally, an HF wet and/or gas etch (Figure 12.10D) is used to remove the sacrificial oxide layer, leaving the diamond film suspended above the Si substrate to form moving MEMS/NEMS structures (Figure 12.10E).

UNCD film stress and ohmic contact of electrode layers on UNCD films

A critical property of UNCD films, which enables fabrication of high-performance MEMS/NEMS structures, is that they exhibit relatively low intrinsic tensile stress that ranges from 100 to 400 MPa (orders of magnitude smaller than for MCD films) [7]. This property may be due to attractive forces between the diamond grains. UNCD films also exhibit very low differential stress (down to 50 MPa/μm) [7], due

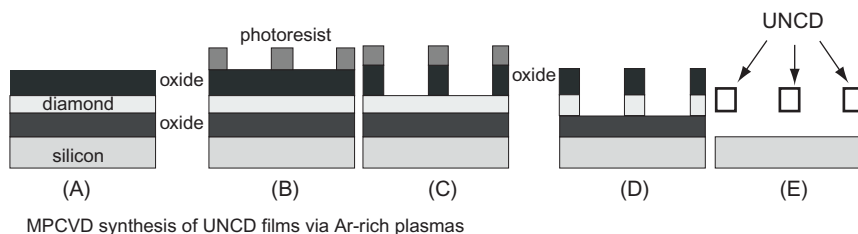


FIGURE 12.10

Schematic showing lithographically based process microfabrication of UNCD–MEMS: (A) deposition of UNCD on SiO₂ sacrificial layer plus masking layer; (B and C) photoresist and lithography; (D) RIE in oxygen plasma; and (E) selective chemical etching of SiO₂ sacrificial layer. This process works very well because UNCD is not etched by any acid used in the fabrication of Si microchips or Si-based MEMS.

Reprinted from Ref. [6]. Copyright (2001), with permission from Elsevier.

to both the microstructure, which does not vary with thickness and the use of nano-diamond-based seeding techniques, which ensure uniform growth and density even in the first few layers of the film.

Another important property of UNCD film surfaces is that sputter-deposited Al, Au, Cr, Cu, Pt, and Ti layers, all about 200 nm thick, have been shown to establish ohmic contact with the surface of UNCD [59]. This property of metallic layers/UNCD interfaces is critical for applications such as electrostatically actuated MEMS and NEMS devices, which require reliable electrical contacts.

Materials integration for hybrid piezoelectric/UNCD-based MEMS/NEMS devices

Real estate is fast becoming a premium in most consumer-based mobile applications. In addition, the current evolution toward ever-decreasing power availability for such applications puts a severe strain in the current integration of electrostatic RF-MEMS components with charge pumps needed to deliver 20–60 V. Such devices may become prohibitive in the future. Thus, alternative low voltage actuation schemes are necessary and are being explored as described in this section. In this respect, low voltage RF-MEMS/NEMS actuation can be achieved by integrating an electrode/piezoelectric/electrode-layered heterostructure on top of a structural UNCD layer used for a MEMS/NEMS structure. Application of a voltage across the piezoelectric layer induces strain (mechanical deformation due to the piezoelectric effect), causing the structural material to deform in the same direction as the piezoelectric layer, thus inducing the MEMS/NEMS structure actuation. In this respect, Auciello's group [60] recently demonstrated the integration of Pt/Pb(Zr_xTi_{1-x})O₃(PZT)/Pt-layered heterostructures, featuring PZT films with excellent piezoelectric and electromechanical coupling coefficients and high remanent polarization, on UNCD structural layers, to produce the first low voltage piezoactuated UNCD–MEMS cantilevers. Theoretical calculations performed by the same group at Argonne demonstrated that diamond is the best platform material for the proposed hybrid structures, including PZT as the piezoelectric actuation layer and UNCD as the structural mechanically robust support layer. The calculations showed that the product resonance frequency/dynamic displacement at resonance is the largest for the PZT/UNCD hybrid compared to the other PZT-based hybrids [60], including Si, nitrides, metals, and insulators. In addition, UNCD films provide the best support material for resonators due to the highest Young's modulus (see Table 12.1). The PZT/UNCD integration was achieved by using robust TiAl or TaAl (named TA) layers with dual functionality as oxygen diffusion barrier and adhesion layers [61] interposed between the Pt/PZT/Pt heterostructure and UNCD layers (Figure 12.11). The novel TA oxygen diffusion barrier layer [61] enabled growing oxide piezoelectric films, like PZT, on a carbon-based layer like UNCD without chemical etching of carbon due to oxygen (see Figure 12.11).

The TA barriers were chosen based on thermodynamic arguments, which indicate that oxygen atoms react preferentially with Ti, Ta, and Al to form stable oxides due to the lowest energy of oxide formation for these elements with respect to all

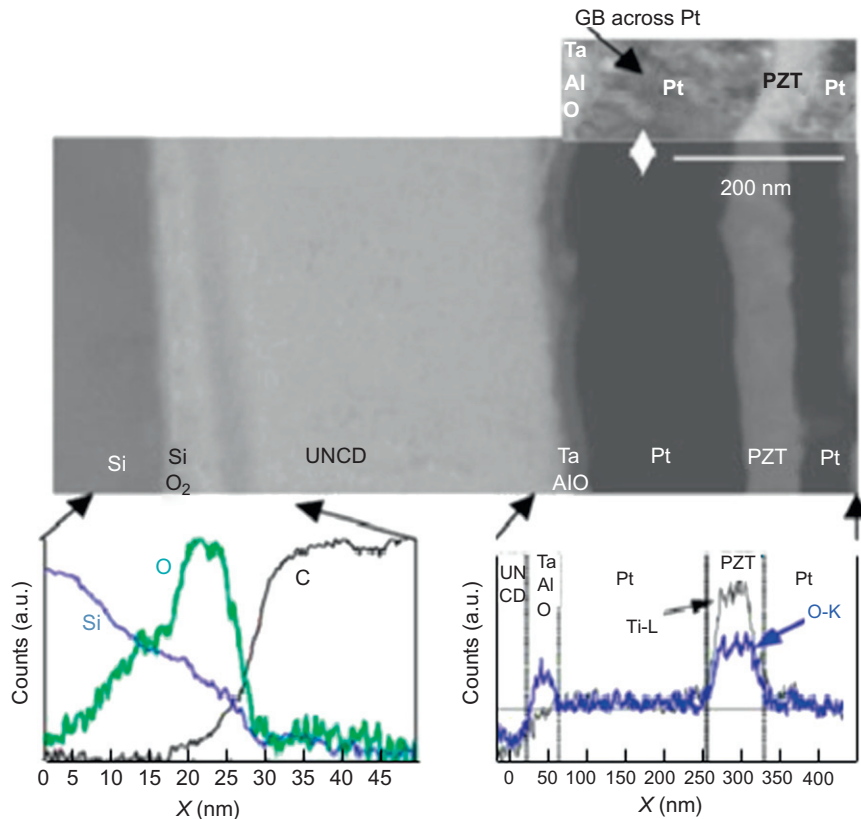


FIGURE 12.11

(Top) Cross-section TEM micrograph of a Pt/PZT/Pt/TA/UNCD heterostructure, showing the composition and microstructure of each layer and the interfaces; (bottom) EELS analysis of the different layers and interfaces shown on the top cross-section TEM images.

Source: Reprinted from Ref. [32]. Copyright (2001), with permission from the American Institute of Physics.

other elements in the periodic table. The TA barrier inhibits oxygen-induced etching of UNCD (carbon) layer during growth of PZT at relatively high temperature (450–500°C) in oxygen.

12.3.2 Examples of MEMS/NEMS devices based on UNCD film technology

Electrostatically actuated UNCD-based MEMS resonators

Recently, several companies (SiTime, Discera) have announced the availability of silicon-based MEMS resonator-based products for timing applications. These devices exhibit very high performance in the low- to mid-MHz range, but are unable to achieve

the same reproducible performance in the high-MHz to low-GHz range. For such applications, silicon-based MEMS resonators usually require the use of higher-order modes [62]. UNCD exhibits the highest measured AV ($\sim 15,700\text{m/s}$) reported in the literature today [63], among most nondiamond materials being used for resonators much higher than for single crystal silicon [64] (8024m/s) and SiC [65] ($11,500\text{m/s}$). Thus, UNCD promises to relax the design and manufacturing complexity of high-frequency resonators. It is relevant to point out that measurements of AV for MCD [66], using the propagation of acoustic Lamb waves in freestanding CVD-MCD films, showed velocities in the range $8700\text{--}12,200\text{m/s}$, which are lower than those measured by our group for our UNCD films. The lowest values reported for these MCD films [66] were recorded for films with the lowest crystal quality and highest nondiamond content. On the other hand, material parameters extracted from the dispersion characteristics of the acoustic signal together with SEM studies suggested that void, microcrack, and grain boundary density were the main factors influencing the propagation of low frequency Lamb waves in the freestanding CVD-MCD films reported in Ref. [66]. On the other hand, comparison between the phase velocities estimated from high-frequency characterization of surface acoustic wave (SAW) devices fabricated with NCD films, and numerical calculations, showed acoustic velocities for CVD-NCD films of up to 9500m/s [67].

As a first demonstration of UNCD-based resonators, simple resonant UNCD cantilevers were fabricated (Figure 12.12A) and used to measure the Q via the ring-down method (Figure 12.12C). The initial linear cantilever UNCD resonators fabricated at Argonne exhibit Q s as high as 11,460 (Figure 12.12D) measured at 11 KHz in air, which yields a frequency- Q product of $\sim 1.2 \times 10^{11}$, indicating promising perspectives for achieving very high Q s at medium- to high-MHz and low-GHz frequencies; once UNCD-based resonators with more efficient geometries (circular) are fabricated, they may yield comparable Q s to those of the circular resonators fabricated with NCD, which have shown the highest Q s in air (35,550) at 498 MHz today, yielding a frequency- Q product of $\sim 1.77 \times 10^{13}$ [23].

A primary driver for the development of high-frequency/high- Q MEMS resonators is for their insertion into communication filters and RF signal processing devices. In addition, these MEMS resonators would also be excellent mass and chemical sensors, particularly if the chemical termination of the surface can be controlled [16]. The new frontier to be explored is whether sensitivity and better response time of the resonators can be obtained by going at higher frequencies (high GHz) via reduction of device dimensions down to the nanoscale. However, at the nanoscale, due to the increase in surface-to-volume ratio, intrinsic dissipative mechanisms may dominate. Thus, there is a need for fundamental studies relating the atomic structure to various dissipative mechanisms in UNCD films, as similarly done previously for other diamonds.

Piezoelectrically actuated UNCD-based MEMS resonators and NEMS switches

MEMS/NEMS devices based on Si and other materials are generally actuated electrostatically, which requires high voltages ($\geq 10\text{V}$). This high voltage actuation

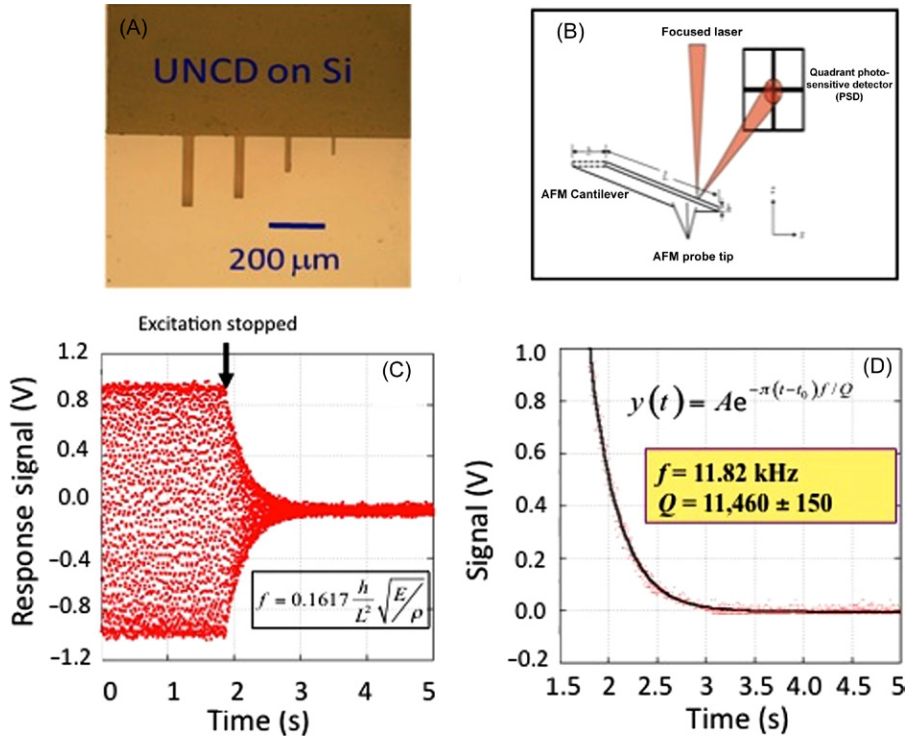


FIGURE 12.12

(A) UNCD resonant cantilevers for measuring Q of simple UNCD resonator; (B) schematic of AFM system measuring Q via reflection of a laser beam from the top of the cantilever with an integrated AFM tip that is in contact with the UNCD cantilevers and vibrates in resonance with them; (C) excitation of the ring-down method to measure Q ; and (D) amplitude versus time curve that yields Q 5 11,460 for the UNCD resonant cantilevers.

Reprinted from Ref. [11]. Copyright (2001), with permission from Elsevier.

would result in much less efficient means of actuating UNCD cantilevers for sensing or actuation applications, and would make it very difficult to integrate the UNCD-based MEMS/NEMS sensors with conventional low voltage CMOS devices to enable monolithically integrated UNCD–MEMS/NEMS/CMOS devices for compact handheld sensors. Thus, research and development at Argonne focused on a novel approach for actuating UNCD cantilevers via integration of a Pt/piezoelectric $\text{Pb}(\text{Zr}_x\text{Ti}_{1-x})\text{O}_3$ (PZT)/Pt heterostructure layer with the UNCD layer used as the mechanically robust, stiff material with high Young's modulus to enable high resonance frequency resonators.

The functionality of the hybrid Pt/PZT/Pt/Ta/UNCD heterostructure is based on the application of an external electric field \vec{E}_3 across the PZT layer, which results in displacement of the ions in the PZT lattice resulting in polarization of

the ferroelectric material as shown in the polarization versus electric field curve (Figure 12.13) and macroscopic mechanical distortion of the PZT layer, which in turn induces bending of the heterostructure (deflection at the free end of the cantilever; Figure 12.14B).

Piezoelectric actuation of 150 μm long UNCD cantilever beams were demonstrated via fabrication of Pt/PZT/Pt/UNCD heterostructured cantilevers (Figure 12.14A), with PZT film thickness of about 70 nm and Pt electrode layers about 50 nm thick. They exhibited deflections up to 5 μm at the end, via excitation with 3 V AC at 1 MHz, and were run for about 1 billion cycles (Figure 12.14B) [60]. More recently, piezoactuated NEMS horizontal switches were demonstrated. The horizontal NEMS switches consisted of Pt/PZT/Pt/UNCD nanostructured beams

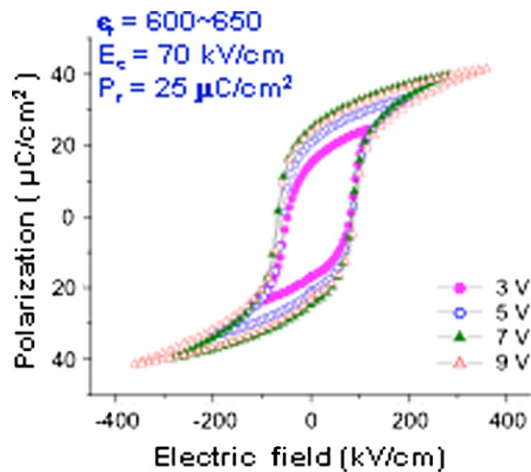


FIGURE 12.13

Polarization versus electric field curve measured for different excitation voltages for a Pt/PZT/Pt capacitor fabricated on top of a UNCD film.

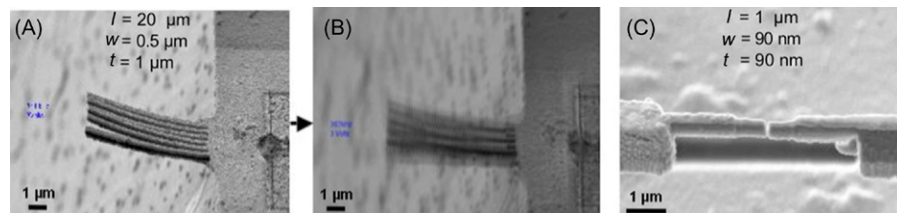


FIGURE 12.14

(A) Layered heterostructured Pt/PZT/Pt/UNCD cantilevers; (B) same cantilevers shown in (A) actuated with 3 AC Volts (1 MHz) applied between the top and bottom Pt electrodes sandwiching the PZT layer, for 1 billion cycles; and (C) layered heterostructured Pt/PZT/Pt/UNCD NEMS switch actuated with 1 AC Volt (1 MHz) for 1 billion cycles.

Reprinted from Ref. [11]. Copyright (2001), with permission from Elsevier.

(1 μm long, 90 nm wide, and 90 nm thick), and were operated for about 1 billion cycles with 1 V at 1 MHz (Figure 12.14C) [11,12].

The NEMS switches are being developed for integration into new logic systems based on these nanomechanical switches as opposed to logic based on solid state transistors. Logics based on NEMS switches would involve much lower energy consumption due to the fact that once opened the NEMS switches exhibit practically zero leakage current, as opposed to the solid state transistor switches.

The initial work described here shows the feasibility of producing high-performance piezoactuated UNCD-based MEMS/NEMS devices for applications to a variety of systems.

Fabrication of monolithic UNCD cantilever/AFM tips and applications

The technology for fabricating monolithic UNCD AFM cantilevers with integrated tips has recently been developed [68,69] and UNCD AFM probes, including electrically conducting (boron-doped) ones are now commercially available (NaDiaProbe™) [70]. They represent the first MEMS-type structures in the market based on UNCD (Figure 12.15A). Tests have demonstrated that UNCD AFM tips exhibit practically no wear (Figure 12.15B) after extensive scanning on different surfaces as opposed to high wear generally observed with conventional Si and Si_3N_4 -based AFM tips.

These probes will find applications in metrology, fabrication of nanostructure, AFM imaging in corrosive liquids, and nanoscale electrical measurements of nanostructures, among many other applications. The UNCD AFM tips represent a substantial improvement over prior diamond AFM tips [71], particularly from the point of view of the much smoother profile of the UNCD tips, which leads to much higher AFM image resolution for scientific purposes and exploration of fabrication of nanoscale structures using AFM-based nanofabrication.

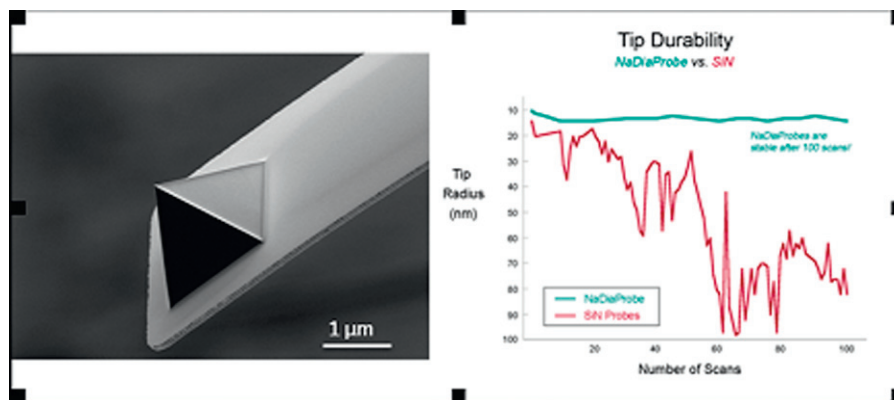
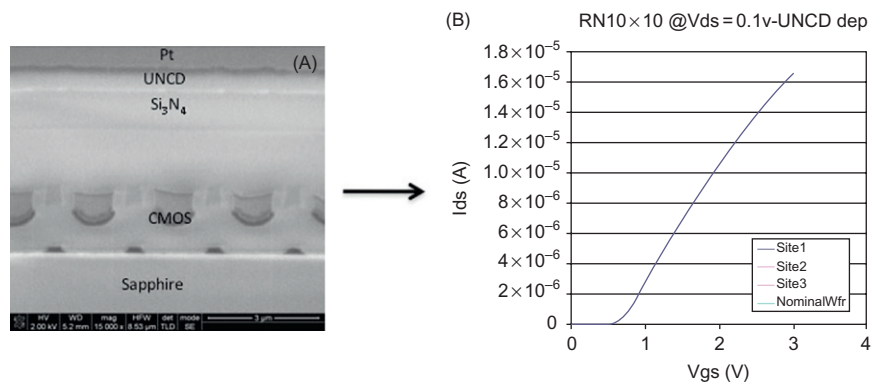


FIGURE 12.15

(A) SEM image of commercially available microfabricated monolithic UNCD AFM cantilever/tip and (B) comparison of wear performance with that of Si_3N_4 AFM tip.

Source: Courtesy of Advanced Diamond Technologies, Inc., with permission from J.A. Carlisle and Prof. R.W. Carpick, University of Pennsylvania.

**FIGURE 12.16**

(A) Cross-section SEM picture of an integrated UNCD film SOS-CMOS device and (B) I–V curves measured for an SOS-CMOS device before and after UNCD deposition (the two curves are practically superimposed showing similar performance without any measurable degradation).

12.3.3 UNCD integration with CMOS devices

A recent technological breakthrough has been the demonstration of integration of UNCD films with CMOS devices [10,11], which provides the basis for the development of a new generation of monolithically integrated diamond MEMS/NEMS/CMOS devices for low-power CMOS driven MEMS/NEMS-based systems. This integration has been achieved due to the fact that UNCD films can be synthesized at $\leq 400^\circ\text{C}$ [5,11], within the CMOS thermal budget. Other groups have reported growing NCD films at low temperature [67]. However, up until now, no demonstration of integration of low temperature NCD films with CMOS devices has been published. The compatibility of the low temperature UNCD process with CMOS was tested by depositing UNCD films directly on the CMOS wafer and testing the performance of CMOS devices before and after the UNCD deposition [8,10,11,73]. A cross-section SEM image of integrated UNCD/CMOS devices fabricated on sapphire for low-loss high-frequency RF systems is shown in Figure 12.16A (see also Ref. [73]). Electrical measurements of CMOS devices before and after UNCD deposition demonstrated that all devices perform to specifications before and after UNCD deposition (see Figure 12.16B).

12.3.4 RF-MEMS switches with UNCD dielectric layer monolithically integrated with CMOS driving devices

Research performed recently by an Argonne National Laboratory–led team involving industry (MEMtronics Corp., Peregrine Semiconductor, Innovative Micro Technology (IMT), and Advanced Diamond Technology (ADT)) and university (University of Pennsylvania and Lehigh University) partners, under a DARPA-HERMIT funded

program, resulted in the development of monolithically integrated RF-MEMS capacitive switches/CMOS devices for insertion into advanced radar and mobile communication applications. For this particular application, UNCD films are used as a dielectric layer with controlled leakage to enable high-performance reliable RF-MEMS capacitive switches with ≥ 100 billion cycles operation. The work performed until now within the DARPA-funded program has resulted in the first world-wide demonstration of RF-MEMS switches with UNCD as the dielectric layer [72,73], based on MEMtronics design, driven by high voltage CMOS devices based on the silicon-on-sapphire technology of Peregrine Semiconductors.

While the performance of RF-MEMS switches has been shown to be compatible with systems requiring these switches as critical components, reliability issues have limited their deployment into military or commercial systems. In the case of capacitive RF-MEMS switches, with conventional SiO_2 or SiN_x dielectric layers on top of the bottom electrode, the charging and discharging time constants of the dielectric, upon application of the voltage to close the switch membrane onto the bottom electrode, are of $10\text{--}100 + \text{s}$ [74]. As the switches operate, charges build up within their dielectric, and they experience a very gradual change in pull-in and release voltages until the ultimate failure of the switch. With charging of the dielectric bulk, this failure is characterized by the release voltage dropping to zero and the device becoming stuck down. After failure, the switch requires a sufficiently long period of time to recover (in which the charges recombine) before it is released.

There are many solutions for lessening the impact of dielectric charging, including hermetic packaging, minimizing the electric field across the dielectric, and tailoring the polarity and waveform of bias control signals to minimize charging. These solutions have provided significant improvements in reliability, but have not proven enough to overcome the dielectric charging, which is currently the main limitation for insertion into the market of RF-MEMS capacitive switches. Recently, there have been many attempts to tailor the dielectric material itself for mitigating charging. The work focused on mitigating charging in RF-MEMS capacitive switching includes growth of layers using atomic layer deposition (ALD), as well as physical and metalorganic CVD techniques. There have also been efforts to manipulate the leakage of the MEMS switch dielectric to bleed off charges and improve reliability. Unfortunately, these techniques have not proven repeatable or robust enough to be generally adopted. Attempts were made by different groups to manipulate the bulk conductivity of the dielectric film to bleed off charges and improve reliability [75]. The attempts involved several techniques, including using atomic layer deposition (ALD) to grow dielectric layers [76]. Unfortunately, these techniques are not repeatable or robust enough to be generally adopted. Researchers have attempted incorporation of nanocrystalline diamond as the switch dielectric for MEMS switches, but were not able to demonstrate significant improvements regarding controlling dielectric charging, and thus reliability [77–79].

More recently, research and development performed by the Argonne-led DARPA team demonstrated that UNCD films with hydrogen incorporated into the grain boundaries provides fast charging and discharging (both in the range of $10\text{--}100\text{s}$ of

microseconds) via a dense network of grain boundaries, providing a new paradigm in charging/discharging of the dielectric layer of RF-MEMS switches to enable robust/reliable RF capacitive MEMS switches. Three major improvements were introduced by the DARPA team to enable a reliable incorporation of diamond films in to RF-MEMS switches [72,73], namely (a) incorporation of the novel UNCD dielectric layer developed by the DARPA team, (b) use of new substrate material (sapphire) as a platform to enable silicon-on-sapphire electronics to achieve monolithically integrated RF-MEMS switches with UNCD dielectric and CMOS devices, and (c) a chrome/tungsten (W)/chrome bottom electrode to accommodate the higher deposition temperature of UNCD ($\sim 400^\circ\text{C}$) relative to silicon dioxide ($<100^\circ\text{C}$), without significant interdiffusion between the electrode and the substrate. The W layer thickness in the bottom electrode was doubled to $\sim 0.5\mu\text{m}$ to compensate for the higher resistivity with respect to the standard gold electrodes and help maintain the switch insertion loss at a low level.

The electromechanical properties of the RF-MEMS switches with the UNCD dielectric layer were characterized by measurements involving sweeping the bias voltage on the bottom electrode and measuring the capacitance of the device (C–V curves). A typical C–V curve is shown in Figure 12.17, which includes an inset with a schematic of the RF-MEMS switch. These switches exhibit actuation voltages in the range of 30–45 V with an on-capacitance ranging from 650 to 800 fF. The on-capacitance is primarily determined by the surface roughness of the lower electrode and the cleanliness of the sacrificial release process. The measured switch off-capacitance ranged from 90 to 105 fF, which includes 52 fF of transmission line capacitance. This means that the MEMS plate and fringing capacitance is ~ 38 –53 fF.

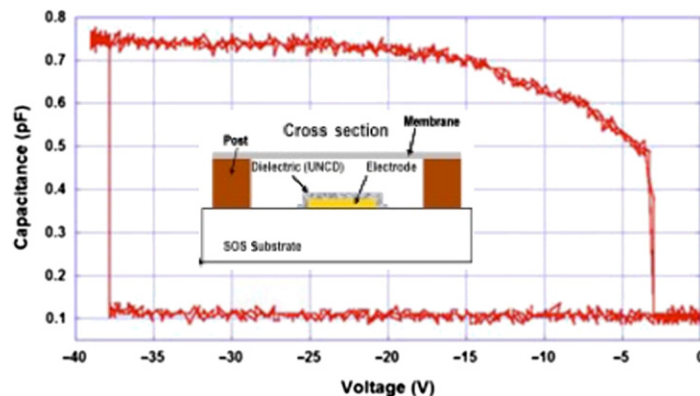


FIGURE 12.17

C–V curve obtained when applying a voltage between the bottom electrode and the membrane of an RF-MEMS switch with UNCD dielectric ($V_p = 38\text{ V}$) and measuring the capacitance change when closing the membrane on the dielectric layer on top of the bottom electrode (the inset shows a schematic of the RF-MEMS switch with the UNCD dielectric layer).

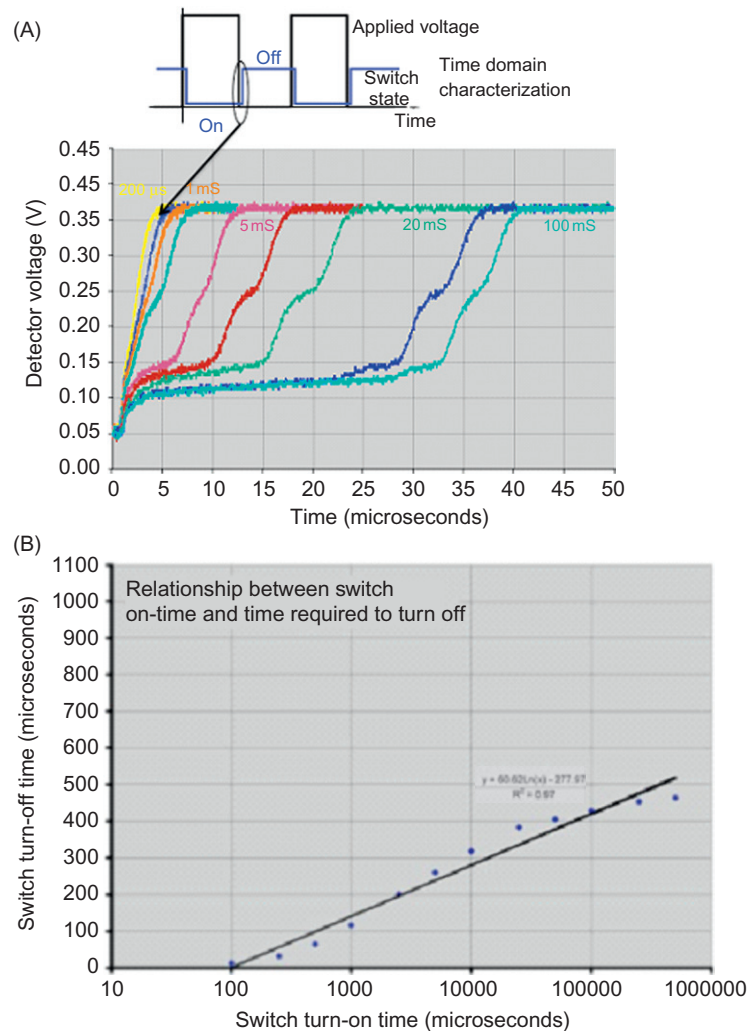
Source: Reprinted from Ref. [72], with permission from IEEE.

The RF performance of the RF-MEMS switch with UNCD dielectric layer is typical of most MEMS capacitive switches. When the shunt switch is in the off-state, the insertion loss is very low, on the order of 0.25 dB at 20 GHz. This is slightly higher than the usual insertion loss of 0.15 dB, and is attributed to the less conductive W metal used for the bottom electrode. When the switch is actuated, isolation is set by the on-capacitance of the device. With 700 fF of on-capacitance, the isolation at 20 GHz is very close to the theoretical value associated with a shunt 700 fF capacitor (7.7 dB). This switch operates more like a switched capacitor (45–725 fF) than a high isolation switch at frequencies below 20 GHz.

Measurements of the on–off states revealed that the RF-MEMS switches with UNCD dielectrics have switching time constants that are 5–6 orders of magnitude faster (~100 ms) than those of switches with conventional oxide or nitride dielectric layers. With these very short time constants, the UNCD-based switch fails very quickly, less than a millisecond after actuation. As is characteristic of bulk charging, the device becomes stuck down. However, after the switch bias is removed, the switch requires a very short time for the charges to dissipate and the switch to release. The switch recovery time is not the typical 5–10 ms switching speed of the oxide or nitride-based switches but is dependent on the amount of charging that occurred during and after failure. Thus, the time required for recovery and release is dependent on the switch on-time. Figure 12.18A shows the release time of the switch as a function of the transmitted RF power, and hence, the switch on-time. The vertical axis is the detector voltage monitoring the position of the membrane. The operating voltage on the lower electrode was –33 V relative to ground. The equipment configuration for this test can be seen in detail in Ref. [80]. Figure 12.18B reveals that the UNCD–RF switch recovery time, t_{OFF} , can take many hundreds of microseconds depending on the switch on-time, t_{ON} . In the most extreme cases, switches required milliseconds to recover.

A plot of the switch recovery (see Ref. [80]) shows that the charging and discharging time constants of the UNCD dielectric layer are very short (in the micro-seconds range). As the switch is actuated and charges, bulk charging aids in the actuation of the switch and there is no perceived difference in actuation time. However, the release of the switch is delayed until the accumulated charges have had sufficient time to recombine and/or dissipate. This has the effect of making the switch release time dependent on the switch on-time and subsequent dissipation of accumulated charges.

The latest optimized RF-MEMS switches with UNCD dielectric layers showed that if the switches were left “on” for 100 s they recovered back to their original condition in less than 50 ms. This implies that if switches are cycled off once out of every 100 s, they will be fully recovered from any effects of charging and are ready to be reused anew. This means that they only have to be turned off 0.00005% of the timeline to operate without charging failure. Continuous switch operation is now reasonably achievable for RF-MEMS capacitive switches with the UNCD dielectric layer. The measured results for these switches demonstrate a new paradigm in switch operation, eliminating the dielectric charging failure that dominated the RF-MEMS switches with oxide or nitrides dielectric layers. However, there is still

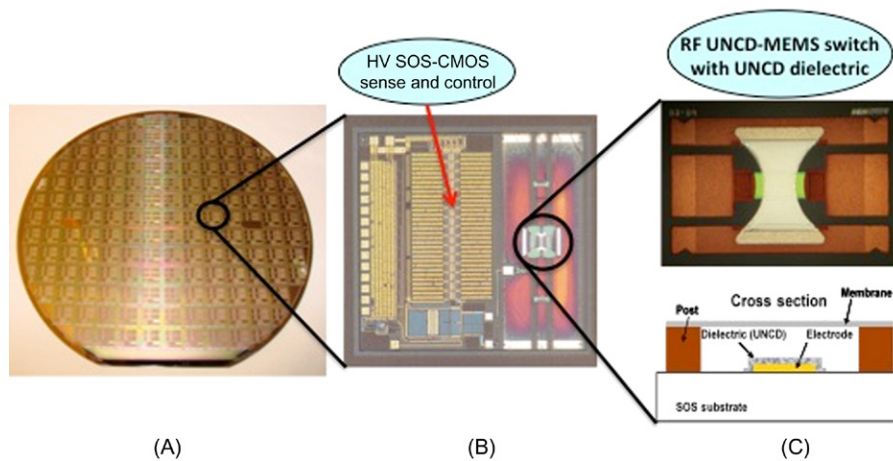
**FIGURE 12.18**

(A) Time domain measurements showing switch recovery dependence with switch on-time and (B) relationship between the switch time-on and the time required to turn the switch off.

Source: Reprinted from [72], with permission from IEEE.

significant development required to fully optimize the materials and materials integration for the RF-MEMS switches with the UNCD dielectric layer.

In any case, the DARPA team demonstrated the first fully operational RF-MEMS switches with UNCD dielectric layers monolithically integrated with CMOS devices fabricated on sapphire 150 mm wafers, with the CMOS devices driving the switches (Figure 12.19).

**FIGURE 12.19**

(A) Sapphire wafer with integrated RF-UNCD/MEMS switches/SOS-CMOS devices; (B) optical microscope picture of integrated RF-UNCD/MEMS switch/SOS-CMOS device; and (C) optical microscope picture (top) and cross-section schematic (bottom) of RF-UNCD/MEMS switch.

Source: Reprinted from Ref. [9].

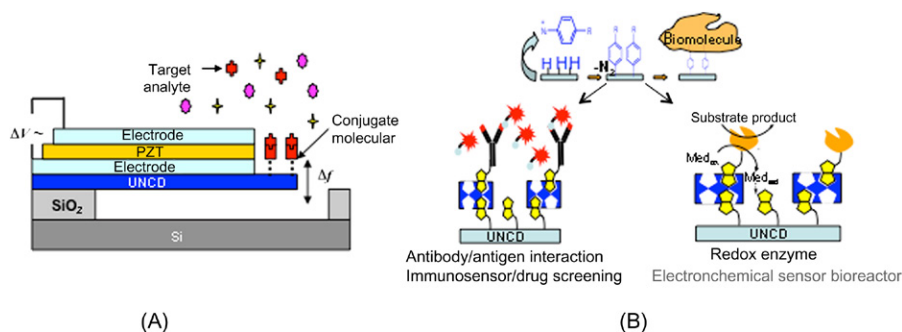
The work described in this section demonstrated the feasibility for integration of RF-MEMS switches with UNCD dielectric layer in commercial radars and mobile communication systems.

12.3.5 MEMS/NEMS biosensors

The research and development described in the section discussing piezoelectrically actuated MEMS/NEMS devices has been useful to provide one of the two key components for developing a new generation of biosensors based on piezoelectrically actuated MEMS/NEMS devices. The second key component for the development of these devices is the demonstrated functionalization of the UNCD surface, which provides the bases for selective attachment of biomolecules on the surface of UNCD resonant MEMS/NEMS structures, which upon absorption of the biomolecules change their resonant frequency, thus providing the basis for the MEMS/NEMS biosensors.

Figure 12.20A shows a schematic of MEMS/NEMS biosensors. The fabrication of the MEMS/NEMS cantilevers or resonators is done following the processes described in Section 12.3. The second component of R&D to develop MEMS/NEMS biosensor based on UNCD is the development of functionalization of the UNCD surface to attach functional molecules, which can selectively grab the biomolecules to be sensed.

Initial research at Argonne demonstrated the feasibility of functionalizing the surface of UNCD thin films [11]. The surface was first combined with a linker,

**FIGURE 12.20**

(A) Schematic of piezoelectrically actuated MEMS biosensor based on hybrid Pt/PZT/Pt/UNCD-MEMS heterostructure and (B) functionalization of the UNCD biosensor base.

which offers the binding sites for biomolecules. Then the proteins were linked to the linker. Different linkers were purchased and synthesized (Figure 12.20B).

All linkers were used to modify the surface of UNCD films deposited on Si substrates, with and without hydrogen plasma treatment. The UNCD surface modification was conducted by exposing the UNCD surface to 254nm UV irradiation in an N_2/Ar environment for more than 12h. In order to identify the presence of the linkers on the UNCD surface, the UNCD surface modified by linker 1 was further linked using an *N*-hydroxysuccinimide group and immobilized S-protein horseradish peroxidase (HRP) and tested by its substrate; UNCD surfaces modified by linker 2 were further linked by S-protein HRP. UNCD surfaces modified by linker 3 were further deprotected and linked by an *N*-hydroxysuccinimide group and immobilized S-protein HRP and tested; and surfaces modified by linker 4 were further tested by Fourier transform infrared (FTIR) and X-ray Photoelectron Spectroscopies (XPS).

The analysis of linked UNCD surfaces showed that there was a change in the surface chemistry after linker attachment. Peaks have shifted to different wave numbers and the intensities of these peaks changed as well. Further experiments are under way to understand the effect of the UNCD surface modification on linker attachment, since this is a critical step toward trapping of biomolecules for detection. Electrochemical surface modification methods are currently under investigation.

The functionalization of UNCD surfaces via exposure to UV light, as described above, generally involves a process that takes about 24h to produce a densely functionalized surface. On the other hand, a new electrochemical process developed at Argonne produces dense functionalized surfaces in 20–30s. The electrochemical functionalization of conductive UNCD thin-film surfaces recently developed at Argonne proceeds via the electrochemical reduction of aryl diazonium cations in a nonaqueous medium [81]. A one-electron transfer reaction leads to the formation of solution-based aryl radicals, which react with the UNCD surface forming covalent CC bonds. Cyclic voltammetry, X-ray photoelectron spectroscopy, contact angle, and ac impedance measurements have been employed to characterize the organic overlayer

and estimate the surface coverage. The grafting of 3,5-dichlorophenyl groups render the UNCD surface hydrophobic, whereas the attachment of 4-nitrophenyl groups makes the surface relatively hydrophilic. The surface coverage estimated from the electrochemical and XPS measurements is as high as 70% of a compact monolayer. The grafted organic layer can be removed at temperatures above 700°C when heated in an ultrahigh vacuum environment. Finally, aniline moieties were achieved via a six-electron transfer reaction, converting the nitrophenyl NO₂ termination to NH₂, which provide the basis for subsequent covalent immobilization of biomolecules such as DNA, peptides, proteins, and molecules used in biowarfare, such as anthrax.

12.4 Future scientific and technological developments based on UNCD films and integration into MEMS/NEMS structures

Recently, Argonne researchers have demonstrated the feasibility of fabricating UNCD nanowires (A.V. Sumant et al., private communication, 2010), which open a broad range of opportunities for studying fundamental phenomena such as electrical and thermal transport in 1D dimensionality at the nanoscale, as well as the possibility of developing biosensors based on functionalized UNCD nanowires. On the other hand, work by other groups is showing that NCD nanowires can be fabricated as well and are being explored for application to biosensors [82].

In another breakthrough development, a University of Wisconsin–Argonne collaboration recently resulted in the demonstration of a novel-layered heterostructure of an electrically conductive NUNCD film [11] covered by an insulating UNCD layer [11], such that this layered structure is used as a multilayer of electrically conductive/insulating UNCD, which provides a nonsacrificial template for repeatable nanowire synthesis [19]. Unlike all other methods for making patterned nanowires, this technique produces large numbers of complex patterned nanowires with controlled diameters from a wide range of materials without intervening clean room processes, and providing a reusable UNCD-based template for growing multifunctional nanowires for science and industrial applications. These UNCD templates could be used to fabricate nanowires, which can subsequently be integrated in NEMS systems.

Finally, given the fact that work by Argonne investigators has demonstrated that UNCD films are extremely biocompatible, it is feasible that UNCD films can be used to develop a new generation of bio-MEMS/NEMS with capability for implantation in the human body to provide different functionalities, such as drug-delivery MEMS/NEMS implantable devices and MEMS/NEMS-based biosensors.

12.5 Conclusions

In conclusion, the fundamental and applied science done to understand the synthesis and properties of the novel material named UNCD, since its invention as a

thin-film material in the early 1990s, and the numerous applications demonstrated until now and those upcoming in the future, have proven that UNCD is truly a multifunctional material that exhibits a broad range of functionalities applicable to a large range of multifunctional devices. Specifically, this chapter provides extensive evidence that UNCD films can be used for developing a new generation of specific MEMS and NEMS devices with superior performance to that of equivalent Si-based MEMS/NEMS devices. Although there is still a wide range of properties that need further detailed investigation, UNCD has already found applications into commercial devices now in the market, introduced by a company spun-off from Argonne National Laboratory, where UNCD was discovered and has been under continuous development for the past 20 years. During the past 20 years, research and development on UNCD has been extremely productive, and given the fact that many groups worldwide are now working on the science and technology of UNCD, it is expected that the future will be even more exciting and productive on the science and technology of UNCD, which has the great potential to enable a new generation of MEMS/NEMS devices with superior performance to that of Si and other materials being explored for this application.

Acknowledgments

This work was supported by US Department of Energy, Office of Science, Office of Basic Energy Sciences—Materials Science, under Contract No. DE-AC02-06CH11357 and DARPA under Contract No. MIPR 06-W238. Use of the Center for Nanoscale Materials was supported by the US Department of Energy, Office of Science, Office of Basic Energy Sciences, under Contract No. DE-AC02-06CH11357. The TEM work was performed at the Electron Microscopy Center of Argonne National Laboratory. The MEMS/NEMS programs are supported by DARPA under Contract No. MIPR 06-W238. The author acknowledges the great contributions of the many scientists, students, and postdoctoral fellows who contributed to the science and technology of UNCD films during the past 20 years, and also to the development of the MEMS/NEMS device fabrication process and demonstration of prototype systems, namely A.R. Krauss, D.M. Gruen, A.V. Sumant, and S. Srinivasan (now at IMT); Y.C. Chen, X.Y. Zhong, B. Kabius, J.M. Hiller, B. Shi, Q. Jin, L. Chen, and X. Xiao (Argonne National Laboratory, Materials Science Division); D.C. Mancini, L. Ocola, D. Czaplewski, R. Divan, and C.S. Miller (Argonne National Laboratory, Center for Nanoscale Materials); J.A. Carlisle (initially Argonne National Laboratory and currently CTO of Advanced Diamond Technologies, Inc, special thanks for his leadership in bringing the UNCD technology to commercialization); N.H. Tai and I.N. Lin (Tamkang University, Taiwan); A.R. Konicek, D.S. Grierson, V.P. Adiga, and R.W. Carpick (Department of Physics, University of Wisconsin-Madison, and Department of Mechanical Engineering and Applied Mechanics, University of Pennsylvania); C. Goldsmith, D. Forehand, and S. O'Brien (MEMtronics Corporation); S. Sampath, A. Datta, and C. Gudeman (IMT); M. Burgener and J. Swonger (Peregrine Semiconductors); S. Pacheco and P. Zurcher (Freescall Semiconductor); and M.P. Zach, D.B. Seley, and D.A. Dissing (Department of Chemistry, University of Wisconsin-Stevens Point). The submitted manuscript has been created by UChicago Argonne, LLC,

Operator of Argonne National Laboratory (“Argonne”). Argonne, a US Department of Energy Office of Science laboratory, is operated under Contract No. DE-AC02-06CH11357. The US Government retains for itself, and others acting on its behalf, a paid-up nonexclusive, irrevocable worldwide license in said article to reproduce, prepare derivative works, distribute copies to the public, and perform publicly and display publicly, by or on behalf of the Government.

References

- [1] D.M. Gruen, S. Liu, A.R. Krauss, J. Luo, X. Pan, *Appl. Phys. Lett.* 64 (1994) 1502.
- [2] D. Zuiker, A.R. Krauss, D.M. Gruen, J.A. Carlisle, L.J. Terminello, S.A. Asher, et al., *Mater. Res. Soc. Proc.* 437 (1996) 211.
- [3] S. Jiao, A.V. Sumant, M.A. Kirk, D.M. Gruen, A.R. Krauss, O. Auciello, *J. Appl. Phys.* 90 (2001) 118.
- [4] J. Birrell, J.A. Carlisle, O. Auciello, D.M. Gruen, J.M. Gibson, *Appl. Phys. Lett.* 81 (2002) 2235.
- [5] X. Xiao, J. Birrell, J.E. Gerbi, O. Auciello, J.A. Carlisle, *J. Appl. Phys.* 96 (2004) 2232.
- [6] A.R. Krauss, O. Auciello, D.M. Gruen, A. Jayatissa, A.V. Sumant, J. Tucek, et al., *Diamond Relat. Mater.* 10 (11) (2001) 1952.
- [7] O. Auciello, J. Birrell, J.A. Carlisle, J.E. Gerbi, X. Xiao, B. Peng, et al., *J. Phys. Condens. Matter.* 16 (16) (2004) R539.
- [8] O. Auciello, S. Pacheco, A.V. Sumant, C. Gudeman, S. Sampath, A. Datta, et al., *IEEE. Microwave. Mag.* 8 (2008) 61.
- [9] O. Auciello, S. Srinivasan, J. Hiller, A.V. Sumant, B. Kabius, *Proc. SPIE* 7318 (2009) 18.
- [10] A.V. Sumant, O. Auciello, H.-C. Yuan, Z. Ma, R.W. Carpick, D.C. Mancini, *Proc. SPIE* 7318 (2009) 17.
- [11] O. Auciello, A.V. Sumant, Status review of the science and technology of ultranancocrystalline diamond (UNCD™) films and application to multifunctional devices, *Diamond Relat. Mater.* 19 (2010) 699.
- [12] A.V. Sumant, O. Auciello, R.W. Carpick, S. Srinivasan, J.E. Butler, *MRS Bull.* 35 (2010) 1.
- [13] A.V. Sumant, A.R. Krauss, D.M. Gruen, O. Auciello, A. Erdemir, M. Williams, et al., *Tribol. Trans.* 48 (2005) 24.
- [14] A.R. Krauss, M.Q. Ding, O. Auciello, D.M. Gruen, Y. Huang, V.V. Zhirnov, et al., *J. Appl. Phys.* 89 (2001) 2958.
- [15] J.M. Garguilo, F.A.M. Koeck, R.J. Nemanich, X.C. Xiao, J.A. Carlisle, O. Auciello, *Phys. Rev. B.* 72 (2005) 165404.
- [16] X. Xiao, J. Wang, J.A. Carlisle, B. Mech, R. Greenberg, R. Freda, et al., *J. Biomed. Mater.* 77B (2) (2006) 273.
- [17] W. Yang, O. Auciello, J.E. Butler, W. Cai, J.A. Carlisle, J.E. Gerbi, et al., *Nat. Mater.* 1 (2002) 253.
- [18] B. Shi, Q. Jin, L. Chen, O. Auciello, *Diamond Relat. Mater.* 18 (2–3) (2009) 596.
- [19] D.B. Seley, D.A. Dissing, A.V. Sumant, R. Divan, S. Miller, O. Auciello, E.A. Terrell, T.S. Shogren, D. Fahrner, J.P. Hamilton, M.P. Zach, *Appl. Mater. Interfaces* 3 (2011) 925.

- [20] B.V. Spitsyn, L.L. Bouilov, B.V. Derjaguin, *J. Cryst. Growth* 52 (1981) 219.
- [21] J.E. Butler, H. Windischmann, *MRS Bull.* 23 (9) (1998) 22.
- [22] M.A. Prelas, G. Popovici, K.L. Biglow (Eds.), Marcel Dekker, New York, NY, 1997; R.S. Sussmann (Ed.), *Handbook of Industrial Diamonds and Diamond Films*, John Wiley & Sons, Chichester, UK, 2009.
- [23] J.E. Butler, A.V. Sumant, *Chem. Vap. Deposit.* 14 (7–8) (2008) 145.
- [24] S. Rotter, in: M. Yoshikawa, Y. Koga, Y. Tzeng, C.P. Klages, K. Miyoshi (Eds.), *Proceedings of the Applied Diamond Conference/Frontier Carbon Technologies-ADC/FCT '99*, MYU, K.K., Tokyo, 1999, p. 25.
- [25] E. Kohn, P. Gluche, M. Adamschik, *Diamond Relat. Mater.* 8 (1999) 934.
- [26] A.V. Sumant, D.S. Grierson, A.R. Konicek, M. Abrecht, P.U.P.A. Gilbert, J.E. Butler, et al., *Diamond. Relat. Mater.* 16 (2007) 718.
- [27] D.M. Gruen, *MRS. Bull.* 23 (9) (1998) 32.
- [28] M. Sternberg, P. Zapol, L.A. Curtiss, *Phys. Rev. B* 68 (2003) 205330.
- [29] P.W. May, N.L. Allan, M.N.R. Ashfold, J.C. Richley, Y.A. Mankelevich, *J. Phys. Condens. Matter.* 21 (2009) 364203.
- [30] P.W. May, J.N. Harvey, J.A. Smith, Y.A. Mankelevich, *J. Appl. Phys.* 99 (2006).
- [31] W.S. Huang, D.T. Tran, J. Asmussen, T.A. Grotjohn, D. Reinhard, *Diamond Relat. Mater.* 15 (2006) 341.
- [32] S. Battacharyya, O. Auciello, J. Birrell, J.A. Carlisle, L.A. Curtiss, A.N. Goyete, et al., *Appl. Phys. Lett.* 79 (10) (2001) 1441–1443. R. Arenal, P. Bruno, D.J. Miller, M. Bleuel, J. Lal, D.M. Gruen, *Phys. Rev. B* 75 (2007) 195431.
- [33] J. Birrell, J.E. Gerbi, J.A. Carlisle, O. Auciello, D.M. Gruen, J.M. Gibson, *J. Appl. Phys.* 93 (2003) 5606.
- [34] P. Achatz, O.A. Williams, P. Bruno, D.M. Gruen, J.A. Garrido, M. Stutzmann, *Phys. Rev. B* 74 (15) (2006) 155429.
- [35] Y.C. Chen, X.Y. Zhong, A.R. Konicek, D.S. Grierson, N.H. Tai, I.N. Lin, et al., *Appl. Phys. Lett.* 92 (2008) 133113.
- [36] A. Gerber, S. Sattel, H. Ehrhardt, J. Robertson, P. Wurzinger, P. Pongratz, *J. Appl. Phys.* 79 (1996) 4388.
- [37] B.R. Stoner, G.-H. Ma, S.D. Wolter, J.T. Glass, *Phys. Rev. B* 45 (1992) 11067.
- [38] Y.C. Lee, S.J. Lin, C.Y. Lin, M.C. Yip, W. Fang, I.N. Lin, *Diamond Relat. Mater.* 15 (2006) 2046.
- [39] Y. Lifshitz, X.M. Meng, S.T. Lee, R. Akhvelidany, A. Hoffman, *Phys. Rev. Lett.* 93 (2004) 056101.
- [40] Y.C. Lee, S.J. Lin, C.T. Chia, H.F. Cheng, I.N. Lin, *Diamond Relat. Mater.* 14 (2005) 296.
- [41] X.Y. Zhong, Y.C. Chen, N.H. Tai, I.N. Lin, J.M. Hiller, O. Auciello, *J. Appl. Phys.* 105 (3) (2009) 034311.
- [42] V.P. Adiga, A.V. Sumant, S. Suresh, C. Gudeman, O. Auciello, J.A. Carlisle, et al., *Phys. Rev. B* 79 (2009) 245403.
- [43] A.R. Konicek, D.S. Grierson, P.U.P.A. Gilbert, W.G. Sawyer, A.V. Sumant, R.W. Carpick, *Phys. Rev. Lett.* (2008) 235502/1–235502/4.
- [44] A.V. Sumant, D.S. Grierson, J.E. Gerbi, J. Birrell, U.D. Lanke, O. Auciello, et al., *Adv. Mater.* 17 (2005) 1039.
- [45] N.N. Naguib, J.W. Elam, J. Birrell, J. Wang, D.S. Grierson, B. Kabius, et al., *Chem. Phys. Lett.* 430 (2006) 345. Also, A.V. Sumant, D.S. Grierson, J.E. Gerbi, J.A. Carlisle, O. Auciello, R.W. Carpick, *Phys. Rev. B* 76 (23) (2007) 235429.

- [46] J. Zhanga, J.W. Zimmer, R.T. Howe, R. Maboudian, *Diamond Relat. Mater.* 17 (1) (2008) 23.
- [47] W. May, W.J. Ludlow, M. Hannaway, J.A. Smith, K.N. Rosser, P.J. Heard, *Mater. Res. Soc. Symp. Proc.* 1039 (2008) 17.
- [48] S. Wang, V.M. Swope, J.E. Butler, T. Feygelson, G.M. Swain, *Diamond Relat. Mater.* 18 (4) (2009) 669.
- [49] C. Liu, X. Xiao, J. Wang, B. Shi, V.P. Adiga, R.W. Carpick, J.A. Carlisle, O. Auciello, et al., *J. Appl. Phys.* 102 (7) (2007) 074115.
- [50] R. Ramesham, P.E. Pehrsson, T.I. Smith, M.F. Rose, *J. Mater. Sci. Mater. Electron.* 8 (1997) 69.
- [51] G. Conte, M.C. Rossi, F. Spaziani, R. Arcangeli, *Diamond Relat. Mater.* 14 (2005) 570.
- [52] F.X. Lu, H.D. Zhang, Y.M. Tong, J.X. Yang, C.M. Li, G.C. Chen, et al., *Diamond Relat. Mater.* 13 (2004) 1714.
- [53] H. Ye, Q.S. Chang, P. Hing, *J. Phys. D Appl. Phys.* 33 (2000) L148.
- [54] M.A. Angadi, T. Watanabe, A. Bodapati, X. Xiao, O. Auciello, J.A. Carlisle, et al., *J. Appl. Phys.* 99 (11) (2006) 114301.
- [55] D.G. Cahill, R.O. Pohl, *Phys. Rev. B* 35 (1987) 4067.
- [56] D.G. Cahill, M. Katiyar, J.R. Abelson, *Phys. Rev. B* 50 (1994) 6077.
- [57] A.V. Sumant, D.S. Grierson, J.E. Gerbi, J. Birrell, U.D. Lanke, O. Auciello, et al., *Adv. Mater.* 17 (2005) 1039.
- [58] M.A. Prelas, G. Popovici, L.K. Bigelow, *Handbook of Industrial Diamonds and Diamond Films*, Marcel Dekker, New York, NY, 1998, p. 1214.
- [59] J.E. Gerbi, O. Auciello, J. Birrell, D.M. Gruen, J.A. Carlisle, B.W. Alphenaar, *Appl. Phys. Lett.* 83 (10) (2003) 2001.
- [60] S. Sudarsan, J. Hiller, B. Kabius, O. Auciello, *Appl. Phys. Lett.* 90 (2007) 134101.
- [61] W. Fan, S. Saha, J.A. Carlisle, O. Auciello, R.P.H. Chang, R. Ramesh, *Appl. Phys. Lett.* 82 (9) (2003) 1452.
- [62] K. Wang, A.-C. Wong, C.T.-C. Nguyen, in: *Proceedings of the IEEE MEMS Conference*, 1999, p. 453.
- [63] V.P. Adiga, A.V. Sumant, S. Suresh, C. Gudeman, O. Auciello, J.A. Carlisle, et al., *Phys. Rev. B* 79 (2009) 245403.
- [64] R. Hull, *Properties of Crystalline Silicon*, IEEE Publishing, Portland, OR, 1999.
- [65] G.L. Harris, *Properties of Silicon Carbide*, IEEE Publishing, Portland, OR, 1995.
- [66] M.D. Whitfield, B. Audic, C.M. Flannery, L.P. Kehoe, G.M. Crean, R.B. Jackman, *J. Appl. Phys.* 88 (2000) 2984. 101063/1, 1286010.
- [67] O. Elmazria, F. Bénédic, M. El Hakiki, H. Moubchir, M.B. Assouar, F. Silva, *Diamond Relat. Mater.* 15 (2–3) (2000) 193.
- [68] K.-H. Kim, N. Moldovan, C. Ke, H.D. Espinosa, X. Xiao, J.A. Carlisle, et al., *Small* 1 (8–9) (2005) 866.
- [69] J. Liu, D.S. Grierson, J. Notbohm, S. Li, S.D. O'Connor, K.T. Turner, et al., *Small* 6 (10) (2010) 1140.
- [70] Advanced Diamond Technologies. <www.thindiamond.com>.
- [71] A. Malave, E. Oesterschulze, W. Kulisch, T. Trenkler, T. Hantschel, W. Vandervorst., *Diamond Relat. Mater.* 8 (2–5) (1999) 283.
- [72] C. Goldsmith, O. Auciello, A. Sumant, J. Carlisle, R. Carpick, A. Datta, et al., *IEEE. Intl. Microwave Symp. Dig.* (2010) 1246.

- [73] O. Auciello, A.V. Sumant, C. Goldsmith, S. O'Brien, S. Sampath, C. Gudeman, et al., Micro- and nanotechnology sensors, systems, and applications—II, in: T. George, S. Islam, A. Dutta (Eds.), *Proc. SPIE*. 7679 (2010) 76791K-1.
- [74] Z. Peng, X. Yuan, J.C.M. Hwang, D. Forehand, C.L. Goldsmith, *Proceedings of the Asia-Pacific Microwave Conference*, 2006.
- [75] John C. Ehmke, Charles L. Goldsmith, Zhimin J. Yao, Susan M. Eshelman et al., Method and apparatus for switching high frequency signals, US Patent 6,391,675 (1999).
- [76] C.F. Herrmann, F.W. Del Rio, D.C. Miller, S.M. George, V.M. Bright, J.L. Ebel, R.E. Strawser, R. Cortez, K.D. Leedy, *Sens. Actuators A* 135 (2007) 262.
- [77] J. Webster, C. Dyck, J. Sullivan, T. Friedmann, A. Carton, *Electron. Lett.* 30 (1) (2004).
- [78] J. Chee, R. Karu, T. Fishe, D. Peroulis, Gallium Arsenide and Other Semiconductor Application Symposium, 2005, p. 581.
- [79] S. Balachandran, D. Hoff, A. Kumar, T. Weller, *IEEE MTT-S International Microwave Symposium Digest*, 2009, p. 1657.
- [80] C.L. Goldsmith, D. Forehand, D. Scarbrough, Z. Peng, C. Palego, J.C.M. Hwang, et al., *Proc. Int. Soc. Opt. Eng.* 6884 (3) (2008).
- [81] J. Wang, M.A. Firestone, O. Auciello, J.A. Carlisle, *Langmuir* 20 (2004) 11450.
- [82] C.E. Nebel, N. Yang, H. Uetsuka, E. Osawa, N. Tokuda, and O. Williams, in: *19th European Conference on Diamond, Diamond-Like Materials, Carbon Nanotubes, Nitrides and Silicon Carbide*, Sites, Spain, 2008.
- [83] W. Jing, J.E. Butler, T. Feygelson, C.T. Nguyen, in: *Proceedings of the 17th IEEE Micro Electro Mechanical Systems International Conference*, The Netherlands, 25–29 January, 2004, p. 641.

Advances in Surface Chemistry of Nanodiamond and Nanodiamond–Polymer Composites

Ioannis Neitzel, Vadym Mochalin, and Yury Gogotsi

Department of Materials Science and Engineering, Drexel University, Philadelphia, PA

CHAPTER OUTLINE

13.1 Introduction	421
13.2 Chemical modification of the surface of NDs.....	422
13.3 Introduction to polymer nanocomposites	426
13.4 Mechanical properties of polymer–ND composites	429
13.4.1 Thermoplastic–ND composites.....	430
<i>Thermoplastic–ND composites for biomedical applications.....</i>	<i>434</i>
<i>Synergetic effects of ND in reinforcing thermoplastic copolymers.....</i>	<i>440</i>
13.4.2 Thermoset–ND composites.....	441
13.4.3 Elastomer–ND composites	445
13.5 Thermal properties of polymer–ND composites	446
13.5.1 Thermal stability of polymer–ND composites.....	446
13.5.2 Thermal conductivity of polymer–ND composites	446
13.6 Optical properties of polymer–ND composites.....	447
13.7 Electromagnetic shielding of polymer–ND composites.....	448
13.8 Other applications for polymer–ND composites	448
13.9 Future work	449
References	450

13.1 Introduction

The unique feature of nanodiamond (ND), as compared to carbon nanotubes (CNTs), graphene, and other carbon nanomaterials with sp^2 bonding is, that its surface chemistry can be fully controlled without compromising the structure and useful properties of the material. ND cannot be used to its full potential without

control of the particle size, surface chemistry, and interior structure, as well as particle agglomeration. To tune NDs' surface, numerous methods including annealing in reactive gases or wet chemistry techniques based on the chemistry of ND surface functional groups can be used. By properly modifying NDs' surface, powders with various surface chemistries for specific applications can be produced, for example powders optimized for incorporation into polymer matrices.

Due to their versatile properties combined with a favorable strength-to-weight ratio, polymer composites find numerous applications in structural, tribological, biomedical, sports, and other industries. A nanocomposite contains fillers smaller than 100 nm in diameter. At these small length scales, the specific surface area becomes large and polymer–filler interactions become increasingly important, changing polymer properties in the vicinity of the surface and forming a new phase called interphase. Tailoring the properties of the interphase allows for engineering the properties of composite materials. The small 5 nm diameter of detonation ND particles in combination with their superior mechanical properties (diamond properties) and rich surface chemistry makes ND an optimal candidate for reinforcing polymer matrices, where it can act through changing the properties of the interphase as well as forming a strong covalent interface with the matrix. This chapter summarizes recent developments in the optimization of the surface chemistry of NDs and its application in polymer matrix composites.

13.2 Chemical modification of the surface of NDs

A distinct feature of ND compared to CNTs and other carbon nanoparticles is the presence of a large number of different functional groups terminating the surface of a ND particle [1]. The layer of surface functional groups is an intrinsic feature of this material. The surface chemistry of ND is rich and surface functionalization of ND can be done to any extent without compromising useful properties of the diamond core. Therefore, our ability to control and tailor the surface chemistry of ND is of paramount importance [1,2], and *vice versa*, without being properly taken into account, the surface chemistry of ND may lead to detrimental effects in many of its applications. For example, strong aggregation of ND could be in part due to the interactions between the surface functional groups of ND particles forming the aggregates [3–5]. Most researchers now agree that after oxidative treatment used for purification, ND has primarily oxygen-containing functional groups terminating its surface [1–3,6,7] as evidenced by IR and Raman spectroscopy [8]. Negative zeta-potential and higher dispersion stability in aqueous solutions at basic pH [9] also indicate the presence of carboxylic groups on the surface of ND. However, the number of carboxylic and other functional groups on the surface of NDs subjected to different purification procedures is still to be precisely measured.

Commercially available ND powders have various surface terminations and, potentially, any of these functional groups can be used for covalent functionalization with known chemical techniques appropriate for each type of these groups.

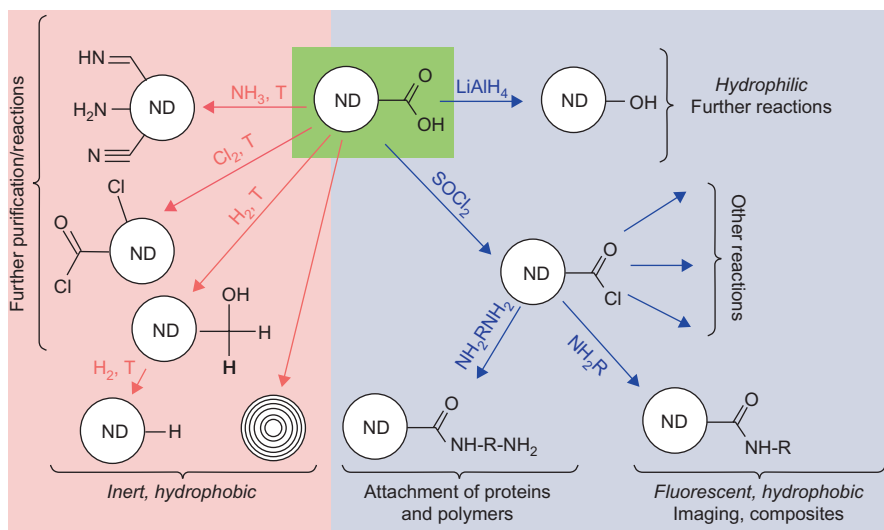


FIGURE 13.1

ND terminated with carboxylic groups (ND-COOH; green region) is a common starting material (and is made by air oxidation or ozone treatment of ND, followed by treatment in aqueous HCl to hydrolyze anhydrides and remove metal impurities). The surface of ND-COOH can be modified by high-temperature gas treatments (red) or ambient-temperature wet chemistry techniques (blue).

Oxidation used for ND purification removes surface carbon layers and creates oxygen-containing functional groups (mainly anhydrides, which are easily transformed into carboxylic groups) thus providing a way to control the surface chemistry of ND in addition to purification [6] and, in this sense, can also be considered as a modification technique. The variety of chemical modification techniques can be divided into gas treatment and wet chemistry techniques (Figure 13.1). Gas treatments are usually performed at elevated temperatures in the range of 400–850°C and suffer from poor selectivity. For example, heating ND in ammonia flow for 1 h at 850°C in an attempt to produce ND terminated with NH₂ groups resulted, in addition to formation of aminogroups, in reduction of C=O groups to C–O–H, and formation of C–H and C≡N groups [10] as well as C=N-containing groups [11,12] (Figure 13.1). These changes were accompanied by a corresponding shift in pH of aqueous dispersions from 4.3 (ND before ammonia treatment) to 8 (ND after ammonia treatment) [11]. Heating in hydrogen gas at 800°C for 2 h [10] and 5 h [13,14] resulted in complete reduction of C=O to C–O–H and formation of C–H groups (“bifunctional surface”). It should be emphasized that hydrogenation in these conditions has never resulted in complete removal of surface O–H groups; however, it may become possible at higher temperatures or longer treatment times (Figure 13.1). Completely hydrogenated hydrophobic

ND is of interest for many applications as well as for comparison with computer modeling performed mainly for hydrogen-terminated clusters. Treatment in chlorine for 1 h at 400°C resulted in formation of acylchloride species and partial removal of C—H- and O—H-containing functional groups [10]. Fluorination in F₂ was reported to form CF groups on ND [15–17]. Annealing of ND in N₂, Ar, or vacuum results in complete removal of surface functional groups, followed by progressive graphitization and conversion of ND into carbon nano-onions [10,18–21], which find applications in energy storage [20], composites [22,23], and catalysis [24].

Compared to gas treatments, wet chemistry reactions can be done in milder conditions and provide a better selectivity (Figure 13.1). Due to their vast variety, all possible wet chemical routes cannot be captured in a single scheme; their number is potentially as large as the number of chemical conversions of various functional groups in organic chemistry. A variety of functionalized NDs were produced with wet chemical functionalization [1,2]. Carboxylated ND was reduced into O—H terminated [25], converted into reactive acyl chlorides with subsequent linking of amines [26,27], diamines were linked *via* the same chemistry yielding aminated ND [28]. Reactive C—Cl and C—F surface species created by gas annealing and photochemical chlorination were further used in numerous wet chemical reactions [14,15,17,29].

O—H-terminated ND can be produced by reduction with borane (BH₃ in tetrahydrofuran) [30] or LiAlH₄ [25], by treatment of ND with Fenton reagent (H₂O₂ + FeSO₄ in a strongly acidic environment) [31,32], or by photochemical reaction of hydrogenated ND with water [33]. Hydroxylated ND was involved in esterification reactions with different acyl chlorides yielding ND terminated with long alkyl chains attached via ester bonds [34]. O—H-terminated ND was also used in silanization with simultaneous de-agglomeration [35].

NH₂-terminated ND is of interest for many composite and biomedical applications. In addition to gas treatment at high temperature mentioned above, which however results in unavoidable formation of other nitrogen-containing groups, selective formation of aminogroups on ND surface was accomplished by covalent linking of amine derivatives to ND. The examples include grafting of nitroaromatic derivatives using diazonium chemistry with subsequent electrochemical reduction of NO₂ into NH₂ [36], attaching of aminated silanes to hydroxylated ND [30], or most recently, a reaction of activated carboxylated ND with diamines [28].

Recent progress in chemical reactions of ND was reviewed in Refs. [1–4]. Examples of functionalization for biomedical applications can be found in [1,30,37,38]. The majority of these techniques are based on the assumption that ND bears carboxylic or hydroxylic groups on its surface, and because hydroxylic groups are usually produced by reduction of carboxylic groups, carboxylated ND can be considered as a universal precursor material for ND functionalization (Figure 13.1).

In addition to organic chemistry of functional groups, ND can be functionalized *via* the chemistry of graphitic carbon either present intrinsically (bucky diamond) or deliberately created through a partial surface graphitization. In this case, it is possible to create strong C—C bonds between ND's graphitic shell and the attached

moiety, whereas the techniques using chemistry of functional groups usually result in the formation of C—X bonds where X is N, O, S, etc. Functionalization of ND's graphitic shells was reported *via* [4 + 2] cycloaddition (Diels-Alder reactions) [39], 1,3-dipolar cycloaddition of azomethine ylides (the Prato reaction) [40], and diazonium chemistry [41]. Diazonium chemistry is a simple and versatile process which, in addition to graphitized ND, was also used with hydrogenated ND [36] to form C—C bonds between the attached moiety and diamond core, and with hydroxylated ND [35] (in the latter case C—O—C bonds are formed). Thus, ND provides numerous options for surface functionalization but the outcome strongly depends on the purity and surface chemistry of the starting material, emphasizing the need to use purified ND with a unified surface chemistry.

Another important task yet to be accomplished is the quantitative analysis of ND surface functional groups. Available data on the number of surface functional groups of NDs are still scarce. Carboxylic groups are among the most common in NDs and are relatively easy to determine due to their acidic character. In one of the earlier studies, the content of COOH was determined by electrostatically mediated adsorption of dodecylamine, where it was assumed that an ionic bond is formed between equivalent COOH and NH₂ [27]. This technique gave an average content of carboxylic groups of 0.9 ± 0.1 mmol per gram of ND, corresponding to ~ 3.9 wt % of COOH in ND. Boehm titration is a widely used technique to quantify different surface functional groups based on their pK_a. The average content of COOH groups on ND measured by this technique was 0.85 COOH per nm² of ND surface [42]. The same research group later reported results of Boehm titration with conductometric detection [43], which gave values from 0.15 to 0.81 COOH groups and from 0 to 0.27 lactone groups per nm² of ND surface, depending on ND modification. The content of O—H groups in hydroxylated ND has been determined in an indirect way by formation of stearyl ester of ND followed by its hydrolysis, dissolution of stearic acid in ethyl acetate, its reaction with NaOH, collection of precipitated sodium stearate, and its conversion back into stearic acid, which was then collected, dried, and determined gravimetrically. Using this technique, the content of O—H groups in hydroxylated ND was found to be 0.13 mmol/g [25]. It should be emphasized that ND is a material, not a substance, and as such has no defined chemical formulae. Therefore, the content of a certain type of functional group for different NDs can be different and largely depends on the history of the sample, i.e., on how it was produced, purified, modified, etc. At the same time, researchers developing advanced applications for this material must know precisely the composition of the ND material they are working with. Therefore, careful qualitative and quantitative characterization of ND is of the utmost importance for successful development of its applications.

With regard to polymer composites, the importance quantitative analysis of different functional groups on ND is emphasized by the interference of ND surface chemistry with the chemistry of polymers first observed by Mochalin et al. [28], when the authors tried to produce aminated ND-epoxy composites with covalent incorporation of ND. Without knowing how many reactive NH₂ groups were introduced with aminated ND into the epoxy-curing agent system it was impossible

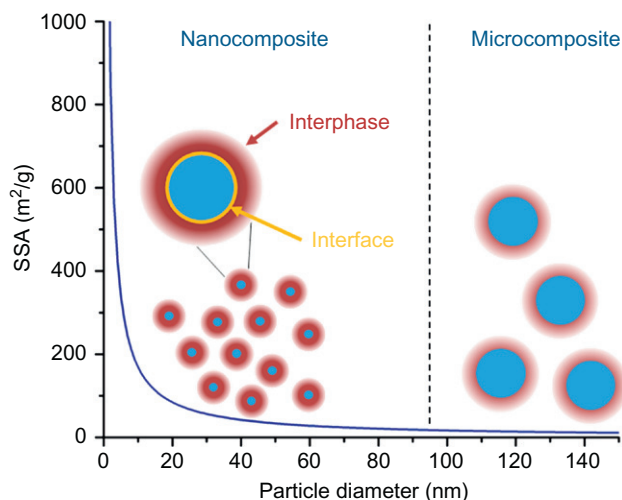
to optimize the mechanical properties of the composites. On the other hand, after quantifying the number of NH_2 groups on ND, the authors were able to calculate how much ND is required to cure the epoxy solely with the aminogroups of ND, yielding composites with unprecedentedly high Young's modulus [44]. For this purpose, the amount of reactive aminogroups on ND was determined by Differential Scanning Calorimetry (DSC) titration of aminated ND with epoxy resin [28]. The authors reported the value of coverage to be of 18–23% of ND's surface atoms in a 5 nm diameter ND particle (or 3.5–4.5 NH_2 groups per nm^2 of ND surface).

13.3 Introduction to polymer nanocomposites

Polymer nanocomposites (PNCs) are of interest due to their unique properties; combining the polymer matrix and filler to create PNCs results in a whole new set of properties that are not found in the individual components. Depending on the material selection, PNCs can be used for various applications—ranging from mechanical and electrical to optical ones. In the vicinity of small particles, polymers have properties different from the bulk polymer, forming a third phase in the two-phase polymer–filler system. This phase, called the “interphase,” exists in both micro- and nanocomposites. To ensure good load and heat transfer from the polymer matrix to a filler, a strong interface between the particle and the interphase is necessary (Figure 13.2). A nanocomposite is a multiphase material in which, in contrast to microcomposites, one of the phases has one, two, or three dimensions of less than 100 nm, or the composite phases have nanoscale distances between them [45]. Hereafter, we will consider only polymer matrix composites with nanoparticles (fillers). The small size of nanofillers results in a large surface area, thus increasing the amount of polymer in contact with the filler. When the volume content of the nanofiller is large enough, the interphase becomes the dominant phase in the composite (Figure 13.2). Therefore, controlling the properties of the interphase holds great potential for tailoring the properties of the nanocomposite.

Since the advent of the era of nanotechnology in the early 1990s, various nanocomposites with different polymers and fillers were studied. For example, CNTs [46] and nanosilica [47] were used for reinforcing the epoxy matrices (Epon828) and (Epon862), respectively. These studies show that mechanical properties can be improved due to the addition of nanofillers. Still, current results are far below the expectations [48]. To some extent, this can be explained by the nonoptimal properties of the fillers used in previous studies. However, general challenges related to design and processing of nanocomposites such as improving nanofiller dispersion quality, interface strength, and properties of the interphase are thought to be the main cause for the apparent underperformance of many nanocomposites.

One major challenge common to all nanoparticles is the formation of clusters and aggregates resulting from the forces acting between nanoparticles and driving their agglomeration in order to minimize surface energy. Although this feature can sometimes be beneficial, for most applications, the agglomeration of nanofillers is

**FIGURE 13.2**

Specific surface area (SSA) as a function of particle diameter. As the particle diameter decreases, the amount of interfacial material increases. For optimal mechanical properties, a strong interface, which transfers load from the filler to the interphase and polymer matrix is mandatory. Composites containing particles smaller than 100 nm fall into the subclass of nanocomposites.

undesirable, since it compromises the distinctive advantages of nanoparticles as compared to their micrometer-sized counterparts. Improving the dispersion of nanoparticles is of major importance to achieve maximal Young's moduli as recently confirmed by computer simulations [49]. Models for nanoparticle–polymer composites that take filler–filler and filler–polymer interactions into account can provide guidance on how to change the surface properties of the fillers to obtain single well dispersed nanoparticles in the polymer [50,51]. In practice, the optimal interaction parameters can be achieved by changing the surface chemistry of the filler and selecting the appropriate functional groups of the polymer molecules.

An optimal nanofiller should have a large surface area (small particle size), and a tailorable surface chemistry allowing to control both, the nanofiller–polymer interface and the interphase (Figure 13.2). Besides these properties, the filler is required to have additional characteristics dictated by a specific application, e.g., good mechanical properties for load-bearing composites, high (or low) electrical conductivity for conducting (or insulating) materials, transparency, or high index of refraction for optical applications.

ND produced by detonation synthesis in large commercial quantities [1,52] represents a perfect nanofiller for many composite applications. It is made of small and uniform particles of ~ 5 nm in diameter and features a large and accessible surface area of $\sim 350 \text{ m}^2/\text{g}$ with a rich and tailorable surface chemistry. It has many

of the unique properties of bulk diamond, including superior thermal conductivity, hardness and Young's modulus, high resistivity, and a high refraction index to name a few. Various gas and wet chemistry treatments can be applied to optimize ND properties for a specific application. Depending on the temperature and atmosphere, graphitized [53], oxidized [6], or hydrogenated NDs [54] can be produced (Figure 13.3A). Synthetic routes to aminated ND [28], ND-NH₂ (Figure 13.3A), or octadecylamine (ODA)-functionalized ND [26] (Figure 13.3B) were recently developed.

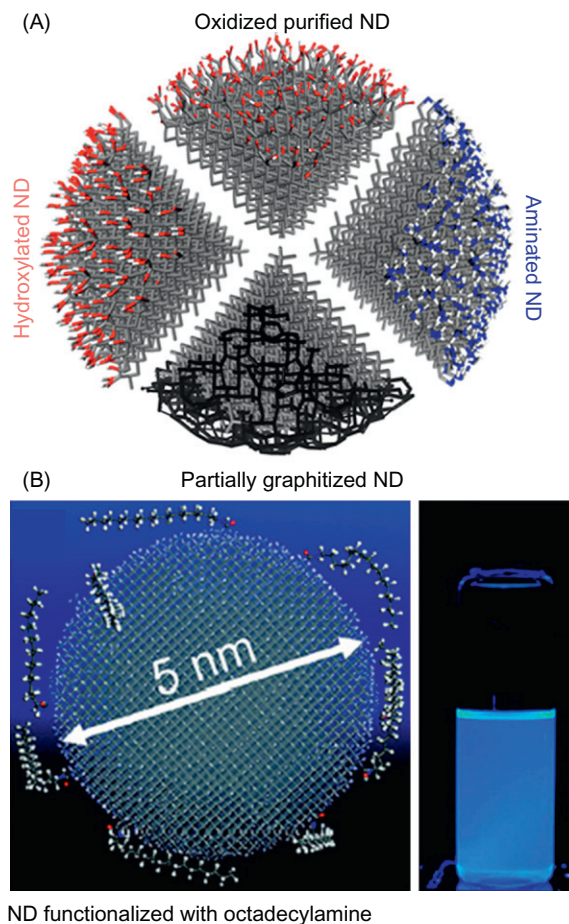


FIGURE 13.3

(A) Computer models showing the different surface chemistries of ND [1] and (B) a model of ND functionalized with ODA [26]. Bright blue fluorescence of this material was observed when dispersed in different hydrophobic solvents. (For interpretation of the references to color in this figure legend, the reader is referred to the web version of this book.)

In this chapter, we summarize the latest developments in the field of polymer–ND composites and show how mechanical, thermal, optical, electrical, and other properties are improved due to the addition of ND.

13.4 Mechanical properties of polymer–ND composites

Due to their high strength-to-weight ratio, polymer composite materials are widely used as structural components. Common examples include fiber reinforced polymer matrices such as carbon–fiber–epoxy composites, which have Young’s moduli of ~ 150 GPa [55]—very close to the values reported for steel. Polymer–particulate composites represent noncontinuous reinforced matrices, where, for example, the stiffness and fracture toughness are improved [56]. Naturally, the filler properties themselves have a major influence on the composite properties. ND particles possess superior mechanical properties such as a higher hardness (10 on Mohs scale) and Young’s modulus (~ 1220 GPa) compared to other materials. In addition, they offer unique tribological properties [57], biocompatibility [1], and show no toxicity so far [58]. ND can be thought of as a universal building block for PNC design since its surface can be modified to virtually any extent in order to create desirable interfaces and influence the interphase with almost any polymer matrix without compromising the properties of the diamond core [6,8], a striking contrast to CNTs and other sp^2 -carbon nanostructures, in which surface functionalization often results in degradation of their properties. For example, a large number of reactive aminogroups were grafted onto the ND surface with subsequent covalent incorporation of aminated ND into the molecular structure of an epoxy polymer (Figure 13.4A and B) without any detrimental effects on the diamond core of the ND particles [28]. Similar functionalizations were reported to destroy the conjugated aromatic network of CNTs and degrade their properties [59].

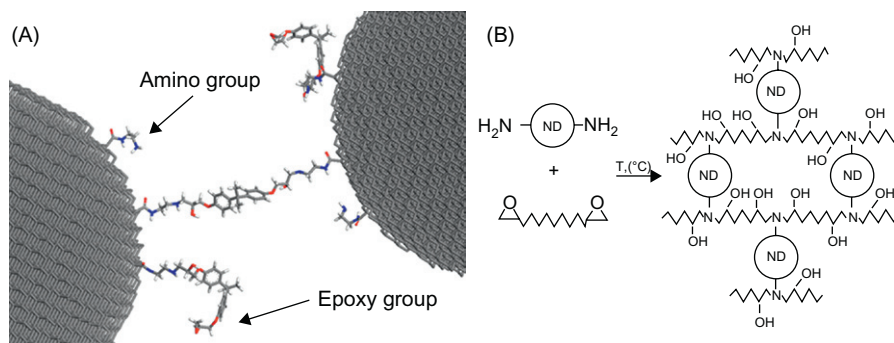


FIGURE 13.4

(A) Computer model showing the covalent incorporation of aminated ND into an epoxy matrix. (B) Schematic of covalent incorporation of aminated ND into a structure of epoxy polymer. In this study, ND was functionalized with ethylenediamine that can react with the epoxide groups of the epoxy Epon828 [28].

In this section, we describe recent developments in PNC–ND design, focusing on the mechanical properties of the composites. We will provide representative examples of how ND can improve these properties and how its surface chemistry can be tailored to achieve the optimal properties. Due to the variety of polymers, we split this section into three subsections following the classic subdivision of polymer matrices into thermoplastic, thermosetting, and elastomeric.

13.4.1 Thermoplastic–ND composites

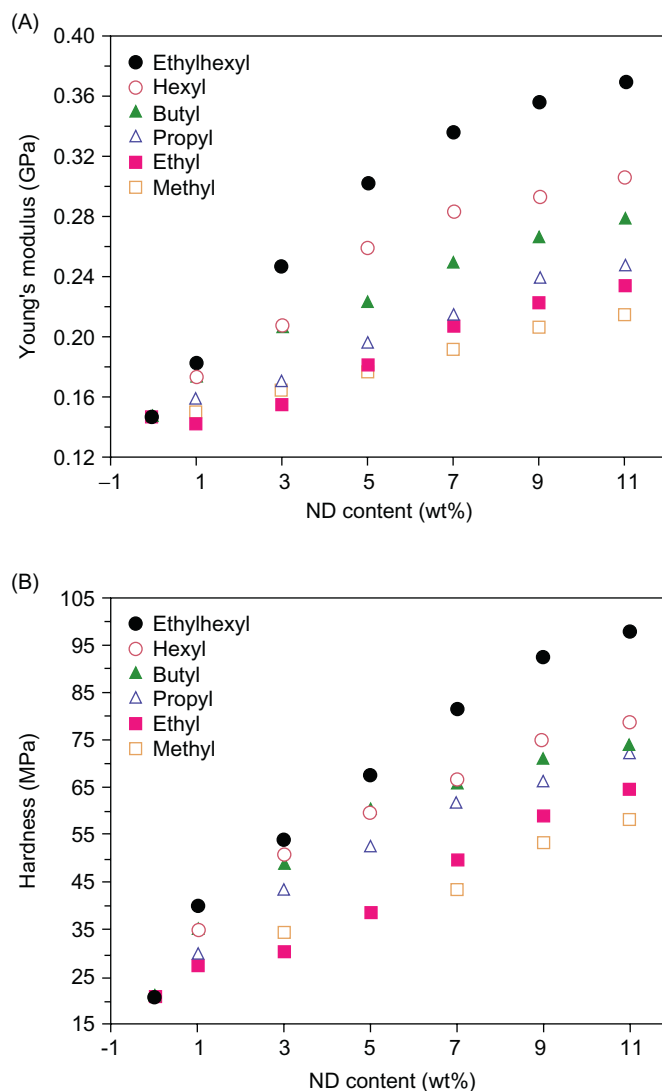
There are several studies on the reinforcement of thermoplastics with ND. Even at low concentrations and without surface functionalization, ND can reinforce some thermoplastics. For example, a reduced mechanical stress, as defined by the Mooney–Rivlin equation, was observed due to the addition of glass beads in combination with only 0.1 wt% of as-received ND to polydimethylsiloxane (PDMS). Viscosity measurements of the melts suggest that ND changes the conformation of PDMS molecules, resulting in improved mechanical properties [60].

Also, improved properties of polyurethane-2-hydroxyethylmethacrylate (PU-PHEMA) with added ND were reported. Increased Young's moduli and glass transition temperatures (T_g) due to the addition of 0.25 wt% of as-received ND were measured and explained by a reaction between NDs' carboxylic groups and the isocyanate groups forming during the polymerization of PU-PHEMA [61].

Polyethylene is a widely used polymer consisting of a $-\text{CH}_2$ backbone, with no side chain functionalities. To improve its affinity to this specific polymer matrix, alkyl chains of variable length were grafted to ND. DSC measurements performed on polyethylene–ND composites indicate an increased crystallinity, crystallization, and melting temperatures of the nanocomposites with increasing ND content and alkyl chain length. Following this trend, Young's moduli and hardness values measured by Atomic Force Microscopy (AFM) were increased by a factor of 2.5 and 4.5, respectively; the increase was larger with longer grafted alkyl chains (Figure 13.5A and B). These improvements were explained by the significant increase in crystallinity of the polymer, providing an example of how the proper selection of ND's surface functionality can be used to design an interphase [62].

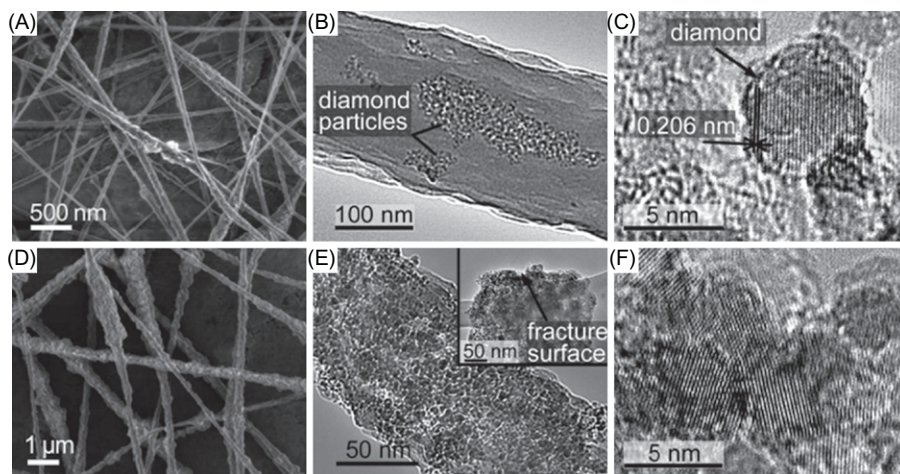
PAN and PA11 nanofibers with high contents of ND show dramatically improved mechanical properties [63]. It should be noted that the ND used in this study was purified by air oxidation, followed by HCl treatment to reduce the content of metals and increase the number of carboxylic groups on ND, as confirmed by Fourier Transform Infrared Spectroscopy (FTIR) measurements. A 400% increase in Young's modulus and a 200% increase in hardness were measured by nanoindentation for the films produced by melting the electrospun ND-PA11 and ND-PAN nanofiber mats.

Interestingly, even at high ND concentrations (up to 20 wt%), these films remain transparent in visible light, while strongly absorbing UV radiation. The electrospun ND-PAN fibers produced in this study contained up to 80 wt% ND, where agglomeration is pronounced at higher concentrations (Figure 13.6). Eventually, performance can be enhanced when dispersion of ND is improved.

**FIGURE 13.5**

Young's modulus (A) and hardness (B) of polyethylene–ND composites as functions of ND content and grafted alkyl chain length to ND [62].

Due to the observed increases in Young's modulus and hardness, both the wear and scratch resistance of the spun ND–polymer films are expected to increase, making this material a promising candidate for optically transparent UV-absorbing scratch- and wear-resistant coatings and paints [63].

**FIGURE 13.6**

Top row: (A) SEM and (B and C) TEM images of electrospun PAN nanofibers with 10wt% ND. Bottom row: (D) SEM images and (E and F) TEM images of electrospun PAN nanofibers with 60wt% ND. ND particles, which have a higher density than PAN, appear as dark spots in TEM images in panels (B) and (E). Inset in panel (E) shows a fracture surface of a polymer-bonded diamond fiber (60wt% of ND in the polymer) [63].

Polymers are commonly used in tribological applications to reduce friction between two surfaces. For example, they are used as bearings between steel counterparts or as wear-reducing coatings in artificial joints [64–67]. Since it is well known that diamond has excellent tribological properties [68], a number of studies addressed the tribological performance of different thermoplastic polymers reinforced by ND.

Polytetrafluoroethylene (PTFE) is a well-known and widely used low-friction polymer with high chemical and thermal stability. To further improve its tribological properties, as-received ND was introduced into this matrix. Reduced friction coefficients and an improved wear resistance with a significant reduction in the wear track width at 23°C and 150°C were measured (Figure 13.7A and B). The reduced wear was explained not only by the low-friction coefficient of ND, but rather by a change in the microstructure of the nanocomposite observed by Scanning Electron Microscopy (SEM) [69]. It has been claimed that PTFE–ND composites can eventually replace metals, such as bronze, in high performance tribological applications.

Another study reported a relationship between ND agglomerate size and the wear performance of PTFE–ND composites. In this study, a decrease in wear was observed for small agglomerates, while larger agglomerates resulted in increased wear [70]. Friction coefficients follow the same trend, indicating that small agglomerate size leads to better properties. Reduction in the wear rate of PTFE–ND composites with 2 wt% of ND and a up to five times decreased wear of polyacrylamide-, polymethylmethacrylate-, and polyethylene-ND composites were observed

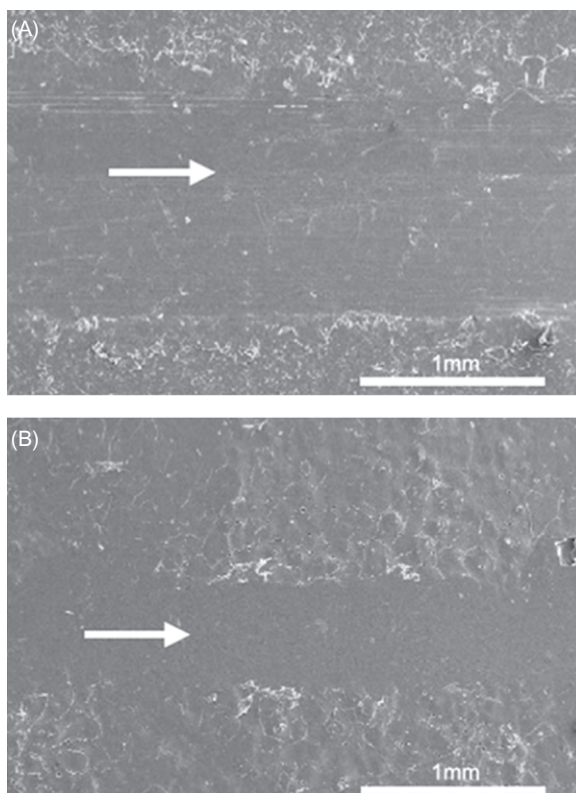


FIGURE 13.7

SEM micrographs on worn surfaces of (A) pure PTFE and (B) a 2 wt% PTFE–ND composite. Tests were performed with a Si_3N_4 counter-body at room temperature [69].

[71]. Studies on polyurethane–ND composites with 0.5 wt% of ND confirmed that tribological properties of different thermoplastics can be improved due to the addition of ND [72].

Development of wear-resistant and low-friction ND-containing coatings that only need to be applied on the surfaces of wearing parts is especially attractive since in this case the amount of ND needed is low.

Also, coating applications require strong adhesion between the substrate and coating. This can also be improved by adding ND. A study on Nylon-11–ND composites reported on a significantly improved adhesion of the polymer coatings to steel due to the addition of 7 wt% purified ND, further emphasizing the great potential of ND in coatings [73].

In summary, as-received ND can be used to reinforce various thermoplastic matrices, but the key to creating more consistent and ultimately strong composites lies in selecting the right surface chemistry of ND for each specific application.

Thermoplastic–ND composites for biomedical applications

Due to nontoxicity and biocompatibility of ND [58], it is an excellent material to reinforce polymers for biomedical applications. Most polymers developed for such applications, in particular biodegradable polymers, suffer from poor mechanical properties, which severely limit their potential for the replacement of metals in applications such as bone fracture fixation. In this section, we give an overview of how ND can improve the mechanical properties of several biocompatible polymers.

A common biodegradable polymer is polyvinyl alcohol (PVA), which has numerous biomedical applications including soft tissue replacements, artificial cartilage, catheters, artificial skin, artificial pancreas, and hemodialysis membranes [74]. Several studies have investigated the use of ND to reinforce PVA. For example, a 40% improved tensile modulus and a 70% larger fracture energy were measured due to the addition of 1 vol.% of ND purified by a treatment with *o*-xylene to remove any adsorbed organics. The observed improved properties were explained by favorable interactions between ND–COOH groups and the hydroxyl groups of PVA [75].

In a similar study, using “Gohsenol NH-18” PVA, a significantly larger improvement in tensile modulus (150%), and increased yield strength and fracture energy were measured. The improvements were explained by an 8% increased crystallinity of PVA and hydrogen bond formation between the hydroxyl groups of PVA and the oxygen-containing surface functional groups and absorbed water of ND. (Figure 13.8) [76].

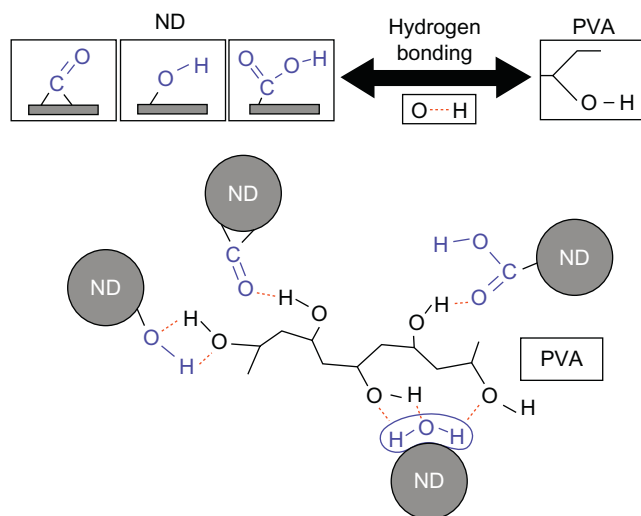


FIGURE 13.8

Illustration of the possible interactions between PVA and NDs' functional groups. Hydrogen bonding between oxygen-containing functional groups on ND and hydroxyl groups of PVA can explain the significant improvement in the mechanical properties of PVA–ND composites [76].

While the measurements above were done on bulk PVA–ND samples, the Young's moduli of PVA–ND composites have also been studied by nanoindentation. The compression modulus and hardness improved by more than 90% and 78%, respectively, due to the addition of only 0.6 wt% acid-purified ND having an increased number of carboxylic groups. DSC data showed a 14% increased crystallinity [77].

The reported differences in the properties of PVA–ND nanocomposites can be explained by the variations in molecular weight of PVA, dispersion states of ND in the polymer, and in the nature and number of ND functional groups. Also, nanoindentation and tensile tests measure mechanical properties on different length scales and the data produced by both can significantly differ. Higher values of Young's modulus and hardness measured by nanoindentation can be due to local variations in ND dispersion and concentration, showing the potential of these composites.

The above studies ascribe the main reason for improved properties to the attractive interactions between ND carboxylic surface groups and hydroxyl groups of the polymer matrix. However, in the case of a Kevlar–ND composite, more than 50% reduced Young's moduli and hardness values were measured by nanoindentation. In this case, the attractive interactions between ND–COOH groups and Kevlar molecules played a detrimental role, destroying the supramolecular structure of the aramide [42]. This example emphasizes the importance of designing the ND–polymer interface in order to achieve a desired performance.

Another common biodegradable polymer is poly-(methyl methacrylate) (PMMA), which is used for example as a dental implant. The impact strength and fracture toughness of PMMA–ND composites were increased due to the addition of only 0.1 wt% of acid-purified ND. At ND contents of 0.8 wt%, Young's modulus was 80% higher and the T_g increased by 20°C. The improved properties are explained by hydrogen bonding between the polymer carbonyl groups and the surface hydroxyl groups of ND [78]. Transmission Electron Microscopy (TEM) micrographs of the produced nanocomposites showed significant agglomeration of ND (Figure 13.9A and B), suggesting that further improvements are possible if that the dispersed single ND particles become available.

Besides the as-received ND, polycarbonate (PC) and PMMA were also reinforced with different functionalized NDs. Hardness and Young's moduli of these nanocomposites were increased by up to 100%, when the appropriate surface functionality was selected. Young's moduli of PC and PMMA with same contents of different functionalized NDs are compared in Figure 13.10. Highest improvements in mechanical properties are obtained when using amide functionalized ND for PMMA and aminofunctionalized ND for PC [79]. Reasons for the better performance of ND functionalized with nitrogen-containing groups remain unknown.

Poly-lactic acid (PLA) is a common biodegradable polymer used in tissue engineering. Storage modulus, tensile modulus, and the tensile strength of PLA were improved due to the addition of 5 wt% ND. The reasons for the better properties might be due to the increased crystallinity of the matrix (measured by DSC) as well as the attractive molecular interactions between ND and PLA molecules as suggested by the increased thermal stability measured by Thermogravimetric Analysis (TGA) [80].

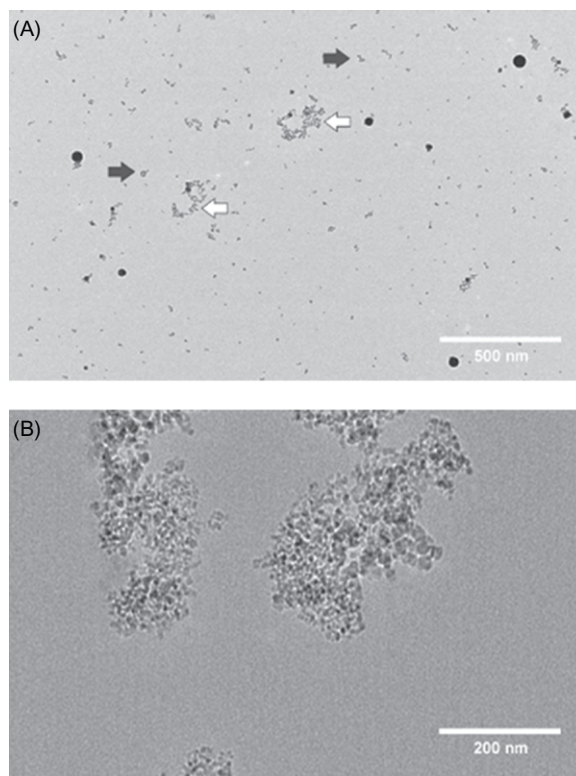


FIGURE 13.9

TEM micrographs of a PMMA-ND nanocomposite showing agglomeration of ND in the polymer matrix (A) at low magnification and (B) at high magnification [78].

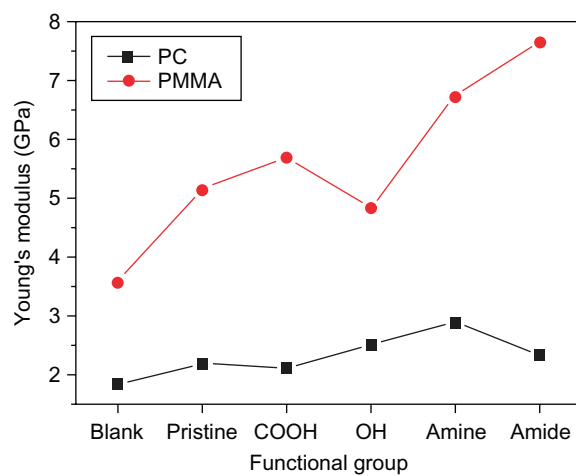


FIGURE 13.10

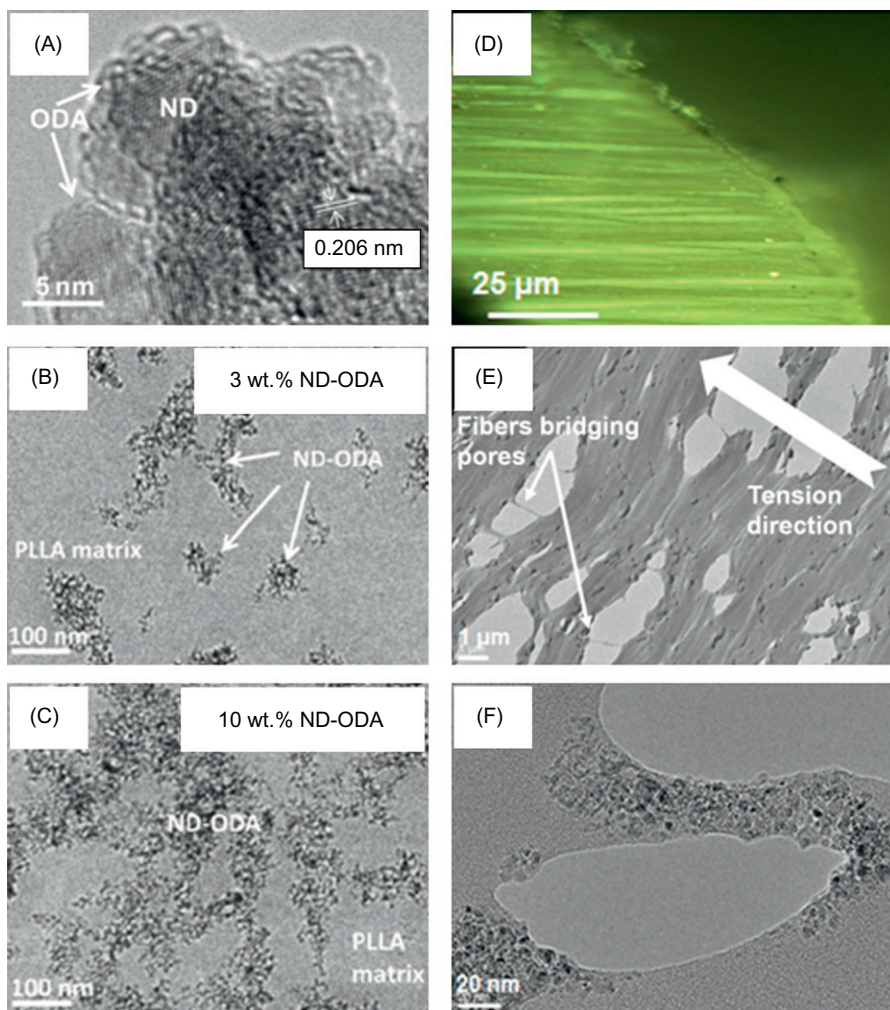
Young's modulus of polycarbonate (PC) and poly-(methyl methacrylate) (PMMA) composites with different functionalized NDs [79].

An optical isomer of PLA, poly-L-(lactic acid) (PLLA), which is used in manufacturing fixation devices for bone fracture surgery, was reinforced by a specifically modified ND for this application. In order to increase the affinity of ND toward the polymer matrix and improve the dispersion of the nanofiller, a hydrophobic amine, Octadecylamine (ODA), was grafted to the ND's surface (Figures 13.3B and 13.11A), resulting in a decrease of nanoparticle–nanoparticle attractive interactions [51] and a better affinity of hydrophobic ND–ODA toward hydrophobic PLLA [81]. Successful covalent binding of ODA to ND was proven by FTIR [26] and confirmed by AFM measurements (Figure 13.12) [83]. In contrast to pristine ND, the resulting ND–ODA material is hydrophobic, providing good dispersion in hydrophobic polymers. TEM images of PLLA–ND–ODA films (Figure 13.11B and C) show single ND–ODA particles and loosely bonded ND–ODA agglomerates dispersed in the matrix. The elongated shape of these agglomerates is essential. According to polymer–nanofiller theory, the high aspect ratio of ND–ODA agglomerates in the composites containing 3 and 10 wt% ND–ODA (Figure 13.11B and C) corresponds to the penultimate step before obtaining single-dispersed particles [84]. Thus, covalent modification of ND with ODA results in a very good dispersion, which translates into mechanical properties: PLLA–ND–ODA composites containing up to 10 wt% ND–ODA showed an up to two times increase in Young's modulus and up to eight times higher hardness when compared to neat PLLA, measured using nanoindentation. As expected, unmodified ND reinforced the PLLA to a lesser extent [81]. The bulk compression modulus of a PLLA–ND–ODA composite containing 10 wt% ND–ODA was increased by 22%, where a 316% increase in fracture energy was observed at the same time. It was suggested that ND–ODA-induced crazing, observed by light microscopy and TEM, is responsible for the large increase in fracture energy (Figure 13.11D–F) [82].

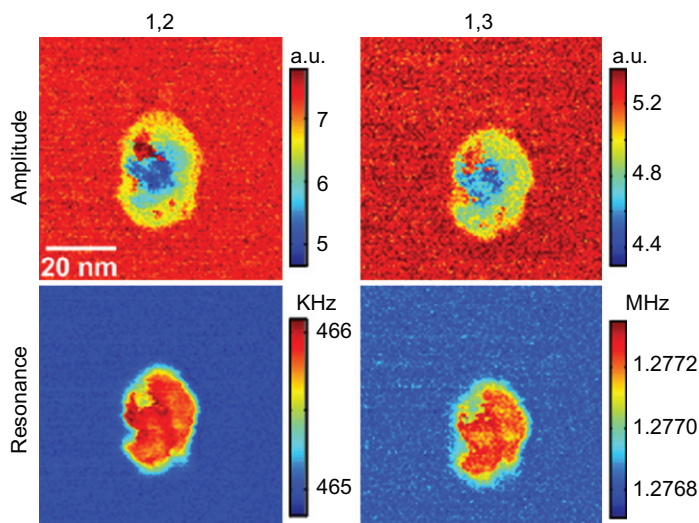
Besides mechanical reinforcement, ND–ODA is blue fluorescent under UV light [26], offering additional options to monitor the performance and replacement of PLLA–ND–ODA composite with growing bone tissue.

In the above studies, the composites were manufactured by solution mixing and casting. Another approach to manufacture nanocomposites is to start from monomers and perform *in situ* polymerization directly on the ND surface. Resulting composites are expected to have an improved dispersion since ND agglomerates can be broken by the growing polymer chains during the reaction. At the same time the polymers are covalently attached to the ND surface, forming the strongest interface between the polymer and ND, which is mandatory for effective load and heat transfer from the matrix to the nanofiller.

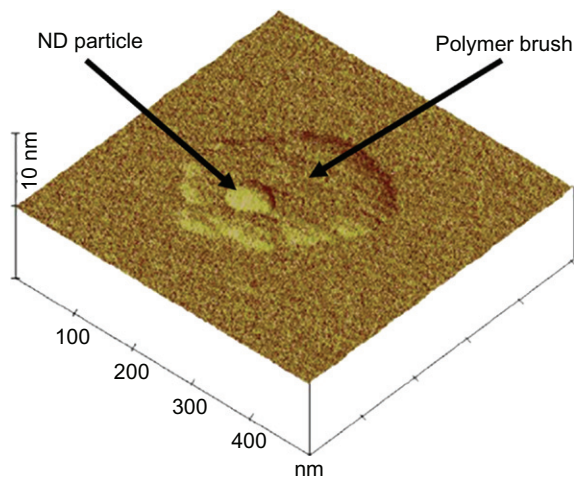
ND with covalently linked polymer chains (ND–polymer brushes) were synthesized using the atom transfer radical polymerization of poly-(iso-butyl methacrylate) at the ND surface. The brushes were characterized by TGA, FTIR, Nuclear Magnetic Resonance spectroscopy (NMR), and AFM. Single ND–polymer brushes were visualized using AFM as shown in Figure 13.13. According to this data, the single ND–polymer brushes can have diameters of up to 300 nm, i.e., ~100 times larger than the diameter of single ND particles [85]. This increase in

**FIGURE 13.11**

TEM images of ND-ODA and PLLA-ND-ODA composites [81]. (A) At high resolution, the grafted ODA chains are seen on ND particles. Low resolution TEM images of PLLA-ND-ODA nanocomposites show good dispersion and reduced agglomeration of ND-ODA particles: composites containing (B) 3 wt% and (C) 10 wt% ND-ODA show high aspect ratio agglomerates, being the penultimate step before obtaining single-dispersed particles according to polymer-nanofiller theory. Light and TEM micrographs of fractured tensile PLLA-ND-ODA specimen containing 10 wt% ND-ODA [82]. (D) Crazing observed using light microscopy. (E) TEM micrograph showing crazing. (F) High-magnification TEM micrograph showing typical pores and fibers bridging a crazing gap in ND-ODA-reinforced PLLA.

**FIGURE 13.12**

AFM scans of ND-ODA particles using generalized phase imaging scans (resonance and amplitude signals are shown), based on broad-band detection and multi-eigenmode operations at different combinations of topographic and Band Excitation (BE) eigenmodes [83]. Due to the high spatial resolution, the grafted ODA molecules to ND become traceable.

**FIGURE 13.13**

AFM scan of a ND-PiBMA-1 polymer brush. The ND-polymer brush has a diameter of 300 nm, ~50 times larger than the pristine ND particle [85].

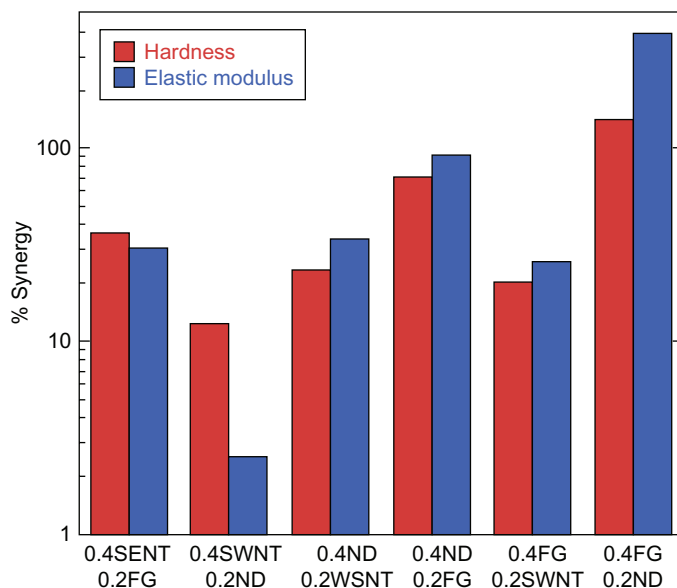


FIGURE 13.14

Synergetic effects of different carbon nanofillers in PVA. The highest synergetic effect was found when few layered graphene (FG) and ND are combined in a PVA composite [88].

single ND particle size due to the attached molecules is important to keep in mind when analyzing particle size by techniques such as dynamic light scattering [81,85].

Using a similar approach, polyimides were grown on ND particles. It was found that the X-ray Diffraction (XRD) peak of polyimide at 4.9° disappeared in ND composites, providing evidence that long range interactions between polyimide chains are disrupted due to the introduction of ND. The produced nanocomposite had a 25% higher Young's modulus and a 15% higher hardness at a ND content of 5 wt% [86].

Synergetic effects of ND in reinforcing thermoplastic copolymers

It was suggested that the combination of two fillers in a nanocomposite may result in synergism with larger improvements in properties, compared to the values expected based on the additive rule. This was demonstrated by combining a micrometer-sized filler with ND: polyurethane foam containing a mixture of 10 μm diameter glass spheres and ND showed a 30% improved strain resistance [87].

In the case of a PVA-based nanocomposite, the strongest synergetic effects were observed when two nanocarbons, few layered graphene and ND, were combined (Figure 13.14). The highest Young's modulus—9.3 GPa, 14 times higher compared to the neat PVA matrix—was achieved when CNTs were used with ND at a total nanofiller loading of only 0.6 wt%. The mechanism of the synergism is still unclear [88].

ND can be used to reinforce various thermoplastic polymers as described above. There seems to be no limitation on the matrix composition; even complex copolymer

matrices can be reinforced by ND. In a study of ethylene-1-octene–ND composites, an example of such a complex copolymer composite, the amount of crystalline orthorhombic phase and its crystallization rate were increased due to the addition of 5 wt% of as-received ND. This resulted in an improved Young's modulus and larger strain-to-failure values [89]. V-shaped ND–copolymer brushes were produced in a different study and might be optimal for copolymer reinforcement [27].

13.4.2 Thermoset–ND composites

Polymer thermosets find numerous applications in industry as adhesives, structural components, polymer concretes, and matrix materials [90,91]. These applications require superior mechanical properties. Similar to thermoplastics, ND can be introduced into the thermosets to improve their mechanical and tribological properties.

A common thermosetting polymer is epoxy, widely used as a matrix material for carbon–fiber reinforced composites [91]. To further improve the mechanical properties of the matrix material and to study the reinforcing potential of ND, epoxy–ND composites with ND contents of up to 35 vol.% were produced. Hardness and Young's moduli of these composites measured by nanoindentation were improved by 300% and 700%, respectively, reaching modulus values of up to 20 GPa and resulting in an increased scratch resistance. At such high ND concentrations, the composite material can be thought of as a ND network infiltrated by a polymer acting as a binder (Figure 13.15A). Direct contact between the ND particles in such composites results in improved thermal conductivity [92]. Furthermore, tribological studies showed that an alumina counter-body was damaged by the ND–epoxy agglomerates contained within these composites, suggesting high hardness of these agglomerates, which can eventually replace micron-sized diamond particles in cutting tools. Average macroscale friction coefficients of epoxy composites containing 7.5 vol.% ND were reduced by a factor of 4 reaching values of 0.1 [93].

While high loadings of ND result in remarkably high hardness and Young's moduli of the epoxy–ND composites, lower concentrations can increase the mechanical properties as well. The bulk Young's modulus measured in tensile tests was 25% higher due to the addition of 0.5 wt% as-received ND also increasing the decomposition temperature. However, due to poor dispersion, the storage modulus of the epoxy composite was significantly reduced with addition of ND [94], emphasizing the importance of a good dispersion to optimize the mechanical properties of ND composite materials.

A study on the mode I and II fracture toughness of epoxy–ND composites has shown that, besides an improved Young's modulus and hardness, the mode II fracture toughness of epoxy–ND composites with ND loadings of 0.1 wt% is increased. This is because ND is thought to hinder shear deformation, improving fracture toughness [95].

To strengthen the epoxy–nanofiller interface, functionalization of the nanofillers was explored. Following the analogy with molecular curing agents, which for epoxy resins are typically amines, nanoparticles were modified in a way to form surface aminogroups that are expected to react with epoxy groups of the resin.

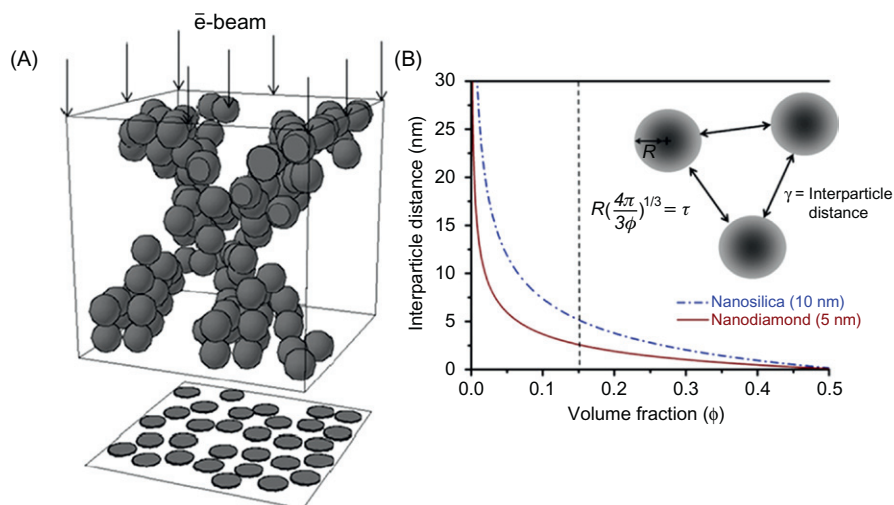
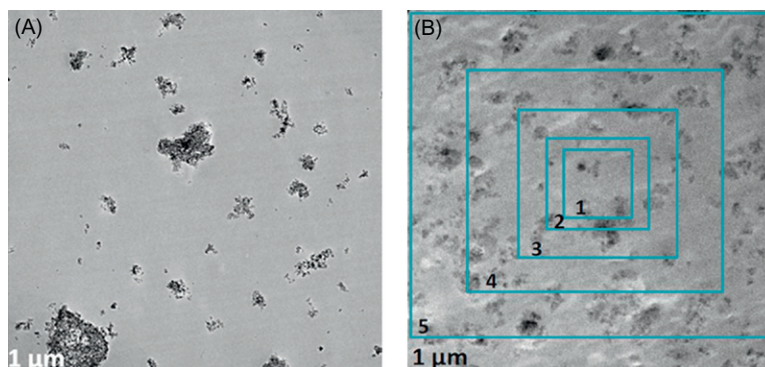


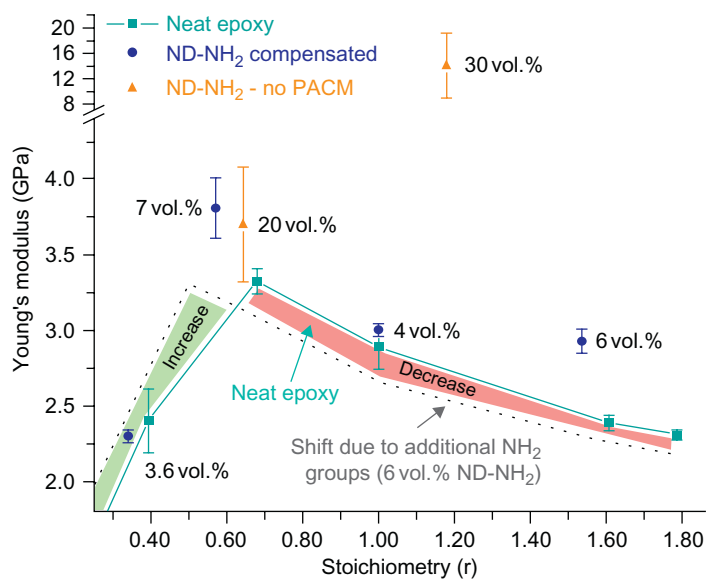
FIGURE 13.15

(A) Model of a high concentration ND composite. Electrons used in TEM imaging pass through the sample. The resulting TEM images give limited information on the 3D structure of the composite. Additional measurements are required to draw further conclusions. (B) Relationship between the volume fraction of the filler and the interparticle distance. In comparison to larger particles, the interparticle separation in ND composites is shorter at lower concentrations and disappears earlier [92].

CNTs functionalized with aminogroups significantly improved the flexural modulus and strength of an epoxy matrix when compared to unmodified CNTs [46]. A route to aminated ND (ND-NH₂) was recently developed by covalent linking ethylenediamine to its surface, making it possible to form a covalently bonded network of ND-NH₂ and epoxy molecules (Figure 13.4A and B) [28]. To confirm covalent bonding between the diamine molecules and ND particles, FTIR, TGA, and DSC studies were performed on ND-NH₂. When ND-NH₂ reacted with the epoxy resin (Figure 13.4B), a strong covalent epoxy-ND interface was formed. The resulting Young's modulus of a composite containing 3.5 vol.% ND-NH₂ was improved by 80% [44]. Also, it was found that to manufacture epoxy-ND-NH₂ composites with uniformly dispersed NDs it is important to use ND-NH₂ that was kept in an inert solvent without drying [28,44] (Figure 13.16A and B). This study also discussed the interference of aminogroups of ND-NH₂ with the aminogroups of curing agent used for this epoxy system: special attention was paid to compensate for the excess of aminogroups introduced by ND-NH₂ in order to keep the right ratio of the amino-to-epoxy groups in the system and to maximize the Young's modulus of the composite. Young's moduli of neat epoxy samples containing an excess of aminogroups, equivalent to the number of aminogroups introduced by 6 vol.% ND-NH₂ have been calculated and are plotted in Figure 13.17 (dotted line). To avoid

**FIGURE 13.16**

(A) TEM image of an epoxy–ND–NH₂ composite manufactured using dried ND–NH₂ powder, showing large ND–NH₂ agglomerates of up to 1 μm in size. (B) TEM images of epoxy–ND–NH₂ composites manufactured with ND–NH₂ stored in Tetrahydrofuran (THF) suspension after the synthesis prior to composite manufacturing, showing improved dispersion due to this adjusted manufacturing process [44].

**FIGURE 13.17**

Young's moduli of neat epoxy, compensated epoxy–ND–NH₂ composites (spheres), and composites cured with ND–NH₂ only (triangles). The effect of the additional aminogroups on Young's modulus introduced by 6 vol.% ND–NH₂ at different stoichiometries is shown as well (dotted gray line) [44].

undesired reduced Young's moduli of the epoxy-ND-NH₂ composites it is critical to compensate for the additionally introduced aminogroups. With proper compensation, the Young's moduli of composites are always higher compared to noncompensated epoxy-ND-NH₂ composites (Figure 13.17, circles) [44]. Remarkably, due to the large number of aminogroups formed on the surface of the NDs, it is possible to cure epoxy solely with ND-NH₂, yielding composites with Young's moduli of up to 20 GPa (Figure 13.17, triangles).

The tribological properties of epoxy-ND-NH₂ composites were studied as well. A composite with a high content of ND-NH₂ (33 vol.%) has a friction coefficient of 0.06 ± 0.02 , 54% less when compared to composites produced with up to 50 vol.% of as-received ND [93]. This friction coefficient value is close to the ones reported for carbide-derived [96] or diamond-like carbon films [97], showing the potential of this composite for tribological applications. AFM line scans on the epoxy-ND composites showed a sharp change in friction force when the AFM tip moved from the matrix to ND clusters composed of as-received ND (Figure 13.18). Composites

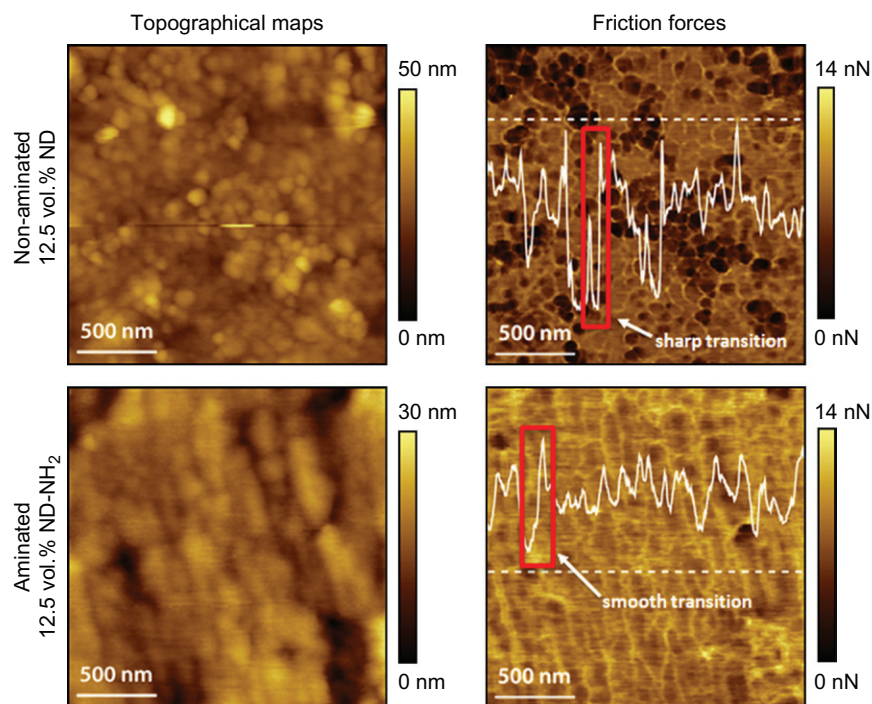


FIGURE 13.18

Topographical and friction force maps recorded with AFM on epoxy-ND composites containing 12.5 vol.% ND and ND-NH₂. AFM line scan shows sharp transitions in frictional forces for composites containing as-received ND, while composites containing ND-NH₂ have a smoother transition in frictional forces [93].

made with aminated ND-NH₂ have a rather different structure: transitions between low- and high-friction force areas are smoother, indicating the formation of an interphase around ND-NH₂ particles that might be responsible for the better performance of these composites (Figure 13.18) [93].

13.4.3 Elastomer–ND composites

Elastomers are a subclass within polymers; an elastomer is defined as a cross-linked, amorphous polymer above its T_g [98]. Elastomers are heavily used in the automobile industry to make tires, braking systems, chassis, interior parts, etc. [99]. In many cases, improvements in mechanical properties of elastomers are required to extend their lifetime and further broaden their applications.

Studies on elastomer–ND composites are rare. However, improved mechanical properties, such as cohesive strength, rupture, and wear resistance were reported for a variety of elastomers including fluorinated elastomers and rubbers [100]. The effect of the surface functionalization of ND on the mechanical properties of polysiloxane films was studied as well, where mechanical properties such as engineering stress and tensile strength were increased due to the addition of silanized ND. The improvement in mechanical properties was attributed to a reduction in ND agglomerate size during a silylation reaction, which removes adsorbed water from the ND surface at the same time, rendering the material hydrophobic (Figure 13.19) [101]. Further studies on the reinforcing mechanisms of ND in elastomeric polymer matrices are required. The covalent incorporation of ND into elastomers is a promising approach that could yield materials with larger strain-to-failure values.

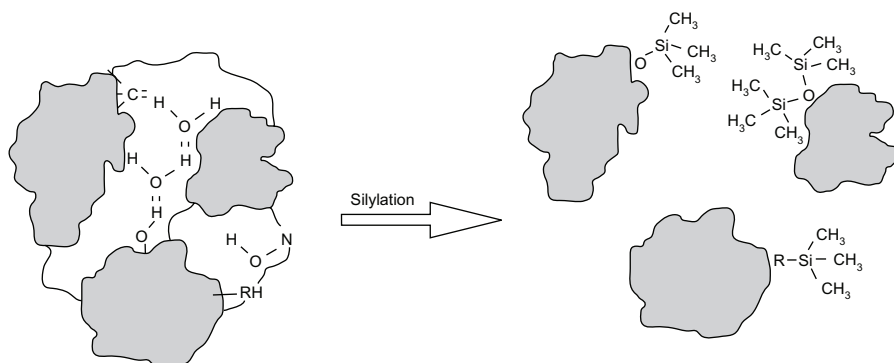


FIGURE 13.19

Scheme of the surface modification of ND with silylation agents: R is the functional group, which contains an “active” proton (OH, NH₂, COOH, etc.). It is suggested that the silylation breaks down ND agglomerates, resulting in improved dispersion [101].

13.5 Thermal properties of polymer–ND composites

A major challenge limiting the application of polymers is their low melting temperature and thermal stability, both resulting in a decay of mechanical properties at relatively low temperatures. The T_g , a common phenomenon responsible for the decrease in mechanical properties of polymers, is in the range of 200°C for epoxy polymers, one of the highest among polymers. In addition to T_g , other thermal properties, such as thermal conductivity and fire resistance need to be further improved to broaden the use of polymers. Here, we discuss the effects of ND on the thermal properties of polymers.

13.5.1 Thermal stability of polymer–ND composites

Addition of ND to PLA resulted in improved mechanical properties, an increased thermal stability, and a lower T_g and crystallization temperature of the composites, measured by TGA [80]. A 20°C increase in T_g and a higher degradation temperature were measured for a liquid crystal polyester, due to the addition of 1 wt% ND [102].

PMMA reinforced with 2 wt% of onion-like carbon (OLC), produced by the annealing of ND [1,103], has a higher T_g and melting temperature, as measured using a capacitance bridge [104]. Resistance to thermal degradation of PMMA was increased in another study due to the addition of 2 wt% of nitric acid–purified ND [23].

It can be concluded that ND and OLC can be used to effectively improve the thermal stability of polymers. Mechanisms for the observed improvements are still under discussion and are believed to result from changes in the polymer conformation taking place in the ND–polymer interphase.

13.5.2 Thermal conductivity of polymer–ND composites

Due to diamond's excellent thermal conductivity, additions of ND can improve the typically poor thermal conductivity of polymers. However, the large interfacial area of nanofillers introduces thermal barriers. To understand if ND can improve the thermal conductivity of polymer matrices, several studies were conducted.

Experimentally, it was shown that the thermal conductivity of polymers is improved due to the addition of ND. In the case of a PDMS, a 15% improvement in thermal conductivity due to the addition of 2 wt% ND was measured by a transient-state technique. This increased thermal conductivity indicates a strong interface between the nanofiller and the polymer matrix, minimizing interfacial phonon scattering [23].

The thermal conductivity in epoxy–ND composites with up to 35 vol.% ND was measured by DSC. These composites are essentially ND bodies infiltrated by epoxy (Figure 13.15A). The interparticle distances of nanosilica and ND at same concentrations are compared in Figure 13.15B. ND's small particle size results in a much smaller interparticle distance at lower filler loadings, making ND advantageous

compared to other nanofillers. The high loadings of ND resulted in a 30% improved thermal conductivity when compared to the neat epoxy [92]. The ND in this study was used as-received. Further improvements in thermal conductivity might be possible when purified or functionalized ND is used to create a stronger ND–polymer interface.

13.6 Optical properties of polymer–ND composites

The optical properties of polymer composites are of interest for various applications. For example, laser beams can be amplified or high refractive index materials can be obtained when introducing nanofillers into polymers [105]. Also, the visual appearance of polymer films, which is of importance, e.g., for packaging or surface finishing, can be tuned by nanofillers [106]. Light adsorbing nanofillers are currently used in cosmetic sunscreens [107]; it is also possible to take advantage of a high-UV absorbance of NDs when incorporating them into polymer films.

Due to its interesting optical properties, discussed in detail in Chapter 14 of this book, including a high refractive index and the ability to strongly adsorb light in the UV range, ND is a promising material to improve the optical properties of polymers.

The strong absorption of ND in the UV range was previously reported; the efficiency of absorption was shown to be a function of agglomerate size, concentration, and surface functionalities [108]. Furthermore, ND with certain naturally or artificially created defects is fluorescent [109]. ND agglomerates can form photonic crystals, where variations in the interparticle distance result in various colors of ND–oil suspensions [110]. Incorporating ND into polymer matrices will make it possible to take advantage of these optical properties.

PA 11 fiber mats containing up to 20 wt% ND were produced by electrospinning and formed visually transparent, UV-absorbing thin films on different substrates upon heating (Figure 13.20). In combination with improved mechanical properties, this material has a great potential for UV-protective, scratch-resistant coatings [63].



FIGURE 13.20

Optical images of electrospun PA 11 nanofibers containing 20 wt% ND (left) before and (right) after heating, which leads to fibers fusing to the surface and forming a transparent UV-absorbing film [63].

The UV-absorbing properties of heat-treated PMMA–OLC composites were also reported [22].

A strong photoluminescence of PDMS–ND composites in UV, blue, and green ranges was observed after proton irradiation, and was the strongest within ND agglomerates. The irradiation has probably resulted in creating a number of fluorescent defect centers in the ND structure [22].

13.7 Electromagnetic shielding of polymer–ND composites

Electromagnetic compatibility (EMC) is essential for any electrical device to function reliably. Thus, it is important to protect electrical devices such as processors, integrated circuits, information processing equipment, and telecommunication units against electromagnetic interference (EMI). Advanced materials such as nanocomposites are expected to have good shielding properties against EMI, when appropriate nanofillers are used [111]. While ND is an insulator, OLC has metallic conductivity. OLC is produced by ND annealing, when sp^3 carbon is converted into sp^2 carbon [1,103]. The sp^3/sp^2 -carbon ratio can be controlled by the annealing temperature and time. OLC consisting of several shells of sp^2 carbon has good EM absorption properties due to its high electron conductivity and highly defective inner shells with electron vacancies that can be polarized [112].

A study on PDMS–OLC composites containing 4 wt% OLC showed that it is possible to improve the electromagnetic shielding of the polymer matrix determined using loss-tangent and dielectric constant measurements [23].

In a different study, the dielectric permittivity of PMMA and polystyrene polymer films was increased due to the addition of OLC (up to 2 vol.%) [104,113]. Additionally, the electrical conductivity of the polystyrene–OLC composites was characterized and showed several orders of magnitude improvement due to the addition of 35 wt% OLC. Both values increased with improved dispersion and reduced agglomerate size. Improved dispersion was achieved with high shear forces during the manufacturing process introduced using a forge-rolling method [113].

13.8 Other applications for polymer–ND composites

Due to its biocompatibility [1] and rich surface chemistry, ND holds great potential for engineering new materials for biomedical applications.

Grafting of polymers to ND has been described above. In a next step, ND can be used as a drug delivery system for oral intake when, for example, functionalized with the biopolymer chitosan. Chitosan can be used as a carrier for various proteins, where proteins get released due to changes in pH. Successful grafting of chitosan to ND was confirmed by FTIR, Raman, and Zeta-potential measurements [114].

Another approach to use ND as a drug carrier in polymer systems was realized by enclosing ND particles into a porous sandwich Parylene C structure (Figure 13.21).

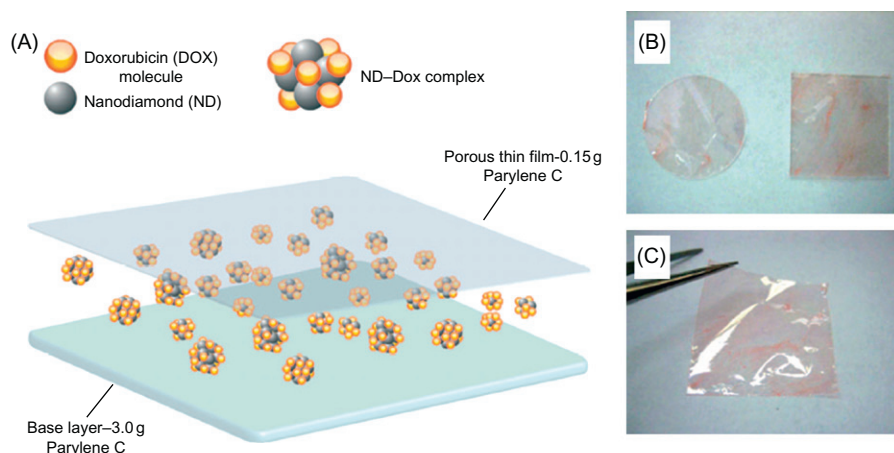


FIGURE 13.21

(A) Illustrated schematic of hybrid film patch for doxorubicin (DOX) delivery with ND. NDs and DOX molecules bound through physical interactions in various configurations are deposited atop a base layer of Parylene. A final layer of Parylene film is then deposited for additional elution control. (B) Hybrid films with a 10g base layer of varied size and shapes. (C) The patch exhibits innate flexibility and a thin physical profile [115].

An FDA-approved biocompatible polymer, Parylene C can be used for local drug delivery when implanted into the human body. Due to the microporosity of the polymer, ND is released at constant rates for prolonged periods, which is often necessary for successful disease treatment [115].

More exotic properties such as the shielding against proton irradiation were reported for polymer–ND composites as well. Changes in the molecular structure of a neat PDMS matrix and a PDMS–ND composite due to proton irradiation were monitored using FTIR and Raman spectroscopy. It was found that cleavage of the polymer backbone was significantly reduced due to the introduction of ND, thus improving the resistance of the polymer to radiation-induced degradation [116].

13.9 Future work

This review of literature illustrates that ND is an excellent material to improve many important properties of various polymer matrices. However, future advances in ND dispersion and optimization of the ND–polymer interface and interphase hold a great and largely unexplored potential for further improvements in properties. To fully explore the opportunities provided by ND in polymer matrix composites, new processing techniques and routes of chemical modification of ND surfaces as well as new, smarter ways to control the ND–polymer interface and interphase need to be developed.

References

- [1] V.N. Mochalin, O. Shenderova, D. Ho, Y. Gogotsi, The properties and applications of nanodiamonds, *Nat. Nanotechnol.* 7 (2012) 11–23.
- [2] A. Krueger, D. Lang, Functionality is key: recent progress in the surface modification of nanodiamond, *Adv. Funct. Mater.* 22 (5) (2012) 890–906.
- [3] A. Krueger, The structure and reactivity of nanoscale diamond, *J. Mater. Chem.* 18 (2008) 1485–1492.
- [4] A. Krueger, Diamond nanoparticles: jewels for chemistry and physics, *Adv. Mater.* 20 (2008) 2445.
- [5] X. Xu, Z. Yu, Y. Zhu, B. Wang, Influence of surface modification adopting thermal treatments on dispersion of detonation nanodiamond, *J. Solid State Chem.* 178 (2005) 688–693.
- [6] S. Osswald, G. Yushin, V. Mochalin, S.O. Kucheyev, Y. Gogotsi, Control of sp^2/sp^3 carbon ratio and surface chemistry of nanodiamond powders by selective oxidation in air, *J. Am. Chem. Soc.* 128 (2006) 11635–11642.
- [7] I. Kulakova, Surface chemistry of nanodiamonds, *Phys. Solid State* 46 (2004) 636–643.
- [8] V. Mochalin, S. Osswald, Y. Gogotsi, Contribution of functional groups to the Raman spectrum of nanodiamond powders, *Chem. Mater.* 21 (2) (2009) 273–279.
- [9] A. Pentecost, S. Gour, V. Mochalin, I. Knoke, Y. Gogotsi, Deaggregation of nanodiamond powders using salt- and sugar-assisted milling, *ACS Appl. Mater. Interfaces* 2 (2010) 3289–3294.
- [10] V.N. Mochalin, S. Osswald, C. Portet, G. Yushin, C. Hobson, M. Havel, et al., in: *Materials Research Society Symposium Proceedings, Materials Research Society Fall meeting, Boston, MA, USA, 2007*, pp. 1039–1103.
- [11] B.V. Spitsyn, J.L. Davidson, M.N. Gradoboev, T.B. Galushko, N.V. Serebryakova, T.A. Karpukhina, et al., Inroad to modification of detonation nanodiamond, *Diamond Relat. Mater.* 15 (2006) 296–299.
- [12] B.V. Spitsyn, M.N. Gradoboev, T.B. Galushko, T.A. Karpukhina, N.V. Serebryakova, I.I. Kulakova, et al., Purification and functionalization of nanodiamond, in: D.M. Gruen, O.A. Shenderova, A.Y. Vul' (Eds.), *Synthesis, Properties and Applications of Ultrananocrystalline Diamond*, Springer, Dordrecht, 2005, pp. 241–252.
- [13] V.V. Korolkov, I.I. Kulakova, B.N. Tarasevich, G.V. Lisichkin, Dual reaction capacity of hydrogenated nanodiamond, *Diamond Relat. Mater.* 16 (2007) 2129–2132.
- [14] G. Lisichkin, V. Korol'kov, B. Tarasevich, I. Kulakova, A. Karpukhin, Photochemical chlorination of nanodiamond and interaction of its modified surface with C-nucleophiles, *Russ. Chem. Bull.* 55 (2006) 2212–2219.
- [15] Y. Liu, V.N. Khabashesku, N.J. Halas, Fluorinated nanodiamond as a wet chemistry precursor for diamond coatings covalently bonded to glass surface, *J. Am. Chem. Soc.* 127 (2005) 3712–3713.
- [16] G.V. Lisichkin, I.I. Kulakova, Y.A. Gerasimov, A.V. Karpukhin, R.Y. Yalkovlev, Halogenation of detonation-synthesised nanodiamond surfaces, *Mendeleev Commun.* 19 (2009) 309–310.
- [17] Y. Liu, Z.N. Gu, J.L. Margrave, V.N. Khabashesku, Functionalization of nanoscale diamond powder: fluoro-, alkyl-, amino-, and amino acid-nanodiamond derivatives, *Chem. Mater.* 16 (2004) 3924–3930.

- [18] V.L. Kuznetsov, A.L. Chuvilin, Y.V. Butenko, I.Y. Malkov, V.M. Titov, Onion-like carbon from ultra-disperse diamond, *Chem. Phys. Lett.* 222 (1994) 343–348.
- [19] C. Portet, G. Yushin, Y. Gogotsi, Electrochemical performance of carbon onions, nanodiamonds, carbon black and multiwalled nanotubes in electrical double layer capacitors, *Carbon* 45 (2007) 2511–2518.
- [20] D. Pech, M. Brunet, H. Durou, P.H. Huang, V. Mochalin, Y. Gogotsi, et al., Ultrahigh-power micrometre-sized supercapacitors based on onion-like carbon, *Nat. Nanotechnol.* 5 (2010) 651–654.
- [21] P. Ganesh, P.R.C. Kent, V. Mochalin, Formation, characterization, and dynamics of onion-like carbon structures for electrical energy storage from nanodiamonds using reactive force fields, *J. Appl. Phys.* 110 (2011) 073506–073508.
- [22] O. Shenderova, C. Jones, V. Borjanovic, S. Hens, G. Cunningham, S. Moseenkov, et al., Detonation nanodiamond and onion-like carbon: applications, in: *Composites*, vol. 205, 2008, p. 2251.
- [23] O. Shenderova, T. Tyler, G. Cunningham, M. Ray, J. Walsh, M. Casulli, et al., Nanodiamond and onion-like carbon polymer nanocomposites, *Diamond Relat. Mater.* 16 (2007) 1213–1217.
- [24] D.S. Su, N.I. Maksimova, G. Mestl, V.L. Kuznetsov, V. Keller, R. Schlogl, et al., Oxidative dehydrogenation of ethylbenzene to styrene over ultra-dispersed diamond and onion-like carbon, *Carbon* 45 (2007) 2145–2151.
- [25] W.W. Zheng, Y.H. Hsieh, Y.C. Chiu, S.J. Cai, C.L. Cheng, C.P. Chen, Organic functionalization of ultradispersed nanodiamond: synthesis and applications, *J. Mater. Chem.* 19 (2009) 8432–8441.
- [26] V.N. Mochalin, Y. Gogotsi, Wet chemistry route to hydrophobic blue fluorescent nanodiamond, *J. Am. Chem. Soc.* 131 (2009) 4594–4595.
- [27] J.L. Cheng, J.P. He, C.X. Li, Y.L. Yang, Facile approach to functionalize nanodiamond particles with V-shaped polymer brushes, *Chem. Mater.* 20 (2008) 4224–4230.
- [28] V.N. Mochalin, I. Neitzel, B.J.M. Etzold, A. Peterson, G. Palmese, Y. Gogotsi, Covalent incorporation of aminated nanodiamond into an epoxy polymer network, *ACS Nano* 5 (2011) 7494–7502.
- [29] V.N. Khabashesku, J.L. Margrave, E.V. Barrera, Functionalized carbon nanotubes and nanodiamonds for engineering and biomedical applications, *Diamond Relat. Mater.* 14 (2005) 859–866.
- [30] A. Kruger, Y.J. Liang, G. Jarre, J. Stegk, Surface functionalisation of detonation diamond suitable for biological applications, *J. Mater. Chem.* 16 (2006) 2322–2328.
- [31] R. Martín, M. Álvaro, J.R. Herance, H. García, Fenton-treated functionalized diamond nanoparticles as gene delivery system, *ACS Nano* 4 (2010) 65–74.
- [32] R. Martín, P. Hydorn, M. Alvaro, H. Garcia, General strategy for high-density covalent functionalization of diamond nanoparticles using Fenton chemistry, *Chem. Mater.* 21 (2009) 4505–4514.
- [33] H.A. Girard, T. Petit, S. Perruchas, T. Gacoin, C. Gesset, J.C. Arnault, et al., Surface properties of hydrogenated nanodiamonds: a chemical investigation, *Phys. Chem. Chem. Phys.* 13 (2011) 11517–11523.
- [34] A. Krueger, T. Boedeker, Deagglomeration and functionalisation of detonation nanodiamond with long alkyl chains, *Diamond Relat. Mater.* 17 (2008) 1367–1370.
- [35] Y.J. Liang, M. Ozawa, A. Krueger, A general procedure to functionalize agglomerating nanoparticles demonstrated on nanodiamond, *ACS Nano* 3 (2009) 2288–2296.

- [36] W.S. Yeap, S.M. Chen, K.P. Loh, Detonation nanodiamond: an organic platform for the Suzuki coupling of organic molecules, *Langmuir* 25 (2009) 185–191.
- [37] A. Krueger, New carbon materials: biological applications of functionalized nanodiamond materials, *Chem. A Eur. J.* 14 (2008) 1382–1390.
- [38] A. Krueger, J. Stegk, Y.J. Liang, L. Lu, G. Jarre, Biotinylated nanodiamond: simple and efficient functionalization of detonation diamond, *Langmuir* 24 (2008) 4200–4204.
- [39] G. Jarre, Y. Liang, P. Betz, D. Lang, A. Krueger, Playing the surface game—Diels-Alder reactions on diamond nanoparticles, *Chem. Commun.* 47 (2011) 544–546.
- [40] D. Lang, A. Krueger, The Prato reaction on nanodiamond: surface functionalization by formation of pyrrolidine rings, *Diamond Relat. Mater.* 20 (2011) 101–104.
- [41] Y.J. Liang, T. Meinhardt, G. Jarre, M. Ozawa, P. Vrdoljak, A. Scholl, et al., Deagglomeration and surface modification of thermally annealed nanoscale diamond, *J. Colloid Interface Sci.* 354 (2011) 23–30.
- [42] M. Comet, V. Pichot, B. Siegert, F. Britz, D. Spitzer, Detonation nanodiamonds for doping Kevlar, *J. Nanosci. Nanotechnol.* 10 (2010) 4286–4292.
- [43] L. Schmidlin, V. Pichot, M. Comet, S. Josset, P. Rabu, D. Spitzer, Identification, quantification and modification of detonation nanodiamond functional groups, *Diamond Relat. Mater.* 22 (2012) 113–117.
- [44] I. Neitzel, V. Mochalin, J. Niu, J. Cuadra, A. Kontsos, G. Palmese, et al., Maximizing Young's moduli of aminated nanodiamond-epoxy composites, *Macromolecules* (2012) submitted.
- [45] P.M. Ajayan, L.S. Schadler, P.V. Braun, *Nanocomposite Science and Technology*, Wiley-VCH, 2003.
- [46] P.-C. Ma, S.-Y. Mo, B.-Z. Tang, J.-K. Kim, Dispersion, interfacial interaction and re-agglomeration of functionalized carbon nanotubes in epoxy composites, *Carbon* 48 (2010) 1824–1834.
- [47] C. Chen, R.S. Justice, D.W. Schaefer, J.W. Baur, Highly dispersed nanosilica-epoxy resins with enhanced mechanical properties, *Polymer* 49 (2008) 3805–3815.
- [48] G.D. Seidel, D.C. Lagoudas, Micromechanical analysis of the effective elastic properties of carbon nanotube reinforced composites, *Mech. Mater.* 38 (2006) 884–907.
- [49] P.D. Spanos, A. Kontsos, A multiscale Monte Carlo finite element method for determining mechanical properties of polymer nanocomposites, *Probab. Eng. Mech.* 23 (2008) 456–470.
- [50] J.B. Hooper, K.S. Schweizer, Contact aggregation, bridging, and steric stabilization in dense polymer-particle mixtures, *Macromolecules* 38 (2005) 8858–8869.
- [51] J.B. Hooper, K.S. Schweizer, Theory of phase separation in polymer nanocomposites, *Macromolecules* 39 (2006) 5133–5142.
- [52] O.A. Shenderova, G. McGuire, Nanocrystalline diamond, in: Y. Gogotsi (Ed.), *Nanomaterials Handbook*, CRC Taylor and Francis Group, Boca Raton, FL, 2006, pp. 203–237.
- [53] O.O. Mykhaylyk, Y.M. Solonin, D.N. Batchelder, R. Brydson, Transformation of nanodiamond into carbon onions: a comparative study by high-resolution transmission electron microscopy, electron energy-loss spectroscopy, x-ray diffraction, small-angle x-ray scattering, and ultraviolet Raman spectroscopy, *J. Appl. Phys.* 97 (2005) 074302–074316.
- [54] O.A. Williams, J. Hees, C. Dieker, W. Jager, L. Kirste, C.E. Nebel, Size-dependent reactivity of diamond nanoparticles, *ACS Nano* 4 (2010) 4824–4830.

- [55] R. Selzer, K. Friedrich, Mechanical properties and failure behaviour of carbon fibre-reinforced polymer composites under the influence of moisture, *Composites Part A Appl. Sci. Manuf.* 28 (1997) 595–604.
- [56] S. Ahmed, F.R. Jones, A review of particulate reinforcement theories for polymer composites, *J. Mater. Sci.* 25 (1990) 4933–4942.
- [57] A. Grill, Tribology of diamondlike carbon and related materials: an updated review, *Surf. Coat. Technol.* 94–95 (1997) 507–513.
- [58] A.M. Schrand, J. Johnson, L. Dai, S.M. Hussain, J.J. Schlager, L. Zhu, et al., Cytotoxicity and genotoxicity of carbon nanomaterials. in: *Safety in Nanoparticles: From Manufacturing to Clinical Applications*, Springer, New York, 2009, pp. 1–29.
- [59] M. Monthieux, B.W. Smith, B. Burteaux, A. Claye, J.E. Fischer, D.E. Luzzi, Sensitivity of single-wall carbon nanotubes to chemical processing: an electron microscopy investigation, *Carbon* 39 (2001) 1251–1272.
- [60] A. Gavrilov, A. Voznyakovskii, Rheological characteristics and relaxation properties of polymer-nanodiamond composites, *Russ. J. Appl. Chem.* 82 (2009) 1041–1045.
- [61] V. Bershtein, L. Karabanova, T. Sukhanova, P. Yakushev, L. Egorova, E. Lutsyk, et al., Peculiar dynamics and elastic properties of hybrid semi-interpenetrating polymer network—3-D diamond nanocomposites, *Polymer* 49 (2008) 836–842.
- [62] A.-Y. Jee, M. Lee, Thermal and mechanical properties of alkyl-functionalized nanodiamond composites, *Curr. Appl. Phys.* 11 (2011) 1183–1187.
- [63] K.D. Behler, A. Stravato, V. Mochalin, G. Korneva, G. Yushin, Y. Gogotsi, Nanodiamond-polymer composite fibers and coatings, *ACS Nano* 3 (2009) 363–369.
- [64] J. Klein, Shear, friction, and lubrication forces between polymer-bearing surfaces, *Annu. Rev. Mater. Sci.* 26 (1996) 581–612.
- [65] J.K. Lancaster, Polymer-based bearing materials: the role of fillers and fibre reinforcement, *Tribology* 5 (1972) 249–255.
- [66] P. Rehbein, J. Wallaschek, Friction and wear behaviour of polymer/steel and alumina/alumina under high-frequency fretting conditions, *Wear* 216 (1998) 97–105.
- [67] M.R. Widmer, M. Heuberger, J. Vörös, N.D. Spencer, Influence of polymer surface chemistry on frictional properties under protein-lubrication conditions: implications for hip-implant design, *Tribol. Lett.* 10 (2001) 111–116.
- [68] J. Robertson, Properties of diamond-like carbon, *Surf. Coat. Technol.* 50 (1992) 185–203.
- [69] J.-Y. Lee, D.-S. Lim, Tribological behavior of PTFE film with nanodiamond, *Surf. Coat. Technol.* 188–189 (2004) 534–538.
- [70] D.P. Lim, J.Y. Lee, D.S. Lim, S.G. Ahn, I.W. Lyo, Effect of reinforcement particle size on the tribological properties of nano-diamond filled polytetrafluoroethylene based coating, *J. Nanosci. Nanotechnol.* 9 (2009) 4197–4201.
- [71] G.S. Bobrovnichii, A.L.D. Skury, S.N. Monteiro, R.C. Tardim, Effect of nanodiamond addition on the mechanical properties of polycrystalline metallic and polymeric composites, *Mater. Sci. Forum* 660–661 (2010) 848–853.
- [72] A. Voznyakovskii, B. Ginzburg, D. Rashidov, D. Tochil'nikov, S. Tuichiev, Structure, mechanical, and tribological characteristics of polyurethane modified with nanodiamonds, *Polym. Sci. Ser. A* 52 (2010) 1044–1050.
- [73] A. Stravato, R. Knight, V. Mochalin, S.C. Picardi, HVOF-sprayed nylon-11 + nanodiamond composite coatings: production and characterization, *J. Therm. Spray Technol.* 17 (2008) 812–817.

- [74] C.M. Hassan, N.A. Peppas, Structure and applications of poly(vinyl alcohol) hydrogels produced by conventional crosslinking or by freezing/thawing methods, in: A. Abe (Ed.), *Biopolymers/PVA Hydrogels/Anionic Polymerisation Nanocomposites*, vol. 153, Springer-Verlag, Berlin, 2000, pp. 37–65.
- [75] T.S. Kurkin, A.N. Ozerin, A.S. Kechek'yan, O.T. Gritsenko, L.A. Ozerina, G.G. Alkhanishvili, et al., The structure and properties of polymer composite fibers based on poly(vinyl alcohol) and nanodiamond of detonation synthesis, *Nanotechnol. Russ.* 5 (2010) 340–351.
- [76] S. Morimune, M. Kotera, T. Nishino, K. Goto, K. Hata, Poly(vinyl alcohol) nanocomposites with nanodiamond, *Macromolecules* 44 (2011) 4415–4421.
- [77] U. Maitra, K.E. Prasad, U. Ramamurty, C.N.R. Rao, Mechanical properties of nanodiamond-reinforced polymer-matrix composites, *Solid State Commun.* 149 (2009) 1693–1697.
- [78] P. Protopapa, E. Kontonasaki, D. Bikiaris, K. Parasekevopoulos, P. Koidis, Reinforcement of a PMMA resin for fixed interim protheses with nanodiamonds, *Dent. Mater. J.* 30 (2010) 222–231.
- [79] A.-Y. Jee, M. Lee, Mechanical properties of polycarbonate and poly(methyl methacrylate) films reinforced with surface-functionalized nanodiamonds, *J. Nanosci. Nanotechnol.* 11 (2011) 533–536.
- [80] Y.-Q. Zhao, K.-T. Lau, J.-k. Kim, C.-L. Xu, D.-D. Zhao, H.-L. Li, Nanodiamond/poly (lactic acid) nanocomposites: effect of nanodiamond on structure and properties of poly (lactic acid), *Composite Part B Eng.* 41 (2010) 646–653.
- [81] Q. Zhang, V.N. Mochalin, I. Neitzel, I.Y. Knoke, J. Han, C.A. Klug, et al., Fluorescent PLLA-nanodiamond composites for bone tissue engineering, *Biomaterials* 32 (2011) 87–94.
- [82] Q. Zhang, V. Mochalin, I. Neitzel, K. Hazeli, J. Niu, A. Kontsos, et al., Multifunctional nanodiamond-PLLA scaffolds for bone tissue engineering: enhanced mechanical strength and biomineralization, *Biomaterials* 33 (2012) 5067–5075.
- [83] S. Guo, S.D. Solares, V. Mochalin, I. Neitzel, Y. Gogotsi, S. Kalinin, et al., Multifrequency imaging in the intermittent contact mode of atomic force microscopy: beyond phase imaging, *Small* 8 (2012) 1264–1269.
- [84] P. Akcora, H. Liu, S.K. Kumar, J. Moll, Y. Li, B.C. Benicewicz, et al., Anisotropic self-assembly of spherical polymer-grafted nanoparticles, *Nat. Mater.* 8 (2009) 354–359.
- [85] L. Li, J. Davidson, C. Lukehart, Surface functionalization of nanodiamond particles via atom transfer radical polymerization, *Carbon* 44 (2006) 2308–2315.
- [86] Q. Zhang, K. Naito, Y. Tanaka, Y. Kagawa, Grafting polyimides from nanodiamonds, *Macromolecules* 41 (2008) 536–538.
- [87] N. Sirotnikin, A. Voznyakovskii, A. Ershova, Model of formation of three-dimensional polyurethane films modified by detonation nanodiamonds, *Phys. Solid State* 46 (2004) 746–747.
- [88] K.E. Prasad, B. Das, U. Maitra, U. Ramamurty, C.N.R. Rao, Extraordinary synergy in the mechanical properties of polymer matrix composites reinforced with 2 nanocarbons, *Proc. Nat. Acad. Sci. U.S.A.* 106 (2009) 13186–13189.
- [89] A.P. Korobko, N.P. Bessonova, S.V. Krashennnikov, E.V. Konyukhova, S.N. Drozd, S.N. Chvalun, Nanodiamonds as modifier of ethylene-1-octene copolymer structure and properties, *Diamond Relat. Mater.* 16 (2007) 2141–2144.
- [90] R. Kotsilkova (Ed.), *Thermoset Nanocomposites for Engineering Applications*, Rapra, 2007, pp. 2–10.
- [91] C. Soutis, Carbon fiber reinforced plastics in aircraft construction, *Mater. Sci. Eng. A* 412 (2005) 171–176.

- [92] I. Neitzel, V. Mochalin, I. Knoke, G.R. Palmese, Y. Gogotsi, Mechanical properties of epoxy composites with high contents of nanodiamond, *Compos. Sci. Technol.* 71 (2011) 710–716.
- [93] I. Neitzel, V. Mochalin, J. Bares, R. Carpick, A. Erdemir, Y. Gogotsi, Tribological properties of nanodiamond-epoxy composites, *Tribol. Lett.* (2012) [10.1007/s11249-012-9978-8](https://doi.org/10.1007/s11249-012-9978-8).
- [94] Z. Spitalsky, A. Kromka, L. Matejka, P. Cernoch, J. Kovarova, J. Kotek, et al., Effect of nanodiamond particles on properties of epoxy composites, *Adv. Compos. Lett.* 17 (2008) 29–34.
- [95] M.R. Ayatollahi, E. Alishahi, S. Shadlou, Mechanical behavior of nanodiamond/epoxy nanocomposites, *Int. J. Fract.* 170 (2011) 95–100.
- [96] B. Carroll, Y. Gogotsi, A. Kovalchenko, A. Erdemir, M.J. McNallan, Effect of humidity on the tribological properties of carbide-derived carbon (CDC) films on silicon carbide, *Tribol. Lett.* 15 (2003) 51–55.
- [97] Y. Liu, A. Erdemir, E.I. Meletis, A study of the wear mechanism of diamond-like carbon films, *Surf. Coat. Technol.* 82 (1996) 48–56.
- [98] A.P. Angelopoulos, Introduction to physical polymer science, *Mol. Cryst. Liq. Cryst. Sci. Technol. A* 381 (2002) 183–184.
- [99] C.A. Harper (Ed.), *Handbook of Plastics, Elastomers, and Composites*, fourth ed. McGraw-Hill 2002, p. 884.
- [100] V.Y. Dolmatov, Composition materials based on elastomer and polymer matrices filled with nanodiamonds of detonation synthesis, *Nanotechnol. Russia* 4 (2009) 556–575.
- [101] V.Y. Dolmatov, Polymer–diamond composites based on detonation nanodiamonds. Part 2, *J. Superhard Mater.* 29 (2007) 65–75.
- [102] D. Sordi, C. De Ruijter, S. Orlanducci, S.J. Picken, E.J.R. Sudhölter, M.L. Terranova, et al., Sulfonated liquid crystalline polyesters as resin matrix for single wall carbon nanotube and nanodiamond composites, *J. Polym. Sci. Part A Polym. Chem.* 49 (2011) 1079–1087.
- [103] O.A. Shenderova, V.V. Zhirnov, D.W. Brenner, Carbon nanostructures, *Crit. Rev. Solid State Mater. Sci.* 27 (2002) 227–356.
- [104] J. Macutkevic, P. Kuzhir, D. Seliuta, G. Valusis, J. Banys, A. Paddubskaya, et al., Dielectric properties of a novel high absorbing onion-like-carbon based polymer composite, *Diamond Relat. Mater.* 19 (2010) 91–99.
- [105] L.L. Beecroft, C.K. Ober, Nanocomposite materials for optical applications, *Chem. Mater.* 9 (1997) 1302–1317.
- [106] J.-H. Yeun, G.-S. Bang, B.J. Park, S.K. Ham, J.-H. Chang, Poly(vinyl alcohol) nanocomposite films: thermo-optical properties, morphology, and gas permeability, *J. Appl. Polym. Sci.* 101 (2006) 591–596.
- [107] S.A. Wissing, R.H. Müller, Cosmetic applications for solid lipid nanoparticles (SLN), *Int. J. Pharm.* 254 (2003) 65–68.
- [108] O. Shenderova, V. Grichko, S. Hens, J. Walch, Detonation nanodiamonds as UV radiation filter, *Diamond Relat. Mater.* 16 (2007) 2003–2008.
- [109] S.-J. Yu, M.-W. Kang, H.-C. Chang, K.-M. Chen, Y.-C. Yu, Bright fluorescent nanodiamonds: no photobleaching and low cytotoxicity, *J. Am. Chem. Soc.* 127 (2005) 17604–17605.
- [110] V. Grichko, T. Tyler, V.I. Grishko, O. Shenderova, Nanodiamond particles forming photonic structures, *Nanotechnology* 19 (2008) 225201.
- [111] X.C. Tong, *Advanced Materials and Design for Electromagnetic Interference Shielding*, vol. 1, CRC Press, Boca Raton, FL, 2008, p. 130.

- [112] O. Shenderova, V. Grishko, G. Cunningham, S. Moseenkov, G. McGuire, V. Kuznetsov, Onion-like carbon for terahertz electromagnetic shielding, *Diamond Relat. Mater.* 17 (2008) 462–466.
- [113] N.N. Gavrilov, A.V. Okotrub, L.G. Bulusheva, O.V. Sedelnikova, I.V. Yushina, V.L. Kuznetsov, Dielectric properties of polystyrene/onion-like carbon composites in frequency range of 0.5–500 kHz, *Compos. Sci. Technol.* 70 (2010) 719–724.
- [114] H.D. Wang, Q.Q. Yang, C.H. Niu, Functionalization of nanodiamond particles with N,O-carboxymethyl chitosan, *Diamond Relat. Mater.* 19 (2010) 441–444.
- [115] R. Lam, M. Chen, E. Pierstorff, H. Huang, E. Osawa, D. Ho, Nanodiamond-embedded microfilm devices for localized chemotherapeutic elution, *ACS Nano* 2 (2008) 2095–2102.
- [116] V. Borjanovic, L. Bisticic, I. Vlasov, K. Furic, I. Zamboni, M. Jaksic, et al., Influence of proton irradiation on the structure and stability of poly(dimethylsiloxane) and poly(dimethylsiloxane)-nanodiamond composite, *J. Vac. Sci. Technol. B* 27 (2009) 2396–2403.

Nanodiamond Nanoparticles as Additives to Lubricants

14

M.G. Ivanov^{a,b} and D.M. Ivanov^a

^a*Ural Federal University named after the First President of Russia B.N. Yeltsin, Yekaterinburg, Russia,*

^b*Adámas Nanotechnologies, Raleigh, NC*

CHAPTER OUTLINE

14.1 Introduction	458
14.1.1 Nanolubricants: state of the art	458
14.1.2 Formulations of industrial oils	458
14.1.3 Nanodiamond particles: properties important in nanolubricants	463
<i>Deagglomeration and fractionation</i>	<i>464</i>
<i>DND zeta potential.....</i>	<i>465</i>
14.2 Formation of ND colloids in oils	466
14.2.1 Stabilization of ND colloids in oils	466
<i>Electrostatic stabilization.....</i>	<i>466</i>
<i>Steric stabilization.....</i>	<i>468</i>
<i>Electrosteric stabilization.....</i>	<i>469</i>
<i>Stabilization by a metal complex</i>	<i>470</i>
<i>Stabilization by covalent surface modification of ND</i>	<i>470</i>
14.2.2 Preparation of ND colloids in oils.....	472
14.3 Tribological properties and mechanism of action of ND-related additives in oil and greases	473
14.3.1 Detonation soot.....	473
14.3.2 Nanodiamond	477
14.3.3 Synergistic lubricating effect of ND with colloid dispersions of solid particles additives.....	479
14.3.4 ND-derived carbon onions	480
14.3.5 Mechanism of action of ND particles.....	483
14.4 Conclusion	485
Acknowledgments.....	485
References	486

14.1 Introduction

The requirements for advanced lubricants are increasingly demanding due to, first, wider range of usage (wider temperature range, higher loads, higher speed of motion in friction pairs), and second the general requirement for increased reliability and service life of machinery. Therefore, it is particularly important to develop specialized antifriction and antiwear materials that prevent and compensate for wear, lower friction, save lubricants, fuel, and electricity, and have good antiscoring properties.

Thus research into extending the service life of such materials continues to be imperative. This is true for studies of both nanostructured coatings of friction surfaces and of new lubricant compositions containing nanoparticles.

14.1.1 Nanolubricants: state of the art

Over the last few years, interest in applications of nanoparticles as lubricant additives has steadily grown due to demonstrated reduction of friction and wear of nanoparticle-containing lubricant formulations. Nanoparticles of LaF_3 [1], polytetrafluoroethylene (PTFE) [2], MoS_2 [3], TiO_2 [4–6], CeO_2 and CaCO_3 [7], PbS [8], lanthanum borate [9], titanium borate [10], zinc borate [11], ferric oxide [12], Ni [13], CaCO_3 [14], and CuO , ZrO_2 , and ZnO [15] have been considered as perspective candidates for lubricant additives. A variety of studies on both inorganic and organic nanoparticles demonstrated their effectiveness as extreme pressure (EP) and antiwear (AW) additives for liquid lubricants. Some studies show that the addition of nanoparticles into lubricant can reduce contact sliding friction by improving performance of the boundary film formed between the sliding surfaces [13,16].

Nanotechnology principles have been utilized in the mid-twentieth century in developing cleaning additives for motor oils. These nanodetergents essentially consist of an inorganic core (15–40 mass%) stabilized by oil-soluble surfactants (20–45 mass%) incorporated into a lubricating base oil [14]. The principal functions performed by detergents in engine oil formulations are (1) acid neutralization, (2) high-temperature detergency, (3) oxidation inhibition, and (4) rust prevention [14]. Indeed detergents, such as overbased sulfonate particles, are examples of nanoadditives that are currently produced on an industrial scale. Therefore, nanoparticles (nanodetergents) are always added to automotive engine oils and the goal of reduction of oxidative degradation of the lubricant is achieved by forming organoacids.

Special among nanomaterials are carbon-based ultrafine additives. Studies of lubricating compositions [16,17] with detonation nanodiamond (DND) and detonation soot (a mixture of DND particles with different forms of sp^2 -bonded carbon) as additives have demonstrated their positive impact on the performance of lubricant compositions, often superior to other nanoparticle fillers.

14.1.2 Formulations of industrial oils

Lubricants are divided into several groups according to application: engine, industrial, transmission, turbine, compressor, and instrument oils. Currently in highest

demand (both by overall production volume and by diversity of products) is the motor oil group for gasoline, diesel, and natural gas engines. The industrial oil group includes oils for hydraulic systems, various guides and bushings, spindles and gearboxes, etc. Transmission oils are used in mechanical, hydromechanical, and hydrostatic transmissions. Especially important is improving the lubricity of motor oils for internal combustion engines.

Pure petroleum-based hydrocarbon blends or lubricants based on synthetic hydrocarbon-type mixtures (polyolefins or esters) do not meet all requirements provided by original equipment manufacturers (OEMs) for lubricating materials used in modern engines or in other applications. The usual solution is the addition of relatively small amounts of certain additive compounds that provide significant improvement of base oil properties with regard to either oxidative degradation or to tribological and other performance characteristics.

Currently there are five groups of major base oils [18]:

1. Group I base stocks contain less than 90% saturates and/or greater than 0.03% sulfur and have a viscosity index greater than or equal to 80 and less than 120.
2. Group II base stocks contain greater than or equal to 90% saturates and less than or equal to 0.03% sulfur and have a viscosity index greater than or equal to 80 and less than 120.
3. Group III base stocks contain greater than or equal to 90% saturates and less than or equal to 0.03% sulfur and have a viscosity index greater than or equal to 120.
4. Group IV base stocks are polyalphaolefins (PAO).
5. Group V base stocks include all other base stocks not included in groups I, II, III, and IV.

To convert base oil into motor oil, various additives are used—up to 25% w/w of the final product. Figure 14.1 provides an example of a final motor oil additive composition [19].

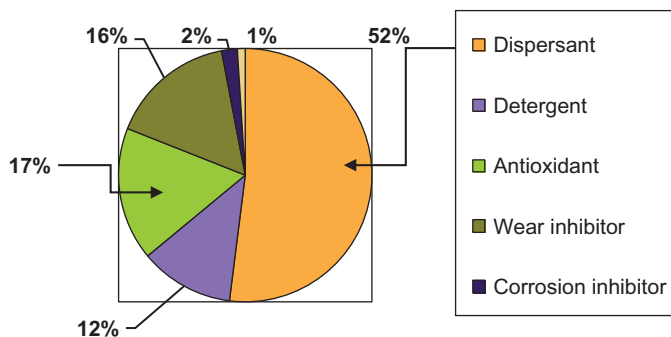


FIGURE 14.1

Illustration of a final composition for a motor oil additive.

Source: Adapted from Ref. [19].

The properties of commercial motor oils are determined by their ability to reduce friction between parts, reduce wear of contact surfaces, prevent sticking and welding, cool the parts, prevent corrosion, and, most importantly, retain these protective properties throughout the entire range of working temperatures and loads for as long as possible.

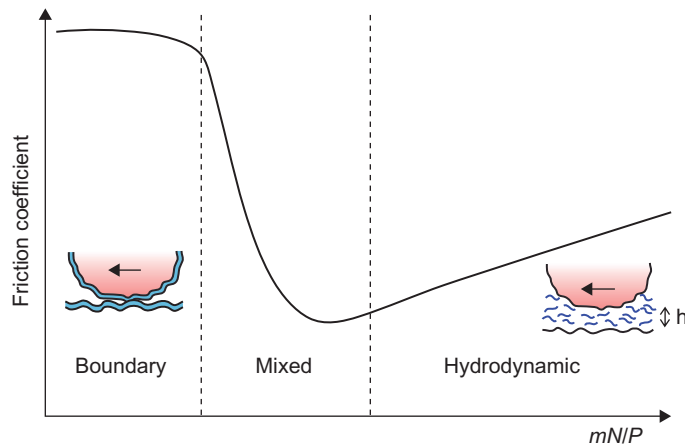
Commercially available motor oils are represented by dozens of products, differing in viscosity and other properties; new products appear periodically, which confirms the difficulty of creating a “universal” lubricant. Obtaining optimum durability (wear) and fuel economy (low friction) of tribological systems, especially where new materials and surfaces or surface treatments are used, relies on the compatibility between the surface and the lubricant.

The ability of crankcase oils to improve fuel economy is critical in vehicles worldwide. It has been estimated [17] that if all U.S. car owners used engine oil that gave them 0.5% fuel economy improvement, then the total cost savings would be \$370 million per year. It is also worth noting that U.S. manufacturers benefit significantly from more fuel-efficient oils: a 1 mpg (mile per gallon) benefit in CAFE (Corporate Average Fuel Economy) is worth ~\$100 million since the manufacturer has more flexibility in the mix of vehicles that they can sell. Therefore, both government regulations and OEMs are key drivers to more fuel-efficient lubricants.

The International Lubricant Standardization and Approval Committee (ILSAC) has issued the GF-5 passenger car motor oil specification. This new specification is the fifth in a series issued by ILSAC to provide improvements in fuel economy, emissions system protection, and engine oil robustness for gasoline engines. The GF-5 specification is designed to help OEMs meet regulatory requirements and provide new benefits to consumers. Specifically, the ILSAC GF-5 *Needs Statement* indicates that additional improvements in fuel economy and fuel economy retention must take place as compared to the ILSAC GF-4 specification [20]. In attempts to meet key challenges expected with ILSAC GF-5, the use of nanolubricants is a recurring theme, as they are beneficial for fuel economy, wear control, deposit control, and oxidation control.

Within the last few years, more restraining ecological requirements are being introduced, limiting use of sulfur- and phosphorus-containing additives (e.g., zinc dialkyldithiophosphates (ZDDP)) in motor oils. In this regard, utilization of nano-carbon-based additives is beneficial. In comparison with existing additives (such as ZDDP), their influence on catalytic activity of the neutralizers of the exhaust gases is minimal. The advantage of carbon-based additives is preserved at both low and high exhaust gas temperatures.

In order to understand the role of nanoparticles-based additives in the reduction of friction and wear, it is necessary to consider lubrication regimes in more detail. The lubricating fluid viscosity, the external load that is carried by the two surfaces, and the speed that the two surfaces move relative to each other are factors determining the thickness of the fluid film between friction surfaces. This, in turn, determines the lubrication regime. The combined effect of the viscosity, load, and speed on the friction losses and how they correspond to the different regimes is typically

**FIGURE 14.2**

Lubrication regimes for engine components and their relationships to friction. The horizontal axis shows a parameter where m is the fluid viscosity, N is the relative speed of the surfaces, and P is the load on the interface per unit bearing width.

Sources: Modified from Refs. [21,22].

represented on the so-called Stribeck curve (Figure 14.2). The basic regimes of fluid film lubrication are (i) hydrodynamic lubrication where two surfaces are separated by a fluid film, (ii) elastohydrodynamic lubrication where two surfaces are separated by a very thin fluid film, (iii) mixed lubrication where two surfaces are partly separated, partly in contact, and (iv) boundary lubrication where two surfaces mostly are in contact with each other even though a fluid is present. In addition to fluid film lubrication, there is solid film lubrication, in which a thin solid film (tribofilm) separates two surfaces.

Moving from the left to the right on the horizontal axis of the Stribeck curve, the effects of increased speed, increased viscosity, or reduced load can be seen [21,22] (Figure 14.2). The combination of low speed, low viscosity, and high load produces boundary lubrication. Boundary lubrication is characterized by little fluid at the interface and large contact area. The lubricating film is about the same thickness as the surface roughness and asperities on the solid surfaces are in contact with each other. This results in very high friction (Figure 14.2). The region of decreasing friction coefficient, down to the minimum of the Stribeck curve is determined as mixed lubrication. The fluid film thickness is slightly greater than the surface roughness, so that there is very little asperity contact, but the surfaces are still in close proximity and affect each other. In a mixed lubrication system, the surface asperities can form miniature nonconformal contacts characterized by a very high pressure build-up in the lubricant in the vicinity of the contact resulting in micro-elastohydrodynamic lubrication. These extremely high local pressures have a significant effect on the fluid viscosity that allows a very thin extremely viscous oil

film to form and support the load. To the right of the mixed lubrication regime, the subsequent increase of the Stribeck curve is referred to as the elastohydrodynamic regime where the two friction surfaces are separated by a lubricant film and no surface contact is present. The hydrodynamic film is formed when the geometry, surface motion, and fluid viscosity combine to increase the fluid pressure enough to support the load. The increased pressure forces the surfaces apart and prevents surface contact. The increase in friction in the hydrodynamic region is caused by the fluid drag (friction produced by the fluid): higher speed results in a thicker fluid film, but it also increases the fluid drag on the moving surfaces.

Thus the boundary regime leads to increased friction, energy loss, wear, and material damage. But, the boundary lubrication regime is unavoidable for most machines during their operating lives, especially during start-up, shutdown, and low speed operation. The boundary regime is very unstable and it determines the limit of serviceability of the friction pair. Thickness and stability of the boundary layer of oil on the working surfaces of engine parts depends on the chemical composition of the oil and the additives, chemical structure of the parts, and the condition of the surfaces. Therefore, special lubricants and additives have been developed to decrease the negative effects of boundary lubrication. In the boundary regime, the presence of nanomodifiers may promote the formation of a protective tribofilm with high plasticity and lubricity, as well as high-load capacity.

It is generally accepted that both the piston assembly and bearings in a modern engine are predominantly in the hydrodynamic lubrication regime, whereas the valve train is in the mixed/boundary lubrication regime [23] (Figure 14.3).

The lubrication role of solid particles introduced in a liquid lubricant depends on the size of the particles, on their amount, and on the geometry of the contact. The introduction of small particles is beneficial in boundary lubrication, but

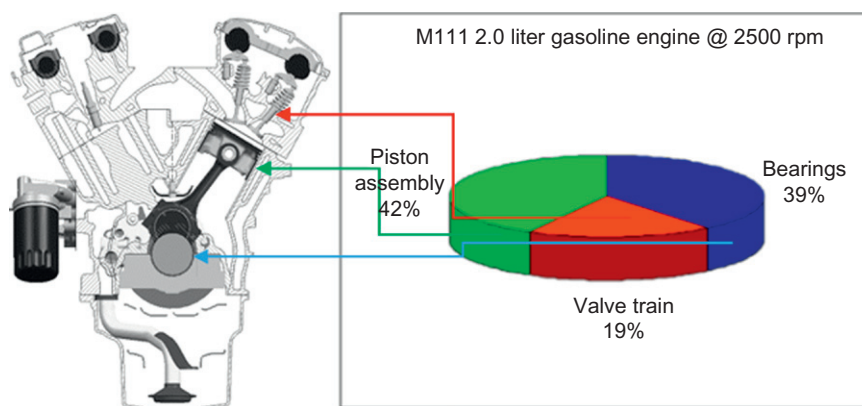


FIGURE 14.3

Predicted engine friction breakdown for a 2.0 liter gasoline engine (total loss = 1.5 kW) (CuO and TiO₂ [23,24]).

particles present in the lubricant have to be of small size so as to allow good fluid circulation within the contact.

Nanolubricant additives have the following effects [25,26]:

- strengthening of surface layers;
- smoothing of the surface with formation of low-angle roughness;
- formation of stable separation layers and of tribochemical products with lubricating properties [27]; and
- improving the stability of rheological parameters of the lubricant at elevated temperatures.

14.1.3 Nanodiamond particles: properties important in nanolubricants

DNDs produced in huge quantities (in tons) by detonation of carbon-containing explosives is one of the most promising nanocolloidal additives. Primary particles of DND are only 4–5 nm in size, but during synthesis and processing they form tight aggregates and agglomerates up to several hundred nanometers in size. While detonation soot (a mixture of DND particles with different forms of sp^2 -bonded carbon (Figure 14.4)) was used for improved tribological properties of industrial oils and greases for decades, highly purified DND with small aggregate sizes is a relatively new nanomaterial additive.

Due to the very active nature of the surface, particle size distributions of the same nanodiamond (ND) significantly varies depending on the solvent. For example, removal of water while drying (oxidizing the nondiamond carbon invariably yields aqueous suspensions) results in formation of strong aggregates [29–31],

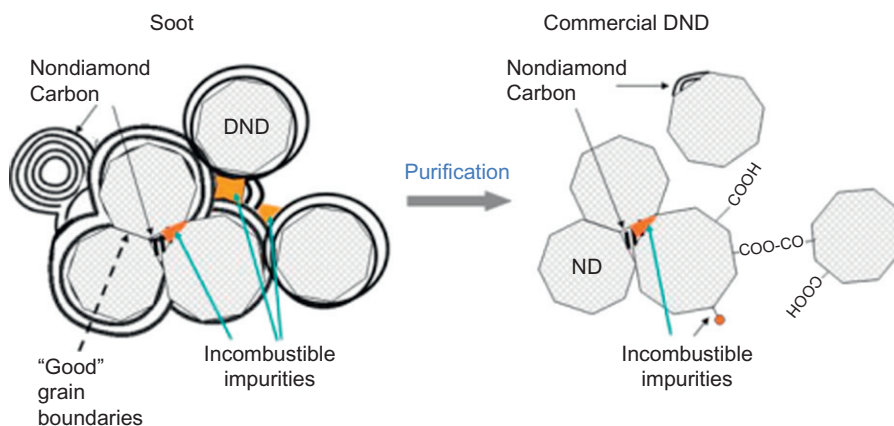


FIGURE 14.4

Tentative scheme of major structural components of detonation soot (left) and commercial DND product (right) [28].

which are difficult to re-suspend in oil; the aggregate sizes can be 500 nm or more, inevitably leading to abrasive erosion of surfaces.

The zeta potential of ND particles is an important parameter, determining the suspension stability. Depending on purification technology and sample history, NDs may have either positive or negative zeta potential. Formation of the different (acidic and basic) surface groups depends on both the chemical treatment of the particles and their surrounding medium.

Therefore, there are fundamental challenges that need to be overcome before widespread industrial use of ND, such as eliminating the large aggregates and improving suspension stability in oil (each group of lubricants according to American petroleum institute (API) classification may require a separate approach). Moreover, it is necessary to ensure compatibility with the existing additives, which vary according to the quality, viscosity, and manufacturer.

This requires developing novel approaches to surface modification of DND by either covalent or noncovalent attachment of functional groups to improve their dispersion properties, as well as to better understand the mechanism of action of NDs in lubricant compositions.

Deagglomeration and fractionation

DND deagglomeration and fractionation issues were considered in detail in a recent review [28]. Here we focus on the processes important for DND applications in lubricant compositions.

Krüger et al. [30] developed methods of mechanical deagglomeration of DND dispersions in suspensions by stirred media milling. Dynamic light scattering (DLS) analysis of typical colloidal solution thus obtained showed 99.4 wt% of single nanoparticles of 4.6 ± 0.8 nm diameter [32]. Krüger and coworkers developed a beads-assisted sonication (BASD) methodology that dispersed ND aggregates and subsequently functionalized the resulting primary particles during the BASD process. Liang et al. [33] developed a versatile and efficient method for the simultaneous deagglomeration and surface functionalization of strongly agglomerated nanoparticles. Their strategy included functionalization of the primary ND particle surfaces with silane and aryl groups.

Pentecost et al. [34] demonstrated that dry media-assisted attrition milling is a simple, inexpensive, and efficient alternative to the current methods of disaggregating ND. This technique uses water-soluble nontoxic and noncontaminating crystalline compounds, such as sodium chloride or sucrose. When milling is complete, the media can be easily removed from the product by water rinsing, which provides an advantage when compared to milling with ceramic microbeads.

Several other methods have been proposed for DND deagglomeration. Xu et al. [35,36,37] developed a two-step deagglomeration procedure that included graphitization of by-products of detonation in a N_2 atmosphere at 1000°C for 1 h followed by oxidation with air at 450°C for several hours.

Williams [38] introduced a new technique to modify the surface of particles with hydrogen, which prevents cluster formation in buffer solution and which is a

perfect starting condition for chemical surface modifications. By annealing aggregated ND powder in hydrogen gas, the large (>100 nm) aggregates are broken down into their core (4 nm) particles. Dispersion of these particles into water via high power ultrasound and fractionation using high-speed centrifugation results in a monodisperse ND colloid, with exceptional long time stability in a wide pH range, and with high positive zeta potential (>60 mV). The large change in zeta potential resulting from this gas treatment demonstrates that ND particle surfaces are able to react with molecular hydrogen at relatively low temperatures, a phenomenon not witnessed with larger (20 nm) diamond particles or bulk diamond surfaces.

Stavrev [39] proposed a method for disaggregation of ND particles in suspension by freezing the suspension several times to a temperature below the boiling point of liquid nitrogen. Treated suspension was subjected to ultrasound with a frequency 18–27 Hz. As a result, primary diamond nanoparticles with a thin carbon shell were produced.

An alternative approach to effectively separate the particles and narrow the size distribution is centrifugal fractionation [40–43]. The centrifugal fractionation approach has drawbacks that mostly originate from the highly irregular shapes (spherical versus elongated chains) of the DND aggregates. While the centrifugal force depends upon the particle shape, the resulting separation is done based upon the combined size/shape factor rather than solely on the size. Importantly, it was recently shown that it is possible to extract 4 nm primary ND particles by ultracentrifugation [44].

DND zeta potential

The type of charge that DND acquires in colloids becomes important in its lubricant applications. Remarkably, there are classes of commercial and modified DNDs with highly positive and highly negative zeta potential values. Different groups, both acidic and basic, found on the ND surface form during the chemical treatment of the nanomaterial.

Thus, some processes of oxidation of soot or further oxidation of ND-containing nondiamond carbon such as the use of singlet oxygen in liquid media, oxygen, or ozone [45,46] in a gas phase result in rather deep oxidation with carboxylic acids groups predominantly on the ND surface. When ND is dispersed in DI water, dissociated acidic groups cause a negative charge on the ND surface [40,47–48].

Revealing the origin of positive zeta potential of ND is more complicated. Previously, a positive charge on the ND surface was attributed to protonation of amino groups in acidic media. At the same time, the amount of alcoholic groups that might also be responsible for a positive zeta potential is also small. Several models of basic oxygen-containing functionalities still being debated include chromene structures, diketone or quinone groups, pyrone-like groups, and electrostatic interactions of protons with the π -electron system of the graphene structures [28]. Pyrone-like structures are combinations of nonneighboring carbonyl and ether oxygen atoms at the edges of a graphene layer.

Zeta potential is one of the most important factors influencing the stability of ND suspensions and plays the main role in electrokinetic processes, reviewed below with regard to electrostatic and electrosteric methods of stabilization of DND suspensions in oil.

14.2 Formation of ND colloids in oils

It has been shown [49] that one of the main features of DND is the presence of diverse surface groups, rendering DND hydrophilic. The low stability to sedimentation of ND dispersions in liquids is well documented in the literature [28]. The problem is further exacerbated by the fact that there are no universal materials such as NDs. NDs supplied are vendor specific, depending on the method of synthesis and purification conditions [28]. Below we consider strategies of DND stabilization in oils and methods of preparation of DND suspensions in oils.

14.2.1 Stabilization of ND colloids in oils

The stabilization of ND colloids and thus the means to preserve their finely dispersed state is a crucial aspect in applications of diamond nanoparticles. The aggregation of ND particles is the bottleneck that hinders its applications. Several general discussions on the stability of colloids and nanoclusters have been already reported [50,51].

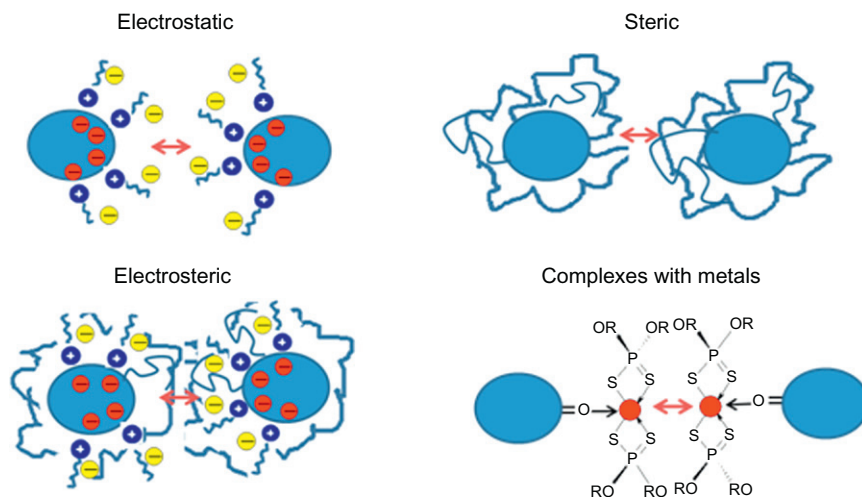
Van der Waals forces are the primary source of attraction between colloidal particles. These forces are always present between particles of similar composition. Therefore, a colloidal dispersion is said to be stable only when a sufficiently strong repulsive force counteracts the van der Waals attraction [52]. Consequently, the use of a stabilizing agent able to induce a repulsive force opposed to the van der Waals forces is necessary to impart stability to nanoparticles in suspensions.

In the present review, based on the stabilizing agents used for nanoparticles, four kinds of stabilization procedures are distinguished: (1) the electrostatic stabilization caused by ionogenic groups present on the surface or due to adsorbed ions, (2) the steric stabilization provided by the presence of bulky groups, (3) the combination of the first two stabilization mechanisms leading to electrosteric stabilization, and finally (4) stabilization with coordination compounds (Figure 14.5).

Electrostatic stabilization

In aqueous systems, there are two kinds of stabilization mechanisms, namely electrostatic stabilization and steric stabilization, while in nonaqueous systems, what really counts is steric stabilization.

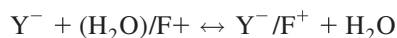
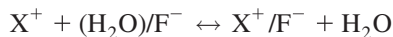
DND particles are inherently hydrophilic due to oxidative treatment of the detonation soot, therefore, it is difficult to disperse DND in nonaqueous systems. As reported by Osawa et al. [53], after drying at 60°C under a vacuum of 30–40 hPa for 2 h, the resulting powder still contains 2–3% of water demonstrating strong

**FIGURE 14.5**

Schematics of major types of nanoparticle stabilization mechanisms: electrostatic repulsion, steric stabilization due to extended chain molecules, the combination of the two (electrosteric), and stabilization with coordination compounds.

adherence of a water shell as a result of the electrostatic field over the facets of particles. Water in DND cannot be removed completely unless heated to 150°C for 15h under high vacuum [53]. Therefore, in general it is always necessary to consider the effect of the hydration shell in applications of DND particles.

Osawa et al. [53] classify perturbations of the nanophase of water on the DND surface by ions and dipolar molecules from bulk water phase as the first step toward understanding and controlling the behavior of DND particles. A salt X^+Y^- will bind in general more strongly than dipolar molecules with the electrostatic field of facets replacing adhered water:



where F^- and F^+ are the facets having strong negative or positive electrostatic field, respectively.

The production of charge on particle surfaces can be due to the presence of ionogenic groups or by adsorption of ionic compounds. The authors of Ref. [54] reported on the mechanical dispersion of diamond particles in aqua suspensions yielding suspensions stabilized with detergents or inorganic salts. Puzyr et al. [55,56] suggested modification of DND in water suspensions with NaCl and complex ions (EDTA) [57], using ultrasound treatment. The adsorption of ionic compounds and their related counter ions on the ND surface generates an electrical double layer around the nanoparticle. If the electric potential associated with the

double layer is high enough, then the electrostatic repulsion will prevent particle aggregation.

Several research groups developed methods of electrostatic stabilization using stabilizing agents with relatively high molecular weight. The authors of Ref. [58] demonstrated that thermally oxidized ND at 420°C (T-ND) is chemically active, favoring the formation of charge-transfer complexes with the amino-containing surfactants such as oleylamine (OLA) and octadecylamine (ODA) and the carboxyl groups on T-ND surface. Through these complexes OLA/ODA are anchored on DND surface, while the nonpolar alkyl chain extends outside and imparts hydrophobic properties to the particle. After being dispersed in tetrahydrofuran (THF), methyl ethyl ketone (MEK), and acetone with one of the surfactants, OLA or ODA, the T-ND showed good dispersion stability; however, the dispersion efficiency of the saturated ODA is not as good as that of the unsaturated OLA. Some steric stabilization takes place in this case too.

An ionic surfactant cetyltrimethylammonium chloride (CTAC) was used [59] in order to prepare hydrophobic NDs by forming the ionic complex $[\text{ND}-\text{COO}^-][\text{CTA}^+]$. The hydrogen ion of the NDs COOH functional group is substituted by the CTA^+ ion forming the ionic complex $[\text{ND}-\text{COO}^-][\text{CTA}^+]$. ND particles functionalized with CTAC were stable in toluene. A steric stabilization mechanism is also likely to act in this case.

Stable dispersions of ND in toluene were also obtained using various surfactants [60] such as sodium bis(2-ethylhexyl) sulfosuccinate (AOT) and cetyltrimethylammonium bromide (CTAB). Interestingly, AOT gives more stable dispersions in toluene. The behavior of sodium oleate utilized for ND dispersion has also been discussed in the literature [54,61].

Steric stabilization

The most straightforward method for promoting steric stabilization of ND suspensions in oil is to use oil-soluble dispersants. The presence of functional groups on the surface of nanoparticles allows their modification by conjugation with oil-soluble oligomeric dispersants to obtain stable suspensions in oil. Such modification will help reduce friction, as well as help prevent nanoparticle aggregation in fluids.

The molecular polymer structure generally plays an important role in steric stabilization. Polymers containing carboxyl groups are the most effective steric stabilizers due to the strong interaction of carboxyl groups with basic sites on the particle surface. On the other hand, the long-chain hydrocarbons in the molecular structures extend from the surface into the nonaqueous solvent providing stabilization. The longer the hydrocarbon chains, the better the stabilization effect. It is also shown in the literature that copolymers are usually more effective in steric stabilization than homopolymers because copolymers consist of more than one type of repeat unit. While one type of repeat unit can act as anchor on a nanoparticle, the other type, well soluble in the nonaqueous solution, provides good dispersivity.

The effect of different kinds of surfactants on the size distribution of ND particles in clean oil was studied by the authors of Ref. [62]. Results show that the dispersing stability of ND modified with surfactants YS-1 and SB-18 simultaneously is much better than those modified with either of them alone because of synergism of the surfactants. And the particle size distribution in the system can be improved remarkably after the adoption of hyperdispersants such as SA-E and SA-F. Anchoring groups of those hyperdispersants can be bonded with the particle surface by chemical and/or hydrogen bonding and their soluble chains are compatible with the dispersion media. A very stable clean-oil-based ND suspension with an average particle size of around 50 nm was prepared [62].

Hyperdispersant SF-1 was used for ND particle surface modification during mechanical deagglomeration [63]. SF-1 is a block copolymer with -NH_2 as the anchoring group and a polyester chain as the oil-soluble block in clean oil. High-speed shear stirring, high energy ultrasonic and vibration milling were used for disintegration at different weight ratios of dispersant to ND: 1:2, 1:1, and 2:1. It was demonstrated that the most efficient ratio resulting in highly dispersed ND was 1:1.

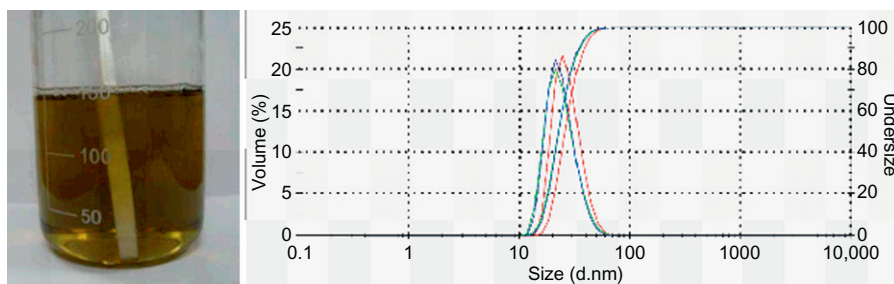
Dispersants for ND particles should provide dispersivity of the ND but not affect the oil composition. Thus, most preferable dispersants for oils are nonionic surfactants [64]. Specific examples of the dispersant for the diamond nanoparticles include polyoxyethylene alkyl ethers, polyoxyethylene dialkylphenol ethers, alkylglycoside, polyoxyethylene fatty acid esters, sucrose fatty acid esters, sorbitan fatty acid esters, polyoxyethylene sorbitan fatty acid esters, and fatty acid alkanolamide.

Electrosteric stabilization

The electrostatic and steric stabilization can be combined to maintain nanoparticle stability in solution (Figure 14.5). This kind of stabilization is generally provided by means of ionic surfactants. When a polyelectrolyte is used as a polymeric surfactant, both steric and electrostatic stabilizing effects are combined in one molecule. These compounds bear a polar head-group able to generate an electric double layer and a lyophobic side chain able to provide steric repulsion.

Authors of Ref. [36] used a diblock polymer as a dispersant to increase the steric repulsion between ND particles in white oils. The polymer was a polyelectrolyte consisting of two parts, a long polyester chain as an oil-soluble block and anchoring groups like amidocyanogen. The authors performed thermal treatment of ND in air with the purpose of increased density of carboxylic groups on ND surface, which interact presumably through electrostatic attraction with the anchoring groups of the dispersant. Enrichment of DND with carboxylic groups improved dispersivity of DND in the presence of the diblock polymer.

Example of stable colloidal suspension of DND in PAO oil with excellent dispersivity is illustrated in Figure 14.6, produced by the authors of Ref. [51] by means of electrosteric stabilization. While the average volumetric particle size of this DND is 10 nm when dispersed in DI water (data not shown), its average volumetric size in PAO-6 oil is also extremely low, only 20 nm, without the presence of larger aggregates (Figure 14.6).

**FIGURE 14.6**

Photographs of colloidal suspension of 0.1% 10nm DND (10nm when dispersed in DI water) in PAO-6 oil and volumetric size distribution of DND shown in PAO-6 oil.

Source: Modified from Ref. [51].

Stabilization by a metal complex

The term *stabilization by a metal complex* has been chosen to describe the use of traditional AW and EP oil additive to stabilize ND colloids.

It has recently been reported by Cholakov et al. [65] that ND can be stabilized by conventional oil additives, namely by oil detergent (neutral and overbased Ca (Mg) alkylaryl sulfonate), dispersant (polyalkenyl succinimide), and EP, AW additives (Zn dithiophosphate or their packages (Figure 14.5)). It was also demonstrated that powders containing soot are more easily stabilized in oils than those with pure diamond [65]. Certain typical oil additives ensure stability higher than that of a commercial product for nanoparticles used for a comparison. Specifically, detergent additives typically introduced into industrial lubricants provided higher stability than specialized dispersants. Ultrasonic treatment has an ambivalent effect and it is very important to determine correctly the time that would produce the required stability.

Stabilization by covalent surface modification of ND

Stabilization of ND in some media by covalent modification through functional surface groups (formed either during removal of nondiamond carbon or in some other way) can be considered as a subset of steric stabilization methods. For example, one of the polymer's terminal groups can be covalently bound to the ND surface (as opposed to chemisorption).

Chemical modification of ND surface occurs at early stages of purification of detonation soot (oxidation using various agents), resulting in formation on the nanoparticle surface of a set of oxygen-containing functional groups (whose exact composition is specific to the method used). Additionally, such purification also removes the noncombustible residues (various metal oxides) [66]. The use of strong chemical treatments or extreme temperatures render the NDs suitable for lubricant use without degrading the crystalline structure (sp^3 bonding) of the all-carbon chemically inert core.

Further modification of ND requires formation of reactive groups on the surface of nanoparticles, which can then participate in downstream reactions. Usually, one of the two treatments is applied: oxidative [41,45,67–69] or reductive [70,71]. We view the oxidative method, resulting in formation of carboxyl groups on the surface and a negative zeta potential, as the preferred way of modification of ND to prepare them for introduction into lubricating compositions.

One of the most effective methods for ND modification for obtaining stable suspensions in various solvents is its oxidation in air at 350–450°C [41,45,67,72]. During oxidation, the surface of individual ND particles reacts with oxygen from the air, producing gaseous carbon oxides. The oxidation process also takes place in the “neck” regions, formed between individual particles during aggregation. Thereby the aggregate is significantly weakened. When the processed powder is transferred into water or other selected solvent, the aggregates readily dissociate, which facilitates preparation of a suspension [72].

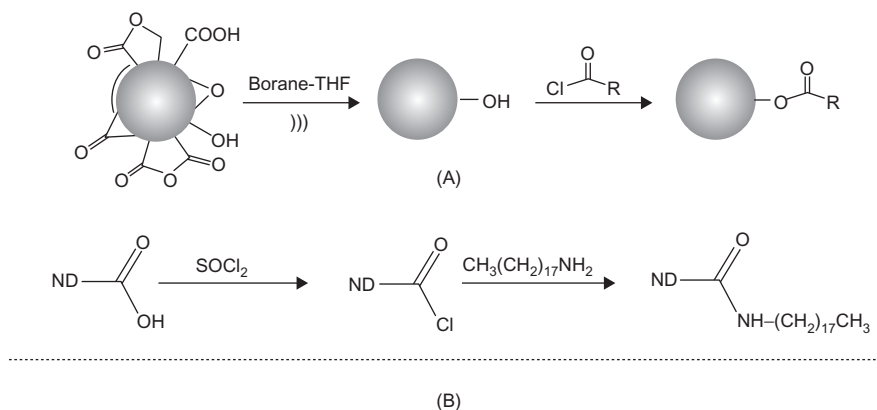
However, a variety of oxygen-containing functional groups present on the diamond surface leads to easy agglomeration of ND due to hydrogen bonding and van der Waals forces acting between the individual particles. HCl treatment of ND conducted after oxidative purification selectively increases the number of surface carboxylic groups due to hydrolysis of anhydrides, esters, lactones, and other groups formed during air oxidation, thus resulting in better suspension stability in polar solvents because of increased negative charge on the surface of the particles upon dissociation of COOH [73].

Other types of primary modification of ND—fluorination [74,75–78] and chlorination [79]—have also been demonstrated by several authors. Further processing yielded ND with alkyl- [80], aryl- [33,81], and fluoroalkyl- [82] derivatization.

By annealing aggregated ND powder in hydrogen gas, the large (>100 nm) aggregates are broken down into their core (4 nm) particles. Dispersion of these particles into water via high power ultrasound and high-speed centrifugation results in a monodisperse ND colloid, with exceptionally long time stability in a wide range of pH, and with high positive zeta potential (>60 mV). The large change in zeta potential resulting from this gas treatment demonstrates that ND particle surfaces are able to react with molecular hydrogen at relatively low temperatures, a phenomenon not witnessed with larger (20 nm) diamond particles or bulk diamond surfaces [83].

Covalent modification of ND with ester groups (Figure 14.7A) was demonstrated in Ref. [33]. Hydrophobic NDs, readily forming suspensions in nonpolar solvents, were synthesized using ODA [84–86] (Figure 14.7B). The aggregate size for DND-ODA particles in chloroform was 28–32 nm [86].

Another DND modification route is their conversion into onion-like graphitic material (onion-like carbon, OLC) at high temperature in an inert atmosphere [87–92]. It was shown that OLC is formed during the annealing of ND [87,93], with intermediate products being represented by particles with a diamond core covered by closed curved graphitic shells (graphite/diamond nanocomposites). Applications of these particles in lubricants will be demonstrated below. Partially graphitized

**FIGURE 14.7**

Esterification of surface hydroxyl groups on detonation diamond can be done by reaction with the respective acid chlorides ($R = \text{alkyl}$) [33] (A) and functionalization of ND with ODA (B).

Source: From Refs. [84–86], with permission.

diamond can be also functionalized [81] similar to DND and different dispersing agents can be, correspondingly, covalently attached.

Among the methods to modify DND for use in lubricant compositions discussed above, DND fluorination and functionalization by CC coupling of the partially graphitized diamond surface using aryl diazonium salts [63] appear to offer the most advantages. Nevertheless, deagglomeration and fractionation are still necessary, as are the above-mentioned methods of stabilization, in particular, steric stabilization.

14.2.2 Preparation of ND colloids in oils

Whatever the purification scheme is, the commercially available powder of DND and its aqueous suspension contain 200 nm particles, which is almost two orders of magnitude larger than the above-mentioned dimension of the ordered diamond crystal lattice of 4–5 nm. The particles in the 200 nm size range constitute most of the commercial product mass. Essentially, until recently the researchers have been dealing not with nanoparticles, but with submicron aggregates with a minimum size of 200–300 nm.

Simple mixing of NDs or detonation soot with the base oil typically fails to yield uniform, stable fine suspensions [94]. The authors suggested reducing the aggregate size by processing the mixture of detonation soot, base oil, and a dispersing agent (vinylsuccimide) in a ball mill for 24 h [95]. The average aggregate size after this treatment was 0.4–10.0 μm , and the suspension was stable for 6 months at a solid fraction 0.5% w/w.

One of the published methods [96] of introducing detonation soot into lubricant oil was realized in a closed-circuit actuated mixer (heated loop with

a pump); the additive was introduced as a suspension in base oil at 2–5% w/w soot concentration and the mixing was conducted at $\sim 100^{\circ}\text{C}$, with subsequent transfer to a sealed tank for cooling. Better results were obtained when the suspension was additionally passed through a mesh filter, magnetic separator, or an ultrasonic homogenizer.

Disintegration of aggregates (either of ND or detonation soot) can be combined with surface modification in the same operation, by processing with a solution of fluorinated oligomer in water, alcohol, or freon [97]. The solvent choice depends on the nature of the oligomer used. Ultrasonic homogenizers were used as a way to intensify the processing.

In Ref. [98], carbon nanopowder suspensions were obtained using ultrasound processing. The peculiar feature of their process was that they used two-step sonication. First, the raw material was sonicated in cleaning-grade alcohol. The solid concentration was 1% w/w. The resultant suspension was dried, yielding powder with aggregate size no larger than 0.5 mm. The second step was to mix the powder with oil, whereupon the mixture was sonicated for 5 min and the aggregates were readily disintegrated. The resulting oil-nanopowder suspension appeared as uniform, nontransparent, viscous liquid. Final nanomaterial content was 0.1% w/w.

A similar method of producing a nanomaterial suspension with simultaneous surface modification with oleic acid was demonstrated in [99]. The authors used a solvent with low surface tension, viscosity, and boiling point (ethanol) to perform modification of DND with oleic acid. The mixture was sonicated (44 kHz) for 4 h and evaporated. The nanoparticles modified by oleic acid exhibit good dispersivity and stability in liquid paraffin.

14.3 Tribological properties and mechanism of action of ND-related additives in oil and greases

In the following sections, we provide details on the performance in lubricants of three major ND-related carbon materials: detonation soot, OLC (containing ND cores), and well-purified ND particles themselves.

14.3.1 Detonation soot

The first report on application of detonation soot in lubricants was published in 1990 [79]. In conventional lubricants (i.e., motor and gear oils, hydraulic fluids), the nanosized detonation soot particles presumably penetrate between the tribosurfaces, forming a film *in situ*, which under boundary lubricating conditions ensures excellent load-carrying and antiwear properties [100]. Claimed benefits include a decrease of the friction coefficient by 20–30% and a reduction of wear by 200% [100–102]. However, evidence has been reported that the effect of detonation soot might be minimal and even negative [103].

Use of detonation soot and ND in oils and lubricants has recently been reviewed by Dolmatov [104] and Zhornik et al. [105]. Table 14.1 (from Ref. [106]) lists the results of testing of several engines with 0.1% detonation soot added to the motor oil. Besides improved (2–6%) fuel economy, the tests demonstrated increased power (4%) and compression (12%). There also was an after-effect, probably as a result of nanoparticles being incorporated into the friction surfaces of the parts.

Nikitin et al. [107] suggested an antifriction additive for motor oil, containing detonation soot, and using a succinimide-type dispersant.

Authors of Ref. [108] suggested a lubricant composition, containing base oil and 0.01–5% detonation soot with size range selected by centrifugation to be one of the following ranges: 10–30, 20–40, 40–80, or 80–120 nm with DND/nondiamond carbon ratios 55:45, 50:50, 35:65, and 25:75, respectively. The composition is manufactured by introducing detonation soot into the base oil followed by mixing, dispersing, and centrifugation with isolation of narrow size ranges of diamond-carbon particles. Table 14.2 summarizes the results of the tests of these compositions, using a four-ball friction tester.

The use of detonation soot as a structural additive in semisolid lubricants was described in Refs. [62,105,109–111]. Tests of lubricants in radial roller bearings [112] have shown that detonation soot addition reduced wear for each of the

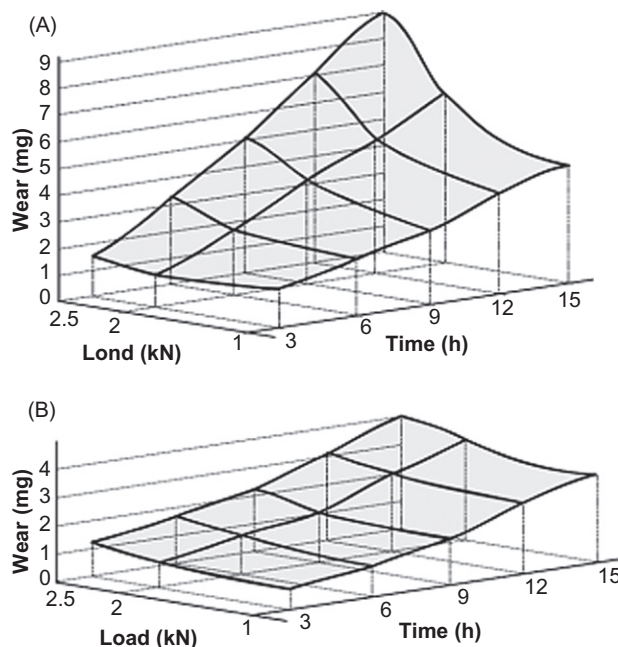
Table 14.1 Engine Test Results for 0.1% Detonation Soot Additive in Motor Oil [106]

Engine	Consumption Reduction (%)		Improvement (%)	
	Gasoline	Oil	Compression	Power
VAZ-2101	6.0	–	12.0	4.4
KamAZ-4310	8.0	14	–	–
Komatsu diesel SA6D-155-4A	2.0	–	–	–
Naval diesel 6NFD48A-2U	5.6	–	–	–

Table 14.2 Test Results for Oil with 0.05% Detonation Soot

Detonation Soot Aggregate Size (nm)	Average Size of Wear Spot (mm)	
	40 kg Load	60 kg Load
80–120	0.395	0.508
40–80	0.367	0.491
20–40	0.317	0.474
10–30	0.305	0.470
Base oil	0.431	0.592

Source: From Ref. [108], with permission.

**FIGURE 14.8**

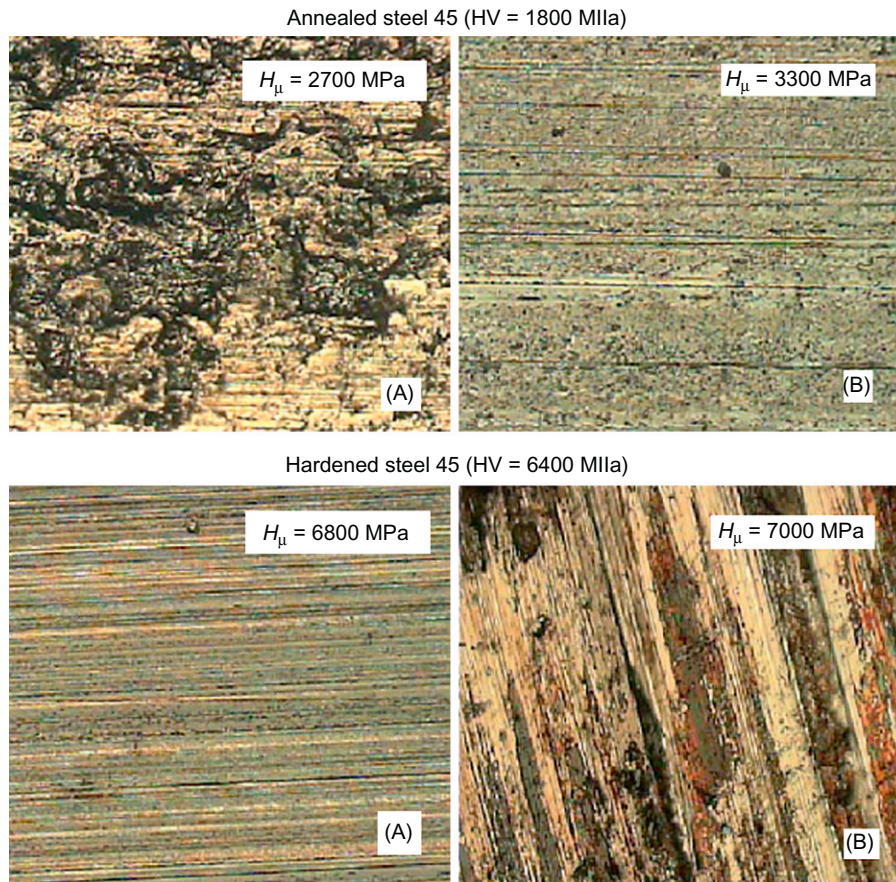
Time course of radial bearing wear for plastic lubricants: (A) TSIATIM-201 and (B) TSIATIM-201+soot (1% w/w, 10nm, 20% DND in soot), 960rpm.

Source: From Ref. [112], with permission.

lubricants studied (lithium grease Litol-24, TSIATIM-201 (similar to US product NLGI-2)) (Figure 14.8). For the semisolid lubricant TSIATIM-201, the bearing wear was reduced by 1.9- to 2.3-fold, for Litol-24 by 1.4- to 1.6-fold.

Road tests of Litol-24 semisolid lubricant were conducted by using it in front wheel bearings of five ZiL-130 trucks and the average distance for the tests was 25,000km. After tests the bearings were visually inspected, and their outer ring wear measured. The wear was shown to be reduced by a factor of 1.5–2 [112]

Analyzing tribological test data, the authors of Refs. [105,113] demonstrated that using detonation soot as a solid additive to semisolid lubricants not only increases critical and welding loads but also affects the wear of the friction surfaces. It has been shown [105] that the grease with the optimal (1.0%) soot additive content has better characteristics (colloidal stability) than the nonmodified grease. The effect strongly depends on the initial hardness of the friction pair materials (Figure 14.9). Modification of Litol-24 lubricant with detonation soot reduces wear of the samples of steel 45 (20–25 HRC) by approximately 30-fold and steel ShKh-15 (35–40 HRC) 5-fold, but for the steel ShKh-15 samples with initial hardness of 62–65 HRC, the wear was actually increased from $I = 7 \cdot 10^{-9}$ to $I = 8 \cdot 10^{-9}$ g/m (Table 14.3).

**FIGURE 14.9**

Microstructure of friction surface after tribotests: (A) Litol-24 and (B) Litol-24+soot; pressure, $P_a = 30 \text{ MPa}$.

Source: From Ref. [105], with permission.

Presumably, increased wear of the friction pairs with an initial hardness ≥ 60 HRC when detonation soot is added to the lubricating medium is due to the processes of local reshaping and brittle degradation of the surface layer with soot particle inclusions, resulting in formation of large agglomerates from the debris, whose presence results in abrasive wear of the friction surfaces.

The authors of Ref. [105] concluded that detonation soot affects the tribosystems in two ways. First, soot changes the structure and properties of a lubricant and increases the carrying capacity of a lubricating film. Second, during friction they facilitate structural transformation of the surface layers of the contacting

Table 14.3 Tribological Characteristics of Formulations Litol-24 with Detonation Soot

Characteristics	The Material of the Friction Pair	Grease	
		Litol-24	Litol-24 + soot
Welding load (N)		1410	1600
Wear rate (l, g/m, 10 ⁻⁷)	Steel 45 (20–25 HRC)	4.04	0.12
	Steel ShKh-15 (35–40 HRC)	0.63	0.12
	Steel ShKh-15 (62–64 HRC)	0.07	0.08

Source: From Ref. [105], with permission.

solids. Such tribomodification results in higher hardness and wear resistance of the friction surface.

14.3.2 Nanodiamond

One of the first works investigating diamond nanoparticles as an oil additive was done by Tao et al. [114]. The authors concluded that under boundary lubricating conditions, the ball-bearing effect of diamond nanoparticles existed between the rubbing surfaces and that the surface polishing and increase in surface hardness due to the presence of diamond nanoparticles were the main reasons for the reduction in wear and friction. Consequent works showed that a lubricant with diamond nanoparticles possessed excellent load-carrying capacity, antiwear, and friction-reduction properties [115,116]. Shen et al. [115] reported that the diamond nanoparticles in base oil exhibited a viscosity-increasing effect and form a thicker film than that in the pure base oil.

The friction and wear behavior at high temperature and high or low load of lubricants containing the ND particles were examined using an SVR multifunctional test system [117]. The friction coefficient of the DND modified by oleic ester was higher than that of the DND modified by a dimer ester and was similar to the nonmodified DND at 500°C. The friction coefficient of the DND-containing lubricant was lower than that of the base oil when the test temperature was below 300°C. It was concluded that DND particles can obviously improve the antiwear and friction-reducing properties of the base oil at high temperature and high load [117].

Reduced friction was observed in a lubricant composition containing less than 0.1 wt% of DND nanoparticles using the Plint-TE77 reciprocating sliding friction tribotester [118]. The mean sliding speed of the specimen was 120 mm/s under the load of 200 N. For the antiwear test, the upper specimen was a chromium-coated steel ball. Two standard oils, an API-SF engine oil (SAE30 LB51153) and a base oil (SAE30 LB51163-11), were used as the test oils. The authors compared DND additives with CuO- and TiO₂-containing additives. Distribution of ND

nanoparticles was not very uniform as compared to CuO and TiO₂, and DND demonstrated the worst friction-reduction behavior, possibly due to large agglomerates of DND used in the work. When CuO and ND were used as additives for the SF oil, the worn scar depths were reduced by 16.7% and 43.3%, respectively, as compared to the SF oil without nanoparticles. The authors speculated that the sphere-like nanoparticles may result in a rolling effect between the rubbing surfaces, and the situation of friction was changed from sliding to rolling [118].

Another group of authors demonstrated that oleic acid-surface-modified diamond and SiO₂ nanoparticles in liquid paraffin provide better tribological properties in terms of load-carrying capacity, antiwear, and friction reduction than pure liquid paraffin [99].

The authors of Ref. [119] investigated the effect of DND additives in a commercial oil for sliding surfaces made from different materials (Figure 14.10). A carbon chromium steel ball was rubbing against various materials such as carbon steels AISI 1045, AISI 1025, and aluminum alloy 6061 in a pin-on-disk tribological test. In the tribological test of an aluminum alloy, the ND particles made the wear tracks of the alloy smoother but the friction and wear were increased. However, for carbon steel pairs, the DND additive reduced the friction force and the wear but made the wear tracks rougher. The carbon content in the steel composition seemed to play a role in the testing results, and wear reduction in the presence of the DND additive took place only under the contact situation of carbon steel pairs [119].

In another publication from the same group [120], the authors investigated the tribological properties of ISO68 standard HN base oil and Mobil 1409 oil for the

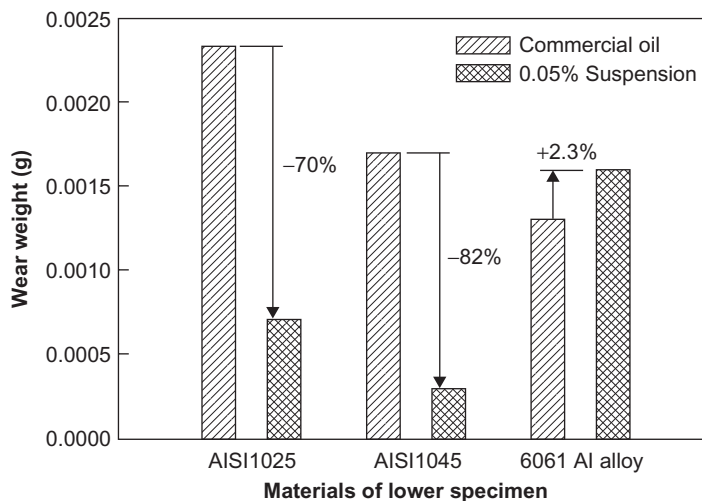


FIGURE 14.10

Wear of various lower specimens tested in the commercial lubricant Mobil 1409 and same with 0.05% ND-containing additive, respectively [119].

same carbon steels and aluminum alloy substrates. Mobil 1409 has the same base stock as ISO68 oil, but also contains some other additives, like EP, AW additives, and others. For carbon steels, AISI 1025 and 1045, the best concentration of DND was 0.05 g/l, while for aluminum alloy the value was 0.10 g/l. The tribological behavior of all substrates was improved. However, their wear mechanisms were different. For the carbon steels, the lubricant's antiwear capability was improved by a mechanism characterized not only by the increased viscosity of the ND suspensions but also by the significant enhancement of the contact surface's toughness possibly due to the embedded NDs from the suspension. For the aluminum alloy, the wear mechanism was dominated mainly by the viscosity of the ND suspension [120].

The authors of Ref. [121] studied the effect of modified DND on tribological properties of industrial oil I-20 and motor oil 10W-40. Steel-steel surfaces with a load range 5.5–58 kg and steel-Babbitt surfaces under constant load 5.5 kg were investigated. Formation of a protecting layer containing DND between friction surfaces was observed resulting in increased wear resistance of the samples.

The authors of Ref. [74] demonstrated that addition of the ND particles into commercial oil CPC R68 resulted in an improvement of antiscuffing performance in the oil samples in a block-on-ring test. The number of scuffing events was reduced after adding the ND particles in the oil with most pronounced effect seen when 2–3 vol.% of the ND was added in the base oil. In a consequent work [74], the same authors demonstrated that the scuffing reduction was due to an increase of the surface hardness under heavy loads when DND was added. The increase in the surface hardness can be attributed to the work hardening effect of DND particles on the rubbing surfaces. Since the addition of ND particles can not only increase the surface hardness during the block-on-ring wear tests, but also reduce the friction power [122], it shows the benefit of using DND to resist scuffing.

Significant reduction of friction coefficient and improvement in fuel economy when using ND additives were demonstrated in several patents by Nakagawa [64,69,123]. The lubricant composition included PAO as a base oil additional constituents: 1% of GMO (glycerin monooleate); 0.01% of diamond nanoparticles having an average primary particle size of 5 nm; and 1% of a nonionic surfactant serving as a dispersant for the diamond nanoparticles and consisting of 5% of polyoxyethylene alkyl ether, and 95% of polyoxyethylene alkyl ether phosphate.

14.3.3 Synergistic lubricating effect of ND with colloid dispersions of solid particles additives

One of the promising ways of using nanomodifiers in lubricating compositions is the utilization of nanoparticles as carriers of functional additives. The synergistic effect of using both NDs and S-, P-containing additives in oils was first demonstrated in Ref. [124].

The authors of Refs. [110,111] demonstrated an example of using detonation soot as a carrier of antiwear fluoropolymers. The functional fluorinated oligomers had the general formulae R^F-R_X , where R^F is the fluorinated radical and R_X is

the terminal functional group (OH, NH₂, COOH, CF₃) [111]. The authors hypothesized that the active additives, introduced into oil, cluster around the soot particles. During frictional interaction, the clusters migrate into the close contact zone. Thus, nanoparticles serve as carriers of active additives, facilitating their transport into the zone. Thereby the activity in the surface layers increases [26,125].

The tribological properties of lubricating compositions based on I-12A oil with DND and PTFE additives were considered in [50,126]. The friction for DND-containing samples (0.026–0.104%) increased by the factor of 1.5–3.5 as compared to low friction synergistic compositions including both DND and PTFE (Figure 14.11), while the friction momentum changed in a manner suggesting formation, under conditions of boundary friction, of a wear-resistant coating—presumably including the nanoparticles.

More recently, authors of Ref. [51] reported synergistic effects of DND on the frictional characteristics of PTFE (MP1100) and Cu-nanoparticle. The best properties were observed for compositions DND-PTFE@Cu and PTFE-DND@Cu in PAO (PTFE additives (Zonyl MP1100)).

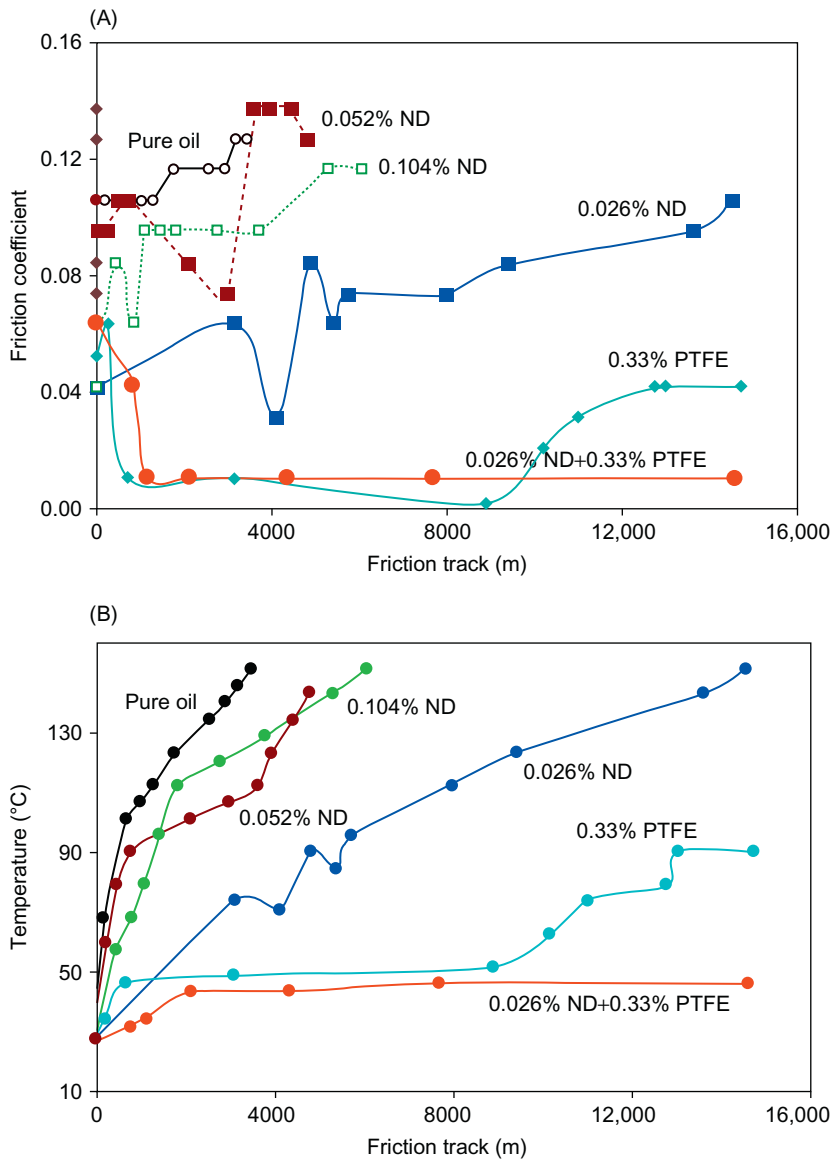
Lubricant composition for high-load friction pairs based on molybdenum disulfide paste with ND additive is described in a Byelorussian patent [61]. Testing has shown that the suggested composition retains high lubricity even at high temperatures, when the efficiency of molybdenum disulfide alone begins to deteriorate. ND additives improve wear resistance through increasing the hardness of contact surfaces, as well as reducing friction through a reduction of surface roughness and partial replacement of sliding friction with rolling friction.

A synergistic effect in a plastic lubricant with various viscosity enhancers and addition of ND, low-MW PTFE, and MoS₂ was shown in the patent given in Ref. [127]. It was demonstrated that the suggested composition had improved antifric-tion and antiscoring properties.

14.3.4 ND-derived carbon onions

ND particles are often used as precursors to carbon onions' synthesis [128] by annealing ND inside a vacuum chamber. Depending on the annealing temperature, synthesized carbon onions have different structures [128]. After annealing at 1600°C, round-shaped carbon onions are formed but they contain a residual diamond core. After annealing at 2000°C, the diamond core disappears but carbon onions become faceted.

Hirata et al. studied the tribological properties of carbon onions used as a solid lubricant between a steel ball and a silicon wafer [129]. Wear observed with carbon onions was lower than that observed with graphite. Low friction coefficients were measured. Hirata also studied the influence of the size of carbon onions as compared to the roughness of the friction surfaces and concluded that carbon onions are effective when their diameter is larger than the surface roughness. Carbon onions formed a layer between two surfaces involving low friction and low wear.

**FIGURE 14.11**

Coefficient of friction (A) and temperature (B) of mineral oil (I-12A) composition with various amounts of ND and PTFE obtained by ring-on-ring technique. Load is 120N, rpm 1000 [50].

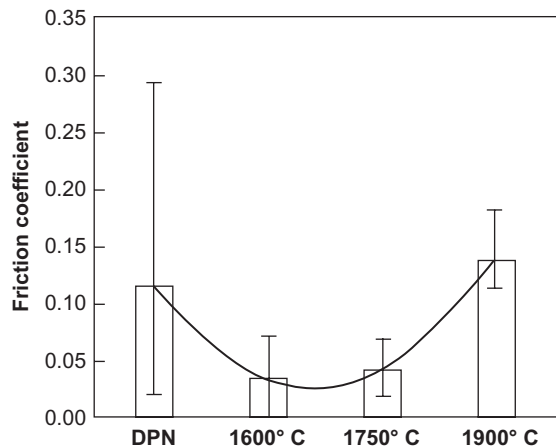
Addition of carbon onions in Krytox 143B, a perfluorinated polyether (PFPE) oil, resulted in a strong reduction of the friction coefficient (0.05 versus 0.13 without carbon onions) with a long lifetime of the oil [130].

Significant improvement in the oil lifetime can be attributed to an ability of carbon onions to serve as a “back-up” lubricant. Interesting results were observed with carbon onions tested in PAO base oil. Matsumoto et al. [131] studied the tribological properties of 0.1 wt% of OLC in PAO for the AISI 52100 steel surfaces. Tribological properties were tested at four different contact pressures by changing the load on the ball or the ball diameter. An AISI 52100 ball with a diameter of 6 mm was used to obtain the Hertzian pressure of 0.83, 1.12, and 1.42 GPa. atomic force microscope (AFM) and scanning tunneling microscopy (STM) revealed the characteristic structure of a low friction film (with friction coefficient (COF) as low as 0.07) formed from the OLC particles.

Joly-Pottuz et al. [27] studied NDs annealed at 1600°C, so that round-shaped carbon onions were formed but they contain a residual diamond core. Another sample was prepared by annealing at 2000°C, where the diamond core disappeared but carbon onions become faceted. Tribological tests were performed at four contact pressures with the two carbon onion samples with/without a diamond core. Comparison of the tribological properties of the two samples at 0.1 wt% of carbon onions in PAO oil indicated similar friction-reducing properties but the sample without ND core presented better antiwear properties. The presence of a diamond core inside the carbon onion was found to be detrimental for the antiwear properties of carbon onions. The presence of this core possibly leads to poor elastic properties of the nanoparticles [27]. It was concluded that a low concentration of onions is sufficient to obtain interesting antiwear properties. These results confirmed the formation of a carbon film with PAO reinforced by the presence of carbon additives. The nano-onions can replace the degraded oil as a lubricant, forming a graphitic material.

Joly-Pottuz et al. [132] also studied carbon nano-onions in comparison with graphite powder as additives in synthetic base oil. Carbon nano-onions and graphite powder were dispersed at 0.1 wt% in a PAO synthetic base oil, using an ultrasonic bath. A pin-on-flat tribometer with both surfaces made of AISI 52100 steel was used for the tribological tests. Measurements were performed in humid ambient air (30–35 RH) and at room temperature (25°C) with a sliding velocity of 2.5 mm/s. Different contact pressures were used to test the lubricant properties: 0.83, 1.12 and 1.42 GPa (corresponding to normal loads of 2, 5, and 10 N, respectively). Carbon nano-onions present better tribological properties than graphite powder when used as lubricant additives in PAO base oil for steel surfaces (specifically antiwear efficiency).

The authors of Ref. [128] performed molecular dynamics simulations of carbon onions placed between sliding diamond-like carbon surfaces at high contact pressure. The results of the simulations demonstrated that the carbon onions were not destroyed in the tribofilm, indicating that the lubrication mechanism of carbon onions in oil may be caused by another reason than formation of graphene sheets. The lubricity of carbon onions at low pressure was principally based on the

**FIGURE 14.12**

Friction properties of COs synthesized at different temperatures.

Source: Modified from Ref. [128].

rolling–sliding of the nanoparticle, as was initially envisaged for this kind of spherical nanoparticle. The authors of Ref. [128] also performed tribological experiments using a pin-on-flat tribometer with both surfaces made of AISI 52100 bearing steel. Carbon onions were added at a concentration of 0.1 wt% to PAO base oil. The addition of carbon onions to PAO resulted in a strong reduction of both friction and wear under boundary lubrication (Figure 14.12).

14.3.5 Mechanism of action of ND particles

The mechanism of action for nanoparticulate lubricant additives in friction is not yet comprehensively understood.

Several mechanisms by which dispersed nanoparticles in lubricants result in lower friction and wear are contemplated in the literature. These mechanisms include (i) formation of a solid lubricant film from nanoparticles under the contact pressure [132,133], (ii) rolling of spherical nanoparticles in the contact zone [134], (iii) reducing asperity contact by filling the valleys of contacting surfaces [135], and (iv) shearing of trapped nanoparticles at the interface without the formation of an adhered film [136]. These mechanisms are especially relevant to mixed and boundary lubrication (Figure 14.13).

Tao et al. [114] suggested for ND particles a “ball-bearing” effect that reduced the wear and friction of steel surfaces contact. The authors also discussed two possibilities that may increase the surface hardness [114]. One is that the particles were pressed and embedded into the rubbing surfaces resulting in dispersion hardening, while the other includes the increased surface hardness due to the surface polishing by the particles leading to densification of the surface.

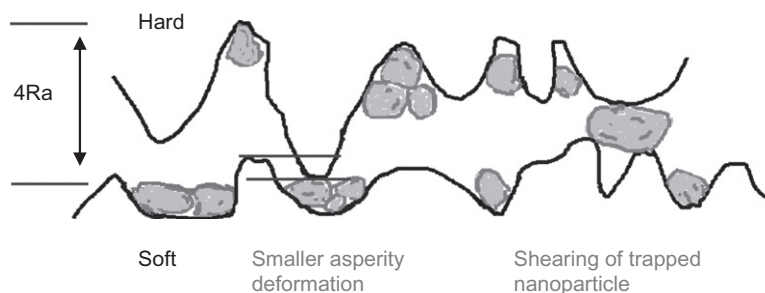
**FIGURE 14.13**

Illustration of two (iii and iv) mechanisms by which nanoparticles affect friction and wear.

Source: Modified from Ref. [137].

Vityaz et al. [25] have suggested an ant-pitting mechanism of action for ND-containing soot whereby during friction of parts made of relatively soft and yielding material the hard nanoparticles, after their release from the structural lattice of the dispersion, are incorporated into the surfaces during friction—with the resultant formation of a dispersion-hardened surface layer, preventing the growth of large fatigue cracks and leading to localized pitting domains instead.

The authors of Ref. [110] suggested that the microabrasive action of nanoparticles leads to formation of a fresh surface with enhanced adsorption activity. That is why the solid-phase ND additives, through their polishing action, activate the surfaces in friction resulting in formation of a more strongly bound adsorbed layers of lubricant. It is probable that in the presence of active antiwear additives, the nanoadditives can provide a synergistic effect of transport and adsorption (chemisorption) of the friction modifier molecule.

A possible mechanism of antiwear action of nanoparticulate additives is formation of stable separation layers on the surfaces during friction, capable of repeated rearrangements without loss of integrity [105,110,125]. It is suggested, in particular, that due to the presence of nanoparticles in the lubricating fluid in the vicinity of the contact, an effective intermediate layer is formed between the parts in friction, which prevents direct contact between the surfaces in the friction pair. This layer is formed by the nanoparticles, which, being deformed under contact pressure and shear forces, gain the ability to alter the surface profile, filling microvoids in the contact zone and thus reducing the contact pressure. The antiwear separation layers formed by nanoparticles have rather good resistance to disintegration under contact pressure and temperature.

It has been established [113] that modification of lubricants with ND additives results in intensification of the work-in processes (mutual adjustment of the starting surfaces), increase of surface microhardness of steel and reduction of wear for initial hardness $HV \geq 5000 \text{ MPa}$ [105]. It has been shown [105] that HM (Hypersonic Electrometallization)-coating of steel Kh18N10T lubricated with the oil modified by soot retain their efficiency under nominal pressures of up to 100 MPa (Table 14.4).

Table 14.4 Microhardness H_μ and Content of Retained Austenite in Surface Layer (Steel Kh18N10T, Oil I-20) [105]

Friction Condition	Microhardness (H_μ , Mpa)	Content of Retained Austenite (vol.%)
Original state	3300	88
$P = 10$ MPa, oil I-20	5000	80
$P = 10$ MPa, oil I-20 + 1% soot	5300	75
$P = 50$ MPa, oil I-20 + 1% soot	5300	60
$P = 100$ MPa, oil I-20 + 1% soot	5500	55

It has been assumed that the nanosized fragmented substructure appears in the surface layer of the coating lubricated with the modified oil in addition to the acceleration of running-in accompanied the $\gamma \rightarrow \alpha$ martensitic transformation.

For hardened steel, due to its low resistance to crack propagation, wear resistance typically deteriorates when friction pairs are lubricated with ND-containing lubricants, and are under heavy contact pressures ($P_a = 20\text{--}30$ MPa).

14.4 Conclusion

Diamond nanoparticles prepared by detonation methods are certainly of great interest as nanolubricants. They demonstrated excellent tribological properties documented by a wide variety of research groups. However, their lubrication mechanism has not yet been completely elucidated. A better understanding of the ND lubrication mechanism will certainly lead to further improved characteristics of the lubricants containing DND. Other carbon nanoparticles, ND-derived carbon onions, also present interesting tribological properties and may find applications as nanolubricants.

Despite doubtless progress in the study of the efficiency of the use of ND as lubricant additive, a number of problems remain to be solved. In particular, it is necessary to outline the conditions when use of DND is beneficial (for example, the hardness properties of the friction surfaces). Further development of new colloiddally stable lubricants based on different classes of oils (petroleum, synthetic, ester-based, etc.) with NDs is required as well as testing of the new compositions. For this purpose, new classes of dispersants should be synthesized, because the aggregation, precipitation, and tribological performance of diamond particles in oils are greatly influenced by their dispersion in the lubricating medium.

Acknowledgments

The authors greatly acknowledge O. Shenderova for the critical reading of the manuscript and helpful comments and A. Shenderova and G. McGuire for the assistance with translation.

References

- [1] J. Zhou, Z. Wu, Z. Zhang, W. Liu, H. Dang, Study on an antiwear and extreme pressure additive of surface coated LaF_3 nanoparticles in liquid paraffin, *Wear* 249 (2001) 333–337.
- [2] E. Fernández Rico, I. Minondoa, D.G. Cuervo, The effectiveness of PTFE nanoparticle powder as an EP additive to mineral base oils, *Wear* 262 (2007) 399–406.
- [3] V.N. Bakunin, G.N. Kuzmina, M. Kasrai, O.P. Parenago, G.M. Bancroft, Tribological behavior and tribofilm composition in lubricated systems containing surface-capped molybdenum sulfide nanoparticles, *Tribol. Lett.* 22 (2006) 289–296.
- [4] H. Chang, Z.Y. Li, M.J. Kao, K.D. Huang, H.M. Wu, Tribological property of TiO_2 nanolubricant on piston and cylinder surfaces, *J. Alloys Compd.* 495 (2010) 481–484.
- [5] Z.S. Hu, J.X. Dong, Study on antiwear and reducing friction additive of nanometer titanium oxide, *Wear* 216 (1998) 92–96.
- [6] Y. Gao, G. Chen, Y. Oli, Z. Zhang, Q. Xuec, Study on tribological properties of oleic acid-modified TiO_2 nanoparticle in water, *Wear* 252 (2002) 454–458.
- [7] G.U. Caixiang, L.I. Qingzhu, G.U. Zhuoming, Z.H.U. Guanyao, Study on application of CeO_2 and CaCO_3 nanoparticles in lubricating oils, *J. Rare Earths* 26 (2008) 163–167.
- [8] S. Chen, W. Liu, L. Yu, Preparation of DDP-coated PbS nanoparticles and investigation of the antiwear ability of the prepared nanoparticles as additive in liquid paraffin, *Wear* 218 (1998) 153–158.
- [9] Z.S. Hu, J.X. Dong, G.X. Chen, J.Z. He, Preparation and tribological properties of nanoparticle lanthanum borate, *Wear* 243 (2000) 43–47.
- [10] Z.S. Hu, J.X. Dong, Study on antiwear and reducing friction additive of nanometer titanium borate, *Wear* 216 (1998) 87–91.
- [11] J.X. Dong, Z.S. Hu, A study of the anti-wear and friction-reducing properties of the lubricant additive, nanometer zinc borate, *Tribol. Int.* 31 (1998) 219–223.
- [12] Z.S. Hu, J.X. Dong, G.X. Chen, Study on antiwear and reducing friction additive of nanometer ferric oxide, *Tribol. Int.* 31 (1998) 355–360.
- [13] S. Qiu, Z. Zhou, J. Dong, G. Chen, Preparation of Ni nanoparticles and evaluation of their tribological performance as potential additives in oils, *J. Tribol.* 123 (2001) 441–443.
- [14] L.K. Hudson, J. Eastoe, P.J. Dowding, Nanotechnology in action: overbased nano detergents as lubricant oil additives, *Adv. Colloid Interface Sci.* 123–126 (2006) 425–431.
- [15] A.H. Battez, R. González, J.L. Viesca, J.E. Fernández, J.M.D. Fernández, A. Machado, et al., CuO , ZrO_2 and ZnO nanoparticles as antiwear additive in oil lubricants, *Wear* 265 (2008) 422–428.
- [16] L. Martin, G.A. Kostjukovich, A. Skaskevich, V.I. Kravchenko, P.A. Vityaz, et al., Methods of creating lubricating materials with nanomodifiers, *J. Friction Wear* 23 (2002) 411–424.
- [17] M. Martin, N. Ohmae, *Nanolubricants*, John Wiley & Sons, 2008, p. 231.
- [18] M.S. Rakow, Petroleum oil refining, (2003), in: G.E. Totten, S.R. Westbrook, R.J. Shah (Eds.), *Fuels and Lubricants Handbook: Technology, Properties, Performance, and Testing*, ASTM Intl., pp. 3–30.
- [19] S.C. Tung, M.L. McMillan, E.P. Becker, S.E. Schwartz, *Handbook of Lubrication and Tribology*, Taylor Francis Group, 2006.
- [20] K. Ferrick, ILSAC/Oil Committee Meeting, Attachment 1, Energy API, 2010.

- [21] D.M. Dresselhuys, H.J. Klok, M.A. Cohen Stuart, R.J. de Vries, G.A. van Aken, E.H.A. de Hoog, *Food Biophys.* 4 (2007) 158–171.
- [22] J.M. Coles, D.P. Chang, S. Zauscher, Molecular mechanisms of aqueous boundary lubrication by mucinous glycoproteins, *Curr. Opin. Colloid Interface Sci.* 15 (2010) 406–416.
- [23] S.C. Tung, M.L. McMillan, Automotive tribology overview of current advances and challenges for the future, *Tribol. Int.* 37 (2004) 517–536.
- [24] R.I. Taylor, Engine friction lubricant sensitivities: a comparison of modern diesel and gasoline engines, *Tribotest* 7 (2000) 37–43.
- [25] P.A. Vityaz, V.I. Zhornik, V.A. Kukareko, A.V. Ivanihnik, et al., Improvement of tribo-technical materials' properties by their modification with nanometer-sized solid components, *Trans. Nat. Acad. Sci. Belarus. Phys. Technical. Ser.* 4 (2008) 45–49.
- [26] V.A. Struk, V.I. Kravchenko, *New Resource-Efficient Technologies and Composite Materials*, Energoatomizdat Publisher House, Moscow, 2004.
- [27] L. Joly-Pottuza, N. Matsumoto, H. Kinoshita, B. Vacher, M. Belin, G. Montagna, et al., Diamond-derived carbon onions as lubricant additives, *Tribol. Int.* 41 (2008) 69–78.
- [28] A.M. Schrand, S.A.C. Hens, O.A. Shenderova, Nanodiamond particles: properties and perspectives for bioapplications, *Solid State Mater. Sci.* 34 (2009) 18–74.
- [29] A. Krüger, The structure and reactivity of nanoscale diamond, *J. Mater. Chem.* 18 (2008) 1485–1492.
- [30] A. Krüger, F. Kataoka, M. Ozawa, T. Fujinoc, Y. Suzuki, A.E. Aleksenskii, et al., Unusually tight aggregation in detonation nanodiamond: identification and disintegration, *Carbon* 43 (2005) 1722–1730.
- [31] E. Osawa, Recent progress and perspectives in single-digit nanodiamond, *Diamond Relat. Mater.* 16 (2007) 2018–2022.
- [32] E. Osawa, Monodisperse single nanodiamond particulates, *Pure Appl. Chem.* 80 (2008) 1365–1379.
- [33] Y. Liang, M. Ozawa, A. Krüger, A general procedure to functionalize agglomerating nanoparticles demonstrated on nanodiamond, *ACS Nano* 3 (2009) 2288–2296.
- [34] A. Pentecost, S. Gour, V. Mochalin, I. Knoke, Y. Gogotsi, Deaggregation of nanodiamond powders using salt- and sugar-assisted milling, *Appl. Mater. Interface* 2 (2010) 3289–3294.
- [35] K. Xu, Q.J. Xue, Deaggregation of ultradispersed diamond from explosive detonation by a graphitization-oxidation method and by hydriodic acid treatment, *Diamond Relat. Mater.* 16 (2007) 277–282.
- [36] X.Y. Xu, Z.M. Yu, Y.W. Zhu, B.C. Wang, Influence of surface modification adopting thermal treatments on dispersion of detonation nanodiamond, *J. Solid State Chem.* 178 (2005) 688–693.
- [37] Xu Kang, Xue Qunji, A new method for deaggregation of nanodiamond from explosive detonation: graphitization–oxidation method, *Phys. Solid State* 46 (2004) 649–650.
- [38] O.A. Williams, J. Hees, C. Dieker, W. Jäger, L. Kirste, C.E. Nebel, Size-dependent reactivity of diamond nanoparticles, *ACS Nano* 4 (2011) 4824–4830.
- [39] S.J. Stavrev, Carbon-containing nanoparticle and method of its production, RU Patent 2004586 (2011).
- [40] I. Larionova, V. Kuznetsov, A. Frolov, O. Shenderova, S. Moseenkov, Mazov, Properties of individual fractions of detonation nanodiamond, *Diamond Relat. Mater.* 15 (2006) 1804–1808.

- [41] O. Shenderova, I. Petrov, J. Walsh, V. Grichko, T. Tyler, G. Cunningham, Modification of detonation nanodiamonds by heat treatment in air, *Diamond Relat. Mater.* 15 (2006) 1799–1803.
- [42] S.I. Chukhaeva, P. Detkov, A. Tkachenko, A. Toropov, Physicochemical properties of fractions isolated from ultradispersed diamonds, *Sverktverd. Mater.* 4 (1998) 29–36.
- [43] S.I. Chukhaeva, Synthesis, properties, and applications of fractionated nanodiamonds, *Phys. Solid State* 46 (2004) 625–628.
- [44] Y. Morita, T. Takimoto, H. Yamanaka, K. Kumekawa, S. Morino, S. Aonuma, et al., A facile and scalable process for size-controllable separation of nanodiamond particles as small as 4 nm, *Small* 4 (2008) 2154–2157.
- [45] I. Petrov, O. Shenderova, V. Grishko, T. Tyler, G. Cunningham, G. McGuire, Detonation nanodiamonds simultaneously purified and modified by gas treatment, *Diamond Relat. Mater.* 16 (2007) 2098–2113.
- [46] G. Cunningham, A.M. Panich, A.I. Shames, I. Petrov, O. Shenderova, Ozone-modified detonation nanodiamonds, *Diamond Relat. Mater.* 17 (2008) 650–654.
- [47] N. Gibson, O. Shenderova, T.J.M. Luo, S. Moseenkov, V. Bondar, A. Puzyr, et al., Colloidal stability of modified nanodiamond particles, *Diamond Relat. Mater.* 18 (2009) 620–626.
- [48] G.A. Chiganova, Aggregation of particles in ultradispersed diamond hydrosols, *Colloid J.* 62 (2000) 238–243.
- [49] A. Krüger, Diamond nanoparticles, jewels for chemistry and physics, *Adv. Mater.* 20 (2008) 2445–2449.
- [50] M.G. Ivanov, V.V. Kharlamov, V.M. Buznik, D.M. Ivanov, S.V. Pavlyshko, A.K. Tsvetkov, Tribological properties of the grease containing polytetrafluoroethylene and ultrafine diamond, *J. Friction Wear* 25 (2004) 99–103.
- [51] M.G. Ivanov, S.V. Pavlyshko, D.M. Ivanov, I. Petrov, O. Shenderova, Synergistic compositions of colloidal nanodiamond as lubricant-additive, *J. Vac. Sci. Technol. B* 28 (2010) 869–877.
- [52] S. Tatsul, R. Richard, *Stabilization of Colloidal Dispersion by Polymer Adsorption*, Marcel Dekker, New York, NY, 1980.
- [53] E. Ōsawa, D. Hob, H. Huang, M.V. Korobov, N.N. Rozhkova, Consequences of strong and diverse electrostatic potential fields on the surface of detonation nanodiamond particles, *Diamond Relat. Mater.* 18 (2009) 904–909.
- [54] X. Xu, Z. Yu, Y. Zhu, B. Wang, Effect of sodium oleate adsorption on the colloidal stability and zeta potential of detonation synthesized diamond particles in aqueous solutions, *Diamond Relat. Mater.* 14 (2005) 206–212.
- [55] A.P. Puzyr, V.S. Bondar, Method of production of nanodiamonds of explosive synthesis with an increased colloidal stability, RU Patent 2252192 (2003).
- [56] V.S. Bondar, A.P. Puzyr, Nanodiamonds for biological investigations, *Phys. Solid State* 46 (2004) 716–719.
- [57] A.P. Puzyr, V.S. Bondar, Nano-size diamond treatment method, RU Patent 2258671 (2005).
- [58] C.-C. Li, C.-L. Huang, Preparation of clear colloidal solutions of detonation nanodiamond inorganic solvents, *Colloids Surf. A Physicochem. Eng. Aspects* 353 (2010) 52–56.
- [59] V. Pichot, K. Bonnot, N. Piazzon, M. Schaefer, M. Comet, D. Spitzer, Deposition of detonation nanodiamonds by Langmuir–Blodgett technique, *Diamond Relat. Mater.* 19 (2010) 479–483.
- [60] U. Maitra, A. Gomathi, C.N.R. Rao, Covalent and noncovalent functionalisation and solubilisation of nanodiamond, *J. Exp. Nanosci.* 3 (2008) 271–278.

- [61] P.A. Vityaz, V.I. Zhornik, V.A. Vereschagin, N.E. Gilchin, Lubricant composition for high-gravity loaded friction units, BY Patent 5906 (2004).
- [62] Y. Zhu, X. Xu, B. Wang, Z. Feng, Surface modification and dispersion of nanodiamond in clean oil, *China Particuology* 2 (2004) 132–134.
- [63] X.Y. Xu, Z.M. Yu, Y.W. Zhu, B. Wan, Dispersion and stability of nanodiamond in clean oil, *Wang Mater. Sci. Forum* 471–472 (2004) 779–783.
- [64] A. Nakagawa, Nanoparticle-containing lubricating oil composition, EP Patent 1980609 (2006).
- [65] G. Cholakov, N. Georgiev, Chr. Ivanova, K. Stanulov, Stability of ultradisperse diamond powder in oil suspensions, *J. Univ. Chem. Technol. Metall.* 40 (2005) 299–306.
- [66] S. Osswald, G. Yushin, V. Mochalin, S.O. Kucheyev, Y. Gogotsi, Control of sp(2)/sp(3) carbon ratio and surface chemistry of nanodiamond powders by selective oxidation in air, *J. Am. Chem. Soc.* 128 (2006) 11635–11642.
- [67] I.A. Apolonskaya, A.V. Tyurnina, P.G. Kopylov, A.N. Obratsov, Thermal oxidation of detonation nanodiamond, *Mosc. Univ. Phys. Bull.* 64 (2009) 433–436.
- [68] S. Osswald, M. Havel, V. Mochalin, G. Yushin, Increase of nanodiamond crystal size by selective oxidation, *Diamond Relat. Mater.* 17 (2008) 1122–1126.
- [69] A. Nakagawa, Y. Mabuchi, Lubricant composition comprising a diamond nanoparticle, EP Patent 1953214 (2008).
- [70] A. Krüger, Y. Liang, G. Jarre, J. Stegk, Surface functionalisation of detonation diamond suitable for biological applications, *J. Mater. Chem.* 16 (2006) 2322–2328.
- [71] L.M. Yung, Nanodiamond compounds synthesized by surface functionalization, US Patent 2010298600 (2010).
- [72] S.K. Gordeev, S.B. Korchagina, Method for preparing powder nanodiamond for producing stable suspension, RU Patent 2302994 (2006).
- [73] K.D. Behler, A. Stravato, V. Mochalin, G. Korneva, G. Yushin, Y. Gogotsi, Nanodiamond-polymer composite fibers and coatings, *ACS Nano* 3 (2010) 363–369.
- [74] V.N. Khabashesku, Y. Liu, N.J. Halas, Fluorinated nanodiamond as a precursor for solid substrate surface coating using wet chemistry, US Patent 7,858,186 (2010).
- [75] T. Nakamura, M. Hasegawa, K. Tsugawa, T. Ohana, M. Ishihara, Y. Koga, Photochemical modification of nanodiamond films with perfluorooctyl functionalities, *Diamond Relat. Mater.* 15 (2006) 678–681.
- [76] V.N. Khabashesku, J.L. Margrave, E.V. Barrera, Functionalized carbon nanotubes and nanodiamonds for engineering and biomedical applications, *Diamond Relat. Mater.* 14 (2005) 859–866.
- [77] Y. Liu, Z. Gu, J.L. Margrave, V.N. Khabashesku, Functionalization of nanoscale diamond powder: fluoro-, alkyl-, amino-, and amino acid-nanodiamond derivatives, *Chem. Mater.* 16 (2004) 3924–3930.
- [78] V.N. Khabashesku, Y. Liu, J.L. Margrave, M.M. Lou, Functionalization of nanodiamond powder through fluorination and subsequent derivatization reactions, US Patent 7,820,130 (2010).
- [79] B.V. Spitsyn, J.L. Davidson, M.N. Gradoboev, T.B. Galushko, N.V. Serebryakova, T.A. Karpukhina, et al., Inroad to modification of detonation nanodiamond, *Diamond Relat. Mater.* 15 (2006) 296–299.
- [80] Y. Liu, G. Zhenning, J.L. Margrave, et al., Functionalization of nanoscale diamond powder: fluoro-, alkyl-, amino-, and amino acid-nanodiamond derivatives, *Chem. Mater.* 16 (2004) 3925–3930.

- [81] Y. Liang, T. Meinhardt, G. Jarre, M. Ozawa, P. Vrdoljak, A. Schöll, et al., Deagglomeration and surface modification of thermally annealed nanoscale diamond, *J. Colloid Interface Sci.* 354 (2011) 23–30.
- [82] T. Nakamura, M. Hasegawa, K. Tsugawa, T. Ohana, M. Ishihara, Y. Koga, Photochemical modification of nanodiamond films with perfluorooctyl functionalities, *Diamond Relat. Mater.* 15 (2006) 678–681.
- [83] O.A. Williams, J. Hees, C. Dieker, W. Jäger, L. Kirste, E. Christoph, et al., Size-dependent reactivity of diamond nanoparticles, *ACS Nano* 4 (2010) 4824–4830.
- [84] V.N. Mochalin, Y. Gogotsi, Wet chemistry route to hydrophobic blue fluorescent nanodiamond, *J. Am. Chem. Soc.* 131 (2009) 4594–4595.
- [85] V. Mochalin, Y. Gogotsi, G. Yushin, K. Behler, J. Detweiler, A. Gurga, Nanodiamond composition and methods of making and using thereof, CA Patent 2692017 (2009).
- [86] Q. Zhang, V.N. Mochalin, I. Neitzeld, Q. Zhang, V. Mochalin, I. Neitzel, et al., Fluorescent PLLA-nanodiamond composites for bone tissue engineering, *Biomaterials* 32 (2011) 87–94.
- [87] V.L. Kuznetsov, A.L. Chuvilin, Y.V. Butenko, I.Y. Mal'kov, V.M. Titov, Onion-like carbon from ultra-disperse diamond, *Chem. Phys. Lett.* 222 (1994) 343–348.
- [88] V.V. Roddatis, V.L. Kuznetsov, Y.V. Butenko, D.S. Sua, R. Schlögl, Transformation of diamond nanoparticles into carbon onions under electron irradiation, *Phys. Chem. Chem. Phys.* 4 (2002) 1964–1967.
- [89] S. Tomita, M. Fujii, S. Hayashi, K. Yamamoto, Electron energy-loss spectroscopy of carbon onions, *Chem. Phys. Lett.* 305 (1999) 225–229.
- [90] H. Mori, E. Taguchi, H. Yasuda, H. Kinoshita, N. Ohmae, Transformation of diamond nanoparticles into onion-like carbon by electron irradiation studied directly inside an ultra-high vacuum transmission electron microscope, *Appl. Phys. Lett.* 86 (2005) 223101.
- [91] V.L. Kuznetsov, Y.V. Butenko, D.M. Gruen, O.A. Shenderova, A.Y. Vul, Synthesis, properties and applications of ultrananocrystalline diamond, *NATO Sci. Ser.* 192 (2005) 199–216.
- [92] S. Tomita, A. Burian, J.C. Dore, D. LeBolloch, M. Fujii, S. Hayashi, Diamond nanoparticles to carbon onions transformation: x-ray diffraction studies, *Carbon* 40 (9) (2002) 1469–1474.
- [93] V.L. Kuznetsov, A.L. Chuvilin, E.M. Moroz, V.N. Kolomiichuk, S.K. Shaikhutdinov, Y.V. Butenko, Effect of explosions on the structure of detonation soots: ultradisperse diamond and onion carbon, *Carbon* 32 (1994) 873–882.
- [94] V.Y. Dolmatov, *Ultradisperse Diamonds of Detonation Synthesis*, Polytechnical University, St. Petersburg, 2003, p. 344.
- [95] F.Z. Badaev, Y.N. Privalko, T.M. Gubarevich, A.I. Shebalin, O.A. Besedina, Method of preparation of carbonaceous suspension in oil, USSR Patent 1658641 (1987).
- [96] V.S. Prochorov, V.A. Yatsenko, Y.F. Hoonis, Method of preparation of lubricating oil, RU Patent 2004586 (1993).
- [97] V.A. Struk, G.A. Kostjukovich, L. Martin, V.I. Kravchenko, A. Ckaskevich, C.V. Avdejchik, et al., Lubricant composition, RU Patent 2248389 (2004).
- [98] N.K. Tolochko, S.E. Mozharov, P.G. Stanovoy, Y.A. Shieniyk, Tribological properties of liquid lubricants with carbon nanoparticle additives, in: *Transactions of International Conference on Science and Applications*, Baranovich State University Publishing, Baranovich, 2007, p. 366.

- [99] D.X. Peng, Y. Kang, R.M. Hwang, S.S. Shyr, Y.P. Chang, Tribological properties of diamond and SiO₂ nanoparticles added in paraffin, *Tribol. Int.* 42 (2009) 911–917.
- [100] M. Shen, J. Luo, S. Wena, The tribological properties of oils added with diamond nano-particles, *Tribol. Trans.* 44 (2001) 494–498.
- [101] V.E. Red'kin, Lubricants with ultradisperse diamond-graphite powder, *Chem. Technol. Fuels Oils* 40 (2004) 164–179.
- [102] Q. Yu-lin, X. Biag-shi, M. Shi-nin, JIN Xian-shi, The tribological properties of the composite additive containing nanometer diamond, *Petroleum Process. Petrochem.* 30 (1999) 12–15.
- [103] T. Xu, X. Tao, Z. Jiazheng, Study on the tribological properties of ultradispersed diamond containing soot as an oil additive, *Tribol. Trans.* 40 (1997) 178–182.
- [104] V.Yu. Dolmatov, Detonation nanodiamonds in oils and lubricants, *J. Superhard Mater.* 32 (2010) 14–20.
- [105] V.I. Zhornik, V.A. Kukareko, M.A. Belotserkovsky, Tribomechanical modification of friction surface by running-in in lubricants with nano-sized diamonds, Nova Science Publishers, Hauppauge, NY, 2011.
- [106] V.F. Komarov, G.V. Sakovich, Nanometer-sized diamond-containing carbon for automotive industry, *Chem. Sustain. Develop.* 13 (2005) 847–850.
- [107] E.V. Nikitin, A.V. Korytnikov, S.Y. Shiusarev, E.V. Filipova, A.I. Danilov, Y.A. Skryabin, Antifricition additive, RU Patent 2054456 (1996).
- [108] V.N. Beljaev, I.S. Larionova, N.M. Kutakova, L.I. Poleva, Lubricant composition and method of preparing said composition, RU Patent 2417252 (2011).
- [109] P.A. Vityaz, V.I. Zhornik, V.A. Kukareko, A.S. Kalinichenko, N.E. Gilnich, The effect of the friction couple material on the triboengineering features of the consistent grease modified with ultradispersed diamonds, *J. Friction Wear* 21 (2000) 527–533.
- [110] Ljuty Martin, A.A. Skaskevich, V.A. Struk, G.A. Kostjukovich, Lubricants with nanomodifiers, *J. Yanko Kupala Grodno State Univ.* 2 (2003) 84–92.
- [111] V.A. Struk, L. Martin, G.A. Kostjukovich, V.I. Kravchenko, A.A. Skaskevich, A.S. Valentinovich, et.al., Lubricant composition, RU Patent 2248389 (2003).
- [112] S.G. Dokshanin, R.S. Privalihin, Application of grease with ultradisiperible component in rolling bearings, *J. Samara Res. Ctr. Russ. Acad. Sci.* 12 (2010) 342–345.
- [113] P.A. Vityaz, V.I. Zhornik, V.A. Kukareko, Tribomodification of friction surfaces by rubbing in nanodiamond-containing lubricating medium, II, in: *International Scientific Conference of Nanostructured Materials*, 2010, p. 536.
- [114] X. Tao, Z. Jiazheng, X. Kang., The ball-bearing effect of diamond nanoparticles as an oil additive, *J. Phys. D Appl. Phys.* 29 (1996) 2932–2937.
- [115] M. Shen, J. Luo, S. Wen, The tribological properties of oils added with diamond nano-particles, *Tribol. Trans.* 44 (2001) 494–498.
- [116] J.X. Zhang, K. Liu, X.G. Hu, Effect of ultra-dispersed diamond nanoparticles as additive on the tribological properties of 15W30 engine oil, *Tribology* 22 (2002) 44–48.
- [117] Q. Yu-lin, S. Xiao-feng, X. Bin-shi, M. Shi-ning, High temperature tribological behaviors of nano-diamond as oil additive, *J. Cent. South. Univ. Technol.* 12 (2005) 181–185.
- [118] Y.Y. Wu, W.C. Tsui, T.C. Liu, Experimental analysis of tribological properties of lubricating oils with nanoparticle additives, *Wear* 262 (2007) 819–825.
- [119] C.C. Chou, S.H. Lee, Rheological behavior and tribological performance of a nanodiamond-dispersed lubricant, *J. Mater. Process. Technol.* 201 (2008) 542–547.

- [120] C.-C. Chou, Lee S.-H., Tribological behavior of nanodiamond-dispersed lubricants on carbon steels and aluminum alloy, *Wear* 269 (2010) 757–762.
- [121] A.P. Puzyr, G.E. Selyutin, V.B. Vorobyov, E.N. Fedorova, K.V. Purtov, V.A. Voroshilov, et al., Prospects of applying detonation nanodiamonds with improved colloidal stability for technical sciences, *Nanotechnika* 8 (2006) 96–106.
- [122] H.Y. Chu, W.C. Hsu, J.F. Lin, The anti-scuffing performance of diamond nanoparticles as an oil additive, *Wear* 268 (2010) 960–967.
- [123] A. Nakagawa, Y. Mabuchi, Lubricant composition comprising a diamond nanoparticle, EP Patent 1953214 (2008).
- [124] Qiao Yu-lin, X.U. Bing-shi, M.A. Shi-nin, The tribological properties of the composite additive containing nanomer diamond, *Petroleum Process. Petrochem.* 30 (3) (1999) 12–15.
- [125] P.A. Vityaz, V.I. Zhornik, V.A. Kukareko, A.I. Kamko, Formation of wear resistant surface structure and their mechanism in friction with lubricant modified ultradispersible diamond-graphite additives. Part 2. Damage model, *J. Friction Wear* 27 (2006) 196–200.
- [126] M.G. Ivanov, S.V. Pavlyshko, D.M. Ivanov, I. Petrov, Gary Mc. Guire, O. Shenderova, Nanodiamond particles as additives in lubricants, in: *Materials Research Society Symposium Proceedings*, p. 1203.
- [127] M.G. Ivanov, D.M. Ivanov, Grease, RU Patent RU 2395563 (2010).
- [128] L. Joly-Pottuz, E.W. Bucholz, Friction properties of carbon nano-onions from experiment and computer simulations, *Tribol. Lett.* 37 (2010) 75–81.
- [129] Qiao Yu-lin, X.U. Bing-shi, M.A. Shi-nin, The tribological properties of the composite additive containing nanomer diamond, *Petroleum Process. Petrochem.* 30 (3) (1999) 12–15.
- [130] K.W. Street, M. Marchetti, R.L. Vander Wal, A.J. Tomasek, Evaluation of the tribological behavior of nano-onions in Krytox 143AB, *Tribol. Lett.* 16 (2004) 143–149.
- [131] N. Matsumoto, L. Joly-Pottuz, H. Kinoshita, N. Ohmae, Application of onion-like carbon to micro and nanotribology, *Diamond Relat. Mater.* 16 (2007) 1227–1230.
- [132] L. Joly-Pottuz, B. Vacher, N. Ohmae, J.M. Martin, T. Epicier, Anti-wear and friction reducing mechanisms of carbon nano-onions as lubricant additives, *Tribol. Lett.* 30 (2008) 69–80.
- [133] Z.S. Hu, R. Lai, F. Lou, L.G. Wang, Z.L. Chen, G.X. Chen, et al., Preparation and tribological properties of nanometer magnesium borate as lubricating oil additive, *Wear* 252 (2002) 370–374.
- [134] Z. Xiaodong, F. Xun, S. Huaqiang, H. Zhengshui, Lubricating properties of Cyanex 302-modified MoS₂ microspheres in base oil 500SN, *Lubrication Sci.* 19 (2007) 71–79.
- [135] L. Rapoport, V. Leshchinsky, I. Lapsker, Y. Volovik, O. Nepomnyashchy, M. Lvovsky, et al., Tribological properties of WS₂ nanoparticles under mixed lubrication, *Wear* 255 (2003) 785–793.
- [136] T. Hisakado, T. Tsukizoe, H. Yoshikawa, Lubrication mechanism of solid lubricants in oils, *J. Lubr. Technol.* 105 (1983) 245–253.
- [137] M. Mosleh, N.D. Atnaf, J.H. Belk, O.M. Nobles, Modification of sheet metal forming fluids with dispersed nanoparticles for improved lubrication, *Wear* 267 (2009) 1220–1225.

Engineering Nanoparticulate Diamond for Applications in Nanomedicine and Biology

15

Han B. Man^a, Kangyi Zhang^b, Erik Robinson^a, Edward K. Chow^c, and Dean Ho^{a,b,d,e}

^aDepartment of Mechanical Engineering, Northwestern University, Evanston, IL,

^bDepartment of Biomedical Engineering, Northwestern University, Evanston, IL

^cG.W. Hooper Foundation, University of California, San Francisco, CA

^dRobert H. Lurie Comprehensive Cancer Center, Northwestern University, Chicago, IL

^eInstitute for Nanobiotechnology in Medicine (IBNAM), Northwestern University, Chicago, IL

CHAPTER OUTLINE

15.1 Nanodiamond synthesis and processing techniques	493
15.1.1 Synthesis and purification.....	494
15.1.2 Deaggregation and surface functionalization	495
15.2 ND therapeutics	499
15.2.1 Biomolecule interactions.....	500
15.2.2 Nanocrystalline diamond.....	503
15.2.3 Gene therapy	505
15.2.4 Fluorescent probes	508
15.2.5 Drug delivery	509
15.3 Future outlook.....	512
Acknowledgments.....	513
References	513

15.1 Nanodiamond synthesis and processing techniques

The rapid development of nanotechnology has served as a foundation for the emergence of nanoparticulate diamond particles due to their advantageous mechanical, chemical, biological, and optical properties [1]. In the case of biomedical applications, nanoscale diamonds functionalized with a wide variety of active chemical groups are ideal for biomolecular interactions. While there are many methods to generate pristine nanodiamonds (NDs), synthesis approaches by detonation and high pressure/high temperature have forged the use of NDs for biomedical and

other nanotechnology applications [1–3]. These synthesis methods have enabled large-scale production with consistent material properties [4].

15.1.1 Synthesis and purification

With regards to the general synthesis and purification of NDs, an explosive charge using trinitrotoluene (TNT) and hexogen, for example, is first ignited in a detonation chamber with a negative oxygen balance. The process of incomplete combustion generates elemental carbon from the explosives themselves, where typical yields of 4–10% of the explosive weight can be obtained [5]. To optimize ND yield, a 3:2 ratio of TNT and hexogen was previously recommended [6]. Detonation NDs are typically ~5 nm in diameter and the upper size limit can be determined by the duration of the detonation shock wave [2].

Rapid cooling (3000 K/min) is critical to reducing or preventing the transformation of NDs to graphite. A “dry” synthesis procedure that has previously been employed utilizes inert gas, such as argon, while a “wet” synthesis methodology utilizes water (ice) as the cooling medium. The resulting detonation soot can contain up to 80 wt% of diamond [5]. After mechanical and magnetic separation of larger debris and magnetic impurities, the detonation soot can still be comprised of nondiamond carbon and metal impurities. Further purification can be done via oxidation. When concentrated acids or corrosive liquid oxidizers (e.g., $\text{H}_2\text{SO}_4/\text{CrO}_3$) are subsequently applied, the oxidization of residual sp^2 -carbon impurities occurs more readily than diamond carbon, thus facilitating its preferential removal [2]. However, this method was originally not optimized for environmental compatibility and expensive treatment of hazardous waste is required. While earlier dry chemistry methods using catalysts can also result in contamination with the ND mixture [7], many of these early methods have been further optimized to enhance their efficiency.

Gas purification methods have been increasingly popular because they can improve efficiency, and remain environmentally friendly and inexpensive [8]. The process also results in surface modification with oxygen-containing acidic chemical groups. Beneficially, these groups facilitate the dispersion of NDs in water. For ozone-purified NDs, carboxylic anhydride groups on the surface enable the formation of highly stable hydrosols over a wide pH range (pH 2–12) [9]. These polydispersed NDs are also stable in organic solvents and the surface anhydrides can remain unaltered for a duration of at least 5 years. In addition to the application of air oxidation, Shenderova et al. also demonstrated that ozone oxidation can better allow the isolation of small size ND fractions.

Air oxidation without ozone enrichment requires a higher treatment temperature but this strategy also eliminates the application of harmful ozone gas, which may play a role in determining the spectrum of applications for which the material is being developed. Osswald et al. has narrowed down the temperature window (400–430°C) for preferential sp^2 graphitic carbon oxidation. Using their methodology, diamond loss is minimized and ~5 nm diamonds of high purity are obtained. One should note that the presence of trace amounts of iron can serve as a catalyst

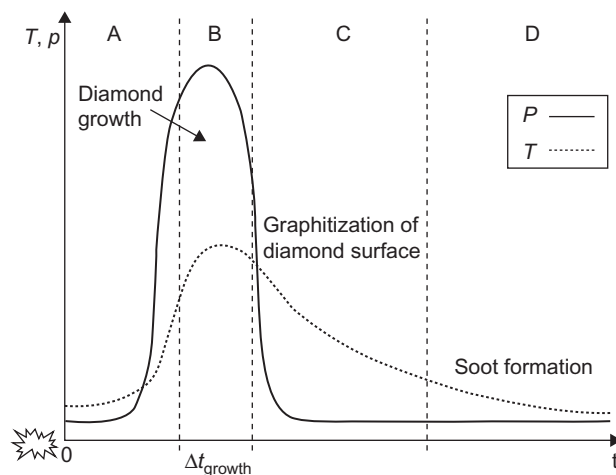
for sp³ to sp² conversion. Thus, significant diamond loss can be avoided by prior acid treatment to remove metal impurities. Selective air oxidation of graphite can also be performed at room temperature conditions when a UV light source is used [10]. The UV light mediates the onset of a photochemical reaction, which generates oxygen radicals O₃ and O for oxidation. In examining the varying methods of treatment, UV treatment can be achieved over the course of 2 days.

15.1.2 Deaggregation and surface functionalization

To apply NDs effectively in the field of drug and gene delivery, the hydrodynamic size must be fine-tuned. While some degree of clustering is often observed, nanoparticles possessing primary particle diameters in ranges below 6 nm can often filter through the capillaries of the glomerulus in the kidney and be cleared rapidly. In addition to these studies, lower primary particle diameter size limits of 8 nm have previously been examined [11,12]. The need to avoid opsonization and phagocytosis by the reticuloendothelial system, and to prevent accumulation of NDs in parts of the body, can also impose upper dimension limit parameters. For cancer therapy, the widely examined size parameters have previously been observed to be approximately in the 100 nm range [13,14]. The nanoparticles should be able to circulate within the bloodstream for a sufficient amount of time to prevent rapid clearance, and to be directed to the site of interest/therapeutic activity. While NDs are highly biocompatible [15], the long-term effects of ND accumulation in the lung, spleen, liver, and kidney are still unknown and continue to be studied. Dye-conjugated ND clusters of ~100–150 nm in diameter comprised of primary particles with single-digit diameters have been shown to be capable of eventual clearance from the body [16].

Another field where particle size/diameter is critical is the application of ND photonic crystals for future photonic devices. Contrary to expectations that photonic crystal formation from nanoparticles require high monodispersity, polydispersed NDs produce exceptional iridescence, which may be particularly relevant for translating these materials toward specific applications [17]. For example, blue color development is observed for NDs between 120 and 180 nm but not for sizes below 100 nm. Hence, unlike biomedical applications, ND aggregates above 100 nm are necessary for light diffraction. The importance of obtaining precise fractions of ND with narrow size distribution is thus paramount for various applications. The centrifugation, or ultracentrifugation, method allows for the separation of ND mixtures into discrete fractions based on properties such as material weight and size. The method is also straightforward and scalable, which is applicable for translation. Motivated by successes in carbon nanotube separation, Morita et al. [18] demonstrated that 4 nm and other ND fractions can be obtained using ultracentrifugation.

In scenarios where pristine NDs spontaneously agglomerate to form diamond aggregates that are several hundred nanometers in diameter, this may determine the specific application of NDs in medicine. Agglomeration can be attributed to the incomplete removal of graphite during purification steps [19]. During the cooling phase after detonation, curved graphitic ribbons and spherical graphitic shells

**FIGURE 15.1**

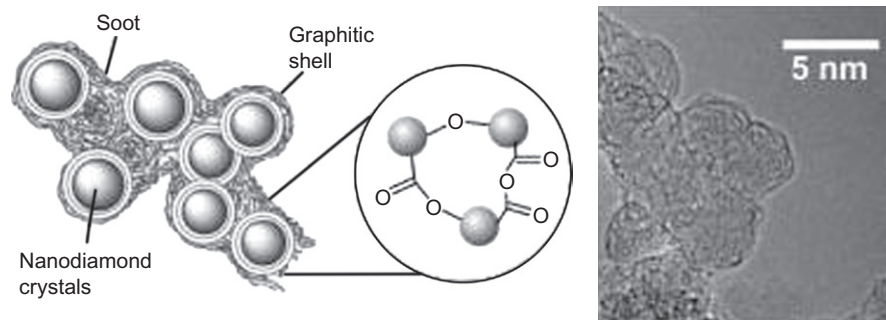
The period for diamond growth occurs during high temperature and pressure. As temperature and pressure decreases, diamond crystal formation stops and graphitization of ND surface occurs. At the same time, “soot embryos,” made up of hundreds of sp^2 -carbon atoms, are formed. These soot embryos then grow into carbon nanoparticles and form aggregates together with the surrounding NDs.

Source: Reprinted with permission from Ref. [20], Copyright 2005 Elsevier Ltd.

are formed on the surface of NDs (Figure 15.1). Soot formation occurs following ND graphitization and this increases the particle diameters to a point where they aggregate. Hence, a core aggregate can be visualized as primary diamond particles grouped together in graphitic soot (Figure 15.2). Chemical groups on the ND surface also result in interparticle covalent interactions, such as ester and anhydride groups [21]. The agglutinates that result are usually in the size range of 100–200 nm or potentially larger. The self-assembly of individual ND particles has been attributed to the intrinsic differential electrostatic charges on the different ND facets [22,23]. The [100] surface facets have been previously observed to be positive while the [111] facets can be negative, although varying degrees of functionalization can mediate varying charge properties to arise. The level of Coulombic interactions and thus agglomeration is determined by particle crystallinity and spatial orientation of the facets, among other attributes.

The tight aggregates of 100–200 nm can be disintegrated to allow for the surface functionalization of primary ND particles with optimal loading [23]. These steps make the NDs useful for attaching therapeutic molecules and also increase the dispersion of NDs in aqueous medium, such as blood.

A variety of oxidized groups, together with amorphous and graphitic carbons, are typically present on ND surfaces after detonation. Surface homogenization of NDs can therefore be performed before synthesizing desired terminal groups for

**FIGURE 15.2**

ND agglomerates of 100–200 nm are typically formed as a result of interparticle bonds and graphitic carbon. Graphitic carbon here refers to the graphitic shells on ND surface and the soot between particles. Examples of covalent bonds as shown here are ether, ester, and anhydride bonds.

Source: Reprinted with permission from Ref. [19], Copyright 2008 Wiley Online Library.

binding biomolecules. Examples of such chemical treatments include borane reduction [21], hydrogenation [24], fluorination [25], and oxidizing acids [26]. Surface homogenization increases the grafting efficiency for other chemical groups as well. The surface can then be more thoroughly modified to suit the attachment of a desired biomolecule, such as biotin [27], or to disperse the NDs in the appropriate solvent for either delivery or subsequent functionalization steps. Besides covalent conjugation of chemical groups to homogenized surfaces, noncovalent modifications such as poly-L-lysine adsorption can also be done [28,29].

Surfactants can be used after deagglomeration to prevent the re-aggregation of ND particles. The anionic surfactant, sodium oleate, can be adsorbed to the NDs in alkaline media to render the zeta potential negative [30]. However, unlike thermal oxidation methods [31], the zeta potentials, and thus electrostatic stability, varies more clearly with the pH values. Li et al. [31] used thermally oxidized ND-COOH particles to react with oleylamine (amino-containing surfactant) to form stable colloidal solutions in organic solvents for at least 3 months. However, for *in vivo* medical applications, stable aqueous dispersions will be more relevant to enhance particle delivery and therapeutic release efficacy.

Initial mechanical means of disintegration were performed using high-speed stirred-media milling with 0.1 mm SiO₂ beads [20]. The milled slurries were then sonicated for 1 h, yielding 4.5 nm ND particles. To further enhance the scalability and sustainability of processing, high-power, horn-type sonotrode-based ultrasonication was then done simultaneously with zirconia bead-milling in an important study from Osawa et al. [32]. Through the use of zirconia beads, primary ND particles could be obtained. Dimethyl sulfoxide as a dispersing solvent was utilized over water because it was a stronger H-bond acceptor. These studies also showed that zirconia bead fragments and graphitic layers on the ND surface could be removed

by using concentrated alkali (14M NaOH) [33]. Zirconia micro-bead wet milling, followed by acid treatment, has subsequently been used to make both nanocrystalline diamond films and ultrananocrystalline diamond (UNCD) (grain size <10 nm) films [34,35]. Monodispersed NDs seeded onto various substrates can thus achieve a very high nucleation density ($>10^{11}$ cm⁻²). In examining another milling procedure, Pentecost et al. proposed dry-milling with water-soluble salts and sugars [36]. Grinding media such as sucrose and NaCl are inexpensive, nontoxic, and easily removed by water rinsing. After 90 min of milling and with pH adjustments, stable colloidal solutions with particle sizes below 20 nm were obtained.

Dispersion and functionalization can also be performed using gas- or plasma-based approaches [9,24,37]. Such techniques are helpful because they are simple, scalable, and inexpensive in high-volume processing. There is also limited contamination observed utilizing these approaches. Efficient and reproducible modification of the ND surface can be done using gas methods as well. For example, hydrogenation by plasma or hydrogen gas removes oxygenated termination such as carboxylic and hydroxyl groups [24,37,38]. Deagglomeration has been achieved by heating NDs in pure hydrogen at 500°C. Hydrogenated ND powder, following ultrasonication and centrifugation procedures, revealed the presence of ~4 nm primary ND particles [38].

Contrary to the conventional thoughts on deagglomeration where sp² graphite should be avoided, some groups have performed graphitization as the first step, followed by air oxidation [39,40]. It can be noted that incomplete removal of graphite can lead to additional aggregation, which can further determine the specific application for the clusters. In this study, while a portion of the NDs was reduced to less than 50 nm, there was formation of new larger aggregates as well for potential additional applications where increased cluster sizes may be needed. The application being explored for the larger ND aggregates can then determine the dimensions of the aggregates or clusters that are formed as a result.

Oxidation in air within a narrow temperature range of 400–430°C has been found to selectively remove sp² graphitic carbon between primary NDs [7]. This was confirmed by TEM imaging observation (Figure 15.3). Oxidative groups on the ND surface can facilitate dispersion in alcohols and water while further modification, namely hydrogenization, can cause the ND particles to disperse well in nonpolar solvents.

Prior studies have shown that the density of carboxyl groups increases on the ND surface as the treatment temperature increases [41]. Heating at 900 K in air resulted in NDs with highly negative zeta potentials for a wide range of pH values (4–11). These negatively charged NDs exhibit interparticle electrostatic repulsion resulting in greater stability in suspension. However, the formation of ether (COC) bonds during heating can cause particle agglomeration. Multistep centrifugation at a spectrum of g-forces can subsequently be used to effectively isolate ND fractions of different sizes [42].

After thermal annealing, the NDs may not be soluble in common solvents and thus undergo additional chemically functionalization for further applications. Prior to chemical grafting of different aryl diazonium salts, the annealed NDs were shown to form less stable aqueous suspensions with sizes above 175 nm [43]. Conjugating –COOH and –SO₃H moieties allow dispersion in aqueous solutions while conjugating NO₂ and bromoethyl moieties can enable dispersion in organic media. Similarly,

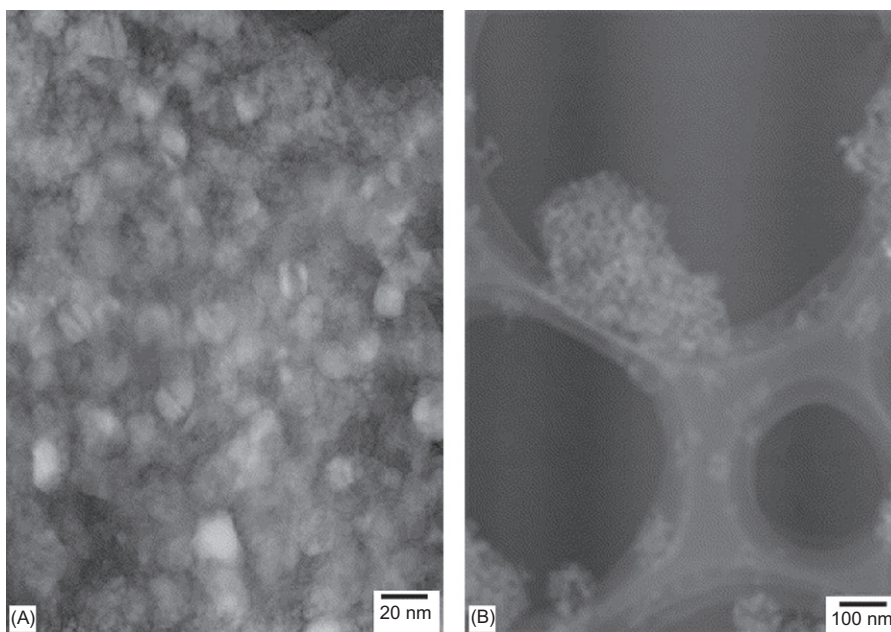


FIGURE 15.3

High-resolution TEM micrographs of (A) dispersed primary ND particles and (B) ND aggregates prior to thermal annealing in air.

Source: Reprinted with permission from Ref. [41], Copyright 2005 Elsevier Ltd.

after air oxidation and thermal annealing, Chang et al. [40] showed that graphitized NDs can be easily functionalized with a wide range of moieties simply by mixing, ultrasonication, and irradiating with microwaves. Compared to unmodified NDs, attached moieties enable the formation of stable suspensions for several days without precipitation. For example, ND–poly(methyl methacrylate) complexes can disperse well in tetrahydrofuran, while ND–poly(acrylic acid) disperses well in water.

15.2 ND therapeutics

Nanoparticles have been studied extensively for potential medical applications due to their biologically relevant attributes [13]. Specifically, NDs possess a unique set of properties, due to their size and composition, which allow them to function as therapeutic carriers in a variety of translationally relevant settings [44]. Biocompatibility is a crucial aspect of any effective therapeutic delivery agent. When NDs were compared to other carbon-based nanoscale materials, including carbon black, multiwalled and single-walled carbon nanotubes, they were shown to be among the most biocompatible within the group [15]. In that study, neuroblastoma cells were evaluated, after exposure to different nanoparticles, using cell viability tests such as mitochondrial function (MTT) and luminescent ATP production assays. NDs have also been

evaluated *in vivo*, for a deeper assessment into the safety of the nanoparticle [45]. Through microinjection and feeding, NDs were delivered into the model organism *Caenorhabditis elegans*, and the interactions were monitored. The researchers observed no abnormalities in differentiation, cellular division, or morphogenesis during embryogenesis. Furthermore, only very low levels of stress response was measured, which further reinforces the safety and stability of NDs.

NDs have consistently demonstrated the ability to function as a platform for drug delivery, which was shown through an initial study of ND-mediated delivery of a small molecule clinical standard chemotherapeutic [46]. These features make them particularly useful in the area of cancer treatment [47]. NDs have shown the ability to mediate the delivery of drugs that are otherwise insoluble in water [48]. The therapeutics Purvalanol A, 4-hydroxytamoxifen, and dexamethasone were effectively dispersed in water after reacting with NDs, and enhancing their stability in suspension. After binding to NDs, various chemotherapeutics also exhibit sustained and constant release, a gentler treatment procedure compared with bare drug. As a result of these properties, NDs have also been incorporated into biomedical devices such as thin-film patches [49]. Parylene was utilized as a base architecture for the thin-film device because of its proven biocompatibility as an implantable material. Nanocrystalline diamond thin films have also been incorporated into a variety of sensors such as an electrochemical biosensor to detect hydrogen peroxide levels [50], as well as a dual-mode sensor that can be used to detect an antimicrobial peptide through optical and electronic cues [51]. The synergistic advantages of NDs, such as drug sequestering, were also incorporated into the device. *In vivo* chemotherapeutic delivery using NDs was also validated in murine models for liver and mammary cancers [16].

Beyond drug delivery, NDs are also capable vehicles for gene therapy to deliver compounds such as plasmid DNA and siRNA [52,53]. NDs are capable of condensing nucleic acid molecules on their surface after they are functionalized with the cationic polymer polyethylenimine (PEI). The resulting ND-based platform protects nucleic acids from degradation until they are delivered into cells. Recently, NDs were used as a vector to administer siRNA into Ewing's sarcoma cells, and tracked using embedded color centers [54]. Nitrogen-vacancy defects are generated by ion beam irradiation of NDs followed by thermal annealing, a scalable method for producing naturally fluorescent nanoscale particles. The fluorescent profile of this particle has low photobleaching, making it an effective cellular tracking agent. Another modality for ND-based tracking studies is in combination with the magnetic resonance imaging (MRI) contrast agent gadolinium (III) (Gd(III)) [55]. The strength of signal produced by an MRI contrast agent is a direct result of its relaxivity, and the ND-Gd(III) complex produced over a 10-fold increase in relaxivity compared with Gd(III) alone, effectively resulting in among the highest ever reported per-Gd relaxivity values. NDs have been demonstrated to be both consistently scalable and effective as a therapeutic agent.

15.2.1 Biomolecule interactions

Work completed to date reveals that NDs can serve as excellent platforms for adsorption of various proteins and biomolecules, while mediating their preserved

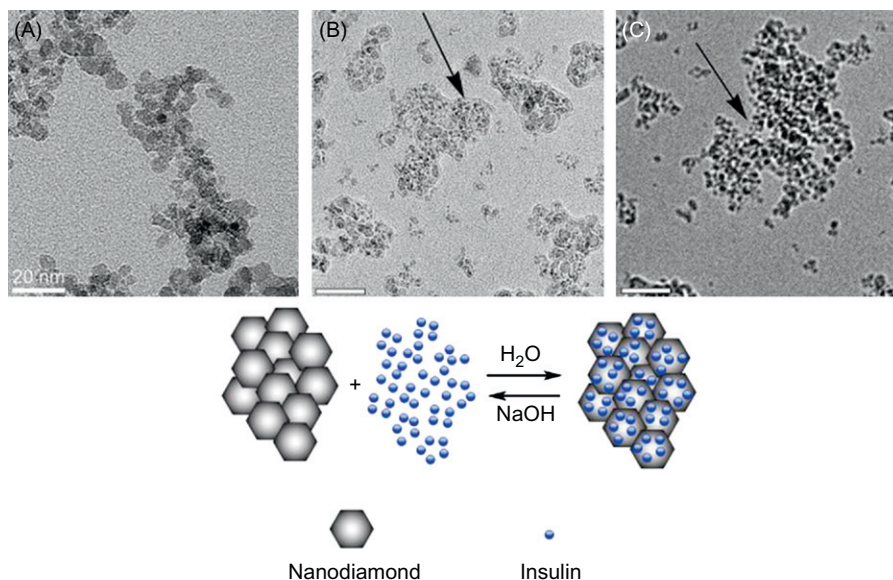


FIGURE 15.4

The effect of NaOH treatment on bare (A) NDs to (B) ND-insulin conjugates is contrasted in the TEM images (above). Exposure of ND-insulin conjugates to NaOH causes desorption of insulin from the surface of the ND, resulting in (C) bare NDs. The graphic (below) further illustrates the adsorption/desorption shift that can take place when NDs and insulin are exposed to varying environments.

Source: Reprinted with permission from Ref. [59], Copyright 2009, Elsevier Ltd.

activity. Numerous researchers have had success in adsorbing different types of proteins onto the ND surface. Initial experiments attempted to adsorb or link proteins, including variants of cytochrome *c* from horse and yeast species, onto NDs. This work demonstrated that the various routes of adsorption mediated through poly-L-lysine or chemical linkage was an effective means of adherence [30]. Efforts involved the physisorption of the protein histone, the enzymes catalase and lysozyme, and various other cholesterol-related enzymes. Adsorption/desorption of proteins and enzymes were noted in addition to enzymatic activity being retained. Furthermore, bolus ND injection subcutaneously and intravenously provided insight into the *in vivo* response to ND solutions in rabbits, yielding positive compatibility findings [56]. Further work revealed the adsorption of the enzyme lysozyme to the ND surface with retention of innate enzymatic activity [57]. Furthermore, there was a synergistic effect to protein absorption of lysozyme when combined with cytochrome *c* [58]. Studies examining the incorporation of therapeutically relevant proteins onto ND surfaces, and the modulation of their affinity to the ND surface under varying pH gradients was also studied (Figure 15.4). This work involving insulin presented NDs as a potential clinically relevant delivery system. This was confirmed by the

adsorption and release of the protein with retained activity, demonstrated through cellular gene expression studies.

Resultantly, the use of therapeutic compounds, specifically proteins, can be successfully adsorbed onto the ND surface and may complement existing medicinal protein-based therapies. Continued protein absorption work, specifically aimed toward the development of biosensor or nanomedicine applications [60], led to the development of the adherence of bovine serum albumin (BSA) to the ND surface [61]. Similarly, this work emphasized pH dependence as a primary mechanism to modulate ND loading and subsequent release of adsorbed compounds. Physisorption of specific targeting proteins, such as alpha-bungarotoxin (α -BTX), increased the range of biomolecules that could be successfully integrated onto the ND [62]. This level of modification points to the increasing role ND-functionalized particles may impart into the biosensor or nanomedicine fields, in addition to the clinical role still being pursued. Recently, interaction of TGF- β antibodies to the ND surface, dependent upon pH gradients, revealed a level of stability when adsorbed but also retained activity upon release. Consequently, the potential to deliver virtually any type of antibody toward a spectrum of potential therapeutic applications (e.g., cancer, inflammation) by means of an ND platform opens up a wide range of therapies, which could be significantly improved upon through the introduction of an ND carrier to promote antibody structure, and the ability to trigger release based on external stimuli.

Another avenue that is being explored is physically linking biomolecules to the surface of NDs through new strategies. Immobilization of IgG antibodies in combination with BSA onto the surface of NDs revealed a method to add specificity and targeting capabilities to the particle [63]. Further, surface modification has also been completed, such as the linking of particular chemical moieties that enhance the binding of certain glycoproteins while simultaneously reducing nonspecific adsorption [64] (Figure 15.5). Other biomolecules, such as biotin, can also be coupled to the ND surface for subsequent conjugation of other biomolecules, and to improve applications in novel biosensor technology [27].

Physical linkage of trypsin indicates that a spectrum of biomolecules can be chemically bonded to the ND surface, while retaining their innate activity. As such, enzymatic activity can be interchangeably modified, depending on the biomolecule required to fit a particular process being explored (e.g., for diagnostics, biological monitoring, signal enhancement) or to enhance proteolytic degradation [65].

Additional work with NDs has led to novel agglomeration of particles applied via a layer-by-layer (LBL) technique, thus arranging NDs into an ordered set of arrays that may be applicable toward nanoscale patterning, drug delivery, and implant coating, among other studies. Agglomeration of NDs onto charged amino acids applied to a glass surface allows for ND aggregates to be formed into discrete layers [66]. These layers can then be doped with various drugs for periods of extended or even combinatorial/sequential release. Additional LBL techniques, such as linking BSA to NDs and then applying these conjugates to surfaces via LBL method, have been completed as well, demonstrating the versatility of this approach. Immobilization of BSA proteins allows for ND packing arrangements

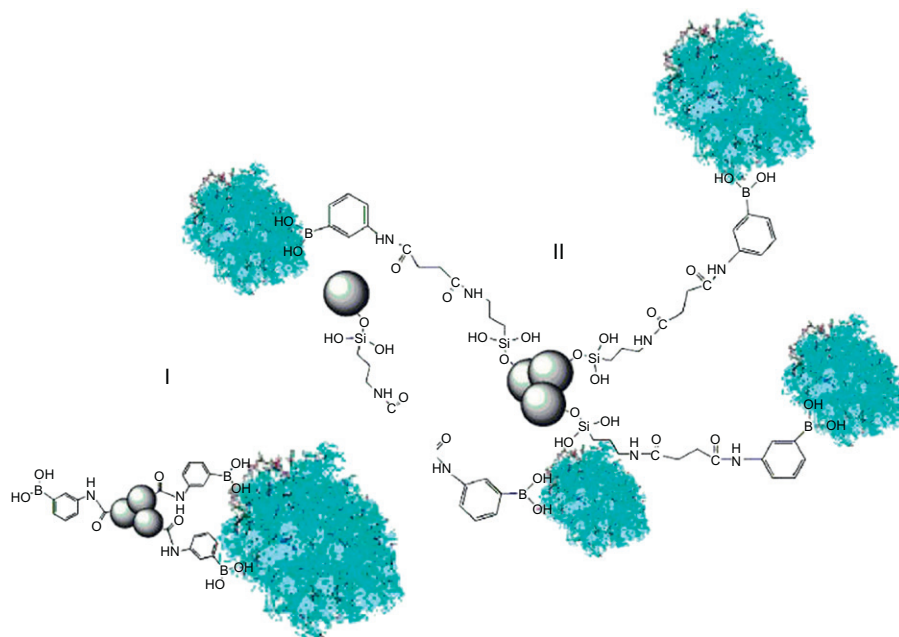


FIGURE 15.5

Glycoprotein adsorption of NDs without a linker peptide present on the ND surface (I). Addition of linker peptides to the ND surface increases the loading capacity of glycoproteins (II). Thus, surface functionalization leads to an increase in loading potential of NDs directed toward biomolecules.

Source: Reprinted with permission from Ref. [64], Copyright 2008, American Chemical Society.

amenable to biosensor applications while remaining scalable [67]. While the two previous LBL techniques are driven by electrostatic interactions, new ND arrays have been created through affixing NDs into ordered arrangements onto self-assembled monolayers [68]. Once these ND arrays have been created, protein absorption and further surface processing can be studied/completed, thus contributing to applications ranging from biosensing to functionally active coatings.

15.2.2 Nanocrystalline diamond

While delivery of biomolecules can be achieved through the use of injectable nanoparticles, specifically NDs, other material interfaces also present amenable surfaces for biomedical purposes like localized therapeutic delivery. One form of deposition, which has seen wide use, is chemical vapor deposition (CVD). The CVD process is suitable to the biomedical arena due to its passive, conformal, and nondestructive nature. There are several forms of CVD that can deposit an assortment of material platforms, from polymers to carbon-based materials. Investigation of polymers deposited through CVD such as parylene-derived films (an inert

biocompatible polymer) has yielded a number of potential therapeutic films [69–71]. Various methodologies have been investigated to determine the value in delaying and sustaining release of underlying/packaged therapeutics.

Expanding on the application of carbon-based materials, UNCD films can possess similar surface properties, which make them particularly applicable toward the medical device and sensor research domains. Preliminary work completed with UNCD films to assess biocompatibility has generated promising results. Silicon chips, coated with a layer of UNCD, demonstrated biocompatibility after being implanted into the eyes of rabbits for 2 weeks, revealing the relevance of UNCD films as potential implant coatings [72]. Exposure of nanocrystalline diamond films to blood-related proteins did not reveal aggregation or nonspecific adsorption, lending to the inert surface appropriate for potential longer-term physiological implantation as well [73].

Dependent upon the end-stage use of related films, cell and protein adhesion may result as in the case of implant or medical device coatings. Cellular response to UNCD films was undertaken and included incorporation of several phenotypically different cell lines such as HeLa, PC12, and MC3T3. Results indicate that the cell lines interacted favorably compared to control surfaces, thus showing that UNCD can serve as a biocompatible surface for biological applications [74]. Further compatibility work, which compared cellular adhesion to chemically modified UNCD surfaces, revealed strong adhesion with certain cell lines. NHDF cells and PC12 cells grown on UNCD and laminin-immobilized UNCD surfaces both displayed positive interaction with the respective substrates [75]. Thus UNCD surfaces are conducive to cellular outgrowth in addition to providing surface integration of biomolecules, specifically adhesive peptides, properties that support their further development as versatile implant coatings.

Further UNCD work focused on the potential application of these surfaces in biomedical, dental, and surgical fields. Morphological analysis coupled with viability assays of L929 and gingival-derived fibroblasts revealed surfaces supportive of tissue growth [76]. Comparatively, UNCD surfaces proved to be biocompatible with the growth of murine-derived fibroblasts onto deposited substrates [77]. With these initial findings, a greater degree of functionality was explored through the coating of UNCD films with collagen networks (Figure 15.6), which in turn was loaded with an anti-inflammatory drug [59]. These hybrid films present a robust coating coupled with adhesive proteins for proper cell growth, while possessing therapeutic molecules for manipulation of cellular responses. Surface analysis and gene expression results highlight the multifunctionalized capability of UNCD films to act as a biocompatible base from which numerous modifications can be achieved [78]. Additional work regarding composite films, incorporating UNCD and amorphous carbon (UNCD/a-C), showed positive results when exposed to BSA and a number of cell types [79]. When UNCD/a-C was compared to nanocrystalline diamond hydrogels, each fared favorably toward bone-derived EPC cells, demonstrating that each substrate was a potentially viable surface for biomedical applications. Results indicate either surface could potentially be employed as a bone implant

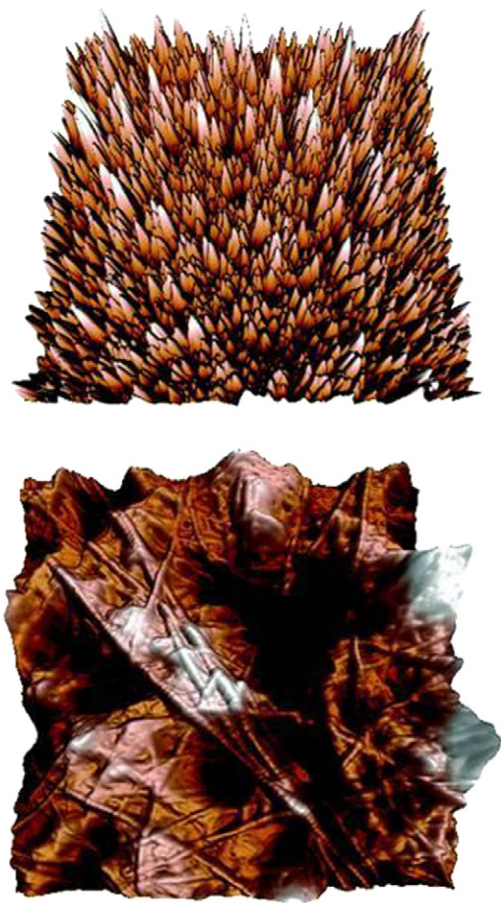


FIGURE 15.6

AFM images of type I collagen applied to UNCD films. The image (above) depicts collagen deposited without dehydration onto the UNCD substrate. Upon subsequent dehydration (below) collagen fibrils can be easily identified on the UNCD surface. The presence of adhesive proteins on diamond-related surfaces allows for adequate cellular adhesion and growth.

Source: Reprinted with permission from Ref. [78], Copyright 2009, American Chemical Society.

coating to prolong implant lifetime due to the protective and compatible properties of the film [80].

15.2.3 Gene therapy

While the idea of gene therapy has been a promising concept for cancer treatment for many years, there are still challenges with developing the appropriate vector to

deliver these genes [81]. Researchers have been providing increasing evidence demonstrating that properly functionalized NDs are capable of being a biocompatible and efficient carrier of gene therapy components. Current gene therapy vehicles, based on liposomal, viral, and polymer materials, are still being developed to overcome issues with unacceptable levels of toxicity. PEI itself is a cationic polymer-based gene delivery vehicle that can be very efficient at high molecular weights (MWs), but can also be very toxic. Remarkably, NDs functionalized with low MW PEI are able to demonstrate high levels of delivery efficiency while maintaining safety.

In one of the first demonstrations of ND-based gene therapy with markedly enhanced efficacy, NDs functionalized with PEI of MW 800Da (PEI800) were able to deliver plasmid DNA into HeLa cells [52]. As a result of ND functionalization, PEI800 complexes were over 70 times more efficient at transfection than PEI800 alone. The process for surface functionalization was simple and scalable since PEI800 was physically adsorbed onto the ND surface after mixing. To confirm the cellular internalization of NDs by HeLa cells, rhodamine-labeled NDs were incubated with the cell line and then analyzed using flow cytometry. The uptake of ND particles by cells was determined to be dependent on time and exposure concentration. The ND–PEI conjugates were also tested for cytotoxicity using a 3-(4,5-dimethylthiazol-2-yl)-2,5-diphenyltetrazolium bromide (MTT) assay, which measures cellular viability through metabolic activity by the production of formazan dyes. All ND-based complexes exhibited significantly higher compatibility, with survival rates over 80% as compared with less than 40% for higher MW PEI25K.

ND and PEI vectors were tested at different mixing ratios with plasmid DNA and the maximum binding ratio was determined. ND–PEI delivery efficacy was subsequently compared with ND alone, and PEI alone, for transfection efficiency using the luciferase plasmid (pLuc) and green fluorescent protein plasmid (pEGF-PLuc). Although delivery with ND–PEI complexes resulted in a 2–3 times lower gene expression than the PEI25K, it was able to demonstrate significantly better biocompatibility. Using the GFP plasmid, the efficacy of gene delivery was easily determined by measuring the increase in fluorescence conferred upon the HeLa cells, using flow cytometry and confocal microscopy. Figure 15.7 shows the quantification of the efficacy of plasmid DNA delivery using ND compared to polymer carriers and other controls. It can be observed that the function of polymer-functionalized NDs outperforms all other vectors. As a result, ND–PEI delivered plasmid DNA to HeLa cells 70 times more efficiently than PEI alone at equivalent concentrations. In addition, ND–PEI treatment resulted in a marked improvement in cellular biocompatibility over high MW PEI. A qualitative improvement of GFP expression in HeLa cells following treatment with ND–PEI vectors as compared with other vectors was observed. This data further validates the enhanced performance of the ND–PEI vector by showing the increased green fluorescence signal. This study was among the first demonstrations of gene delivery using an ND-based system delivering plasmid DNA, and this study served as the foundation for the ND-mediated delivery of small interfering RNA (siRNA) with enhanced safety compared to commercial standards.

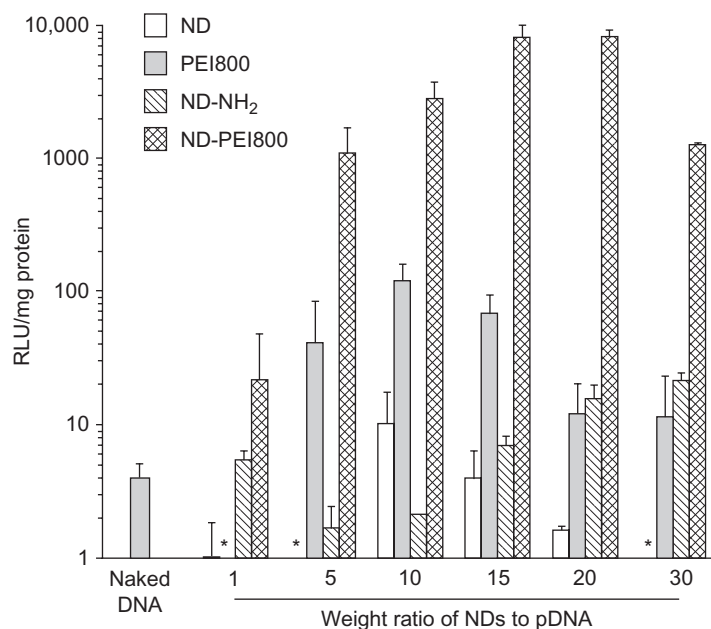
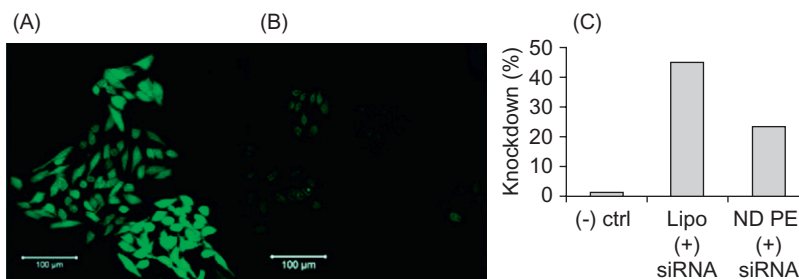


FIGURE 15.7

Quantification of the gene expression of the pLuc plasmid demonstrates the performance of various transfection agents. The advantage of ND-PEI is evident as ND-PEI is able to outperform all other vectors across different weight ratios of ND to pDNA.

Source: Reprinted with permission from Ref. [52], Copyright 2009, American Chemical Society.

In another study of ND-mediated delivery of nucleic acid therapeutics, researchers also utilized polymer-functionalized diamond particles for gene therapy, and in this case utilized fluorescent NDs (fNDs) with nitrogen defects, which exhibit an inherent fluorescence [54]. Researchers adsorbed siRNA onto the functionalized nanoparticles and were able to track their internalization by monitoring the fluorescence of the NDs. The siRNA was transported into Ewing's sarcoma cells and the specific inhibition of the EWS/Fli-1 gene expression was decreased as a result. In previous work, PEI functionalized NDs delivered siRNA into breast cancer cells [53]. These cells already contained the GFP-encoding gene in its genome, while anti-GFP siRNA was introduced using various vectors. Compared with a standard polymeric delivery agent Lipofectamine, transfections that were performed in the presence of serum proteins resulted in improved performance by ND-PEI (Figure 15.8). Alhaddad et al. [54] also examined the therapeutic potential of siRNA delivery by ND-PEI by testing the gene knockdown of the EWS-Fli1 gene in Ewing's sarcoma cells. A rare genetic bone cancer, Ewing's sarcoma is predominantly caused by chromosomal translocations that result in protein mutation. Therefore, treatments have been derived from the suppression of the expression of this gene. In addition to PEI, researchers also examined the

**FIGURE 15.8**

Confocal microscope images showing the expression (A) and subsequent knockdown (B) of GFP in M4A4 cells. Part (C) shows the percentage knockdown conferred by ND–PEI compared to Lipofectamine and a negative control.

Source: Reprinted with permission from Ref. [53], Copyright 2010, American Chemical Society.

use of another cationic polymer coating, poly(allylamine hydrochloride) (PAH), which was bound to the surface of the NDs. Cytotoxicity assays using NIH/3T3 murine fibroblast cells determined that ND–PAH remained less toxic than the commonly used commercial Lipofectamine agent. By using FITC-labeled siRNA molecules and the inherent fluorescence of the fNDs, a confocal image after a 4 h incubation confirmed the co-localization of both the ND and siRNA in the perinuclear region of the cell. When mRNA levels were measured, it was determined that ND–PEI was the most efficient of the ND-based vectors, inhibiting the expression of EWS-Flt1 by ~50%. This compares very closely with Lipofectamine at 65%, but when performed in the presence of serum-containing medium, that value subsequently dropped to 20%. The improved performance of ND–PEI in realistic biological conditions is further reinforced by its vastly improved biocompatibility compared to Lipofectamine, increasing its potential for translation. These findings agreed very well with the Chen et al. study utilizing ND–PEI to silence GFP expression, and exemplifies the potential of NDs as a therapeutic modality for gene therapy.

15.2.4 Fluorescent probes

ND-based fluorescent probes offer several advantages over current fluorescent labeling [82]. Fluorescent probes are important tools for tracking and visualization [83], but some are limited by photoblinking, photobleaching, and cytotoxicity. NDs can be transformed into fluorescent labels after introducing nitrogen-vacancy centers through irradiation from an electron beam followed by high-temperature annealing. ND probes represent improvements over current fluorescent markers by being photostable, nanodisperse, scalable, and biocompatible. In addition, their absorption and emission wavelengths are typically above that of endogenous biomolecules. Some proteins, such as flavins and collagens, auto-fluoresce at low wavelengths, but the ND fluorescent signal is unaffected due to higher absorption and emission

wavelengths [82]. ND fluorescence is remarkably stable, sustaining a constant signal for up to 300 s. This compares very favorably with industry standard dyes, such as AlexaFluor 546, which typically photobleaches after several seconds. Along with high contrast and stability, these ND probes are also manufactured in a scalable method [84]. Researchers have been able to use low-energy helium ion bombardment to create defects in the ND structure, instead of the higher-energy electron bombardment [85]. The result is a method that is more efficient in vacancy production per ion dosage by over two orders of magnitude. Because of the long lifetime of the signal, researchers were also able to track the intracellular movements of fluorescent NDs in 3D. Improvements to the fluorescent ND production process have yielded single particle (5 nm) fluorescence with intermittence that can be finely regulated [86]. With a variety of beneficial properties and ongoing improvements in fluorescent ND production [87], there is significant promise for their use in biological applications.

15.2.5 Drug delivery

The area where NDs have shown the most tangible benefits has been in drug delivery, specifically toward cancer therapy. Important characteristics of an efficient drug carrier are dispersability and stability in biological conditions, scalability, biocompatibility, and diverse functionality to transport a variety of therapeutics. Modeling of NDs has shown that the shape of the ND is a truncated octahedron, with many distinct facets [88]. Regarding these facets, it is suggested that water molecules align themselves in opposing orientations on differently charged facets (e.g., $\langle 111 \rangle$, $\langle 100 \rangle$), leading to a strongly bound, nanoscale layer of water on the ND surface, which may play a role in mediating improvements in areas ranging from drug delivery to imaging. Since neighboring facets have oppositely oriented water molecules, each cluster of water molecules can exert an attractive force to the bordering clusters, causing a dense and robust hydration layer. This contributes significantly to ND stability in water.

NDs have been shown to deliver a wide spectrum of drugs as well as exhibiting marked levels of biocompatibility. This safety was supported in HeLa cells as well as mouse 489–2 osteoprogenitor cells [89]. Cell viability remained constant for up to concentrations of 200 $\mu\text{g}/\text{ml}$ incubated for 48 h as determined via cell viability assays. According to alkaline phosphatase staining, in progenitor cells, the ability to differentiate was not reduced by increasing concentrations of NDs. To test uptake characteristics, a clathrin-specific inhibitor, phenyl arsine oxide, resulted in a reduction in ND uptake while a caveolae-specific inhibitor did not. This suggests that NDs can be internalized through energy-dependent clathrin-mediated endocytosis, which explains NDs' advantage in delivering therapeutics into cells.

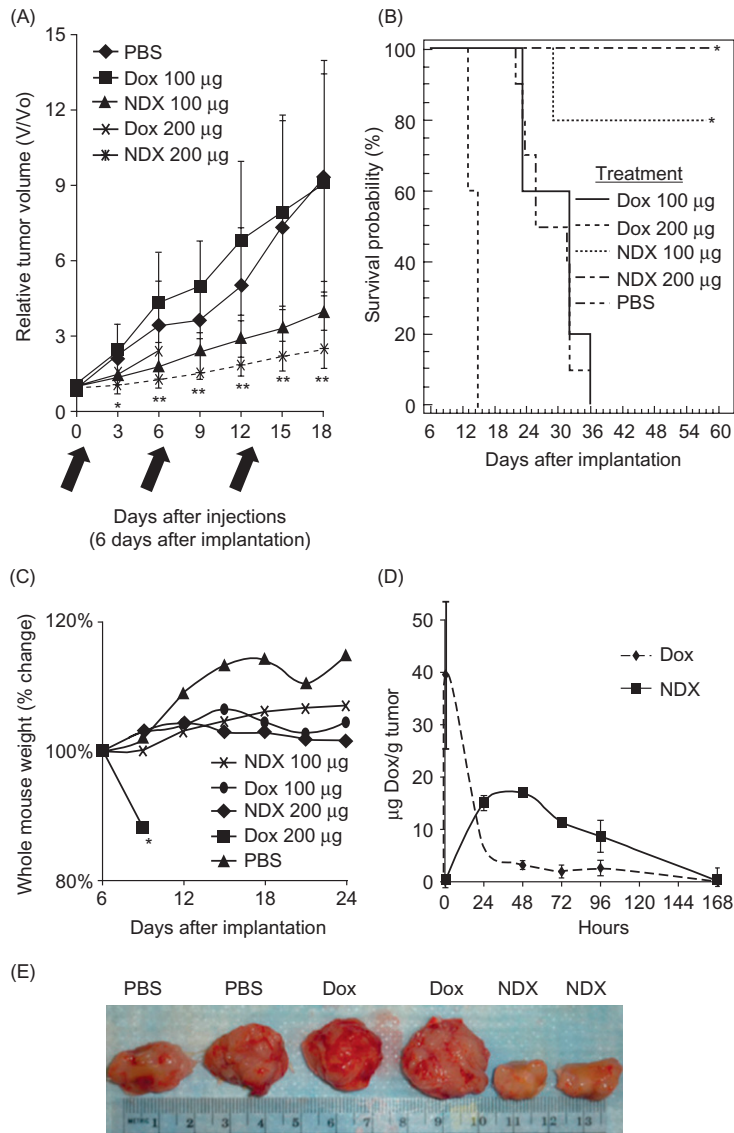
ND-mediated efficiency of drug delivery has also been validated comprehensively *in vivo*, confirming the clinical relevance of this nanoscale material [16]. In the study, the common chemotherapeutic Doxorubicin (Dox) was physically adsorbed onto the ND surface. Previous modeling work has suggested that the charged facets on the ND surface are what allow drugs such as Dox to bind very

strongly to the ND [88]. The result is a facile and scalable production process, adding to the feasibility of this treatment modality. This ND–Dox (NDX) platform was tested in drug-resistant liver and mammary cancer tumors in murine models. Many cancer types become difficult to treat after repeat administration of chemotherapeutics because of acquired drug resistance. Drug-efflux proteins, cell surface proteins in charge of removing intracellular toxins, become over-expressed as cells experience increased exposure to toxic drugs such as Dox. However, it was shown that NDX could bypass efflux pumps and effectively deliver drugs into cancer cells. Favorable biological response was measured for high ND dosages. Levels of sera interleukin-6 (IL-6), an indicator of systemic inflammation, and serum alanine transferase, an indicator of liver function, were not affected by the presence of even large dosages of NDs. Furthermore, Dox bound to NDs exhibited a 10-fold increase in circulation halftime which may play a role in reducing the need for the constantly repeated administration of toxic therapeutics. ND clearance and biodistribution was investigated using dye-labeled particle clusters. By day 10, clearance of a significant dose of the NDs from the lung, spleen, kidney, and liver were all observed. Continued studies will be performed to assess the degree of long-term whole body clearance and safety.

High concentrations of drug loading in the NDX platform also enhance its therapeutic efficacy. Elevated localized drug concentrations coupled with increased therapeutic retention can overcome drug efflux, which can become necessary when treating resistant tumors. Drug retention of NDX was tested against Dox alone in MDCK cells that overexpress the MDR drug transport protein. Following drug incubation, a marked improvement in drug retention was observed for ND-delivered drug versus drug alone. Drug treatments were also tested with the drug-efflux inhibitor Verapamil, revealing that NDX function is not affected while Dox alone showed increased effect, demonstrating that the mechanism of resistant was indeed mediated by efflux pumps. Increased drug retention mediated by NDX compared to the unmodified drug within both a drug-resistant liver and mammary tumor model was also demonstrated *in vivo*.

Subsequently, mice bearing LT2-Myc liver and 4T1 mammary tumors were treated weekly by tail vein injection of NDX, unmodified Dox, ND alone, and a PBS control. In the highly resistant 4T1 tumors, drug amounts up to 200 μ g resulted in accelerated animal mortality/decreased drug tolerance. On the other hand, NDX was able to treat tumors by reducing their size and weight. In the 4T1 model, low unmodified Dox alone dosages did not affect tumors, while the higher dosages resulted in no mouse survival by day 15 (Figure 15.9). NDX administration of the normally lethal Dox dosages resulted in the elimination of the peripheral toxic effects of Dox, while simultaneously enabling even further enhanced tumor volume reduction. Furthermore, NDX administration resulted in the absence of notable myelosuppression, the dose-limiting side effect of chemotherapy, when compared to the administration of unmodified Dox clinical standard, which caused notable myelosuppression.

The confirmation of the ND platform to overcome drug resistance *in vivo* has potential to be clinically relevant. Current attempts at blocking drug efflux, using chemical inhibitors such as verapamil, have been limited by toxicity, low efficacy,

**FIGURE 15.9**

NDX is able to effectively treat tumors in a murine model more effectively than drug alone. Part (A) demonstrates that NDX, at two equivalent drug dosages, is able to reduce tumor weight more effectively than drug alone. Part (E) is the corresponding images showing the reduction of tumor size. Part (B) is a Kaplan–Meier survival plot showing that NDX results in improved mouse survival. Parts (C) and (D) show the progression of whole mouse weight and drug retention by tumors over 168h, respectively.

Source: Reprinted with permission from Ref. [16], Copyright 2011, American Association for the Advancement of Science.

and lack of specificity. ND-based delivery of drugs represents a general approach that may be able to circumvent these challenges. The wide spectrum of treatment modalities that NDs are capable of harnessing is evidence of the considerable promise of ND-based therapeutics.

15.3 Future outlook

While NDs have demonstrated numerous biologically applicable features, such as tunable small molecule loading and delivery, and robust fluorescent profiles, there still remains additional research needed to realize their full potential. Modifications such as controlling surface chemistry for the attachment of multiple moieties (e.g., targeting, therapeutic, imaging) will improve upon the multifunctionality of the ND platform. It is also important to engineer processing techniques to produce ND systems based on primary particle sizes. After many observed successes with regards to safety and efficacy of therapy in murine models, additional testing in larger animals will be required before NDs can be validated in a clinical setting. Modeling of the complex facet behavior of the NDs from first principle, using quantum and molecular dynamic simulations, will increase our ability to acutely control the particle. A diverse modeling framework, utilizing experimental input parameters and validated by experiment results, will provide a foundation for the optimization of various ND structures for biological applications. These simulations will establish the groundwork for realistic continuum-scale modeling and analysis, such as finite-element modeling, which will be able to inform real-world therapeutic development.

In addition to fundamental examination of optimization of ND surface properties, as our understanding of the complex diseases such as cancer increases, it is clear that a wide diversity in molecular mechanisms and characteristics of these diseases exists, and that this can be harnessed and targeted by versatile nanomedicine-based approaches. Nanomedicine-based therapy can potentially be tailored to treat specific patients as diagnostics and therapy move toward being more personalized depending on unique patient characteristics. In order for nano-enabled drug-delivery approaches to successfully be clinically utilized in treating complex diseases, these platforms must possess specific properties that are translationally relevant. This includes the ability to specifically target specific sites of disease to potentially increase efficacy and reduce toxicity. This is particularly clear in cancer, where different subtypes of cancer in the same tissue express specific proteins depending on the tumor cell of origin as well as the driving oncogenes. In breast cancer, epidermal growth factor receptor (EGFR) is over-expressed in the case of triple-negative breast cancers (TNBC) [90]. TNBC is one of the most aggressive forms of breast cancer and is often associated with poor treatment outcomes when addressed by conventional nonspecific therapies that can also present significant adverse outcomes. Therapeutic delivery platforms that are enhanced through the use of nanotechnology can potentially be used to specifically target proteins such as EGFR to deliver drugs specifically to cancer cells and thereby enhance the

specificity of cancer cell treatment while limiting systemic effects of these drugs. Another property required of a successful nanotherapeutic platform is versatility in delivering multiple classes of drug compounds and targeting moieties. There is a clear need for this capability as therapeutics used in complex diseases can include a variety of molecules including small molecules, proteins, and genetic material such as siRNA. Additionally, the nanoparticles that serve as the foundation of these vehicles must be biocompatible in order to minimize inflammatory or toxic reactions in patients. This is important to mitigating the adverse effects of drug treatment, which can serve as a barrier to translation and widespread clinical use. Finally, the dimensions of drug-delivery vehicles and the foundational components of the platform are important as targeting to disease sites such as tumors as well as clearance of nonnative particles requires specific size requirements [91,92]. As discussed in this chapter, it is clear that NDs meet many of these requirements for a successful drug-delivery platform. Continued work harnessing the versatility of NDs allows us to begin to realize their full therapeutic potential as a powerful tool in nanomedicine.

Acknowledgments

D.H. gratefully acknowledges support from the National Science Foundation CAREER Award (CMMI-0846323), Mechanics of Materials grant CMMI-0856492, Center for Scalable and Integrated NanoManufacturing (DMI-0327077), DMR-1105060, V Foundation for Cancer Research Scholars Award, Wallace H. Coulter Foundation Translational Research Award, American Chemical Society Petroleum Research Fund Grant 47121-G10, and National Cancer Institute grant U54CA151880 (the content is solely the responsibility of the authors and does not necessarily represent the official views of the National Cancer Institute or the National Institutes of Health), National Cancer Institute grant 1R01CA159178-01, and European Commission funding program FP7-KBBE-2009-3.

References

- [1] A.M. Schrand, S.A.C. Hens, O.A. Shenderova, Nanodiamond particles: properties and perspectives for bioapplications, *Crit. Rev. Solid State Mater. Sci.* 34 (1–2) (2009) 18–74.
- [2] Krueger, The structure and reactivity of nanoscale diamond, *J. Mater. Chem.* 18 (2008).
- [3] O.A. Shenderova, *Ultrananocrystalline Diamond: Synthesis, Properties, and Applications*, William Andrew, Norwich, NY, 2006.
- [4] V.Y. Dolmatov, Detonation nanodiamonds: synthesis, structure, properties and applications, *Usp. Khim.* 76 (4) (2007) 375–397.
- [5] V.Y. Dolmatov, Detonation synthesis ultradispersed diamonds: properties and applications, *Russ. Chem. Rev.* 70 (607) (2001).
- [6] J.A. Viecelli, Carbon particle phase transformation kinetics in detonation waves, *J. Appl. Phys.* 88 (683) (2000).
- [7] S. Osswald, G. Yushin, V. Mochalin, S.O. Kucheyev, Y. Gogotsi, Control of sp(2)/sp(3) carbon ratio and surface chemistry of nanodiamond powders by selective oxidation in air, *J. Am. Chem. Soc.* 128 (35) (2006) 11635–11642.

- [8] I. Petrov, O. Shenderova, V. Grishko, V. Grichko, T. Tyler, G. Cunningham, et al., Detonation nanodiamonds simultaneously purified and modified by gas treatment, *Diamond. Relat. Mater.* 16 (12) (2007) 2098–2103.
- [9] O. Shenderova, A. Koscheev, N. Zaripov, I. Petrov, Y. Skryabin, P. Detkov, et al., Surface chemistry and properties of ozone-purified detonation nanodiamonds, *J. Phys. Chem. C* 115 (20) (2011) 9827–9837.
- [10] L.M. Apatiga, A. Castaneda-Miranda, C. Menchaca, V.M. Castano, Selective oxidation of graphite on diamond films induced by UV exposure, *Inorg. Mater.* 38 (1) (2002) 31–33.
- [11] J. Rao, Shedding light on tumors using nanoparticles, *ACS Nano* 2 (10) (2008) 1984–1986.
- [12] J.A. Barreto, W. O'Malley, M. Kubeil, B. Graham, H. Stephan, L. Spiccia, Nanomaterials: applications in cancer imaging and therapy, *Adv. Mater.* 23 (12) (2011) H18–H40.
- [13] M.E. Davis, Z. Chen, D.M. Shin, Nanoparticle therapeutics: an emerging treatment modality for cancer, *Nat. Rev. Drug. Discov.* 7 (9) (2008) 771–782.
- [14] E. Gullotti, Y. Yeo, Extracellularly activated nanocarriers: a new paradigm of tumor targeted drug delivery, *Mol. Pharm.* 6 (4) (2009) 1041–1051.
- [15] A.M. Schrand, H. Huang, C. Carlson, J.J. Schlager, E. Ōsawa, S.M. Hussain, et al., Are diamond nanoparticles cytotoxic?, *J. Phys. Chem. B* 111 (1) (2006) 2–7.
- [16] E.K. Chow, X.Q. Zhang, M. Chen, R. Lam, E. Robinson, H.J. Huang, et al., Nanodiamond therapeutic delivery agents mediate enhanced chemoresistant tumor treatment, *Sci. Transl. Med.* 3 (73) (2011) 73ra21.
- [17] V. Grichko, Nanodiamond particles forming photonic structures, *Nanotechnology* 19 (22) (2008).
- [18] Y. Morita, T. Takimoto, H. Yamanaka, K. Kumekawa, S. Morino, S. Aonuma, et al., A facile and scalable process for size-controllable separation of nanodiamond particles as small as 4 nm, *Small* 4 (12) (2008) 2154–2157.
- [19] A. Krueger, Diamond nanoparticles: jewels for chemistry and physics, *Adv. Mater.* 20 (12) (2008) 2445–2449.
- [20] A. Krueger, Y. Liang, G. Jarre, J. Stegk, Surface functionalisation of detonation diamond suitable for biological applications, *J. Mater. Chem.* 16 (24) (2006) 2322–2328.
- [21] A.S. Barnard, Self-assembly in nanodiamond agglutinates, *J. Mater. Chem.* 18 (34) (2008) 4038–4041.
- [22] A.S. Barnard, M. Sternberg, Crystallinity and surface electrostatics of diamond nanocrystals, *J. Mater. Chem.* 17 (45) (2007) 4811–4819.
- [23] A. Krüger, F. Kataoka, M. Ozawa, T. Fujino, Y. Suzuki, A.E. Aleksenskii, et al., Unusually tight aggregation in detonation nanodiamond: identification and disintegration, *Carbon* 43 (8) (2005) 1722–1730.
- [24] H.A. Girard, J.C. Arnault, S. Perruchas, S. Saada, T. Gacoin, J.P. Boilot, et al., Hydrogenation of nanodiamonds using MPCVD: a new route toward organic functionalization, *Diamond Relat. Mater.* 19 (7–9) (2010) 1117–1123.
- [25] Y. Liu, Z. Gu, J.L. Margrave, V.N. Khabashesku, Functionalization of nanoscale diamond powder: fluoro-, alkyl-, amino-, and amino acid-nanodiamond derivatives, *Chem. Mater.* 16 (20) (2004) 3924–3930.
- [26] J.B. Donnet, E. Fousson, T.K. Wang, M. Samirant, C. Baras, M.P. Johnson, Dynamic synthesis of diamonds, *Diamond Relat. Mater.* 9 (3–6) (2000) 887–892.

- [27] A. Krueger, J. Stegk, Y. Liang, L. Lu, G. Jarre, Biotinylated nanodiamond: simple and efficient functionalization of detonation diamond, *Langmuir* 24 (8) (2008) 4200–4204.
- [28] A. Krueger, New carbon materials: biological applications of functionalized nanodiamond materials, *Chem. Eur. J.* 14 (5) (2008) 1382–1390.
- [29] L.C.L. Huang, H.-C. Chang, Adsorption and immobilization of cytochrome *c* on nanodiamonds, *Langmuir* 20 (14) (2004) 5879–5884.
- [30] L.C.L. Huang, H.C. Chang, Adsorption and immobilization of cytochrome *c* on nanodiamonds, *Langmuir* 20 (14) (2004) 5879–5884.
- [31] C.-C. Li, C.-L. Huang, Preparation of clear colloidal solutions of detonation nanodiamond in organic solvents, *Colloids Surf. A Physicochemical Eng. Aspects* 353 (1) (2010) 52–56.
- [32] M. Ozawa, Preparation and behavior of brownish, clear nanodiamond colloids, *Adv. Mater.* 19 (9) (2007) 1201–1206.
- [33] Ō Eiji, Recent progress and perspectives in single-digit nanodiamond, *Diamond Relat. Mater.* 16 (12) (2007) 2018–2022.
- [34] O.A. Williams, M. Nesladek, M. Daenen, S. Michaelson, A. Hoffman, E. Osawa, et al., Growth, electronic properties and applications of nanodiamond, *Diamond Relat. Mater.* 17 (7–10) (2008) 1080–1088.
- [35] O.A. Williams, O. Douhéret, M. Daenen, K. Haenen, E. Ōsawa, M. Takahashi, Enhanced diamond nucleation on monodispersed nanocrystalline diamond, *Chem. Phys. Lett.* 445 (4–6) (2007) 255–258.
- [36] A. Pentecost, S. Gour, V. Mochalin, I. Knoke, Y. Gogotsi, Deaggregation of nanodiamond powders using salt- and sugar-assisted milling, *ACS Appl. Mater. Interfaces* 2 (11) (2010) 3289–3294.
- [37] J.-C. Arnault, T. Petit, H. Girard, A. Chavanne, C. Gesset, M. Sennour, et al., Surface chemical modifications and surface reactivity of nanodiamonds hydrogenated by CVD plasma, *Phys. Chem. Chem. Phys.* 13 (24) (2011) 11481–11487.
- [38] O.A. Williams, J. Hees, C. Dieker, W. Jager, L. Kirste, C.E. Nebel, Size-dependent reactivity of diamond nanoparticles, *ACS Nano* 4 (8) (2010) 4824–4830.
- [39] K. Xu, Q. Xue, A new method for deaggregation of nanodiamond from explosive detonation: graphitization-oxidation method, *Phys. Solid State* 46 (4) (2004) 649–650.
- [40] I.P. Chang, K.C. Hwang, J.-A.A. Ho, C.-C. Lin, R.J.R. Hwu, J.-C. Horng, Facile surface functionalization of nanodiamonds, *Langmuir* 26 (5) (2009) 3685–3689.
- [41] X. Xu, Z. Yu, Y. Zhu, B. Wang, Influence of surface modification adopting thermal treatments on dispersion of detonation nanodiamond, *J. Solid State Chem.* 178 (3) (2005) 688–693.
- [42] O. Shenderova, I. Petrov, J. Walsh, V. Grichko, V. Grishko, T. Tyler, et al., Modification of detonation nanodiamonds by heat treatment in air, *Diamond Relat. Mater.* 15 (11–12) (2006) 1799–1803.
- [43] Y. Liang, T. Meinhardt, G. Jarre, M. Ozawa, P. Vrdoljak, A. Schöll, et al., Deagglomeration and surface modification of thermally annealed nanoscale diamond, *J. Colloid Interface Sci.* 354 (1) (2011) 23–30.
- [44] V.N. Mochalin, O. Shenderova, D. Ho, Y. Gogotsi, The properties and applications of nanodiamonds, *Nat. Nano* 7 (1) (2012) 11–23.
- [45] N. Mohan, C.-S. Chen, H.-H. Hsieh, Y.-C. Wu, H.-C. Chang, *In vivo* imaging and toxicity assessments of fluorescent nanodiamonds in *Caenorhabditis elegans*, *Nano Lett.* 10 (9) (2010) 3692–3699.
- [46] H. Huang, E. Pierstorff, E. Osawa, D. Ho, Active nanodiamond hydrogels for chemotherapeutic delivery, *Nano Lett.* 7 (11) (2007) 3305–3314.

- [47] D. Ho, Beyond the sparkle: the impact of nanodiamonds as biolabeling and therapeutic agents, *ACS Nano* 3 (12) (2009) 3825–3829.
- [48] M. Chen, E.D. Pierstorff, R. Lam, S.-Y. Li, H. Huang, E. Osawa, et al., Nanodiamond-mediated delivery of water-insoluble therapeutics, *ACS Nano* 3 (7) (2009) 2016–2022.
- [49] R. Lam, M. Chen, E. Pierstorff, H. Huang, E. Osawa, D. Ho, Nanodiamond-embedded microfilm devices for localized chemotherapeutic elution, *ACS Nano* 2 (10) (2008) 2095–2102.
- [50] J. Rubio-Retama, J. Hernando, B. López-Ruiz, A. Härtl, D. Steinmüller, M. Stutzmann, et al., Synthetic nanocrystalline diamond as a third-generation biosensor support, *Langmuir* 22 (13) (2006) 5837–5842.
- [51] P.K. Ang, K.P. Loh, T. Wohland, M. Nesladek, E. Van Hove, Supported lipid bilayer on nanocrystalline diamond: dual optical and field-effect sensor for membrane disruption, *Adv. Funct. Mater.* 19 (1) (2009) 109–116.
- [52] X.Q. Zhang, M. Chen, R. Lam, X.Y. Xu, E. Osawa, D. Ho, Polymer-functionalized nanodiamond platforms as vehicles for gene delivery, *ACS Nano* 3 (9) (2009) 2609–2616.
- [53] M. Chen, X.-Q. Zhang, H.B. Man, R. Lam, E.K. Chow, D. Ho, Nanodiamond vectors functionalized with polyethylenimine for siRNA delivery, *J. Phys. Chem. Lett.* 1 (21) (2010) 3167–3171.
- [54] A. Alhaddad, M.-P. Adam, J. Botsoa, G. Dantelle, S. Perruchas, T. Gacoin, et al., Nanodiamond as a vector for siRNA delivery to Ewing sarcoma cells, *Small* 7 (21) (2011) 3087–3095.
- [55] L.M. Manus, D.J. Mastarone, E.A. Waters, X.-Q. Zhang, E.A. Schultz-Sikma, K.W. MacRenaris, et al., Gd(III)-nanodiamond conjugates for MRI contrast enhancement, *Nano Lett.* 10 (2) (2009) 484–489.
- [56] A.P. Puzyr, A.V. Baron, K.V. Purtov, E.V. Bortnikov, N.N. Skobelev, O.A. Moginaya, et al., Nanodiamonds with novel properties: a biological study, *Diamond Relat. Mater.* 16 (12) (2007) 2124–2128.
- [57] E. Perevedentseva, P.J. Cai, Y.C. Chiu, C.L. Cheng, Characterizing protein activities on the lysozyme and nanodiamond complex prepared for bioapplications, *Langmuir* 27 (3) (2011) 1085–1091.
- [58] T.T.-B. Nguyen, H.-C. Chang, V.W.-K. Wu, Adsorption and hydrolytic activity of lysozyme on diamond nanocrystallites, *Diamond Relat. Mater.* 16 (4–7) (2007) 872–876.
- [59] X.L. Kong, L.C.L. Huang, C.M. Hsu, W.H. Chen, C.C. Han, H.C. Chang, High-affinity capture of proteins by diamond nanoparticles for mass spectrometric analysis, *Anal. Chem.* 77 (1) (2005) 259–265.
- [60] H.-D. Wang, C.H. Niu, Q. Yang, I. Badea, Study on protein conformation and adsorption behaviors in nanodiamond particle–protein complexes, *Nanotechnology* 22 (14) (2011).
- [61] K.-K. Liu, C. Mei-Fang, P.-Y. Chen, T.J.F. Lee, C.-L. Cheng, C.-C. Chang, et al., Alpha-bungarotoxin binding to target cell in a developing visual system by carboxylated nanodiamond, *Nanotechnology* 19 (20) (2008).
- [62] K.V. Purtov, A.I. Petunin, A.E. Burov, A.P. Puzyr, V.S. Bondar, Nanodiamonds as carriers for address delivery of biologically active substances, *Nanoscale Res. Lett.* 5 (3) (2010) 631–636.
- [63] W.S. Yeap, Y.Y. Tan, K.P. Loh, Using detonation nanodiamond for the specific capture of glycoproteins, *Anal. Chem.* 80 (12) (2008) 4659–4665.

- [64] L. Wei, W. Zhang, H. Lu, P. Yang, Immobilization of enzyme on detonation nanodiamond for highly efficient proteolysis, *Talanta* 80 (3) (2010) 1298–1304.
- [65] H. Huang, E. Pierstorff, E. Osawa, D. Ho, Protein-mediated assembly of nanodiamond hydrogels into a biocompatible and biofunctional multilayer nanofilm, *ACS Nano* 2 (2) (2008) 203–212.
- [66] H.-D. Wang, Q. Yang, C.H. Niu, I. Badea, Protein-modified nanodiamond particles for layer-by-layer assembly, *Diamond Relat. Mater.* 20 (8) (2011) 1193–1198.
- [67] Y.L. Liu, K.W. Sun, Protein functionalized nanodiamond arrays, *Nanoscale Res. Lett.* 5 (6) (2010) 1045–1050.
- [68] M. Chen, H. Huang, E. Pierstorff, E. Shin, E. Robinson, D. Ho, Parylene-encapsulated copolymeric membranes as localized and sustained drug delivery platforms, *Ann. Biomed. Eng.* 37 (10) (2009) 2003–2017.
- [69] E. Pierstorff, R. Lam, D. Ho, Nanoscale architectural tuning of parylene patch devices to control therapeutic release rates, *Nanotechnology* 19 (44) (2008).
- [70] E.M. Robinson, R. Lam, E.D. Pierstorff, D. Ho, Localized therapeutic release via an amine-functionalized poly-*p*-xylene microfilm device, *J. Phys. Chem. B* 112 (37) (2008) 11451–11455.
- [71] X.C. Xiao, J. Wang, C. Liu, J.A. Carlisle, B. Mech, R. Greenberg, et al., *In vitro* and *in vivo* evaluation of ultrananocrystalline diamond for coating of implantable retinal microchips, *J. Biomed. Mater. Res. Part B* 77B (2) (2006) 273–281.
- [72] R.J. Narayan, W. Wei, C. Jin, M. Andara, A. Agarwal, R.A. Gerhardt, et al., Microstructural and biological properties of nanocrystalline diamond coatings, *Diamond Relat. Mater.* 15 (11–12) (2006) 1935–1940.
- [73] P. Bajaj, D. Akin, A. Gupta, D. Sherman, B. Shi, O. Auciello, et al., Ultrananocrystalline diamond film as an optimal cell interface for biomedical applications, *Biomed. Microdevices* 9 (6) (2007) 787–794.
- [74] K.F. Chong, K.P. Loh, S.R.K. Vedula, C.T. Lim, H. Sternschulte, D. Steinmuller, et al., Cell adhesion properties on photochemically functionalized diamond, *Langmuir* 23 (10) (2007) 5615–5621.
- [75] M. Amaral, P.S. Gomes, M.A. Lopes, J.D. Santos, R.F. Silva, M.H. Fernandes, Cytotoxicity evaluation of nanocrystalline diamond coatings by fibroblast cell cultures, *Acta Biomater.* 5 (2) (2009) 755–763.
- [76] B. Shi, Q. Jin, L. Chen, O. Auciello, Fundamentals of ultrananocrystalline diamond (UNCD) thin films as biomaterials for developmental biology: embryonic fibroblasts growth on the surface of (UNCD) films, *Diamond Relat. Mater.* 18 (2–3) (2009) 596–600.
- [77] R.A. Shimkunus, E. Robinson, R. Lam, S. Lu, X. Xu, X.-Q. Zhang, et al., Nanodiamond–insulin complexes as pH-dependent protein delivery vehicles, *Biomaterials* 30 (29) (2009) 5720–5728.
- [78] H. Huang, M. Chen, P. Bruno, R. Lam, E. Robinson, D. Gruen, et al., Ultrananocrystalline diamond thin films functionalized with therapeutically active collagen networks, *J. Phys. Chem. B* 113 (10) (2009) 2966–2971.
- [79] W. Kulisch, C. Popov, D. Gilliland, G. Ceccone, J.P. Reithmaier, F. Rossi, UNCD/a-C nanocomposite films for biotechnological applications, *Surf. Coat Tech.* 206 (4) (2011) 667–675.
- [80] L. Ivanova, C. Popov, I. Kolev, B. Shivachev, J. Karadjov, M. Tarassov, et al., Nanocrystalline diamond containing hydrogels and coatings for acceleration of osteogenesis, *Diamond Relat. Mater.* 20 (2) (2011) 165–169.

- [81] J.A. Roth, R.J. Cristiano, Gene therapy for cancer: what have we done and where are we going?, *J. Natl. Cancer Inst.* 89 (1) (1997) 21–39.
- [82] C.C. Fu, H.Y. Lee, K. Chen, T.S. Lim, H.Y. Wu, P.K. Lin, et al., Characterization and application of single fluorescent nanodiamonds as cellular biomarkers, *Proc. Natl. Acad. Sci. U.S.A.* 104 (3) (2007) 727–732.
- [83] J.-I. Chao, E. Perevedentseva, P.-H. Chung, K.-K. Liu, C.-Y. Cheng, C.-C. Chang, et al., Nanometer-sized diamond particle as a probe for biolabeling, *Biophys. J.* 93 (6) (2007) 2199–2208.
- [84] J.-P. Boudou, P.A. Curmi, F. Jelezko, J. Wrachtrup, P. Aubert, M. Sennour, et al., High yield fabrication of fluorescent nanodiamonds, *Nanotechnology* 20 (35) (2009) 235602.
- [85] Y.-R. Chang, H.-Y. Lee, K. Chen, C.-C. Chang, D.-S. Tsai, C.-C. Fu, et al., Mass production and dynamic imaging of fluorescent nanodiamonds, *Nat. Nanotechnol.* 3 (5) (2008) 284–288.
- [86] C. Bradac, T. Gaebel, N. Naidoo, M.J. Sellars, J. Twamley, L.J. Brown, et al., Observation and control of blinking nitrogen-vacancy centres in discrete nanodiamonds, *Nat. Nano* 5 (5) (2010) 345–349.
- [87] G. Dantelle, A. Slablab, L. Rondin, F. Lainé, F. Carrel, P. Bergonzo, et al., Efficient production of NV colour centres in nanodiamonds using high-energy electron irradiation, *J. Lumin.* 130 (9) (2010) 1655–1658.
- [88] E. Ōsawa, D. Ho, H. Huang, M.V. Korobov, N.N. Rozhkova, Consequences of strong and diverse electrostatic potential fields on the surface of detonation nanodiamond particles, *Diamond Relat. Mater.* 18 (5–8) (2009) 904–909.
- [89] V. Vijayanthimala, Y.-K. Tzeng, H.-C. Chang, C.-L. Li, The biocompatibility of fluorescent nanodiamonds and their mechanism of cellular uptake, *Nanotechnology* 20 (42) (2009) 425103.
- [90] E.A. Rakha, M.E. El-Sayed, A.R. Green, A.H. Lee, J.F. Robertson, I.O. Ellis, Prognostic markers in triple-negative breast cancer, *Cancer* 109 (1) (2007) 25–32.
- [91] S.W. Jang, M. Wientjes, D. Lu, S. Au, Drug delivery and transport to solid tumors, *Pharm. Res.* 20 (2003) 1337–1350.
- [92] M.L. Schipper, G. Iyer, A.L. Koh, Z. Cheng, Y. Ebenstein, A. Aharoni, et al., Particle size, surface coating, and PEGylation influence the biodistribution of quantum dots in living mice, *Small* 5 (1) (2009) 126–134.

Characterization of Detonation Nanodiamonds for Biocompatibility

16

Amanda M. Schrand^a and Jonathan B. Lin^b

^a*Air Force Research Laboratory, Munitions Directorate Eglin AFB, Eglin, FL*

^b*Department of Neuroscience and Behavioral Biology, Emory University, Atlanta, GA*

CHAPTER OUTLINE

16.1	Introduction.....	519
16.2	Worker, patient, and environmental safety: priorities	520
16.3	Methods for studying biocompatibility at the cellular and organism levels	522
16.4	Factors influencing nanoparticle biocompatibility	526
16.5	Studies of ND biocompatibility.....	526
16.5.1	Biological peculiarities of carbon nanoparticles	526
16.5.2	Historical perspective on diamond particle biocompatibility studies	529
16.5.3	ND property-biocompatibility relationship: <i>in vitro</i> studies.....	529
16.5.4	ND size studies.....	530
16.5.5	Influence of ND surface chemistry and contaminants	530
16.5.6	ND intracellular localization and kinetics: an important consideration for long-term biocompatibility	531
16.6	<i>In vivo</i> considerations for ND biocompatibility	534
16.7	Future goals for biological assessment of NDs.....	538
	References	540

16.1 Introduction

There has been an explosion of potential applications for nanodiamonds (NDs) due to their large-scale production [1] and commercial availability (Diamond Center, PlasmaChem) in designer forms. However, it is the purity, fluorescence, variety of surface modifications, and high biocompatibility that have contributed to their popularity among other carbon nanoparticles. Indeed, NDs can maintain most, if

not all, of their inherently desirable properties upon surface functionalization (such as fluorescence and biocompatibility) in contrast to many other forms of carbon or more traditional nanoparticles such as semiconductor quantum dots (see recent reviews in Refs. [2–5]). Furthermore, they can be imaged with multiple modalities including Raman spectroscopy, fluorescent confocal microscopy, and electron microscopy [6–9]. It is the goal of this chapter to review the current literature on ND biocompatibility by first prefacing the ultimate goal of biocompatibility studies, to better understand the benefits and risks of nanoparticles to workers, patients, and the environment. The remainder of the chapter will address the current methods for studying biocompatibility as well as a historical perspective of diamond in foreign particle and inflammatory response. The reader will be presented with an overview of factors influencing nanoparticle biocompatibility followed by specific factors responsible for ND biocompatibility through the exploration of *in vitro* and *in vivo* data. The conclusion of the chapter will suggest future considerations for biological assessment and important biological implications that may be encountered during the quest for the most effective use of NDs for any purpose. For a more thorough review of ND properties and perspectives for bioapplications, see Ref. [3].

16.2 Worker, patient, and environmental safety: priorities

Due to the vast array of compositions and surface properties, the biological effects of nanoparticles have received attention from several U.S. government regulatory agencies, such as the Environmental Protection Agency (EPA), Food and Drug Administration (FDA), National Institute for Occupational Safety and Health (NIOSH), and Occupational Safety and Health Administration (OSHA). These government agencies, along with public and private organizations, are working closely with scientists to establish safety guidelines and advance the understanding of nanoparticles for the larger global aim of producing sustainable and significant advances for humankind. Although the beneficial effects of nanoparticles are not typically incorporated as part of the risk assessment process, sharing these findings would be beneficial to the scientific community. For example, proposed mechanisms responsible for the positive health effects of ND include (1) its ability to act as a polyradical cluster and regulate free radical processes due to its abundance of unpaired electrons [10–12] and (2) the strong adsorption characteristics [13] and hydrophilic surface groups ($-\text{OH}$, $-\text{NH}_2$, $-\text{C}(\text{O})\text{NH}_2$), which actively adsorb pathogenic viruses and other microorganisms.

The establishment of exposure limits and appropriate doses is a prerequisite for understanding undesirable attributes, properly disposing of waste products, and limiting their impact on microorganisms and plants [14–16]. With this said, the disease potential of supposedly biocompatible nanoparticles in individuals with existing medical conditions can still be high, and there can be an increased susceptibility to disease after exposure to nanoparticles [17]. For example, the link between particulate air pollution and increased cardiovascular morbidity and mortality is well documented, where increases in respirable particulate matter have been associated

with increased plasma viscosity, changes in blood parameters (i.e., fibrinogen, red blood cell counts), arterial vasoconstriction, and increased heart rate variability [18]. Furthermore, multiple avenues for nanoparticle administration and exposure may require specific limits. For example, the LD₅₀ oral value in rats was >7000 mg/kg (compared with an LD₅₀ of 3000 mg/kg for sodium chloride orally administered to rats), but the dermal and injection limits are virtually unknown [19]. Therefore, lessons learned in the medical community with regard to particulates should be tested alongside the laboratory experiments for additional insight.

The strong potential benefits of NDs for medical purposes warrant special consideration of long-term consequences related to the route of administration, localization, clearance, and bio-persistence within the body. In medicinal preparations used for oncology, gastroenterology, or dermatology (burns, skin diseases), NDs can be used as additives to intensify the action of other components. Already purified NDs have been shown to normalize blood pressure, detoxify the gastrointestinal system, and remedy cancerous conditions [19]. The effective coupling of biocompatible NDs to enzymes or drugs has been shown to effectively kill bacteria [20] or cancer cells [21] (see Ref. [3] and Chapter 15 for more information). Therefore, the attachment of bioactive molecules to any of the variety of ND forms (i.e., substrate, film, or particulate) can lead to a profound effect on ND distribution, targeting, and medicinal effectiveness throughout the body (Figure 16.1).

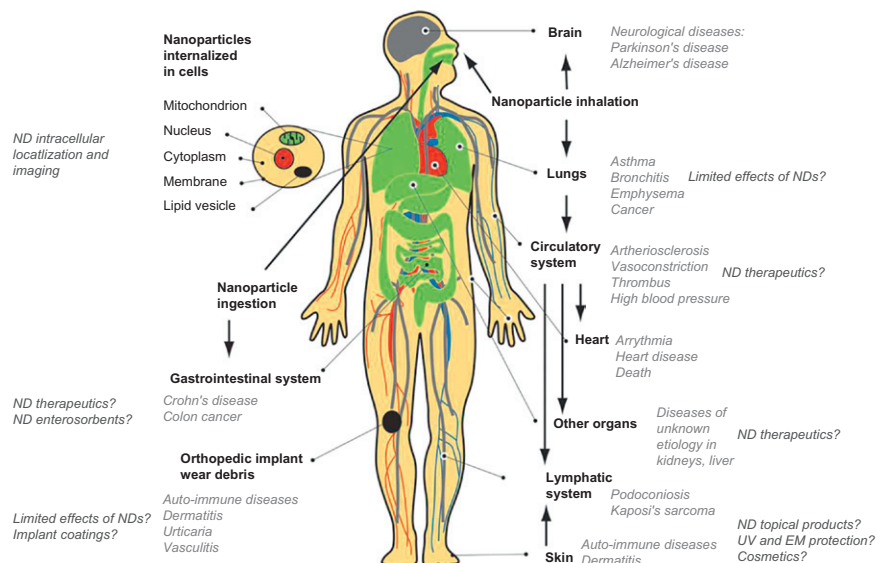


FIGURE 16.1

Schematic of human body with pathways of exposure for nanoparticles, affected organs, and associated diseases from epidemiological *in vivo* and *in vitro* studies.

Source: Adapted from [165] with permission.

From an environmental safety and utility perspective, NDs may serve multiple purposes. For example, the synthesis of NDs can be accomplished from molecules of explosives, even utilizing old munitions, such as composition B, which provide both a source of carbon and energy for the conversion. This can be considered an environmentally friendly and economically viable method for recycling munitions. The detonation takes place in a closed chamber filled with an inert gas or water (ice) coolant, called “dry” or “wet” synthesis, respectively. The resultant product, detonation soot, is a mixture of diamond particles 4–5 nm in diameter with other carbon allotropes and impurities [22] (see Chapter 5 for more information). Other uses of NDs for environmental remediation can include water purification similar to other active carbons [23].

It cannot be emphasized enough that the number of outstanding questions regarding long-term nanoparticle safety and biomedical use has greatly outweighed firm answers. Therefore, the intentional assessment of nanoparticle properties throughout their life cycle, including alterations in their properties upon incorporation into substrates [24], nanocomposites [25,26], and fluids, will provide the most relevant safe handling and clinical information. Understanding the benefits and risks is the utmost priority for personnel working with NDs (and other nanoparticles) as well as prospective patients. Taking into account these considerations, the remainder of the chapter will cover the established methods, historical context, and current understanding of the factors responsible for the biocompatibility of NDs.

16.3 Methods for studying biocompatibility at the cellular and organism levels

The evaluation of possible detrimental health consequences or potential therapeutic applications of nanoparticles is routinely performed with both *in vitro* cell cultures and *in vivo* animal studies [27,28]. *In vitro* studies rapidly and inexpensively provide an initial assessment of biocompatibility and carrier efficiency (i.e., drugs and fluorescent labels) in cell models. Cells used in *in vitro* studies may represent likely routes of nanoparticle (NP) exposure and have included alveolar macrophages (respiratory inhalation), keratinocytes and fibroblasts (integument breach), neuroblastoma or PC-12 cells (nervous system translocation), blood cells (platelets, neutrophils, monocytes), and epithelial cells (circulatory injection) or particular cancer cells [155] (HeLa, A549 human lung carcinoma cells, HT-29 human colorectal adenocarcinoma cells, Ewing’s sarcoma, etc). Therefore, the choice of cell type in biocompatibility studies may be based upon the ability of nanoparticles to interfere with or contribute to an immune response at the site of exposure (i.e., keratinocytes in the epidermis) or for targeting of the nanoparticles to certain locations to aid in recovering normal function (i.e., destruction of cancer cells).

The primary assay that has been used to evaluate cell health after exposure to nanoparticles is the (3-(4,5-Dimethylthiazon-2-yl)-2,5-diphenyltetrazolium bromide) (MTT) assay. The ability of mitochondria in living cells to chemically reduce a tetrazolium salt, thereby changing its color from yellow to purple, provides a method to spectroscopically monitor reductions in cell viability after nanoparticle

exposure compared to untreated cells. Similar tetrazolium dye assays include (2,3-bis[2-methoxy-4-nitro-5-sulfophenyl]-2H-tetrazolium-5-carboxanilide) (XTT) and 4-[3-(4-iodophenyl)-2-(4-nitrophenyl)-2H-5-tetrazolio]-1,3-benzene disulfonate (WST). Other complementary methods of evaluating the cellular effects of nanoparticles include, but are not limited to, morphological examination, trypan blue dye exclusion, neutral red uptake by lysosomes (neutral red (NR) assay), thymidine uptake, propidium iodide staining, cell counts, reactive oxygen species (ROS) production, cellular permeability barrier breakdown (i.e., lactase dehydrogenase assay), mitochondrial membrane permeability, chemiluminescent luminole reaction measurement, glutathione alterations (i.e., glutathione (GSH)), genetic analyses, protein expression, and activation of proinflammatory cytokines (i.e., interleukin (IL)-6, IL-8, tumor necrosis factor (TNF)- α) [24] (Table 16.1). Additionally, characterization of the pathways for ND internalization, degradation, and release at the cellular level contribute to understanding biocompatibility. Examples of nanoparticle uptake mechanisms

Table 16.1 Physicochemical Properties of NDs for Biomedical Applications

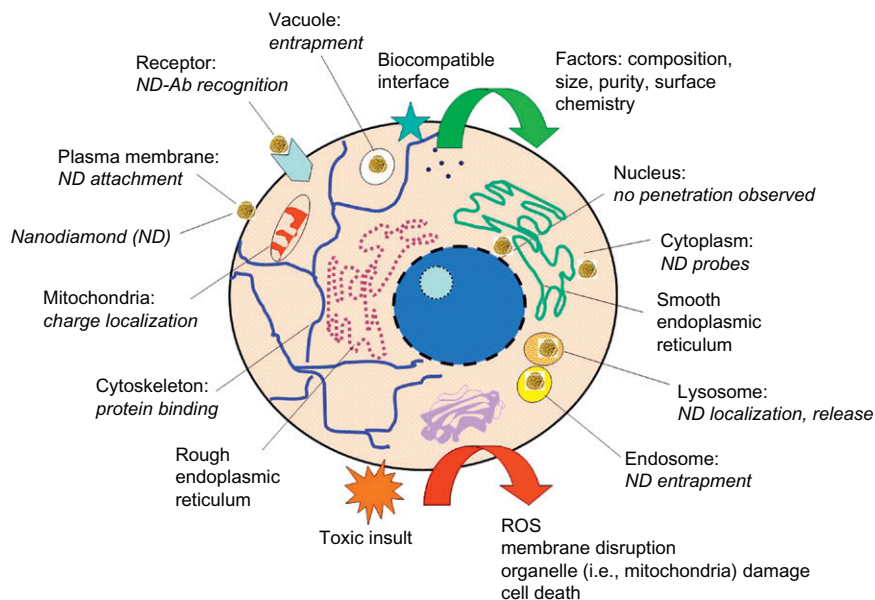
Property	Characteristics	Application/Benefit
Structural	Small size of primary monocrystalline particles (~2–10 nm)	Unique interactions with bio-compounds on same size scale
	Availability of variable sizes and narrow size fractions	Diverse applications based on size (UV protection, photonic structures)
	Different forms (i.e., particulate, coating/film, substrate)	Tailorability for different bio-environments
	Large specific surface area (300–400 m ² /g)	High affinity/adsorption capacity for binding proteins, enzymes; enterosorbents, purification
	Low porosity/permeability of films	Component of small pore membranes for ultrafiltration or nonporous membrane for extended time storage
Chemical	High specific gravity (3.5 g/cm ³)	Dense structure for solid phase support
	Chemically resistant to degradation/corrosion, pH stability	Implants, coatings, films, substrates for cell growth
	High chemical purity	Biocompatible interface
	Possible sp ² carbon shells	Adsorption of hydrophobic biomolecules; electromagnetic (EM) radiation absorption for thermal therapy
	Numerous oxygen containing groups on surface	Hydrophilic, water-dispersible suspensions for further coupling to bio-entities/into other matrices

(Continued)

Table 16.1 Physicochemical Properties of NDs for Biomedical Applications
(Continued)

Property	Characteristics	Application/Benefit
Biological	Ease of surface functionalization (chemical, photochemical, mechanochemical, enzymatic, plasma- and laser-assisted methods)	Attachment of drugs and biomolecules; polymer, metal composite materials
	Radiation/ozone resistance	X-ray, protective coatings and surfaces, detection devices
	Large number of unpaired electrons on the surface	Free radical scavenger/multiple radical donor; electrochemistry
	High biocompatibility, low toxicity	Cell, tissue, organ, and organism studies
Optical	Readily bind bioactive substances (i.e., proteins, DNA) with retained functionality	Targeted therapeutics/ molecules, labels, hormones, inhibitors, antigens, drugs
	Solid phase carrier	Multiple cell delivery methods including ballistic, transfection
	Photoluminescence: nonphotobleaching, nonblinking, originates from nitrogen-vacancy defects	Fluorescent probe and imaging tool for biolabeling
Mechanical	High refractive index, optical transparency	Scattering optical label for live cells, possible UV sunscreen
	Unique Raman spectral signal	Nondestructive detection with living cells
	High strength and hardness	Composite additive; possible cell lysis; ballistic delivery to tissues and cells; autoclaving
Electrochemical	Fine abrasive	Homogenization of composites/ cosmetics, skin polishing
	Electrochemical plating with metals	Improves durability, life of medical instruments/implants
	Redox behavior of DND	Chem/biosensors; potential production of ROS
Thermal	Can withstand very high/low temperatures	Sterilization (i.e., autoclave), composite manufacturing, liquid nitrogen storage
Technical	Inexpensive, mass production (i.e., detonation synthesis)	Commercial availability
	Exist naturally in meteorites and laboratory synthesized by diverse techniques	Availability of various quality/ purity samples

Adapted from Ref. [3].

**FIGURE 16.2**

Schematic representation of a mammalian cell showing some possible interactions with ND particles including surface binding, intracellular entrapment, and localization resulting in biocompatibility or toxic effects.

Source: Reproduced with permission from Ref. [3].

include temperature/energy-dependent endocytosis [29,30] and nonphagocytic uptake mechanisms based on diffusion or adhesive interactions [31] as well as other nonspecific uptake mechanisms including pinocytosis, patocytosis, or membrane ruffling that may unsuspectingly traffic nanoparticles into cells. Therefore, at the cellular level, inflammatory responses are characterized by interactions with and uptake into cells, damage to lysosomal membranes, leakage of lytic enzymes, and increased expression of proinflammatory mediators and cytokines. Correspondingly, the generation of ROS and subsequent oxidative stress [32] is the leading mechanistic paradigm to explain the toxic efforts of nanoparticles (Figure 16.2).

The choice of animal for studies of nanoparticle biocompatibility may be influenced by several factors including genetic similarity to humans, size, cost, ease of handling, and reproduction rate. However, neither *in vitro* nor *in vivo* studies can ultimately predict the consequences of some drugs and chemicals in humans, which can produce unique effects even among different rodent species. [33–36]. For example, rat studies have shown that nanoparticles can translocate from the lungs to the blood circulation and other organs, while most of the human studies of short-term exposure to carbon nanoparticles have not [37]. Additional differences in the breathing patterns and the structure of the respiratory tract between rodents and humans result in differences in delivered dose to the upper and lower airways [157].

16.4 Factors influencing nanoparticle biocompatibility

There is evidence that smaller, nanosized particles induce greater toxicity compared to larger or soluble materials of identical composition [38–41]. In addition to their small size, a multitude of other physicochemical properties have been implicated in the distinct biological effects of nanoparticles. For example, the synthesis, purification (typically oxidation using liquid or ozone-enriched air) and functionalization conditions can alter biocompatibility in addition to size, shape (i.e., carbon nanotubes versus nano-onions or nanohorns; TiO₂ rods versus dots, Au spheres versus rods), surface charge, elemental impurities/release of soluble impurities, surface defects/terminations, crystal structure (i.e., TiO₂ anatase versus rutile or amorphous versus crystalline SiO₂), surface chemistry (i.e., hydrophilic versus hydrophobic), porosity as well as macro- and microstructure (i.e., ropes, aggregates) of the final product [38,42–60,158–160]. Therefore, during the pursuit for novel uses of nanoparticles, it is imperative to independently assess the biocompatibility of nanosized particles even if materials of similar composition are currently being used in biomedical applications.

16.5 Studies of ND biocompatibility

16.5.1 Biological peculiarities of carbon nanoparticles

In contrast to the historical perspective that carbon-based materials present minimal reactivity toward cells of the body [61], nanosized carbons are characterized by very small sizes, high surface-to-volume ratios, and reactive surface chemistries, which can impact cellular permeability and dynamics [62,63]. However, not all carbon-based nanoparticles present similar biocompatibility profiles. For example, Schrand et al. [64] demonstrated differential biocompatibility between neuronal and lung cell lines after exposure to aqueous suspensions of carbon nanoparticles (ND, carbon black (CB), multi-walled carbon nanotube (MWNT), single-walled carbon nanotube (SWNT)) at concentrations from 25 to 100 µg/ml for 24 h with the MTT assay. The trend for biocompatibility was ND>CB>MWNT>SWNT. The lung cells (macrophages) were more greatly affected by the presence of carbon nanoparticles generating up to five times the amount of ROS compared to the neuroblastoma cells after exposure to either MWNTs or SWNTs. However, there was a lack of ROS generation from either cell line after incubation with the NDs as well as intact mitochondrial membranes further supporting the low toxicity of NDs. These studies suggest a complex role for cell-specific responses and purity (i.e., residual catalyst content) in the inflammatory response as well as other factors that may be related to dispersion/aggregation dynamics. By comparison, the incubation of fluorescently labeled NDs (5–100 µg/ml, 24 h) with three different cell types revealed no significant differences in biocompatibility compared to control cells (MTT assay) (Figure 16.3A). The different cell lines were representative of both rodent and human cell lines including murine neuroblastoma (N2A), human skin cells

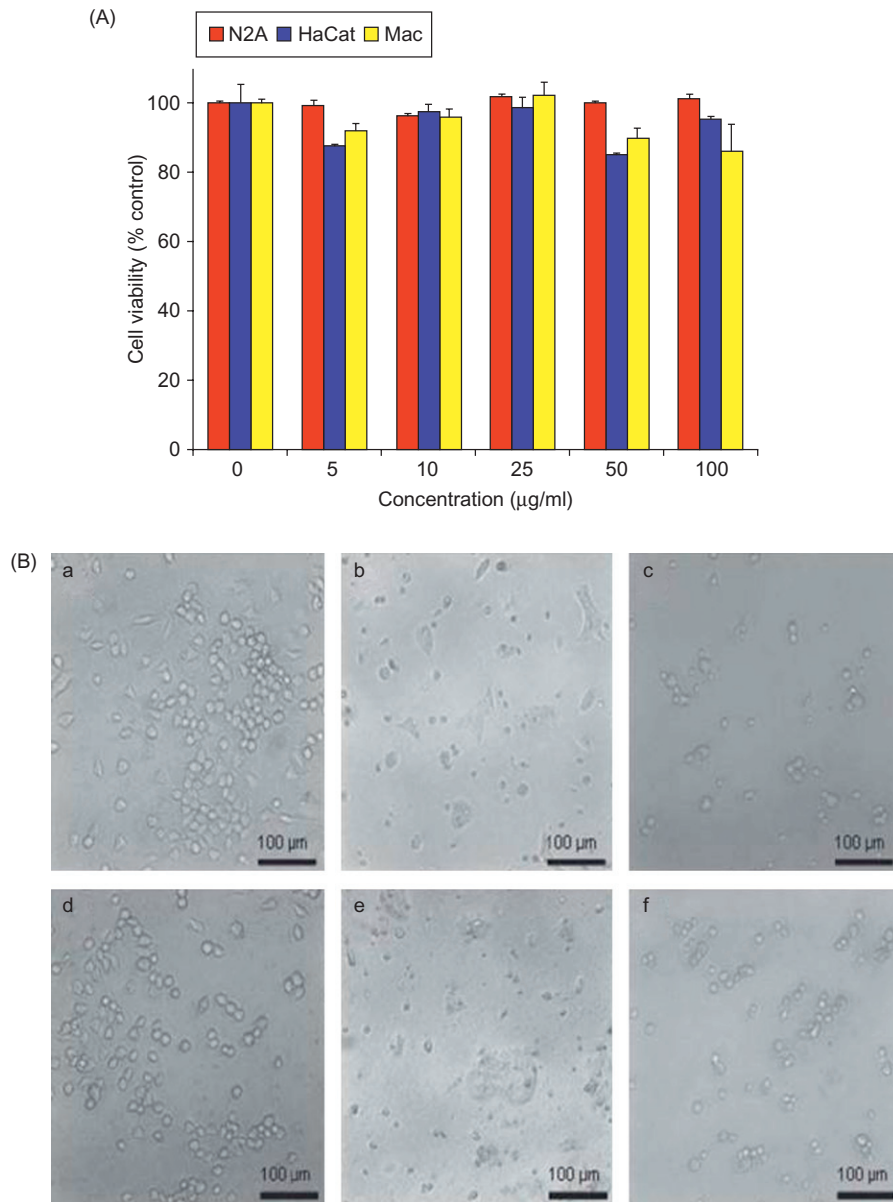


FIGURE 16.3

(A) MTT viability assessment and morphological evaluation of N2A, HaCat, and macrophage cells after 24 h of incubation with 0–100 mg/ml of ND-T. Triplicate experiments show no significant difference in viability after exposure to ND-T compared to untreated controls. (B) Phase contrast light microscopy of (a, c, and e) controls and (b, d, and f) cells incubated with 100 mg/ml ND-T. (a and b) N2A cells, (c and d) HaCat cells, and (e and f) macrophages. There were no morphological changes compared to the controls.

Source: Reproduced with permission from Ref. [9].

(HaCat), and rat alveolar macrophage (CRL-2192). Additionally, morphological examination did not show any alterations in cell shape compared to the controls (Figure 16.3B).

Although there has been no direct link between the primary dimension of carbon nanoparticles and their resultant biocompatibility, Jia et al. [65] found that the toxicity of carbon nanoparticles followed a mass sequence of biocompatibility with C60 > quartz > MWNT > SWNT in alveolar macrophages after exposure for 6 h. By comparison, Grabinski et al. [66] found that larger carbon fibers or carbon nanofibers were more biocompatible than MWNTs or SWNTs in mouse keratinocytes (HEL-30). Smaller-sized carbon black (14 nm) compared to larger-sized carbon black (260 nm) increased the production of ROS and MIP2 mRNA expression [161,162]. In contrast, other studies have shown that smaller or shorter carbon nanotubes were more biocompatible than larger-sized carbon nanotubes or carbon fibers [67–70].

The examination of carbon nanoparticles with regard to both size and surface chemistry was studied by Liu et al. [71]. They examined the biocompatibility of carboxylated and uncarboxylated NDs and carbon nanotubes (CNTs) in human lung A549 epithelial cells and HFL-1 normal fibroblasts [71]. Treatment with ND or carboxylated ND (cND, 5 and 100 nm) at concentrations ranging from 0.1 to 100 µg/ml for 4 h followed by recovery for 24–48 h did not affect the overall cell morphology including the cytoskeleton or nuclei, did not reduce cell viability per the MTT assay, and did not alter the expression of protein extracts via sodium dodecyl sulfate-polyacrylamide gel electrophoresis (SDS-PAGE) analysis. The smaller 5 nm cNDs slightly reduced viability compared to the larger 100 nm cNDs, but with no significance. In contrast, uncarboxylated CNTs (10–50 nm and 100–200 nm) significantly decreased cell viability at concentrations as low as 0.1 µg/ml in A549 cells, or 1 µg/ml in HFL-1 cells, compared to concentrations greater than 10 µg/ml for carboxylated CNTs (cCNTs). There was also a more pronounced cytotoxic effect for the longer 100–200 nm cCNTs compared to the shorter 10–50 nm cCNTs [71].

Therefore, to date, research shows that when compared side-by-side to other carbon nanomaterials (carbon nanotubes, fullerenes), NDs are consistently better tolerated by cells [59,60,64,66,67,72–80]. One major factor in the variability between studies is the purity of the samples. Impurities (or contaminants) such as residual metal catalysts (i.e., Fe, Ni, Co) in carbon nanotubes, and other materials containing Fe and transition metals [81–83], are now routinely screened prior to and during toxicity studies. Although NDs are not synthesized via metal catalysts, metal contaminants are introduced from the containers used for the detonation of ND, which must be removed by postsynthesis purification procedures [84]. For example, some initial ND powders contained ~5.7% Fe, which was reduced to ~1.2% Fe ([85]; see Chapter 5).

It is the aim of the following sections to summarize the properties that contribute to a biocompatible interface between NDs and cells in culture or after various routes of administration to animals. Factors such as particle size, concentration, exposure time, and cell-type specific responses will be examined with an appropriate comparison between micron-sized diamond particles and nanosized diamond particles.

16.5.2 Historical perspective on diamond particle biocompatibility studies

Due to its low reactivity, diamond was frequently chosen as an inert, negative control particle in many early scientific studies examining possible links between particulate wear debris from implantable materials or coatings and respirable dusts (i.e., asbestos, quartz) and disease conditions (i.e., inflammation, arthritis, fibrosis). For example, diamond particles internalized by neutrophils resulted in no chemotactic activity [86], did not produce ROS [87,88], and had no effect on degranulation or secretion of cell motility factors [89]. *In vitro* studies of macrophages exposed to micron-sized diamond dust demonstrate that it is nonfibrogenic [90], does not affect cell viability for at least 30 h [91], and does not activate or change the cell morphology or production of interleukin 1- β [92]. In fibroblasts, micron-sized diamond particles did not induce fibrogenic activity [91,93], did not induce the release of proliferation factors [90], and had no mitogenic effect [94]. In mouse embryo 3T3 Balb/c cells or differentiated human umbilical venous endothelial cell, a variety of ceramics (Al_2O_3 , $\text{ZrO}_2/\text{Y}_2\text{O}_3$, AlN, B_4C , BN, SiC, Si_3N_4 , TiB_4 , TiC, TiN), including diamond and graphite powder, did not induce any cytotoxic effects [95]. Additionally, rabbit blood exposed to diamond powder did not produce any detectable hemolysis after 60 min although the diamond powders contained elemental impurities (0.05 wt% Al, 0.05 wt% Fe, 0.15 wt% Si, and 1.00 wt% Zr) [96]. Furthermore, these low concentrations of impurities were not cytotoxic to other cell lines in culture [95]. Therefore, these studies collectively indicate that diamond particles are not involved in a foreign particle inflammatory response.

16.5.3 ND property-biocompatibility relationship: *in vitro* studies

Although the majority of the literature, including our previous work [3,9,24,64,80], has demonstrated high biocompatibility for different types of NDs, there are some studies that have shown negative effects in blood cells and deeper at the genomic level [24,97]. Therefore, smaller, nanosized diamonds are being scrutinized for biological interactions due to their superior physicochemical properties for incorporation into cutting-edge biomedical innovations (i.e., nanosized therapeutic carriers, probes, labels) (see Ref. [3]).

By definition, well-purified NDs are almost perfect crystalline structures with negligible fractions of nondiamond carbon. They consist of polyhedra with a diamond core built up of sp^3 carbon, which may be partially coated by a graphitic shell or amorphous carbon with dangling bonds terminated by various functional groups. An additional characteristic feature of NDs are nitrogen impurities (up to 2–3 wt%), which can form complexes in the core of ND particles, and the presence of twins and grain boundaries in the crystallites [2]. A summary of ND properties for consideration in biocompatibility or toxicity studies is presented in Table 16.1.

16.5.4 ND size studies

Investigations into size-dependent biological behavior of NDs have not proven any measurable differences. For example, an early study on ND biocompatibility by Yu et al. [98] investigated relatively large synthetic abrasive diamond powders (type 1b, 100 nm, Micron+ MDA, synthesized by Element Six, acid purified) that were proton-beam irradiated to introduce very stable, bright, and internal fluorescent nitrogen-vacancy defects [98]. They found very high viability, indicative of *in vitro* biocompatibility, with human kidney cells (293T) after 3 h of incubation at concentrations up to 400 $\mu\text{g/ml}$ assessed with the MTT assay. Smaller, nonfluorescent, detonation NDs (2–10 nm, supplied by NanoCarbon Research Institute Inc.) at lower maximum concentrations ($\leq 100 \mu\text{g/ml}$) over longer periods of time (typically 24 h) were studied by Schrand et al. from 2007 to 2009 [3,24,64,80] and Huang et al. [21] in other cell lines. Liu et al. [71] found that there were slight, but not significant, reductions in cell viability after incubation with smaller 5 nm cNDs compared to larger 100 nm cNDs.

16.5.5 Influence of ND surface chemistry and contaminants

The effects of processing techniques (i.e., oxidation procedures, aggregate disintegration, and high temperature heat treatment) [67,68,72,99] on NDs should be evaluated with regard to alterations in the surface chemistry, which may impact on cellular functions (see Chapter 13). The impact of surface chemistry on 2–10 nm detonation-produced NDs, purified with strong acids or bases, on cell viability was examined by Schrand et al. [64]. At concentrations up to 100 $\mu\text{g/ml}$, all of the NDs, containing surface groups such as $-\text{COOH}$, $-\text{COONa}$, and $-\text{SO}_3\text{Na}$, were nontoxic to a variety of cell types including neuroblastomas, macrophages, PC-12 cells, and keratinocytes after 24 h with the MTT assay. The most noticeable difference between two cell types (neuroblastoma and macrophage) was in the amount of carbon nanoparticles internalized by the cells, which was likely related to the greater decreased viability and increased ROS for the macrophages. The inherent function of the macrophages to initiate an inflammatory response or programmed cell death may also occur to a greater extent in this immune cell. However, despite these proposed cell-specific differences, there was a lack of ROS generation and a retention of mitochondrial membrane integrity in cell lines incubated with NDs.

Studies on the biocompatibility of acid purified NDs in RAW 264.7 murine macrophages by Huang et al. [21] monitored the response of genes involved in inflammation including the production of three different cytokines (IL-6, $\text{TNF}\alpha$, nitric oxide synthase (iNOS)), and the Bcl-x gene involved in apoptotic behavior/toxicity. After 24–72 h of incubation with 100 $\mu\text{g/ml}$ NDs, no significant change in the expression of the cytokines was detected with the real time polymerase chain reaction (RT-PCR) compared to controls. Additional experiments examining morphological changes and DNA fragmentation in macrophages as well as viability with the MTT assay in HT-29 human colorectal adenocarcinoma cells revealed the high innate biocompatibility of the NDs.

In addition to surface chemistry alterations (see Chapter 13), other contaminants to the underlying elemental composition can include residual ceramic or other abraded material fragments from mechanical (bead milling) or ultrasonic processing for aggregate disruption (i.e., ZrO_2 in ND from stir-media milling for dispersion), fragments of graphitic/amorphous structure at grain boundaries, and ~2 wt% fullerene-like conjugated sp^2 carbon [84,100,101]. More recently, there has been progress in dry milling with water-soluble salts and sugars, which show promise as biocompatible and environmentally friendly alternatives for aggregate disruption [102]. Other considerations for effects on biocompatibility include various levels of nitrogen doping [103], or residual solvents from dispersion processes that may be inherently toxic such as tetrahydrofuran or dimethyl sulfoxide [104,105]. Functionalization of NDs with biomolecules for biological applications did not seem to induce cytotoxicity in Chinese hamster ovary (CHO) cells, and these functionalized NDs retained their ability to localize intracellularly [106].

Of concern, however, are some other studies, which have suggested that NDs may possess some deleterious effects toward biological organisms. For example, Silbajoris et al. [107] found that ND particles can induce up to 14-fold increases in IL-8 expression in human airway epithelial cells. IL-8 is a chemokine involved in the inflammatory; this upregulation implies that the ND particles retain the ability to trigger an inflammatory response when inhaled. Moreover, embryonic stem cells have been shown to yield moderately increased expression of DNA proteins, such as p53 and MOGG-1, when they are incubated with NDs [97]. This response was more pronounced when the cells were exposed to oxidized NDs rather than pure NDs, implying a role of surface chemistry. Still, these levels are much lower than those observed when cells were incubated with MWNTs, suggesting that NDs may still be the most biocompatible and promising in relation to other forms of NPs.

Studies with stable and fluorescent rhodamine-labeled NDs incubated with both animal and human cell lines did not induce morphological changes and maintained high viabilities at concentrations up to 100 $\mu\text{g}/\text{ml}$ [8,9]. Studies with fluorescently labeled NDs by Vijayanthimala et al. [108] also did not implicate any toxicity at exposures for 5 h at concentrations as high as 100–200 $\mu\text{g}/\text{ml}$ across multiple cytotoxicity endpoints. The mechanisms of uptake and intracellular localization will be examined in greater detail in the following section.

16.5.6 ND intracellular localization and kinetics: an important consideration for long-term biocompatibility

The kinetics of both nonfluorescent and fluorescent ND entry and localization inside cells has been examined with microscopic, radio-labeling, and spectroscopic techniques. Internalized ND aggregates localized within the cytoplasm, but not within the nucleus [9,98,109–111]. Recently, the authors of this review and other groups [108,112] have addressed this issue by using fluorescent NDs to track their localization into cells based on time and concentration [9]. Schrand et al. [9] initially performed transmission electron microscopy (TEM) on N2A

cells to investigate the time-dependent uptake of ND into cells as well as determine their localization prior to confocal microscopy studies. The TEM studies enabled both verification of uptake and higher resolution subcellular localization of NDs. Images in Figure 16.4 show the fluorescent NDs outside cells (white arrows), internalized into membrane-bound structures resembling early endosomes inside cells (black arrows) as well as free in the cytoplasm after lysosomal processing (Figure 16.4I). The presence of ND aggregates increases over time from 1 to 6 h (Figure 16.4A–H) compared to 24 h where larger pockets were found (Figure 16.4I–L). The ND aggregates inside the intracellular vacuoles were ~500 nm in size. Several images suggest that the NDs, after coming into contact with the cell membrane, are brought inside by an endocytic mechanism where they remain close to the edge of the membrane, but do not appear to enter the nucleus. The addition of endocytosis and exocytosis inhibitors allows for diminished uptake and increased accumulation, respectively, which further corroborates cellular behavior in response to NDs. Additionally, the degradation of the membrane-bound structure containing the NDs was found in some areas after 24 h (Figure 16.4I).

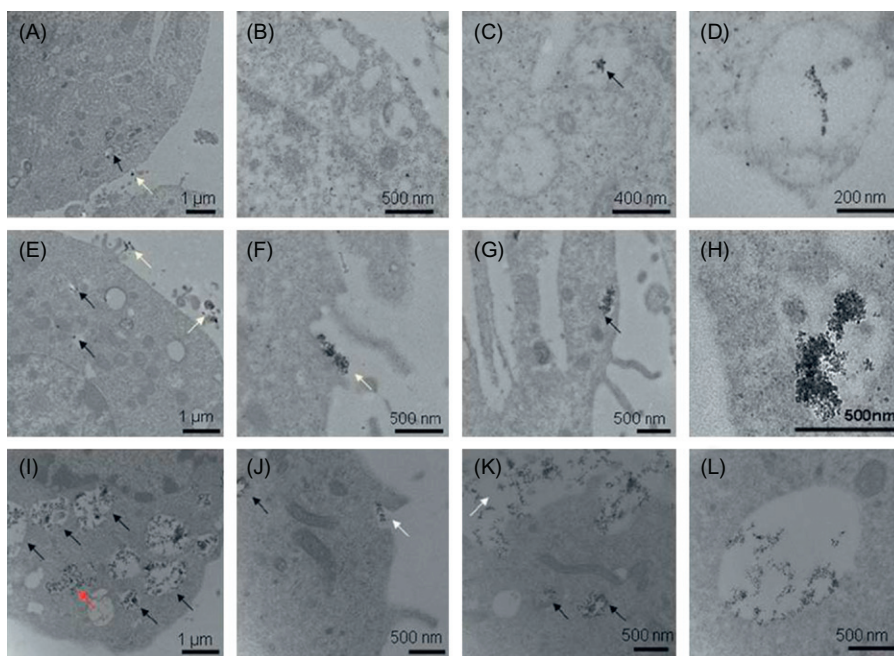


FIGURE 16.4

Internalization and localization of NDs into N2A cells with TEM: (A–D) after 1 h incubation, (E–H) after 6 h incubation, and (I–L) after 24 h incubation. Notice the time-dependent accumulation of fluorescent NDs (ND-T) both in the cytoplasm and intracellular vacuoles.

Source: Reproduced with permission from Ref. [9].

Because an endocytic mechanism appeared to be at work, the co-localization of ND in distinct subcellular locations was probed with organelle-specific stains for early endosomes and lysosomes in a chronological study [9]. Confirmation of the increased uptake of NDs over time was demonstrated with confocal microscopy after static incubation with $10\mu\text{g/ml}$ of NDs over 1–24 h (Figure 16.5). Early endosomes are observed during the early stages of clathrin-dependent endocytosis as membrane vesicles pinch off containing extracellular transports including NPs. Lysosomes are single-membrane compartments found in most eukaryotic cells that are responsible for the breakdown of materials. In the case of endocytosis, lysosomes develop gradually from late endosomes, which are vesicles that initially carry materials into the cell. The coalescence of the endosome with the low pH environment of the lysosome causes the degradation and release of the contents. Therefore, we expect to observe early localization of ND to endosomes, followed by localization to lysosomes, and finally to the cytosol. In cells fixed and stained for detecting early endosomes, control N2A cells show diffuse green staining with some punctate spots that represent invaginating early endosomes (Figure 16.5A). After 1 h, green punctate dots can still be observed; however, there is some overlap

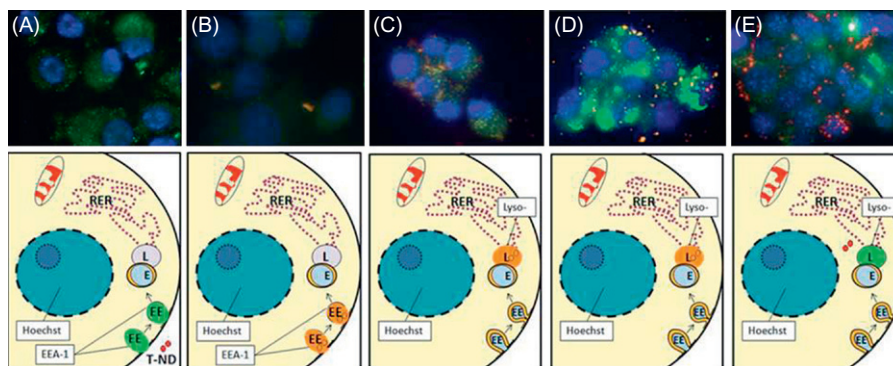


FIGURE 16.5

Confocal microscopy of N2A cells for co-localization of ND-T ($10\mu\text{g/ml}$) and early endosomes or lysosomes after various time points. Labels: ND-T (red), Hoechst nuclear dye (blue), and LysoTracker/EEA1 (green). Combined red and green signals, indicative of co-localization of ND-T in lysosomes or early endosomes, appear in yellow or orange. (A) Control with EEA1, (B) 1 h, stained for EEA1, (C) 3 h, stained for LysoTracker, (D) 6 h, stained for LysoTracker, and (E) 24 h, stained for LysoTracker. Notice that not all ND-T is localized to lysosomes, but some NDs are free in the cytoplasm and not all lysosomes contain ND-T. Images were taken at 60x magnification. EEA1 at 3, 6, and 24 h and LysoTracker at 0 and 1 h were omitted for clarity and ease of presentation.

of red signal from ND with the green dots, suggesting that there is early and rapid localization to early endosomes (Figure 16.5B). After 3 h, there was some overlapping of the red signal from ND and the green signal representative of lysosomes resulting in yellow spots, suggesting that ND co-localized with the lysosomes (Figure 16.5C). After 6 h, the density of this overlap greatly increased, suggesting that movement to the lysosomes follows early endosomes localization (Figure 16.5D). After 24 h, most of the ND appeared to be released from the lysosomes and was found in the cytoplasm as red aggregates while the lysosomes remained stained in green (Figure 16.5E).

Other studies have confirmed that fluorescent NDs rely upon energy-dependent clathrin-mediated endocytosis to enter the cell [108]. Similarly, Liu et al. [113] provided evidence to suggest that cNDs enter cells via both clathrin-mediated endocytosis and macropinocytosis. Moreover, the surface charge of fluorescent NDs has been shown to affect uptake: the uptake of poly-L-lysine-coated fluorescent NDs was better than that of oxidative-acid-purified fluorescent NDs at the same concentration. In addition, NDs may enter cells through the process of phagocytosis: Karpukhin et al. [114] demonstrated that detonation nanodiamonds (DNDs) may be phagocytosed by neutrophils, leading to ROS production. A more recent study has implicated that fluorescent nanodiamonds (FNDs) may exit the cellular cytosol through the process of exocytosis. For example, Fang et al. [112] demonstrated through flow cytometry that up to 30% of FNDs exocytosed from 3T3-L1 preadipocytes after 6 days. However, exocytosis was much lower for HeLa and 489-2.1 cells, implicating the crucial effect of cell type. The occurrence of exocytosis suggests that the presence of fluorescent NDs within the cell is a dynamic equilibrium process.

16.6 *In vivo* considerations for ND biocompatibility

The use of animals including mice, rats, and rabbits for *in vivo* nanotoxicity studies allows a more in-depth understanding of nanoparticle kinetics. However, even within the same animal model, there has been a great divergence in toxicity results for pulmonary studies of carbon nanotubes in animals [103,115–120] or C60 in aquatic species and animals [105,121–126]. It is suspected that differences in the starting materials (i.e., metal impurities, residual solvent) or administration routes/procedures may be responsible for the varied biocompatibility results. In contrast, micron- or nanosized diamonds show consistently positive results for *in vivo* applications. For example, micron-sized diamond particles did not contribute to inflammation when introduced to implant traversing canals in rabbits [127], canine knee joints [86], or the complement system [128] and NDs do not affect the weight or reproductive ability of mice or induce inflammation in rats [19,129–133,163].

Unfortunately, the early *in vivo* studies with detonation NDs were complicated by the low colloidal stability and high polydispersity, which made it difficult to establish dose–response relationships. In one study, ND suspensions in starch gel were orally introduced to animals with a catheter in order to increase the

sedimentation stability [134]. Other treatments to remove contaminants and further functionalize the surface of NDs with hydrophilic surface moieties (i.e., oxy, carboxyl, carbonyl groups) were used to produce medical-quality ND hydrosols. The ability to prepare stable and sterile ND hydrosols that could be cryogenically stored and administered by various methods led to a series of long-term experiments in animals including mice, rats, and dogs. The species-specific responses to 0.002–1.0 wt% ND administered by different means (i.e., oral, intravenous, intramuscular) were studied and summarized below [129,130,132–135].

In mice, completely replacing water in the animals' diet with 0.002–0.05 wt% ND hydrosols from 3 to 6 months neither caused death nor affected the growth or internal organ (liver, lungs, heart, kidneys, and pancreas) weight dynamics compared to control animal [129,133,135]. Further, the substitution of water with ND hydrosols did not influence mouse reproductive ability, for at least the first three generations as animals consuming ND hydrosols from birth produced healthy offspring [129–131]. Within the duration of the experiments, the total amount of ND delivered to the animals was between 16 and 450 mg per mouse depending on the concentration of ND in hydrosols [135]. The effects of NDs on blood cells and blood plasma chemistry were examined after prolonged substitution of water with ND hydrosols [129,133,135] with minimal changes.

Similar studies in rats showed that intramuscularly injected NDs localized at the injection sites as gelatinous clots that contained considerable amounts of protein components on their surface [129,135]. However, no pronounced visual or histological manifestations of inflammation were detected. The low toxicity was confirmed with an estimated median lethal dose (LD_{50}) of >7000 mg/kg compared to an LD_{50} of 3000 mg/kg for sodium chloride orally administered to rats [19]. In another series of experiments, dogs intravenously injected with 0.3–20 ml of sterile ND hydrosols in glucose (0.001–5 wt%) did not die after the dosage [135].

Studies have also exposed NDs to mice via intratracheal instillation [136]. This study reported that the NDs localized largely to the lung, although there is also distribution in the spleen, liver, bone, and heart. The authors implied that there could be dose-dependent toxicity in these organs based on histological and biochemical evaluation. Similarly, Yuan et al. found that NDs mostly accumulated in the liver after intravenous injection with the spleen and lung being other target organs [156]. Approximately 60% of the initial NDs remained in the liver and ~8% remained in the lung both 30 min and 28 days after initial exposure, with potentially cytotoxic effects. Finally, Rojas et al. [137] reported similar results with amino-functionalized DNDs, with the majority of particles localized to the lung, spleen, and liver. These particles were excreted through the urinary tract. The addition of surfactant agents did not change the biodistribution, although it did diminish excretion through the urinary tract.

These studies suggest that the significant amount of NDs that make it inside the cell may pose a significant cytotoxic risk at the *in vivo* level. In support of this concern, Marcon et al. reported that cNDs could induce embryotoxicity and teratogenicity, interfering with neurulation and gastrulation with high mortality in *Xenopus laevis* embryos [164].

Recent studies of fluorescently labeled NDs either fed to or microinjected into *Caenorhabditis elegans* worms [138] demonstrate that bioconjugation can tailor the localization to either the intestinal lumen (bare NDs) or intestinal walls (dextran or bovine serum albumin (BSA)-coated NDs). By comparison, microinjected NDs are dispersed in the distal gonad and oocytes at ~30 min after injection and effectively delivered to the embryos (Figure 16.6). The injected NDs are present in the cytoplasm of many cells in the early embryos (Figure 16.6B), but are predominantly localized to the intestinal cells of the late embryo (Figure 16.6C). A comparison of the worm's life spans, brood sizes, and ROS production demonstrate that both the life span and the potential for progeny production are unaffected by the treatments with either dextran- or BSA-coated NDs. Therefore, the longevity of *C. elegans* measured over 25 days, the reproductive potential measured over 4 days, and the stress response after 4 h did not produce any deleterious effects compared to controls.

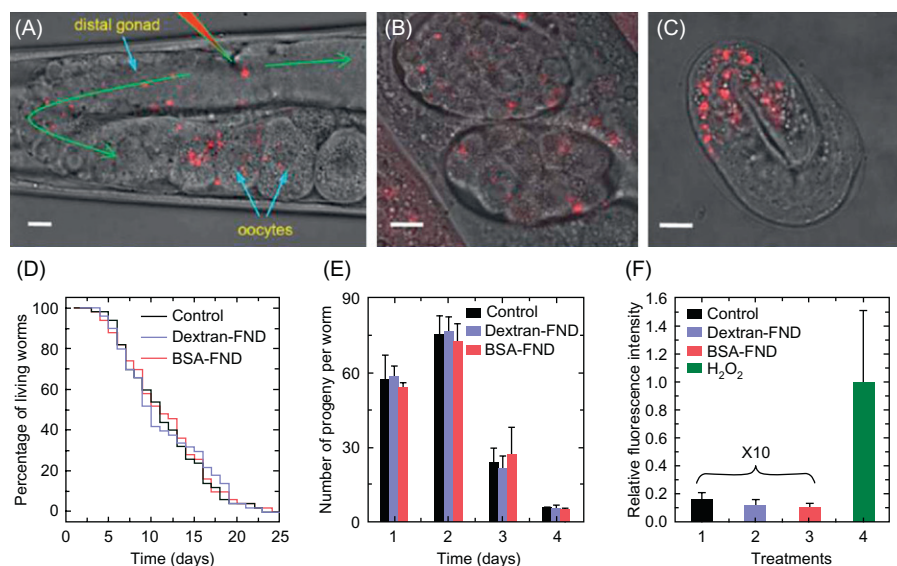


FIGURE 16.6

Microinjection of bare fluorescent NDs into *C. elegans*. (A–C) Epifluorescence/DIC-merged images of (A) an injected worm and (B) its progeny at the early and (C) late embryonic stages. Green arrows indicate bulk streaming of NDs with cytoplasmic materials and the red triangle indicates the site of injection. Scale bars are 10 μm . (D–F) Comparison of life span, brood size, and ROS assays for *C. elegans*—(D) life span, (E) brood size, and (F) ROS level of the worms treated with bioconjugated, fluorescent NDs. In part (F), a hydrogen peroxide treatment was used as the positive control for the ROS assay. Note that the data of the untreated control and the ND treatments were magnified 10-fold for clarity.

Source: Reproduced with permission from Ref. [139].

Yuan et al. [140] investigated the pulmonary effects and localization of NDs in mice intratracheally administered with 1 mg/kg NDs and examined at 1–28 days postexposure. There were no long-term signs of biochemical, ultrastructural, or histopathological alterations, but there was a temporary lung index increase at the early time point of 1 day postexposure. Further, the ND burden within alveolar macrophages decreased over time were removed over time. Representative histopathological and TEM imaging of lung tissue from mice intratracheally instilled with 1 mg/kg NDs-50 at 1 day postexposure is shown in Figure 16.7. The normal lung architecture indicates that exposures to NDs does not produce detectable pulmonary toxicity (Figure 16.7A and B). The high-resolution TEM images of lung tissue show NDs localized to phagosomes within macrophages (Figure 16.7C and D).

Cumulatively, these past *in vivo* studies suggest that NDs possess enormous potential based on their biodistribution throughout animal models. Moreover, their cytotoxicity does not appear to be a major concern, although there seems to be some disagreement depending upon the animal model utilized and the particular end points that are assessed. However, most importantly, NDs appear to possess

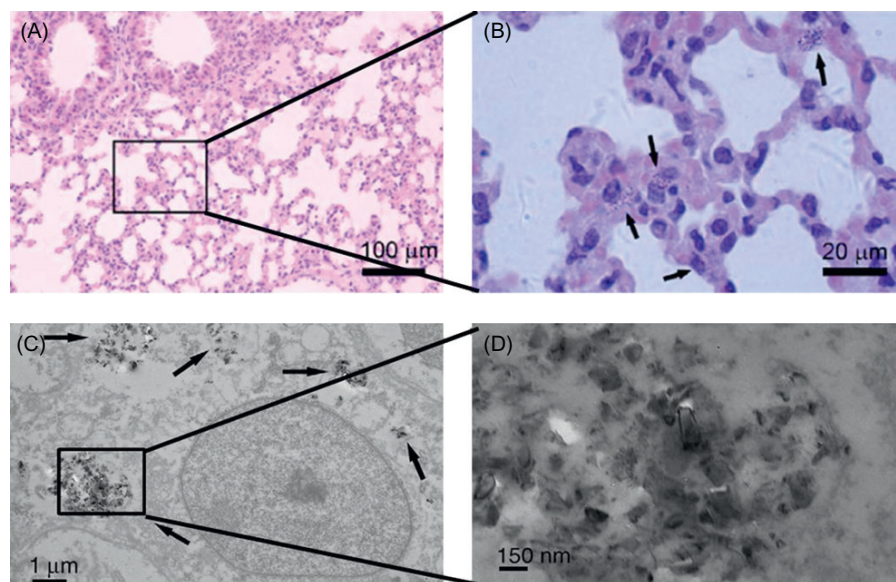


FIGURE 16.7

Histopathological imaging of lung tissue from mice intratracheally instilled with 1 mg/kg NDs-50 at 1 day postexposure. (A) The normal lung architecture indicates that exposure to NDs does not produce detectable pulmonary toxicity. (B) Higher magnification of area in (A). (C and D) High-resolution TEM images of lung tissue showing NDs entrapped in phagosomes. (D) Higher magnification of area in (C). The black arrows point to the entrapped ND aggregates throughout the tissue.

Source: Reproduced with permission from Ref. [141].

valuable biological effects and properties characteristic of an enterosorbent (detoxifying agent), which may be exploited in potential biomedical and bioengineering applications.

16.7 Future goals for biological assessment of NDs

The current body of research on NDs overwhelmingly suggests that they are biocompatible with many mammalian cell lines [21,64,80,98]. Regardless of the size of the NDs, both *in vivo* and *in vitro* studies of NDs of varying purities with conjugations to fluorophores or other biomolecules retained levels of cell high viability and minimal protein and genomic alterations. However, the role of ND size should be examined in a systematic manner because 5 nm NDs, which have >15% of the carbon atoms on their surface, have shown different properties than 100 nm NDs [142]. An understanding of size effects is further complicated by the dynamic nature of nanoparticles in fluids, including protein corona formation, tight or loose aggregate formation, and cellular surface interactions. At this time, most nanoparticles, including NDs, cannot be controlled as individual particles in biological environments to target entry into the cell nucleus or across tightly controlled barriers (i.e., blood–brain barrier) without direct microinjection or other invasive methods. It will still be interesting, however, to quantify the uptake amount of NDs into individual cells or systems to partially elucidate size-dependent effects on biocompatibility. With regard to advancing testing methods, the strength of *in vitro* biocompatibility studies could be improved by providing consistent positive and negative controls and benchmark nanoparticles to assess the validity of the toxicity assays. This includes independent testing of the solvents or surfactants incorporated with the nanoparticles as well as common matrices in the case of polymer nanocomposites. Because micron-sized diamond particles were chosen, negative control particles for other ceramics, nanosized diamonds could be proposed as control particles for nanosized carbon biocompatibility studies. However, the properties would need to be uniform, of high purity, and the binding of the biochemical assay probes (i.e., MTT or ROS) should continue to be scrutinized for directly interfering with the toxicity assay results [143,144].

Advances in ND synthesis methods, purification procedures, and functionalization routes necessitates further investigation into the mechanisms responsible for either the positive or negative effects. Unfortunately, the detailed purity and surface chemistry of the NDs used in many experiments has not been detailed alongside the biocompatibility results, making it difficult to ascertain the significance, if any, of the impurities and surface functional groups. Further, these surface groups may be masked by biomolecules such as serum proteins, which effectively “coat” the ND surface. Alternatively, the surface groups or impurities may be unstable or soluble thereby releasing unwanted chemical species into the biological environment. Given the number of chemical species applied to NDs in recent experiments, it is essential to better understand the evolving properties of NDs in biological

environments related to the cellular response and kinetics. A recent review by Zhu et al. [145] discusses the implications of complex ND-based drug-imaging-targeting delivery systems on biocompatibility.

The recent animal studies have shown great progress in examining the biocompatibility of NDs with promising results. However, extensive fundamental studies will be required before clearly understanding the long-term bio-effects of NDs. In particular, questions remain regarding (1) the doses used during the studies, (2) optimal routes of administration (oral, intratracheal, intravenous, etc.), (3) the effects of their very small primary particle size for translocation into unintended areas of the body or cell, (4) proper tracking, and (5) clearance/bio-persistence. The use of radiotracers [136] has aided the tracking of NDs, however, there are conflicting results for localization to the lung, liver, kidney, heart, and blood with or without effects, which need to be clarified. For example, Zhang et al. [136] administered 20× the dose of Yuan et al. [140]. Further, the few studies that demonstrate negative effects at the cellular and genomic level upon exposure to NDs should be clarified in the context of the ND properties, cell lines, and assays. For example, the intratracheal administration of NDs did not produce pulmonary toxicity and allowed clearance by macrophages, but certain cell types may be less robust during the early embryonic stages [97,146]. Mechanical damage has not been shown, although it should not be ruled out due to different synthesis and processing methods, which could result in sharp edges and bio-persistence similar to studies with micron-sized diamond particles [139,141]. Side effects of such phenomena could include respiratory ailments, alterations in fluid composition [147–149], malfunctioning transport [64,71,98], or accumulation and resistance to elimination by cells or tissues. For example, although the NDs were routed to lysosomes, they were unable to be degraded within 24h and accumulated in the cytoplasm [9]. Although many cells of the body undergo cell death through natural cellular renewal processes (i.e., skin and lung macrophages), the localization and cell-specific differences should also be considered in the mechanism of nanoparticle uptake, accumulation, and localization for truly understanding biocompatibility [64,150].

Before NDs are incorporated into health care products, such as skin creams, shaving gels, or toothpastes, the penetration depth of NDs into the skin or gums would need to be evaluated (Figure 16.1). The biomedical use of NDs in implantable materials should carefully examine the mechanism and extent of direct ND interaction with cellular membranes and proteins, and fluid electrolyte/osmotic balance should be elucidated in more complex systems. The exciting, yet preliminary, results of the human and animal anticancer effects of ND need systematic probing of the mechanisms at work including specific cell-signaling pathways and gene expression by high throughput microarrays similar to studies performed with carbon nanotubes [151–153]. Therefore, the structure-property relationship for NDs and biocompatibility are not straightforward and must be considered on a case-by-case basis due to the high degree of variations (i.e., synthesis methods, differences between manufacturers, laboratories, methods, purification procedures, functionalization routes, chemicals, and further alterations to ND properties during their life

cycle), which further complicate gaining an accurate understanding of the properties responsible for both detrimental and beneficial effects on biological systems.

References

- [1] Y.R. Chang, H.Y. Lee, K. Chen, et al., Mass production and dynamic imaging of fluorescent nanodiamonds, *Nat. Nanotechnol.* 3 (2008) 284–288.
- [2] V.N. Mochalin, O. Shenderova, D. Ho, Y. Gogotsi, The properties and applications of nanodiamonds, *Nat. Nanotechnol.* 7 (2012) 11–23.
- [3] A.M. Schrand, S.A.C. Hens, O.A. Shenderova, Nanodiamond particles: properties and perspectives for bioapplications, *Crit. Rev. Solid State Mater. Sci.* 34 (2009) 45–54.
- [4] D. Ho, Beyond the sparkle: the impact of nanodiamonds as biolabeling and therapeutic agents, *ACS Nano.* 3 (12) (2009) 3825–3829.
- [5] Y. Xing, L. Dai, Nanodiamonds for nanomedicine, *Nanomedicine* 4 (2009) 207–218.
- [6] J.I. Chao, E. Perevedentseva, P.H. Chung, et al., Nanometer-sized diamond particle as a probe for biolabeling, *Biophys. J.* 93 (2007) 2199–2208.
- [7] I.P. Chang, K.C. Hwang, C.S. Chiang, Preparation of fluorescent magnetic nanodiamonds and cellular imaging, *J. Am. Chem. Soc.* 130 (2008) 15476–15481.
- [8] A.M. Schrand, Characterization and *in vitro* biocompatibility of engineered nanomaterials, in: *The School of Engineering, University of Dayton, Dayton, OH, 2007*, pp. 93–123.
- [9] A.M. Schrand, J.B. Lin, S. Ciftan Hens, S.M. Hussain, Temporal and mechanistic tracking of cellular uptake dynamics with novel surface fluorophore-bound nanodiamonds, *Nanoscale* 3 (2011) 435–445.
- [10] V.Y. Dolmatov, L.N. Kostrova, Detonation-synthesized nanodiamonds and the feasibility of developing a new generation of medicinals, *Superhard Mater.* 3 (2000) 82–85.
- [11] V.Y. Dolmatov, Detonation Synthesis Ultradispersed Diamonds, Russian ed., Publishing House of Saint-Petersburg State Polytechnic University, Saint-Petersburg, 2003.
- [12] T.A. Nachalnaya, V.G. Malogolovets, G.A. Podzerei, Y.I. Nikitin, N.V. Novikov, Y.A. Polkanov, Special features of structure and physico-mechanical properties of natural diamonds of Ukraine, *Superhard Mater.* 22 (2000) 33–41.
- [13] T.N. Barushkina, V.G. Aleinikov, B.B. Donster, G.I. Savvakina, Chemical modification of diamond surface with ozone, Russian ed., in: *Proceedings of Institute of Superhard Materials of Ukrainian Academy of Sciences, 1990*, pp. 41–48.
- [14] V. Grichko, V. Grishko, O. Shenderova, Nanodiamond bullets and their biological targets, *Nanobiotechnology* 2 (1–2) (2006) 37–42.
- [15] D. Lin, B. Xing, Phytotoxicity of nanoparticles: inhibition of seed germination and root growth, *Environ. Pollut.* 150 (2) (2007) 243–260.
- [16] A. Morozan, L. Stamatina, F. Nastase, A. Dumitru, S. Vulpe, C. Nastase, et al., The biocompatibility microorganisms-carbon nanostructures for applications in microbial fuel cells, *Phys. Status Solid A* 204 (2007) 1797–1803.
- [17] K. Inoue, H. Takano, R. Yanagisawa, S. Hirano, M. Sakurai, A. Shimada, et al., Effects of airway exposure to nanoparticles on lung inflammation induced by bacterial endotoxin in mice, *Environ. Health Perspect.* 114 (9) (2006) 1325–1330.
- [18] P. Hoet, A. Nemmar, B. Nemery, M. Hoylaerts, Hemostatic and thrombotic effects of particulate exposure: assessing the mechanisms, in: N. Monteiro-Riviere,

- C.L. Tran (Eds.), *Nanotoxicology: Characterization, Dosing, and Health Effects*, Informa Healthcare, New York, 2007, pp. 247–266.
- [19] V.Y. Dolmatov, Application of detonation nanodiamond, in: O.A. Shenderova, D.M. Gruen (Eds.), *Ultra Nanocrystalline Diamond: Synthesis, Properties, and Applications*, William Andrew, Norwich, NY, 2006, p. 513.
 - [20] E. Perevedentseva, C.Y. Cheng, P.H. Chung, J.S. Tu, Y.H. Hsieh, C.L. Cheng, The interaction of the protein lysozyme with bacteria *E. coli* observed using nanodiamond labelling, *Nanotechnology* 18 (31) (2007) 1–7.
 - [21] H. Huang, E. Pierstorff, E. Osawa, D. Ho, Active nanodiamond hydrogels for chemotherapeutic delivery, *Nano Lett.* 7 (2007) 3305–3314.
 - [22] O.A. Shenderova, V.V. Zhirnov, D.W. Brenner, Carbon nanostructures, *Crit. Rev. Solid State Mater. Sci.* 27 (2002) 227.
 - [23] J. Lee, J. Kim, J. Kim, H. Kang, Novel electrode for water purification based on nanodiamonds, 220th ECS Meeting, Abstract #2346, The Electrochemical Society, 2011.
 - [24] A.M. Schrand, J. Johnson, L. Dai, S.M. Hussain, J.J. Schlager, L. Zhu, et al., Cytotoxicity and genotoxicity of carbon nanoparticles, in: T. Webster (Ed.), *Safety of Nanoparticles: From Manufacturing to Clinical Applications*, Springer Publishing, Brown University, Providence, RI, 2008.
 - [25] L. Pramatarova, R. Dimitrova, E.P.T. Spassov, et al., Peculiarities of hydroxyapatite/nanodiamond composites as novel implants, *J. Phys. Conf. Ser.* 93 (2007) 012049.
 - [26] Q. Zhang et al., Fluorescent PLLA–nanodiamond composites for bone tissue engineering, *Biomaterialia* 32 (2011) 87–94.
 - [27] F.A. Barile, P.J. Dierickx, U. Kristen, In vitro cytotoxicity testing for prediction of acute human toxicity, *Cell. Biol. Toxicol.* 10 (1994) 155–162.
 - [28] G. Eisenbrand, B. Pool-Zobel, V. Baker, M. Balls, B.J. Blaauboer, A. Boobis, et al., Methods of *in vitro* toxicology, *Food Chem. Toxicol.* 40 (2–3) (2002) 193–236.
 - [29] N. Jia, Q. Lian, H. Shen, C. Wang, X. Li, Z. Yang, Intracellular delivery of quantum dots tagged antisense oligodeoxynucleotides by functionalized multiwalled carbon nanotubes, *Nano Lett.* 7 (10) (2007) 2976–2980.
 - [30] L. Cao, X. Wang, M.J. Meziani, F. Lu, H. Wang, P.G. Luo, et al., Carbon dots for multiphoton bioimaging, *J. Am. Chem. Soc.* 129 (37) (2007) 11318–11319.
 - [31] M. Geiser, B. Rothen-Rutishauser, N. Kapp, S. Schurch, W. Kreyling, H. Schulz, et al., Ultrafine particles cross cellular membranes by nonphagocytic mechanisms in lungs and in cultured cells, *Environ. Health Perspect.* 113 (11) (2005) 1555–1560.
 - [32] A. Nel, T. Xia, L. Madler, N. Li, Toxic potential of materials at the nanolevel, *Science* 311 (5761) (2006) 622–627.
 - [33] G. Oberdörster, A. Maynard, K. Donaldson, V. Castranova, J. Fitzpatrick, K. Ausman, et al., Principles for characterizing the potential human health effects from exposure to nanoparticles: elements of a screening strategy, Part. *Fibre Toxicol.* 2 (2005) 8.
 - [34] S.L. Brown, S.M. Brett, M. Gough, J.V. Rodricks, R.G. Tardiff, D. Turnbull, Review of interspecies risk comparisons, *Regul. Toxicol. Pharmacol.* 8 (1988) 191–206.
 - [35] R.L. Brent, Utilization of juvenile animal studies to determine the human effects and risks of environmental toxicants during postnatal developmental stages, *Birth. Defects. Res. B. Dev. Reprod. Toxicol.* 71 (5) (2004) 303–320.
 - [36] R.L. Brent, Utilization of animal studies to determine the effects and human risks of environmental toxicants (drugs, chemicals, and physical agents), *Pediatrics* 113 (Suppl. 4) (2004) 984–995.

- [37] E.D. Kuempel, Estimating nanoparticle dose in humans: issues and challenges, in: N.A. Monteiro-Riviere, C.L. Tran (Eds.), *Nanotoxicology: Characterization, Dosing, and Health Effects*, Informa Healthcare, p. 141.
- [38] G. Oberdörster, J.N. Finkelstein, C. Johnston, R. Gelein, C. Cox, R. Baggs, et al., Acute pulmonary effects of ultrafine particles in rats and mice, *Res. Rep. Health Eff. Inst.* 5 (2000) 74.
- [39] K. Donaldson, D. Brown, A. Clouter, R. Duffin, W. Macnee, L. Renwick, et al., The pulmonary toxicology of ultrafine particles, *J. Aerosol. Med.* 15 (2) (2002) 213–220.
- [40] L. Braydich-Stolle, S. Hussain, J.J. Schlager, M.C. Hofmann, *In vitro* cytotoxicity of nanoparticles in mammalian germline stem cells, *Toxicol. Sci.* 88 (2) (2005) 412–419.
- [41] S.M. Hussain, K.L. Hess, J.M. Gearhart, K.T. Geiss, J.J. Schlager, *In vitro* toxicity of nanoparticles in BRL 3A rat liver cells, *Toxicol. In Vitro* 19 (7) (2005) 975–983.
- [42] G. Oberdörster, A. Maynard, K. Donaldson, V. Castranova, J. Fitzpatrick, K. Ausman, et al., Principles for characterizing the potential human health effects from exposure to nanoparticles: elements of a screening strategy, Part. *Fibre Toxicol.* 2 (8) (2005).
- [43] T. Ashikaga, M. Wada, H. Kobayashi, M. Mori, Y. Katsumura, H. Fukui, et al., Effect of the photocatalytic activity of TiO₂ on plasmid DNA, *Mutat. Res.* 466 (2000) 1.
- [44] D.M. Brown, V. Stone, P. Findlay, W. Macnee, K. Donaldson, Increased inflammation and intracellular calcium caused by ultrafine carbon black is independent of transition metals or other soluble components, *Occup. Environ. Med.* 57 (2000) 685.
- [45] D.M. Brown, M.R. Wilson, W. Macnee, V. Stone, K. Donaldson, Size-dependent proinflammatory effects of ultrafine polystyrene particles: a role for surface area and oxidative stress in the enhanced activity of ultrafines, *Toxicol. Appl. Pharmacol.* 175 (2001) 191.
- [46] D. Hohn, Y. Steinfartz, R.P. Schins, A.M. Knaapen, G. Martra, B. Fubini, et al., The surface area rather than the surface coating determines the acute inflammatory response after instillation of fine and ultrafine TiO₂ in the rat, *Int. J. Hyg. Environ. Health* 205 (2002) 239.
- [47] B. Rehn, F. Seiler, S. Rehn, J. Bruch, M. Maier, Investigations on the inflammatory and genotoxic lung effects of two types of titanium dioxide: untreated and surface treated, *Toxicol. Appl. Pharmacol.* 189 (2003) 84.
- [48] A. Hoshino, F. Kujioka, T. Oku, M. Suga, Y.F. Sasaki, T. Ohta, et al., Physicochemical properties and cellular toxicity of nanocrystal quantum dots depend on their surface modification, *Nano Lett.* 4 (2004) 2163.
- [49] M. Muller, S. Mackeben, C.C. Muller-Goymann, Physicochemical characterisation of liposomes with encapsulated local anaesthetics, *Int. J. Pharm.* 1–2 (2004) 139.
- [50] L. Ding, J. Stilwell, T. Zhang, O. Elboudwarej, H. Jiang, J.P. Selegue, et al., Molecular characterization of the cytotoxic mechanism of multiwall carbon nanotubes and nano-onions on human skin fibroblast, *Nano Lett.* 5 (2005) 2448.
- [51] C. Kirchner, T. Liedl, S. Kudera, T. Pellegrino, A. Munoz Javier, H.E. Gaub, et al., Cytotoxicity of colloidal CdSe and CdSe/ZnS nanoparticles, *Nano Lett.* 5 (2005) 331.
- [52] K. Soto, A. Carrasco, T. Powell, K. Garza, L. Murr, Comparative *in vitro* cytotoxicity assessment of some manufactured nanoparticulate materials characterized by transmission electron microscopy, *J. Nanopart. Res.* 7 (2005) 145.
- [53] B.D. Chithrani, A.A. Ghazani, W.C. Chan, Determining the size and shape dependence of gold nanoparticle uptake into mammalian cells, *Nano Lett.* 6 (2006) 662.
- [54] C.M. Sayes, F. Liang, J.L. Hudson, J. Mendez, W. Guo, J.M. Beach, et al., Functionalization density dependence of single-walled carbon nanotubes cytotoxicity *in vitro*, *Toxicol. Lett.* 161 (2006) 135.

- [55] H.W. Chen, S.F. Su, C.T. Chien, W.H. Lin, S.L. Yu, C.C. Chou, et al., Titanium dioxide nanoparticles induce emphysema-like lung injury in mice, *FASEB J.* 20 (2006) 2393.
- [56] D.B. Warheit, T.R. Webb, C.M. Sayes, V.L. Colvin, K.L. Reed, Pulmonary instillation studies with nanoscale TiO₂ rods and dots in rats: toxicity is not dependent upon particle size and surface area, *Toxicol. Sci.* 91 (2006) 227.
- [57] Z.P. Xu, Q.H. Zeng, G.Q.L. Gq, A.B. Ui, Inorganic nanoparticles as carriers for efficient cellular delivery, *Chem. Eng. Sci.* 61 (2006) 1027.
- [58] S. Pal, Y.K. Tak, J.M. Song, Does the antibacterial activity of silver nanoparticles depend on the shape of the nanoparticle? A study of the gram-negative bacterium *Escherichia coli*, *Appl. Environ. Microbiol.* 73 (2007) 1712.
- [59] V.E. Kagan, Y.Y. Tyurina, V.A. Tyurin, N.V. Konduru, A.I. Potapovich, A.N. Osipov, et al., Direct and indirect effects of single walled carbon nanotubes on RAW 264.7 macrophages: role of iron, *Toxicol. Lett.* 165 (2006) 88.
- [60] K. Pulskamp, S. Diabate, H.F. Krug, Carbon nanotubes show no sign of acute toxicity but induce intracellular reactive oxygen species in dependence on contaminants, *Toxicol. Lett.* 168 (2007) 58.
- [61] R.A. Freitas, Jr., *Nanomedicine*, vol. IIA: Biocompatibility, Landes Bioscience, Georgetown, TX, 2003.
- [62] R.H. Hurt, M. Monthieux, A. Kane, Toxicology of carbon nanoparticles: status, trends, and perspectives on the special issue, *Carbon* 44 (2006).
- [63] L. Dai (Ed.), *Carbon Nanotechnology: Recent Developments in Chemistry, Physics, Materials Science and Device Applications*, Elsevier: Amsterdam, 2006.
- [64] A.M. Schrand, L. Dai, J.J. Schlager, S.M. Hussain, E. Osawa, Differential biocompatibility of carbon nanotubes and nanodiamonds, *Diamond. Relat. Mater.* 16 (2007) 2118.
- [65] G. Jia, H. Wang, L. Yan, X. Wang, R. Pei, T. Yan, et al., Cytotoxicity of carbon nanoparticles: single-wall nanotube, multi-wall nanotube, and fullerene, *Environ. Sci. Technol.* 39 (2005) 1378.
- [66] C. Grabinski, S. Hussain, K. Lafdi, L. Braydich-Stolle, J. Schlager, Effect of particle dimension on biocompatibility of carbon nanoparticles, *Carbon* 45 (2007) 2828.
- [67] A. Magrez, S. Kasas, V. Salicio, N. Pasquier, J.W. Seo, M. Celio, et al., Cellular toxicity of carbon-based nanoparticles, *Nano Lett.* 6 (2006) 1121.
- [68] Y. Sato, A. Yokoyama, K. Shibata, Y. Akimoto, S. Ogino, Y. Nodasaka, et al., Influence of length on cytotoxicity of multi-walled carbon nanotubes against human acute monocytic leukemia cell line THP-1 *in vitro* and subcutaneous tissue of rats *in vivo*, *Mol. Biosyst.* 1 (2005) 176.
- [69] R.L. Price, K.M. Haberstoh, T.J. Webster, Improved osteoblast viability in the presence of smaller nanometer dimensioned carbon fibres, *Nanotechnology* 15 (2004) 892.
- [70] C. Liu, H. Huang, P. Song, S. Fan, Machining carbon nanotubes into uniform slices, *J. Nanosci. Nanotechnol.* 7 (2007) 4473.
- [71] K. Liu, C. Cheng, C. Chang, et al., Biocompatible and detectable carboxylated nanodiamond on human cell, *Nanotechnology* 18 (2007) 325102.
- [72] C.M. Sayes, A.M. Gobin, K.D. Ausman, J. Mendez, J.L. West, V.L. Colvin, Nano-C60 cytotoxicity is due to lipid peroxidation, *Biomaterials* 26 (2005) 7587.
- [73] A.A. Corona-Morales, A. Castell, E. Al., Fullerene C60 and ascorbic acid protect cultured chromaffin cells against levodopa toxicity, *J. Neurosci. Res.* 71 (2003) 121.
- [74] G. Bogdanovic, V. Kojic, A. Dordevic, J. Canadanovic-Brunet, M. Vojinovic-Miloradov, V.V. Baltic, Modulating activity of fullerol C60(OH)₂₂ on doxorubicin-induced cytotoxicity, *Toxicol. In Vitro* 18 (2004) 629.

- [75] N.A. Monteiro-Riviere, A.O. Inman, Y.Y. Wang, R.J. Nemanich, Surfactant effects on carbon nanotube interactions with human keratinocytes, *Nanomedicine* 1 (2005) 293.
- [76] N.A. Monteiro-Riviere, R.J. Nemanich, A.O. Inman, Y.Y. Wang, J.E. Riviere, Multi-walled carbon nanotube interactions with human epidermal keratinocytes, *Toxicol. Lett.* 155 (2005) 377.
- [77] F.A. Witzmann, N.A. Monteiro-Riviere, Multi-walled carbon nanotube exposure alters protein expression in human keratinocytes, *Nanomedicine* 2 (2006) 158.
- [78] C.M. Sayes, A.A. Marchione, K.L. Reed, D.B. Warheit, Comparative pulmonary toxicity assessments of C60 water suspensions in rats: few differences in fullerene toxicity *in vivo* in contrast to *in vitro* profiles, *Nano Lett.* 7 (2007) 2399.
- [79] C.M. Sayes, K.L. Reed, D.B. Warheit, Assessing toxicity of fine and nanoparticles: comparing *in vitro* measurements to *in vivo* pulmonary toxicity profiles, *Toxicol. Sci.* 97 (2007) 163.
- [80] A.M. Schrand, H. Huang, C. Carlson, J.J. Schlager, E. Osawa, S.M. Hussain, et al., Are diamond nanoparticles cytotoxic?, *J. Phys. Chem. B* 111 (2007c) 2.
- [81] L.N. Daniel, Y. Mao, T.C. Wang, C.J. Markey, S.P. Markey, X. Shi, et al., DNA strand breakage, thymine glycol production, and hydroxyl radical generation induced by different samples of crystalline silica *in vitro*, *Environ. Res.* 71 (1995) 60.
- [82] J.C. Ball, A.M. Straccia, W.C. Young, A.E. Aust, The formation of reactive oxygen species catalyzed by neutral, aqueous extracts of NIST ambient particulate matter and diesel engine particles, *J. Air Waste Manage. Assoc.* 50 (2000) 1897.
- [83] J.F. Long, W.J. Waldman, R. Kristovich, M. Williams, D. Knight, P.K. Dutta, Comparison of ultrastructural cytotoxic effects of carbon and carbon/iron particulates on human monocyte-derived macrophages, *Environ. Health Perspect.* 113 (2005) 170.
- [84] E. Osawa, Recent progress and perspectives in single-digit nanodiamond, *Diamond. Relat. Mater.* 16 (2007) 2018.
- [85] V.S. Bondar, A.P. Puzyr, Nanodiamonds for biological investigations, *Phys. Solid State* 46 (2004) 716.
- [86] R.L. Tse, P. Phelps, Polymorphonuclear leukocyte motility *in vitro*. V. Release of chemotactic activity following phagocytosis of calcium pyrophosphate crystals, diamond dust, and urate crystals, *J. Lab. Clin. Med.* 76 (1970) 403.
- [87] F.K. Higson, O.T. Jones, Oxygen radical production by horse and pig neutrophils induced by a range of crystals, *J. Rheumatol.* 11 (1984) 735.
- [88] M. Hedenborg, M. Klockars, Quartz-dust-induced production of reactive oxygen metabolites by human granulocytes, *Lung* 167 (1989) 23.
- [89] A. Swan, B. Dularay, P. Dieppe, A comparison of the effects of urate, hydroxyapatite and diamond crystals on polymorphonuclear cells: relationship of mediator release to the surface area and adsorptive capacity of different particles, *J. Rheumatol.* 17 (1990) 1346.
- [90] J.A. Schmidt, C.N. Oliver, J.L. Lepe-Zuniga, I. Green, I. Gery, Silica-stimulated monocytes release fibroblast proliferation factors identical to interleukin 1. A potential role for interleukin 1 in the pathogenesis of silicosis, *J. Clin. Invest.* 73 (1984) 1462.
- [91] A.C. Allison, J.S. Harington, M. Birbeck, An examination of the cytotoxic effects of silica on macrophages, *J. Exp. Med.* 124 (1966) 141.
- [92] L. Nordsletten, A.K. Hogasen, Y.T. Kontinen, S. Santavirta, P. Aspenberg, A.O. Aasen, Human monocytes stimulation by particles of hydroxyapatite, silicon carbide and diamond: *in vitro* studies of new prosthesis coatings, *Biomaterials* 17 (1996) 1521.
- [93] H.G. Luhr, Comparative studies on phagocytosis of coal powders of various carbonification grades, also of quartz and diamond powders in tissue cultures, *Arch. Gewerbepathol Gewerbehyg* 16 (1958) 355.

- [94] H.S. Cheung, M.T. Story, D.J. Mccarty, Mitogenic effects of hydroxyapatite and calcium pyrophosphate dihydrate crystals on cultured mammalian cells, *Arthritis Rheum.* 27 (1984) 668.
- [95] I. Dion, L. Bordenave, F. Lefebvre, R. Bareille, C. Baquey, J.R. Monties, et al., Physico-chemistry and cytotoxicity of ceramics Part II: Cytotoxicity of ceramics, *J. Mater. Sci. Mater. Med.* 5 (1994) 18.
- [96] I. Dion, M. Lahaye, R. Salmon, C. Baquey, J.R. Monties, P. Havlik, Blood haemolysis by ceramics, *Biomaterials* 14 (1993) 107.
- [97] Y. Xing, W. Xiong, L. Zhu, et al., DNA damage in embryonic stem cells caused by nanodiamonds, *ACS Nano.* 5 (2011) 2376–2384.
- [98] S.J. Yu, M.W. Kang, H.C. Chang, K.M. Chen, Y.C. Yu, Bright fluorescent nanodiamonds: no photobleaching and low cytotoxicity, *J. Am. Chem. Soc.* 127 (2005) 17604.
- [99] M. Bottini, S. Bruckner, K. Nika, N. Bottini, S. Bellucci, A. Magrini, et al., Multi-walled carbon nanotubes induce T lymphocyte apoptosis, *Toxicol. Lett.* 160 (2006) 121.
- [100] A. Krueger, F. Kataoka, M. Ozawa, T. Fujino, Y. Suzuki, A.E. Aleksenskii, et al., Unusually tight aggregation in detonation nanodiamond: identification and disintegration, *Carbon* 43 (2005) 1722.
- [101] H.J. Huang, L.M. Dai, D.H. Wang, L.S. Tan, E. Osawa, Large-scale self-assembly of dispersed nanodiamonds, *J. Mater. Chem.* 18 (2008) 1347.
- [102] A. Pentecost, S. Gour, V. Mochalin, I. Knoke, Y. Gogotsi, Deaggregation of nanodiamond powders using salt- and sugar-assisted milling, *ACS Appl. Mater. Interfaces* 2 (2010) 3289–3294.
- [103] J.C. Carrero-Sanchez, A.L. Elias, R. Mancilla, G. Arrellin, H. Terrones, J.P. Laclette, et al., Biocompatibility and toxicological studies of carbon nanotubes doped with nitrogen, *Nano Lett.* 6 (2006) 1609.
- [104] S.K. Manna, S. Sarkar, J. Barr, K. Wise, E.V. Barrera, O. Jejelowo, et al., Single-walled carbon nanotube induces oxidative stress and activates nuclear transcription factor-kappaB in human keratinocytes, *Nano Lett.* 5 (2005) 1676.
- [105] E. Oberdörster, S. Zhu, T. Blickley, P. McClellan-Green, M. Haasch, Ecotoxicology of carbon-based engineered nanoparticles: effects of fullerene (C60) on aquatic organisms, *Carbon* 44 (2006) 1112.
- [106] S. Vial, C. Mansuy, S. Sagan, T. Irinopoulou, F. Burlina, J.P. Boudou, et al., Peptide-grafted nanodiamonds: preparation, cytotoxicity and uptake, *Chembiochem* 9 (13) (2008) 2113–2119.
- [107] R. Silbajoris, J.M. Huang, W.-Y. Cheng, L. Dailey, T.L. Tal, I. Jaspers, et al., Nanodiamond particles induce IL-8 expression through a transcript stabilization mechanism in human airway epithelial cells, *Nanotoxicology* 3 (2009) 152–160.
- [108] V. Vijayanthimala, Y.-K. Tzeng, H.-C. Chang, C.-L. Li, The biocompatibility of fluorescent nanodiamonds and their mechanism of cellular uptake, *Nanotechnology* 20 (2009) 425103.
- [109] C.C. Fu, H.Y. Lee, K. Chen, T.S. Lim, H.Y. Wu, P.K. Lin, et al., Characterization and application of single fluorescent nanodiamonds as cellular biomarkers, *Proc. Natl. Acad. Sci. U.S.A.* 104 (2007) 727.
- [110] F. Neugart, A. Zappe, F. Jelezko, C. Tietz, J.P. Boudou, A. Krueger, et al., Dynamics of diamond nanoparticles in solution and cells, *Nano Lett.* 7 (2007) 2588.
- [111] A.M. Schrand, Characterization and *in vitro* biocompatibility of engineered nanoparticles, in: *The School of Engineering, University of Dayton, Dayton, OH, 2007.*

- [112] C.-Y. Fang, V. Vijayanthimala, C.-A. Cheng, S.-H. Yeh, C.-F. Chang, C.-L. Li, et al., The exocytosis of fluorescent nanodiamond and its use as a long-term cell tracker, *Small* 7 (23) (2011) 3363–3370.
- [113] K.K. Liu, C.C. Wang, C.L. Cheng, et al., Endocytic carboxylated nanodiamond for the labeling and tracking of cell division and differentiation in cancer and stem cells, *Biomaterials* 30 (2009) 4249–4259.
- [114] A.V. Karpukhin, N.V. Avkhacheva, R.Y. Yakovlev, I.I. Kulakova, V.A. Yashin, G.V. Lisichkin, et al., Effect of detonation nanodiamonds on phagocyte activity, *Cell. Bio. Int.* 35 (7) (2011) 727–733.
- [115] C.W. Lam, J.T. James, R. McCluskey, R.L. Hunter, Pulmonary toxicity of single-wall carbon nanotubes in mice 7 and 90 days after intratracheal instillation, *Toxicol. Sci.* 77 (2004) 126.
- [116] D.B. Warheit, B.R. Laurence, K.L. Reed, D.H. Roach, G.A. Reynolds, T.R. Webb, Comparative pulmonary toxicity assessment of single-wall carbon nanotubes in rats, *Toxicol. Sci.* 77 (2004) 117.
- [117] A.A. Shvedova, E.R. Kisin, R. Mercer, A.R. Murray, V.J. Johnson, A.I. Potapovich, et al., Unusual inflammatory and fibrogenic pulmonary responses to single-walled carbon nanotubes in mice, *Am. J. Physiol. Lung. Cell. Mol. Physiol.* 289 (2005) L698.
- [118] J. Muller, F. Huaux, N. Moreau, P. Misson, J.F. Heilier, M. Delos, et al., Respiratory toxicity of multi-wall carbon nanotubes, *Toxicol. Appl. Pharmacol.* 207 (2005) 221.
- [119] K. Donaldson, R. Aitken, L. Tran, V. Stone, R. Duffin, G. Forrest, et al., Carbon nanotubes: a review of their properties in relation to pulmonary toxicology and workplace safety, *Toxicol. Sci.* 92 (2006) 5.
- [120] T.K. Leeuw, R.M. Reith, R.A. Simonette, M.E. Harden, P. Cherukuri, D.A. Tsyboulski, et al., Single-walled carbon nanotubes in the intact organism: near-IR imaging and biocompatibility studies in *Drosophila*, *Nano Lett.* 7 (2007) 2650.
- [121] T. Tsuchiya, I. Oguri, Y.N. Yamakoshi, N. Miyata, Novel harmful effects of [60]fullerene on mouse embryos *in vitro* and *in vivo*, *FEBS Lett.* 393 (1996) 139.
- [122] T.H. Ueng, J.J. Kang, H.W. Wang, Y.W. Cheng, L.Y. Chiang, Suppression of microsomal cytochrome P450-dependent monooxygenases and mitochondrial oxidative phosphorylation by fullereneol, a polyhydroxylated fullerene C60, *Toxicol. Lett.* 93 (1997) 29.
- [123] C.Y. Usenko, S.L. Harper, R.L. Tanguay, *In vivo* evaluation of carbon fullerene toxicity using embryonic zebrafish, *Carbon* 45 (2007) 1891.
- [124] G.L. Baker, A. Gupta, M.L. Clark, B.R. Valenzuela, L.M. Staska, S.J. Harbo, et al., Inhalation toxicity and lung toxicokinetics of C60 fullerene nanoparticles and microparticles, *Toxicol. Sci.* 101 (2008) 122.
- [125] A.A. Tykhomyrov, V.S. Nedzvetsky, V.K. Klochkov, G.V. Andrievsky, Nanostructures of hydrated C60 fullerene (C60HyFn) protect rat brain against alcohol impact and attenuate behavioral impairments of alcoholized animals, *Toxicology* 246 (2008) 158.
- [126] A. Baun, N.B. Hartmann, K. Grieger, K.O. Kusk, Ecotoxicity of engineered nanoparticles to aquatic invertebrates: a brief review and recommendations for future toxicity testing, *Ecotoxicology* 17 (2008) 387.
- [127] P. Aspenberg, A. Anttila, Y.T. Konttinen, R. Lappalainen, S.B. Goodman, L. Nordsletten, et al., Benign response to particles of diamond and SiC: bone chamber studies of new joint replacement coating materials in rabbits, *Biomaterials* 17 (1996) 807.
- [128] M. Doherty, J.T. Whicher, P.A. Dieppe, Activation of the alternative pathway of complement by monosodium urate monohydrate crystals and other inflammatory particles, *Ann. Rheum. Dis.* 42 (1983) 285.

- [129] A.P. Puzyr, V.S. Bondar, S.E. Al., Dynamics of the selected physiological responses in laboratory mice under the prolonged oral administration of nanodiamonds suspensions, *Siberian Med. Obozrenie (Siberian Med. Rev.)* 4 (2004) 19 (in Russian).
- [130] A.P. Puzyr, V.S. Bondar, Z.Y. Selimhanova, A.G. Tyan, E.V. Bortnikov, E.V. Injevatkin, Results of studies of possible applications of detonation nanodiamonds as enterosorbents, *Siberian Med. Obozrenie (Siberian Med. Rev.)* 2–3 (2004) 25 (in Russian).
- [131] V. Bondar, D. Baron, et al., Changes in bio-chemical parameters of blood plasma at administration of nanodiamond to laboratory animals, *Bull. Siberian Med.* 4 (2005) 182.
- [132] A.P. Puzyr, V.S. Bondar, Z.Y. Selimkhanova, A.G. Tyan, E.V. Inzhevatkin, E.V. Bortnikov, Results of *in vitro* and *in vivo* studies using detonation nanodiamonds/complex systems under extreme conditions, *KSC SB RAS, Krasnoyarsk* 229 (2005).
- [133] A.P. Puzyr, V.S. Bondar, Z.Y. Selimkhanova, A.G. Tyan, E.V. Inzhevatkin, V.S. Bondar, et al., Physiological parameters of laboratory animals at oral administration of nanodiamond hydrosols, *Bull. Siberian Med.* 4 (2005) 185.
- [134] V.Y. Dolmatov, L.N. Kostrova, Detonation-synthesized nanodiamonds and the feasibility of developing a new generation of medicinals, *Superhard Mater.* 3 (2000) 82.
- [135] A.P. Puzyr, E.V. Bortnikov, N.N. Skobelev, A.G. Tyan, Z. Yu, G.G. Selimkhanova, et al., A possibility of using of intravenous administration of sterile colloids of modified nanodiamonds, *Siberian Med. Obozrenie (Siberian Med. Rev.)* 1 (2005) 20.
- [136] X. Zhang, J. Yin, C. Kang, J. Li, Y. Zhu, W. Li, et al., Biodistribution and toxicity of nanodiamonds in mice after intratracheal instillation, *Toxicol. Lett.* 198 (2) (2010) 237–243.
- [137] S. Rojas, J.D. Gispert, R. Martin, et al., Biodistribution of amino-functionalized diamond nanoparticles. *In vivo* studies based on ¹⁸F radionuclide emission, *ACS Nano.* 5 (2011) 5552–5559.
- [138] N. Mohan, C.S. Chen, H.H. Hsieh, Y.C. Wu, H.C. Chang, *In vivo* imaging and toxicity assessments of fluorescent nanodiamonds in *Caenorhabditis elegans*, *Nano Lett.* 10 (2010) 3692–3699.
- [139] H. Maxwell, *The Poisoner's Handbook*, Loompanics Unlimited, Port Townsend, WA, 1988.
- [140] Y. Yuan, X. Wang, G. Jia, et al., Pulmonary toxicity and translocation of nanodiamond in mice, *Diamond Relat. Mater.* 19 (2010) 291–299.
- [141] G. Davies, *Diamond*, Adam Hilger Ltd., Bristol, 1984.
- [142] J.S. Tu, E. Perevedentseva, P.H. Chung, C.L. Cheng, Size-dependent surface CO stretching frequency investigations on nanodiamond particles, *J. Chem. Phys.* 125 (2006) 174713.
- [143] N.A. Monteiro-Riviere, A.O. Inman, B.M. Barlow, R.E. Baynes, Dermatotoxicity of cutting fluid mixtures: *in vitro* and *in vivo* studies, *J. Toxicol. Cutaneous Ocul. Toxicol.* 25 (2006) 235.
- [144] J.M. Worle-Knirsch, K. Pulskamp, H.F. Krug, Oops they did it again! Carbon nanotubes hoax scientists in viability assays, *Nano Lett.* 6 (2006) 1261.
- [145] Y. Zhu, J. Li, W. Li, Y. Zhang, X. Yang, N. Chen, et al., The biocompatibility of nanodiamonds and their application in drug delivery systems, *Theranostics* 2 (3) (2012) 302–3112.
- [146] L. Marcon, F. Riquet, D. Vicogne, S. Szunerits, J.-F. Bodart, R. Boukherroub, Cellular and *in vivo* toxicity of functionalized nanodiamond in *Xenopus* embryos, *J. Mater. Chem.* (2010) 8064–8069.

- [147] V.S. Bondar, I.O. Pozdnyakova, A.P. Puzyr, Applications of nanodiamonds for separation and purification of proteins, *Phys. Solid State* 46 (2004) 758.
- [148] L.C. Huang, H.C. Chang, Adsorption and immobilization of Cytochrome c on nanodiamonds, *Langmuir* 20 (2004) 5879.
- [149] T.S. Huang, Y. Tzeng, Y.K. Liu, Y.K. Chen, K.R. Walker, R. Guntupalli, et al., Immobilization of antibodies and bacterial binding on nanodiamond and carbon nanotubes for biosensor applications, *Diamond. Relat. Mater.* 13 (2004) 1098.
- [150] M. Ricarda-Lorenz, V. Holzapfel, A. Musyanovych, K. Nothelfer, P. Walther, H. Frank, et al., Uptake of functionalized, fluorescent-labeled polymeric particles in different cell lines and stem cells, *Biomaterials* 27 (2006) 2820.
- [151] L. Ding, J. Stilwell, T. Zhang, O. Elboudwarej, H. Jiang, J.P. Selegue, et al., Molecular characterization of the cytotoxic mechanism of multiwall carbon nanotubes and nano-onions on human skin fibroblast, *Nano Lett.* 5 (2005) 2448.
- [152] D. Cui, F. Tian, C.S. Ozkan, M. Wang, H. Gao, Effect of single wall carbon nanotubes on human HEK293 cells, *Toxicol. Lett.* 155 (2005) 73.
- [153] M.J. Cunningham, S.R. Magnuson, M.T. Falduto, Gene expression profiling of nanoscale materials using a systems biology approach, *Toxicol. Sci.* 84 (2005) 9.
- [154] A. Bahman, O.T. Price, Deposition of ultrafine (nano) particles in the human lung, *Inhal. Toxicol.* 19 (13) (2007) 1045–1054.
- [155] A.M. Schrand, K. Szcublewski, J.J. Schlager, L. Dai, S.M. Hussain, Interaction and biocompatibility of multi-walled carbon nanotubes in PC-12 cells, *Int. J. Neuroprotect. Neuroregen.* 3 (2007) 115.
- [156] Y. Yuan, Y. Chen, J.H. Liu, H. Wang, Y. Liu, Biodistribution and fate of nanodiamonds *in vivo*, *Diamond Relat. Mater.* 18 (2009) 95–100.
- [157] B. Asgharian, OT Price, Deposition of ultrafine (nano) particles in the human lung, *Inhal. Toxicol.* 19 (13) (2007) 1045–1054.
- [158] A.A. Shvedova, V. Castranova, E.R. Kisin, D. Schwegler-Berry, A.R. Murray, V.Z. Gandelsman, et al., Exposure to carbon nanotube material: assessment of nanotube cytotoxicity using human keratinocyte cells, *J. Toxicol. Environ. Health A* 66 (2003) 1909.
- [159] S. Garibaldi, C. Brunelli, V. Bavastrello, G. Ghigliotti, C. Nicolini, Carbon nanotube biocompatibility with cardiac muscle cells, *Nanotechnology* 17 (2006) 391.
- [160] P. Wick, P. Manser, L.K. Limbach, U. Dettlaff-Weglikowska, F. Krumeich, S. Roth, et al., The degree and kind of agglomeration affect carbon nanotube cytotoxicity, *Toxicol. Lett.* 168 (2007) 121.
- [161] M.R. Wilson, J.H. Lightbody, K. Donaldson, J. Sales, V. Stone, Interactions between ultrafine particles and transition metals *in vivo* and *in vitro*, *Toxicol. Appl. Pharmacol.* 184 (2002) 172.
- [162] P.S. Gilmour, A. Ziesenis, E.R. Morrison, M.A. Vickers, E.M. Drost, I. Ford, et al., Pulmonary and systemic effects of short-term inhalation exposure to ultrafine carbon black particles, *Toxicol. Appl. Pharmacol.* 195 (2004) 35.
- [163] A.P. Puzyr, D.A. Neshumayev, S.V. Tarskikh, G.V. Makarskaia, V. Dolmatov, V.S. Bondar, Destruction of human blood cells upon interaction with detonation nanodiamonds in experiments *in vitro*, *Biofizika* 50 (2005) 101.
- [164] L. Marcon, Z. Kherrouche, J. Lyskawa, D. Fournier, D. Tulasne, P. Woisel, et al., Preparation and characterization of Zonyl-coated nanodiamonds with antifouling properties, *Chem. Commun. (Camb)* 47 (2011) 5178–5180.
- [165] C. Buzea, I.I. Pacheco Blandino, K. Robbie, Nanomaterials and nanoparticles: sources and toxicity, *Biointerphases* 2 (2007) MR17–MR172.

Index

Note: Page numbers followed by “f” and “t” refer to figures and tables respectively.

A

- Absolute rates of ND graphitization, 203–205
- Absorption contrast, *see* Mass-thickness contrast
- Advanced Diamond Technology (ADT), 384–387, 408–409
- Agglomerated detonation nanodiamond
 - usefulness of, 166–170
- Agglutinated single-nano diamond (SND), 166
- Agglutination, 165–166
- Argon-dominated plasma discharge, 58
- Atomic force microscope (AFM), 317
 - of ND-ODA particles, 439f
 - of ND-PiBMA-1 polymer brush, 439f
- Atomic layer deposition (ALD), 409
- Attrition mill, 173f

B

- “Ball-bearing” effect, 477, 483
- Base oils, major
 - groups of, 459
- Beads-assisted sonication (BASD) methodology, 464
- Beads-milling, 171–175
- Benzene, 155–156
- Berman–Simon line, 4
- Bias-enhanced nucleation and growth process (BEN-BEG), 388–389
- Biomolecule interactions, of NDs, 500–503
- Blinking mechanism, 318, 328
 - and NV center, 346–349
- Boehm titration, 425
- Bovine serum albumin (BSA), 502
- Bright-field TEM imaging
 - and electron diffraction of ND material, 293–294
- Bulk properties of UNCD, 87–97
 - grain boundaries (GBs), structure of, 89–91
 - model generation, 87–89
 - sp²/sp³ composition in, 95–96
 - specific heat and Debye temperature, 92–95
 - thermal stability of, 95–96
 - vibrational spectra, 91–92
- Bulk thermal stability study, 274–277, 279–281

C

- Caenorhabditis elegans*, 499–500, 536
- CAFE (Corporate Average Fuel Economy), 460
- Carbide-derived diamond, 158
- Carbon, phase stability of, 4–5
- Carbon and carbon/explosive mixture
 - NDs production from, 145
- Carbon nanotubes (CNTs), 42, 86, 154, 421–422
 - CNTs-diamond hybrid nanomaterials, 97–98
- Carbon onions, ND-derived, 480–483
- Carnot efficiency, 359, 362
- Cavitation-assisted synthesis of nanodiamonds, 155–156
- Cavity ring down spectroscopy, 59
- Cetyltrimethylammonium bromide (CTAB), 468
- Cetyltrimethylammonium chloride (CTAC), 468
- Chapman–Jouguet (CJ) plane, 146–147
- Chemical vapor deposition (CVD), 171, 248–249
 - dc GD CVD films, 251
 - diamond films, 250–252
 - diamond growth process, 66f
 - HF CVD diamond films, 250
 - MW CVD nanodiamond films, 250
 - technique-based synthesis of nanodiamonds, 156–157
- Chitosan, 448
- Clausius, 359–360
- Closed curved graphitic structures (CCGS), 217–221
- CMOS devices, UNCD integration with, 408
 - RF-MEMS switches with, 408–413
- Cobalt particles, 221, 222
- Coherent interfacial Coulombic interaction (CICI), 167, 169
- Common neighbor analysis (CNA), 89–91
- Computational methodologies, 86–87
 - classical MD simulations, 86
 - DFTB calculations, 86–87
 - of diamond nanoparticles, 9–13
- Confocal microscopy, of N2A cells, 533f
- Core agglutinate, 167
 - deagglomeration of, 169
- Core-loss EELS
 - ND carbon K-edge ELNES, 299–300
- Core-loss STEM-EELS analysis, 302f
- Crankcase oils, 460

D

- Deagglomeration of detonation nanodiamond, 165
 - agglutinates, usefulness of, 166–170
 - beads-milling, 172–175
 - methods of, 170–172
 - primary particles, 175–176
- Debye temperature of UNCD models, 92–95, 94f
- Deliberate dopants, 30–32
- Density functional based tight binding (DFTB), 367
- Density functional theory (DFT) methods, 14
- Detonation nanodiamond (DND), 135–142, 458
 - agglomerated
 - usefulness of, 166–170
 - deagglomeration of, 165
 - beads-milling, 172–175
 - methods of, 170–172
 - primary particles, 175–176
 - zeta potential, 465–466
- Detonation nanodiamonds' characterization, 292
 - ESR spectroscopy, 313–314
 - NEXAFS spectroscopy, 305–307
 - photoluminescence spectroscopy, 315–321
 - confocal PL spectroscopy of single DND particles, 316–320
 - PL spectroscopy of HPHT-sintered DND, 320–321
 - time-resolved PL, 316
- TEM and electron energy-loss spectroscopy, 292–305
 - aberration-corrected high-resolution
 - imaging at low acceleration voltage, 294–296
 - bright-field TEM imaging and electron diffraction of ND material, 293–294
 - core-loss EELS, ND carbon K-edge ELNES, 299–300
 - local dopant detection and coordination determination, 300–305
 - low-loss EELS, 298–299
 - scanning TEM, 296–297
- XRD and small-angle X-ray scattering, 308–313
 - microstructure of NDs from X-ray data, 311–313
 - SAXS, 309–311
 - X-ray diffraction, 308–309
- Detonation nanodiamonds' characterization for
 - biocompatibility, 519
 - biological assessment of, 538–540
 - environmental safety, 520–522
 - influencing factors, 526
 - in vivo* considerations for ND biocompatibility, 534–538
 - patient safety, 520–522
 - physicochemical properties of, 523–524t
 - studies of, 526–534
 - carbon nanoparticles, biological peculiarities of, 526–528
 - diamond particle biocompatibility studies, 529
 - ND intracellular localization and kinetics, 531–534
 - ND property-biocompatibility relationship, 529
 - ND size studies, 530
 - ND surface chemistry and contaminants, 530–531
 - studying methods for, at cellular and organism levels, 522–525
 - worker safety, 520–522
- Detonation products (DPs), 135–137
- DFTB theory, application of, 116–117
- Diamondoids, 141, 142–143
- Diamond polycrystalline films, 249
- Differential scanning calorimetry (DSC), 196
- Differential thermal analysis (DTA), 190
- Diffraction contrast, 293
- Diffuse reflectance Fourier transform infrared spectroscopy (DRIFTS), 190
- Dimethyl sulfoxide, 497–498
- Dopants, 25–37
- Doxorubicin (Dox), 509–510
- Drug delivery, 509–512
- Dynamically synthesized NDs, 149–152
- Dynamic light scattering (DLS) analysis, 464

E

- Elastic recoil detection (ERD), 393
- Elastic recoil detection analysis (ERDA), 249
- Elastomer–ND composites, of polymer–ND composites, 445
- Elastomers, 445
- Electromagnetic compatibility (EMC), 448
- Electromagnetic interference (EMI), 448
- Electromagnetic shielding, of polymer–ND composites, 448
- Electron energy loss spectroscopy (EELS), 108–109, 111–112, 292, 297–305
 - core-loss EELS
 - local dopant detection and coordination determination, 300–305
 - ND carbon K-edge ELNES, 299–300
 - formation of sp^2 -bonded carbon on NDs, 193
 - low-loss EELS, 298–299

- in transmission electron microscopy (TEM), 113–114
- zero-loss region, 298
- Electron–E-vibration interaction, 336
- Electron paramagnetic resonance (EPR), 134, 330–331
- Electron spin echo (ESE) technique, 313–314
- Electron spin resonance (ESR), 292
- Electrospun PA 11 nanofibers
 - optical images of, 447f
- Electrostatically actuated UNCD-based MEMS resonators, 403–404
- Electrostatic stabilization, 469
 - of ND colloids in oils, 466–468
- Emission quenching by graphite sp^2 layer, 344
- Energy conversion, nanocarbons in, 357
 - entropy-of-mixing of charge carriers with quantum states, 359–361
 - nanosilicon carbide core/graphene shell nanoensembles, 370–376
 - thermoelectric properties of core/shell UNCD/graphene, 362–370
- Energy-loss near-edge structure (ELNES), 299
- Energy systems, components of, 357–358
- Entropy-of-mixing of charge carriers with quantum states, 359–361
- Environmental Protection Agency (EPA), 520
- Epidermal growth factor receptor (EGFR), 512–513
- ESR spectroscopy, 313–314
- External stimuli, stability in response to, 17–22
 - annealing and thermal activation, 17–19
 - pressure- and irradiation-induced transformations, 19–20
 - under anionic and cationic charge, 20–22

F

- Fluorescent NDs (fNDs), 507–508
- Fluorescent probes, 508–509
- Food and Drug Administration (FDA), 520
- Förster resonance energy transfer, 329
- Fourier transform infrared (FTIR) spectroscopy, 189–190
- Fourier-transformed infrared (FTIR) absorption, 249
- Full width at half maximum (FWHM), 373
- Functional defects, 25–37

G

- Gene therapy, 505–508
 - for cancer treatment, 505–508
- Grain-boundary (GB) regions, 86, 87–88

- structure of, 89–91
- Graphene, 421–422
- Graphene shell nanoensembles
 - synthesis and properties of, 370–376
- Graphite, 135–137
- Graphitic layers, 166–167
- Graphitization, 275–276, 278–279, 280
- Graphitization of diamond, 221–225
 - catalytic graphitization, 221–225
 - onset temperature of, 196–198
 - experimental approaches, 198–200
 - estimation of diamond fraction in intermediates, 198–199
 - kinetic model, 199–200
 - kinetic parameters for 1370–1860 K
 - temperature range
 - absolute rates, 203–205
 - Arrhenius plot, 201f
 - migration rates, 204t
 - temperature regions, 200–205
 - mechanism of
 - cleavage energies of diamond planes, 206–207
 - diamond surface reconstruction, 205–206
 - formation of closed curved graphitic structure on diamond surface, 217–221
 - graphite/diamond interfaces, 209–217
 - nanocarbon species formation via, 211–217
 - shape of diamond particles, 207–209
 - OLC and sp^3/sp^2 nanocomposites, 226–231
 - in presence of oxygen and hydrogen-containing gases, 225–226
- Green fluorescent protein plasmid (pEGF-PLuc), 506
- Growth of UNCD, 55–63
 - high renucleation rate, 62–63
 - plasma discharge region, 56–59
 - species arriving at growth surface, 60–61

H

- HAADF-STEM imaging, 296–297
- Hall-effect measurements, 116
- HeLa cells, 506
- HF CVD diamond films, 250, 253
- High-energy electron irradiation, synthesis of nanodiamonds with, 157–158
- High-energy explosives
 - NDs production from, 145–149
- High-energy XRD (HEXRD), 308
- High-pressure high-temperature (HPHT) diamonds, 309, 341

High-resolution electron energy-loss spectroscopy (HR-EELS), 261–274
 hydrogen and carbon bonding configuration of nanoscale-defined hydrogenated polycrystalline diamond surface, 261–264
 impact of diamond grain size on the shape of, 265–274
 High-resolution transmission electron microscopy (HRTEM), 108–109, 292, 363
 Historical development of UNCD films, 53–55
 HITACHI S-4700, 362
 HOMO-LUMO gap, 369f
 Hot filament CVD (HFCVD), 385–386
 Hot-filament CVD (HFCVD) UNCD synthesis, 75–78
 first report and principle of, 75–76
 HFCVD (U)NCD synthesis, 77–78
 nanocrystalline versus UNCD, 77
 scaling and current reactor technology, 76–77
 HPHT diamond
 synthesis of nanodiamonds from, 152–154
 Hydrogen
 bonding and concentration of, 247
 in diamond, 248–249
 graphitization of NDs, 225–226
 Hydrogen-associated Raman peaks
 clarification of, through isotopic exchange induced modifications, 255–258
 Hydrogenated diamond surface, 248
 Hydrogenated nanodiamond, 171
 Hydrogen atom concentrations
 in polycrystalline diamond films, 250–252
 Hydrogen-based plasma discharge, 56, 58
 Hydrogen bonding configuration, in diamond film, 254–261
 by HR-EELS, 261–274
 by Raman spectroscopy, 254–261
 Hydrogen concentration, 249–250
 versus crystalline size, 254t
 impact of, on shape of Raman spectra, 258–260
 secondary ion mass spectroscopy (SIMS), 252–254

I

Impurities, 25–37
 incidental, 28–30
 Incoherent interfacial Coulombic interactions (IICIs), 167
 Industrial oil group, 458–459
 Industrial oils
 formulations of, 458–463

Infrared (IR) spectroscopy
 main bands for surface groups on NDs, 188
 Insulator–metal transition, mechanism underlying, 116
 Interfacial Coulombic bonds (ICBs), 167
 Interfacial Coulombic interaction, 167
 International Lubricant Standardization and Approval Committee (ILSAC), 460
 Interphase, 422
 Intrinsic defects, 25–28
 Iron particles, 221, 222

K

Kekule graphene structure, 367
 Kelvin, Lord, 359–360
 Kevlar–ND composite, 435
 Krytox 143B, carbon onions in, 482

L

Large-area UNCD synthesis, 63–75
 experimental description and methodologies, 64–68
 experimental procedures and results, 70–75
 reactor operating road maps, 68–70
 Laser ablation process
 synthesis of nanodiamonds by, 154–155
 Lax graphite sp^2 layer, 344
 Layer-by-layer (LBL) technique, 502–503
 Light adsorbing nanofillers, 447
 Low-loss EELS, 298–299
 Low-nitrogen concentration diamonds, 337–339
 Lubricants, nanoparticles as additives, 457
 Luciferase plasmid (pLuc), 506
 Luminescence intermittency, 328
 Luminescent NDs, surface hydrogenation effect on, 346f

M

Magnetic nanotip, 329
 Mass-thickness contrast, 293
 MEMS and NEMS devices based on UNCD films, 399–415
 biosensors, 413–415
 bulk and surface properties, 389–393
 CMOS devices, integration with, 408
 electrostatically actuated UNCD-based MEMS resonators, 403–404
 fabrication of monolithic UNCD cantilever/
 AFM tips and applications, 407

films and integration into MEMS/NEMS structures, 415
 materials integration and process strategies for fabrication, 399–403
 materials integration for hybrid piezoelectric, 402–403
 photolithography plus RIE processes for surface micromachining fabrication, 401
 piezoelectrically actuated UNCD-based MEMS resonators and NEMS switches, 404–407
 RF-MEMS switches with UNCD dielectric layer integrated with CMOS driving devices, 408–413
 selective seeding and growth process for fabrications, 400–401
 stress and ohmic contact of, 401–402
 Merged diode, 125–126
 Methyl ethyl ketone (MEK), 468
 Microcrystalline diamond (MCD), 55
 Microcrystalline diamond films synthesis, 385–388
 Microelectromechanical/nanoelectromechanical systems (MEMS/NEMS), 384
 Micron-sized diamond crystals, 156
 Micron-sized single particles
 with nanocrystalline structure, 134
 Micro-Raman spectrum, of UNCG, 375f
 Microwave cavity plasma reactors (MCPRs), 64–65, 64f
 Microwave chemical vapor deposition nanodiamond films, 250, 253
 Microwave plasma-assisted chemical vapor deposition (MPACVD), scaling up, 63–75
 background, 63
 experimental description and methodologies, 64–68
 experimental procedures and results, 70–75
 reactor operating road maps, 68–70
 Microwave plasma enhanced chemical vapor deposition (MPCVD), 385–386
 Microwave plasma enhanced chemical vapor deposition (MWPECVD), 105, 109–111
 Modified neglect of diatomic overlap (MNDO) method, 9
 Molecular-dynamics (MD) studies, 86
 Molecular mechanics (MM) simulations, 217–219
 Monocrystalline nanoparticles, 141
 Mooney–Rivlin equation, 430
 Motor oil, 458–459
 commercially available, 460
 Multiwalled carbon nanotubes, 154
 Mypolex, 134, 135

N

Nanocarbon particles, 175–176
 coexistence of, 16–17
 theoretical modeling of, 13–15
 Nanocarbon phase diagrams, 5–7
 Nanocarbons, 17
 in energy conversion, 357
 ensembles, 362–370
 entropy-of-mixing of charge carriers with quantum states, 359–361
 nanosilicon carbide core/graphene shell nanoensembles, 370–376
 thermoelectric properties of core/shell UNCD/graphene, 362–370
 stability of, 184–186
 Nanocrystalline diamond (NCD), 53–54, 77, 145, 255, 274, 385–388, 503–505
 thin films, 500
 Nanodiamond(s)
 agglomeration, 495–496
 bulk thermal stability study, 274–277, 279–281
 carbon K-edge ELNES, 299–300
 characterization for biocompatibility
 biological assessment of, 538–540
 carbon nanoparticles, biological peculiarities of, 526–528
 diamond particle biocompatibility studies, 529
 environmental safety, 520–522
 influencing factors, 526
 intracellular localization and kinetics, 531–534
 in vivo considerations for ND
 biocompatibility, 534–538
 patient safety, 520–522
 physicochemical properties of, 523–524t
 property-biocompatibility relationship, 529
 size studies, 530
 studying methods for, at cellular and organism levels, 522–525
 surface chemistry and contaminants, 530–531
 worker safety, 520–522
 colloids in oils
 by covalent surface modification of ND, 470–472
 by metal complex, 470
 electrostatic stabilization, 466–468
 electrosteric stabilization, 469
 formation of, 466–473
 preparation of, 472–473
 stabilization of, 466–472

- Nanodiamond(s) (*Continued*)
 - steric stabilization, 468–469
 - deaggregation and surface functionalization, 495–499
 - ND–PEI treatment, 506
 - particles, action mechanism of, 483–485
 - powder, 427–428
 - surface thermal stability study, 278–281
 - synthesis and processing techniques, 493–499
 - synthesis and purification, 494–495
 - therapeutics, 499–512
 - biomolecule interactions, 500–503
 - drug delivery, 509–512
 - fluorescent probes, 508–509
 - gene therapy, 505–508
 - nanocrystalline diamond, 503–505
- Nanodiamond films
 - deposition of, 248
 - Raman spectra of, 276, 277f
- Nanodiamond particles, synthesis of
 - by laser ablation, 154–155
 - carbide-derived diamond, 158
 - from carbon and carbon/explosive mixture, 145
 - cavitation-assisted synthesis, 155–156
 - CVD-technique-based synthesis, 156–157
 - detonation nanodiamonds (DNDs) discovery,
 - history of, 135–141
 - dynamically synthesized NDs, 149–152
 - future outlook, 159
 - with high-energy electron irradiation, 157–158
 - from high-energy explosives, 145–149
 - from HPHT diamond, 152–154
 - methods of, 141–159
 - recent methods of, 158–159
 - types of NDs, 141–159, 143f
- Nanographite (NG) shells, 362
- Nanolubricants, state of art, 458
- Nanoparticles
 - as additives to lubricants, 457
 - detonation soot, 473–477
 - nanodiamond, 477–479
 - ND colloids in oils, 466–473
 - ND-derived carbon onions, 480–483
 - ND particles, of action mechanism, 483–485
 - ND-related additives in oil and greases, 473–485
 - preparation of, 472–473
 - stabilization of, 466–472
 - synergistic lubricating effect, of ND, 479–480
 - definition of, 175–176
 - state of art, 458
 - industrial oil formulations of, 458–463
 - nanodiamond particles, 463–466
- Nanoropes, 7
- Nanoscale-defined hydrogenated polycrystalline diamond surface
 - carbon bonding configuration of, 261–264
- Nanosilicon carbide core
 - synthesis and properties of, 370–376
- Nanowires (NWs), 109
- National Institute for Occupational Safety and Health (NIOSH), 520
- Near-edge X-ray absorption fine structure (NEXAFS) spectroscopy, 111–112, 274, 305–307, 387–388
- total electron yield (TEY), 274
 - of ultrananocrystalline diamond (UNCD), 307
- Nitrogen, 107–108
- Nitrogen-incorporated UNCD (NUNCD), 387–388
- Nitrogen-vacancy (NV) center, 327–328
 - diamond matrix size and surface effects on
 - emission properties, 344–349
 - blinking, 346–349
 - emission quenching by lax graphite sp^2 layer, 344
 - surface functional groups, effects of, 345–346
 - electronic structure and emission properties of, 330–336, 332f
 - electronic model, 334–335
 - electron paramagnetic resonance (EPR)
 - signal, 330–331
 - nonselective excitation and detection, 333
 - parameter justification, 335–336
 - spin polarization, 333, 334
 - interconversion between negative and neutral charge states, 336–340
 - in nanoscale diamond, 134
 - photoconversion processes, 338f
 - tunneling probability of the photoexcited electron, 347f
 - ultra-small NV–NDs, production and understanding of, 341–344
 - theoretical modeling, 342–344
- Non-Kekule graphene structure, 367
- n*-type nanocrystalline diamond (NCD) films, 103
 - applications, 125–126
 - chemical inertness and wetting of, 125
 - electronic properties, 115–119
 - electron field emission, 117–119
 - thermal conductivity, 119
 - transport properties, 115–117
 - mechanical properties, 124–125
 - n*-type (nitrogen) carbon materials, 104–106
 - optical properties, 119–120

physical and chemical properties of, 114–125
 structural and compositional analysis of,
 108–114
 synthesis of, 106–108
 and growth mechanism, 106–108
 vibrational properties, 121–124
 Number density effect, 169–170
 NV–ND luminescence analysis, 345t

O

Occupational Safety and Health Administration
 (OSHA), 520
 Octadecylamine (ODA), 468
 Oils, 458–463
 Oleylamine (OLA), 468
 Onion-like carbon (OLC), 6–7, 446
 graphitization of NDs, 226–231
 model of ND annealing and OLC formation
 with holes, 212–217
 TEM images, 184f
 Operating field map, 68–69, 69f, 70
 Optical centers and functional defects, 32–37
 Optical emission spectroscopy (OES), 70, 106
 Optical properties, of polymer–ND composites,
 447–448
 Original Equipment Manufacturers (OEMs), 459
 OVITO, 89–91
 Oxygen
 graphitization of NDs, 225–226

P

Parylene, 500
 PDMS–OLC composites, 448
 PEI800 complexes, 506
 Perfluorinated polyether (PFPE), 482
 Phase stability of carbon, 4–5
 Phase transitions of diamond at nanoscale, 182–183
 catalytic graphitization by metal clusters,
 221–225
 graphitization in presence of oxygen and
 hydrogen, 225–226
 kinetics of diamond graphitization, 198–205
 experimental approaches for study, 198–200
 kinetic parameters for 1370–1860 K
 temperature range, 200–205
 mechanism of diamond graphitization
 cleavage energies of diamond planes,
 206–207
 diamond surface reconstruction, 205–206
 formation of closed curved graphitic
 structure on diamond surface, 217–221

graphite–diamond interfaces, 209–211
 nanocarbon species formation via, 211–217
 shape of diamond particles, 207–209
 OLC and sp^3/sp^2 nanocomposites, 226–231
 stability of nanocarbons, 184–186
 stability of surface species, 186–198
 onset temperature of ND graphitization,
 196–198
 sp^2 -bonded carbon in pristine NDs,
 193–196
 surface groups of NDs, 186–198
 thermal stability of ND surface groups,
 189–193
 TEM images, 184f, 185f
 Phosphorus, 105–106
 Photobleaching, 328
 Photoconversion, 338f, 339
 Photoluminescence spectroscopy, 292, 315–321
 confocal PL spectroscopy of single DND
 particles, 316–320
 PL spectroscopy of HPHT-sintered DND,
 320–321
 time-resolved PL of DND, 316
 Piezoelectrically actuated UNCD-based MEMS
 resonators and NEMS switches, 404–407
 Plasma discharge region, 56–59
 Plasma synthesis of UNCD films, 68–70
 growth of UNCD, 55–63
 high renucleation rate, 62–63
 plasma discharge region, 56–59
 species arriving at growth surface, 60–61
 hot-filament CVD UNCD synthesis, 75–78
 first report and principle of, 75–76
 HFCVD (U)NCD synthesis, 77–78
 nanocrystalline versus UNCD, 77
 scaling and current reactor technology,
 76–77
 MPACVD process, scaling up, 63–75
 background, 63
 experimental description and methodologies,
 64–68
 experimental procedures and results, 70–75
 reactor operating road maps, 68–70
 step-flow growth mechanism, 62
 Poly(allylamine hydrochloride) (PAH), 507–508
 Polycrystalline diamond, 134
 Polycrystalline diamond films, 250–252
 hydrogen atom concentrations in, 252–254
 Polycrystalline ND powder, 141
 Polydimethylsiloxane (PDMS), 430
 Polyethylene, 430
 Polyethylenimine (PEI), 500
 Poly-lactic acid (PLA), 435

Polymer nanocomposites (PNCs), 426–429
 Polymer–ND composites
 applications for, 448–449
 elastomer–ND composites, 445
 electromagnetic shielding of, 448
 mechanical properties of, 429–446
 optical properties of, 447–448
 thermal conductivity of, 446–447
 thermal properties of, 446–447
 thermal stability of, 446
 thermoplastic–ND composites, 430–441
 for biomedical applications, 434–440
 synergetic effects of ND, 440–441
 thermoset–ND composites, 441–445
 Poly-(methyl methacrylate) (PMMA), 435
 Polytetrafluoroethylene (PTFE), 432
 Polyvinyl alcohol (PVA), 434
 Poly-L-(lactic acid) (PLLA), 437
 Poly-L-lysine-coated fluorescent NDs, 534
 Primary particles, 175–176
 Pyrone-like structure, 465

Q

Quantum dot blinking, 346–348

R

Raman spectra of nanocarbon ensembles, 363f
 Raman spectra of nanodiamond diamond films,
 276–277, 277f
 Raman spectroscopy, 254–261
 of different diamond samples, 259f
 formation of sp^2 -bonded carbon on NDs, 193
 hydrogen-associated Raman peaks
 clarification of, through isotopic exchange
 induced modifications, 255–258
 impact of diamond grain size and hydrogen
 concentration on, 258–260
 Reactor operating road maps, 68–70
 Reducing sphere model, 199–200
 Renishaw micro-Raman RM2000, 362
 Renucleation in UNCD discharge, 62–63
 RF-MEMS switches, 409–410
 Ring-on-ring technique, 481f

S

Scanning electron microscopy (SEM), 68, 108–109,
 362, 398
 Scanning TEM (STEM), 292, 296–297
 Secondary ion mass spectrometry (SIMS), 112,
 252–254

Second-generation reactive empirical bond-order
 (REBO-II) potential, 86
 Seebeck coefficient, 360, 363
 Single-digit ND particles, 134, 141, 329
 Single-nano diamond (SND), 166
 Single-spinsensitive magnetometry, 329
 Single-walled carbon nanotubes, 7, 97, 104–105
 Small-angle X-ray scattering (SAXS), 308
 formation of sp^2 -bonded carbon on NDs, 193
 Sodium dodecyl sulfatepolyacrylamide gel
 electrophoresis (SDS-PAGE), 528
 Spatial-resolved EELS (SR-EELS) measurements,
 113–114
 Specific heat of UNCD models, 92–95
 Spin and orbit in color centers, 330
 Spin-lattice relaxation time, 333–334
 Spin-orbit interaction, 335
 Stability of diamond at nanoscale
 carbon, phase stability of, 4–5
 computational modeling, of diamond
 nanoparticles, 9–13
 deliberate dopants, 30–32
 external stimuli, stability in response to, 17–22
 annealing and thermal activation, 17–19
 pressure- and irradiation-induced
 transformations, 19–20
 under anionic and cationic charge, 20–22
 incidental impurities, 28–30
 intrinsic defects, 25–28
 morphology, 8–17
 nanocarbon particles
 coexistence of, 16–17
 theoretical modeling of, 13–15
 nanocarbon phase diagrams, 5–7
 optical centers and functional defects, 32–37
 quasi-1D nanocarbon, stability of, 37–42
 diamond nanorods and nanowires,
 morphology of, 38–41
 hybrid 1D structures, 41–42
 stability, 8–17
 structure, 8–17
 surface passivation and functionalization, 22–25
 in nitrogen-rich environments, 24–25
 in oxygen-rich environments, 23–24
 Step-flow growth mechanism, 62
 Steric stabilization, 468–469
 of ND colloids in oils, 468–469
 Stribeck curve, 460–461
 Substitutional nitrogen, 105
 Surface functional groups, in NV emission,
 345–346
 Surface passivation and functionalization, 22–25

- in nitrogen-rich environments, 24–25
- in oxygen-rich environments, 23–24
- Surface sensitive techniques, 248
- Surface terminating groups, 280
- Surface thermal stability study, 278–281
- Synthesis and properties of UNCD films, 383
 - bulk and surface properties of, 389–393
 - dielectric properties of, 393–396
 - electrical properties of, 393
 - films and integration into MEMS/NEMS structures, 415
 - integration with CMOS devices, 408
 - MEMS and NEMS devices, 389–403
 - electrostatically actuated UNCD-based MEMS resonators, 403–404
 - fabrication of monolithic UNCD cantilever/AFM tips and applications, 407
 - materials integration and process strategies for fabrication of, 399–403
 - materials integration for hybrid piezoelectric, 402–403
 - MEMS/NEMS biosensors, 413–415
 - photolithography plus RIE processes for surface micromachining fabrication of, 401
 - piezoelectrically actuated UNCD-based MEMS resonators and NEMS switches, 404–407
 - selective seeding and growth process for fabrications, 400–401
 - stress and ohmic contact of electrode layers on, 401–402
 - microcrystalline diamond thin films, 385–388
 - nanocrystalline diamond thin films, 385–388
 - new advances on, 388–389
 - bias-enhanced nucleation/bias-enhanced growth, 388–389
 - properties of, 398–399
 - as biomaterial for MEMS/NEMS devices implantable in human body, 398–399
 - RF-MEMS switches
 - with UNCD dielectric layer monolithically integrated with CMOS driving devices, 408–413
 - thermal properties of, 396–398
 - ultrananocrystalline diamond thin films, 385–388
- Synthesis of nanodiamond (ND) particles, *see* Nanodiamond particles, synthesis of

T

- Temperature-programmed desorption (TPD), 189–190

- Tetrahydrofuran (THF), 468
- Theoretical studies of UNCD properties, 85
 - bulk properties of, 87–97
 - grain-boundary (GB) regions, structure of, 89–91
 - model generation, 87–89
 - sp²/sp³ composition in, 95–96
 - specific heat and Debye temperature, 92–95
 - thermal stability of, 95–96
 - vibrational spectra, 91–92
 - carbon nanotubes (CNT)-diamond hybrid nanomaterials, 97–98
 - computational methodologies, 86–87
 - classical MD simulations, 86
 - DFTB calculations, 86–87
- Thermal conductivity, of polymer–ND composites, 446–447
- Thermal properties, of polymer–ND composites, 446–447
- Thermal stability, of polymer–ND composites, 446
- Thermionic emission mechanism, 117
- Thermoelectric properties of core/shell UNCD/graphene, 362–370
 - ensembles, 362–370
- Thermogravimetric analysis (TGA), 190
- Thermoplastic–ND composites, of polymer–ND composites, 430–441
 - for biomedical applications, 434–440
 - synergetic effects of ND, 440–441
- Thermoset–ND composites, of polymer–ND composites, 441–445
- Tight-binding approach, 86–88
- T-PA-like bonds, thermal decomposition of, 281
- Transient-state technique, 446
- Transmission electron microscopy (TEM), 68, 108–109, 111–114, 166–167, 249, 292, 387–388, 531–532
 - and electron energy-loss spectroscopy, 292–305
 - aberration-corrected high-resolution imaging at low acceleration voltage, 294–296
 - bright-field TEM imaging and electron diffraction of ND material, 293–294
 - core-loss EELS, ND carbon K-edge ELNES, 299–300
 - local dopant detection and coordination determination, 300–305
 - low-loss EELS, 298–299
 - scanning TEM, 296–297
 - formation of sp²-bonded carbon on NDs, 193

Transmission electron microscopy (TEM)
 (Continued)
 images, of graphene sputtered structures, 372f
 ND-ODA composites, 438f
 PLLA-ND-ODA composites, 438f
 of PMMA-ND nanocomposite, 436f
 Transmission oils, 458–459
 Trans-polyacetylene (TPA) segments, 121
 Trinitrotoluene (TNT), 494
 Triple-negative breast cancers (TNBC), 512–513

U

Ultra Apex Mill, 172
 Ultradispersed diamond (UDD), *see* Detonation
 nanodiamond (DND)
 Ultradispersed NDs, 329
 Ultrananocrystalline diamond (UNCD) films, 103–
 106, 260, 274–282, 497–498, *see also* *n*-type
 nanocrystalline diamond (NCD) films
 bulk thermal stability study, 274–277
 bulk versus surface thermal stability, 279–281
 nitrogen-doping level in, 112
 surface thermal stability study, 278–279
 Ultrananocrystalline diamond thin films, 385–388
 Ultrananocrystalline graphene (UNCG), 370–371, 376
 Ultra-small NV-NDs, 341–344
 oxidative etching in air/oxygen, 342
 structural and electronic disorder, theoretical
 characterization of, 343f

surface-cleaning procedure, 342
 theoretical modeling, 342–344
 top-down approach, 341–342

V

Vibrational spectroscopy, AK

W

White light absorption spectroscopy, 59

X

Xenopus laevis, 535
 X-ray diffraction (XRD), 292
 formation of sp^2 -bonded carbon on NDs, 193
 X-ray photoelectron spectroscopy (XPS), 108–109,
 111–112
 XRD and small-angle X-ray scattering, 308–313
 microstructure of NDs from X-ray data,
 311–313
 SAXS, 309–311
 X-ray diffraction, 308–309
 Young's modulus
 of polycarbonate (PC), 436f
 of poly-(methyl methacrylate) (PMMA), 436f
 Zinc dialkyldithiophosphates (ZDDP), 460
 Zirconia beads, 172–175